$$\rho \frac{D\underline{\mathbf{u}}}{Dt} = -\nabla p + \left[\nabla \cdot \underline{\underline{\tau}}\right] + \rho \underline{\mathbf{g}} \tag{5.4}$$

The full form of Eq. 5.4 is presented in Table VI of the appendix.

5.1.2 The Generalized Newtonian Fluid

The viscosity of most polymer melts is *shear thinning* and temperature dependent. The shear thinning effect is defined as the reduction in viscosity at high rates of deformation. This phenomenon occurs because at high rates of deformation the molecules are stretched out, enabling them to slide past each other with more ease, hence, lowering the bulk viscosity of the melt. Figure 5.3 clearly shows the shear thinning behavior and temperature dependence of the viscosity for a selected number of thermoplastics. The figure also illustrates ranges of rate of deformation that are typical for various processing techniques. To take into consideration *non-Newtonian effects*, it is common to use a viscosity model that is a function of the strain rate and temperature to calculate the stress tensor[2] in Eq. 5.4:

$$\underline{\underline{\tau}} = \eta\left(\dot{\gamma}, T\right)\dot{\gamma} \tag{5.5}$$

where η is the viscosity and $\underline{\underline{\dot{\gamma}}}$ the *strain rate* or *rate of deformation tensor* defined by

$$\underline{\underline{\dot{\gamma}}} = \nabla \underline{\mathbf{u}} + \nabla \underline{\mathbf{u}}^{t} \tag{5.6}$$

where $\nabla \underline{\mathbf{u}}$ represents the velocity gradient tensor. This model describes the *Generalized Newtonian Fluid*. In Eq. 5.5, $\dot{\gamma}$ is the magnitude of the strain rate tensor and can be written as

$$\dot{\gamma} = \sqrt{\frac{1}{2} II} \tag{5.7}$$

where II is the second invariant of the strain rate tensor defined by

$$II = \sum_i \sum_j \dot{\gamma}_{ij}\, \dot{\gamma}_{ji} \tag{5.8}$$

The strain rate tensor components in Eq. 5.8 are defined by

$$\dot{\gamma}_{ij} = \frac{\partial u_i}{\partial x_j} + \frac{\partial u_j}{\partial x_i} \tag{5.9}$$

The temperature dependence of the polymer's viscosity is normally factored out as

$$\eta\left(T, \dot{\gamma}\right) = f\left(T\right)\eta\left(\dot{\gamma}\right) \tag{5.10}$$

2 As will be shown later, this is only true when the elastic effects are negligible during deformation of the polymeric material.

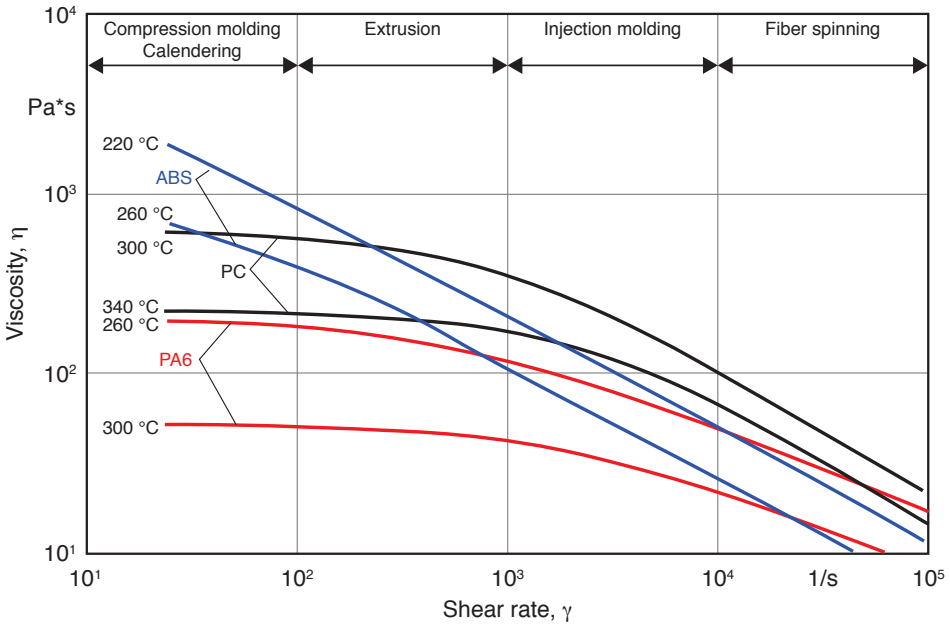

Figure 5.3 Viscosity curves for a selected number of thermoplastics

where for small variations in temperature, $f(T)$ can be approximated using an exponential function such as

$$f(T) = \exp\left(-a\left(T - T_0\right)\right) \tag{5.11}$$

However, a variation in temperature corresponds to a shift in the time scale. A shift commonly used for semi-crystalline polymers is the Arrhenius shift, which is written as

$$a_T(T) = \frac{\eta_0(T)}{\eta_0(T_0)} = \exp\left(\frac{E_0}{R}\left(\frac{1}{T} - \frac{1}{T_0}\right)\right) \tag{5.12}$$

where E_0 is the activation energy, T_0 a reference temperature, and R the gas constant. Using this shift, the viscosity curves measured at different temperatures can be translated to generate a master curve at a specific temperature. Figure 5.4 [9] presents the viscosity of a low density polyethylene with measured values shifted to a reference temperature of 150 °C. For the shift in Fig. 5.4, an activation energy E_0= 54 kJ/mol was used.

Several models that are used to represent the strain rate dependence of polymer melts are presented later in this chapter.

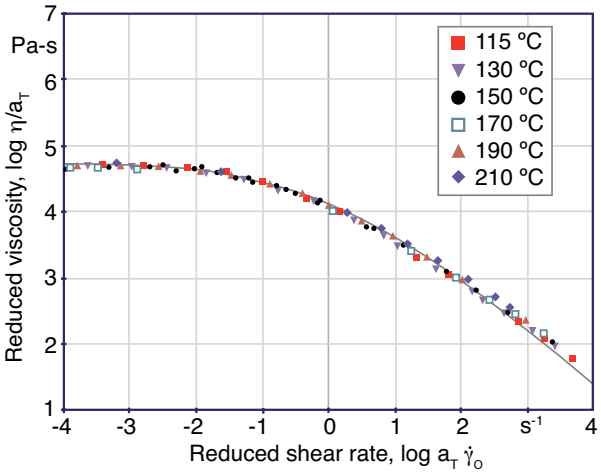

Figure 5.4 Reduced viscosity curve for a low density polyethylene at a reference temperature of 150 °C

5.1.3 Normal Stresses in Shear Flow

The tendency of polymer molecules to "curl-up" while they are being stretched in shear flow results in normal stresses in the fluid. For example, shear flows exhibit a deviatoric stress defined by

$$\tau_{xy} = \eta(\dot{\gamma})\dot{\gamma}_{xy} \tag{5.13}$$

Measurable normal stress differences, $N_1 = \tau_{xx} - \tau_{yy}$ and $N_2 = \tau_{yy} - \tau_{zz}$ are referred to as the *first* and *second normal stress differences*. The first and second normal stress differences are material dependent and are defined by

$$N_1 = \tau_{xx} - \tau_{yy} = -\psi_1(\dot{\gamma}, T)\dot{\gamma}_{xy}^2 \tag{5.14}$$

$$N_2 = \tau_{yy} - \tau_{zz} = -\psi_2(\dot{\gamma}, T)\dot{\gamma}_{xy}^2 \tag{5.15}$$

The material functions ψ_1 and ψ_2 are called the primary and secondary normal stress coefficients, and are also functions of the magnitude of the strain rate tensor and temperature. The first and second normal stress differences do not change in sign when the direction of the strain rate changes. This is reflected in Eqs. 5.14 and 5.15. Figure 5.5 [9] presents the first normal stress difference coefficient for the low density polyethylene melt shown in Fig. 5.4 at a reference temperature of 150 °C. The second normal stress difference is difficult to measure and is often approximated by

$$\psi_2(\dot{\gamma}) \approx -0.1\psi_1(\dot{\gamma}) \tag{5.16}$$

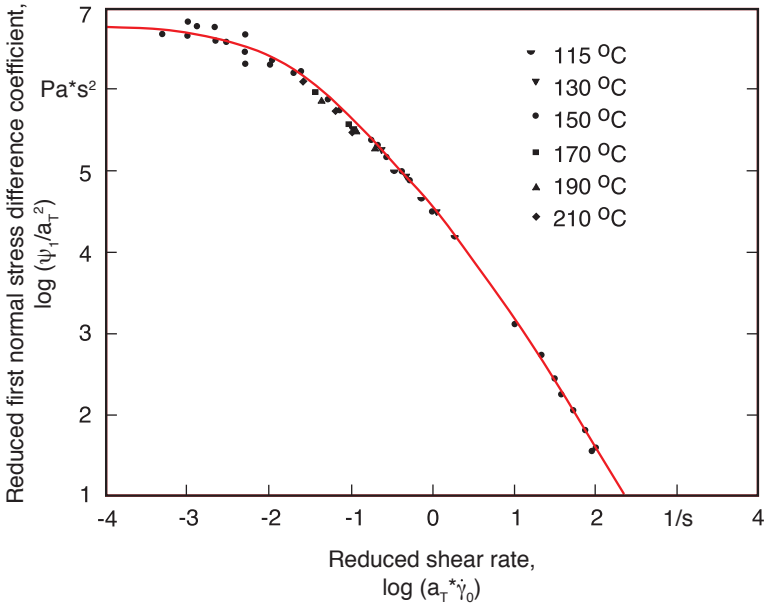

Figure 5.5 Reduced first normal stress difference coefficient for a low density polyethylene melt at a reference temperature of 150 °C

5.1.4 Deborah Number

A useful parameter often used to estimate the elastic effects during flow is the Deborah number[3], De. The Deborah number is defined by

$$De = \frac{\lambda}{t_p} \tag{5.17}$$

3 From the Song of Deborah, Judges 5 : 5 – "*The mountains flowed before the Lord.*" M. Reiner is credited for naming the Deborah number; *Physics Today*, (January 1964).

© Wolfgang Cohnen, 1998. Coyote Buttes North 1 Second Wave, Arizona.

where λ is the relaxation time of the polymer and t_p is a characteristic process time. The characteristic process time can be defined by the ratio of characteristic die dimension and average speed through the die. A Deborah number of zero represents a viscous fluid and a Deborah number of ∞ an elastic solid. As the Deborah number becomes > 1, the polymer does not have enough time to relax during the process, resulting in possible deviations in extrudate dimension or irregularities, such as *extrudate swell*[4], *shark skin,* or even *melt fracture*.

Although many factors affect the amount of extrudate swell, fluid "memory" and normal stress effects are the most significant ones. However, abrupt changes in boundary conditions, such as the separation point of the extrudate from the die, also play a role in the swelling or cross section reduction of the extrudate. In practice, the fluid memory contribution to die swell can be mitigated by lengthening the land length of the die. This is schematically depicted in Fig. 5.6. A long die land separates the polymer from the manifold long enough to allow it to "forget" its past shape.

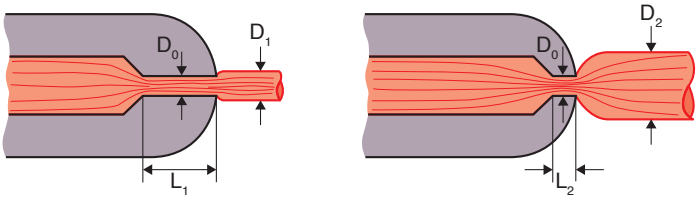

Figure 5.6 Schematic diagram of extrudate swell during extrusion

Waves in the extrudate may also appear as a result of high speeds during extrusion that do not allow the polymer to relax. This phenomenon is generally referred to as *shark skin* and is shown for a high density polyethylene in Fig. 5.7a [10]. It is possible to extrude at such high speeds that an intermittent separation of melt and inner die walls occurs, as shown in Fig. 5.7b. This phenomenon is often referred to as the *stick-slip effect* or *spurt flow* and is attributed to high shear stresses between the polymer and the die wall. This phenomenon occurs when the shear stress is near the critical value of 0.1 MPa [11–13]. If the speed is further increased, a helical geometry is extruded, as shown for a polypropylene extrudate in Fig. 5.7c. Eventually, the speeds become so high that a chaotic pattern develops, such as the one shown in Fig. 5.7d. This well-known phenomenon is called *melt fracture*. The

4 It should be pointed out that Newtonian fluids, which do not experience elastic or normal stress effects, also show some extrudate swell or reduction. A Newtonian fluid that is being extruded at high shear rates reduces its cross-section to 87% of the diameter of the die, whereas if extruded at very low shear rates, it swells to 113% of the diameter of the die. This swell is due to inertia effects caused by the change from the parabolic velocity distribution inside the die to the flat velocity distribution of the extrudate.

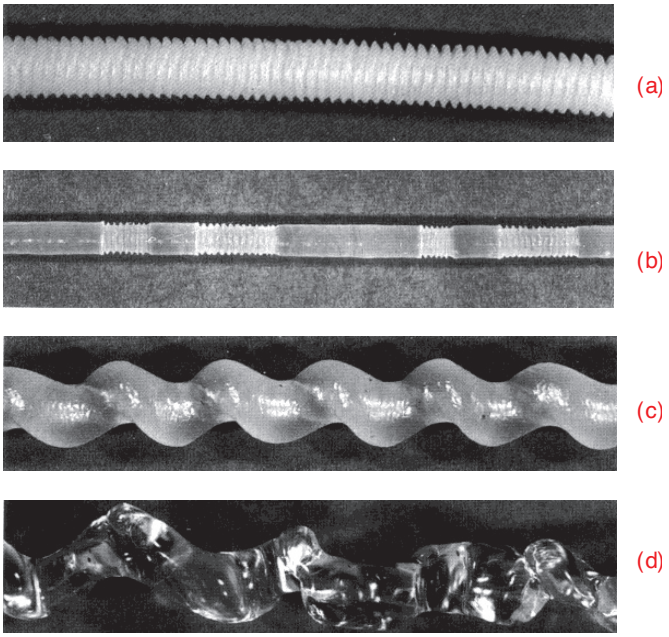

Figure 5.7 Various shapes of extrudates under melt fracture

shark skin effect is rarely experienced with linear polymers, which tend to experience spurt flow

It has been reported that the critical shear stress is independent of the melt temperature, but inversely proportional to the weight average molecular weight [14, 12]. However, Vinogradov et al. [15] presented results showing that the critical stress was independent of molecular weight, except for low molecular weights. Dealy and co-workers [16], and Denn [17] provide an extensive overview of various melt fracture phenomena that is recommended reading.

To summarize, the Deborah number and the size of the deformation imposed upon the material during processing determine how to most accurately model the system. Figure 5.8 [1] helps visualize the relation between time scale, deformation, and applicable model. At small Deborah numbers, the polymer can be modeled as a Newtonian fluid, and at very high Deborah numbers the material can be modeled as a Hookean solid. In between, the viscoelastic region is divided in two areas: the linear viscoelastic region for small deformations, and the non-linear viscoelastic region for large deformations. Linear viscoelasticity was briefly discussed in Chapter 2.

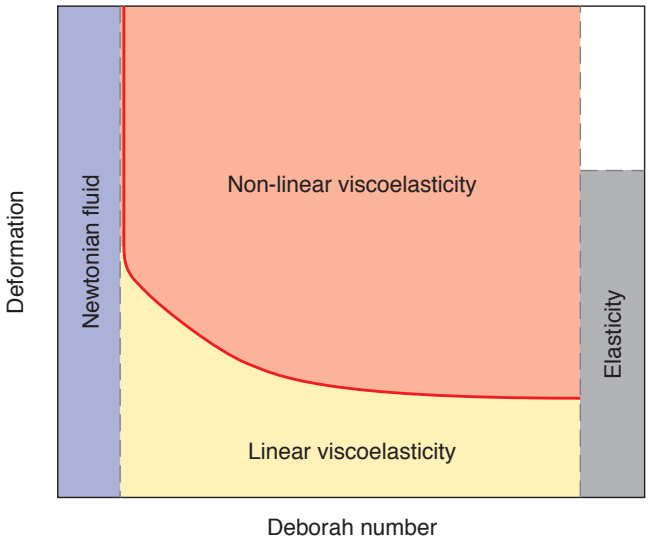

Figure 5.8 Schematic of Newtonian, elastic, linear, and non-linear viscoelastic regimes as a function of deformation and Deborah number during deformation of polymeric materials

5.2 Viscous Flow Models

Strictly speaking, the viscosity η, measured with shear deformation viscometers, should not be used to represent the elongational terms located on the diagonal of the stress and strain rate tensors. Elongational flows are briefly discussed later in this chapter. A rheologist's task is to find the models that best fit the data for the viscosity represented in Eq. 5.5. Some of the models used by polymer processors on a day-to-day basis to represent the viscosity of industrial polymers are presented in the next section.

5.2.1 The Power Law Model

The power law model proposed by Ostwald [18] and de Waale [19] is a simple model that accurately represents the shear thinning region in the viscosity versus strain rate curve but neglects the Newtonian plateau present at small strain rates. The power law model can be written as follows:

$$\eta = m(T)\dot{\gamma}^{n-1} \tag{5.18}$$

where m is referred to as the *consistency index* and n the *power law index*. The consistency index may include the temperature dependence of the viscosity such as represented in Eq. 5.11, and the power law index represents the shear thinning behavior of the polymer melt. Figure 5.9 presents normalized velocity distributions inside a tube for a fluid calculated using the power law model with various power law indices. It should be noted that the limits of this model are

$$\eta \to 0 \text{ as } \dot{\gamma} \to \infty \quad \text{and} \quad \eta \to \infty \text{ as } \dot{\gamma} \to 0$$

The infinite viscosity at zero strain rates leads to an erroneous result for regions of zero shear rate, such as at the center of a tube. This results in a predicted velocity distribution that is flatter at the center than the experimental profile. In computer simulation of polymer flows, this problem is often overcome by using a truncated model such as

$$\eta = m_0(T)\dot{\gamma}^{n-1} \quad \text{for} \quad \dot{\gamma} > \dot{\gamma}_0 \quad \text{and} \tag{5.19a}$$

$$\eta = m_0(T) \qquad \text{for} \quad \dot{\gamma} \le \dot{\gamma}_0 \tag{5.19b}$$

where m_0 represents a zero shear rate ($\dot{\gamma}_0$) viscosity. Table 5.1 presents a list of typical power law and consistency indices for common thermoplastics.

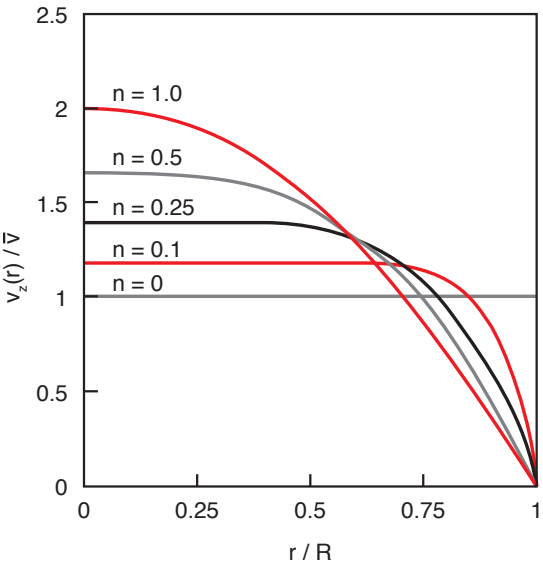

Figure 5.9 Pressure flow velocity distributions inside a tube for fluids with various power law indices

Table 5.1 Power Law and Consistency Indices for Common Thermoplastics

Polymer	m (Pa-s^n)	n	T (°C)
Polystyrene	2.80×10^4	0.28	170
High density polyethylene	2.00×10^4	0.41	180
Low density polyethylene	6.00×10^3	0.39	160
Polypropylene	7.50×10^3	0.38	200
Polyamide 66	6.00×10^2	0.66	290
Polycarbonate	6.00×10^2	0.98	300
Polyvinyl chloride	1.70×10^4	0.26	180

5.2.2 The Bird-Carreau-Yasuda Model

A model that fits the whole range of strain rates was developed by Bird and Carreau [20] and Yasuda [21]; it contains five parameters:

$$\frac{\eta - \eta_\infty}{\eta_0 - \eta_\infty} = \left[1 + \left|\lambda\dot{\gamma}\right|^a\right]^{(n-1)/a} \tag{5.20}$$

where η_0 is the zero shear rate viscosity, η_∞ is an infinite shear rate viscosity, λ is a time constant, n is the power law index and a is a constant, which in the original Bird-Carreau model is $a = 2$. In many cases, the infinite shear rate viscosity is negligible, reducing Eq. 5.20 to a three parameter model. Equation 5.20 was modified by Menges, Wortberg, and Michaeli [22] to include a temperature dependence using a WLF relation. The modified model, which is used in commercial polymer data banks, is written as follows:

$$\eta = \frac{k_1 a_T}{\left[1 + k_2 \dot{\gamma} a_T\right]^{k_3}} \tag{5.21}$$

where the shift a_T applies well for amorphous thermoplastics and is written as

$$\ln a_T = \frac{8.86\left(k_4 - k_5\right)}{101.6 + k_4 - k_5} - \frac{8.86\left(T - k_5\right)}{101.6 + T - k_5} \tag{5.22}$$

Table 5.2 presents constants k_i for Carreau-WLF (amorphous) and Carreau-Arrhenius models (semi-crystalline) for various common thermoplastics. In addition to the temperature shift, Menges, Wortberg and Michaeli [22] measured a pressure dependence of the viscosity and proposed the following model, which includes both temperature and pressure viscosity shifts:

$$\log\eta\left(T, p\right) = \log\eta_0 + \frac{8.86\left(T^* - T_s\right)}{101.6 + T^* - T_s} - \frac{8.86\left(T - T_s + 0.02p\right)}{101.6 + \left(T - T_s + 0.02p\right)} \tag{5.23}$$

where p is in bar, and the constant 0.02 represents a 0.02 K shift per bar[5]. In the above equation, the first term represents a shift between the measured temperature T^* and the reference temperature T_s. The second term represents the temperature and pressure shifts between the actual temperature and the reference temperature, as well as between 1 bar and the actual pressure. Hence, in the above model a rise in pressure is equivalent to a drop in temperature.

Table 5.2 Constants for Carreau-WLF (Amorphous) and Carreau-Arrhenius (Semi-Crystalline) Models for Various Common Thermoplastic

Polymer	k_1 (Pa-s)	k_2 (s)	k_3	k_4 (°C)	k_5 (°C)	T_0 (°C)	E_0 (J/mol)
Polystyrene	1777	0.064	0.73	200	123	–	–
High density polyethylene	24198	1.38	0.60	–	–	200	22272
Low density polyethylene	317	0.015	0.61	–	–	189	43694
Polypropylene	1386	0.091	0.68	–	–	220	427198
Polyamide 66	44	0.00059	0.40	–	–	300	123058
Polycarbonate	305	0.00046	0.48	320	153	–	–
Polyvinyl chloride	1786	0.054	0.73	185	88	–	–

5.2.3 The Bingham Fluid

The Bingham fluid is an empirical model that represents the rheological behavior of materials that exhibit a "no flow" region below certain yield stresses, τ_Y, such as polymer emulsions and slurries. Since these materials flow like a Newtonian liquid above the yield stress, the Bingham model can be represented by

$$\eta = \infty \quad \text{or} \quad \dot{\gamma} = 0 \quad \tau \le \tau_Y \tag{5.24a}$$

$$\eta = \mu_0 + \frac{\tau_y}{\dot{\gamma}} \quad \tau \ge \tau_Y \tag{5.24b}$$

Here, τ is the magnitude of the deviatoric stress tensor and is computed in the same way as in Eq. 5.7.

5.2.4 Elongational Viscosity

In polymer processes, such as fiber spinning, blow molding, thermoforming, foaming, certain extrusion die flows, and compression molding with specific processing conditions, the major mode of deformation is elongational.

5 This constant can be in the range of 0.01 to 0.03.

To illustrate elongational flows, consider the fiber spinning process shown in Fig. 5.10.

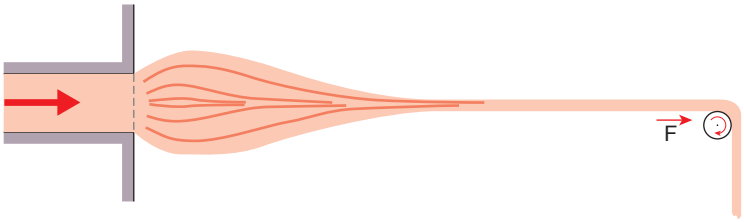

Figure 5.10 Schematic diagram of a fiber spinning process

A simple elongational flow is developed as the filament is stretched with the following components for the rate of deformation:

$$\dot{\gamma}_{11} = -\dot{\varepsilon} \tag{5.25a}$$

$$\dot{\gamma}_{22} = -\dot{\varepsilon} \tag{5.25b}$$

$$\dot{\gamma}_{33} = -2\dot{\varepsilon} \tag{5.25c}$$

where $\dot{\varepsilon}$ is the elongation rate, and the off-diagonal terms of $\dot{\gamma}_{ij}$ are all zero. The diagonal terms of the total stress tensor can be written as

$$\sigma_{11} = -p - \eta\dot{\varepsilon} \tag{5.26a}$$

$$\sigma_{22} = -p - \eta\dot{\varepsilon} \tag{5.26b}$$

and

$$\sigma_{33} = -p + 2\eta\dot{\varepsilon} \tag{5.26c}$$

Since the only outside forces acting on the fiber are in the axial or 3 direction, for the Newtonian case, σ_{11} and σ_{12} must be zero. Hence,

$$p = -\eta\dot{\varepsilon} \quad \text{and} \tag{5.27}$$

$$\sigma_{33} = 3\eta\dot{\varepsilon} = \bar{\eta}\dot{\varepsilon} \tag{5.28}$$

which is known as *elongational viscosity or Trouton viscosity* [23]. This is analogous to elasticity where the following relation between elastic modulus, E, and shear modulus, G, can be written

$$\frac{E}{G} = 2(1+\nu) \tag{5.29}$$

where v is Poisson's ratio. For the incompressibility case, where $v = 0.5$, Eq. 5.29 reduces to

$$\frac{E}{G} = 3 \tag{5.30}$$

Figure 5.11 [24] shows shear and elongational viscosities for two types of polystyrene. In the region of the Newtonian plateau, the limit of 3, shown in Eq. 5.28, is quite clear. Figure 5.12 presents plots of elongational viscosities as a function of stress for various thermoplastics at common processing conditions. It should be emphasized that measuring elongational or extensional viscosity is an extremely difficult task. For example, in order to maintain a constant strain rate, the specimen must be deformed uniformly exponentially. In addition, a molten polymer

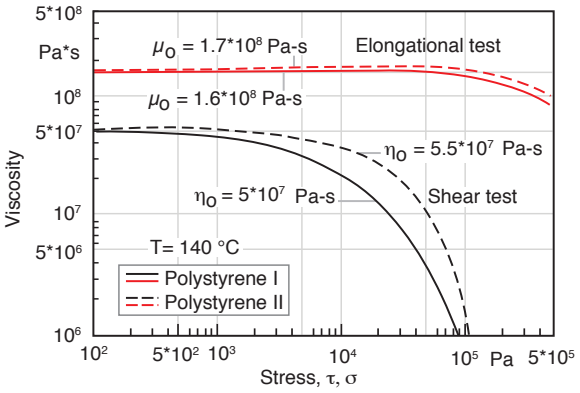

Figure 5.11 Shear and elongational viscosity curves for two types of polystyrene

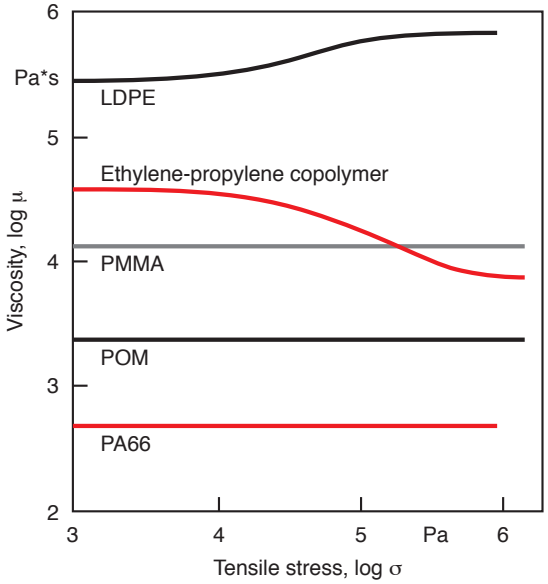

Figure 5.12 Elongational viscosity curves as a function of tensile stress for several thermoplastics

must be tested completely submerged in a heated, neutrally buoyant liquid at constant temperature.

5.2.5 Rheology of Curing Thermosets

The conversion or cure dependent viscosity of a curing thermoset polymer increases as the molecular weight of the reacting polymer increases. For the vinyl ester, whose curing history[6] is shown in Fig. 5.13 [25], the viscosity behaves as shown in Fig. 5.14 [25]. Hence, a complete model for viscosity of a reacting polymer must contain the effects of strain rate, $\dot{\gamma}$, temperature, T, and degree of cure, c, such as

$$\eta = \eta\left(\dot{\gamma}, T, c\right) \tag{5.31}$$

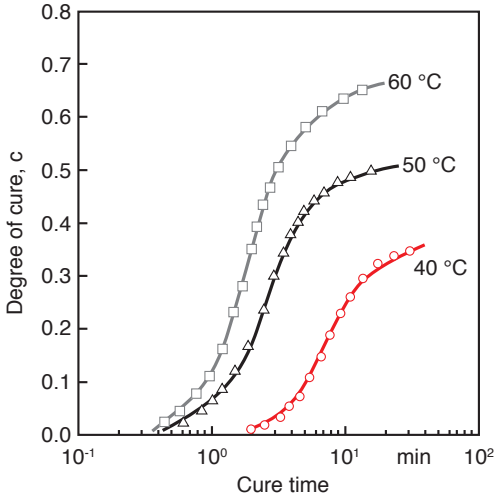

Figure 5.13 Degree of cure as a function of time for a vinyl ester at various isothermal cure conditions

There are no generalized models that include all these variables for thermosetting polymers. However, extensive work has been done on the viscosity of polyurethanes [26, 27] used in reaction injection molding processes. An empirical relation, sometimes referred to as the Castro-Macosko model, which models the viscosity of these mixing-activated polymers, given as a function of temperature and degree of cure, is written as

$$\eta = \eta_0 e^{E/RT}\left(\frac{c_g}{c_g - c}\right)^{C_1 + C_2 c} \tag{5.32}$$

6 A more in-depth view of curing and solidification processes of thermosetting polymers is given in Chapter 7.

where E is the activation energy of the polymer, R is the ideal gas constant, T is the temperature, c_g is the gel point[7], c the degree of cure, and C_1 and C_2 are constants that fit the experimental data. Figure 5.15 shows the viscosity as a function of time and temperature for a 47 % MDI-BDO P(PO-EO) polyurethane, and Fig. 5.16 shows the viscosity as a function of degree of cure.

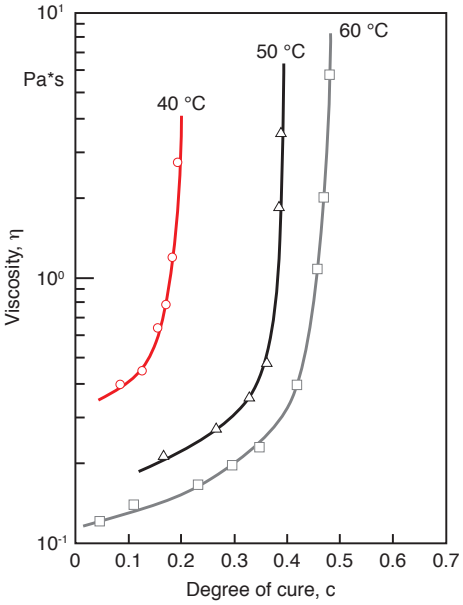

Figure 5.14 Viscosity as a function of degree of cure for a vinyl ester at various isothermal cure conditions

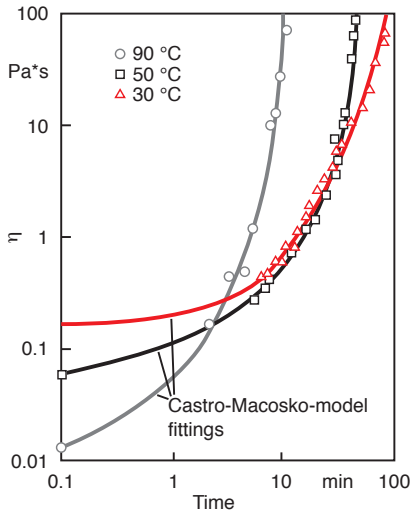

Figure 5.15 Viscosity as a function of time for a 47 % MDI-BDO P(PO-EO) polyurethane at various isothermal cure conditions

7 At the gel point the change of the molecular weight with respect to the degree of cure goes to infinity. Hence, it can be said that at this point all the molecules are interconnected.

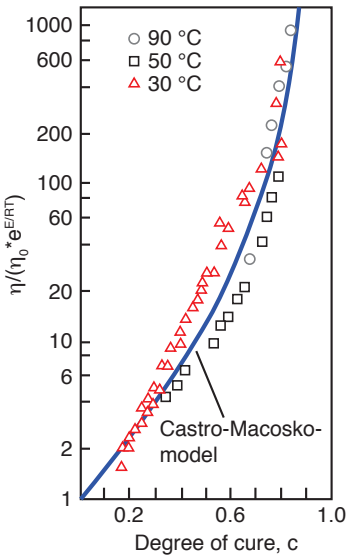

Figure 5.16 Viscosity as a function of degree of cure for a 47% MDI-BDO P(PO-EO) polyurethane at various isothermal cure conditions

5.2.6 Suspension Rheology

Particles suspended in a material, such as in filled or reinforced polymers, have a direct effect on the properties of the final article and on the viscosity during processing. Numerous models have been proposed to estimate the viscosity of filled liquids [28–32]. Most models proposed are a power series of the form[8]

$$\frac{\eta_f}{\eta_0} = 1 + a_1\phi + a_2\phi^2 + a_3\phi^3 + \ldots \tag{5.33}$$

The linear term in Eq. 5.33 represents the narrowing of the flow passage caused by the filler that is passively entrained by the fluid and sustains no deformation, as shown in Fig. 5.17. For instance, Einstein's model, which only includes the linear term with a_1= 2.5, was derived based on a viscous dissipation balance. The quadratic term in the equation represents the first-order effects of interaction between the filler particles. Geisbüsch suggested a model with a yield stress, where the strain rate of the melt increases by a factor κ as

$$\eta_f = \frac{\tau_0}{\dot{\gamma}} + \kappa\eta_0\left(\kappa\dot{\gamma}\right) \tag{5.34}$$

For high deformation stresses, which are typical in polymer processing, the yield stress in the filled polymer melt can be neglected. Figure 5.18 compares Geisbüsch's experimental data to Eq. 5.33 using the coefficients derived by Guth [30].

8 The model developed by Guth in 1938 best fits experimental: $\frac{\eta_f}{\eta_0} = 1 + 2.5\varphi + 14.1\varphi^2$

However, a full analysis of the first-order particle interactions gives an analytical value for the quadratic term of 6.96.

The data and Guth's model seem to agree well. A comprehensive survey on particulate suspensions was given by Gupta [33], and one on short-fiber suspensions by Milliken and Powell [34].

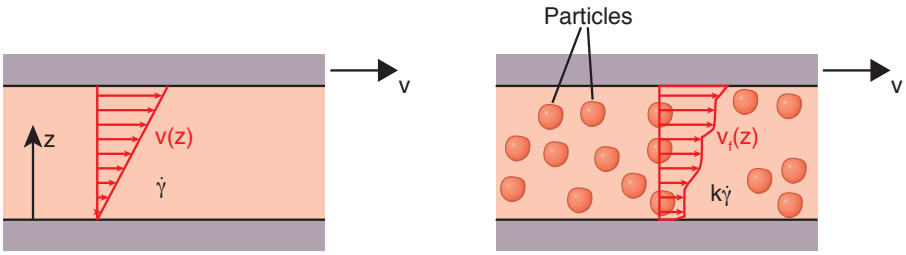

Figure 5.17 Schematic diagram of strain rate increase in a filled system

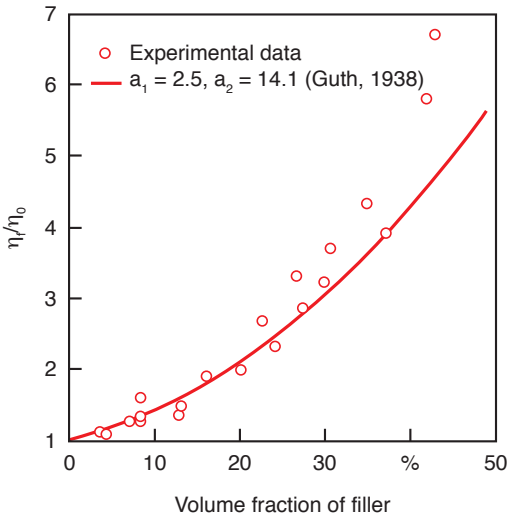

Figure 5.18 Viscosity increase as a function of volume fraction of filler for polystyrene and low density polyethylene containing spherical glass particles with diameters ranging between 36 μm and 99.8 μm

5.3 Simplified Flow Models Common in Polymer Processing

Many polymer processing operations can be modeled using simplified geometries and material models. This section presents several isothermal flow models in simple geometries using a Newtonian viscosity and a power-law viscosity as described in Eq. 5.18. Although it is very common to simplify analyses of polymer processes by assuming isothermal conditions, most operations are non-isothermal because they include melting and are often influenced by viscous dissipation. Hence, the temperature of the polymer melt ranges between T_g (for amorphous polymers) or T_m (for semi-crystalline polymers) and the heater temperature T_w (the subscript w is often used for "wall") and often exceeds T_w due to viscous dissipation. An estimate of the maximum temperature rise due to viscous heating is given by

$$\Delta T_{\max} = \frac{\eta v_0^2}{8k} \tag{5.35}$$

where v_0 represents a characteristic velocity in the flow system, such as plate velocity in a simple shear flow, and k represents the thermal conductivity. To estimate the importance of viscous dissipation, the Brinkman number, Br, is often computed

$$Br = \frac{\eta v_0^2}{k\left(T_w - T_{g\ or\ m}\right)} \tag{5.36}$$

The Brinkman number is the ratio of the heat generated via viscous dissipation and the heat conducted out of the system via conduction. A Brinkman number > 1 implies that the temperature field will be affected by viscous dissipation. The choice of temperatures in the denominator of the equation depends on the type of material and problem being analyzed.

5.3.1 Simple Shear Flow

Simple shear flows, as represented in Fig. 5.19, are very common in polymer processing, such as inside extruders as well as in certain coating flows. The flow field in simple shear is the same for all fluids and is described by

$$v_z = v_0 \frac{y}{h} \tag{5.37}$$

for the velocity distribution and

$$Q = \frac{v_0 h W}{2} \tag{5.38}$$

for the volumetric throughput, where W represents the width of the plates.

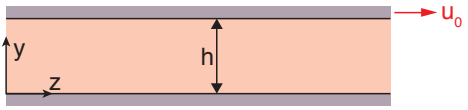

Figure 5.19 Schematic diagram of a simple shear flow

5.3.2 Pressure Flow Through a Slit

The pressure flow through a slit, as depicted in Fig. 5.20, is encountered in flows through extrusion dies or inside injection molds. The flow field for a Newtonian fluid is described by

$$v_z(y) = \left(\frac{h^2 \Delta p}{8\mu L}\right)\left[1 - \left(\frac{2y}{h}\right)^2\right] \tag{5.39}$$

and

$$Q = \frac{Wh^3 \Delta p}{12\mu L} \tag{5.40}$$

for the net volumetric throughput. When using the power-law model, the flow field is described by

$$v_z(y) = \left(\frac{h}{2(s+1)}\right)\left(\frac{h\Delta p}{2mL}\right)^s \left[1 - \left(\frac{2y}{h}\right)^{s+1}\right] \tag{5.41}$$

and

$$Q = \frac{Wh^2}{2(s+2)}\left(\frac{h\Delta p}{2mL}\right)^s \tag{5.42}$$

for the throughput, where $s = 1/n$, and n the power-law index.

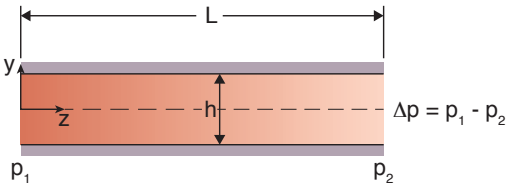

Figure 5.20 Schematic diagram of pressure flow through a slit

5.3.3 Pressure Flow through a Tube – Hagen-Poiseuille Flow

Pressure flow through a tube (Fig. 5.21), or Hagen-Poiseuille flow, is the type that exists inside the runner system in injection molds, as well as in extrusion dies and inside the capillary viscometer. For a Newtonian fluid, the flow field inside a tube is described by

$$v_z(r) = \frac{R^2 \Delta p}{4\mu L}\left[1 - \left(\frac{r}{R}\right)^2\right] \tag{5.43}$$

and

$$Q = \frac{\pi R^4 \Delta p}{8 \mu L} \tag{5.44}$$

for the throughput.

Using the power law model, the flow through a tube is described by

$$v_z(r) = \frac{R}{1+s}\left(\frac{R\Delta p}{2mL}\right)^s \left[1 - \left(\frac{r}{R}\right)^{s+1}\right] \tag{5.45}$$

and

$$Q = \left(\frac{\pi R^3}{s+3}\right)\left(\frac{R\Delta p}{2mL}\right)^s \tag{5.46}$$

for the throughput.

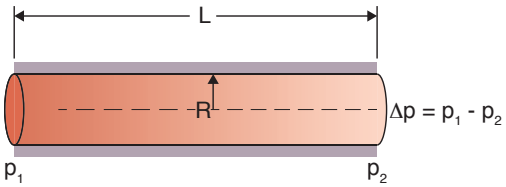

Figure 5.21 Schematic diagram of pressure flow through a tube

5.3.4 Couette Flow

The Couette device, as depicted in Fig. 5.22, is encountered in bearings and in certain types of rheometers. It is also used as a simplified flow model for mixers and extruders. The Newtonian flow field in a Couette device is described by

$$v_\theta(r) = \frac{\Omega}{\kappa^2 - 1}\left(\frac{R_0^2 - r^2}{r}\right) \tag{5.47}$$

where $= R_0 / R_i$. Using the power law model, the flow field inside a Couette device is described by

$$v_\theta(r) = \frac{\Omega}{\kappa^{2s} - 1}\left(\frac{R_0^{2s} - r^{2s}}{r^{2s-1}}\right) \tag{5.48}$$

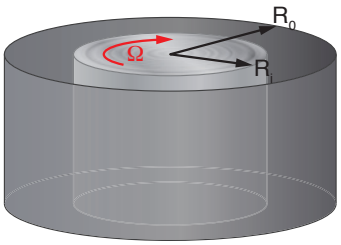

Figure 5.22 Schematic diagram of a Couette device

5.4 Viscoelastic Flow Models

Viscoelasticity has already been introduced in Chapter 3, based on linear viscoelasticity. However, in polymer processing large deformations are imposed on the material, requiring the use of non-linear viscoelastic models. There are two types of general, non-linear viscoelastic flow models: the differential type and the integral type.

5.4.1 Differential Viscoelastic Models

Differential models have traditionally been the choice for describing the viscoelastic behavior of polymers when simulating complex flow systems. Many differential viscoelastic models can be described using the general form

$$Y\underline{\underline{\tau}} + \lambda_1 \underline{\underline{\tau}}_{(1)} + \lambda_2 \left(\underline{\underline{\dot{\gamma}}} \cdot \underline{\underline{\tau}} + \underline{\underline{\tau}} \cdot \underline{\underline{\dot{\gamma}}} \right) + \lambda_3 \left(\underline{\underline{\tau}} \cdot \underline{\underline{\tau}} \right) = \eta_0 \underline{\underline{\dot{\gamma}}} \tag{5.49}$$

where $\underline{\underline{\tau}}_{(1)}$ is the *first contravariant convected time derivative* of the deviatoric stress tensor and represents rates of change with respect to a convected coordinate system that moves and deforms with the fluid. The *convected derivative* of the deviatoric stress tensor is defined as

$$\underline{\underline{\tau}}_{(1)} = \frac{D\underline{\underline{\tau}}}{D_t} - \left(\nabla \underline{v}^t \cdot \underline{\underline{\tau}} + \underline{\underline{\tau}} \cdot \nabla \underline{v} \right) \tag{5.50}$$

The constants in Eq. 5.49 are defined in Table 5.3 for various viscoelastic models commonly used to simulate polymer flows. A review by Bird and Wiest [6] provides a more complete list of existing viscoelastic models, and Giacomin et al. renewed the interest in co-rotational models [35].

The *upper convective model* and the *White-Metzner model* are very similar, with the exception that the White-Metzner model incorporates the strain rate effects of the relaxation time and the viscosity. Both models provide a first order approximation to flows in which shear rate dependence and memory effects are important. However, both models predict zero second normal stress coefficients. The *Giesekus model* is molecular-based, non-linear in nature and describes the power law region for viscosity and both normal stress coefficients. The *Phan-Thien Tanner models* are based on network theory and give non-linear stresses. Both the Giesekus and Phan-Thien Tanner models have been successfully used to model complex flows.

Table 5.3 Definition of Constants in Eq. 5.49

Constitutive model	Y	λ_1	λ_2	λ_3
Generalized Newtonian	1	0	0	0
Upper convected Maxwell	1	λ_1	0	0
White-Metzner	1	$\lambda_1(\dot{\gamma})$	0	0
Phan-Thien Tanner-1	$e^{-\varepsilon(\lambda/\eta_0)tr\underline{\underline{\tau}}}$	λ_1	$\frac{1}{2}\xi\lambda$	0
Phan-Thien Tanner-2	$1-\varepsilon(\lambda/\eta_0)tr\underline{\underline{\tau}}$	λ	$\frac{1}{2}\xi\lambda$	0
Giesekus	1	λ_1	0	$-(\alpha\lambda_1/\eta_0)$

An overview of viscoelastic flow models with a literature review on the subject is given by Giacomin et al. [6] and Phan-Thien [36], and details on numerical implementation of viscoelastic models are given by Osswald and Hernández-Ortiz [37]. As an example of the application of differential models to predict flow of polymeric liquids, it is worth mentioning the work by Dietsche and Dooley [38], who evaluated the White-Metzner, the Phan-Thien Tanner-1, and the Giesekus models by comparing finite element[9] and experimental results of the flow inside multi-layered coextrusion dies. Figure 5.23 [39] presents the progression of a matrix of colored circular polystyrene strands flowing in an identical polystyrene matrix down a channel with a square cross section of 0.95 × 0.95 cm. The cuts in the figure are shown at intervals of 7.6 cm.

The circulation pattern caused by the secondary normal stress differences inside non-circular dies were captured well by the Phan-Thien Tanner and Giesekus models but, as expected, not by the White-Metzner model. Figure 5.24 presents flow patterns predicted by the Phan-Thien Tanner model along with the experimental rearrangement of 165 initially horizontal layers of polystyrene in square, rectangular, and tear-drop shaped dies[10]. In all three cases, the shapes of the circulation patterns were predicted accurately. The flow simulation of the square die predicted a velocity on the order of 10^{-5} m/s along the diagonal of the cross section, which was in agreement with the experimental results. Holmes et al. [40] simulated the viscoelastic secondary flows in square ducts using a finite volume approach. Single mode and multimode Giesekus and Phan-Thien Tanner (PTT) models were implemented and were able to reproduce full three-dimensional (3D) flow through the square ducts. Results for low density polyethylene (LDPE), polystyrene, and polycarbonate were all in agreement with experiments [39] and FEM simulation [38].

9 They used the commercially available code POLYFLOW for their simulation.

10 These geometries are typical for distribution manifolds used in sheeting dies.

Also worth mentioning is work done by Baaijens [41], who evaluated the Phan-Thien Tanner models 1 and 2, and the Giesekus models. He compared finite element results to measured isochromatic birefringence patterns using complex experiments with polymer melts and solutions. His simulation results predicted the general shape of the measured birefringence patterns. He found that at high Deborah numbers, the Phan-Thien Tanner models converged much more easily than the Giesekus model.

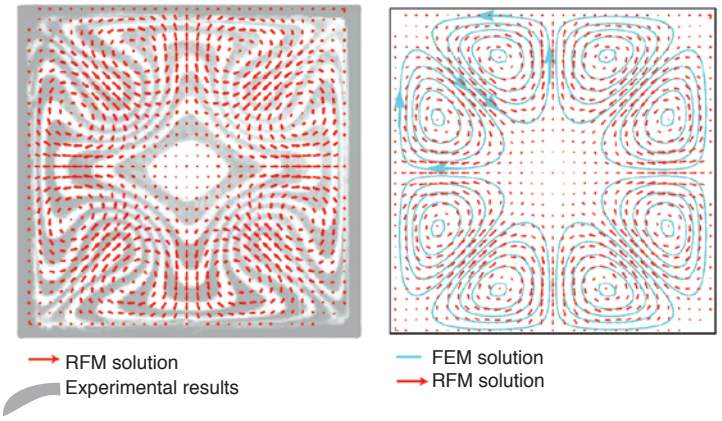

Figure 5.23 Polystyrene strand profile progression in a square die

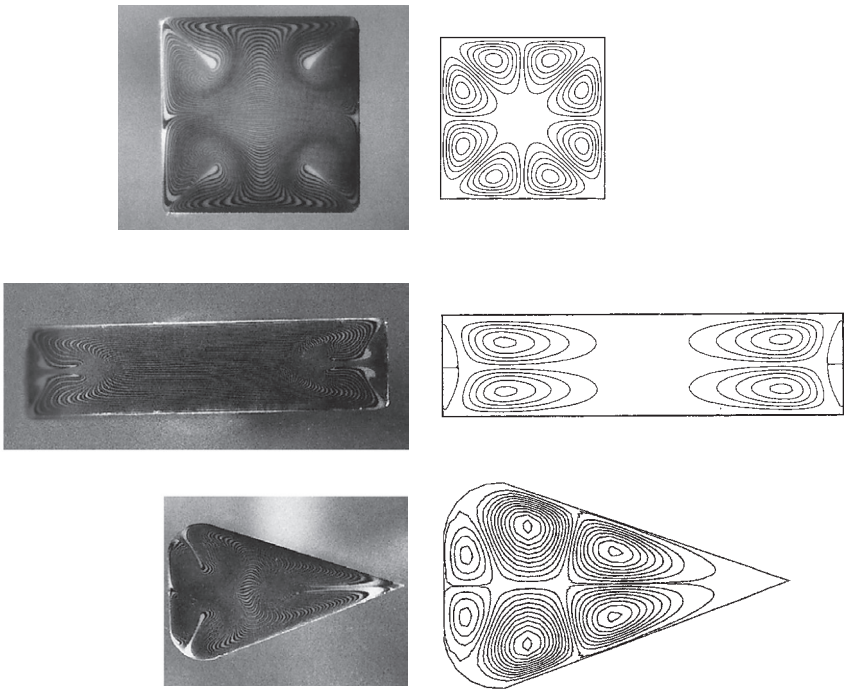

Figure 5.24 Comparison between experimental and predicted flow patterns of polystyrene in square, rectangular, and tear-drop shaped dies

5.4.2 Integral Viscoelastic Models

Integral models with a memory function have been widely used to describe the viscoelastic behavior of polymers and to interpret their rheological measurements [9, 42]. In general the single integral model can be described as

$$\underline{\underline{\tau}} = \int_{-\infty}^{t} M\left(t-t'\right)\underline{\underline{S}}\left(t'\right)dt' \tag{5.51}$$

where $M\left(t-t'\right)$ is a memory function and $\underline{\underline{S}}\left(t'\right)$ *is* a deformation dependent tensor defined by

$$\underline{\underline{S}}\left(t'\right) = \phi_1\left(I_1, I_2\right)\underline{\underline{\gamma}}_{[0]} + \phi_2\left(I_1, I_2\right)\underline{\underline{\gamma}}^{[0]} \tag{5.52}$$

where I_1 and I_2 are the first invariant of the Cauchy and Finger strain tensors, respectively.

Table 5.4 [43–47] defines the constants ϕ_1 and ϕ_2 for various models. In Eq. 5.52, $\underline{\underline{\gamma}}_{[0]}$ and $\underline{\underline{\gamma}}^{[0]}$ are the *finite strain tensors* given by

$$\underline{\underline{\gamma}}_{[0]} = \underline{\underline{\Delta}}^{t} \cdot \underline{\underline{\Delta}} - \underline{\underline{\delta}} \quad \text{and} \tag{5.53}$$

$$\underline{\underline{\gamma}}^{[0]} = \underline{\underline{\delta}} - \underline{\underline{E}} \cdot \underline{\underline{E}}^{t} \tag{5.54}$$

Table 5.4 Definition of Constants in Eq. 5.52

Constitutive model	ϕ_1	ϕ_2
Lodge rubber-like liquid	1	0
K-BKZ*	$\frac{\partial W}{\partial I_1}$	$\frac{\partial W}{\partial I_2}$
Wagner**	$e^{-\beta\sqrt{\alpha I_1 + (1-\alpha) I_2 - 3}}$	0
Papanastasiou-Scriven-Macosko***	$\frac{\alpha}{(\alpha-3)+\beta I_1 + (1-\beta) I_2}$	0

* $W(I_1,I_2)$ represents a potential function which can be derived from empiricisms or molecular theory.
** Wagner's model is a special form of the K-BKZ model
*** The Papanastasiou-Scriven Macosko model is also a special form of the K-BKZ model.

The terms $\underline{\underline{\Delta}}$ and $\underline{\underline{E}}$ are displacement gradient tensors[11] defined by

$$\Delta_{ij} = \frac{\partial x_i'\left(x', t, t'\right)}{\partial x_j} \quad \text{and} \tag{5.55}$$

11 Another combination of the displacement gradient tensors often used are the *Cauchy strain tensor* and the *Finger strain tensor* defined by $\underline{\underline{B}}^{-1} = \underline{\underline{\Delta}}^{t} \cdot \underline{\underline{\Delta}}$ and $\underline{\underline{B}} = \underline{\underline{E}} \cdot \underline{\underline{E}}^{t}$, respectively.

$$E_{ij} = \frac{\partial x_i\left(x', t', t\right)}{\partial x_j'} \tag{5.56}$$

where the components Δ_{ij} measure the displacement of a particle at past time t' relative to its position at present time t, and the terms E_{ij} measure the material displacements at time t relative to the positions at time t'.

A memory function $M\left(t-t'\right)$ that is often applied and that leads to commonly used constitutive equations is written as

$$M\left(t-t'\right) = \sum_{k=1}^{n} \frac{\eta_k}{\lambda_{k^2}} \exp\left(-\frac{t-t'}{\lambda_k}\right) \tag{5.57}$$

where λ_k and η_k are relaxation times and viscosity coefficients at the reference temperature T_{ref}, respectively.

Once a memory function has been specified one can calculate several material functions using [4]

$$\eta\left(\dot{\gamma}\right) = \int_0^{\infty} M\left(s\right) s\left(\phi_1 + \phi_2\right) ds \tag{5.58}$$

$$\psi_1\left(\dot{\gamma}\right) = \int_0^{\infty} M\left(s\right) s^2\left(\phi_1 + \phi_2\right) ds \tag{5.59}$$

$$\psi_2\left(\dot{\gamma}\right) = \int_0^{\infty} M\left(s\right) s^2\left(\phi_2\right) ds \tag{5.60}$$

For example, Figs. 5.25 and 5.26 present the measured [48] viscosity and first normal stress difference data, respectively, for three blow molding high density polyethylene grades along with a fit obtained from the Papanastasiou-Scriven-Macosko [47] form of the K-BKZ equation. A memory function with a relaxation

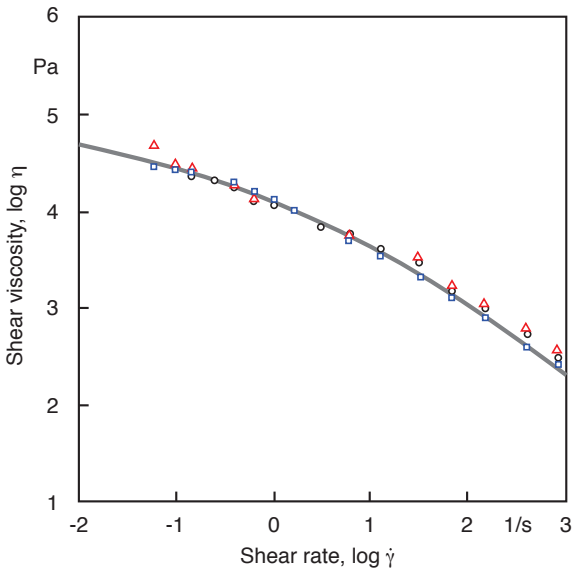

Figure 5.25 Measured and predicted shear viscosity for various high density polyethylene resins at 170 °C

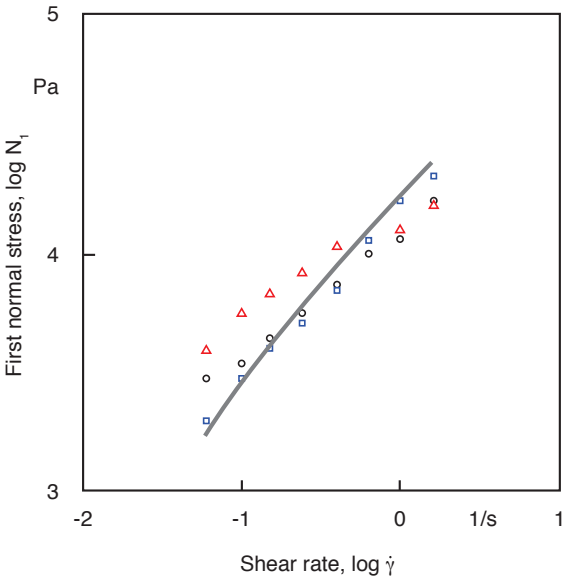

Figure 5.26 Measured and predicted first normal stress difference for various high density polyethylene resins at 170 °C

spectrum of 8 relaxation times was used. The coefficients used to fit the data are summarized in Table 5.5 [42]. The viscosity and first normal stress coefficient data presented in Figs. 5.4 and 5.5 where fitted with the Wagner [9] form of the K-BKZ equation [9]. Luo and Mitsoulis used the K-BKZ model with the data in Table 5.5 to simulate the flow of HDPE through annular dies. Figure 5.27 [42] shows simulation results for a converging, a straight, and a diverging die geometry. The results shown in Fig. 5.27 were in good agreement with experimental results[12].

Table 5.5 Material Parameter Values in Eq. 5.57 for Fitting Data of High Density Polyethylene Melts at 170 °C

k	λ_k (s)	η_k (Pa·s)
1	0.0001	52
2	0.001	148
3	0.01	916
4	0.1	4210
5	1.0	8800
6	10.0	21,200
7	100.0	21,000
8	1000.0	600

12 The degree of the agreement between experiment and simulation varied between the resins.

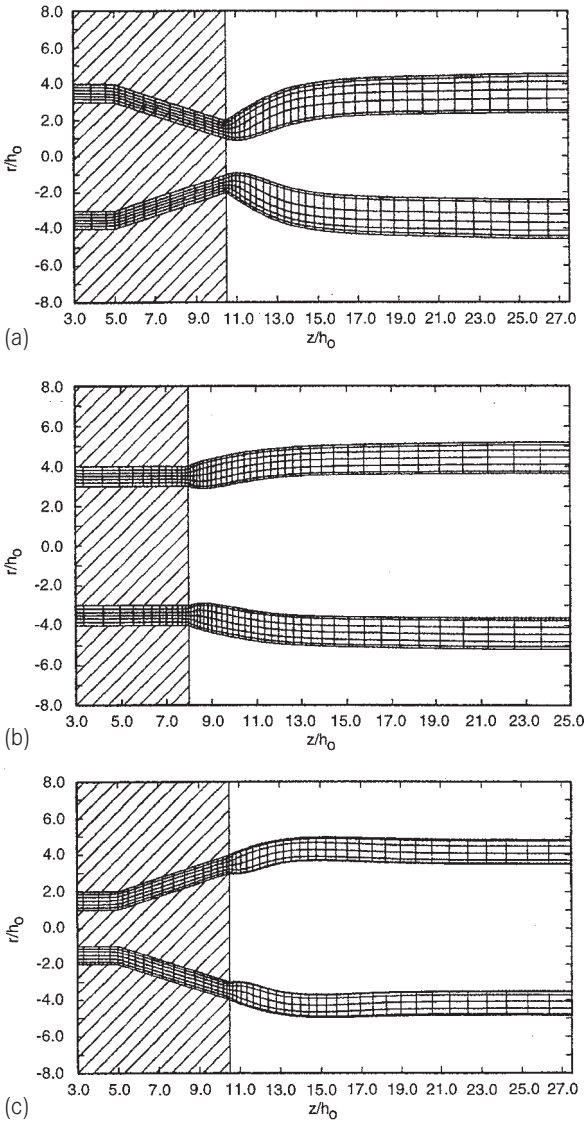

Figure 5.27 Predicted extrudate geometry for: (a) converging, (b) straight, and (c) diverging annular dies

5.5 Rheometry

In industry there are various ways to qualify and quantify the properties of a polymer melt. The techniques range from simple analyses for checking the consistency of the material at certain conditions, to more complex measurements to evaluate viscosity and normal stress differences. This section includes three such techniques to give the reader a general idea of current measuring techniques.

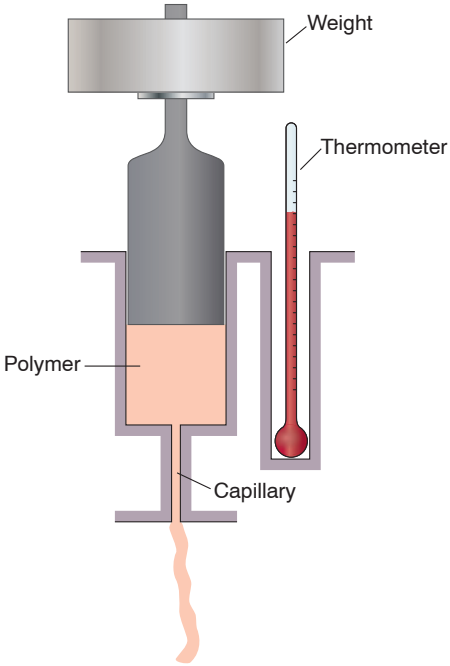

Figure 5.28 Schematic diagram of an extrusion plastometer used to measure melt flow index

5.5.1 The Melt Flow Indexer

The melt flow indexer is often used in industry to characterize a polymer melt and as a simple and quick means of quality control. It takes a single point measurement using standard testing conditions specific to each polymer class on a ram type extruder or extrusion plastometer, as shown in Fig. 5.28. The standard procedure for testing the flow rate of thermoplastics using an extrusion plastometer is described in the ASTM D1238 test [49]. During the test, a sample is heated in the barrel and extruded from a short cylindrical die using a piston actuated by a weight. The weight of the polymer in grams extruded during the 10-minute test is the melt flow index (MFI) of the polymer.

5.5.2 The Capillary Viscometer

The most common and simplest device for measuring viscosity is the capillary viscometer. Its main component is a straight tube or capillary, and it was first used to measure the viscosity of water by Hagen [50] and Poiseuille [51]. A capillary rheometer has a pressure driven flow for which the velocity gradient or strain rate and also the shear rate will be maximum at the wall and zero at the center of the flow, making it a non-homogeneous flow.

Since pressure driven viscometers employ non-homogeneous flows, they can only measure steady shear functions such as viscosity, $\eta(\dot{\gamma})$. However, they are widely used because they are relatively inexpensive to build and simple to operate. Despite their simplicity, long capillary viscometers provide the most accurate viscosity data available. Another major advantage is that the capillary rheometer has no free surfaces in the test region, unlike other types of rheometers, such as the cone and plate rheometers, which we will discuss in the next section. When the strain rate dependent viscosity of polymer melt is measured, capillary rheometers may be the only satisfactory method of obtaining such data at shear rates > 10 s^{-1}. This is important for processes with higher rates of deformation, such as mixing, extrusion, and injection molding. Because its design is basic and it only needs a pressure head at its entrance, capillary rheometers can easily be attached to the end of a screw- or ram-type extruder for on-line measurements. This makes the capillary viscometer an efficient tool for industry.

The basic features of the capillary rheometer are shown in Fig. 5.29. A capillary tube of radius R and length L (Fig. 5.21) is connected to the bottom of a reservoir. Pressure drop and flow rate through this tube are used to determine the viscosity.

To derive the viscosity relation, the following assumptions are made:

- no velocity in the r and θ directions (Fig. 5.21),
- the polymer is incompressible, and
- fully developed, steady, isothermal, laminar flow.

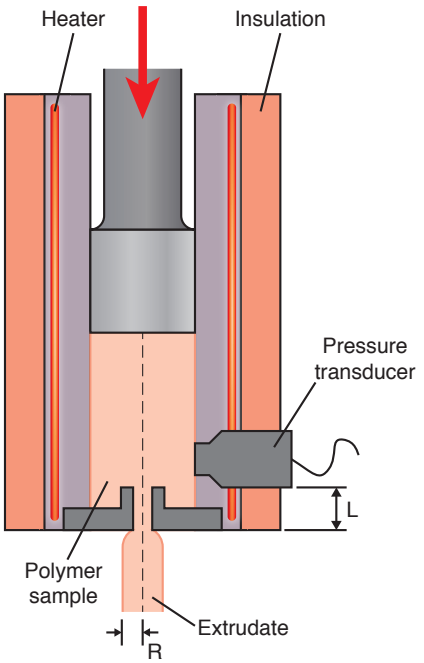

Figure 5.29 Schematic diagram of a capillary viscometer

The capillary viscometer can be modeled using the z-component of the equation of motion in terms of stress, τ, as

$$0 = \frac{dp}{dz} + \frac{1}{r}\frac{d}{dr}\left(r\tau_{rz}\right) \tag{5.61}$$

where,

$$\frac{dp}{dz} = \frac{p_0 - p_L}{L} \tag{5.62}$$

Integrating for the shear stress term gives:

$$\tau_{rz} = \frac{\left(p_0 - p_L\right)r}{2L} + \frac{C_1}{r} \tag{5.63}$$

The constant C_1 is taken to be zero because the stress cannot be infinite at the tube axis.

5.5.3 Computing Viscosity Using the Bagley and Weissenberg-Rabinowitsch Equations

At the wall the shear stress is:

$$\tau_{r=R} = \tau_w = \frac{R}{2}\frac{\left(p_0 - p_L\right)}{L} = \frac{R}{2}\frac{\Delta p}{L} \tag{5.64}$$

Equation 5.64 requires that the capillary be sufficiently long to assure a fully developed flow where end effects are insignificant. However, due to end effects the actual pressure profile along the length of the capillary exhibits a curvature. The effect is shown schematically in Fig. 5.30 [52] and was corrected by Bagley [53] using the end correction e as,

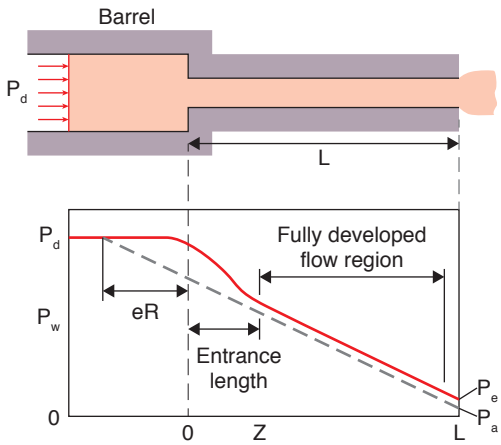

Figure 5.30 Entrance effects in a typical capillary viscometer

$$\tau_w = \frac{1}{2}\frac{\left(p_0 - p_L\right)}{\left(L/R + e\right)} \tag{5.65}$$

The correction factor e at a specific shear rate can be found by plotting pressure drop for various capillary L/D ratios as shown in Fig. 5.31 [52].

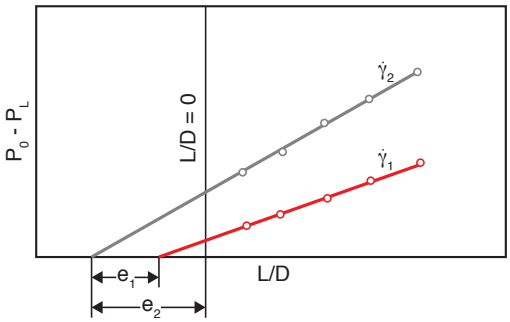

Figure 5.31 Bagley plots for two shear rates

The equation for shear stress can now be written as

$$\tau_{rz} = \frac{r}{R}\tau_w \tag{5.66}$$

To obtain the shear rate at the wall, $\frac{dv_z}{dr}$, the Weissenberg-Rabinowitsch [54] equation can be used

$$-\frac{dv_z}{dr} = \dot{\gamma}_w = \frac{1}{4}\dot{\gamma}_{aw}\left(3 + \frac{d\left(\ln Q\right)}{d\left(\ln \tau\right)}\right) \tag{5.67}$$

where, $\dot{\gamma}_{aw}$ is the apparent or Newtonian shear rate at the wall and is written as

$$\dot{\gamma}_{aw} = \frac{4Q}{\pi R^3} \tag{5.68}$$

The shear rate and shear stress at the wall are now known. Therefore, using the measured values of the flow rate, Q, and the pressure drop, $p_0 - p_L$, the viscosity can be calculated using

$$\eta = \frac{\tau_w}{\dot{\gamma}_w} \tag{5.69}$$

5.5.4 Viscosity Approximation Using the Representative Viscosity Method

A simplified method to compute viscosity, developed by Schümmer and Worthoff [55], takes advantage of the fact that Newtonian and shear thinning materials have a common streamline at which the strain rate is the same. This is schematically represented in Fig. 5.32, where the common streamline is located at r_s. The posi-

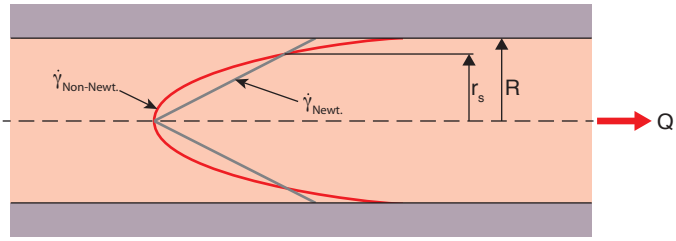

Figure 5.32 Strain rate distribution in Newtonian and non-Newtonian fluids flowing through a capillary

tion of that streamline is related to the power law index and varies between 0.7715 R and 0.8298 R for power law indices between 1.4 and 0.25. A close approximation is given by[13]

$$r_s \approx \frac{\pi}{4} R = 0.7854\ R \tag{5.70}$$

and the strain rate at that point is given by

$$\bar{\dot{\gamma}} = \frac{4}{\pi} \frac{Q}{R^4} r_s \approx \frac{Q}{R^3} \tag{5.71}$$

The shear stress at the location r_s can be calculated using

$$\bar{\tau} = \left(\frac{p_0 - p_L}{L} \right) \frac{r_s}{2} \approx \frac{\pi}{8} R \left(\frac{p_0 - p_L}{L} \right) \tag{5.72}$$

5.5.5 The Cone-Plate Rheometer

The cone-plate rheometer is often used to measure the viscosity and the primary and secondary normal stress coefficient functions as functions of shear rate and temperature. The geometry of a cone-plate rheometer is shown in Fig. 5.33. Because the angle θ_0 is very small, typically $< 5°$, the shear rate can be considered to be constant and is given by

$$\dot{\gamma}_{\theta\phi} = \frac{\Omega}{\theta_0} \tag{5.73}$$

where Ω is the angular velocity of the cone. The shear stress can also be considered constant and can be related to the measured torque, T,

$$\tau_{\theta\phi} = \frac{3T}{2\pi R^3} \tag{5.74}$$

The viscosity function can now be obtained from

13 The value $\pi/4$ was not mathematically derived but offers a significant simplification to the equations with a final error in viscosity of less than 5%.

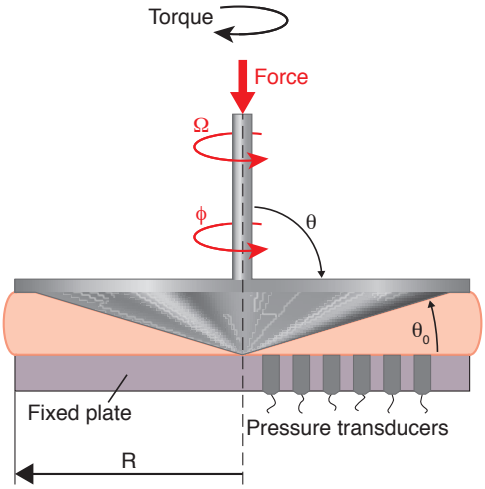

Figure 5.33 Schematic diagram of a cone-plate rheometer

$$\eta\left(\dot{\gamma}_{\theta\phi}\right)=\frac{\tau_{\theta\phi}}{\dot{\gamma}_{\theta\phi}} \tag{5.75}$$

The primary normal stress coefficient function, ψ_1, can be calculated by measuring the force, F, required to maintain the cone in place and can be computed using

$$\psi_1=\frac{2F}{\pi R^2\dot{\gamma}^2} \tag{5.76}$$

Although it is also possible to determine the secondary stress coefficient function from the normal stress distribution across the plate, it is very difficult to get accurate data.

5.5.6 The Couette Rheometer

Another rheometer commonly used in industry is the concentric cylinder or Couette flow rheometer schematically depicted in Fig. 5.34. The torque, T, and rotational speed, Ω, can be easily measured. The torque is related to the shear stress that acts on the inner cylinder wall and can be computed as follows:

$$\tau_i=\frac{T}{2\pi r_i^2 L} \tag{5.77}$$

If we consider a power-law fluid confined between the outer and inner cylinder walls of a Couette device, the shear rate at the inner wall can be computed using

$$\dot{\gamma}_i=\frac{2\Omega}{n\left(1-\left(r_i/r_0\right)^{2/n}\right)} \tag{5.78}$$

The power-law index can be determined with experimental data using

$$n=\frac{d\log\tau_i}{d\log\Omega} \tag{5.79}$$

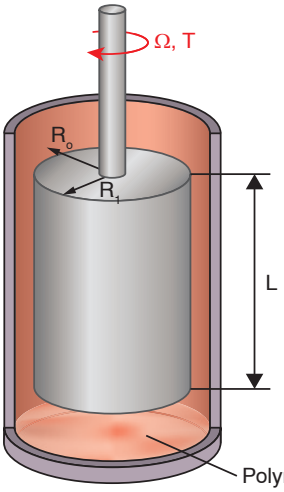

Figure 5.34 Schematic diagram of a Couette rheometer

Once the shear strain rate and stress are known, the viscosity can be computed using

$$\eta = \frac{\tau_i}{\dot{\gamma}} \tag{5.80}$$

The major sources of error in a concentric cylinder rheometer are the end-effects. One way of minimizing these effects is by providing a large gap between the inner cylinder end and the bottom of the closed end of the outer cylinder.

5.5.7 Extensional Rheometry

It should be emphasized that the shear behavior of polymers measured with the equipment described in the previous sections is by no means an indicator of the extensional behavior of polymer melts. Extensional rheometry is the least understood field of rheology. The simplest way to measure extensional viscosities is to stretch a polymer rod held at elevated temperatures at a speed that maintains a constant strain rate as the rod reduces its cross-sectional area. The viscosity can easily be computed as the ratio of instantaneous axial stress to elongational strain rate. The biggest problem when trying to perform this measurement is to hold the rod at its ends as it is pulled apart. The most common way to grab the specimen is with toothed rotary clamps to maintain a constant specimen length [56]. A schematic of Meissner's extensional rheometer incorporating rotary clamps is shown in Fig. 5.35 [56].

Another set-up that can be used to measure extensional properties avoiding clamping problems and without generating orientation during the measurement is the lubricating squeezing flow [57], which generates an equibiaxial deformation. A schematic of this apparatus is shown in Fig. 5.36.

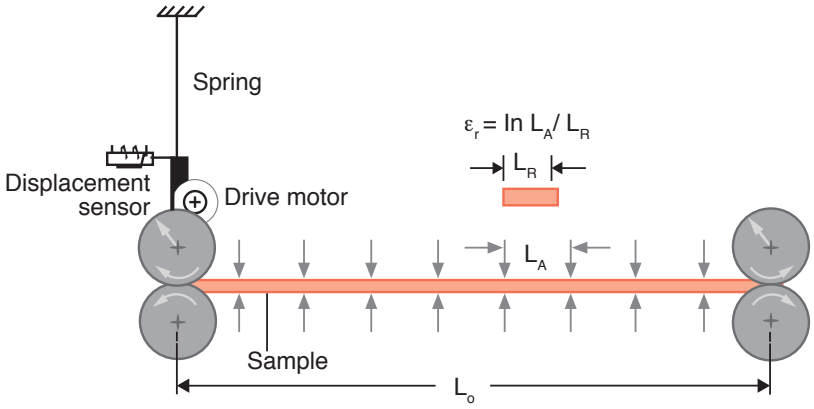

Figure 5.35 Schematic diagram of an extensional rheometer

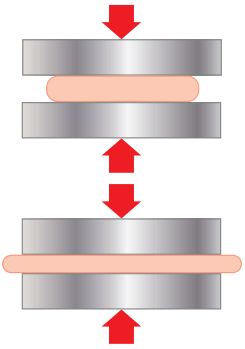

Figure 5.36 Schematic diagram of squeezing flow

It is clear from the apparatus description on Fig. 5.35 that carrying out tests to measure extensional rheometry is a very difficult task. One of the major problems arises because of the fact that, unlike with shear tests, it is not possible to achieve steady state condition with elongational rheometry tests. The reason is that the cross-sectional area of the test specimen is constantly diminishing. Figure 5.37 [56] shows this effect by comparing shear and elongational rheometry data for polyethylene.

Finally, another equibiaxial deformation test is carried out by blowing a bubble and measuring the pressure required and the size of the bubble during the test. This test has been successfully used to measure extensional properties of polymer membranes for blow molding and thermoforming applications. Here, a sheet is clamped between two plates with circular holes and a pressure differential is introduced to deform it. The pressure applied and the resulting deformation of the sheet are monitored with time and related to extensional properties of the material. Assuming an incompressible material, the instantaneous thickness of the sheet can be computed using the notation shown in Fig. 5.38:

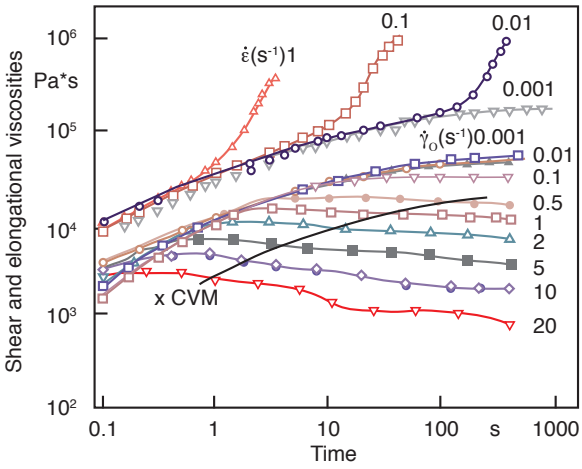

Figure 5.37 Development of elongational and shear viscosities during deformation for polyethylene samples

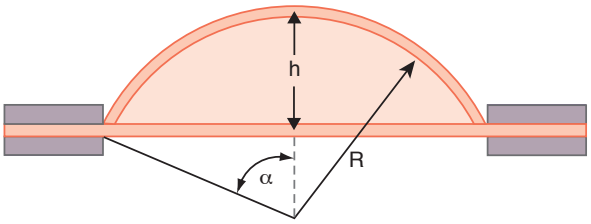

Figure 5.38 Schematic diagram of sheet inflation

$$t = t_0\left(\frac{D^2}{8Rh}\right) \tag{5.81}$$

The instantaneous radius of curvature of the sheet is related to bubble height by

$$R = \frac{D^2}{8h} + \frac{h}{2} \tag{5.82}$$

The biaxial strain can be computed using

$$\varepsilon_B = \ln\left(\frac{2\alpha R}{D}\right) \tag{5.83}$$

and the biaxial stress can be calculated using

$$\sigma_B = \frac{R\Delta P}{2t} \tag{5.84}$$

For more detail on extensional rheometry, beyond the scope of this book, the reader should refer to the literature [58].

5.6 Surface Tension

Although surface tension is generally not included in rheology chapters, it does play a significant role in the deformation of polymers during flow, especially during dispersive mixing of polymer blends. Surface tension, σ_s, between two materials appears as a result of different intermolecular interactions. In a liquid-liquid system, surface tension manifests itself as a force that tends to maintain the surface between the two materials to a minimum. Thus, the equilibrium shape of a droplet inside a matrix that is at rest is a sphere. When three phases touch, such as liquid, gas, and solid, they result in different contact angles depending on the surface tension between the three phases. Figure 5.39 schematically depicts three different cases. In case 1, the liquid perfectly wets the surface with a continuous spread, leading to a wetting angle of zero. Case 2, with moderate surface tension effects, shows a liquid that has a tendency to flow over the surface with a contact angle between zero and $\pi/2$. In case 3, with a high surface tension effect, the liquid does not wet the surface, which results in a contact angle greater than $\pi/2$. In Fig. 5.39, σ_s denotes the surface tension between the gas and the solid, σ_l the surface tension between the liquid and the gas, and σ_{sl} the surface tension between the solid and liquid. Using geometry one can write

$$\cos\theta = \frac{\sigma_s - \sigma_{sl}}{\sigma_l} \tag{5.85}$$

The wetting angle can be measured using simple techniques such as a projector, as shown schematically in Fig. 5.40. This technique, originally developed by Zisman [59], can be used in the ASTM D2578 [60] standard test. Here, droplets of known surface tension, σ_l, are applied to a film. The measured values of cos ϕ are plotted as a function of surface tension, σ_1, as shown in Fig. 5.41, and extrapolated to find the *critical surface tension*, σ_c, required for wetting.

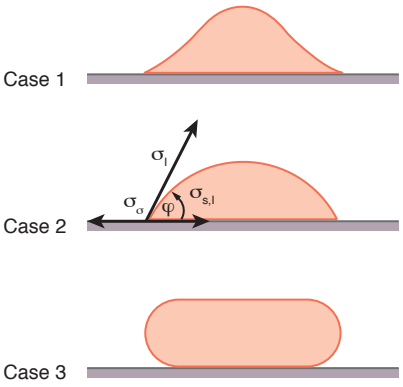

Figure 5.39 Schematic diagram of contact between liquids and solids with various surface tension effects

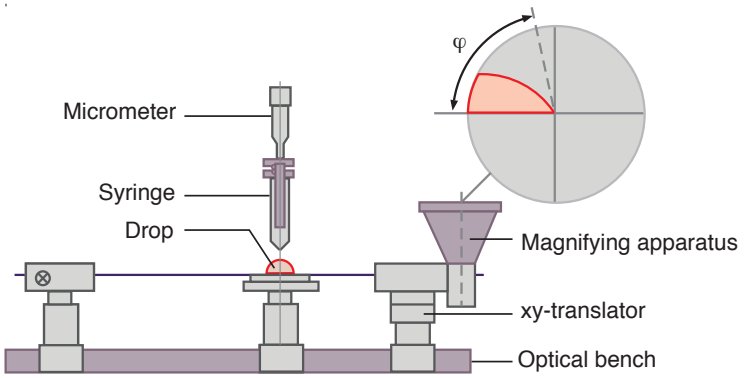

Figure 5.40 Schematic diagram of apparatus to measure contact angle between liquids and solids

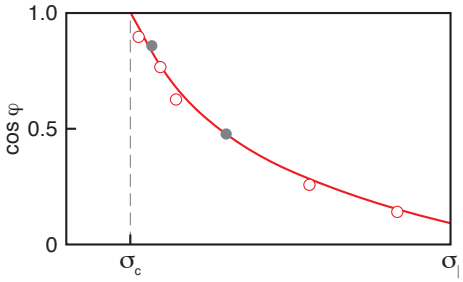

Figure 5.41 Contact angle as a function of surface tension

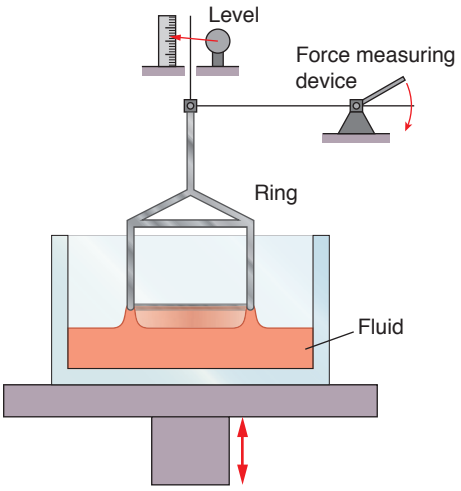

Figure 5.42 Schematic diagram of a tensiometer used to measure surface tension of liquids

For liquids of low viscosity, a useful measurement technique is the tensiometer, schematically represented in Fig. 5.42. Here, the surface tension is related to the force it takes to pull a platinum ring from a solution. Surface tension values for

selected polymers are listed in Table 5.6 [61], for some solvents in Table 5.7 [62], and surface tension values between polymer-polymer systems in Table 5.8 [61].

Furthermore, Hildebrand and Scott [63] found a relationship between the solubility parameter[14], δ, and surface tension, σ_s for polar and non-polar liquids. Their relationship can be written as [64]

$$\sigma_s = 0.24\delta^{2.33}V^{0.33} \tag{5.86}$$

where V is the molar volume of the material. The molar volume is defined by

$$V = \frac{M}{\rho} \tag{5.87}$$

where M is the molar weight. It should be noted that the values in Eqs. 5.86 and 5.87 must be expressed in cgs (centimeter-gram-second) units.

There are many areas in polymer processing and in engineering design with polymers in which surface tension plays a significant role; they include mixing of polymer blends, which is discussed in detail in Chapter 6 of this book, adhesion, treatment of surfaces to make them non-adhesive, and sintering.

During manufacturing it is often necessary to coat and crosslink a surface with a liquid adhesive or bonding material. To enhance adhesion it is often necessary to raise surface tension by oxidizing the surface, by creating COOH groups, using flames, etching or releasing electrical discharges. These approaches are also used when enhancing the adhesion properties of a surface before painting.

On the other hand it is often necessary to reduce adhesiveness of a surface, e.g., when releasing a product from the mold cavity or when coating a pan to give it nonstick properties. A material that is often used for this purpose is polytetrafluoroethylene (PTFE), mostly known by its trade name of teflon.

Table 5.6 Typical Surface Tension Values of Selected Polymers at 180 °C

Polymer	σ_s (N/m)	$\partial\sigma_s/\partial T$ (N/m/°C)
Polyamide resins (290 °C)	0.0290	–
Polyethylene (linear)	0.0265	-5.7×10^{-5}
Polyethylene terephthalate (290 °C)	0.027	–
Polyisobutylene	0.0234	-6.6×10^{-5}
Polymethyl methacrylate	0.0289	-7.6×10^{-5}
Polypropylene	0.0208	-5.8×10^{-5}
Polystyrene	0.0292	-7.2×10^{-5}
Polytetrafluoroethylene	0.0094	-6.2×10^{-5}
Polyvinyl acetate	0.0259	-6.6×10^{-5}

14 Solubility parameter is defined in Chapter 6.

Table 5.7 Surface Tension for Several Solvents

Solvent	σ_s (N/m)
n-Hexane	0.0184
Formamide	0.0582
Glycerin	0.0634
Water	0.0728

Table 5.8 Surface Tension between Polymers

Polymer	σ_s (N/m)	$\partial\sigma_s/\partial T$ (N/m/°C)	T (°C)
PE-PP	1.1×10^{-3}	–	140
PE-PS	5.1×10^{-3}	2.0×10^{-5}	180
PE-PMMA	9.0×10^{-3}	1.8×10^{-5}	180
PP-PS	5.1×10^{-3}	–	140
PS-PMMA	1.6×10^{-3}	1.3×10^{-5}	140

Finally, during the sintering process, surface tension plays a key role, especially when bringing together pairs of particles at high temperatures without applying pressure. Using the notation for the sintering process presented in Fig. 5.43, Menges and Reichstein [65] developed the relation

$$x^2 \approx \frac{\sigma_s D t}{\eta} \tag{5.88}$$

where, σ_s is the surface tension, t is time, and η the viscosity.

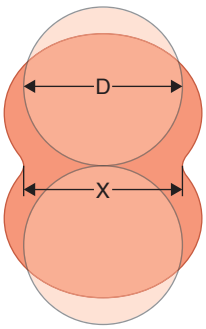

Figure 5.43 Schematic of the sintering process

Examples

1. Derive the equation that describes the pressure driven velocity field inside a tube of constant diameter (Eq. 5.43).

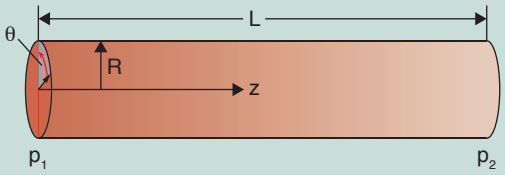

Figure 5.44 Tube geometry and coordinate system

In our solution scheme, we must first choose a coordinate system:

Next we must state our assumptions:

- no variations in the θ direction: $\frac{\partial}{\partial \theta} = u_\theta = 0$,
- steady state: $\frac{\partial}{\partial t} = 0$,
- no velocity in the radial direction: $u_r = 0$.

The continuity equation (Appendix I) reduces to

$$\frac{\partial u_z}{\partial z} = 0$$

Using the reduced continuity equation and the above assumptions, only the z-component of the equation of motion (Appendix I) is needed

$$0 = -\frac{\partial p}{\partial z} + \mu\left[\frac{1}{r}\frac{\partial}{\partial r}\left(r\frac{\partial u_z}{\partial r}\right)\right]$$

Letting $\frac{\partial p}{\partial z} = \frac{\Delta p}{L}$ and integrating gives

$$r\frac{\partial u_z}{\partial r} = \frac{r^2}{2\mu}\left(\frac{\Delta p}{L}\right) + C_1$$

Since $\frac{\partial v_z}{\partial r} = 0$ at $r = 0$, $C_1 = 0$. Integrating again, we get

$$u_z = \frac{r^2}{4\mu}\left(\frac{\Delta p}{L}\right) + C_2$$

Since $v_z = 0$ at $r = R$, the above equation becomes

$$u = \frac{R^2 \Delta p}{4\mu L}\left[1 - \left(\frac{r}{R}\right)^2\right]$$

2. Derive the equation that describes the annular flow in a wire coating process. The wire travels through the annulus at a speed, U, and we assume that the pressure inside the die equals atmospheric pressure. Use the notation presented in Fig. 5.45. Assume a power law viscosity.

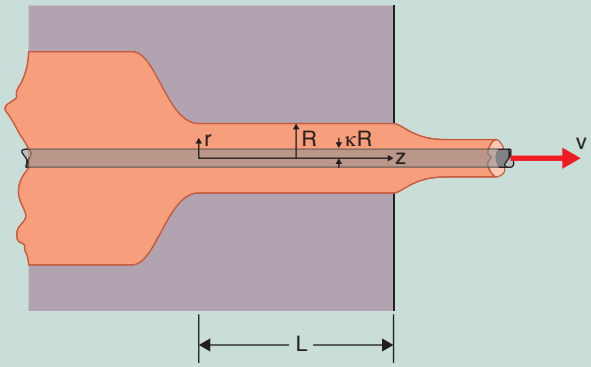

Figure 5.45 Wire coating process geometry and coordinate system

When solving this problem, we make similar assumptions as in Example 1. This results in $\frac{\partial}{\partial\theta} = u_\theta = 0$, $\frac{\partial}{\partial t} = 0$ and $u_r = 0$. Here too, the continuity equation reduces to

$$\frac{\partial u_z}{\partial z} = 0$$

However, the pressure gradient, $\frac{\partial p}{\partial z}$, can be neglected. Because this problem is non-Newtonian, we need to use the general equation of motion (Appendix 1). The z-component reduces to

$$\frac{\partial}{\partial r}\left(r\tau_{rz}\right) = 0$$

Next, we define the deviatoric stress as a function of rate of deformation using

$$\tau_{rz} = \eta\left(T,\dot{\gamma}\right)\dot{\gamma}_{rz} = m_0\dot{\gamma}^{n-1}\dot{\gamma}_{rz}$$

Since the only deformation that occurs is the shear deformation in the *rz*-plane, the magnitude of the rate of deformation tensor is given by

$$\dot{\gamma} = \dot{\gamma}_{rz} = \frac{\partial u_z}{\partial r}$$

The equation of motion, can now be written as

$$\frac{\partial}{\partial r}\left(rm_0\left[\frac{\partial u_z}{\partial r}\right]^n\right) = 0$$

Integrating this equation twice, and applying two boundary conditions, $v_z = V$ at $r = \kappa R$, and $v_z = 0$ at $r = R$ we get

$$u_z = U\frac{\left[\frac{r}{R}\right]^{1-\frac{1}{n}} - 1}{\kappa^{1-\frac{1}{n}} - 1}$$

3. Formulate a design equation for the end-fed sheeting die shown in Fig. 5.46 so that the extruded sheet is of uniform thickness. Your job is to specify the length of the approach zone or die land as a function of the manifold direction to achieve uniform flow. The manifold diameter is constant and the flow can be assumed isothermal with a Newtonian viscosity of η.

After assigning a coordinate system and assuming the notation presented in Fig. 5.47, the flow of the manifold can be represented using the Hagen-Poiseuille equation as

$$Q = \frac{\pi R^4}{8\eta}\left(-\frac{dp}{dz}\right)$$

and the flow in the die land (per unit width) using slit flow

$$q = \frac{h^3}{12\eta}\left(-\frac{dp}{dl}\right) = \frac{h^3}{12\eta}\left(\frac{p}{L_L}\right)$$

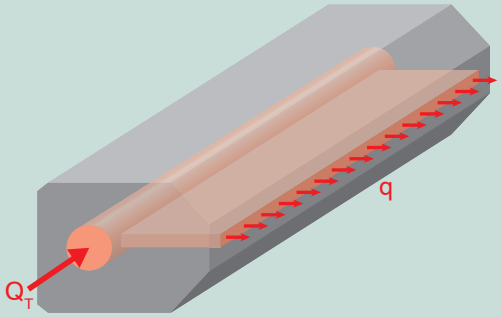

Figure 5.46 Schematic of an end-fed sheeting die

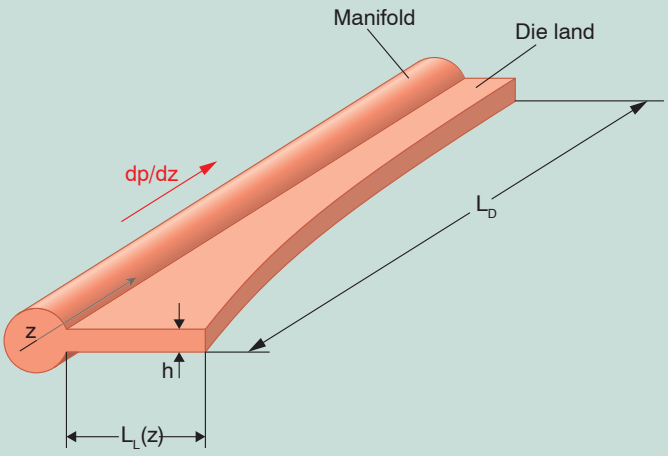

Figure 5.47 End-fed sheeting die coordinates and dimensions

A manifold that leads to a uniform sheet must deliver a constant throughput along the die land. Performing a flow balance within the differential element shown in Fig. 5.48 results in

$$Q(z+\Delta z)-Q(z)-q(z)\Delta z=0$$

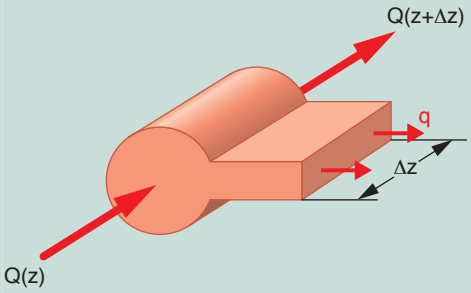

Figure 5.48 Differential element of an end-fed sheeting die

and letting $\Delta z \to 0$ results in

$$\frac{dQ}{dz}=-q=\text{constant}$$

If we integrate and let $Q=Q_T$ at $z=0$ and $Q=0$ at $z=L_D$ we get

$$Q(z)=Q_T\left(1-\frac{z}{L_D}\right)$$

Hence,

$$\frac{dQ}{dz}=-\frac{Q_T}{L_D}=-\frac{h^3}{12\eta}\frac{p(z)}{L_L(z)}$$

which results in

$$L_L(z)=\frac{h^3}{12\eta}\frac{L_D}{Q_T}p(z)$$

where $p(z)$ is unknown. We can now rewrite the manifold equation as

$$\frac{dp}{dz}=-\frac{8\eta}{\pi R^4}Q_T\left(1-\frac{z}{L_D}\right)$$

and then, letting $p=p_0$ at $z=0$, we get

$$p=p_0-\frac{8\eta Q_T L_D}{\pi R^4}\left[\left(\frac{z}{L_D}\right)-\frac{1}{2}\left(\frac{z}{L_D}\right)^2\right]$$

which leads to a land length of

$$L_L=\frac{h^3 L_D p_0}{12\eta Q_T}-\frac{2h^3 L_D^2}{3\pi R^4}\left[\left(\frac{z}{L_D}\right)-\frac{1}{2}\left(\frac{z}{L_D}\right)^2\right]$$

Problems

1. During the filling stage of the injection molding cycle, would the pressure requirements for a PP with a MFI = 10 be larger or smaller, relative to a PP with a MFI = 4? Why?
2. Model the viscosity of the PE-LD shown in Fig. 5.4 using the power law model and the Bird-Carreau model.
3. Derive the equation that predicts the volumetric throughput during pressure flow through a slit, assuming a Newtonian viscosity (Eq. 5.40).
4. Derive the Hagen-Poiseuille equation for a power law fluid (Eq. 5.46).
5. You are to extrude a polystyrene sheet through a die with a land length of 0.1 m. What is the maximum speed you can extrude the sheet if you are extruding polystyrene with the viscoelastic properties presented in Fig. 3.44 of Chapter 3.
6. The metering section of a single screw extruder can be modeled using a combination of shear flow and pressure flow between parallel plates. Derive the relation between volumetric throughput versus pressure build-up, Δp, in a melt extruder of a Newtonian fluid. Hint: Use the notation given in Chapter 6.
7. In Example 5.2, obtain an expression for the flow rate, coating thickness, and the axial force required to pull the wire through the die.
8. Formulate the design equation for an end-fed sheeting die such as the one in Example 3. Unlike the example, the new die should have a variable radius manifold as in Fig. 5.48. In this case, the axial distance from the manifold center to the die exit must be constant.

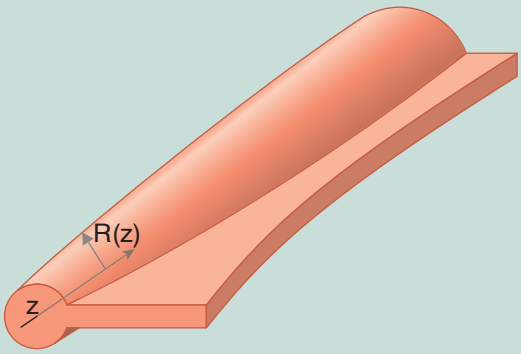

Figure 5.49 End-fed, variable diameter manifold sheeting die coordinates and dimensions

9. State the differences between a shear flow and an extensional flow.

10. The design department of an injection molding company has decided to increase the thickness of your product by a factor of 2. How does this modification affect the cooling time?
11. What assumptions must be made in order to use Eq. 5.40 to model the pressure flow through an annular die?
12. The tube in Example 1 is now set up vertically. How does this change the velocity profile if gravity is considered?

References

[1] Morrison, F., *Understanding Rheology*, Oxford University Press, New York, (2001).

[2] Dealy, J.M., and Larson, R.G., *Structure and Rheology of Molten Polymers*, Hanser Publishers, Munich, (2006).

[3] Tanner, R.I., *Engineering Rheology*, 2nd ed., Oxford University Press, New York, (2000).

[4] Bird, R.B., Armstrong, R.C., and Hassager, O., *Dynamics of Polymeric Liquids*, 2nd ed., Vol.1, John Wiley & Sons, New York, (1987).

[5] Giacomin, A.J., Osswald, T.A., and Rudolph, N.M., *Understanding Plastics Rheology*, Hanser Publishers, Munich, (2012).

[6] Bird, R.B., and J.M. Wiest, *Annu. Rev. Fluid Mech., 27,* 169, (1995).

[7] Tucker III, C.L., *Fundamentals of Computer Modeling for Polymer Processing*, Hanser Publishers, Munich, (1989).

[8] Osswald, T.A., *Understanding Polymer Processing,* Hanser Publishers, Munich, (2010).

[9] Laun, H.M., *Rheol. Acta, 17*, 1, (1978).

[10] Agassant, J.-F., Avenas, P., Sergent, J.-Ph., and Carreau, P.J., *Polymer Processing: Principles and Modeling*, Hanser Publishers, Munich, (1991).

[11] Vinogradov, G.V., Malkin, A.Y., Yanovskii, Y.G., Borisenkova, E.K., Yarlykov, B.V., and Berezhnaya, G.V., *J. Polym. Sci. Part A-2, 10*, 1061, (1972).

[12] Vlachopoulos, J., and Alam, M., *Polym. Eng. Sci., 12*, 184, (1972).

[13] Hatzikiriakos, S.G., and Dealy, J.M., *ANTEC Tech. Papers, 37*, 2311 (1991).

[14] Spencer, R.S., and Dillon, R.D., *J. Colloid Inter. Sci., 3*, 163, (1947).

[15] Vinogradov, G.V., Malkin, A.Y., Yanovskii, Y.G., Borisenkova, E.K., Yarlykov, B.V., and Berezhnaya, G.V., *J. Polym. Sci. Part A-2, 10*, 1061, (1972).

[16] Hatzikiriakos, S.G., and Dealy, J.M., *J. Rheol., 36*, 845, (1992).

[17] Denn, M.M., *Annu. Rev. Fluid Mech., 22*, 13, (1990).

[18] Ostwald, W., *Kolloid-Z.*, *36*, 99, (1925).

[19] de Waale, A., *Oil and Color Chem. Assoc. Journal, 6,* 33, (1923).

[20] Carreau, P.J., Ph.D. Thesis, University of Wisconsin-Madison, USA, (1968).

[21] Yasuda, K., Armstrong, R.C., and Cohen, R.E., *Rheol. Acta, 20*, 163, (1981).

[22] Menges, G., Wortberg, F., and Michaeli, W., *Kunststoffe, 68*, 71, (1978).

[23] Trouton, F.T., *Proc. Roy. Soc., A77*, (1906).

[24] Münstedt, H., *Rheol. Acta, 14,* 1077, 92, (1975).

[25] Han, C.D. and Lem, K.W., *J. Appl. Polym. Sci.,* 29, 1879, (1984).

[26] Castro, J.M. and Macosko, C.W., *AIChe J., 28*, 250, (1982).

[27] Castro, J.M., Perry, S.J., and Macosko, C.W., *Polymer Comm., 25*, 82, (1984).

[28] Einstein, A., *Ann. Physik, 19,* 549, (1906).

[29] Guth, E., and Simha, R., *Kolloid-Zeitschrift, 74*, 266, (1936).

[30] Guth, E., *Proceedings of the American Physical Society*, (1937); *Physical Review, 53*, 321, (1938).

[31] Batchelor, G.K., *Annu. Rev. Fluid Mech.*, *6*, 227, (1974).

[32] Geisbüsch, P., Ph.D. Thesis, IKV, RWTH-Aachen, Germany, (1980).

[33] Gupta, R.K., *Flow and Rheology in Polymer Composites Manufacturing*, Ed. S.G. Advani, Elsevier, Amsterdam, (1994).

[34] Milliken, W.J., and Powell, R.L., *Flow and Rheology in Polymer Composites Manufacturing*, Ed. S.G. Advani, Elsevier, Amsterdam, (1994).

[35] A.J. Giacomin, R.B. Bird, L.M. Johnson, and A.W. Mix, *J. Non-Newton. Fluid Mech.*, *166*, 1081–1099, (2012).

[36] Phan-Thien, N., *Understanding Viscoelasticity*, Springer Verlag, Berlin, (2010).

[37] Osswald, T.A., and Hernández-Ortiz, *Polymer Processing – Modeling and Simulation*, Hanser Publishers, Munich, (2006).

[38] Dietsche, L., and Dooley, J., *SPE ANTEC, 53*, 188, (1995).

[39] Dooley, J., and Hughes, K., *SPE ANTEC, 53*, 69, (1995).

[40] Holmes, L., Favero, J., and Osswald, T.A., *Polym. Eng. Sci,* DOI 10.1002/pen (2012).

[41] Baaijens, J.P.W., *Evaluation of Constitutive Equations for Polymer Melts and Solutions in Complex Flows*, Ph.D. Thesis, Eindhoven University of Technology, Eindhoven, The Netherlands, (1994).

[42] Luo, X.-L., and Mitsoulis, E., *J. Rheol., 33*, 1307, (1989).

[43] Lodge, A.S., *Elastic Liquids*, Academic Press, London, (1960).

[44] Kaye, A., *Non-Newtonian Flow in Incompressible Fluids*, CoA Note No.134, The College of Aeronautics, Cranfield, (1962).

[45] Bernstein, B., Kearsley, E., and Zapas, L., *Trans. Soc. Rheol., 7*, 391, (1963).

[46] Wagner, M.H., *Rheol. Acta, 18*, 33, (1979).

[47] Papanastasiou, A.C., Scriven, L.E., and Macosko, C.W., *J. Rheol.*, *27*, 387, (1983).

[48] Orbey, N., and Dealy, J. M., *Polym. Eng. Sci., 24*, 511, (1984).

[49] ASTM, 8.01, Plastics (I), ASTM, Philadelphia, (1994).

[50] Hagen, G. H. L., *Annalen der Physik, 46*, 423, (1839).

[51] Poiseuille, L. J., *Comptes Rendus 11*, 961, (1840).

[52] Dealy, J. M., *Rheometers for Molten Plastics*, Van Nostrand Reinhold Company, New York, (1982).

[53] Bagley, E. B., *J. Appl. Phys., 28*, 624, (1957).

[54] Rabinowitsch, B., *Z. Phys. Chem., 145*, 1, (1929).

[55] Schümmer, P., and Worthoff, R.H., *Chem. Eng. Sci., 38*, 759, (1978).

[56] Meissner, J., *Rheol. Acta, 10*, 230, (1971).

[57] Chatrei, Sh., Macosko, C.W., and Winter, H. H., *J. Rheol., 25* , 433, (1981).

[58] Macosko, C. W., *Rheology: Principles, Measurements and Applications*, VCH, (1994).

[59] Zisman, W. A., *Ind. Eng. Chem., 55*, 19, (1963).

[60] ASTM, 8.02, Plastics (II), ASTM, Philadelphia, (1994).

[61] Wu, S., *J. Macromol. Sci. – Revs. Macromol. Chem., C10*, 1, (1974).

[62] Owens, D. K. and Wendt, R. C., *J. Appl. Polymer Sci., 13*, 1741, (1969).

[63] Hildebrand, J. and Scott, R. L., *The Solubility of Non-Electrolytes*, 3rd ed., Reinhold Publishing Co., New York, (1949).

[64] Van Krevelen, D. W., *Properties of Polymers*, 4th ed., Elsevier, Amsterdam, (2009).

[65] Reichstein, H., Ph.D. thesis, IKV, RWTH-Aachen, (1982).

PART 2

Influence of Processing on Properties

6 Introduction to Processing

The mechanical properties and the performance of a finished product are always the result of a sequence of events. Manufacturing of a plastic part begins with material choice in the early stages of part design. Then follows processing, which determines the properties of the final part and freezes them into place. During design and manufacturing of any plastic product one must always be aware that material, processing, and design properties all go hand-in-hand and cannot be decoupled. This approach is often referred to as the six P's: polymer, processing, product, performance, post-consumer life, and profit. This chapter presents the most important polymer processing techniques available today[1]. Extrusion[2] is covered first, followed by mixing processes and injection molding[3]. Secondary shaping operations are discussed next. At the end of the chapter other processes, such as calendering, coating, compression molding, and rotational molding are presented.

6.1 Extrusion

During extrusion, a polymer melt is pumped through a shaping die and formed into a profile. This profile can be a plate, a film, a tube, or have any cross-sectional shape. Ram-type extruders were first built by J. Bramah in 1797 to extrude seamless lead pipes. The first ram-type extruders for rubber were built by Henry Bewley and Richard Brooman in 1845. In 1846, a patent for cable coating was filed for trans-gutta-percha and cis-hevea rubber and the first insulated wire was laid across the Hudson River for the Morse Telegraph Company in 1849. The first screw extruder was patented by Mathew Gray in 1879 for the purpose of wire coating. However, the screw pump can be attributed to Archimedes, and the actual inven-

1 An in-depth view of polymer processing is given by Tadmor and Gogos [1].

2 For further reading on extrusion we recommend Rauwendaal's book [2].

3 For further reading on injection molding we recommend Osswald, Turng, and Gramann [3].

tion of the screw extruder in polymer processing by A.G. DeWolfe of the United States dates to the early 1860s. The first extrusion of thermoplastic polymers was done at the Paul Troester Maschinenfabrik in Hannover, Germany in 1935.

Although ram and screw extruders are both used to pump highly viscous polymer melts through passages to generate specified profiles, they are based on different principles. The schematic in Fig. 6.1 shows the principles ruling ram extruders, screw extruders, and other pumping systems.

The ram extruder is a positive displacement pump based on the pressure gradient term of the equation of motion. Here, as the volume is reduced, the fluid is displaced from one point to the other, resulting in a pressure rise. The gear pump, widely used in the polymer processing industry, also works on this principle. On the other hand, a screw extruder is a viscosity pump that works based on the pressure gradient term and the deformation of the fluid, represented as the divergence of the deviatoric stress tensor in Fig. 6.1. The centrifugal pump, based on the fluid inertia, and the Roman aqueduct, based on the potential energy of the fluid, are also represented in the figure and are typical of low viscosity liquids.

In today's polymer industry, the most commonly used extruder is the single screw extruder, schematically depicted in Fig. 6.2. The single screw extruder can have

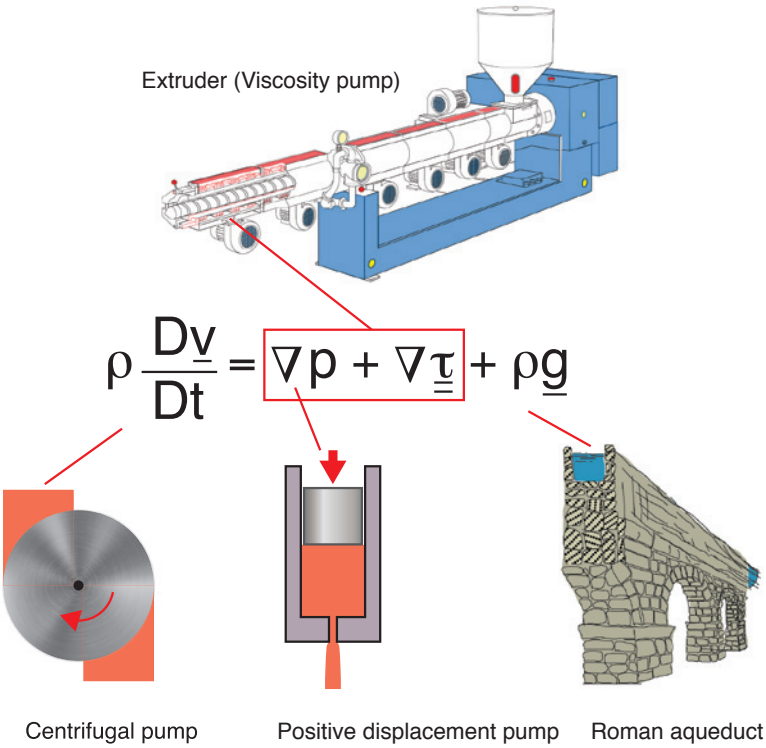

Figure 6.1 Schematic of pumping principles

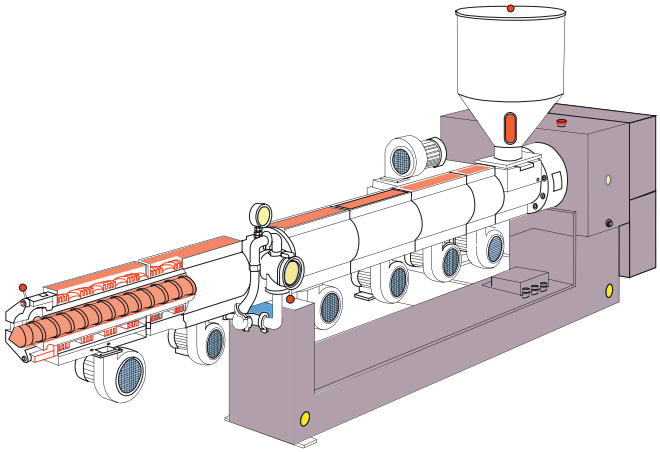

Figure 6.2 Schematic of a single screw extruder (Reifenhäuser)

either a smooth inside barrel surface, then it is called a conventional single screw extruder, or a grooved feed zone, then it is called a grooved feed extruder. In some cases, an extruder can have a degasing zone, required to extract moisture, volatiles, and other gases that form during the extrusion process.

Another important class of extruders are the twin screw extruders, schematically depicted in Fig. 6.3. Twin screw extruders may have co-rotating or counter-rotating screws, and the screws may be intermeshing or non-intermeshing. Twin screw extruders are primarily employed as mixing and compounding devices and as polymerization reactors. The mixing aspects of single and twin screw extruders are detailed later in this chapter.

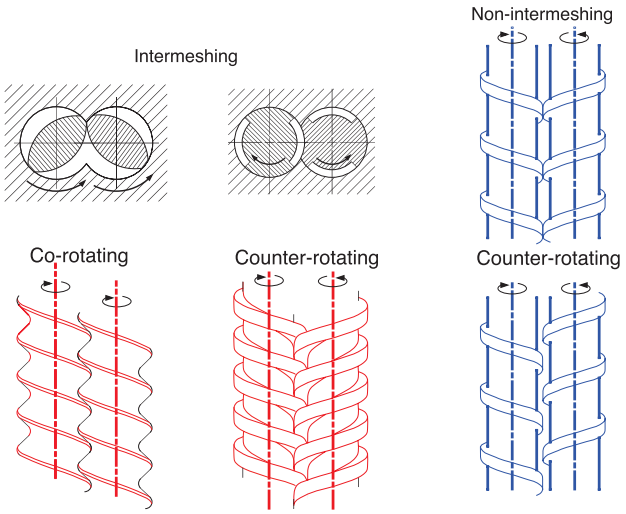

Figure 6.3 Schematic of different twin screw extruders

6.1.1 The Plasticating Extruder

The plasticating single screw extruder is the most common equipment in the polymer industry. It can be part of an injection molding unit but it can also be found in numerous other extrusion processes, including blow molding, film blowing, and wire coating. A schematic of a plasticating or three-zone, single screw extruder with its most important elements is given in Fig. 6.4. Table 6.1 presents typical extruder dimensions and relationships common in single screw extruders.

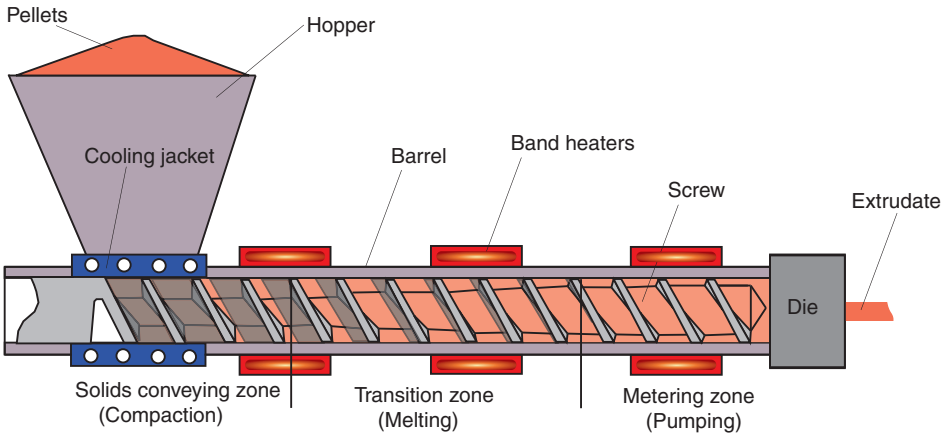

Figure 6.4 Schematic of a plasticating single screw extruder

Table 6.1 Typical Extruder Dimensions and Relationships (the Notations in Table 6.1 are Defined in Fig. 6.5.)

L/D	Length to diameter ratio
	20 or less for feeding or melt extruders
	25 for blow molding, film blowing, and injection molding
	30 or higher for vented extruders or high output extruders
D	Standard diameter
US (inches)	0.75, 1.0, 1.5, 2, 2.5, 3.5, 4.5, 6, 8, 10, 12, 14, 16, 18, 20, and 24
Europe (mm)	20, 25, 30, 35, 40, 50, 60, 90, 120, 150, 200, 250, 300, 350, 400, 450, 500, and 600
Φ	Helix angle
	17.65° for a square pitch screw where $L_s = D$
	New trend: $0.8 < L_s/D < 1.2$
h	Channel depth in the metering section
	(0.05–0.07) D for $D < 30$ mm
	(0.02–0.05) D for $D > 30$ mm

Table 6.1 Typical Extruder Dimensions and Relationships *(continued)*

β	Compression ratio: $h_{feed} = \beta h$ 2 to 4
δ	Clearance between the screw flight and the barrel 0.1 mm for $D < 30$ mm 0.15 mm for $D > 30$ mm
N	Screw speed 1–2 rev/s (60–120 rpm) for large extruders 1–5 rev/s (60–300 rpm) for small extruders
V_b	Barrel velocity (relative to screw speed) = πDN 0.5 m/s for most polymers 0.2 m/s for unplasticized PVC 1.0 m/s for LDPE

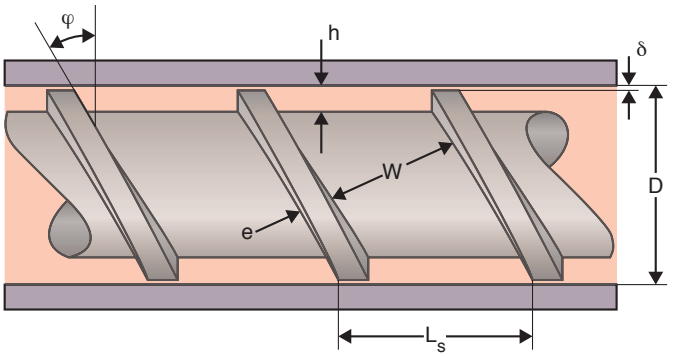

Figure 6.5 Schematic diagram of a screw section

The plasticating extruder can be divided into three main zones:

- The solids conveying zone
- The melting or transition zone
- The metering or pumping zone

The tasks of a plasticating extruder are to:

- Transport the solid pellets or powder from the hopper to the screw channel
- Compact the pellets and move them down the channel
- Melt the pellets
- Mix the polymer into a homogeneous melt
- Pump the melt through the die

The pumping capability and characteristic of an extruder can be represented with sets of die and screw characteristic curves. Figure 6.6 presents such curves for a conventional (smooth barrel), single screw extruder.

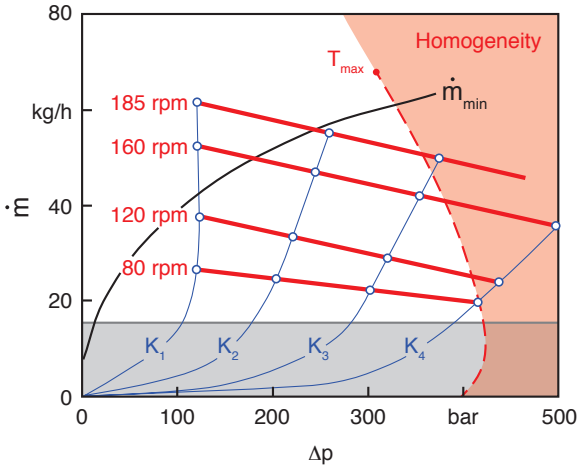

Figure 6.6 Screw and die characteristic curves for a 45 mm diameter extruder for an LDPE

The die characteristic curves are K_1, K_2, K_3, and K_4 in ascending order of die restriction. Here, K_1 represents a low resistance die, such as for a thick plate, and K_4 represents a restrictive die, such as is used for film. The different screw characteristic curves represent different screw rotational speeds. In a screw characteristic curve the point of maximum throughput and no pressure build-up is called the point of open discharge. This occurs when there is no die. The point of maximum pressure build-up and no throughput is called the point of closed discharge. This occurs when the extruder is plugged.

Shown in Fig. 6.6 are also lines that represent critical aspects encountered during extrusion. The curve labeled T_{max} represents the conditions at which excessive temperatures are reached as a result of viscous heating. The feasibility line $(\dot{m}_{min})$ represents the throughput required for an economically feasible system. The processing conditions to the right of the homogeneity line render a thermally and physically heterogeneous polymer melt.

6.1.1.1 The Solids Conveying Zone

The task of the solids conveying zone is to move the polymer pellets or powders from the hopper to the screw channel. Once the material is in the screw channel, it is compacted and transported down the channel. The process to compact the pellets and to move them can only be accomplished if the friction at the barrel surface exceeds the friction at the screw surface. This can be visualized assuming the material inside the screw channel to be a nut sitting on a screw. As we rotate the screw without applying outside friction, the nut (polymer pellets) rotates with the screw without moving in the axial direction. As we apply outside forces (barrel friction), the rotational speed of the nut is less than the speed of the screw, causing

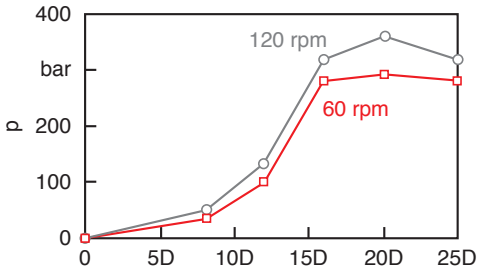

Figure 6.7 Conventional extruder pressure distribution

it to slide in the axial direction. Virtually, the solid polymer is now "unscrewed" from the screw.

To maintain a high coefficient of friction between the barrel and the polymer, the feed section of the barrel must be cooled, usually with cold water cooling lines. The frictional forces also result in a pressure rise in the feed section. This pressure compresses the solids bed, which continues to travel down the channel as it melts in the transition zone. Figure 6.7 presents the pressure build-up in a conventional, smooth barrel extruder. In these extruders, most of the pressure required for pumping and mixing is generated in the metering section.

The simplest mechanism for ensuring high friction between the polymer and the barrel surface is grooving its surface in the axial direction [4, 5]. Extruders with a grooved feed section where developed by Menges and Predöhl [4, 5] in 1969, and are called grooved feed extruders. To avoid excessive pressures that can lead to barrel or screw failure, the length of the grooved barrel section must not exceed 3.5 D. A schematic diagram of the grooved section in a single screw extruder is presented in Fig. 6.8. The key factors that propelled the development and refine-

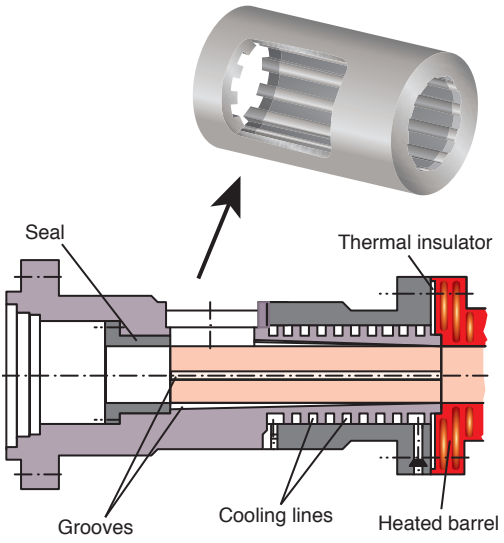

Figure 6.8 Schematic diagram of the grooved feed section of a single screw extruder

ment of the grooved feed extruder were processing problems, excessive melt temperature, and reduced productivity encountered with materials that exhibit high viscosity and low coefficients of friction, such as high molecular weight polyethylenes and polypropylenes.

In a grooved feed extruder, the conveying and pressure build-up tasks are assigned to the feed section. Figure 6.9 shows the pressure build-up in a single screw extruder with a grooved feed section. The high pressures in the feed section lead to the main advantages over conventional systems. Grooved feed systems achieve higher productivity, and higher melt flow stability and pressure invariance. This is demonstrated by the screw characteristic curves shown in Fig. 6.10; these screw characteristic curves represent a 45 mm diameter grooved feed extruder with comparable mixing sections and die openings as the one shown in Fig. 6.6.

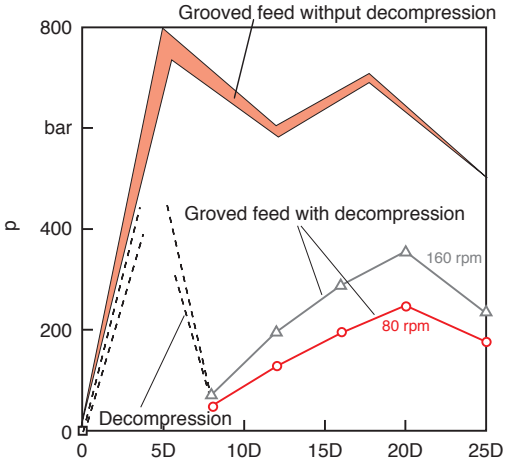

Figure 6.9 Grooved feed extruder pressure distribution

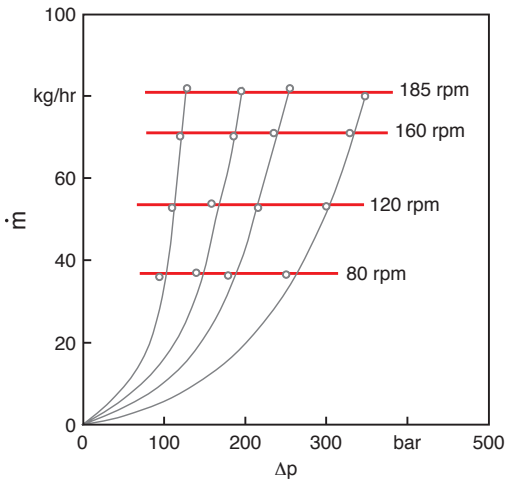

Figure 6.10 Screw and die characteristic curves for a grooved feed 45 mm diameter extruder processing an LDPE

The behavior of the two extruders in Figs. 6.6 and 6.10 are best compared if the throughput and the pressure build-up are non-dimensionalized. The dimensionless throughput is

$$\hat{m} = \frac{\dot{m}}{\rho N D^3} \tag{6.1}$$

and the dimensionless pressure build-up is

$$\Delta\hat{p} = \frac{\Delta p D}{m N^n L_c} \tag{6.2}$$

where L represents the total channel length and for a 25 L/D extruder is

$$L_c = \frac{25D}{\sin(\phi)} \tag{6.3}$$

where ϕ is assumed to be 17.65° (square pitch). Figure 6.11 presents the results shown in Figs. 6.6 and 6.10 after throughput and pressure build-up were rendered dimensionless using Eqs. 6.2 and 6.3. The figure clearly shows the higher productivity of the grooved feed extruder for which the throughput is at least 50% higher than that observed with the conventional system for a comparable application. Used with care, Fig. 6.11 can also be used for scale-up.

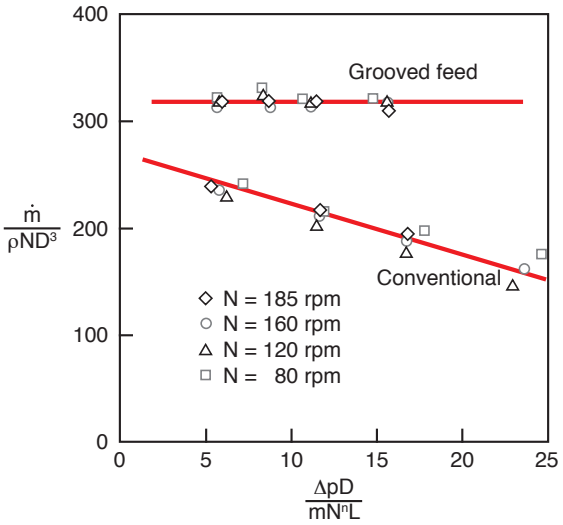

Figure 6.11 Dimensionless screw characteristic curves for conventional and grooved feed extruders

6.1.1.2 The Melting Zone

The melting or transition zone is the portion of the extruder where the material melts. The length of this zone is a function of the material properties, screw geometry, and processing conditions. During melting, the size of the solid bed shrinks

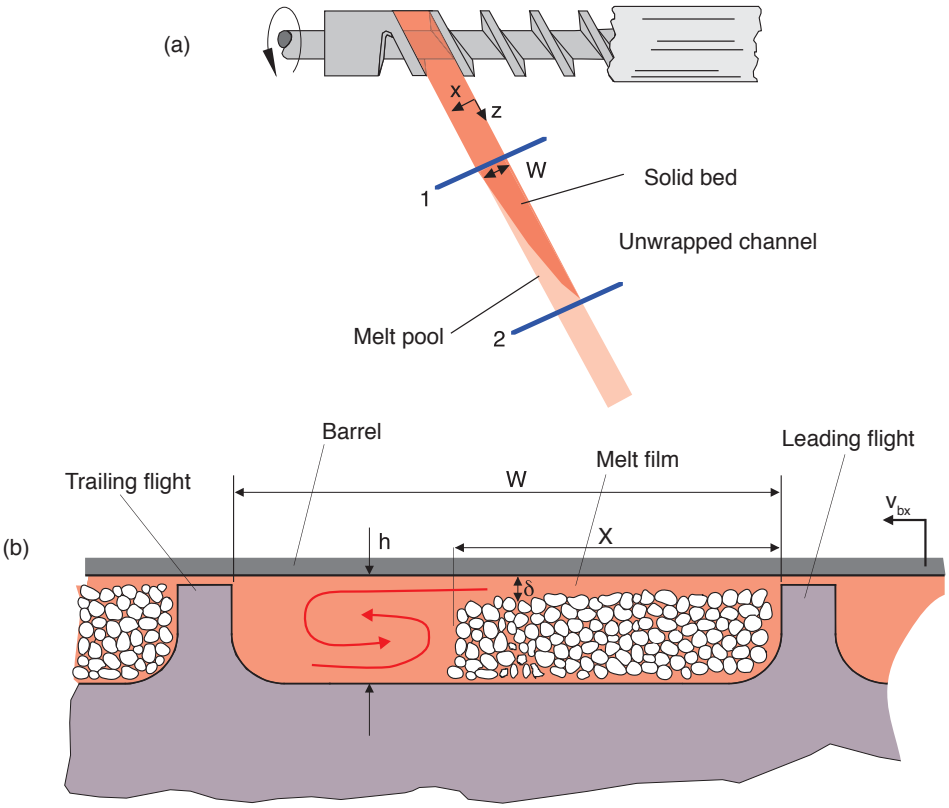

Figure 6.12 (a) Solids bed in an unwrapped screw channel and (b) screw channel cross section

as a melt pool forms at its side, as depicted in Fig. 6.12 (a), which shows the polymer unwrapped from the screw channel.

Figure 6.12 (b) presents a cross section of the screw channel in the melting zone. The solid bed is pushed against the leading flight of the screw as freshly molten polymer is wiped from the melt film into the melt pool by the relative motion between the solids bed and the barrel surface.

Knowing where the melt starts and ends is important when designing a screw for a specific application. The most widely used model to predict melting in a plasticating single screw extruder is the well-known Tadmor Model [5]. Using the Tadmor Model, the solid bed profile in the single screw extruder can be accurately predicted. Figure 6.13 presents the experimental and predicted solids bed profile of an LDPE in a single screw extruder. The material properties and processing conditions used in the calculations are given in Table 6.2.

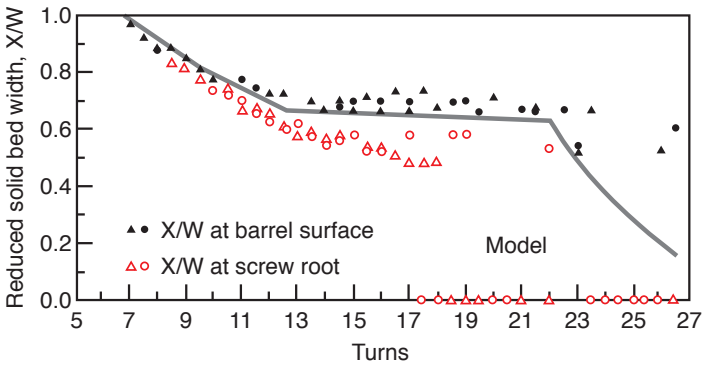

Figure 6.13 Predicted (Tadmor Model) and experimental solids bed profile

Table 6.2 Extruder Parameters, Processing Conditions, and Material Properties for the Solids Bed Profile Shown in Fig. 6.13.

Extruder Geometry:	
	Square pitch screw, D = 63.5 mm, L/D = 26.5, W = 54.16 mm
	Feed zone – 12.5 turns h_1= 9.4 mm
	Transition zone – 9.5 turns h_1= 9.4 mm h_2= 3.23 mm
	Metering zone – 4.5 turns h_2= 3.23 mm
Processing Conditions:	
	T_0= 24 °C T_b= 149 °C N = 60 rpm Δp = 204 bar $\dot{m}$ = 61.8 kg/h
Material properties (LDPE):	
	Viscosity: n = 0.345 a = 0.01 °C^{-1} m_0= 5.6 × 10^4 Pa-s^n T_m = 110 °C
	Thermal:
	k_m= 0.1817 W/m°C C_m= 2.596 kJ/kg°C C_s= 2.763 kJ/kg°C
	ρ_{bulk}= 595 kg/m^3 ρ_s= 915.1 kg/m^3 ρ_m= 852.7 + 5.018 × 10^{-7}p − 0.4756 T
	λ= 129.8 kJ/kg

From experiment to experiment there are always large variations in the experimental solids bed profiles. The variations in this section of the extruder are caused by slight variations in processing conditions and by the uncontrolled solids bed break-up towards the end of melting. This effect can be eliminated by introducing a screw with a barrier flight that separates the solids bed from the melt pool. The Maillefer screw and the barrier screw in Fig. 6.14 are commonly used to ensure high quality and reproducibility. The Maillefer screw maintains a constant solids bed width, using the melt-removal mechanism during melting most effectively, while the barrier screw uses a constant channel depth with a gradually decreasing solids bed width.

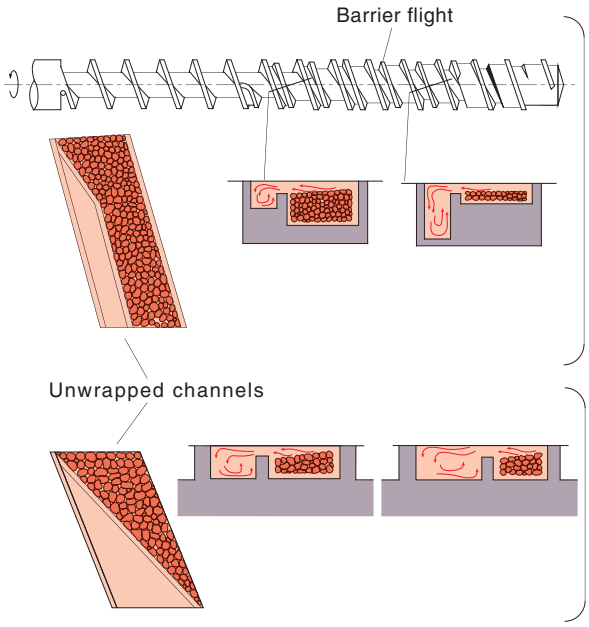

Figure 6.14 Schematic diagram of screws with different barrier flights

6.1.1.3 The Metering Zone

The metering zone is the most important section in melt extruders and conventional single screw extruders that rely on it to generate sufficient pressures for pumping. The pumping capabilities in the metering section of a single screw extruder can be estimated by solving the equation of motion with appropriate constitutive laws. For a Newtonian fluid in an extruder with a constant channel depth, the screw and die characteristic curves for different cases are represented in Fig. 6.15. The figure shows the influence of the channel depth on the screw charac-

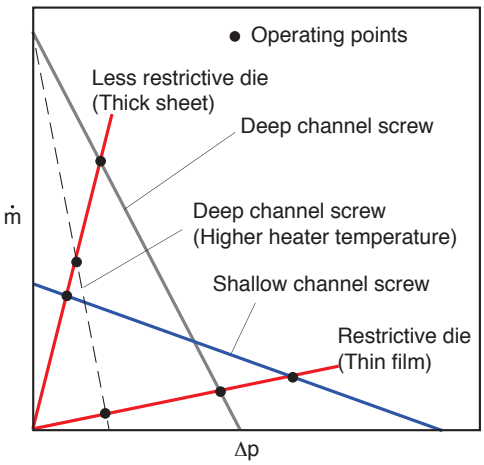

Figure 6.15 Screw characteristic curves (Newtonian fluids)

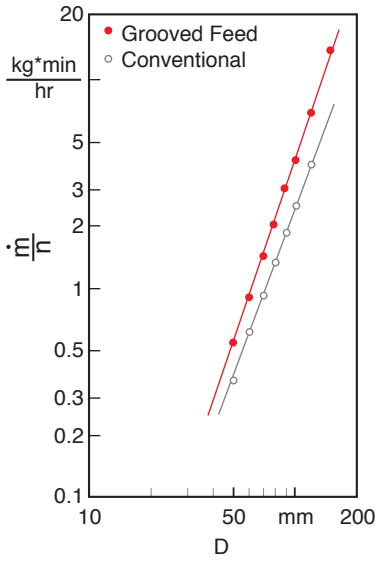

Figure 6.16 Throughput for conventional and grooved feed extruders

teristic curves. A restrictive extrusion die would clearly work best with a shallow channel screw, and a less restrictive die would render the highest productivity with a deep channel screw.

In both the grooved barrel and the conventional extruder, the diameter of the screw determines the metering or pumping capacity of the extruder. Figure 6.16 presents typical normalized mass throughput as a function of screw diameter for both systems.

6.1.2 Extrusion Dies

The extrusion die shapes the polymer melt into its final profile. The extrusion die is located at the end of the extruder and is used to extrude

- Flat films and sheets
- Pipes and tubular films (e. g., for bags)
- Filaments and strands
- Hollow profiles (e. g., for window frames)
- Open profiles

As shown in Fig. 6.17, depending on the functional needs of the product, several rules of thumb should be followed when designing an extruded plastic profile. These are:

- Avoid thick sections. Thick sections add to the material cost and increase sink marks caused by shrinkage.

- Minimize the number of hollow sections. Hollow sections add to die cost and make the die more difficult to clean.
- Generate profiles with constant wall thickness. Constant wall thickness in a profile makes it easier to control the thickness of the final profile and results in a more even crystallinity distribution in semi-crystalline profiles.

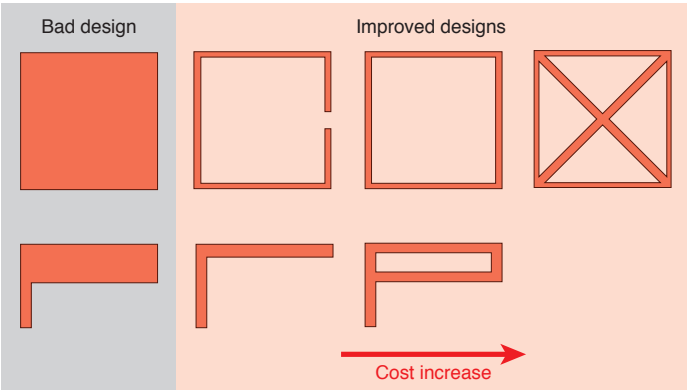

Figure 6.17 Extrusion profile designs

6.1.2.1 Sheeting Dies

One of the most widely used extrusion dies is the coat-hanger sheeting die. A sheeting die, such as depicted in Fig. 6.18, is formed by the following elements:

- Manifold: evenly distributes the melt to the approach or land region
- Approach or land: carries the melt from the manifold to the die lips
- Die lips: perform the final shaping of the melt
- Flex lips: for fine tuning when generating a uniform profile

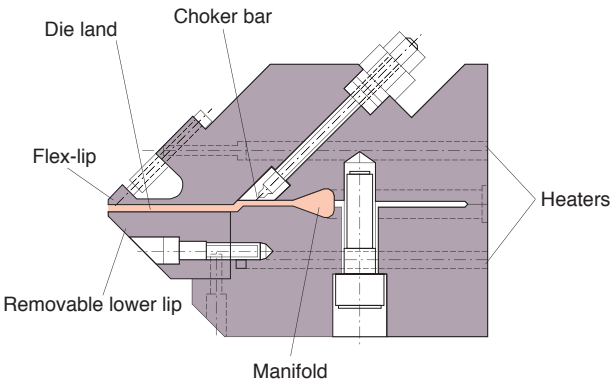

Figure 6.18 Cross section of a coat-hanger die

To generate a uniform extrudate geometry at the die lips, the geometry of the manifold must be specified appropriately. Figure 6.19 presents the schematic of a coat-hanger die with a pressure distribution that corresponds to a die that renders a uniform extrudate. It is important to mention that the flow though the manifold and the approach zone depend on the non-Newtonian properties of the polymer extruded. So the design of the die depends on the shear thinning behavior of the polymer. Hence, a die designed for one material does not necessarily work for another.

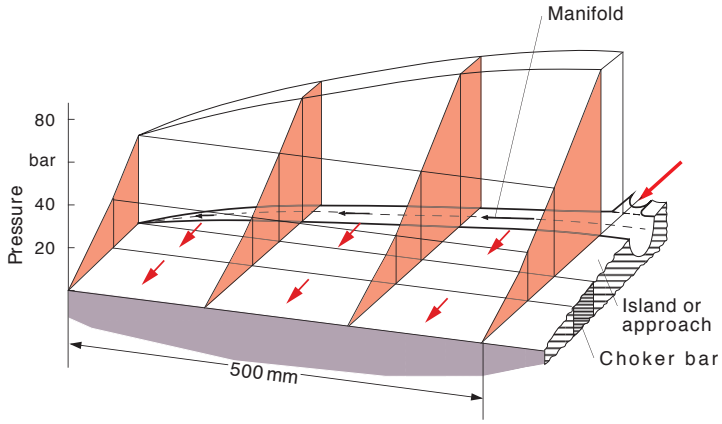

Figure 6.19 Pressure distribution in a coat-hanger die

6.1.2.2 Tubular Dies

In a tubular die, the polymer melt exits through an annulus. These dies are used to extrude plastic pipes and tubular film. The film blowing operation is discussed in more detail later in this chapter.

The simplest tubing die is the spider die, depicted in Fig. 6.20. Here, a symmetric mandrel is attached to the body of the die by several legs. The polymer must flow around the spider legs, causing weld lines along the pipe or film. These weld lines, visible streaks along the extruded tube, are weaker regions.

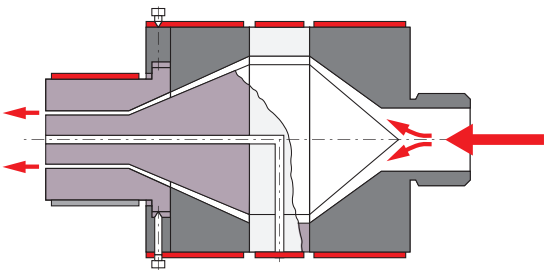

Figure 6.20 Schematic of a spider leg tubing die

To overcome weld line problems, a cross-head tubing die is often used. Here, the die design is similar to that of the coat-hanger die, but wrapped around a cylinder. This die is depicted in Fig. 6.21. Because the polymer melt must flow around the mandrel, the extruded tube exhibits one weld line. In addition, although the eccentricity of a mandrel can be controlled using adjustment screws, there is no flexibility to perform fine tuning such as in the coat-hanger die. This can result in tubes with uneven thickness distributions.

The spiral die, commonly used to extrude tubular blown films, eliminates weld line effects and produces a thermally and geometrically homogeneous extrudate. The polymer melt in a spiral die flows through several feed ports into independent spiral channels wrapped around the circumference of the mandrel. This type of die is schematically depicted in Fig. 6.22.

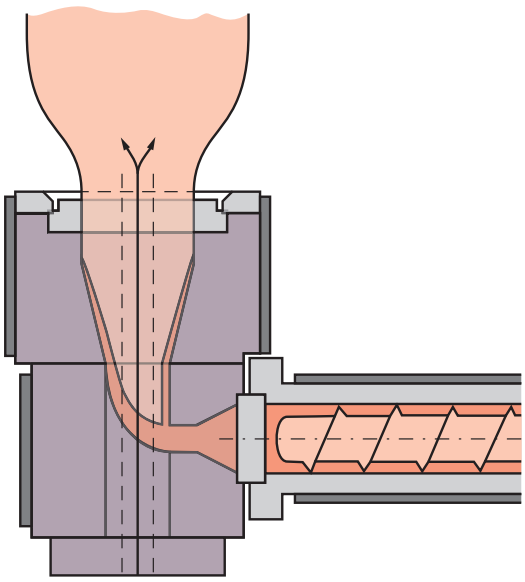

Figure 6.21 Schematic of a cross-head tubing die used in film blowing

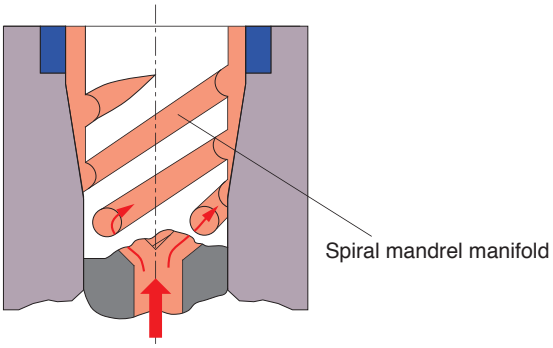

Figure 6.22 Schematic of a spiral die

6.2 Mixing Processes

Today, most processes involve some form of mixing. As discussed in the previous section, an integral part of a screw extruder is a mixing zone. In fact, most twin screw extruders are primarily used as mixing devices. Similarly, the plasticating unit of an injection molding machine often has a mixing zone. This is important because the quality of the finished product in almost all polymer processes depends in part on how well the material was mixed. Both the material properties and the formability of the compound into shaped parts are highly influenced by the mixing quality. Hence, a better understanding of the mixing process helps to optimize processing conditions and to increase part quality.

The process of polymer blending or mixing is accomplished by distributing or dispersing a minor or secondary component within a major component serving as a matrix. The major component can be thought of as the continuous phase and the minor components as distributed or dispersed phases in the form of droplets, filaments, or agglomerates.

When creating a polymer blend, one must always keep in mind that the blend will probably be re-melted in subsequent processing or shaping processes. For example, a rapidly cooled system, frozen as a homogenous mixture, can separate into phases because of coalescence when re-heated. For all practical purposes, such a blend is not processable. To avoid this problem, compatibilizers, which are macromolecules used to ensure compatibility in the boundary layers between the two phases, are commonly added [6].

The mixing can be distributive or dispersive. The morphology development of polymer blends is determined by three competing mechanisms: distributive mixing, dispersive mixing, and coalescence. Figure 6.23 presents a model, proposed by Macosko and co-workers [6], that helps us visualize the mechanisms governing morphology development in polymer blends. The process begins when a thin tape of polymer is melted away from the pellet. As the tape is stretched, surface tension causes it to rip and form threads. These threads stretch and reduce in radius, until surface tension becomes significant enough to cause Rayleigh disturbances, which break the threads down into small droplets.

There are three general categories of mixtures that can be created:

- Homogeneous mixtures of compatible polymers,
- Single phase mixtures of partly incompatible polymers, and
- Multi-phase mixtures of incompatible polymers.

Table 6.3 lists examples of compatible, partially incompatible, and incompatible polymer blends.

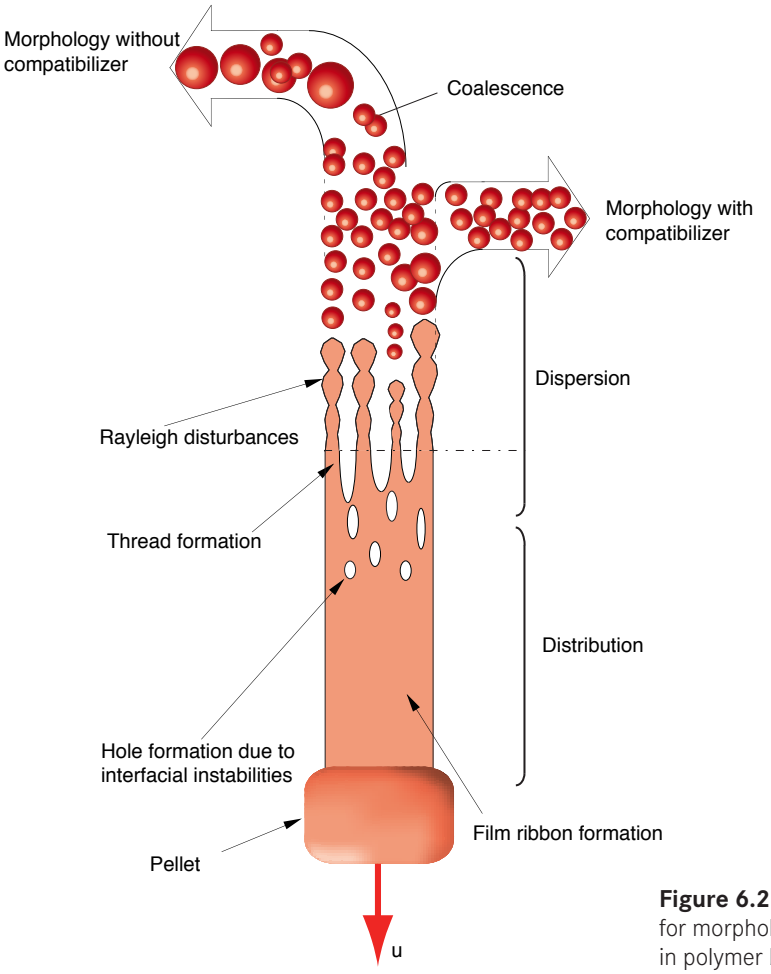

Figure 6.23 Mechanism for morphology development in polymer blends

Table 6.3 Common Polymer Blends

Compatible polymer blends
Natural rubber and polybutadiene
Polyamides (e.g., PA 6 and PA 66)
Polyphenylene ether (PPE) and polystyrene
Partially incompatible polymer blends
Polyethylene and polyisobutylene
Polyethylene and polypropylene (5% PE in PP)
Polycarbonate and polybutylene terephthalate
Incompatible polymers blends
Polystyrene/polyethylene blends
Polyamide/polyethylene blends
Polypropylene/polystyrene blends

6.2.1 Distributive Mixing

Distributive mixing or laminar mixing of compatible liquids is usually characterized by the distribution of the droplet or secondary phase within the matrix. This distribution is achieved by imposing large strains on the system such that the interfacial areas between the two or more phases increase and the local dimensions, or striation thicknesses, of the secondary phases decrease. This concept is shown schematically in Fig. 6.24 [7]. The figure shows a Couette flow device with the secondary component having an initial striation thickness of δ_0. As the inner cylinder rotates, the secondary component is distributed through the system with constantly decreasing striation thickness; striation thickness depends on the strain rate of deformation, which makes it a function of position. The total strain that a droplet or secondary phase undergoes is defined by

$$\gamma(\tau) = \int_0^{\tau} \dot{\gamma}(t)\,dt \tag{6.4}$$

where $\dot{\gamma}$ is the magnitude of the strain rate of deformation defined by Eqs. 5.7 and 5.8, and τ is an arbitrary point in time. For a sphere, which is deformed into an ellipsoid, the total strain can be related to the striation thickness using

$$\delta = 2R\left(1+\gamma^2\right)^{-0.25} \tag{6.5}$$

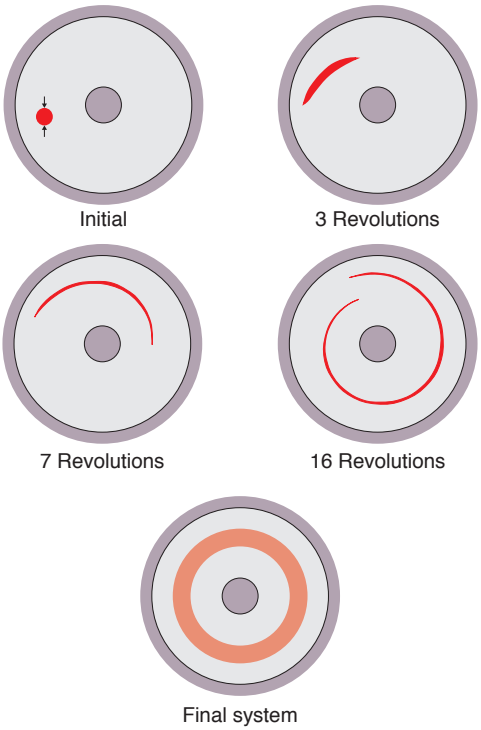

Figure 6.24 Experimental results of distributive mixing in Couette flow, and schematic of the final mixed system

6.2.1.1 Effect of Orientation

Imposing large strains on the system is not always sufficient to achieve a homogeneous mixture. The type of mixing device, initial orientation, and position of the two or more fluid components play a significant role in the quality of the mixture. For example, the mixing mechanism shown in Fig. 6.24 homogeneously distributes the melt within the region contained by the streamlines cut across by the initial secondary component. The final mixed system is shown in Fig. 6.24. Figure 6.25 [8] shows another variation of initial orientation and arrangement of the secondary component. Here, the secondary phase cuts across all streamlines, which leads to a homogeneous mixture throughout the Couette device, under appropriate conditions.

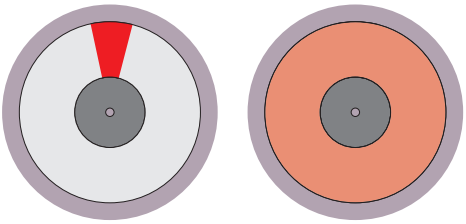

Figure 6.25 Schematic of distributive mixing in Couette flow

A common way of quantifying mixing is by following the growth of the interface between the primary and secondary fluids. In a simple shear flow, a simple expression relates the growth of the interface, the strain, and the orientation of the area of the secondary fluid with respect to the flow direction [9]:

$$\frac{A}{A_0} = \gamma \cos\alpha \tag{6.6}$$

where A_0 is the initial interface area, A is the final interface area, γ is the total strain and α the angle that defines the orientation of the surface, or normal vector, with respect to the direction of flow. Figure 6.26 [2] demonstrates this concept. Here, both cases (a) and (b) start with equal initial areas, A_0, and undergo the same amount of strain, $\gamma = 10$. The circular secondary component in (a) has a surface that is randomly oriented, between 0 and 2π, whereas most of the surface of the elongated secondary component in (b) is oriented at $\pi/2$ leading to negligible growth of the interfacial area. An ideal case would have been a long slender secondary component with a surface oriented in the direction of flow or vertically between the parallel plates. Hence, the maximum interface growth inside a simple shear mixer can be achieved, if the direction of the interface is maintained in an optimal orientation $(\cos\alpha = 1)$. In a simple shear flow this would require a special stirring mechanism that would maintain the interface between the primary and secondary fluid components in a vertical position. Erwin [10] and Ng [11] demonstrated this in an experimental study that involved placing black and white poly-

ethylene blocks in a Couette device (Fig. 6.27a). Figure 6.27b shows that after applying a small amount of shear, the surfaces that were originally oriented in the radial direction have stretched a certain amount and have changed their orientation. It is clear from the photograph that the same surface tends to align with the planes of shear, reducing the mixing efficiency of the process. Hence, in order to increase the effectiveness of the mixer Ng [11] took the Couette content and cut it into new blocks, that were placed inside the Couette device rotated by 90° (Fig. 6.27c). This changed the orientation of the surfaces back to a position where they can more effectively feel the effects of deformation. By repeating this procedure several times, Erwin and co-workers [10, 11] were able to demonstrate that the area growth is also a function of the number of re-orientations that occur during the mixing process. If N is the total number of shearing stages, separated by a re-orientation, the area growth can be computed using

$$\frac{A}{A_0} = \left(\frac{\gamma_{Total}}{N} \right)^N \tag{6.7}$$

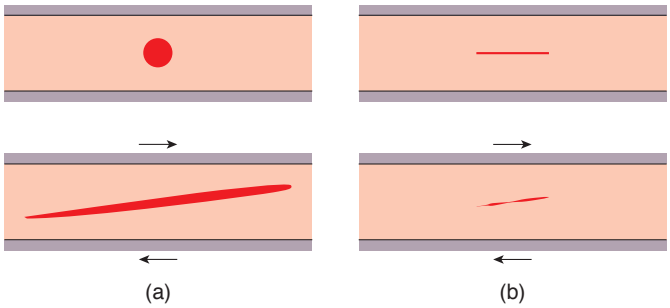

Figure 6.26 Effect of initial surface orientation on distributive mixing

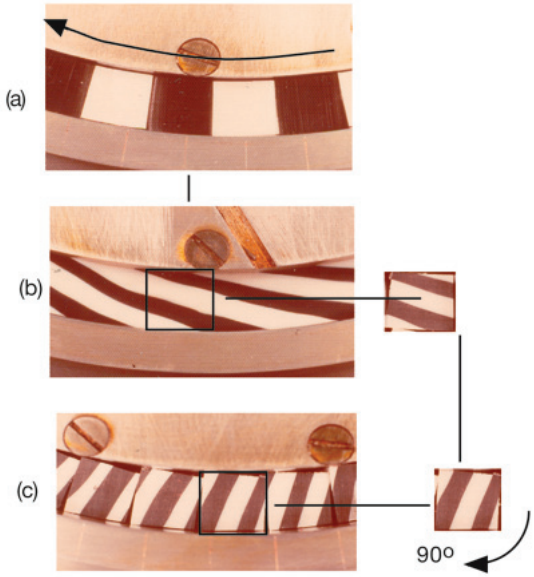

Figure 6.27 Couette deformation and reorientation scheme

where γ_{Total} is the total strain applied during the process. Using this concept, Erwin [10] demonstrated that the upper bound for the ideal mixer is found in a mixer that applies a plane strain extensional flow or pure shear flow to the fluid and where the surfaces are maintained ideally oriented during the whole process; this occurs when $N = \infty$ and each time an infinitesimal amount of shear is applied. In such a system the growth of the interfacial areas follows the relation given by

$$\frac{A}{A_0} = e^{\gamma_{Total}/2} \tag{6.8}$$

In Erwin's ideal mixer the amount of mixing increases in an exponential fashion, compared to a linear increase when the orientation of the fluids' interfaces remains undisturbed.

6.2.2 Dispersive Mixing

Dispersive mixing in polymer processing involves breaking a secondary immiscible fluid or an agglomerate of solid particles and dispersing them throughout the matrix. Here, the imposed strain is not as important as the imposed stress, which causes the system to break-up. Hence, the type of flow inside a mixer plays a significant role for the break-up of solid particle clumps or fluid droplets when dispersing them throughout the matrix.

6.2.2.1 Break-Up of Particulate Agglomerates

The most common example of dispersive mixing of particulate solid agglomerates is the dispersion and mixing of carbon black into a rubber compound. The dispersion of such a system is schematically represented in Fig. 6.28. However, the break-up of particulate agglomerates is best explained using an ideal system of two small spherical particles that need to be separated and dispersed during a mixing process.

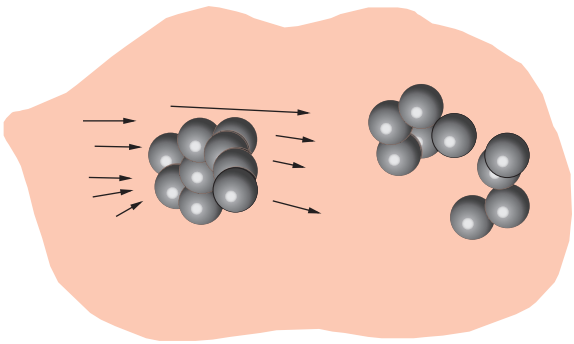

Figure 6.28 Break-up of particulate agglomerates during flow

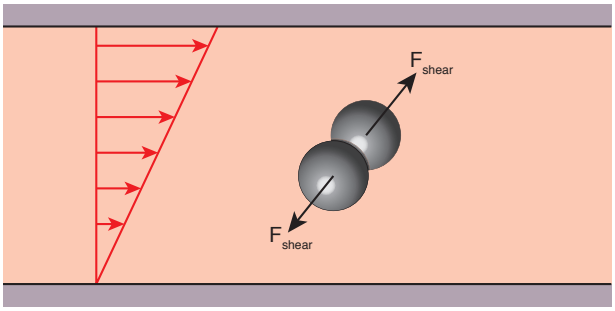

Figure 6.29 Force applied to a two-particle agglomerate in simple shear flow

If the mixing device generates a simple shear flow, as shown in Fig. 6.29, the maximum separation forces acting on the particles as they travel on their streamline occur when they are oriented in a 45° position as they continuously rotate during flow. The magnitude of the force trying to separate the "agglomerate" is given by [12]

$$F_{shear} = 3\pi\eta\dot{\gamma}r^2 \tag{6.9}$$

where η is the viscosity of the carrier fluid, $\dot{\gamma}$ the magnitude of the strain rate tensor, and r are the radii of the particles.

However, if the flow field generated by the mixing device is a pure elongational flow, such as shown in Fig. 6.30, the particles will always be oriented at 0°, the position of maximum force. The magnitude of the force for this system is given by

$$F_{shear} = 6\pi\eta\dot{\gamma}r^2 \tag{6.10}$$

which is twice as high as the maximum force generated by the system that produces a simple shear flow. In addition, in elongational flow, the agglomerate is

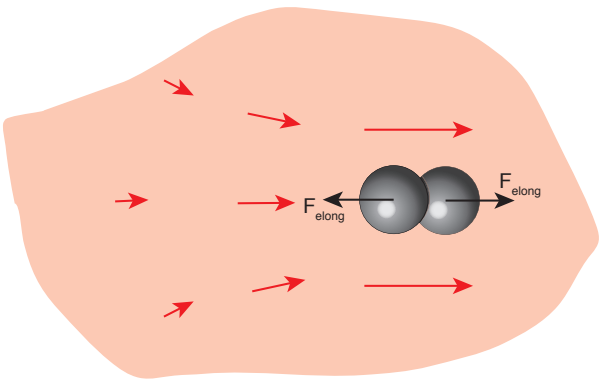

Figure 6.30 Force applied to a two-particle agglomerate in elongational flow

always oriented in the direction of maximum force generation, whereas in simple shear flow the agglomerate tumbles quickly through the position of maximum force[4].

The above analysis makes it clear that for mixing processes that require break-up and dispersion of agglomerates, elongation is the preferred mode of deformation. This is only valid if the magnitude of the rate of deformation tensor can be kept the same in elongation as in shear. Hence, when optimizing mixing devices it is important to know which mode of deformation is dominant. This can be accomplished by computing a flow number, or Manas-Zloczower number (M_z) [13], defined by

$$M_z = \frac{\dot{\gamma}}{\dot{\gamma} - \omega} \tag{6.11}$$

where $\dot{\gamma}$ is the magnitude of the rate of deformation tensor and ω the magnitude of the vorticity tensor. A Manas-Zloczower number of 0 implies pure rotational flow, a value of 0.5 represents simple shear flow, and pure elongational flow is implied when M_z = 1.

6.2.2.2 Break-Up of Fluid Droplets

In general, droplets inside an incompatible matrix tend to stay or become spherical due to the natural tendencies of the drop trying to maintain the lowest possible surface to volume ratio. However, a flow field within the mixer applies a stress to the droplets, causing them to deform. If this stress is high enough, it will eventually cause the drops to disperse. The droplets will disperse when the surface tension can no longer maintain their shape in the flow field and the filaments break-up into smaller droplets. This phenomenon of dispersion and distribution continues to repeat itself until the deviatoric stresses of the flow field can no longer overcome the surface tension of the new droplets formed.

As can be seen, the mechanism of fluid agglomerate break-up is similar in nature to solid agglomerate break-up in the sense that both rely on forces to disperse the particulates. Hence, elongation is also the preferred mode of deformation when breaking up fluid droplets and threads, making the Manas-Zloczower number, M_Z, an indispensable quantity when quantifying mixing processes that deal with such systems.

A parameter commonly used to determine whether a droplet will disperse is the capillary number defined by

$$Ca = \frac{\tau R}{\sigma_s} \tag{6.12}$$

4 A full description of the relation between flow field and rotation of fibers and agglomerates is given in Chapter 7.

where τ is the flow induced or deviatoric stress, R the characteristic dimension of the droplet, and σ_s the surface tension that acts on the drop. The capillary number is the ratio of flow stresses to droplet surface stresses. Droplet break-up occurs when a critical capillary number, Ca_{crit}, is reached. This break-up can be seen in Fig. 6.31 [1], which shows the disintegration of a Newtonian thread in a Newtonian matrix. Because of the continuously decreasing thread radius, the critical capillary number will be reached at some specific point in time. Due to the competing deviatoric stresses and surface forces, the cylindrical shape becomes unstable and small disturbances at the surface lead to a growth of capillary waves. These waves are commonly referred to as Rayleigh disturbances. Disturbances with various wavelengths form on the cylinder surface, but only those with a wavelength greater than the circumference $\left(2\pi R_0\right)$ of the thread lead to a monotonic decrease of the interfacial area.

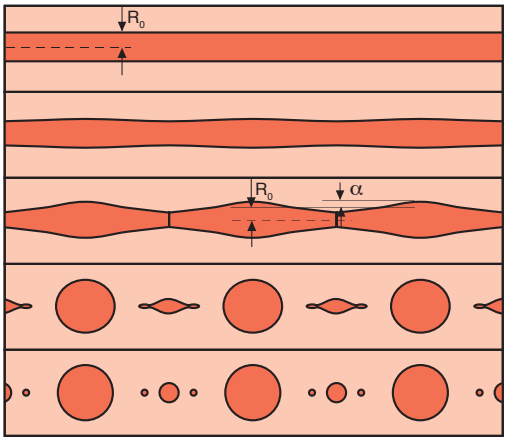

Figure 6.31 Disintegration of a Newtonian 0.35 mm diameter castor oil thread in a Newtonian silicone oil matrix. Redrawn from photographs taken every second

Figure 6.32 [14] shows the critical capillary number as a function of viscosity ratio, η_2 / η_1, and flow type, described by the mixing parameter λ. For a viscosity ratio of 1 the critical capillary number is of order 1 [1]. Distributive mixing is implied when Ca is much greater than Ca_{crit} because the interfacial stress is much smaller than shear stresses. Here, the capillary waves that would cause droplet break-up will not develop. Dispersive mixing is implied when Ca is close to the value of the critical Ca or when interfacial stresses are almost equal to the deviatoric stresses causing droplet break-up. In addition, break-up can only occur if enough time is given for this to happen. The disturbance amplitude, α, is assumed to grow exponentially as

$$\alpha = \alpha_0 e^{qt} \tag{6.13}$$

where α_0 is the initial disturbance amplitude, sometimes assumed to be 0.3% of the thread radius, and the growth rate q is defined by

$$q = \frac{\sigma_s \Omega}{2\eta_1 R_0} \tag{6.14}$$

In the above equation R_0 represents the initial radius of the thread and Ω a dimensionless growth rate presented in Fig. 6.33 as a function of viscosity ratio for the wavelength disturbance amplitude, which leads to break-up. The time required for break-up, t_b, can now be computed using the above equations as

$$t_b = \frac{1}{q} \ln\left(\alpha_b / \alpha_0\right) \tag{6.15}$$

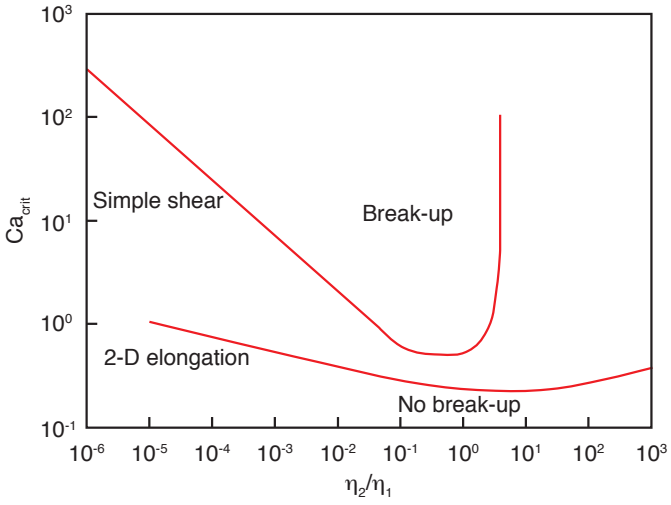

Figure 6.32 Critical capillary number for drop break-up as a function of viscosity ratio in a simple shear and a 2-D elongational flow

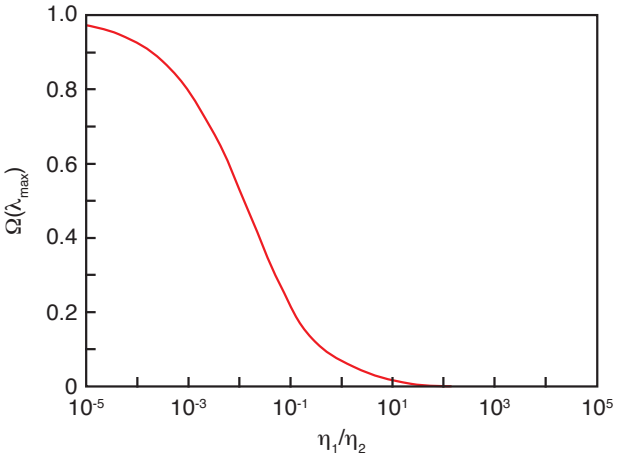

Figure 6.33 Dominant growth rate of interfacial disturbances as a function of viscosity ratio

where α_b is the amplitude at break-up, which for a sinusoidal disturbance is $\alpha_b = \sqrt{2/3}R_0$. The break-up time decreases as the critical capillary number is exceeded. The reduced break-up time t_b^* can be approximated using [14]

$$t_b^* = t_b \left(\frac{Ca}{Ca_{crit}} \right)^{-0.63} \tag{6.16}$$

As mentioned earlier, surface tension plays a large role in the mixing process, especially when dealing with dispersive mixing when the capillary number approaches its critical value. Because of the stretching of the interfacial area, due to distributive mixing, the local radii of the suspended components decrease, causing surface tension to play a role in the process. It should also be noted that once the capillary number assumes a value below the critical *Ca*, only slight deformations occur and internal circulation maintains an equilibrium elliptical droplet shape in the flow field as schematically represented in Fig. 6.34. At that point, the mixing process reduces to the distribution of the dispersed droplets. Analytical and numerical investigations of stable droplet shapes for $Ca < Ca_{crit}$ in simple shear flow have been performed by several investigators [15–17]. Figure 6.32 also shows that at viscosity ratios above 4 simple shear flows are not able to break-up fluid droplets.

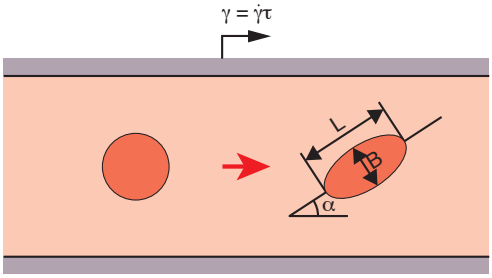

Figure 6.34 Schematic of droplet deformation in simple shear flow

6.2.3 Mixing Devices

The final properties of a polymer component are heavily influenced by the blending or mixing process that takes place during processing or as a separate step in the manufacturing process. As mentioned earlier, when measuring the quality of mixing it is also necessary to evaluate the efficiency of mixing. For example, the amount of power required to achieve the highest mixing quality for a blend may be unrealistic or unachievable. This section presents some of the most commonly used mixing devices encountered in polymer processing.

In general, mixers can be classified in two categories: internal batch mixers and continuous mixers. Internal batch mixers, such as the Banbury type mixer, are the

oldest type of mixing devices in polymer processing and are still widely used in the rubber compounding industry. Industry often also uses continuous mixers because they combine mixing in addition to their normal processing tasks. Typical examples are single and twin screw extruders that often have mixing heads or kneading blocks incorporated into their system.

6.2.3.1 Static Mixers

Static mixers or motionless mixers are pressure-driven continuous mixing devices through which the melt is pumped, rotated, and divided, leading to effective mixing without the need for movable parts and mixing heads. One of the most commonly used static mixers is the twisted tape static mixer schematically shown in Fig. 6.35. Figure 6.36 [19] shows computed streamlines relative to the twist in the wall. As the fluid is rotated by the dividing wall, the interfaces between the fluids increase. The interfaces are then re-oriented by 90° once the material enters a new section. Figure 6.36 shows a typical trajectory of a particle as it travels on a streamline in section N of the static mixer and ends on a different streamline after entering the next section, N+1. The stretching-re-orientation sequence is repeated until the number of striations is so high that a seemingly homogeneous mixture is achieved. Figure 6.37 shows a sequence of cuts down a Kenics static mixer[5]. From the figure it can be seen that the number of striations increases from section to section by 2, 4, 8, 16, 32, etc., which can be computed using

$$N = 2^n \tag{6.17}$$

where N is the number of striations and n is the number of sections in the mixer.

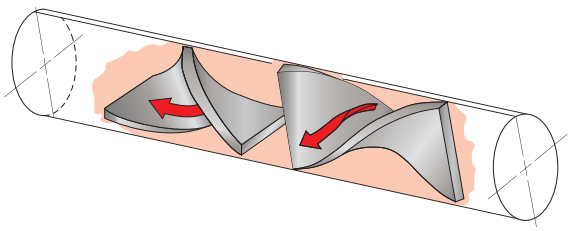

Figure 6.35 Schematic diagram of a Kenics static mixer

6.2.3.2 Banbury Mixer

The Banbury type mixer, schematically shown in Fig. 6.38, is perhaps the most commonly used internal batch mixer. Internal batch mixers are high intensity mixers that generate complex shearing and elongational flows that work especially

5 Courtesy Chemineer, Inc., North Andover, Massachusetts.

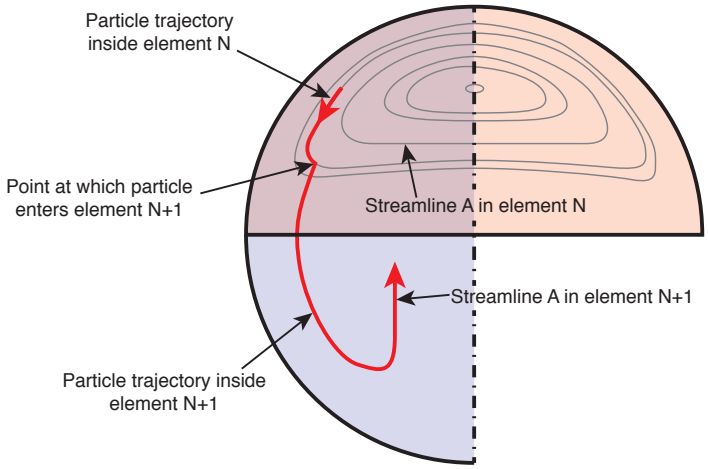

Figure 6.36
Simulated streamlines inside a Kenics static mixer section

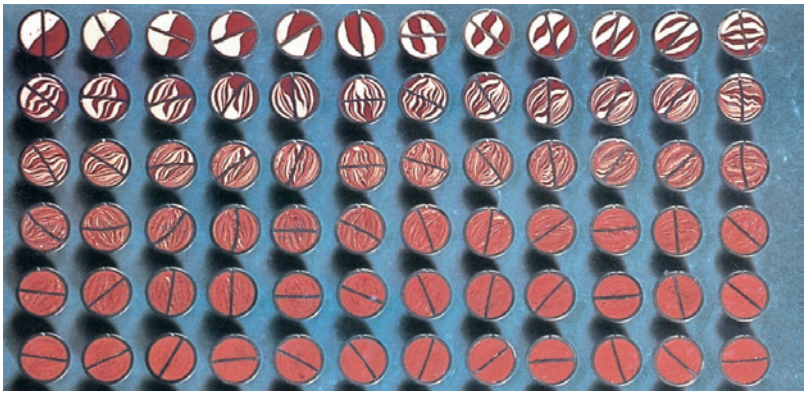

Figure 6.37 Experimental progression of the layering of colored resins in a Kenics static mixer

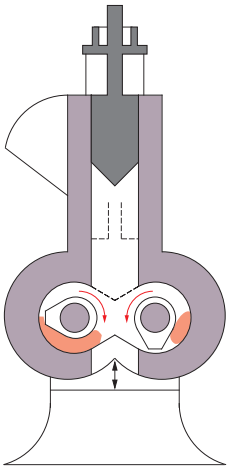

Figure 6.38
Schematic diagram of a Banbury type mixer

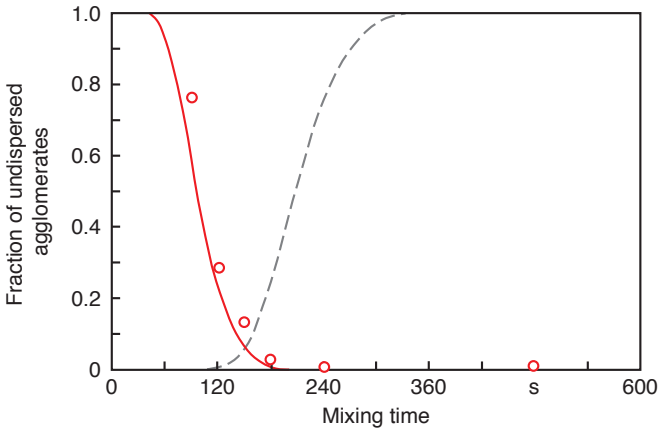

Figure 6.39 Fraction of undispersed carbon black larger than 9 μm as a function of mixing time inside a Banbury mixer; (O) denotes experimental results and solid line theoretical predictions; broken line denotes the fraction of aggregates smaller than 500 nm.

well for the dispersion of solid particle agglomerates within polymer matrices. One of the most common applications for high intensity internal batch mixing is the break-up of carbon black agglomerates into rubber compounds. The dispersion of agglomerates is strongly dependent on mixing time, rotor speed, temperature, and rotor blade geometry [18]. Figure 6.39 [15, 21] shows the fraction of undispersed carbon black as a function of time in a Banbury mixer at 77 rpm and 100 °C. The broken line in the figure represents the fraction of particles smaller than 500 nm.

6.2.3.3 Mixing in Single Screw Extruders

Mixing caused by the cross-channel flow component can be further enhanced by introducing pins in the flow channel. These pins can sit either on the screw, as shown in Fig. 6.40 [22], or on the barrel, as shown in Fig. 6.41 [23]. The extruder with the adjustable pins on the barrel is generally referred to as QSM-extruder[6]. In both cases the pins disturb the flow by re-orienting the surfaces between fluids and by creating new surfaces by splitting the flow. Figure 6.42 presents a photograph of the channel contents of a QSM-extruder. The photograph clearly demonstrates the re-orientation of the layers as the material flows past the pins. The pin type extruder is especially necessary for the mixing of high viscosity materials such as rubber compounds; thus, it is often called a cold feed rubber extruder. This machine is widely used in the production of rubber profiles of any shape and size.

6 QSM is abbreviated for the German *Quer Strom Mischer,* which translates into cross-flow mixing.

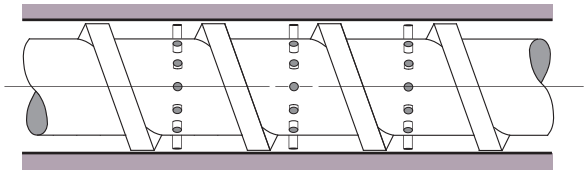

Figure 6.40 Pin mixing section on the screw of a single screw extruder

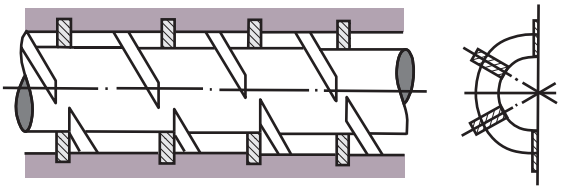

Figure 6.41 Pin barrel extruder (Quer Strom Misch Extruder)

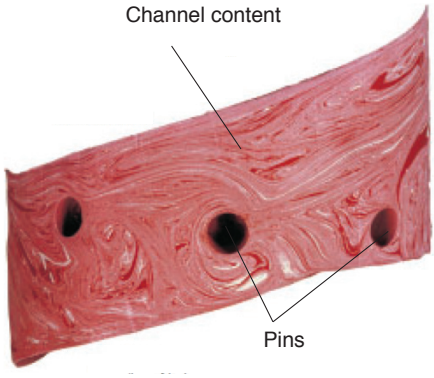

Figure 6.42 Photograph of the unwrapped channel contents of a pin barrel extruder (Courtesy of Paul Troester Maschinenfabrik, Hannover, Germany)

For lower viscosity fluids, such as thermoplastic polymer melts, the mixing action caused by the cross-flow is often not sufficient to re-orient, distribute, and disperse the mixture, making it necessary to use special mixing sections. Re-orientation of the interfaces between primary and secondary fluids and distributive mixing can be induced by any disruption in the flow channel. Figure 6.43 [22] presents commonly used distributive mixing heads for single screw extruders. These mixing heads introduce several disruptions in the flow field that have proven to perform well in mixing.

As mentioned earlier, dispersive mixing is required when breaking down particle agglomerates or when surface tension effects exist between primary and secondary fluids in the mixture. To disperse such systems, the mixture must be subjected to large stresses. Barrier-type screws are often sufficient to apply high stresses to the polymer melt. However, more intensive mixing can be applied by using a mixing head. When using barrier-type screws or a mixing head, as shown in Fig. 6.44 [22], the mixture is forced through narrow gaps, causing high stresses in the melt.

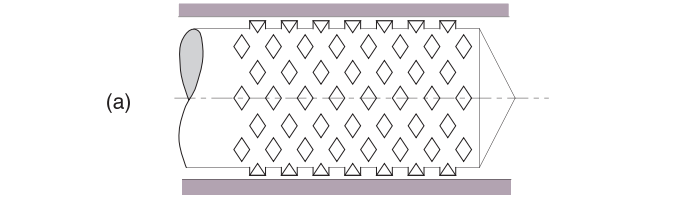

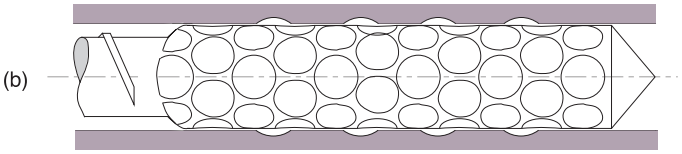

Figure 6.43 Distributive mixing sections: (a) pineapple mixing section, (b) cavity transfer mixing section

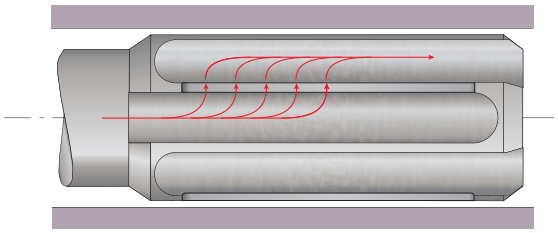

Figure 6.44 Maddock or Union Carbide mixing section

It should be noted that dispersive as well as distributive mixing heads cause resistance to the flow, which results in viscous heating and pressure losses during extrusion.

6.2.3.4 Co-Kneader

The co-kneader is a single screw extruder with pins on the barrel and a screw that oscillates in the axial direction. Figure 6.45 shows a schematic diagram of a co-kneader. The pins on the barrel practically wipe the entire surface of the screw, making it the only self-cleaning single-screw extruder. This results in reduced residence time, which makes it suitable for processing thermally sensitive materials. The pins on the barrel also disrupt the solid bed, creating dispersed melting

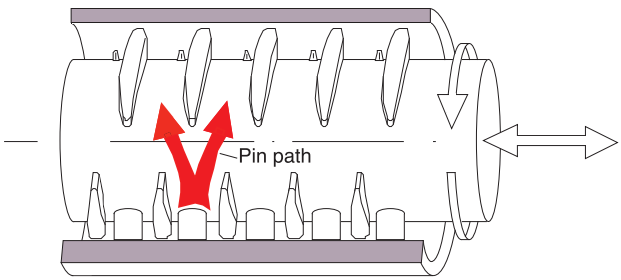

Figure 6.45 Schematic diagram of a co-kneader

[24] which improves the overall melting rate while reducing the overall temperature in the material.

A simplified analysis of a co-kneader gives a number of striations per L/D of [25]

$$N_s = 2^{12} \tag{6.18}$$

which means that over a section of $4D$ the number of striations is $2^{12}(4) = 2.8E14$. A detailed discussion on the co-kneader is given by Rauwendaal [25] and Elemans [26].

6.2.3.5 Twin Screw Extruders

In the past two decades, twin screw extruders have developed into the best available continuous mixing devices. In general, they can be classified into intermeshing and non-intermeshing, and co-rotating and counter-rotating twin screw extruders[7]. Intermeshing twin screw extruders render a self-cleaning effect, which compensates for the residence time of the polymer in the extruder. The self-cleaning geometry for a co-rotating, double-flighted twin screw extruder is shown in Fig. 6.46. The main characteristic of this type of configuration is that the surfaces of the screws are sliding past each other, constantly removing the polymer that is stuck to the screw.

In the last two decades, the co-rotating twin screw extruder systems have established themselves as efficient continuous mixers, including reactive extrusion. In essence, the co-rotating systems provide high pumping efficiency caused by the

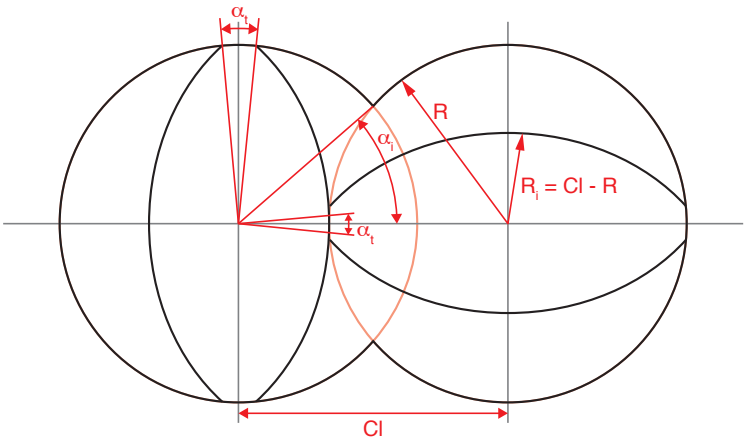

Figure 6.46 Geometry description of a double-flighted, co-rotating, self-cleaning, twin screw extruder

7 A complete overview of twin screw extruders is given by White, J. L., *Twin Screw Extrusion-Technology and Principles*, Hanser Publishers, Munich, (1990).

double transport action of the two screws. Counter-rotating systems generate high stresses because of the calendering action between the screws, making them efficient machines to disperse pigments and lubricants[8].

Several studies have been performed to evaluate the mixing capabilities of twin screw extruders. Noteworthy are two studies performed by Lim and White [27, 28] that evaluated the morphology development in a 30.7 mm diameter co-rotating [17] and a 34 mm diameter counter-rotating [18] intermeshing twin screw extruder. In both studies a 75/25 dry-mixed blend of polyethylene and polyamide 6 pellets was fed into the hopper at 15 kg/h. Small samples were taken along the axis of the extruder and evaluated using optical and electron microscopy.

Figure 6.47 shows the morphology development along the screws at positions marked A, B, C, and D for a counter-rotating twin screw extruder configuration without special mixing elements. The dispersion of the blend becomes visible by the reduction of the characteristic size of the polyamide 6 phase. Figure 6.48 is a plot of the weight average and number average domain size of the polyamide 6 phase along the screw axis. The weight average phase size at the end of the extruder was measured to be 10 µm and the number average 6 µm. By replacing sections of the screw with one kneading-pump element and three special mixing elements, the final weight average phase size was reduced to 2.2 µm and the number average to 1.8 µm, as shown in Fig. 6.49.

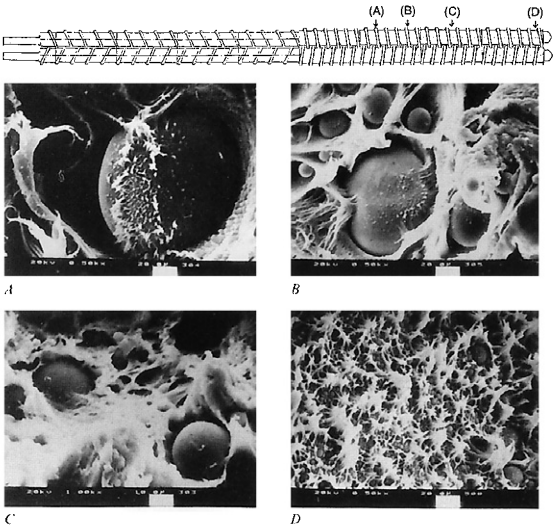

Figure 6.47 Morphology development inside a counter-rotating twin screw extruder

8 There seems to be considerable disagreement about co- versus counter-rotating twin screw extruders between different groups in the polymer processing industry and academic community.

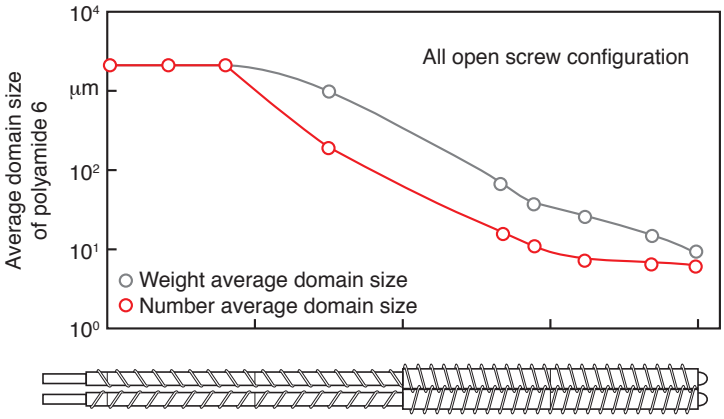

Figure 6.48 Number and weight average of polyamide 6 domain sizes along the screws for a counter-rotating twin screw extruder

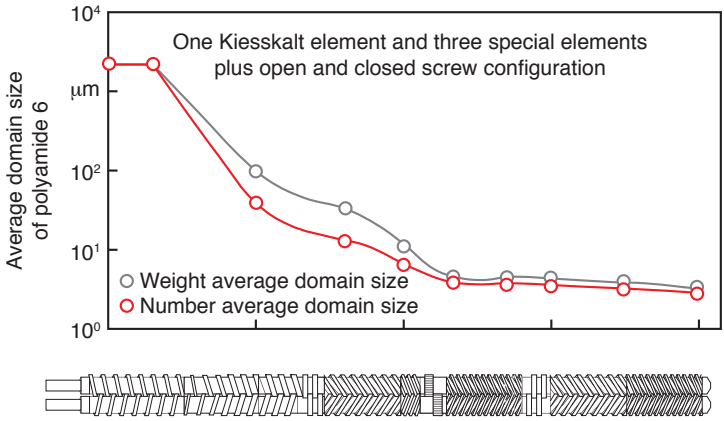

Figure 6.49 Number and weight average of polyamide 6 domain sizes along the screws for a counter-rotating twin screw extruder with special mixing elements

Using a co-rotating twin screw extruder with three kneading disk blocks, a final morphology with polyamide 6 weight average phase sizes of 2.6 µm was achieved. Figure 6.50 shows the morphology development along the axis of the screws. When comparing the outcome of both counter-rotating (Fig. 6.49) and co-rotating (Fig. 6.50) screw, it is clear that both extruders achieve a similar final mixing quality. However, the counter-rotating extruder achieved the final morphology much earlier in the screw than the co-rotating twin screw extruder. A possible explanation for this is that the blend traveling through the counter-rotating configuration melted earlier than in the co-rotating geometry. In addition, the phase size was slightly smaller, possibly due to the calendering effect between the screws in the counter-rotating system.

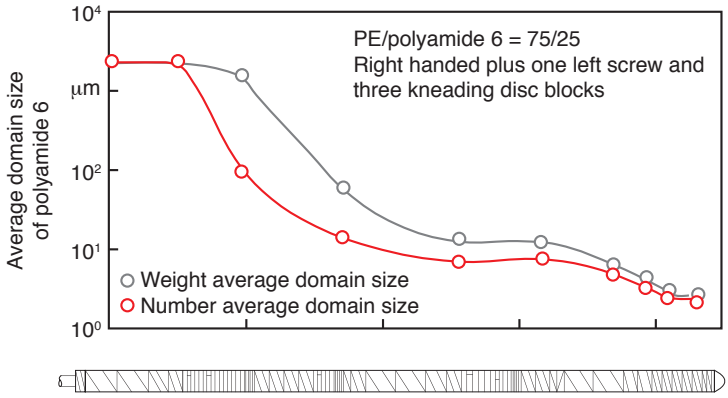

Figure 6.50 Number and weight average of polyamide 6 domain sizes along the screws for a co-rotating twin screw extruder with special mixing elements

6.2.4 Energy Consumption During Mixing

Energy consumption is of extreme importance when assessing and comparing various mixing devices. High energy requirements for optimal mixing mean high costs and expensive equipment. The power consumption per unit volume of a deforming Newtonian fluid is given by [29]

$$p = 2\mu\left[\left(\frac{\partial v_x}{\partial x}\right)^2+\left(\frac{\partial v_y}{\partial y}\right)^2+\left(\frac{\partial v_z}{\partial z}\right)^2\right]+\mu\left[\left(\frac{\partial v_x}{\partial y}+\frac{\partial v_y}{\partial x}\right)^2+\left(\frac{\partial v_y}{\partial z}+\frac{\partial v_z}{\partial y}\right)^2+\left(\frac{\partial v_x}{\partial z}+\frac{\partial v_z}{\partial x}\right)^2\right] \tag{6.19}$$

Erwin [30] used the above equation to assess the energy input requirements for different types of mixing flows: simple shear, pure shear, and extensional flows. Table 6.4 presents flow fields and energy requirements for various flows described by Erwin [30]. For example, to produce a mixture such that A/A_0 = 10^4 in time $t_0 = 100$ s for a fluid with viscosity $\mu = 10^4\,\text{Pa}\cdot\text{s}$, in a mixer that deforms the fluid with an elongational flow, 96 kJ/m^3 of energy input are needed. Because the flow is steady, this requires a power input of 0.96 kW/m^3 for 100 s. In a mixer that deforms the fluid in a biaxial extensional flow the energy required is 24 kJ/m^3 with 0.24 kW/m^3 of power input. For the same amount of mixing, a mixer that deforms the fluid in pure shear requires an energy input of 40 kJ/m^3 or a steady power input of 0.4 kW/m^3 for 100 s. A device that deforms the fluid in simple shear requires a total energy input of 4 × 107 kJ/m^3 or a steady power input of 40,000 kW/m^3 for a 100 second period to achieve the same amount of mixing.

Table 6.4 Energy Input Requirements for Various Flow Mixers

Flow type	Flow field	Power	Energy input
Extensional flow (elongational)	$v_x = Gx$ $v_y = -Gy/2$ $v_z = -Gz/2$	$3\mu G^2$	$\frac{12\mu}{t_0}\left(\ln\left(\frac{5A}{4A_0}\right)\right)^2$
Extensional flow (biaxial)	$v_x = -Gx$ $v_y = Gy/2$ $v_z = Gz/2$	$3\mu G^2$	$\frac{3\mu}{t_0}\left(\ln\left(\frac{5A}{4A_0}\right)\right)^2$
Pure shear	$v_x = -hx$ $v_y = -Hy$ $v_z = 0$	$2\mu(h^2 + H^2)$	$\frac{4\mu}{t_0}\left(\ln\left(2\frac{A}{A_0}\right)\right)^2$
Simple shear	$v_x = -Gy$ $v_y = 0$ $v_z = 0$	μG^2	$\frac{4\mu}{t_0}\left(\frac{A}{A_0}\right)^2$

From this it is clear that, in terms of energy and power consumption, simple shear flows are significantly inferior to extensional flows.

6.2.5 Mixing Quality and Efficiency

In addition to the Manas-Zloczower number, strain, and capillary number, several parameters have been developed by various researchers in the polymer industry to quantify the efficiency of the mixing processes. Some have used experimentally measured parameters while others have used mixing parameters that are easily calculated from computer simulation.

A parameter used in visual experiments is the batch homogenization time (BHT). This parameter is defined as the time it takes for a material to become homogeneously colored inside the mixing chamber after a small sample of colored pigment is placed near the center of the mixer. A downfall to this technique is that the observed homogenized time can be quite subjective.

To describe the state of the dispersion of fillers in a composite material, Suetsugu [31] used a dispersion index defined as:

$$\text{Dispersion index} = 1 - \phi_a \tag{6.20}$$

where ϕ_a is a dimensionless area that the agglomerates occupy and is defined by:

$$\phi_a = \frac{\pi}{4A\phi}\sum d_i^2 n_i \tag{6.21}$$

where A is the area under observation, ϕ the volume fraction of the filler, d_i the diameter of the agglomerate, and n_i the number agglomerates. The dispersion

index ranges between 0 for the worst case of dispersion and 1 when no agglomerates remain in the system.

A commonly used method to analyze the mixing capabilities of the extruder is the residence time distribution (RTD). It is calculated by monitoring the output of the extruder with the input of a secondary component. Two common response techniques are the step input response and the pulse input response shown in Fig. 6.51 [22]. The response of the input provides information on the mixing and conveying performance of the extruder. The RTD response to a pulse input for an ideal mixing situation is shown in Fig. 6.52. The figure shows a quick response to the input with a constant volume fraction of the secondary component until there is no material left.

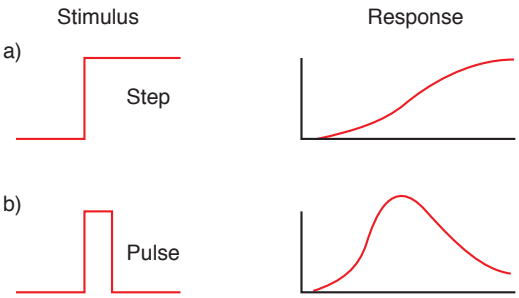

Figure 6.51 Step input and pulse input residence time distribution responses

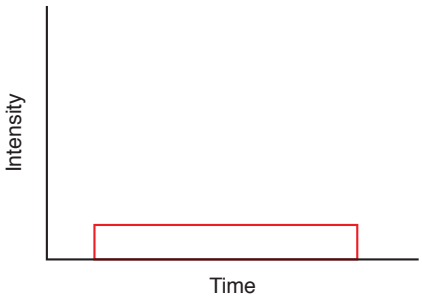

Figure 6.52 Ideal residence time distribution response to a pulse input

Using computer simulation, velocities, velocity gradients, and particle tracking can be computed with some degree of accuracy – depending on the computational method and assumptions made. Using information from a computer simulation, several methods to quantify mixing have been developed. Poincaré sections are often used to describe the particle paths during the mixing process. The Poincaré section shows the trajectory of several particles during the mixing process. They can be very useful in locating stagnation points, recirculation regions, and in detecting symmetric flow patterns where no exchange exists across the planes of symmetry – all issues that hinder mixing.

6.2.6 Plasticization

Solvents, commonly referred to as plasticizers, are sometimes mixed into a polymer to dramatically alter its rheological and/or mechanical properties. Plasticizers are used as processing aids because they have the same impact as raising the temperature of the material. Hence, the lowered viscosities at lower temperatures reduce the risk of thermal degradation during processing. For example, cellulose nitrite would thermally degrade during processing without the use of a plasticizer.

Plasticizers are more commonly used to alter a polymer's mechanical properties, such as stiffness, toughness, and strength. For example, adding a plasticizer such as dioctylphthalate (DOP) to PVC can reduce its stiffness by three orders of magnitude and lower its glass transition temperature to –35 °C. In fact, a highly plasticized PVC is rubbery at room temperature. Table 6.5 [45] presents some common plasticizers with the polymers they plasticize and their applications.

Because moisture is easily absorbed by polyamides, slightly modifying their mechanical behavior, it can be said that water acts as a plasticizing agent with

Table 6.5 Commercial Plasticizers and Their Applications

Plasticizer	Polymers	Plasticizer type
Dioctyl phthalate (DOP)	Polyvinyl chloride and copolymers	General purpose, primary plasticizer
Tricresyl phosphate (TCP)	Polyvinyl chloride and copolymers, cellulose acetate, cellulose nitrate	Flame retardant, primary plasticizer
Dioctyl adipate (DOA)	Polyvinyl chloride, cellulose acetate, butyrate	Low temperature plasticizer
Dioctyl sebacate (DOS)	Polyvinyl chloride, cellulose acetate, butyrate	Secondary plasticizer
Adipic acid polyesters (MW = 1500–3000)	Polyvinyl chloride	Non-migratory secondary plasticizer
Sebacic acid polyesters (MW = 1500–3000)	Polyvinyl chloride	Non-migratory secondary plasticizer
Chlorinated paraffin (%Cl = 40–70) (MW = 600–1000)	Most polymers	Flame retardant, plasticizer extenders
Bi- and terphenyls (also hydrogenated)	Aromatic polyesters	Various
N-ethyl-toluene sulfonamide	Polyamides	General purpose, primary plasticizer
Sulfonamide-formaldehyde resins	Polyamides	Non-migratory secondary plasticizers

these materials. Figure 6.53 shows the equilibrium water content for polyamide 6 and 66 as a function of the ambient relative humidity. This moisture absorption causes the polyamide to expand or swell as shown in Fig. 6.54.

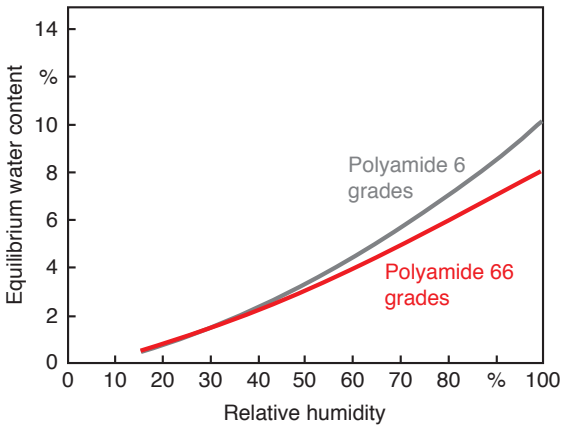

Figure 6.53 Equilibrium water content as a function of relative humidity for polyamide 6 and polyamide 66 (Courtesy of Bayer AG, Germany)

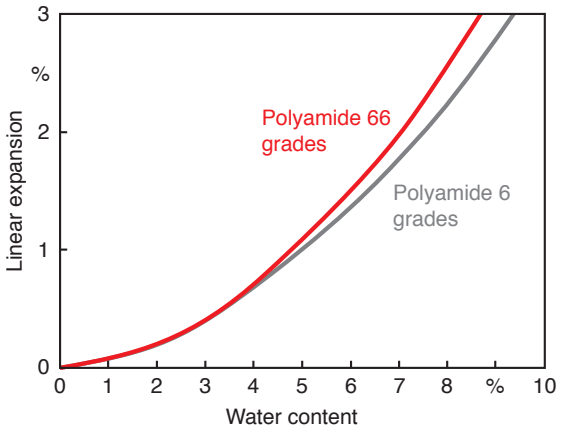

Figure 6.54 Linear expansion as a function of water content for polyamide 6 and polyamide 66 (Courtesy of Bayer AG, Germany)

The behavior of polymers toward solvents depends in great part on the nature of the solvent and on the structure of the polymer molecules. If the basic building block of the macromolecule and the solvent molecule are the same or of similar nature, the absorption of a solution will lead to swelling. If a sufficient amount is added, the polymer will dissolve in the solvent. Crystalline regions of a semi-crystalline thermoplastic are usually not affected by solvents, whereas amorphous regions are easily penetrated. In addition, the degree of crosslinking in thermosets and elastomers has a great influence on whether a material can be permeated by solvents. The shorter the distances between the linked molecules, the less solvent molecules can permeate and give mobility to chain segments. While elastomers

can swell in the presence of a solvent, highly cross-linked thermosets do not swell or dissolve.

The amount of solvent that is absorbed depends not only on the chemical structure of the two materials but also on the temperature. An increase in temperature reduces the covalent forces of the polymer, therefore solubility becomes higher. Although it is difficult to determine the solubility of polymers, there are some rules to estimate it. The simplest rule is: same dissolves same (i.e., when both – polymer and solvent – have the same valence forces, solubility exists).

The solubility of a polymer and a solvent can be addressed from a thermodynamic point of view using the familiar Gibbs free energy equation

$$\Delta G = \Delta H - T\Delta S \tag{6.22}$$

where ΔG is the change in free energy, ΔH is the change in enthalpy, ΔS the change in entropy, and T the temperature. If ΔG in Eq. 6.22 is negative, solubility is possible. A positive ΔG suggests that the polymer and the solvent do not "want" to mix, which means solubility can only occur if $\Delta H < T\Delta S$. On the other hand, $\Delta H \approx 0$ implies that solubility is the natural lower energy state. The change in entropy is very small when dissolving a polymer, therefore the determining factor whether solution will occur or not is the change in enthalpy, ΔH. Hildebrand and Scott [46] proposed a useful equation that estimates the change in enthalpy during the formation of a solution. The Hildebrand equation is stated by

$$\Delta H = V\left(\left(\frac{\Delta E_1}{V_1}\right)^{1/2} - \left(\frac{\Delta E_2}{V_2}\right)^{1/2}\right)^2 \phi_1\phi_2 \tag{6.23}$$

where V is the total volume of the mixture, V_1 and V_2 the volumes of the solvent and polymer, ΔE_1 and ΔE_2 their energy of evaporation and, ϕ_1 and ϕ_2 their volume fractions. Equation 6.23 can be simplified to

$$\Delta H = V\left(\delta_1 - \delta_2\right)^2 \phi_1\phi_2 \tag{6.24}$$

where δ is called the solubility parameter and is defined by

$$\delta = \left(\frac{\Delta E}{V}\right)^{1/2} \tag{6.25}$$

If the solubility parameters of the substances are nearly equal, they will dissolve. As a rule-of-thumb it can be stated that if $|\delta_1 - \delta_2| < 1$ $(\text{cal/cm}^3)^{1/2}$, solubility will occur [47]. The units $(\text{cal/cm}^3)^{1/2}$ are usually referred to as Hildebrands. Solubility parameters for various polymers are presented in Table 6.6 [48], and for various solvents in Table 6.7 [48].

Figure 6.55 [49] shows a schematic diagram of the swelling and dissolving behavior of crosslinked and uncrosslinked polymers as a function of the solubility or solubility parameter, δ_s, of the solvent. When the solubility parameter of the poly-

mer and the solvent approach each other, the uncrosslinked polymer becomes unconditionally soluble. However, if the same polymer is crosslinked, it is only capable of swelling. The amount of swelling depends on the degree of crosslinking.

Table 6.6 Solubility Parameter for Various Polymers

Polymer	$\delta\left(\text{cal}/\text{cm}^3\right)^{1/2}$
Polytetrafluoroethylene	6.2
Polyethylene	7.9
Polypropylene	8.0
Polyisobutylene	8.1
Polyisoprene	8.3
Polybutadiene	8.6
Polystyrene	9.1
Poly(vinyl acetate)	9.4
Poly(methyl methacrylate)	9.5
Polycarbonate	9.9
Polysulfone	9.9
Poly(vinyl chloride)	10.1
Polyethylene terephthalate	10.2
Polyamide 6	11.0
Cellulose nitrate	11.5
Poly(vinylidene chloride)	12.2
Polyamide 66	13.6
Polyacrylonitrile	15.4

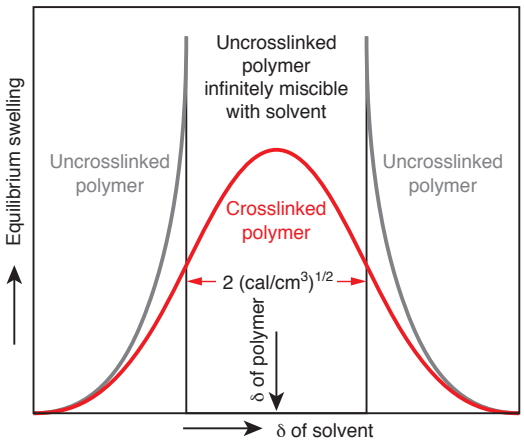

Figure 6.55 Equilibrium swelling as a function of solubility parameter for crosslinked and uncrosslinked polymers

Table 6.7 Solubility Parameter of Various Plasticizers and Solvents

Solvent	$\delta\left(\text{cal}/\text{cm}^3\right)^{1/2}$
Acetone	10.0
Benzene	9.1
Di-butoxyethyl phthalate (Dronisol)	8.0
n-Butyl alcohol	11.4
Sec-butyl alcohol	10.8
Butyl stearate	7.5
Chlorobenzene	9.6
Cyclohexanone	9.9
Dibutyl phenyl phosphate	8.7
Dibutyl phthalate	9.3
Dibutyl sebacate	9.2
Diethyl phthalate	10.0
Di-n-hexyl phthalate	8.9
Diisodecyl phthalate	7.2
Dimethyl phthalate	10.7
Dioctyl adipate	8.7
Dioctyl phthalate (DOP)	7.9
Dioctyl sebacate	8.6
Dipropyl phthalate	9.7
Ethyl acetate	9.1
Ethyl alcohol	12.7
Ethylene glycol	14.2
2-Ethylhexyl diphenyl phosphate (Santicizer 141)	8.4
N-ethyl-toluene sulfonamide (Santicizer 8)	11.9
Hydrogenated terphenyl (HB-40)	9.0
Kronisol	8.0
Methanol	14.5
Methyl ethyl ketone	9.3
Nitromethane	12.7
n-Propyl alcohol	11.9
Toluene	8.9
Tributyl phosphate	8.2
1,1,2-trichloro-1,2,2-trifluoroethane (freon 113)	7.2
Trichloromethane (chloroform)	9.2
Tricresyl phosphate	9.0
Triphenyl phosphate	9.2
Water	23.4
Xylene	8.8

6.3 Injection Molding

Injection molding is the most important process used to manufacture plastic products. Today, more than one-third of all thermoplastic materials are injection molded and more than half of all polymer processing equipment is used for injection molding. The injection molding process is ideally suited to manufacture mass-produced parts of complex shapes requiring precise dimensions. The process goes back to 1872 when the Hyatt brothers patented their stuffing machine to inject cellulose into molds. However, today's injection molding machines are mainly related to the reciprocating screw injection molding machine patented in 1956. A modern injection molding machine with its most important elements is shown in Fig. 6.56. The major components of the injection molding machine are the plasticating unit, clamping unit, and the mold.

Today, injection molding machines are classified by the following international convention[9]

$$\text{Manufacturer} \quad T / P$$

where T is the clamping force in metric tons and P is defined as

$$P = \frac{V_{max} p_{max}}{1000} \tag{6.26}$$

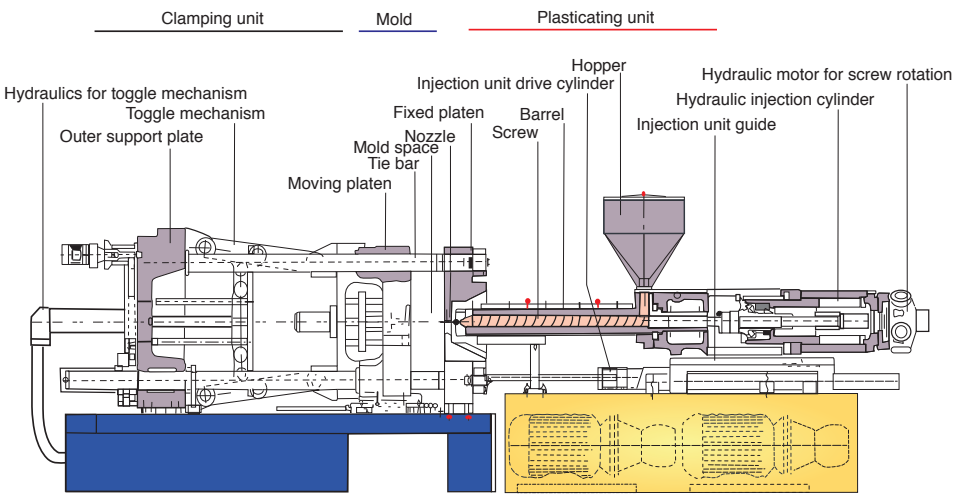

Figure 6.56 Schematic of an injection molding machine

9 The old US convention uses MANUFACTURER T-v where T is the clamping force in British tons and v the shot size in ounces of polystyrene.

where V_{max} is the maximum shot size in cm^3 and p_{max} is the maximum injection pressure in bar. The clamping forced T can be as low as 1 metric ton for small machines, and as high as 11,000 tons.

6.3.1 The Injection Molding Cycle

The sequence of events during the injection molding of a plastic part, as shown in Fig. 6.57, is called the injection molding cycle. The cycle begins when the mold closes, followed by the injection of the polymer into the mold cavity. Once the cavity is filled, a holding pressure is maintained to compensate for material shrinkage. In the next step, the screw turns, feeding the next shot to the front of the screw. This causes the screw to retract as the next shot is prepared. Once the part is sufficiently cool, the mold opens and the part is ejected.

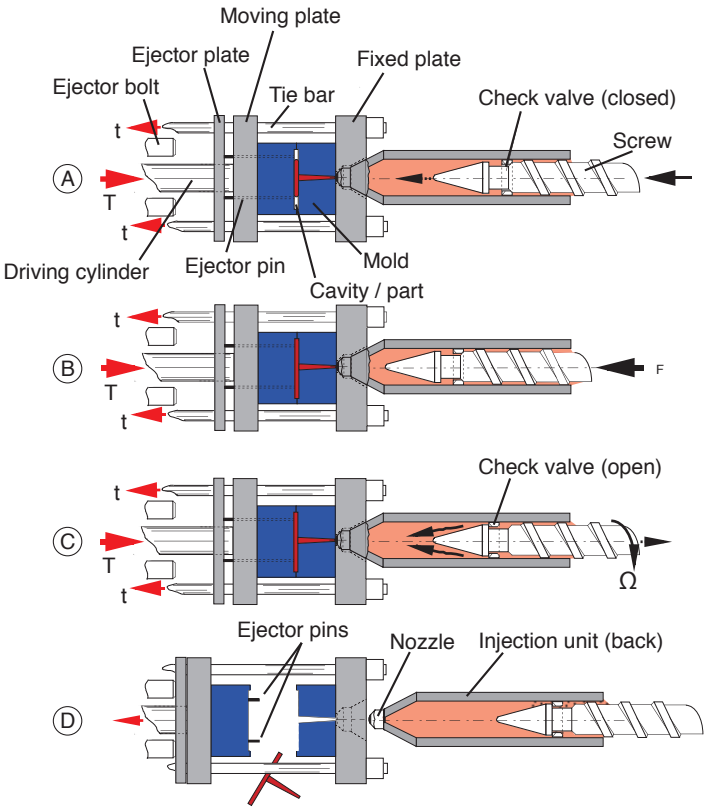

Figure 6.57
Sequence of events during an injection molding cycle

Figure 6.58 presents the sequence of events during the injection molding cycle. The figure shows that the cycle time is dominated by the cooling of the part inside the mold cavity. The total cycle time can be calculated using

$$t_{\text{cycle}} = t_{\text{closing}} + t_{\text{cooling}} + t_{\text{ejection}} \tag{6.27}$$

where the closing and ejection times, t_{closing} and t_{ejection}, can last from a fraction of second to a few seconds, depending on the size of the mold and machine. The cooling times, which dominate the process, depend on the maximum thickness of the part. The cooling time for a plate-like part of thickness h can be estimated using

$$t_{\text{cooling}} = \frac{h^2}{\pi\alpha} \ln\left(\frac{8}{\pi^2}\frac{T_m - T_w}{T_D - T_w}\right) \tag{6.28}$$

and for a cylindrical geometry of diameter D using

$$t_{\text{cooling}} = \frac{D^2}{23.14\alpha} \ln\left(0.692\frac{T_m - T_w}{T_D - T_w}\right) \tag{6.29}$$

where T_m represents the temperature of the injected melt, T_w the temperature of the mold wall, T_D the average temperature at ejection, and α the thermal diffusivity.

Using the average part temperature history and the cavity pressure history, the process can be followed and assessed using the p-v-T diagram, as depicted in Fig. 6.59

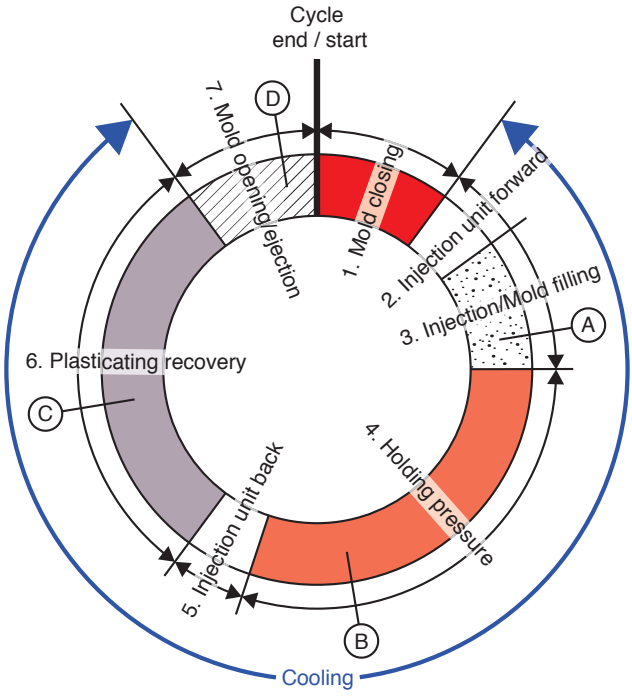

Figure 6.58 Injection molding cycle

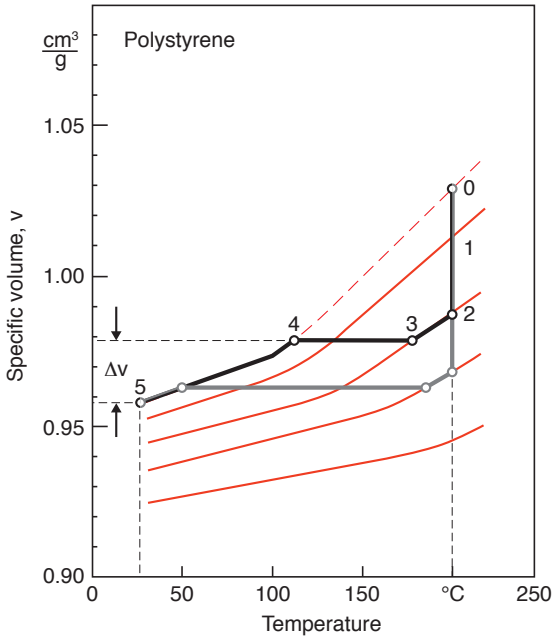

Figure 6.59 Trace of two different injection molding cycles in a p-v-T diagram

[32–33]. To follow the process on the p-v-T diagram, we must transfer both the temperature and the pressure at matching times. The diagram reveals four basic processes: an isothermal injection (0–1) with pressure rising to the holding pressure (1–2), an isobaric cooling process during the holding cycle (2–3), an isochoric cooling after the gate freezes with a pressure drop to atmospheric (3–4), and then isobaric cooling to room temperature (4–5).

The point on the p-v-T diagram at which the final isobaric cooling begins (4) controls the total part shrinkage, Δv. This point is influenced by the two main processing conditions – the melt temperature, T_m, and the holding pressure, P_H, as can be clearly seen when raising the holding pressure. Of course, there is an infinite combination of conditions that render acceptable parts, bound by minimum and maximum temperatures and pressures. Figure 6.60 presents the molding diagram with all limiting conditions. The melt temperature is bound by a low temperature that results in a short shot or unfilled cavity and a high temperature that leads to material degradation. The hold pressure is bound by a low pressure that leads to excessive shrinkage or low part weight and a high pressure that causes flash.

Flash results when the cavity pressure force exceeds the machine clamping force, leading to melt flow across the mold parting line. The holding pressure determines the corresponding clamping force required to size the injection molding machine.

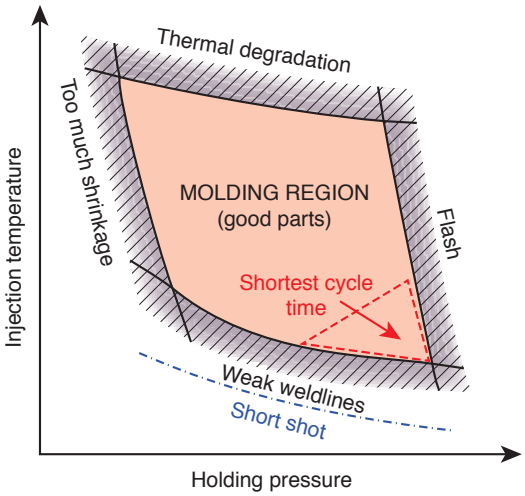

Figure 6.60 The molding diagram

An experienced polymer processing engineer can usually determine which injection molding machine is appropriate for a specific application. For the untrained polymer processing engineer, finding this appropriate holding pressure and its corresponding mold clamping force can be difficult.

With difficulty one can control and predict the component's shape and residual stresses at room temperature. For example, sink marks in the final product are caused by material shrinkage during cooling, and residual stresses can lead to environmental stress cracking under certain conditions [35].

Warpage in the final product is often caused by processing conditions that lead to asymmetric residual stress distributions through the part thickness. The formation of residual stresses in injection molded parts is attributed to two major coupled factors: cooling and flow stresses. The first and most important is the residual stress formed as a result of rapid cooling, which leads to large temperature variations.

6.3.2 The Injection Molding Machine

6.3.2.1 The Plasticating and Injection Unit

A plasticating and an injection unit are shown in Fig. 6.61. The major tasks of the plasticating unit are to melt the polymer, to accumulate the melt in the screw chamber, to inject the melt into the cavity, and to maintain the holding pressure during cooling.

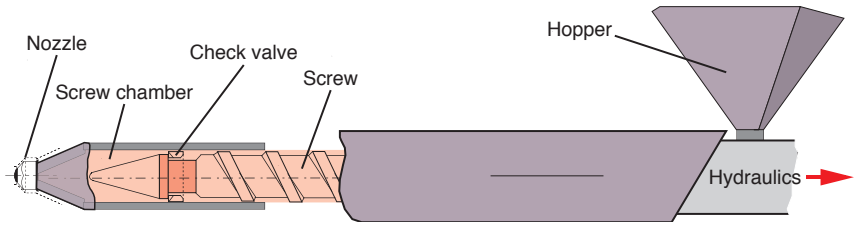

Figure 6.61 Schematic of the plasticating unit

The main elements of the plasticating unit are:

- Hopper
- Screw
- Heater bands
- Check valve
- Nozzle

The hopper, heating bands, and the screw are similar to a plasticating single screw extruder, except that the screw in an injection molding machine can slide back and forth to allow for melt accumulation and injection. This characteristic gives it the name reciprocating screw. For quality purposes, the maximum stroke in a reciprocating screw should be set smaller than 3*D*.

Although the most common screw used in injection molding machines is the three-zone plasticating screw, two-stage vented screws are often used to extract moisture and monomer gases just after the melting stage.

The check valve, or non-return valve, is located at the end of the screw and enables it to work as a plunger during injection and packing preventing polymer melt from flowing back into the screw channel. A check valve and its function during operation is depicted in Fig. 6.57 and in Fig. 6.61. A high quality check valve allows less than 5 % of the melt back into the screw channel during injection and packing.

The nozzle is at the end of the plasticating unit and fits tightly against the sprue bushing during injection. We distinguish between open shut-off nozzle types. The open nozzle is the simplest, rendering the lowest pressure consumption.

6.3.2.2 The Clamping Unit

The job of a clamping unit in an injection molding machine is to open and close the mold, and to close the mold tightly to avoid flash during the filling and holding. Modern injection molding machines have two predominant clamping types: mechanical and hydraulic.

Figure 6.62 presents a toggle mechanism in the open and closed mold positions. Although the toggle is essentially a mechanical device, it is actuated by a hydraulic cylinder. The toggle mechanism has the advantage that, as the mold approaches

closure, the available closing force increases and the closing decelerates significantly. However, the toggle mechanism only transmits its maximum closing force when the system is fully extended.

Figure 6.63 presents a schematic of a hydraulic clamping unit in the open and closed positions. The advantages of the hydraulic system is that a maximum clamping force is attained at any mold closing position and that the system can take different mold sizes without major system adjustments.

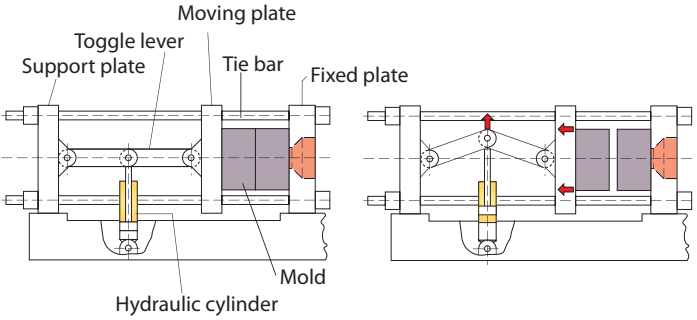

Figure 6.62 Clamping unit with a toggle mechanism

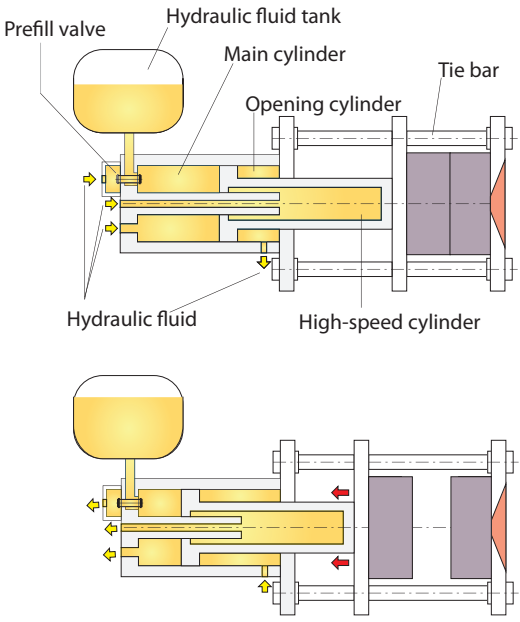

Figure 6.63 Hydraulic clamping unit

6.3.2.3 The Mold Cavity

The central point in an injection molding machine is the mold. The mold distributes polymer melt into and throughout the cavities, shapes the part, cools the melt, and ejects the finished product. As depicted in Fig. 6.64, the mold is custom-made and consists of the following elements:

- Sprue and runner system
- Gate
- Mold cavity
- Cooling system (thermoplastics)
- Ejector system

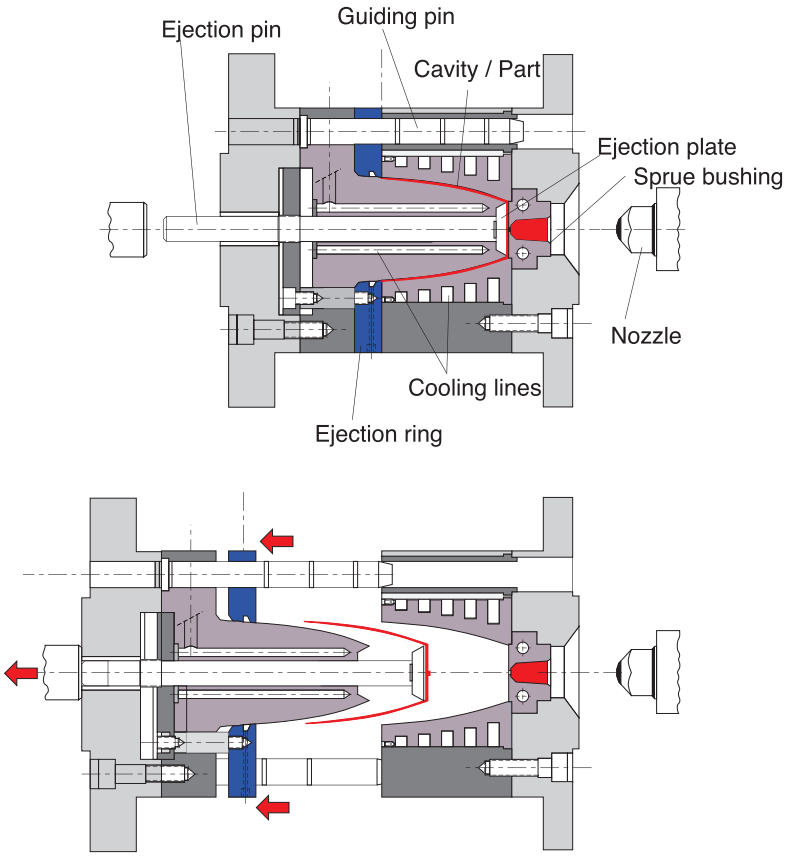

Figure 6.64 An injection mold

During mold filling, the melt flows through the sprue and is distributed into the cavities by the runners, as seen in Fig. 6.65.

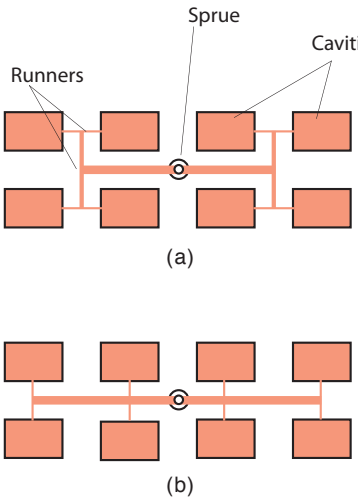

Figure 6.65 Schematic of different runner system arrangements

The runner system in Fig. 6.65 (a) is symmetric which ensures that all cavities fill at the same time and causing the polymer to fill all cavities in the same way. The disadvantage of this balanced runner system is that the flow paths are long, leading to high material and pressure consumption. On the other hand, the asymmetric runner system shown in Fig. 6.65 (b) leads to parts of different quality. Equal filling of the mold cavities can also be achieved by varying runner diameters. There are two types of runner systems – cold and hot runners. Cold runners are ejected with the part, and are trimmed after part removal. The advantage of the cold runner is lower mold cost. The hot runner keeps the polymer at its melt temperature. The material stays in the runner system after ejection, and is injected into the cavity in the following cycle. There are two types of hot runner system: externally and internally heated. The externally heated runners have a heating element surrounding the runner that keeps the polymer isothermal. The internally heated runners have a heating element running along the center of the runner, maintaining a polymer melt that is warmer at its center and possibly solidified along the outer runner surface. Although a hot runner system considerably increases mold cost, its advantages include elimination of trim and lower pressures for injection. Various arrangements of hot runners are schematically depicted in Fig. 6.66. It should be noted that there are two parting lines in a hot runner cavity system, and that the second parting line is only opened during maintenance of the molds.

When large items are injection molded, the sprue sometimes serves as the gate, as shown in Fig. 6.67. The sprue must be subsequently trimmed, often requiring further surface finishing. On the other hand, a pin-type gate (Fig. 6.67) is a small

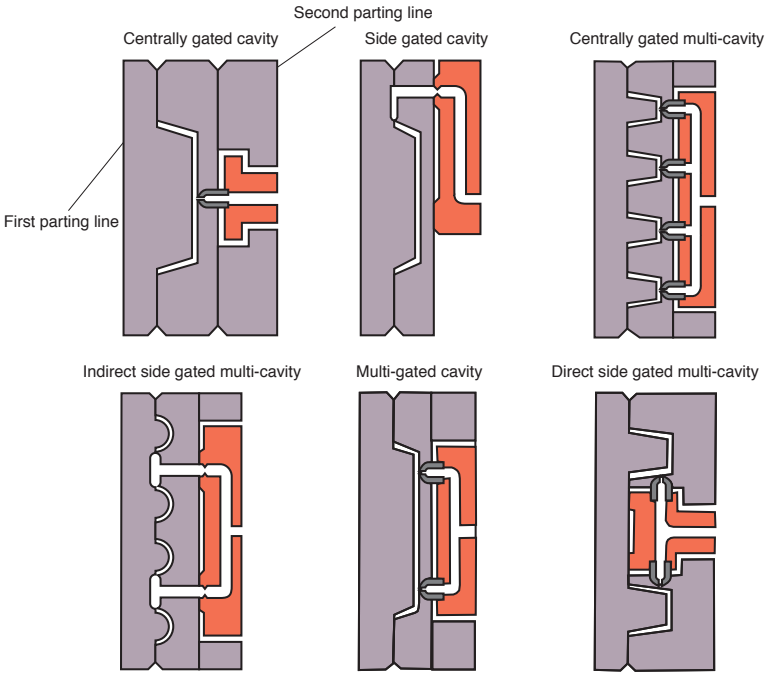

Figure 6.66 Various hot runner system arrangements

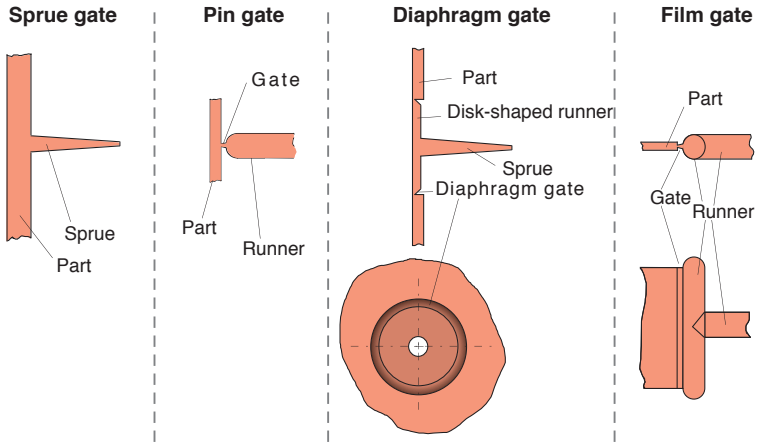

Figure 6.67 Schematic of different gating systems

orifice that connects the sprue or the runners to the mold cavity. The part is easily broken off from such a gate, leaving only a small mark that usually does not require finishing. Other types of gates, also shown in Fig. 6.67, are film gates, used to eliminate orientation, and disk or diaphragm gates for symmetric parts such as compact discs.

6.4 Special Injection Molding Processes[10]

There are several variations of injection molding processes, many of which are still under development. Furthermore, due to the diversified nature of these special injection molding processes, there is no unique method to categorize them. Figure 6.68 attempts to schematically categorize special injection molding processes for thermoplastics. The most common special injection molding processes are multi-component injection molding, co-injection molding, gas assisted injection molding, injection-compression molding, reaction injection molding, and injection molding of liquid silicone rubber.

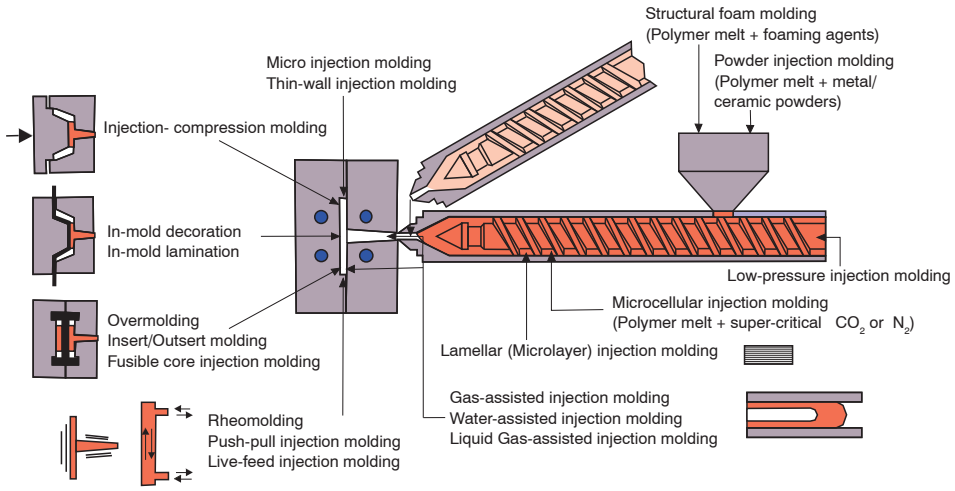

Figure 6.68 Schematic classification of special injection molding processes for thermoplastics

6.4.1 Multi-Component Injection Molding

Multi-component (or multi-color) injection molding is used to inject two or more components through different runner and gate systems at different stages during the molding process. Each component is injected using its own plasticating unit. The molds are often located on a turntable. Multi-color automotive stop lights are molded this way. In multi-component processes, often two incompatible materials are molded or one component is cooled sufficiently so that the two components do

10 Parts of this section are based on Turng, L. S., Injection Molding Processes, A chapter in Injection Molding Handbook, 2nd ed., Eds. Osswald, T. A., Gramann, P. J., and Turng, L. S., Hanser Publishers, Munich, (2007).

not adhere to each other. For example, to mold a ball and socket system, either the ball or the socket of the linkage is molded first. The component that is injected first is allowed to cool somewhat before the second component is molded in. This results in a perfectly movable system; if the socket is injected first, the assembly will be loose and if the ball is molded first, the assembly will be tight, as the socket shrinks over the ball. This type of injection molding process is used to replace tedious assembling tasks and is becoming popular in countries where labor costs are high. Hence, this type of process is referred to as *assembly injection molding*. A commonly used method of multi-component injection molding employs a rotating mold and multiple injection units, as shown in Fig. 6.69. Once the insert is molded, a hydraulic or electric servo drive rotates the core and the part by 180 degrees (or 120 degrees for a three-shot part), allowing alternating polymers to be injected. This is the fastest and most common method because two or more parts can be molded in every cycle. Another variation of multi-component injection molding involves automatically expanding the original cavity geometry using retractable (movable) cores or slides while the insert is still in the mold. This process is called core-pull or core-back, as shown in Fig. 6.70. To be specific, the core retracts after

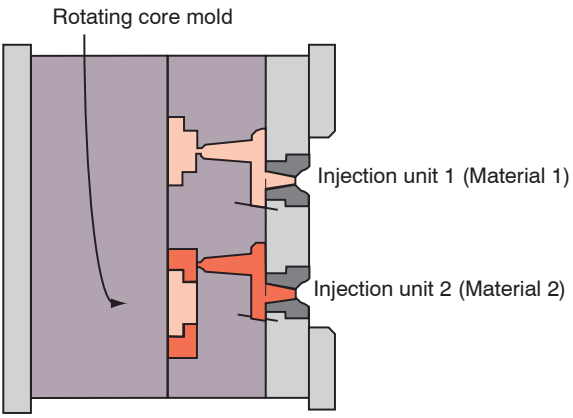

Figure 6.69 Schematic diagram of a rotating mold used to produce multi-component injection molded parts

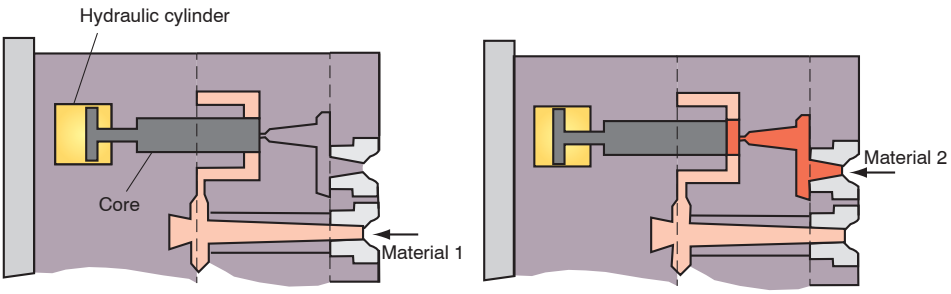

Figure 6.70 Schematic diagram of multi-component injection molding using a *core pull* or a *core back* technique

the insert has solidified to create open volume to be filled by the second material within the same mold.

6.4.2 Co-Injection Molding

In contrast to multi-color or multi-component injection molding, co-injection molding uses the same gate and runner system. Here, the component that will form the outer skin of the part is injected first, followed by the core component. Figure 6.71 illustrates the typical sequences of the co-injection molding process using the *one-channel technique* and the resulting flow of skin and core materials inside the cavity. This is accomplished with the use of a machine that has two separate, individually controllable injection units and a common injection nozzle block with a switching head. Due to the flow behavior of the polymer melts and the solidification of skin material, a frozen layer of polymer starts to grow from the colder mold walls. The polymer flowing in the center of the cavity remains molten. As the core material is injected, it flows within the frozen skin layers, pushing the molten skin

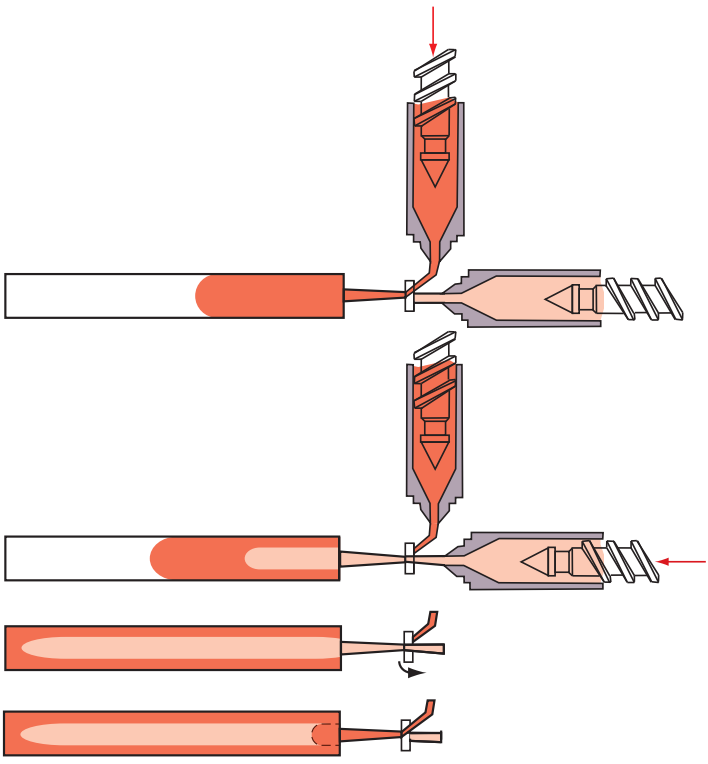

Figure 6.71 Sequential co-injection molding process

material at the hot core to the extremities of the cavity. Because of the fountain-flow effect at the advancing melt front, the skin material at the melt front will show up at the region adjacent to the mold walls. This process continues until the cavity is nearly filled, with skin material appearing on the surface and the end of the part. Finally, a small additional amount of skin material is injected again to purge the core material away from the sprue so that it will not appear on the part surface in the next shot. When not enough skin material is injected prior to the injection of core material, the skin material may sometimes be depleted during the filling process and the core material will show up on portions of the surface and the end of the part that is last filled. This is referred to as *core surfacing* or *core breakthrough*. There are other variations to the sequential (namely, skin-core-skin, or A-B-A) co-injection molding process. In particular, one can start to inject the core material while the skin material is being injected (i. e., A-AB-B-A). That is, a majority of skin material is injected into a cavity, followed by a combination of both skin and core materials flowing into the same cavity, and then followed by the balance of the core material to fill the cavity. Again, an additional small amount of skin injection will cap the end of the sequence, as described previously. In addition to the one-channel technique configuration, two- and three-channel techniques have been developed that use nozzles with concentric flow channels to allow simultaneous injection of skin and core materials.

6.4.3 Gas-Assisted Injection Molding (GAIM)

The gas-assisted injection molding (GAIM) process begins with a partial or nearly full injection of polymer melt into the mold cavity, followed by injection of an inert gas (typically nitrogen) into the core of the polymer melt through the nozzle, sprue, runner, or directly into the cavity. The compressed gas takes the path of least resistance, flowing toward the melt front, where the pressure is lowest. As a result, the gas penetrates and hollows out a network of predesigned, thick-sectioned gas channels, displacing molten polymer at the hot core to fill and pack out the entire cavity. As depicted in Fig. 6.72, gas assisted injection, as well as other fluid assisted injection molding technologies, work based on several variations of two principles. The first principle is based on partially filling a mold cavity and completing the mold filling by displacing the melt with a pressurized fluid. Figure 6.73 presents the gas-assisted injection molding process cycle based on this principle. With the second principle, the cavity is nearly or completely filled and the molten core is evacuated into a secondary cavity. This secondary cavity can be either a side cavity that will be scrapped after demolding, a side cavity that will result in an actual part, or the melt shot cavity in front of the screw in the plasticating unit of the injection molding machine. In the latter, the melt is reused in the next molding cycle. In the so-called gas-pressure control process, the compressed gas is injected

with a regulated gas pressure profile, either constant, ramped, or stepped. In the *gas-volume control process*, gas is initially metered into a compression cylinder at preset volume and pressure; then, it is injected under pressure generated from reducing the gas volume by movement of the plunger. Conventional injection mold-

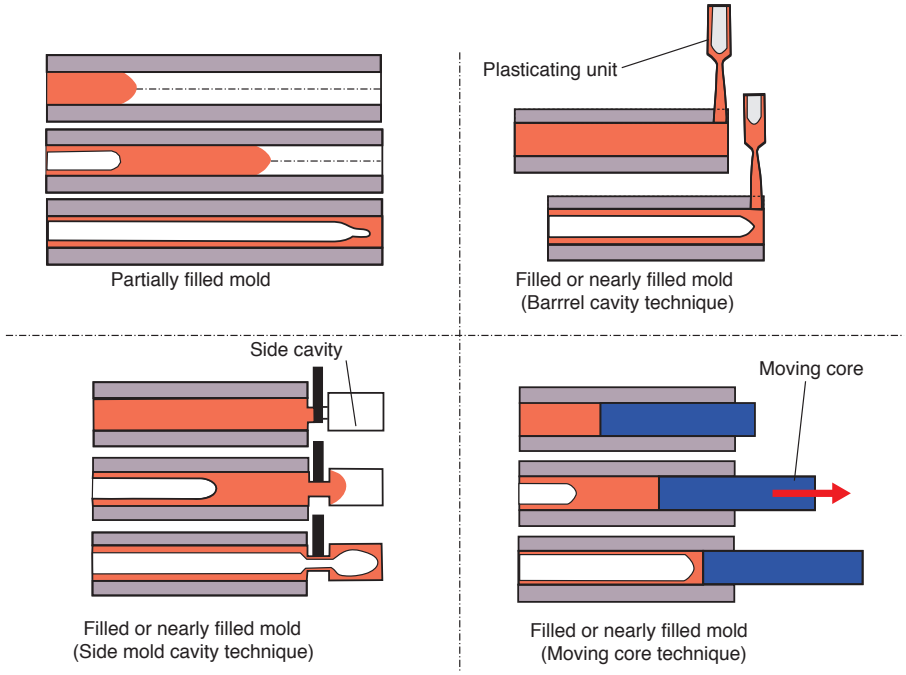

Figure 6.72 Schematic classification of fluid-assisted injection molding processes

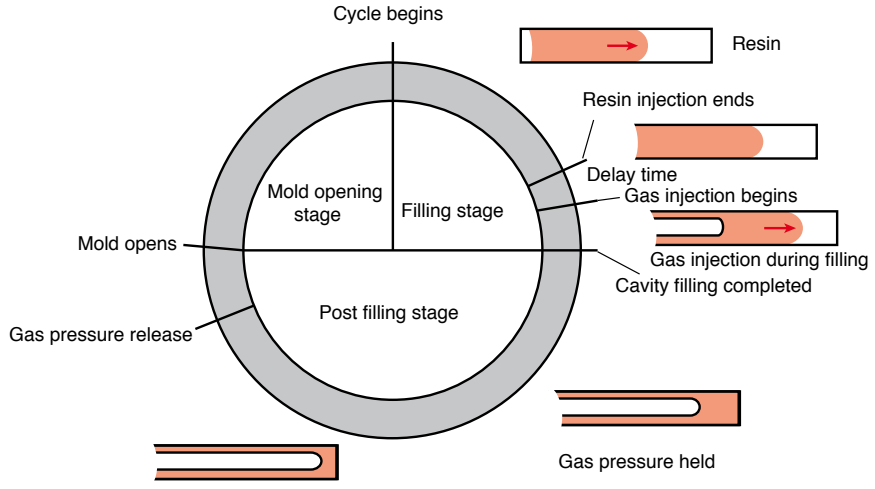

Figure 6.73 Gas-assisted injection molding cycle [3]

ing machines with precise shot volume control can be adapted for gas-assisted injection molding with add-on conversion equipment, a gas source, and a control device for gas injection, as schematically depicted in Fig. 6.74. Gas-assisted injection molding, however, requires a different approach to product, tool, and process design due to the need for control of additional gas injection and the layout and sizing of gas channels to guide the gas penetration in a desirable fashion.

The gas-assisted injection molding process is a special form of a more general category of *fluid-assisted injection molding*. Another process that falls under this category is *water-assisted injection molding*. The main difference of this latter process is that water is incompressible and has a much higher thermal conductivity and heat capacity than air. Consequently, this leads to significant reductions in cycle time.

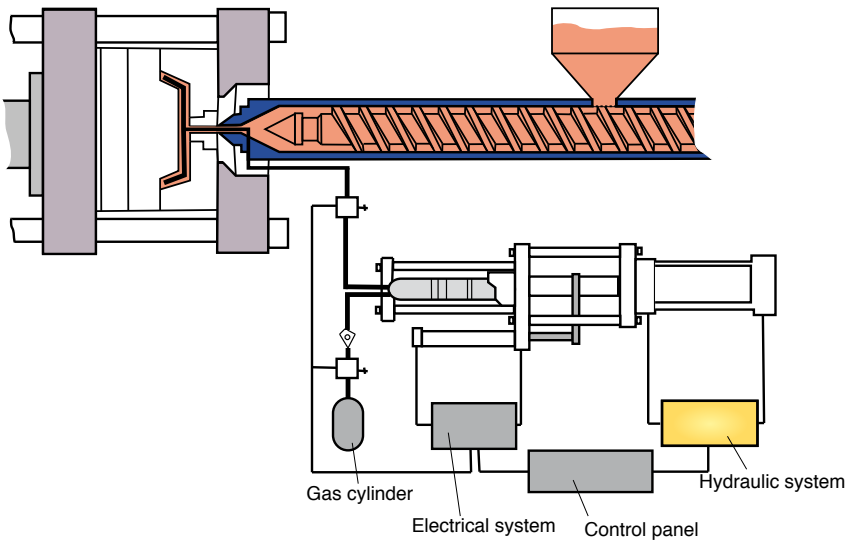

Figure 6.74 Schematic diagram of a typical injection molding machine adapted for gas-assisted injection molding with an add-on gas-compression cylinder and accessory equipment [3]

6.4.4 Injection-Compression Molding

The injection-compression molding (ICM) is an extension of conventional injection molding by incorporating a mold compression action to compact the polymer material for producing parts with dimensional stability and surface accuracy. In this process, the mold cavity initially has an enlarged cross-section, which allows polymer melt to proceed readily to the extremities of the cavity under relatively low pressure. At some time during or after filling, the mold cavity thickness is reduced by a mold-closing movement, which forces the melt to fill and pack out the entire

cavity. This mold compression action results in a more uniform pressure distribution across the cavity, leading to more homogenous physical properties and less shrinkage, warpage, and molded-in stresses than are possible with conventional injection molding. The injection-compression molding process is schematically depicted in Fig. 6.75. A potential drawback associated with the two-stage sequential ICM is the *hesitation* or *witness* mark resulting from flow stagnation during injection-compression transition. To avoid this surface defect and to facilitate continuous flow of the polymer melt, *simultaneous ICM* activates mold compression while resin is being injected. The primary advantage of ICM is the ability to produce dimensionally stable, relatively stress-free parts, at a low pressure, clamp tonnage (typically 20 to 50 % lower than with injection molding), and reduced cycle time. For thin-wall applications, difficult-to-flow materials, such as polycarbonate, have been molded as thin as 0.5 mm. Additionally, the compression of a relatively circular charge significantly lowers molecular orientation, consequently leading to reduced birefringence, improving the optical properties of a finished part. ICM is the most suitable technology for the production of high-quality and cost-effective CDs/DVDs as well as many types of optical lenses.

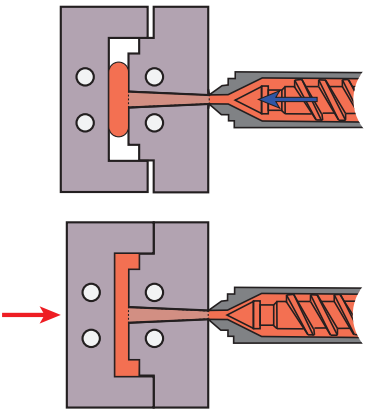

Figure 6.75 Schematic of the injection-compression molding process [3]

6.4.5 Reaction Injection Molding (RIM)

Reaction injection molding (RIM) involves mixing of two reacting liquids in a mixing head before injecting the low-viscosity mixture into mold cavities at relatively high injection speeds. The liquids react in the mold to form a cross-linked solid part. Figure 6.76 presents a schematic of a high pressure polyurethane injection system. The mixing of the two components occurs at high speeds in *impingement mixing heads*. Low pressure polyurethane systems, such as the one schematically presented in Fig. 6.77, require mixing heads with a mechanical stirring device.

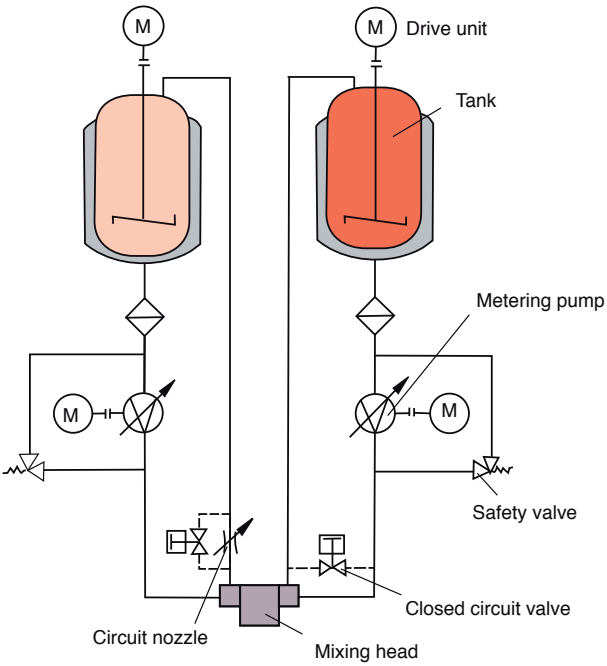

Figure 6.76 Schematic diagram of a high pressure polyurethane injection system

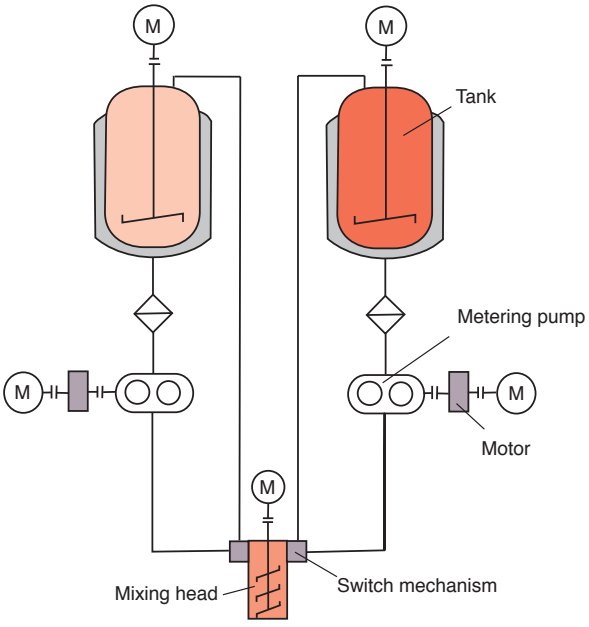

Figure 6.77 Schematic diagram of a low pressure polyurethane injection system

The short cycle times, low injection pressures, and clamping forces, coupled with superior part strength and heat and chemical resistance of the molded part make RIM well suited for the rapid production of large, complex parts, such as automotive bumper covers and body panels. Reaction injection molding is a process for rapid production of complex parts directly from monomers or oligomers. Unlike thermoplastic injection molding, the shaping of solid RIM parts occurs through polymerization (crosslinking or phase separation) in the mold rather than solidification of the polymer melts. RIM is also different from thermoset injection molding in that the polymerization during RIM is activated via chemical mixing rather than thermally activated by the warm mold. During the RIM process, the two liquid reactants (e.g., polyol and an isocyanate, which are the precursors for polyurethanes) are metered in the correct proportion into a mixing chamber where the streams impinge at a high velocity and start to polymerize prior to being injected into the mold. Due to the low-viscosity of the reactants, the injection pressures are typically very low, even though the injection speed is fairly high. Because of the fast reaction rate, the final parts can be de-molded in typically less than one minute. There are a number of RIM variants. For example, in the so-called reinforced reaction injection molding (RRIM) process, fillers, such as short glass fibers or glass flakes, have been used to enhance the stiffness, maintain dimensional stability, and reduce material cost of the part. As another modification of RIM, structural reaction injection molding (SRIM) is used to produce composite parts by impregnating a reinforcing glass fiber-mat (preform) pre-placed inside the mold with the curing resin. Resin transfer molding (RTM) is very similar to SRIM in that it also employs reinforcing glass fiber-mats to produce composite parts; however, the resins used in RTM are formulated to react more slowly, and the reaction is thermally activated as it is in thermoset injection molding. The capital investment for molding equipment for RIM is lower compared with that for injection molding machines. Finally, RIM parts generally exhibit greater mechanical and heat-resistant properties due to the resulting crosslinked structure. The mold and process designs for RIM become generally more complex because of the chemical reaction during processing. For example, slow filling may cause premature gelling, which results in short shots, whereas fast filling may induce turbulent flow, creating internal porosity. Moreover, the low viscosity of the material tends to cause flash that requires trimming. Another disadvantage of RIM is that the reaction with isocyanate requires special environmental precaution due to health issues. Finally, like many other thermosetting materials, the recycling of RIM parts is not as easy as that of thermoplastics. Polyurethane materials (rigid, foamed, or elastomeric) have traditionally been synonymous with RIM as they and urea urethanes account for more than 95 % of RIM production.

6.4.6 Liquid Silicone Rubber Injection Molding

Injection molding of liquid silicone rubber (LSR) has evolved over the past 35 years. Due to the thermosetting nature of the material, liquid silicone injection molding requires special treatment, such as intensive distributive mixing, while maintaining a low material temperature before it is pushed into the heated cavity and vulcanized. Figure 6.78 schematically depicts an LSR injection molding process. Liquid silicone rubbers are supplied in barrels or hobbocks. Because of their low viscosity, these rubbers can be pumped through pipelines and tubes to the vulcanization equipment. The two components (labeled component A and B in the figure) are pumped through a static mixer by a metering pump. One of the components contains the catalyst, which is typically platinum based. A coloring paste as well as other additives can also be added before the material enters the static mixer section. In the static mixer the components are well mixed and then transferred to the cooled metering section of the injection molding machine. The static mixer renders a very homogeneous material, allowing for products that are not only very consistent throughout the part, but also from part to part. This is in contrast to solid silicone rubber materials purchased pre-mixed and partially vulcanized. Hard silicone rubbers are processed by transfer molding and result in less material

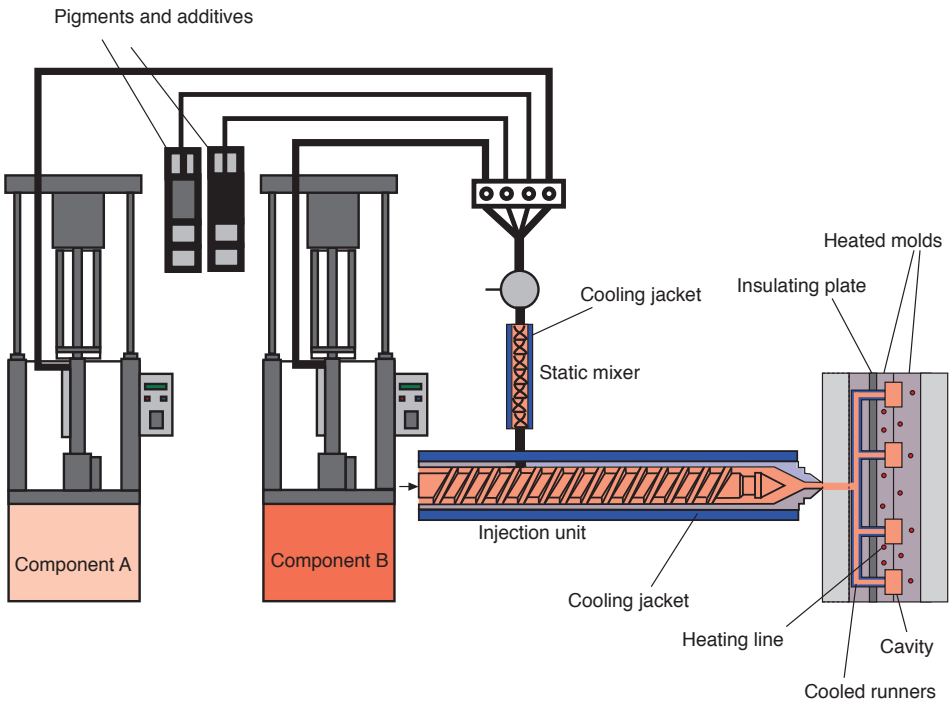

Figure 6.78 Schematic diagram of a liquid silicone rubber injection molding system

consistency and control, leading to higher part variability. Additionally, solid silicone rubber materials are processed at higher temperatures and require longer vulcanization times. From the metering section of the injection molding machine, the compound is pushed through cooled sprue and runner systems into a heated cavity where the vulcanization takes place. The cold runner and general cooling result in minimal loss of material in the feed lines. The cooling allows production of LSR parts with nearly zero material waste, eliminating trimming operations, and yielding significant savings in material cost. Silicone rubber is a family of thermoset elastomers that have a backbone of alternating silicone and oxygen atoms and methyl or vinyl side groups. Silicone rubbers constitute about 30 % of the silicone family, making them the largest group of that family. Silicone rubbers maintain their mechanical properties over a wide range of temperatures and the presence of methyl-groups in silicone rubbers makes these materials extremely hydrophobic. Typical applications for liquid silicone rubber are products that require high precision, such as seals, sealing membranes, electric connectors, multi-pin connectors, infant products where smooth surfaces are desired, such as bottle nipples, medical applications, as well as kitchen goods such as baking pans, spatulas, etc.

6.5 Secondary Shaping

Secondary shaping operations, such as extrusion blow molding, film blowing, and fiber spinning occur immediately after the extrusion profile emerges from the die. The thermoforming process is performed on sheets or plates previously extruded and solidified. In general, secondary shaping operations consist of mechanical stretching or forming of a preformed cylinder, sheet, or membrane.

6.5.1 Fiber Spinning

Fiber spinning is used to manufacture synthetic fibers. During fiber spinning, a filament is continuously extruded through an orifice and stretched to diameters of 100 µm or smaller. The process is schematically depicted in Fig. 6.79. The molten polymer is first extruded through a filter or screen pack, to eliminate small contaminants. The melt is then extruded through a spinneret, a die composed of multiple orifices. A spinneret can have between one and 10,000 holes. The fibers are then drawn to their final diameter, solidified, and wound onto a spool. The solidification takes place either in a water bath or by forced convection. When the fiber solidifies in a water bath, the extrudate undergoes an adiabatic stretch before cool-

ing begins in the bath. Forced convection cooling, which is more commonly used, leads to a non-isothermal spinning process.

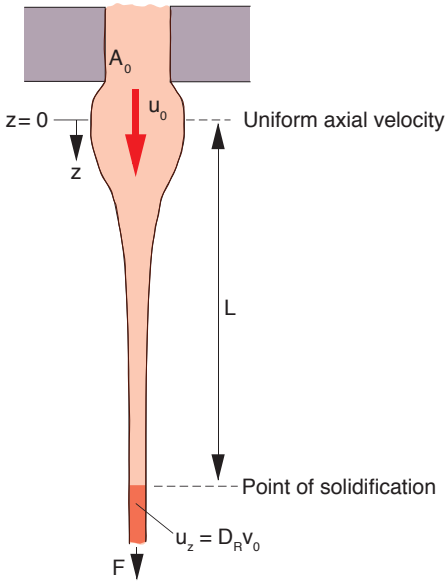

Figure 6.79 The fiber spinning process

The drawing and cooling processes determine the morphology and mechanical properties of the final fiber. For example, ultra high molecular weight HDPE fibers with high degrees of orientation in the axial direction can have the stiffness of steel with today's fiber spinning technology.

Of major concern during fiber spinning are the instabilities that arise during drawing, such as brittle fracture, Rayleigh disturbances, and draw resonance. Brittle fracture occurs when the elongational stress exceeds the melt strength of the drawn polymer melt. The instabilities caused by Rayleigh disturbances are like those causing filament break-up during dispersive mixing as discussed in Chapter 5. Draw resonance appears under certain conditions and manifests itself as periodic fluctuations that result in diameter oscillation.

6.5.2 Film Production

6.5.2.1 Cast Film Extrusion

In a cast film extrusion process, a thin film is extruded through a slit onto a chilled, highly polished, turning roll where it is quenched from one side. The speed of the roller controls the draw ratio and final film thickness. The film is then sent to a second roller for cooling of the other side. Finally, the film passes through a system

of rollers and is wound onto a roll. A typical film casting process is depicted in Fig. 6.80 and 6.81. The cast film extrusion process exhibits stability problems similar to those encountered in fiber spinning [36].

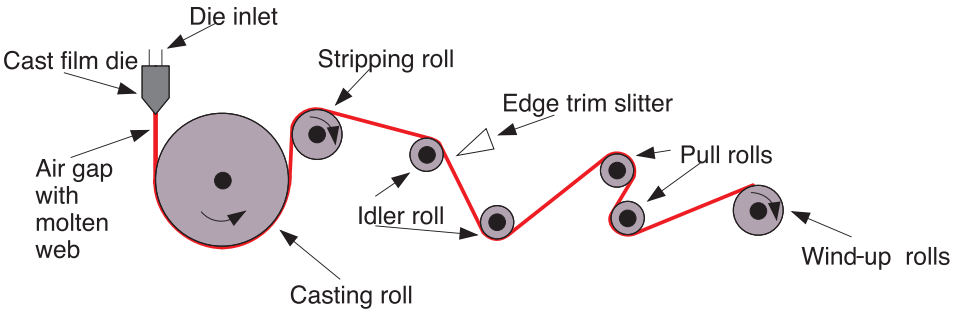

Figure 6.80 Schematic of a film casting operation

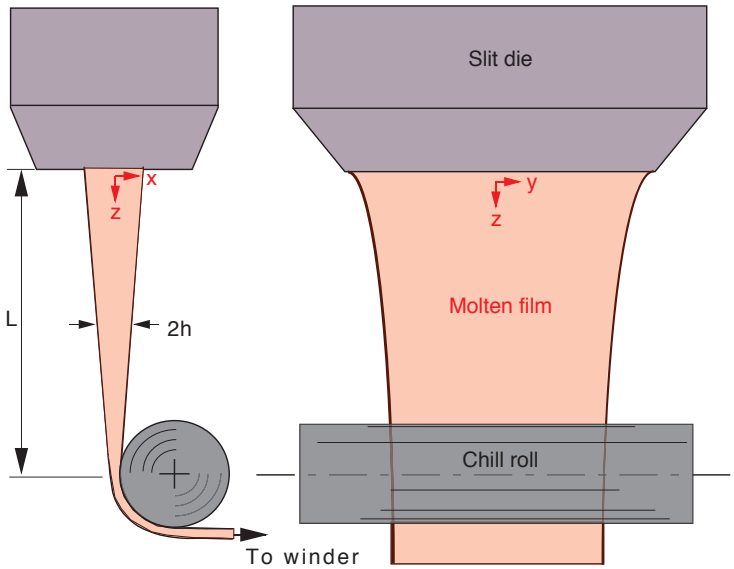

Figure 6.81 Film casting

6.5.2.2 Film Blowing

In film blowing, a tubular cross-section is extruded through an annular die, normally a spiral die, and is drawn and inflated until the freezing line is reached. Beyond this point, the stretching is practically negligible. The process is schematically depicted in Fig. 6.82 [37] and Fig. 6.83. The advantage of film blowing over casting is that the induced biaxial stretching renders a stronger and less permea-

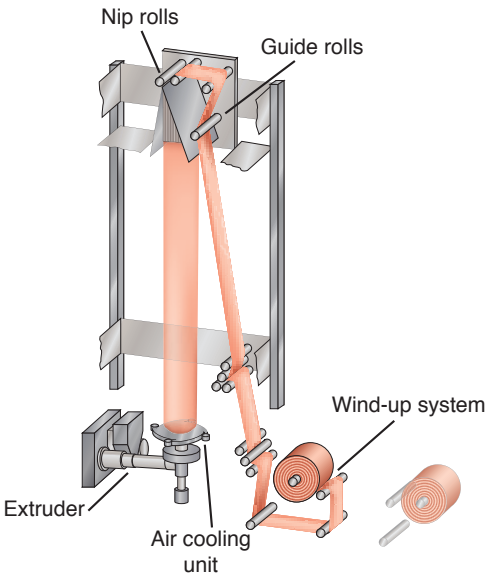

Figure 6.82
Film blowing

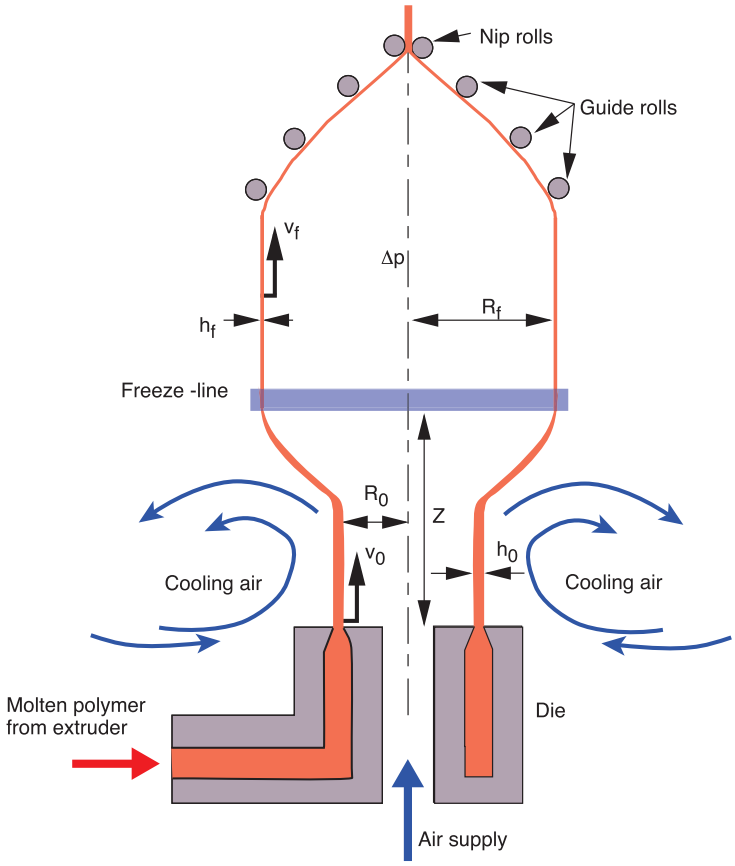

Figure 6.83
Film blowing, detail

ble film. Film blowing is mainly used with less expensive materials such as polyolefins. Polymers with lower viscosity, such as PA and PET, are better manufactured using the cast film process.

The extruded tubular profile passes through one or two air rings to cool the material. The tube interior is maintained at a certain pressure by blowing air into the tube through a small orifice in the die mandrel. The air is retained in the tubular film, or bubble, by collapsing the film well above its freeze-off point and tightly pinching it between rollers. The size of the tubular film is calibrated between the air ring and the collapsing rolls.

6.5.3 Blow Molding

The predecessor of the blow molding process was the blowing press developed by Hyatt and Burroughs in the 1860s to manufacture hollow celluloid articles. Polystyrene was the first synthetic polymer used for blow molding during World War II and polyethylene was the first material to be implemented in commercial applications. Until the late 1950s, the main application for blow molding was the manufacture of LDPE articles such as squeeze bottles.

Blow molding produces hollow articles that do not require a homogeneous thickness distribution. Today, HDPE, LDPE, PP, PET, and PVC are the most common materials used for blow molding.

6.5.3.1 Extrusion Blow Molding

In extrusion blow molding, a parison or tubular profile is extruded and inflated into a cavity with the specified geometry. The blown article is held inside the cavity until it is sufficiently cool. Figure 6.84 [38] presents a step-by-step schematic of the blow molding process.

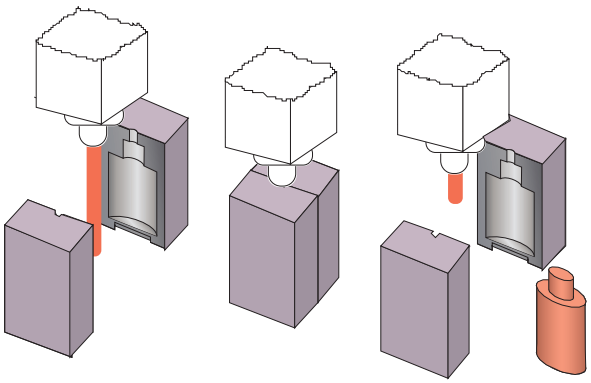

Figure 6.84 Schematic of the extrusion blow molding process

During blow molding, one must generate the appropriate parison length such that the trim material is minimized. Another means of saving material is generating a parison of variable thickness, usually referred to as parison programming, such that an article with an evenly distributed wall thickness is achieved after stretching the material. An example of a programmed parison and finished bottle thickness distribution is presented in Fig. 6.85 [39].

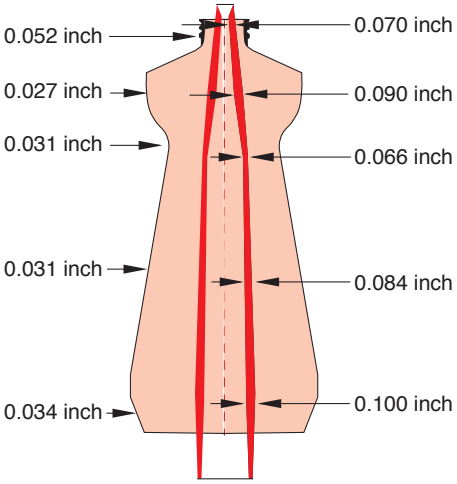

Figure 6.85 Wall thickness distribution in the parison and the part

A parison of variable thickness can be generated by moving the mandrel vertically during extrusion, as shown in Fig. 6.86. A thinner wall not only results in material savings but also reduces the cycle time due to the shorter required cooling times.

As expected, the largest portion of the cycle time is the cooling of the blow molded container in the mold cavity. Most machines utilize multiple molds in order to increase production. Rotary molds are often used in conjunction with vertical or horizontal rotating tables (Fig. 6.87 [37]).

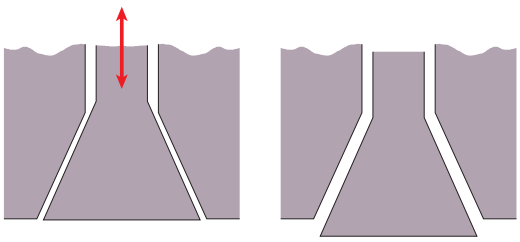

Figure 6.86 Moving mandrel used to generate a programmed parison

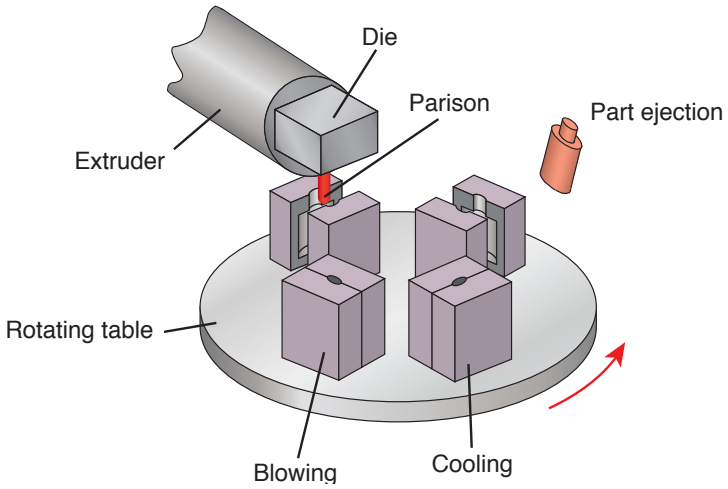

Figure 6.87 Schematic of an extrusion blow molder with a rotating table

6.5.3.2 Injection Blow Molding

Injection blow molding depicted in Fig. 6.88 [38] begins by injection molding the parison onto a core and into a mold with finished bottle threads. The formed parison has a thickness distribution that leads to reduced thickness variations throughout the container. Before blowing the parison into the cavity, it can be mechanically stretched to orient molecules axially, Fig. 6.89 [38]. The subsequent blowing operation introduces tangential orientation. A container with biaxial molecular orientation exhibits higher optical (clarity) and mechanical properties and lower permeability. Injection blow molding processes can move seamlessly from injection to blowing or a re-heating stage of the cooled parison may be incorporated.

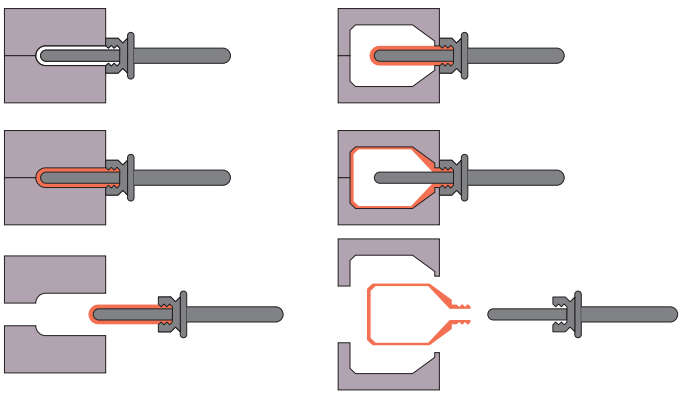

Figure 6.88 Injection blow molding

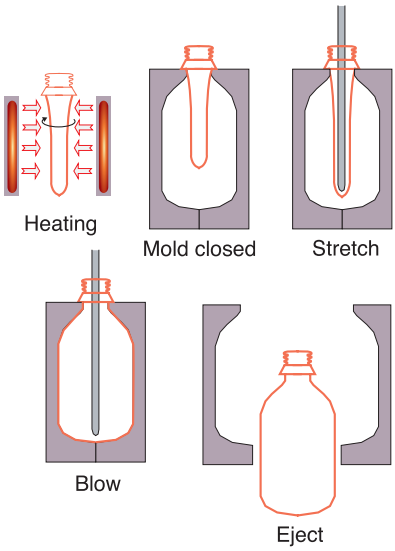

Figure 6.89 Stretch blow molding

The advantages of injection blow molding over extrusion blow molding are:

- Pinch-off and therefore post-mold trimming are eliminated
- Controlled container wall thickness
- Dimensional control of the neck and screw-top of bottles and containers

Disadvantages include higher initial mold cost, the need for both injection and blow molding units, and lower volume production.

6.5.3.3 Thermoforming

Thermoforming is an important secondary shaping method of plastic film and sheet. Thermoforming consists of warming the plastic sheet and forming it into a cavity or over a tool using vacuum, air pressure, and mechanical means. During the 18th Century, tortoiseshells and hooves were thermoformed into combs and other shapes. The process was refined during the mid-19th Century to thermoform various cellulose nitrate articles. During World War II, thermoforming was used to manufacture acrylic aircraft cockpit enclosures, canopies, and windshields, as well as translucent covers for outdoor neon signs. During the 1950s, the process made an impact on the mass production of cups, blister packs, and other packaging commodities. Today, in addition to packaging, thermoforming is used to manufacture refrigerator liners, pick-up truck cargo box liners, shower stalls, bathtubs, as well as automotive trunk liners, glove compartments, and door panels.

A typical thermoforming process is presented in Fig. 6.90 [37]. The process begins by heating the plastic sheet slightly above the glass transition temperature for amorphous polymers, or slightly below the melting point for semi-crystalline materials.

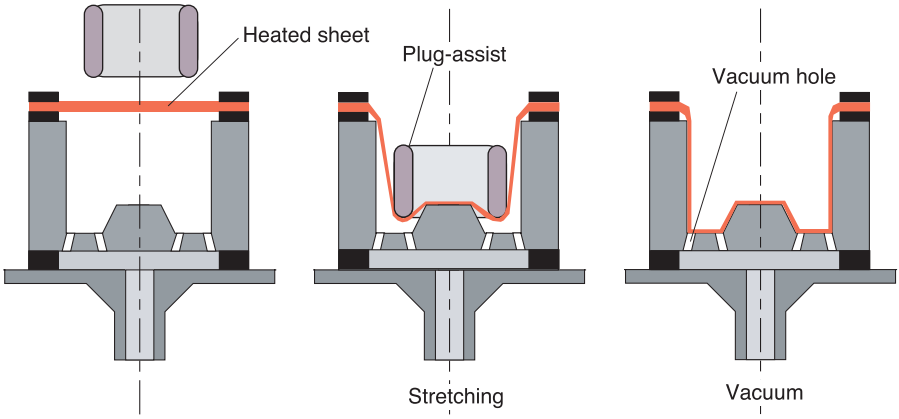

Figure 6.90 Plug-assist thermoforming using vacuum

Although both amorphous and semi-crystalline polymers are used for thermoforming, the process is easiest with amorphous polymers because they have a wide rubbery temperature range above the glass transition temperature. At these temperatures the polymer is easily shaped, but still has enough rigidity to hold the heated sheet without much sagging. Most semi-crystalline polymers lose their strength rapidly once the crystalline structure breaks up above the melting temperature.

The heating is achieved using radiative heaters and the temperature reached during heating must be high enough for sheet shaping, but low enough so the sheets do not droop into the heaters. One key requirement for successful thermoforming is to bring the sheet to a uniform forming temperature. The sheet is then shaped into the cavity over the tool. This can be accomplished in several ways. Most commonly a vacuum sucks the sheet onto the tool, stretching the sheet until it contacts the tool surface. The main problem here is the irregular thickness distribution that arises throughout the part. Hence, the main concern of the process engineer is to optimize the system such that the differences in thickness throughout the part are minimized. This can be accomplished in many ways but is most commonly done by plug-assist. Here, as the plug pushes the sheet into the cavity, only the parts of the sheet not touching the plug-assist stretch. Because the unstretched portions of the sheet must remain hot for subsequent stretching, the plug-assist is made of a low thermal conductivity material such as wood or hard rubber. The initial stretch is followed by a vacuum for final shaping. Once cooled, the product is removed.

To reduce thickness variations in the product, the sheet can be pre-stretched by forming a bubble at the beginning of the process. This is schematically depicted in Fig. 6.91 [37]. The mold is raised into the bubble, or a plug-assist pushes the bubble into the cavity, and a vacuum finishes the process.

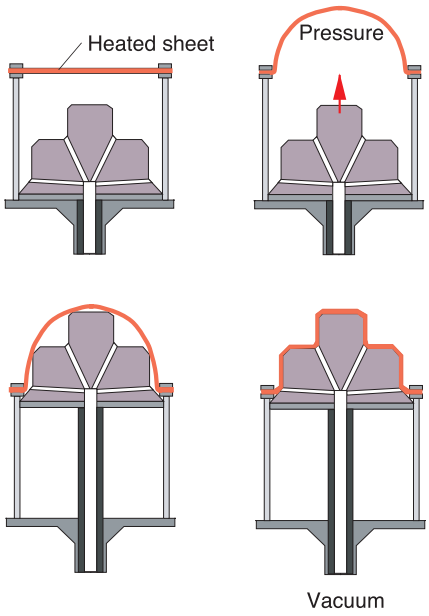

Figure 6.91 Reverse draw thermoforming with plug-assist and vacuum

One of the main reasons for the rapid growth and high volume of thermoformed products is that the tooling costs for a thermoforming mold are much lower than for injection molding.

6.6 Calendering

In a calender line, the polymer melt is transformed into films and sheets by squeezing it between pairs of co-rotating high precision rollers. Calenders are also used to produce certain surface textures that may be required for different applications. Today, calendering lines are used to manufacture PVC sheet, floor covering, rubber sheet, and rubber tires. They are also used to texture or emboss surfaces. When producing PVC sheet and film, calender lines have a great advantage over extrusion processes because of the shorter residence times, resulting in a lower requirement for stabilizers. This is a cost effective approach because stabilizers are a major part of the overall expense of processing these polymers.

Figure 6.92 [37] presents a typical calender line for manufacturing PVC sheet. A typical system is composed of:

- Plasticating unit
- Calender

- Cooling unit
- Accumulator
- Wind-up station

In the plasticating unit, which is represented by the internal batch mixer and the strainer extruder, the material is melted and mixed and then fed in a continuous stream between the nip of the first two rolls. In another variation of the process, the mixing may take place elsewhere, and the material is simply reheated on the roll mill. Once the material is fed to the mill, the first pair of rolls controls the feeding rate, while subsequent rolls in the calender calibrate the sheet thickness. Most calender systems have four rolls as does the one in Fig. 6.92, which is an inverted L- or F-type system. Other typical roll arrangements are shown in Fig. 6.93 and 6.94. After passing through the main calender, the sheet can be passed through a secondary calendering operation for embossing. The sheet is then passed through a series of chilling rolls where it is cooled from both sides in an alternating fashion. After cooling, the film or sheet is wound.

One of the major concerns in a calendering system is generating a film or sheet with a uniform thickness distribution and tolerances as low as ± 0.005 mm. To achieve this, the dimensions of the rolls must be precise. It is also necessary to compensate for roll bowing resulting from high pressures in the nip region. Roll bowing is a structural problem that can be mitigated by placing the rolls in a slightly crossed pattern, rather than completely parallel, or by applying moments to the roll ends to counteract the separating forces in the nip region.

Calendering can be modeled by assuming steady state, laminar flow and isothermal conditions.

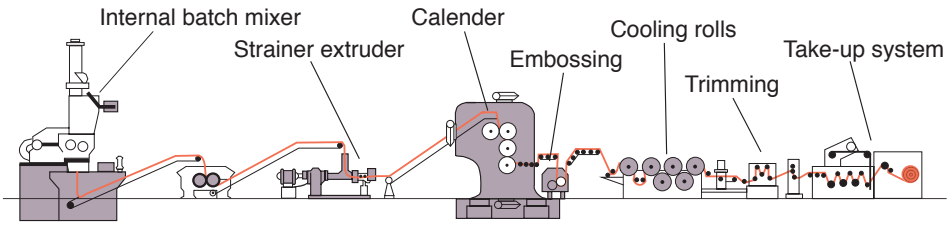

Figure 6.92 Schematic of a typical calendering process (Berstorff GmbH)

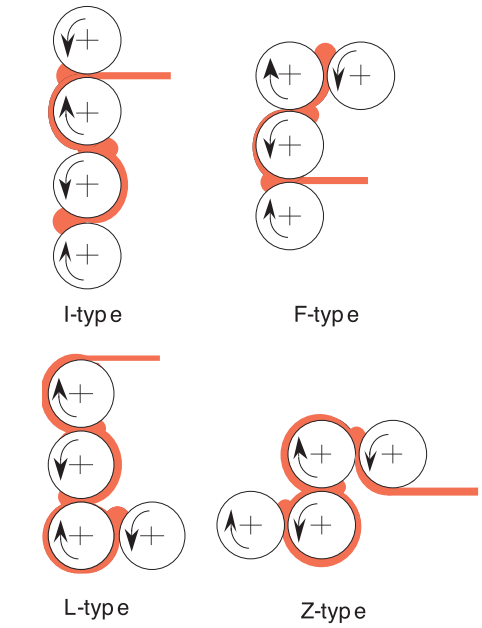

Figure 6.93 Calender arrangements

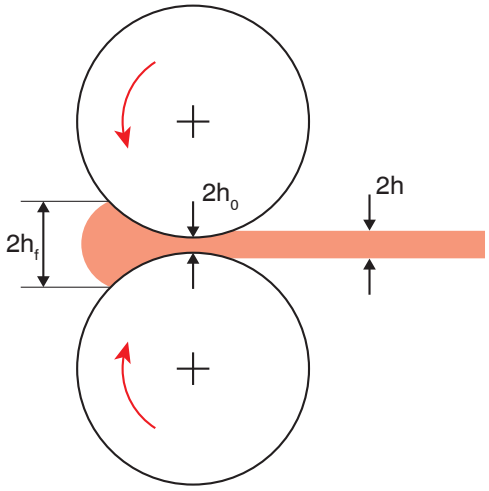

Figure 6.94 Schematic of the calendering process

6.7 Coating

In coating operations, a liquid film is continuously deposited on a moving, flexible, or rigid substrate. Coating is done on metal, paper, photographic films, audio and video tapes, and adhesive tapes. Typical coating processes include wire coating, dip coating, knife coating, roll coating, slide coating, and curtain coating.

In wire coating, a wire is continuously coated with a polymer melt by pulling the wire through an extrusion die. The polymer resin is deposited onto the wire using the drag flow generated by the moving wire and sometimes a pressure flow generated by the back pressure of the extruder. The process is schematically depicted in Fig. 6.95[11]. The second normal stress differences, generated by the high shear deformation in the die, help keep the wire centered in the annulus [40].

Dip coating is the simplest and oldest coating operation. Here, a substrate is continuously dipped into a fluid and withdrawn with one or both sides coated with the fluid. Dip coating can also be used to coat individual objects that are dipped and withdrawn from the fluid. The fluid viscosity and density and the speed and angle of the surface determine the coating thickness.

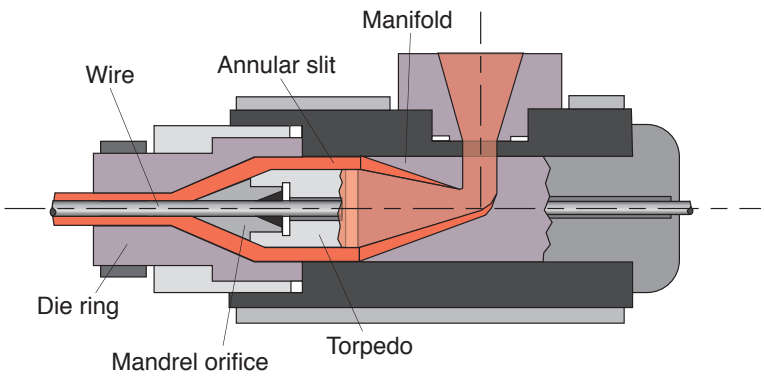

Figure 6.95 Wire coating process

Knife coating, depicted in Fig. 6.96, consists of metering the coating material onto the substrate from a pool of material, using a fixed rigid or flexible knife. The knife can be normal to the substrate or angled and the bottom edge can be flat or tapered. The thickness of the coating is nearly half the gap between the knife edge and the

11 Other wire coating processes extrude a tubular sleeve that adheres to the wire via stretching and vacuum. This is called tube coating.

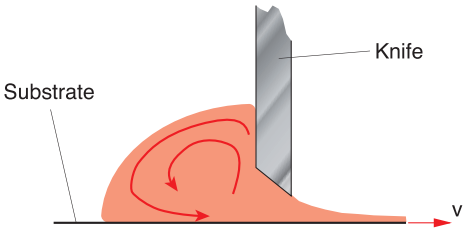

Figure 6.96 Schematic of a knife coating process

moving substrate or web. A major advantage of a knife edge coating system is its simplicity and relatively low maintenance.

Roll coating consists of passing a substrate and the coating simultaneously through the nip region between two rollers. The physics governing this process is similar to calendering, except that the fluid adheres to both the substrate and the opposing roll. The coating material is a low viscosity fluid, such as a polymer solution or paint, and is picked up from a bath by the lower roll and applied to one side of the substrate. The thickness of the coating can be as low as a few μm and is controlled by the viscosity of the coating liquid and the nip dimension. This process can be configured as either forward roll coating for co-rotating rolls or reverse roll coating for counter-rotating rolls (Fig. 6.97). The reverse roll coating process delivers the most accurate coating thicknesses.

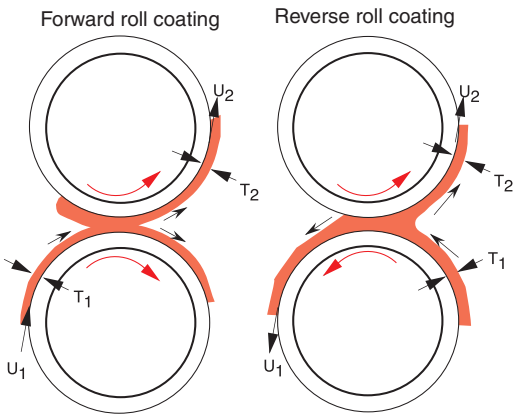

Figure 6.97 Schematic of forward and reverse roll coating processes

Slide coating and curtain coating, schematically depicted in Fig. 6.98, are commonly used to apply multi-layered coatings. However, curtain coating has also been widely used to apply single layers of coatings to cardboard sheet. In both methods, the coating fluid is pre-metered.

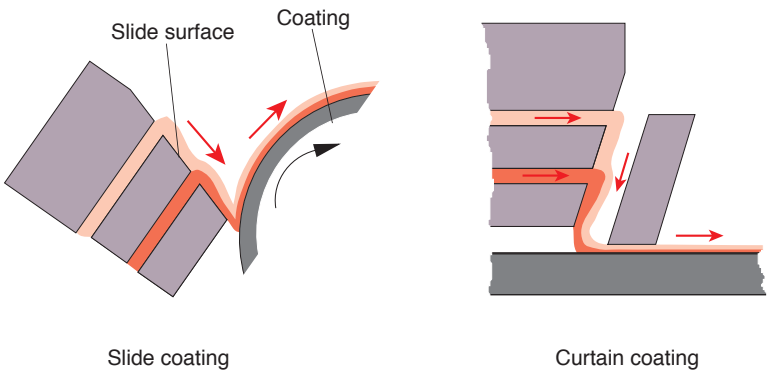

Figure 6.98 Slide and curtain coating

■ 6.8 Compression Molding

Compression molding is widely used in the automotive industry to produce parts that are large, thin, lightweight, strong, and stiff. It is also used in the household goods and electrical industries. Compression molded parts are formed by squeezing a charge, often glass fiber reinforced, inside a mold cavity, as depicted in Fig. 6.99. The matrix can be either a thermoset or a thermoplastic material. The oldest and still widest used material for compression molded products is phenolic.

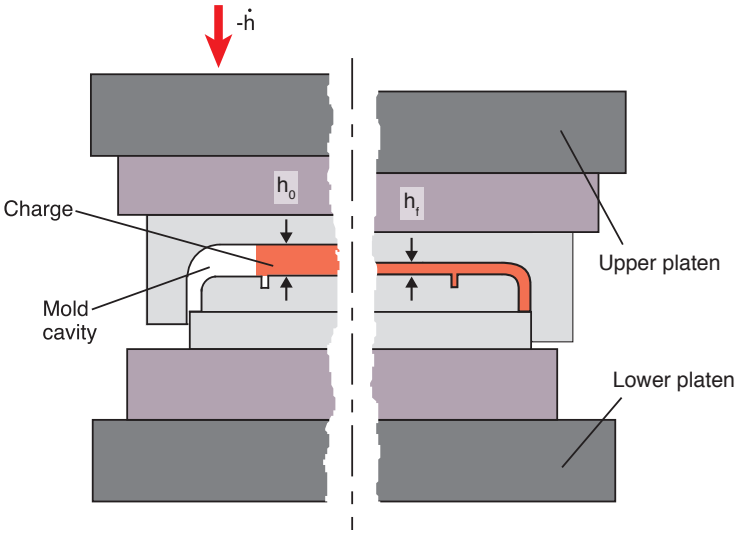

Figure 6.99 Compression molding process (h_0= charge thickness, h_f= part thickness, and $\dot{h}$ = closing speed)

The thermoset materials used to manufacture fiber reinforced compression molded articles is unsaturated polyester sheet or bulk, reinforced with glass fibers, known as sheet molding compound (SMC) or bulk molding compound (BMC). In SMC, the 25 mm long reinforcing fibers are randomly oriented in the plane of the sheet and make up for 20 – 30 % of the molding compound's volume fraction. A schematic diagram of an SMC production line is depicted in Fig. 6.100 [41]. When producing SMC, the chopped glass fibers are sandwiched between two carrier films previously coated with unsaturated polyester-filler matrix. A fiber reinforced thermoplastic charge is often called a glass mat reinforced thermoplastic (GMT) charge. The most common GMT matrix is polypropylene. More recently, long fiber reinforced thermoplastics (LFT) have become common. Here, sausage shaped charges are deposited on the mold by an extruder.

During processing of thermoset charges, the SMC blank is cut from a preformed roll and is placed between heated cavity surfaces. Generally, the mold is charged with 1 to 4 layers of SMC, each layer about 3 mm thick, which initially cover about half the mold cavity's surface. During molding, the initially randomly oriented glass fibers assume an orientation, leading to anisotropic properties in the finished product. When processing GMT charges, the preforms are cut and heated between radiative heaters. Once heated, they are placed inside a cooled mold that rapidly closes and squeezes the charges before they cool and solidify.

One of the main advantages of the compression molding process is the low fiber attrition during processing. Here, relatively long fibers can flow in the melt avoiding the fiber damage common during plastication and cavity filling during injection molding.

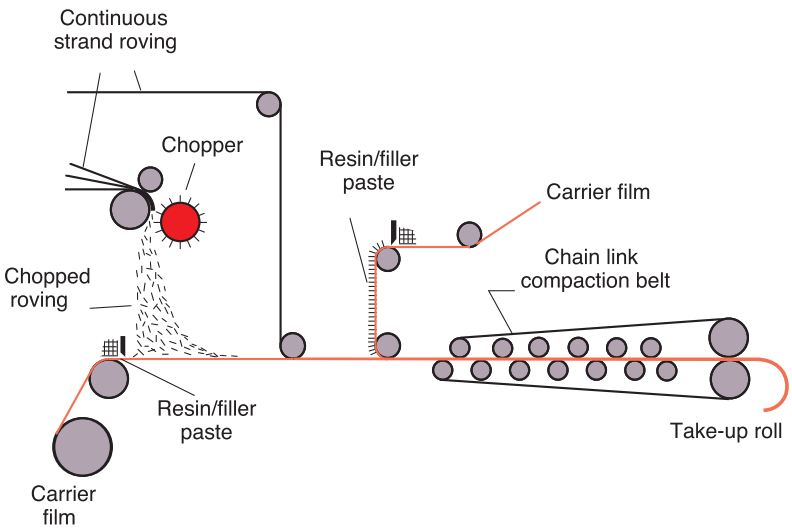

Figure 6.100 SMC production line

An alternate process is injection-compression molding. Here, a charge is injected through a large gate, followed by a compression cycle. The material used in the injection compression molding process is called bulk molding compound (BMC), which is reinforced with shorter fibers, generally 1 cm long, with an unsaturated polyester matrix. The main benefit of injection compression molding over compression molding is automation. The combination of injection and compression molding leads to lower degrees of fiber orientation and fiber attrition compared to injection molding.

6.9 Foaming

In a foam or a foamed polymer, a cellular or porous structure has been generated through the addition and reaction of physical or chemical blowing agents. The basic steps of foaming are cell nucleation, expansion or cell growth, and cell stabilization. Nucleation occurs when, at a given temperature and pressure, the solubility of a gas is reduced, leading to saturation, expelling the excess gas to form a bubble. Nucleating agents, such as powdered metal oxides, are used for initial bubble formation. The bubbles reach an equilibrium shape when their inside pressure balances their surface tension and surrounding pressures. The cells formed can be completely enclosed (closed cell foam) or can be interconnected (open cell foam).

In physical foaming processes a gas such as nitrogen or carbon dioxide is introduced into the polymer melt. Physical foaming also occurs after heating a melt that contains a low boiling point fluid, causing it to vaporize. For example, the heat-induced volatilization of low boiling point liquids, such as pentane and heptane, is used to produce polystyrene foams. Also, foaming occurs during volatilization from the exothermic reaction of gases produced during polymerization, such as the production of carbon dioxide during the reaction of isocyanate with water. Physical blowing agents are added to the plasticating zone of the extruder or molding machine. The most widely used physical blowing agent is nitrogen. Liquid blowing agents are often added to the polymer in the plasticating unit or in the die.

Chemical blowing agents are usually powders introduced in the hopper of the molding machine or extruder. Chemical foaming occurs when the blowing agent thermally decomposes, releasing large amounts of gas. The most widely used chemical blowing agent for polyolefins is azodicarbonamide.

In mechanical foaming, a gas dissolved in a polymer expands upon reduction of the processing pressure.

The foamed structures commonly generated are either homogeneous foams or integral foams. Figure 6.101 [42] presents the various types of foams and their corre-

sponding characteristic density distributions. In integral foam, the unfoamed skin surrounds the foamed inner core. This type of foam can be achieved during injection molding and extrusion and it replaces the sandwiched structure also shown in Fig. 6.101.

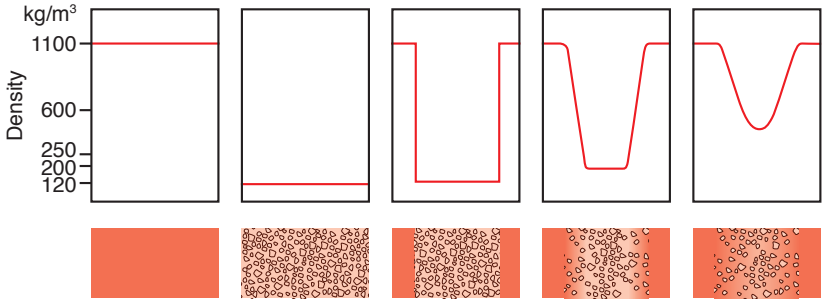

Figure 6.101 Schematic of various foam structures

Today, foams are of great commercial importance and are primarily used in packaging and as heat and noise insulating materials. Examples of foamed materials are polyurethane foams, expanded polystyrene (EPS), and expanded polypropylene particle foam (EPP).

Polyurethane foam is perhaps the most common foaming material and it exemplifies chemical foaming techniques. Here, two low viscosity components, a polyol and an isocyanate, are mixed with a blowing agent such as pentane. When manufacturing semi-finished products, the mixture is deposited on a moving conveyor belt where it is allowed to rise, like a loaf of bread contained within shaped paper guides. The result is a continuous polyurethane block that can be used, among others, in the upholstery and mattress industries.

The basic material to produce expanded polystyrene products is small pearls produced by suspension polymerization of styrene with 6 – 7 % of pentane as a blowing agent. To process the pearls they are placed in pre-expanding machines heated with steam until their temperature reaches 80 to 100 °C. To enhance their expansion, the pearls are allowed to cool in a vacuum and then to age and dry in ventilated storage silos before the shaping operation. Polystyrene foam is used extensively in packaging, but its uses also extend to the construction industry as a thermal insulating material, as well as for shock absorption in children's safety seats and bicycle helmets.

Expanded polypropylene particle foam is similar in to EPS but is characterized by its excellent impact absorption and chemical resistance. Its applications are primarily in the automotive industry as bumper cores, sun visors and knee cushions, to name a few.

6.10 Rotational Molding

Rotational molding is used to make hollow objects. Here, a carefully measured amount of powdered polymer, typically polyethylene, is placed in a mold. The mold is then closed and placed in an oven where the mold turns about two axes as the polymer melts, as depicted in Fig. 6.102. During heating and melting, which occur at oven temperatures between 250 and 450 °C, the polymer is deposited evenly on the mold's surface. To ensure uniform thickness, the axes of rotation should not coincide with the centroid of the molded product. The mold is then cooled and the solid part is removed from the mold cavity. The parts can be as thick as 1 cm, and still be manufactured with relatively low residual stresses. The reduced residual stress and the controlled dimensional stability of the rotational molded product depend in great part on the cooling rate after the mold is removed from the oven. A mold that is cooled too fast yields warped parts. Usually, a mold is first cooled with air to start the cooling slowly, followed by a water spray for faster cooling.

The main advantages of rotational molding over blow molding are the uniform part thickness and the low cost involved in manufacturing the mold. In addition, large parts, such as play structures or kayaks, can be manufactured more economically than with injection molding or blow molding. The main disadvantage of the process is the long cycle time for heating and cooling of the mold and polymer.

Figure 6.103 presents the air temperature inside the mold in a typical rotational molding cycle for polyethylene powders [43]. The process can be divided into six distinct phases (see also Fig. 6.103):

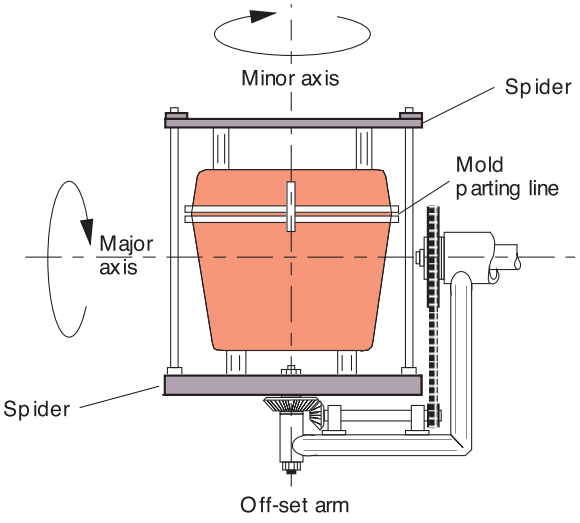

Figure 6.102 Schematic of the rotational molding process

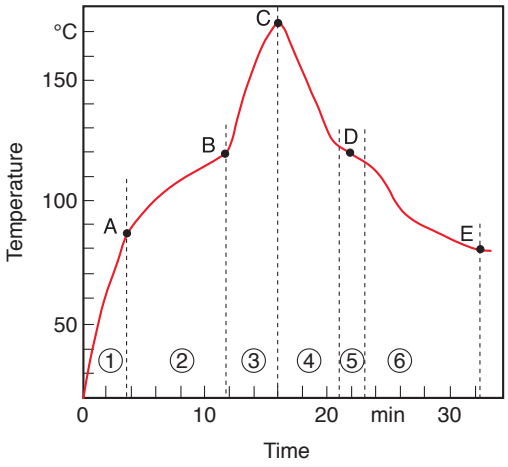

Figure 6.103 Typical air temperature in the mold while rotomolding polyethylene parts

1. Induction or initial air temperature rise
2. Melting and sintering
3. Bubble removal and densification
4. Pre-cooling
5. Crystallization of the polymer melt
6. Final cooling

The induction time can be significantly reduced by pre-heating the powder, and the bubble removal and cooling stage can be shortened by pressurizing the material inside the mold. The melting and sintering of the powder during rotational molding depends on the rheology and geometry of the particles. This phenomenon was studied in depth by Bellehumeur and Vlachopoulos [44].

■ 6.11 Computer Simulation in Polymer Processing

Computer simulation of polymer processes offers the tremendous advantage of enabling designers and engineers to consider virtually any geometric and processing option without incurring the expense associated with prototype mold or die making or the material waste of time-consuming trial-and-error procedures [50]. The ability to try new designs or concepts on the computer gives the engineer the opportunity to detect and fix problems before beginning production. Additionally, the process engineer can determine the sensitivity of processing parameters with regard to the quality and properties of the final part. For example, computer aided

engineering (CAE) offers the designer the flexibility to determine the effect of different gating scenarios, runner designs, or cooling line locations when designing an injection mold.

However, process simulation is not a panacea. As with any modeling technique, there are limitations caused by assumptions in the constitutive material models, or geometric simplifications of the model cavity. For example, there is a tendency in the industry to continuously decrease the part thickness of injection molded parts. Thickness reductions increase the pressure requirements during mold filling, with typical pressures reaching 2,000 bar. Such pressures have a profound effect on the viscosity and thermal properties of the melt; effects that in great part are not accounted for in commercially available software.

The first step of CAE in process design and optimization is to transform a solid model, such as the model for a PA 6 housing presented in Fig. 6.104, into a finite element mesh that can be used by the simulation software package. Typically, a fairly three-dimensional geometric model is transformed into a mid-plane model that essentially represents a two-dimensional geometry oriented in three-dimensional space. A finite element model is then generated on the mid-plane surface. Basically, the most common injection molding models use this approach to represent the geometry of the part. While most injection molded parts are thin and planar and would be well represented with such a model (Hele-Shaw model [51]), some injection molded parts are of smaller aspect ratios, or have three-dimensional features that make these models invalid.

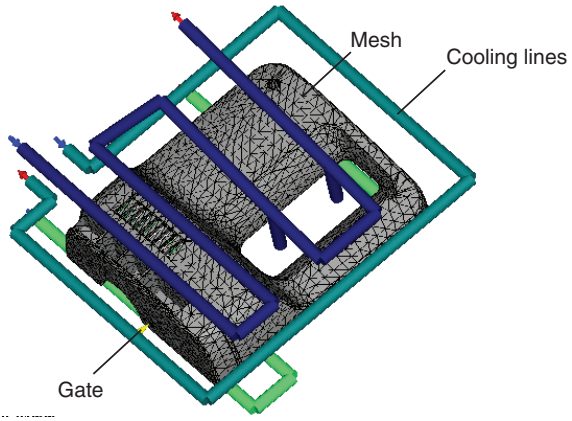

Figure 6.104 Finite element mesh of the mid-plane surface of a part and mold cooling line locations (Courtesy SIMCON Kunststofftechnische Software GmbH)

6.11.1 Mold Filling Simulation

Using a finite element mesh, such as the one presented in Fig. 6.104, in conjunction with the control volume approach, a simulation package solves a coupled energy and momentum balance, resulting in a mold filling pattern that not only

includes the non-Newtonian effects present in the flow of polymer melts, but also the effect that the cooling has on the melt flow inside the mold cavity.

The mold filling analysis and the resulting filling pattern can be used to predict the formation of weld lines (knit lines when dealing with fiber reinforced composite parts) and gas entrapment. These can cause weak spots and surface finish problems that can lead to cracks and failure of the final part, as well as esthetic problems in the finished product. Figure 6.105 presents the predicted 60 % filled mold of the part and gate presented in Fig. 6.104. The pressure and clamping force requirements are also needed information during part and process design. Both are computed by commercial injection molding software. In simulations where the rheology of the material is well defined, along with proper geometry and processing conditions, the accuracy can be quite high. Figure 6.106 presents a comparison of experimental and predicted short shots; as can be seen, prediction and simulation agree.

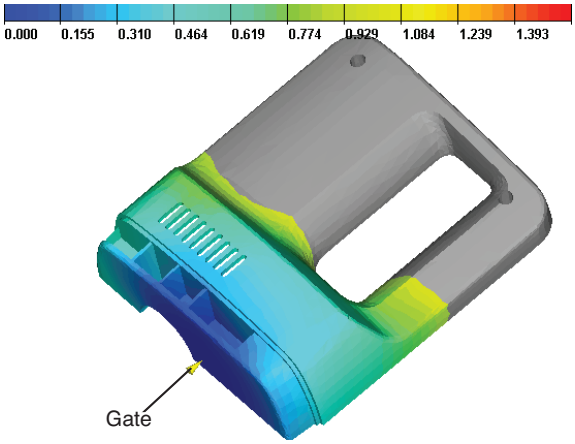

Figure 6.105 Short at 60 % fill of the part presented in Figure 6.104 (Courtesy SIMCON Kunststoff-technische Software GmbH)

Figure 6.106 Experimental and simulated 92 % short shot of an automotive cup holder (Courtesy CoreTech System Co., Ltd.)

6.11.2 Orientation Predictions

Molecular and filler orientation have a profound effect on the properties of the finished part. Molecular orientation will not only influence the mechanical properties of the polymer, but also its optical quality. For example, birefringence is controlled by molecular orientation, which must be kept low for products that require certain optical properties, such as lenses. The Folgar-Tucker model has been implemented into various, commercially available injection and compression mold filling simulation programs. Figure 6.107 presents a comparison between predicted and experimental birefringence patterns. For the polycarbonate lens shown in the figure, the birefringence pattern is directly related to molecular orientation.

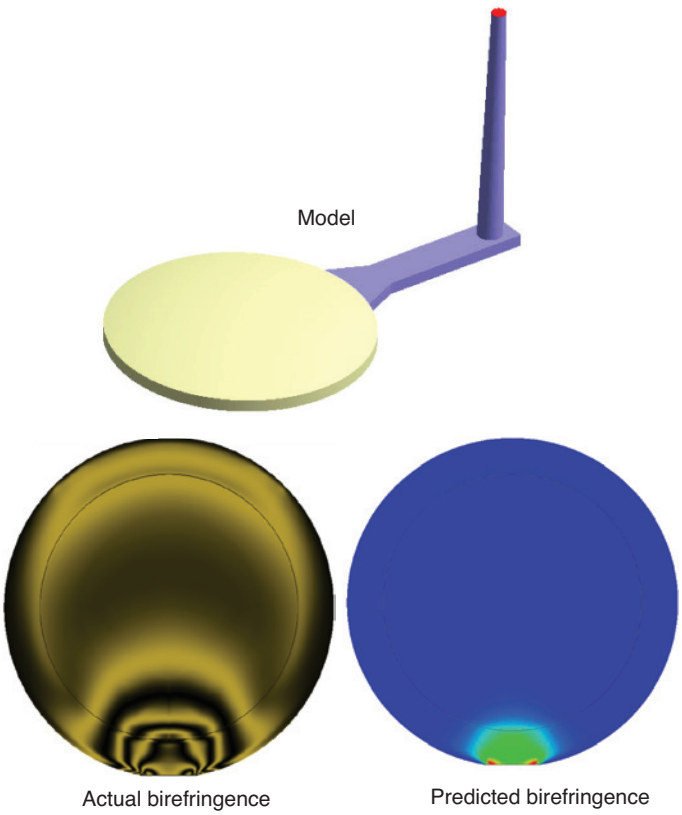

Figure 6.107 Experimental and simulated birefringence pattern in a polycarbonate lens (Courtesy CoreTech System Co., Ltd.)

6.11.3 Shrinkage and Warpage Predictions

Shrinkage and warpage are directly related to residual stresses that result from locally varying strain fields that occur during the curing or solidification stage of a manufacturing process. Such strain gradients are caused by non-uniform thermo-mechanical properties and temperature variations inside the mold cavity. Shrinkage due to cure can also play a dominant role in the residual stress development in thermosetting polymers and becomes important for fiber reinforced thermosets; shrinkage is also a concern when sink marks appear in thick sections or ribbed parts. When processing thermoplastic materials, shrinkage and warpage in a final product depend on the molecular orientation and residual stresses that form during processing. The molecular or fiber orientation and the residual stresses inside the part in turn depend on the flow and heat transfer during the mold filling, packing, and cooling stage of the injection molding process. To predict the residual stress in the finished part, modern software packages characterize the thermomechanical response of the polymer from melt to room temperature using the p-v-T behavior of the material, in conjunction with the temperature dependent stress-strain behavior. Figure 6.108 presents the warped geometry of the part depicted in Fig. 6.104 after mold removal and cooling. The warpage is usually depicted graphically as total amount of deflection as well as superposing deflected part geometry and mold geometry. Minimizing warpage is one of the biggest concerns for the design engineer. This is sometimes achieved by changing the formulation of the resin. Further reduction in warpage can also be achieved by changing the number and location of gates. Although trial-and-error solutions are still the most feasible with today's technology and are commonly done, computer optimization often reduces cost.

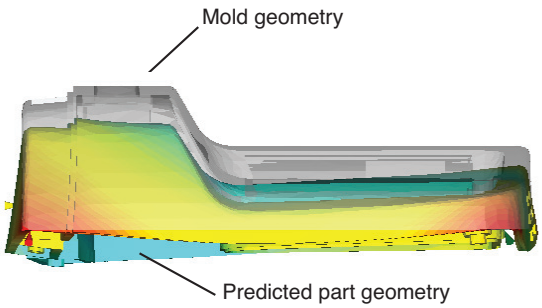

Figure 6.108 Predicted warped geometry after mold removal and cooling of the part presented in Figure 6.104 (Courtesy SIMCON Kunststofftechnische Software GmbH)

Examples

1. You are to use a 45 mm diameter single screw extruder to create a polycarbonate/polypropylene polymer blend. The maximum screw rotation is 160 rpm and the screw channel depth is 4 mm. Assuming a barrel temperature of 300 °C, a surface tension between the two polymers of 8×10^{-3} N/m, and using the viscosity curves given in in the appendix of this book, determine:
   - whether one can disperse 20% PC into 80% PP
   - whether one can disperse 20% PP into 80% PC
   - the minimum size of the dispersed phase

   We start this problem by first calculating the average speed in the extruder using

   $$v_0 = \pi Dn = \pi(45)(160)(1/60) = 377 \text{ mm/s}$$

   which results in an average rate of deformation of

   $$\dot{\gamma} = \frac{v_0}{h} = \frac{377 \text{ mm/s}}{4 \text{ mm}} = 94 \text{ s}^{-1}$$

   From the viscosity curves we get $\eta_{PC} \approx 600$ Pa · s and $\eta_{PP} \approx 150$ Pa · s. Using Fig. 6.32 we can deduce that one cannot disperse polycarbonte into polypropylene using a single screw extruder that only induces shear deformation, because $\eta_{PC}/\eta_{PP} > 4$. On the other hand, one can disperse polypropylene into polycarbonate using the same single screw extruder.

   Using Fig. 6.32 we can see that dispersive mixing for a $\eta_{PC}/\eta_{PP} > 0.25$ will occur at $Ca_{crit} \approx 0.7$. Hence, neglecting the effects of coalescence we can calculate the minimun size of the dispersed phase using

   $$Ca_{crit} = 0.7 = \frac{\tau R}{\sigma_s} = \frac{600(94)R}{8 \text{ x } 10^{-3}} \rightarrow D = 2R = 0.2 \text{ µm}$$

   To achieve this dispersion we must maintain the stresses for an extended period.

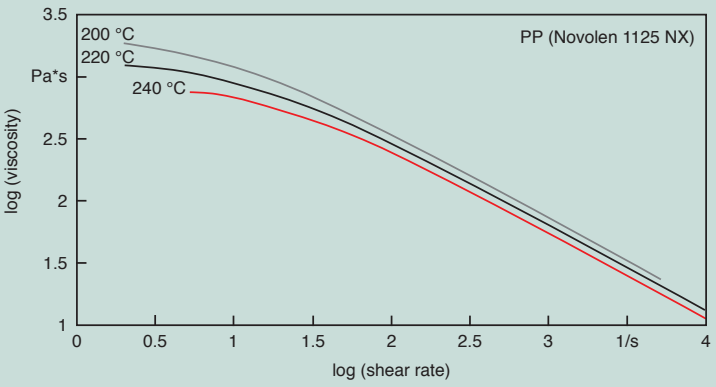

Figure 6.109 Viscosity curves for a polypropylene

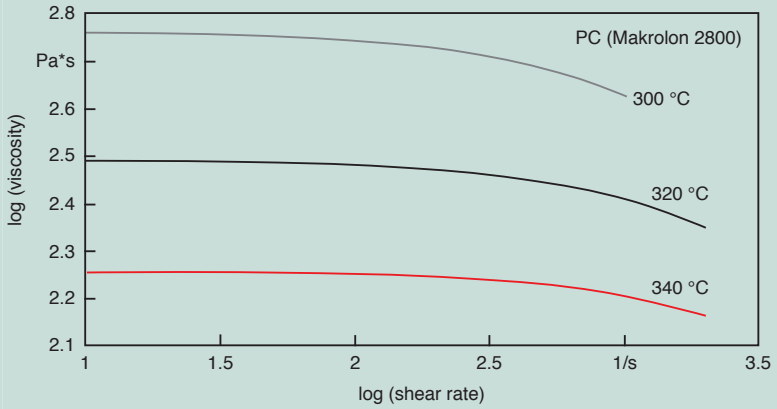

Figure 6.110 Viscosity curves for a polycarbonate

2. You are to determine the maximum clamping force and injection pressure required to mold an ABS suitcase with a filling time, t_{fill}, of 2.5 seconds. Use the dimensions shown in Fig. 6.111, an injection temperature, T_i, of 227 °C (500 K), and a mold temperature, T_m, of 27 °C (300 K). The properties necessary for the calculations are also given below.

Table 6.8 Properties for ABS

$n = 0.29$	$\rho = 1020\ kg/m^3$
$m_0 = 29 \times 10^6\ Pa - s^n$	$C_p = 2343\ J/Kg/K$
$a = 0.01369/K$	$k = 0.184 W/m/K$

To aid the polymer processing engineer in finding required injection pressures and corresponding mold clamping forces, Stevenson [34] generated a set of dimensionless groups and corresponding graphs for non-isothermal mold filling of non-Newtonian polymer melts. We start this problem by first laying the suitcase flat and determining the required geometric factors (Fig. 6.112). From the suitcase geometry, the longest flow path, R, is 0.6 m and the radius of the projected area, R_p, is 0.32 m.

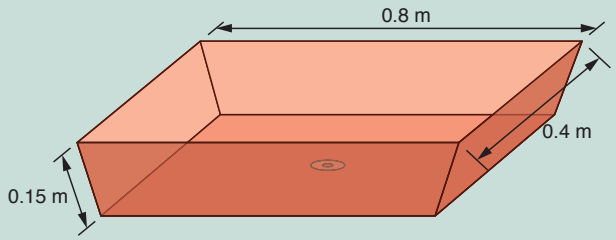

Figure 6.111 Suitcase geometry

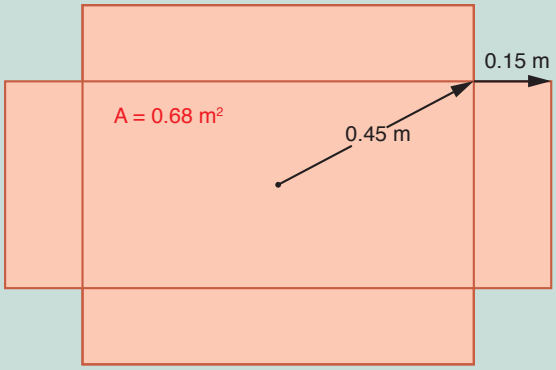

Figure 6.112 Lay-flat suitcase

Using the notation in Fig. 6.111 and a viscosity defined by

$$\eta = m_0 e^{-a\left(T-T_{ref}\right)} \left|\dot{\gamma}\right|^{n-1}$$

four dimensionless groups are defined.

- The dimensionless temperature β determines the intensity of the coupling between the energy equation and the momentum balance. It is defined by

$$\beta = a\left(T_i - T_m\right) \tag{6.30}$$

where T_i and T_m are the injection and mold temperatures, respectively.

- The dimensionless time is the ratio of the filling time, t_{fill}, and the time for thermal equilibrium via conduction, defined by

$$\tau = \frac{t_{fill} K}{h^2 \rho C_p} \tag{6.31}$$

- The Brinkman number Br is the ratio of the energy generated by viscous dissipation and the energy transported by conduction. For a non-isothermal, non-Newtonian model it is

$$Br = \frac{m_0 e^{-aT_i} h^2}{k\left(T_i - T_m\right)} \left(\frac{R}{t_{fill} h}\right)^{n+1} \tag{6.32}$$

- The power-law index n of the Ostwald and deWaale model reflects the shear thinning behavior of the polymer melt. Once the dimensionless parameters are calculated, the dimensionless injection pressures $\left(\Delta p/\Delta p_l\right)$ and dimensionless clamping forces $\left(F/F_l\right)$ are read from Figs. 6.113 to 6.106. The isothermal pressure and force are computed using

$$\Delta p_l = \frac{m_0 e^{-aT_i}}{1-n} \left[\frac{1+2n}{2n} \frac{R}{t_{fill} h}\right]^n \left(\frac{R}{h}\right) \tag{6.33}$$

and

$$F_l = \pi R^2 \left(\frac{1-n}{3-n}\right) \Delta p_l \tag{6.34}$$

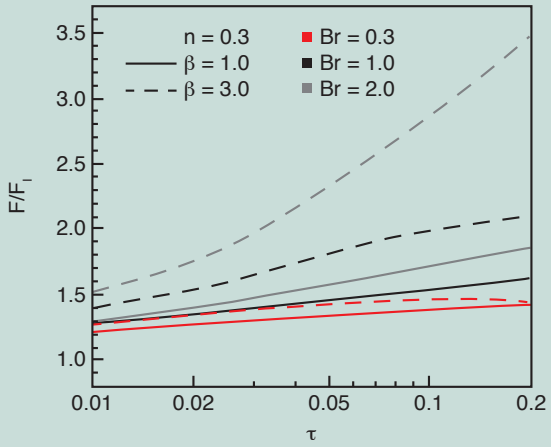

Figure 6.113
Dimensionless clamping force versus dimensionless groups

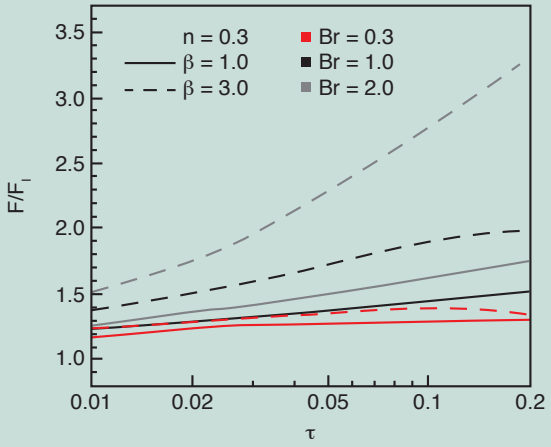

Figure 6.114
Dimensionless clamping force versus dimensionless groups

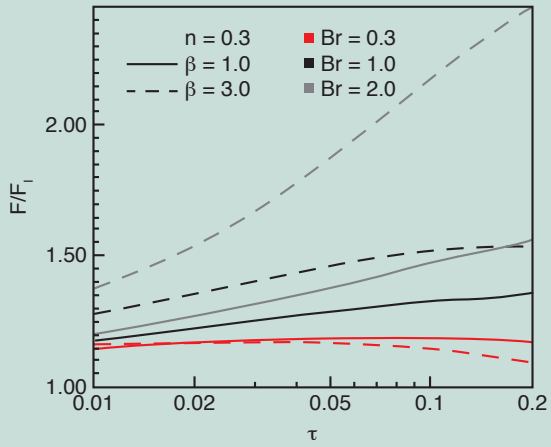

Figure 6.115
Dimensionless injection pressure versus dimensionless groups

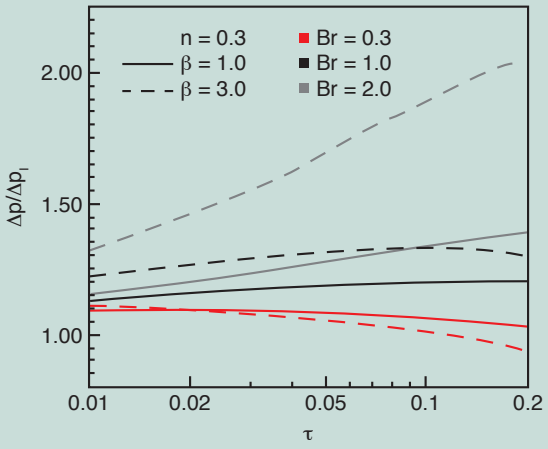

Figure 6.116
Dimensionless injection pressure versus dimensionless groups

Using the data given for ABS and the dimensions for the laid-flat suitcase we can compute the dimensionless groups as

$$\beta = 0.01369(500-300) = 2.74$$

$$\tau = \frac{2.5(0.184)}{(0.001)^2(1020)(2343)} = 0.192$$

$$Br = \frac{(29\text{x}10^6)e^{-0.01369(500)}(0.001)^2}{0.184(500-300)}\left(\frac{0.6}{2.5(0.001)}\right)^{0.29+1} = 0.987$$

The isothermal injection pressure and clamping force are computed using Eqs. 6.30 to 6.34.

$$\Delta p_I = \frac{29\text{x}10^6 e^{-0.01369(500)}}{1-0.29}\left(\frac{1+2(0.29)}{2(0.29)}\frac{0.6}{2.5(0.001)}\right)^{0.29}\left(\frac{0.6}{0.001}\right) = 171\ \text{MPa}$$

$$F_I = \pi(0.6)^2\left(\frac{1-0.29}{3-0.29}\right)(17.1\text{x}10^7) = 50.7\text{x}10^6\ \text{N}$$

We now look up $\Delta p/\Delta p_I$ and F/F_I in Figs. 6.113 to 6.116. Since little change occurs between $n = 0.3$ and $n = 0.5$, we choose $n = 0.3$. However, for other values of n we can interpolate or extrapolate. For $\beta = 2.74$, we interpolate between 1 and 3 as

$$\beta = 1 \rightarrow \Delta p/\Delta p_I = 1.36 \text{ and } F/F_I = 1.65$$

$$\beta = 3 \rightarrow \Delta p/\Delta p_I = 1.55 \text{ and } F/F_I = 2.1$$

$$\beta = 2.74 \rightarrow \Delta p/\Delta p_I = 1.53 \text{ and } F/F_I = 2.04$$

$$\Delta p = \left(p / \Delta p_l \right) \Delta p_l = 262 \text{ MPa} = 2{,}260 \text{ bar}$$

$$F = \left(F / F_l \right) F_l = 10.3 \times 10^7 \text{ N} = 10{,}300 \text{ metric tons}$$

Since the part exceeds the projected area, Fig. 6.117 can be used to correct the computed clamping force. The clamping force can be corrected for an R_p= 0.32 m using Fig. 6.117 and $R_p/R = 0.53$.

$$F_{projected} = (0.52)10{,}300 = 5{,}356 \text{ metric tons}$$

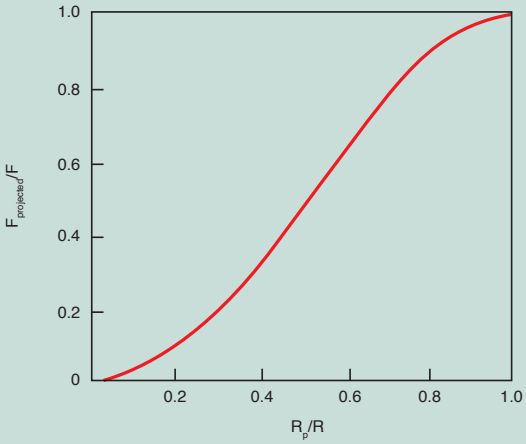

Figure 6.117
Clamping force correction for the projected area

For our suitcase cover, where the total volume is 1,360 cc and total part area is 0.68 m², the above numbers are too high. A useful rule-of-thumb is a maximum allowable clamping force of 2 ton/in². Here, we have greatly exceeded that number. Normally, approx. 3,000 metric ton/m² are allowed in commercial injection molding machines. For example, a typical injection molding machine[12] with a shot size of 2,000 cc has a maximum clamping force of 630 metric ton with a maximum injection pressure of 1,400 bar. A machine with much larger clamping forces and injection pressures is suitable for much larger parts. For example, a machine with a shot size of 19,000 cc allows a maximum clamping force of 6,000 metric ton with a maximum injection pressure of 1,700 bar. For this example we must reduce the pressure and clamping force requirements. This can be accomplished by increasing the injection and mold temperatures or by reducing the filling time. Recommended injection temperatures for ABS range between 210 and 240 °C and recommended mold temperatures range between 40 and 90 °C.[13] As can be seen, there is room for adjustment in the processing conditions, so the above procedure should be repeated using new conditions.

12 MINIFLOW, Injection Molding Simulation, The Madison Group PPRC, Madison, WI.
13 The recommended reference for such values is the CAMPUS® material data bank.

3. Let us consider the multi-cavity injection molding process shown in Fig. 6.118. To achieve equal part quality, the filling time for all cavities must be balanced. For the case in question, we need to balance the cavities by solving for the runner radius. For a balanced runner system the flow rates into all cavities must match. For a given flow rate Q, length L, and radius R_1, we can also solve for the pressure at the runner system junctures. Assuming an isothermal flow of a non-Newtonian shear thinning polymer with viscosity η, we can compute the radius for a part molded of polystyrene with a consistency index of 2.8×10^4 Pa · s^n and a power law index (n) of 0.28.

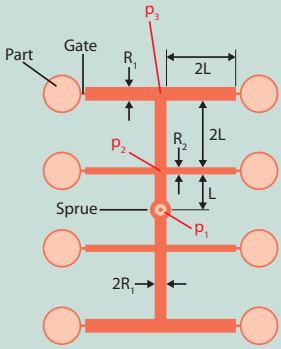

Figure 6.118 Runner system lay-out

The flow through each runner section is governed by Eq. 5.46, and the various sections can be represented using:

$$\text{Section 1: } 4Q = \left(\frac{\pi(2R_1)^3}{s+3}\right)\left(\frac{2R_1(P_1 - P_2)}{2mL}\right)^s$$

$$\text{Section 2: } 2Q = \left(\frac{\pi(2R_1)^3}{s+3}\right)\left(\frac{2R_1(P_2 - P_3)}{2m(2L)}\right)^s$$

$$\text{Section 3: } Q = \left(\frac{\pi R_2^3}{s+3}\right)\left(\frac{R_2(P_2 - 0)}{2m(2L)}\right)^s$$

$$\text{Section 4: } Q = \left(\frac{\pi R_1^3}{s+3}\right)\left(\frac{R_1(P_3 - 0)}{2m(2L)}\right)^s$$

Using values of L = 10 cm, R_1 = 4 mm, and Q = 20 cm^3/s, the unknown parameters, P_1, P_2, P_3, and R_2 can be obtained using the preceding equations. The equations are non-linear and must be solved in an iterative manner. For the given values, a radius R_2 of 3.4 mm would result in a balanced runner system, with pressures P_1 = 265.7 bar, P_2 = 230.3 bar, and P_3 = 171.9 bar. For comparison, if one had assumed a Newtonian model with the same consistency index and a power law index of 1.0, a radius, R_2 of 3.9 mm would have resulted, with much higher required pressures of P_1 = 13,926 bar, P_2 = 12,533 bar, and P_3 = 11,140 bar. The difference is due to shear thinning.

Problems

1. You are to extrude a 100 mm wide high density polyethylene sheet using a 40 mm diameter single screw extruder with distributive as well as dispersive mixing heads. The screw characteristic curve is shown in Fig. 6.119[14].
   The die can be approximated by a 100 mm wide and 100 mm long slit. On the graph in Fig. 6.119 draw the die characteristic curves for dies with 1 mm and 1.5 mm thick slits. Will it be feasible to extrude a sheet through a 1.5 mm thick slit? If yes, what screw speed would you choose? What about a 1 mm thick slit?
   Why do your die characteristic curves cross over the ones shown in the graph? Note that the data in the graph was measured experimentally with a variable restriction (valve) die.
   Typical power law constants for HDPE at 180 °C are m = 20,000 Pa·s^n and n = 0.41. Use a specific gravity for HDPE of 0.95.

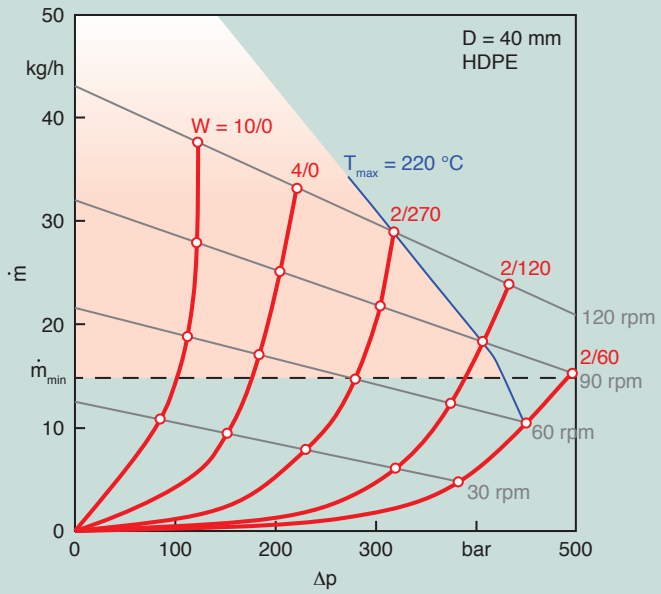

Figure 6.119 Process characteristic curves for a 45 mm diameter conventional extruder

2. Estimate the striation thickness of a 3 mm diameter pigmented polystyrene pellet in a polystyrene matrix after traveling through a 20 turn, 45 mm diameter, 5 mm constant channel depth, single screw extruder. Assume open discharge conditions. Use 100 rpm rotational speed.

14 Courtesy of ICIPC, Medellín, Colombia.

3. Someone in your company proposes to use an existing square pitch 150 mm diameter plasticating single screw extruder as a mixing device for a 40/60 PS/PP polymer blend. The metering section is 5 turns long and has a channel depth of 10 mm. Will dispersion of the polystyrene occur for a screw rotation of 60 rpm? Assume open discharge and a temperature of 220 °C. Use viscosity data given in example 6.1 and Fig. 6.32.
4. Someone in your company proposes to use an existing square pitch 150 mm diameter plasticating single screw extruder as a mixing device for a 40/60 PP/PS polymer blend. The metering section is 5 turns long and has a channel depth of 10 mm. Will dispersion of the polypropylene occur for a screw rotation of 60 rpm? Will there be enough time for dispersion? Assume open discharge and a temperature of 220 °C. Use viscosity data given in problems 6.3 and in Fig. 6.120.

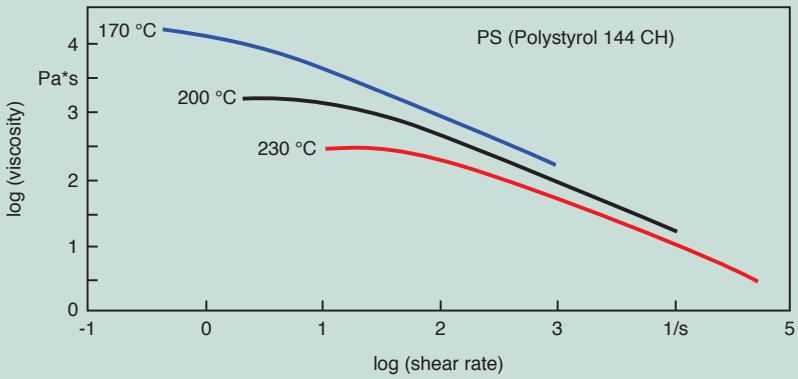

Figure 6.120 Viscosity curves for a polystyrene

5. A thin polyamide 66 component is injection molded under the following conditions:
   - The melt is injected at 275 °C to a maximum pack/hold pressure of 800 bar.
   - The 800 bar pack/hold pressure is maintained until the gate freezes off, at which point the part is at an average temperature of 175 °C.
   - The pressure drops to 1 bar as the part cools inside the cavity.
   - The part is removed from the mold and cooled to 25 °C.
   - Draw the whole process on the p-v-T diagram.
   - Estimate the final part thickness if the mold thickness is 1 mm. For thin injection molded parts, most of the shrinkage leads to part thickness reduction.

6. Do the screw and die characteristic curves correspond to a conventional or a grooved single screw extruder?
A die can be approximated with a 1 mm diameter and 30 mm long capillary. On the graph below draw the die characteristic curve for the given die.
Typical power law constants for HDPE at 180 °C are m = 20,000 Pa·s^n and n = 0.41. Use a specific gravity for HDPE of 0.95.

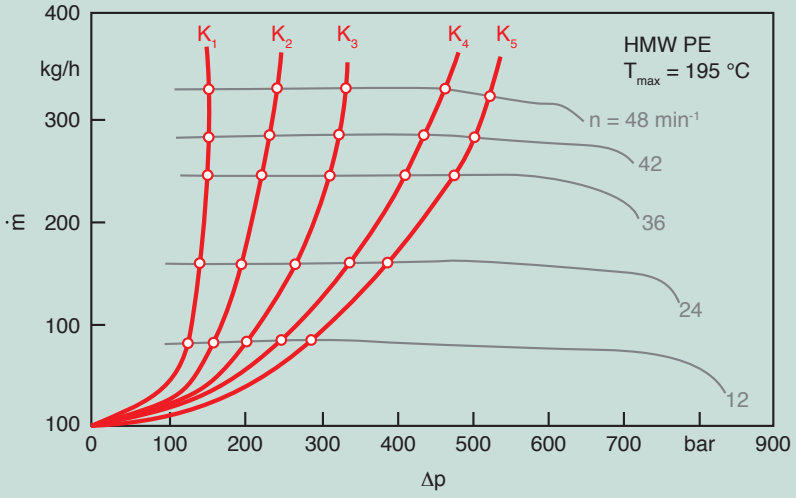

Figure 6.121 Process characteristic curves for a 45 mm diameter extruder

7. An internal batch mixer maintains shear rates, $\dot{\gamma}$, of 100 s^{-1} for extended periods. In the mixer you want to disperse LDPE in a PS matrix at 170 °C. What is the size of the dispersed phase? Will the PS still be transparent? Use viscosity data given in Problem 6.4 and in Fig. 6.122.

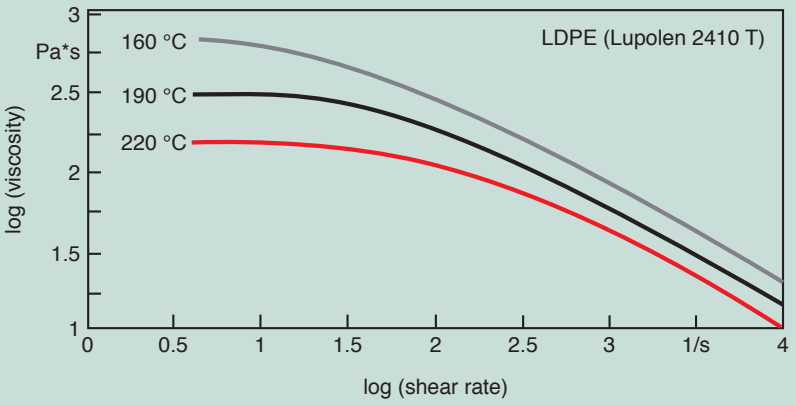

Figure 6.122 Viscosity curves for a low density polyethylene

8. Design a balanced runner system for the mold in Example 6.3 if you are to injection mold a polystyrene product. Assume a power-law model with a consistency index, m, of 2.8 × 104 Pa·s^n, and a power-law index, n, of 0.28.
9. Estimate the cooling time for the ABS suitcase presented in Example 6.2, if demolding occurs when the average part temperature is below 60 °C.
10. What are the required clamping force and injection pressure, if the filling time in Example 6.2 is increased from 2.5 s to 3 s?
11. What are the required clamping force and injection pressure, if the mold temperature in Example 6.2 is increased from 27 °C to 90 °C ?
12. What are the required clamping force and injection pressure, if the injection temperature in Example 6.2 is increased from 227 to 240 °C?
13. Measure and plot the wall thickness distribution on a PE-HD one gallon milk container.
14. Measure and plot the wall thickness distribution on a small thermoformed individual coffee cream container.

References

[1] Tadmor, Z., and Gogos, C.G., *Principles of Polymer Processing*, 2nd ed., John Wiley & Sons, New York, (2006).

[2] Rauwendaal, C., *Mixing in Polymer Processing*, Marcel Dekker, Inc., New York, (1991).

[3] Osswald, T.A., Turng, L.S., and Gramann, P.J., 2nd ed., *Injection Molding Handbook*, Hanser Publishers, Munich, (2007).

[4] Menges, G., and Predöhl, W., *Plastverarbeiter, 20*, 79, (1969).

[5] Menges, G., and Predöhl, W., *Plastverarbeiter, 20*, 188, (1969).

[6] Scott, C.E., and Macosko, C.W., *Polymer Bulletin, 26*, 341, (1991).

[7] Gramann, P.J., Stradins, L., and Osswald, T.A., *Intern. Polym. Proc., 8*, 287, (1993).

[8] Osswald, T.A., *Understanding Polymer Processing*, Hanser Publishers, Munich, (2010).

[9] Erwin, L., *Polym. Eng. & Sci., 18,* 572, (1978).

[10] Erwin, L., *Polym. Eng. & Sci., 18*, 738, (1978).

[11] Ng, K.Y., M.S. Thesis, University of Wisconsin-Madison, (1979).

[12] Tadmor, Z., *Ind. Eng. Fundam., 15*, 346, (1976).

[13] Cheng, J., and Manas-Zloczower, I., *Intern. Polym. Proc., 5*, 178, (1990).

[14] Grace, H.P., *Chem. Eng. Commun., 14*, 225, (1982).

[15] Cox, R.G., *J. Fluid Mech., 37*, 3, 601–623, (1969).

[16] Bentley, B.J. and Leal, L.G., *J. Fluid Mech., 167*, 241–283, (1986).

[17] Stone, H.A. and Leal, L.G., *J. Fluid Mech., 198*, 399–427, (1989).

[18] Biswas, A., and Osswald, T.A., unpublished research, (1994).

[19] Gramann, P.J., M.S. Thesis, University of Wisconsin-Madison, (1991).

[20] Manas-Zloczower, I., Nir, A., and Tadmor, Z., *Rubber Chemistry and Technology, 55*, 1250, (1983).

[21] Boonstra, B.B., and Medalia, A.I., *Rubber Age*, March and April, (1963).

[22] Rauwendaal, C., *Polymer Extrusion*, 4th ed., Hanser Publishers, Munich, (2001).

[23] Menges, G., and Harms, E., *Kautschuk und Gummi, Kunststoffe, 25*, 469, (1972).

[24] Rauwendaal, C., *SPE ANTEC* 39, 2232, (1993).

[25] Rauwendaal, C., Mixing in Reciprocating Extruders, A chapter in *Mixing and Compounding of Polymers*, 2nd ed., Ed. I. Manas-Zloczower, Hanser Publishers, Munich, (2009).

[26] Elemans, P.H.M., Modeling of the cokneater, A chapter in *Mixing and Compounding of Polymers*, 2nd ed., Ed. I. Manas-Zloczower, Hanser Publishers, Munich, (2009).

[27] Lim, S. and White, J.L., *Intern. Polym. Proc., 8*, 119, (1993).

[28] Lim, S. and White, J.L., *Intern. Polym. Proc., 9*, 33, (1994).

[29] Bird, R.B., Steward, W.E., and Lightfoot, E.N., *Transport Phenomena*, 2nd ed., John Wiley & Sons, New York, (2004).

[30] Erwin, L., *Polym. Eng. & Sci., 18*, 1044, (1978).

[31] Suetsugu, Y., *Intern. Polym. Proc., 5*, 184, (1990).

[32] Greener, J., *Polym. Eng. Sci., 26*, 886 (1986).

[33] Michaeli, W., and Lauterbach, M., *Kunststoffe, 79*, 852 (1989).

[34] Stevenson, J.F., *Polym. Eng. Sci., 18*, 577 (1978).

[35] Naranjo, A, Noriega, M., Osswald, T.A., Roldán, A. and Sierra, J., *Plastics Testing and Characterization – Industrial Applications*, Hanser Publishers, Munich, (2006).

[36] Anturkar, N.R., and Co, A., *J. Non-Newtonian Fluid Mech., 28*, 287 (1988).

[37] Menges, G., *Einführung in die Kunststoffverarbeitung,* Hanser Publishers, Munich (1986).

[38] Rosato, D.V., *Blow Molding Handbook*, Hanser Publishers, Munich (1989).

[39] Modern Plastics Encyclopedia, 53, McGraw-Hill , New York (1976).

[40] Tadmor, Z., and Bird, R.B., *Polym. Eng. Sci, 14*, 124 (1973).

[41] Denton, D.L, *The Mechanical Properties of an SMC-R50 Composite*, Owens-Corning Fiberglas Corporation (1979).

[42] Shutov, F.A., *Integral/Structural Polymer Foams*, Springer-Verlag, Berlin (1986).

[43] Crawford, R.J., *Rotational Molding of Plastics*, Research Studies Press, Somerset (1992).

[44] Bellehumeur, C.T., and Vlachopoulos, J., *SPE 56th Antec*, (1998).

[45] Mascia, L., *The Role of Additives in Plastics*, John Wiley & Sons, New York, (1974).

[46] Hildebrand, J. and Scott, R.L., *The Solubility of Non-Electrolytes*, 3rd ed., Reinhold Publishing Co., New York, (1949).

[47] Rosen, S.L., *Fundamental Principles of Polymeric Materials*, 2nd. ed., John Wiley & Sons, Inc., New York, (1993).

[48] Janssen, J.M.H., Ph.D. Thesis, Eindhoven University of Technology, The Netherlands, (1993).

[49] Van Krevelen, D.W., *Properties of Polymers*, 4th ed., Elsevier, Amsterdam, (2009).

[50] Osswald, T.A., and Hernández, J.P., *Polymer Processing – Modeling and Simulation*, Hanser Publishers, Munich, (2006).

[51] Hele-Shaw, H.S., *Proc. Roy. Inst., 16,* 49 (1899).

7 Anisotropy Development During Processing

The mechanical properties and dimensional stability of a molded polymer part are strongly dependent upon the anisotropy of the finished part[1]. The structure of the final part, in turn, is influenced by the design of the mold cavity, e.g., the type and position of the gate, and by the various processing conditions, such as injection speed, melt or compound temperatures, mold cooling or heating rates, and others. The amount and type of filler or reinforcing material also has a great influence on the quality of the final part.

This chapter discusses the development of anisotropy during processing of thermoset and thermoplastic polymer parts and presents basic analyses that can be used to estimate anisotropy in the final product.

7.1 Orientation in the Final Part

During processing, the molecules, fillers, and fibers are oriented in the flow direction and greatly affect the properties of the final part. Because there are large differences in the processing of thermoplastic and thermoset polymers, the two will be discussed individually in the next two sections.

7.1.1 Processing Thermoplastic Polymers

When thermoplastic components are manufactured, the polymer molecules become oriented. The molecular orientation is induced by the deformation of the polymer melt during processing. The flexible molecular chains get stretched, and because of their entanglement they cannot relax fast enough before the part cools and solidifies. At lower processing temperatures this phenomenon is multiplied, leading to even higher degrees of molecular orientation. This orientation impacts

1 This chapter primarily deals with the anisotropy development of injection and compression molded parts.

the stiffness and strength properties of the polymer component. Orientation also gives rise to *birefringence*, or *double refraction*, a phenomenon discussed in Chapter 12. The various degrees of molecular orientation and the different main directions of orientation in the material introduce a variable refractive index field, n (x, y, z), throughout the part. The value of the refractive index, n, depends on the relative orientation of the molecules, or the molecular axes, and on the direction of the light shining through the part.

As polarized light travels through a part, a series of colored lines called *isochromatics* become visible or appear as shown in Fig. 7.1. The isochromatics are lines of equal molecular orientation and numbered from zero, at the region of no orientation, up with increasing degrees of orientation. A zero degree of orientation is usually the place in the mold that fills last and the degree of orientation increases towards the gate. Figure 7.2 shows schematically how molecular orientation is related to birefringence. The layers of highest orientation are near the outer surfaces of the part with orientation increasing towards the gate.

The degree of orientation increases and decreases, depending on the various processing conditions and the materials used [1]. For example, Fig. 7.3 shows two discs molded from different polymers, polycarbonate and polystyrene. Polycarbonate shows a much lower degree of molecular orientation than polystyrene, making it better suited to manufacture optical products such as CDs. It can also be said that when decreasing the thickness of a part the velocity gradients increase, leading to higher degrees of orientation. In subsequent sections of this chapter we will discuss how orientation is directly related to rates of deformation or velocity gradients.

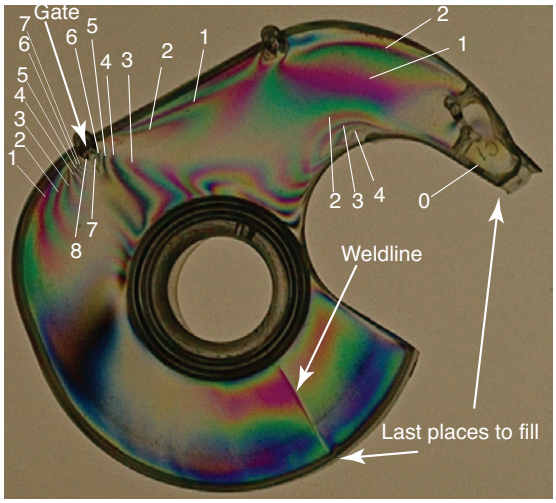

Figure 7.1 Isochromatics in a polycarbonate specimen of 1.7 mm wall thickness

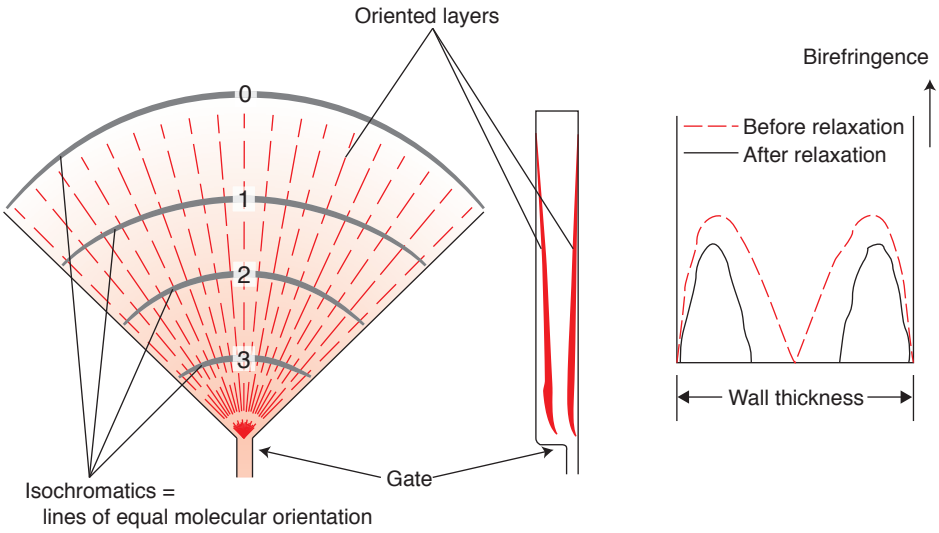

Figure 7.2 Orientation birefringence in a quarter disk

Orientation is also related to the process used to manufacture the part. For example, Fig. 7.4 [1] shows two injection molded polycarbonate parts molded with different injection molding machines: a piston-type and a screw-type machine. It is obvious that the cover made with the piston-type injection molding machine has much higher degrees of molecular orientation than the one manufactured using the screw-type injection molding machine. Destructive tests revealed that it was impossible to produce a part that is sufficiently crack-proof when molded with a piston-type molding machine.

The articles in Figs. 7.1, 7.3, and 7.4 were injection molded – a common processing method for thermoplastic polymers. Early studies have already shown that a

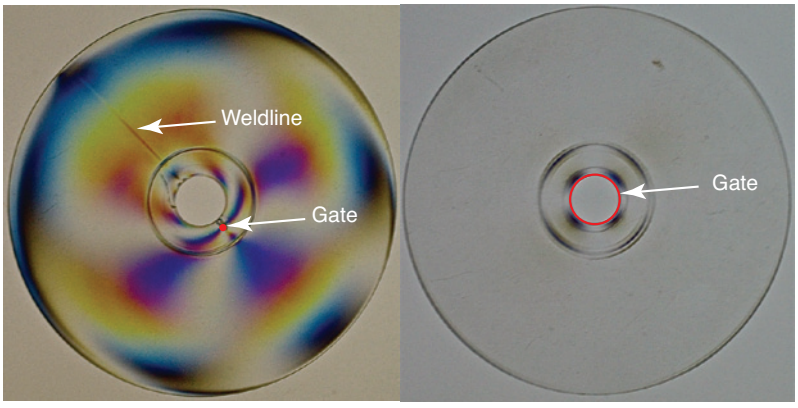

Figure 7.3 Isochromatics in polycarbonate and polystyrene discs

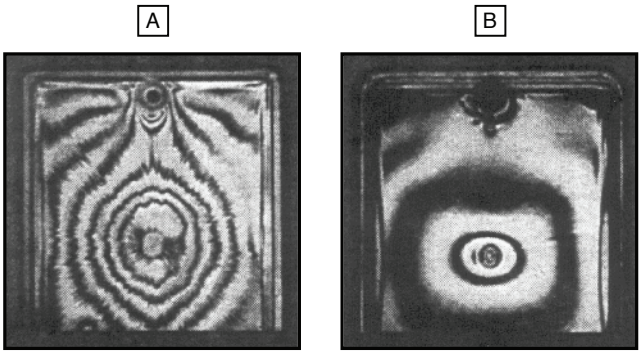

Figure 7.4 Isochromatics in polycarbonate parts molded with (left) piston-type and (right) screw-type injection molding machines

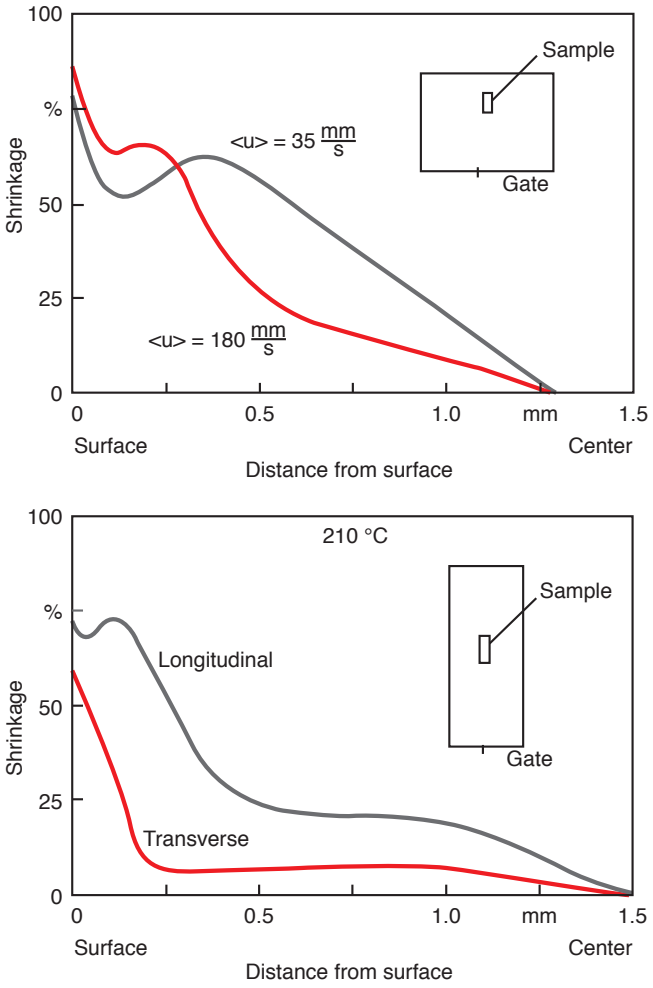

Figure 7.5 Shrinkage distribution of injection molded polystyrene plates

molecular orientation distribution exists across the thickness of thin injection molded parts [2]. Figure 7.5 [2] shows the shrinkage distribution in both longitudinal and transverse flow direction for two different plates. The curves demonstrate the degree of anisotropy that develops during injection molding, and the influence of the part's geometry on this anisotropy.

Polycarbonate compact disks serve as an example of how to use the birefringence patterns in polymer parts to detect severe manufacturing problems [3, 4]. Figure 7.6 shows the birefringence distribution in the *rz*-plane of a 1.2 mm thick disk molded from polycarbonate. The figure shows how the birefringence is highest at the surface of the disk and lowest just below the surface. Towards the inside of the disk the birefringence rises again and drops somewhat toward the central core of the disk. A similar phenomenon was observed in glass fiber reinforced [5–7] and liquid crystalline polymer [8] injection molded parts that showed large variations in fiber and molecular orientation through the thickness.

All these findings support earlier claims that molecular or filler orientation in injection molded parts can be divided into seven layers, schematically represented in Fig. 7.7 [1]. The seven layers may be described as follows:

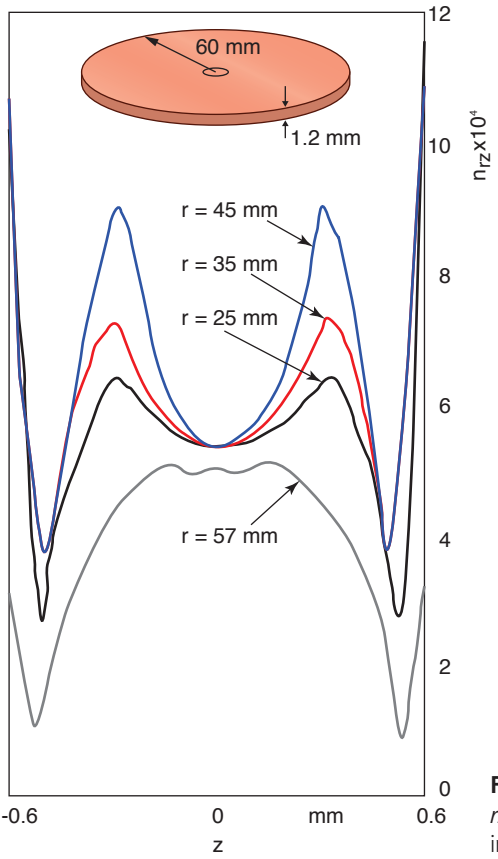

Figure 7.6 Birefringence distribution in the *rz*-plane at various radius positions; numbers indicate radial position

- Two thin outer layers with a biaxial orientation, random in the plane of the disk;
- Two thick layers next to the outer layers with a main orientation in the flow direction;
- Two thin randomly oriented transition layers next to the center core;
- One thick center layer with a main orientation in the circumferential direction.

There are three mechanisms that lead to high degrees of orientation in injection molded parts: fountain flow effect, radial flow, and holding pressure induced flow.

The *fountain flow effect* [9] is caused by the no-slip condition on the mold walls, which forces material from the center of the part to flow outward to the mold surfaces as shown in Fig. 7.8 [10]. As the figure schematically represents, the melt that flows inside the cavity freezes upon contact with the cooler mold walls. The melt subsequently entering the cavity flows between the frozen layers, forcing the melt skin at the front to stretch and unroll onto the cool wall where it freezes instantly.

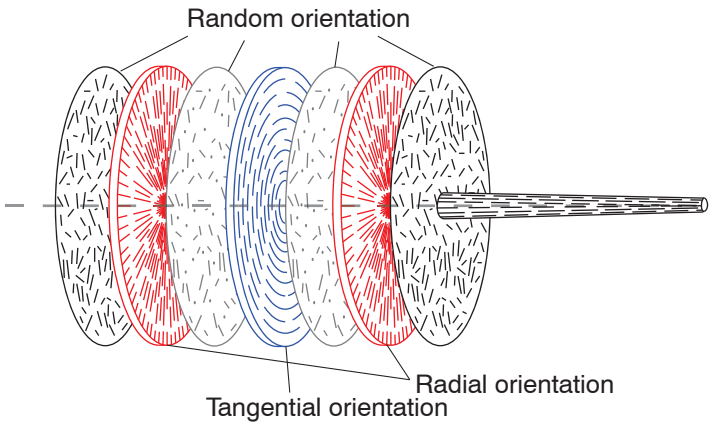

Figure 7.7 Filler orientation in seven layers of a centrally injected disk

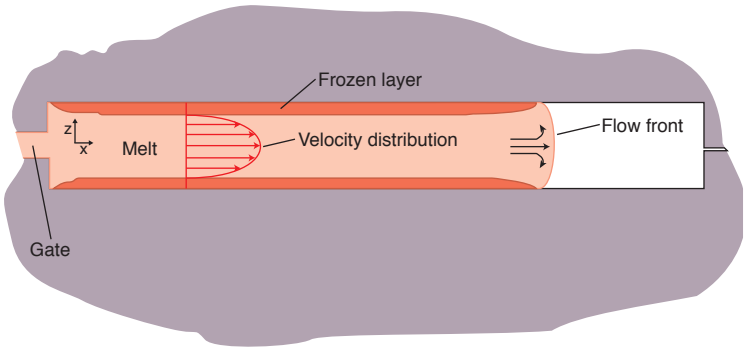

Figure 7.8 Flow and solidification mechanisms through the thickness during injection molding

The molecules that move past the free flow front are oriented in the flow direction and laid on the cooled mold surface, which freezes them into place, though allowing some relaxation of the molecules after solidification. Using computer simulation, the fountain flow effect has been extensively studied [11]. Figure 7.9 a and b [12] show simulated instantaneous velocity vectors and streamlines during the isothermal mold filling of a Newtonian fluid[2]. Fig. 7.9 c and d show the velocity vectors relative to the moving flow front. Figure 7.10 [13] presents the predicted shape and position of the tracer relative to the flow front along with the streamlines for a non-Newtonian non-isothermal fluid model. The square tracer mark is stretched as it flows past the free flow front, and is deposited against the mold wall, pulled upward again and is eventually deformed into a V-shaped geometry. Eventually, the movement of the outer layer is stopped as it cools and solidifies.

Radial flow is the second mechanism that often leads to orientation perpendicular to the flow direction in the central layer of an injection molded part. This mechanism is schematically represented in Fig. 7.11. As the figure suggests, the material

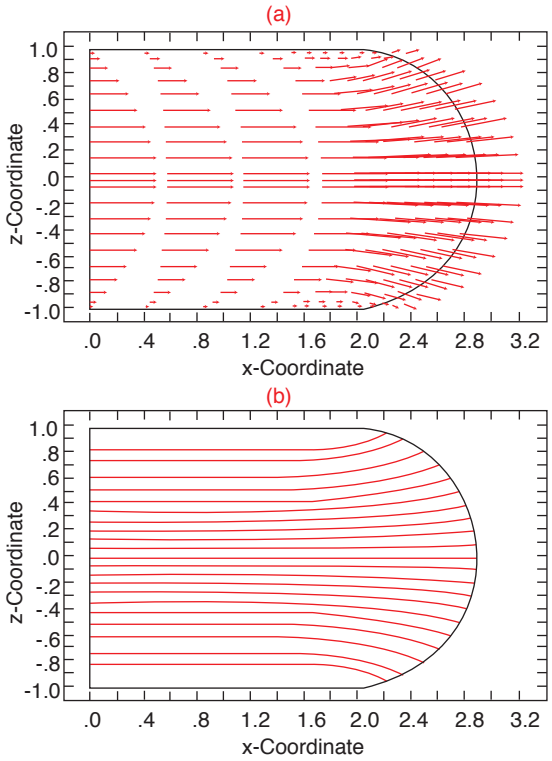

Figure 7.9 Fountain flow effect: (a, b) Actual velocity vectors and streamlines *(continued)*

2 The isothermal and Newtonian analysis should only serve to explain the mechanisms of fountain flow. The non-isothermal nature of the injection molding process plays a significant role in the orientation of the final part and should not be left out in the analysis of the real process.

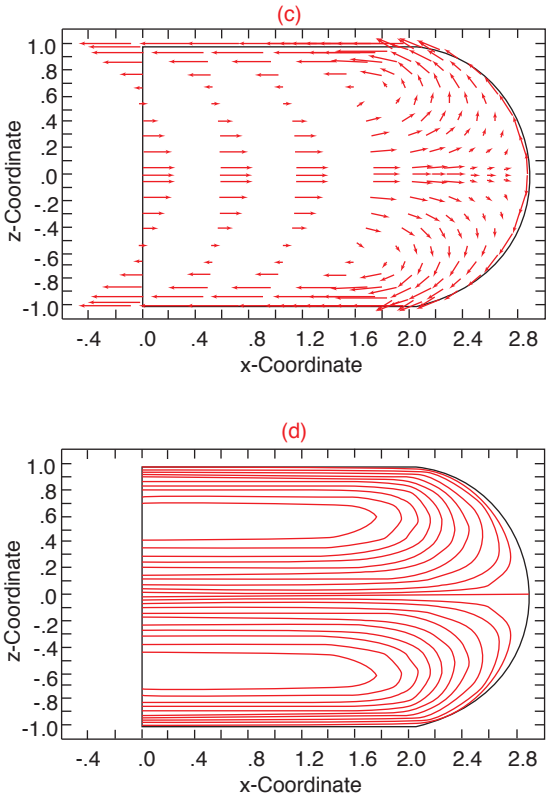

Figure 7.9 *(continued)* Fountain flow effect: (c, d) relative to the moving front velocity vectors and streamlines

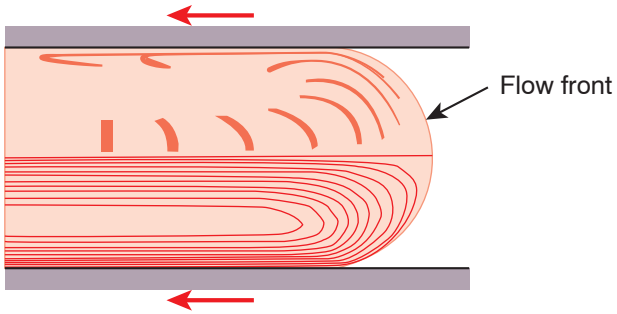

Figure 7.10 Deformation history of a fluid element and streamlines that move with the flow front for frame of reference

that enters through the gate is transversely stretched while it radially expands as it flows away from the gate. This flow is well represented in today's commonly used commercial injection mold filling software programs.

Finally, the flow induced by the holding pressure as the part cools leads to additional orientation in the final part. This flow is responsible for the spikes in the curves shown in Figs. 7.5 and 7.6.

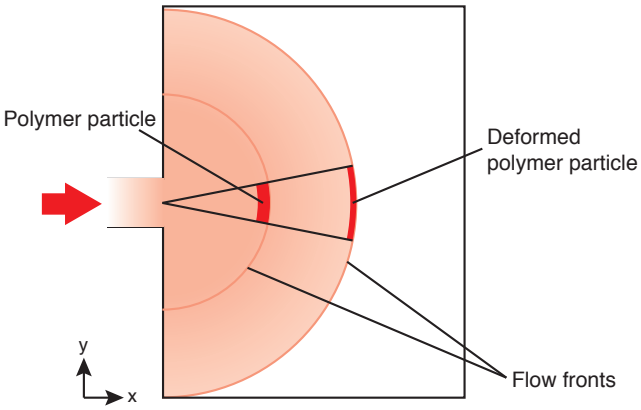

Figure 7.11 Deformation of the polymer melt during injection molding

7.1.2 Processing Thermoset Polymers

During the manufacture of thermoset parts molecular orientation does not develop because of the crosslinking that occurs during the solidification or curing reaction. A thermoset polymer solidifies as it undergoes an exothermic reaction and forms a tight network of inter-connected molecules.

However, many thermoset polymers are reinforced with filler materials, such as glass fiber, wood flour, among others. These composites are molded via transfer molding, compression molding, or injection-compression molding. The properties of the final part are dependent on the filler orientation. In addition, the thermal expansion coefficients and the shrinkage of these polymers are highly dependent on the type and volume fraction of filler being used. Different forms of orientation may lead to varying strain fields, which may cause warpage in the final part. This topic will be discussed in the next chapter.

During the processing of filled thermoset polymers the material deforms uniformly through the thickness, with slip occurring at the mold surface as shown schematically in Fig. 7.12 [14]. Several researchers have studied the development of fiber orientation during transfer molding and compression molding of sheet molding

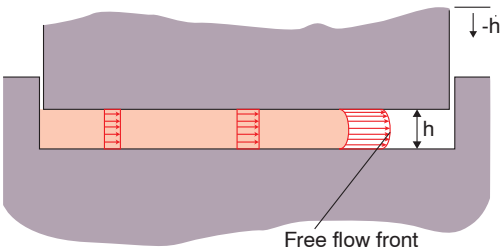

Figure 7.12 Velocity distribution during compression molding with slip between material and mold surface

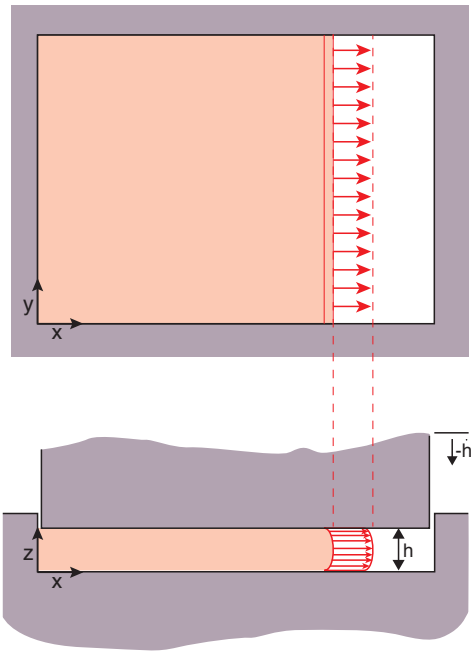

Figure 7.13 Schematic of extensional flow during compression molding

compound (SMC) parts [15]. During compression molding, a thin SMC charge is placed in a heated mold cavity and squeezed until the charge covers the entire mold surface. An SMC charge is composed of a polyester resin with approx. 10% by volume of calcium carbonate filler and 20–50% by volume glass fiber content. The fibers are usually 25 mm long and the final part thickness is 1–5 mm. Hence, the fiber orientation can be described with a planar orientation distribution function.

To determine the relationship between deformation and final orientation in compression molded parts, it is common to mold rectangular plates with various degrees of extensional flow, as shown in Fig. 7.13. These plates are molded with a small fraction of their glass fibers impregnated with lead so that they become visible in a radiograph. Figure 7.14 shows a computer generated picture from a radiograph, taken from a plate where the initial charge coverage was 33% [15, 16]. In Fig. 7.14, about 2000 fibers are visible; digitizing techniques resulted in the histogram of these fibers presented in Fig. 7.15 and depict the fiber orientation distribution in the plate. Such distribution functions are very common in compression or transfer molded parts and lead to high degrees of anisotropy throughout a part.

Furthermore, under certain circumstances, filler orientation may lead to crack formation as shown in Fig. 7.16 [1]. Here, the part was transfer molded through two gates, which led to a knit line and filler orientation shown in the figure. Knit lines are crack-like regions with a significantly lower number of fibers bridging across, lowering the strength across the region to that of the matrix material. A better way

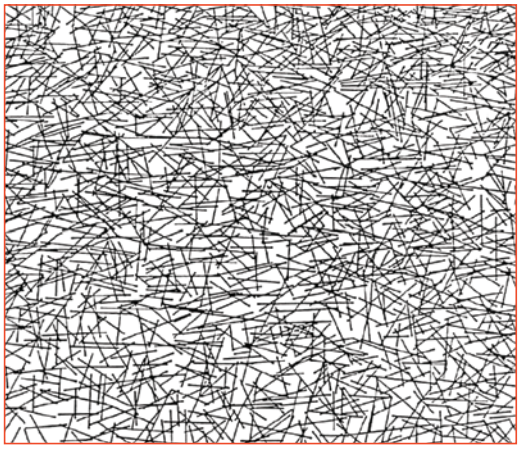

Figure 7.14 Computer redrawn plot of fibers in a radiograph of a rectangular SMC plate

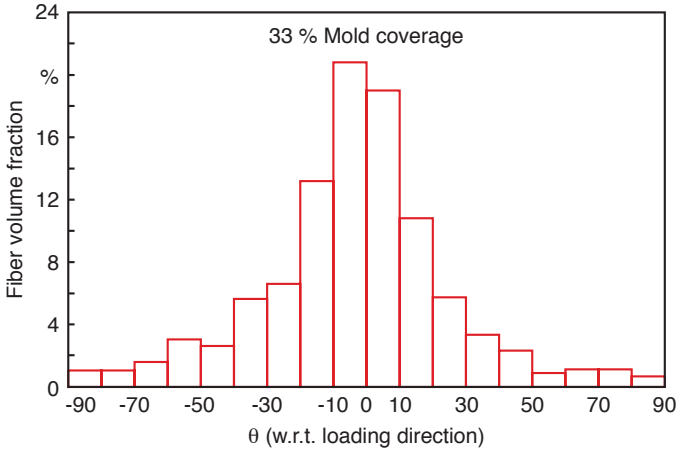

Figure 7.15 Measured fiber orientation distribution histogram in a plate with 33% initial mold coverage and extensional flow during mold filling

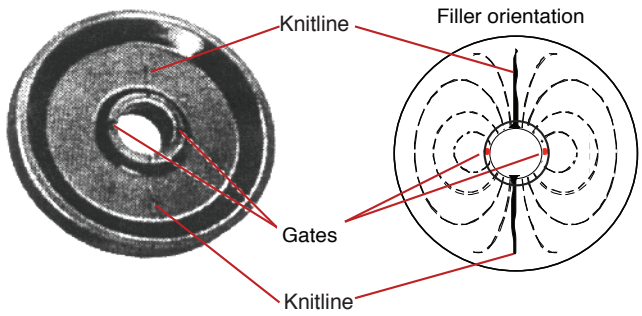

Figure 7.16 Formation of knit lines in a fiber filled thermoset pulley

to mold the part of Fig. 7.16 would be to inject the material through a ring-type gate, which would result in an orientation distribution mainly in the circumferential direction.

In compression molding, knit lines are common when multiple charges are placed inside the mold cavity or when charges with re-entrant corners are used, as shown in Fig. 7.17 [18]. However, a re-entrant corner does not always imply the formation of a knit line. For example, when squeezing a very thick charge, an equibiaxial deformation results, and knit line formation is avoided. On the other hand, a very thin charge will have a friction dominated flow leading to knit line formation at the beginning of flow. Knit lines may also form when there are large differences in part thickness and when the material flows around thin regions as demonstrated in Fig. 7.18. Here, a crack forms as the material flows past the thinner section of the body panel. It is interesting to point out that usually the thin region will eventually be punched out to give room to headlights, door handles, etc.

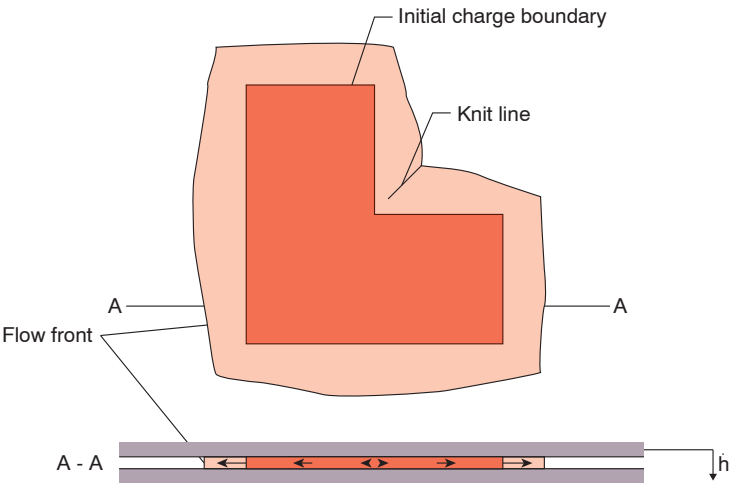

Figure 7.17 Knit line formation in an L-shaped charge for a squeeze ratio of 2

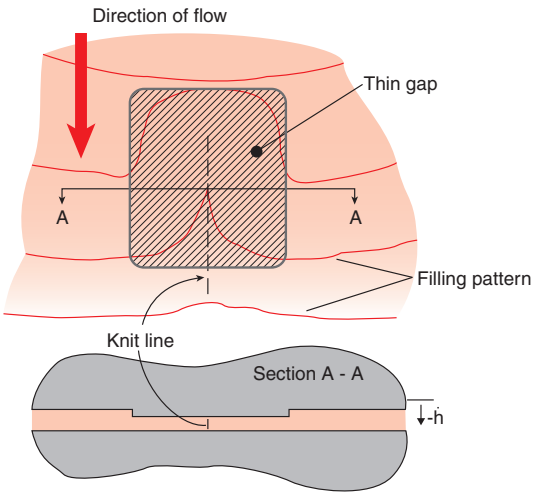

Figure 7.18 Schematic of knit line formation as SMC is squeezed through a narrow gap during compression molding

7.2 Predicting Orientation in the Final Part

In general, the orientation of a particle, such as a fiber, is described by two angles, ϕ and θ, as shown in Fig. 7.19. These angles change over time as the polymer flows through a die or is stretched or sheared during mold filling. In many cases the angular orientation of a particle can be described by a single angle, ϕ, because many complex three-dimensional flows can be reduced to planar flows such as the squeezing flow shown in Figs. 7.12 and 7.13 or the channel flow shown in Fig. 7.20. In squeezing flow, the z-dimension is very small compared to the other dimensions, whereas in channel flow, the z-dimension is much larger than the other dimensions. Channel flow is often encountered inside extrusion dies, and

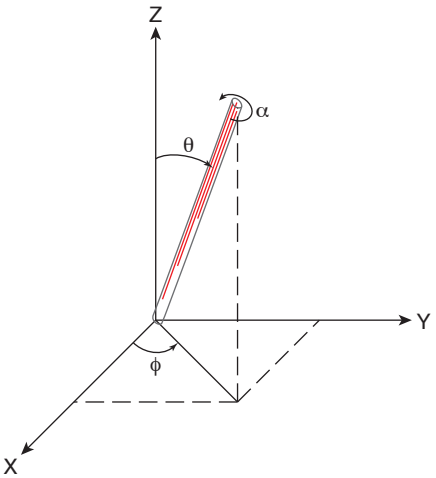

Figure 7.19 Fiber in a three-dimensional coordinate system

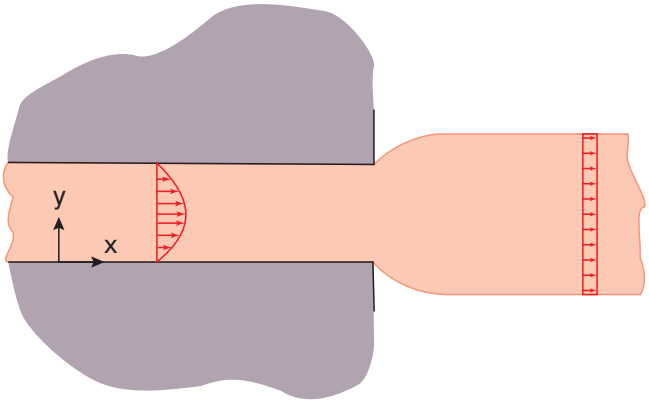

Figure 7.20 Schematic of two-dimensional channel flow

squeezing flow is common in compression molding where the fiber length is much larger than the thickness of the part. In both cases the fiber is allowed to rotate about the *z*-axis, with the channel flow having a three-dimensional orientation and the squeezing flow a planar orientation distribution. Due to the simplicity of planar orientation distributions and their applicability to a wide range of applications, we will limit our discussion to two-dimensional systems that can be handled with planar models. However, it should be pointed out that for many polymer articles, such as injection molded parts, a planar orientation is not sufficient to describe the angular position of the fillers or molecules. Because the topic of three-dimensional orientation distribution function is beyond the scope of this book, the reader is encouraged to consult the literature [6, 7].

7.2.1 Planar Orientation Distribution Function

The state of particle orientation at a point can be fully described by an orientation distribution function, $\psi(\phi, x, y, t)$. The distribution is defined such that the probability of a particle, located at *x*, *y* at time *t*, being oriented between angles ψ_1 and ψ_2, is given by.

$$P(\phi_1 < \phi < \phi_2) = \int_{\phi_1}^{\phi_2} \psi(\phi, x, y, t) d\phi \tag{7.1}$$

This is graphically depicted in Fig. 7.21. For simplicity, the *x, y, t* from the orientation distribution function can be dropped.

Because one end of a particle is indistinguishable from the other, the orientation distribution function must be periodic:

$$\psi(\phi) = \psi(\phi + \pi) \tag{7.2}$$

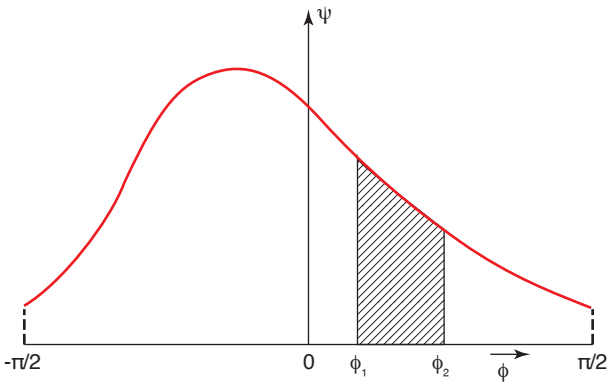

Figure 7.21 Orientation distribution function

Because all particles are located between $-\pi/2$ and $\pi/2$, the orientation distribution function must be normalized such that

$$\int_{-\pi/2}^{\pi/2} \psi(\phi)\, d\phi = 1 \tag{7.3}$$

The orientation distribution function changes constantly as the particles travel within a deforming fluid element. Assuming the fiber density is homogeneous throughout the fluid and remains so during processing[3], a balance around a differential element in the distribution function can be performed. This is graphically represented in Fig. 7.22. Here, the rate of change of the fiber density of the differential element, shown in the figure, should be the difference between the number of particles that move into and out of the control volume in a short time period Δt. This can be written as

$$\frac{\psi(\phi)\Delta\phi}{\Delta t} = \psi(\phi)\dot{\phi}(\phi) - \psi(\phi+\Delta\phi)\dot{\phi}(\phi+\Delta\phi) \tag{7.4}$$

Letting Δt and $\Delta\psi \to 0$ reduces Eq. 7.4 to

$$\frac{\partial\psi}{\partial t} = -\frac{\partial}{\partial\phi}(\psi\dot{\phi}) \tag{7.5}$$

This expression is known as the *fiber density continuity equation*. It states that a fiber that moves out of one angular position must move into a neighboring one, conserving the total number of fibers. If the initial distribution function, ψ_0, is known, an expression for the angular velocity of the particle, $\dot{\phi}$, must be found to solve for Eq. 7.5 and determine how the distribution function varies in time. The next sections present various models that can be used to determine the angular rotation of a slender, fiber-like particle.

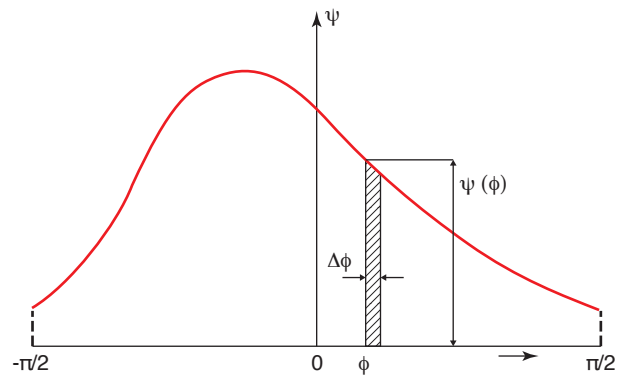

Figure 7.22 Differential element in an orientation distribution function

3 It is common knowledge that the fiber density is not constant throughout the part. However, this assumption is reasonable for predicting fiber orientation distribution functions.

7.2.2 Single Particle Motion

The motion of molecules, particles, or fibers can often be described by the motion of a rigid single rod in a planar flow. The analysis is further simplified assuming that the rod is of infinite aspect ratio, that is, the ratio of length to diameter, L/D, is infinite. Using the notation in Fig. 7.23 a, the fiber-end velocities can be broken into x and y components and rotational speed of the rod can be computed as a function of velocity gradients and its angular position:

$$\dot{\phi} = -\cos\phi\sin\phi\frac{\partial u_x}{\partial x} - \sin^2\phi\frac{\partial u_x}{\partial y} + \cos^2\phi\frac{\partial u_y}{\partial x} + \sin\phi\cos\phi\frac{\partial u_y}{\partial y} \tag{7.6}$$

Applying this equation to a simple shear flow as shown in Fig. 7.24, the rotational speed reduces to

$$\dot{\phi} = -\frac{\partial u_x}{\partial y}\sin^2\phi \tag{7.7}$$

Figure 7.25 shows the rotational speed, $\dot{\phi}$, as a function of angular position, ϕ, and Fig. 7.26 shows the angular position of a fiber as a function of time for a fiber with an initial angular position of 90°. It should be clear that for this model ($L/D = \infty$) all fibers will eventually reach their 0° position and stay there.

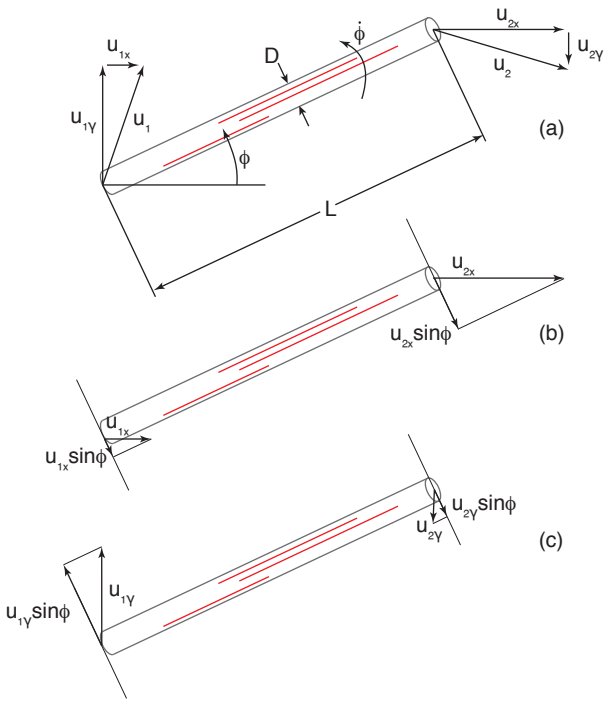

Figure 7.23 Fiber motion in planar flows

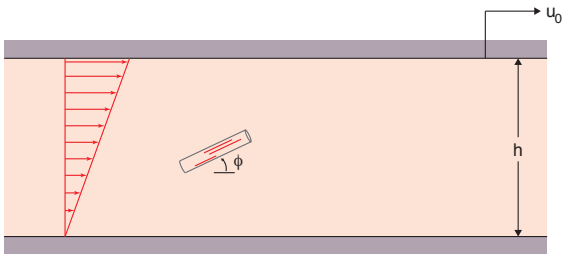

Figure 7.24 Schematic of fiber motion in simple shear flow

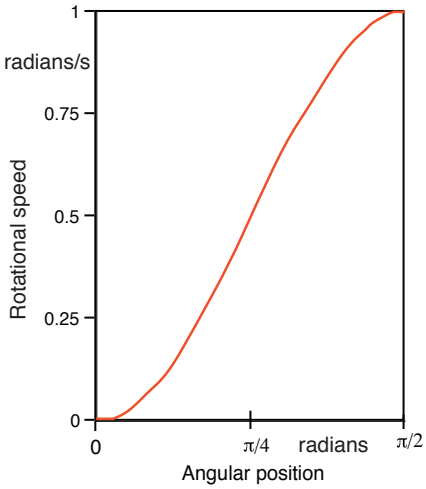

Figure 7.25 Rotational speed of a fiber with $L/D = \infty$ in a simple shear flow

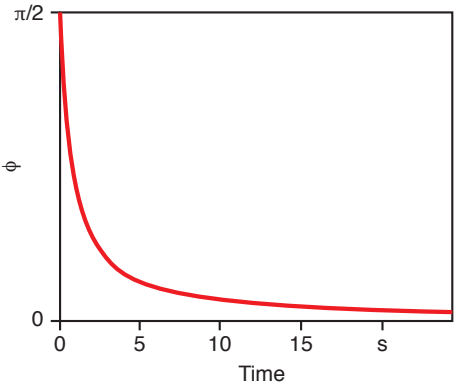

Figure 7.26 Angular position of a fiber with $L/D = \infty$ in a simple shear flow

7.2.3 Jeffery's Model

The rotational speed of a single particle, as described in Eq. 7.6, is only valid for an infinite L/D ratio, because the model does not include the rotational speed contribution caused by the thickness dimension of the particle. The thickness term was included in the classical equation derived by Jeffery [19] and describes the rota-

tional motion of a single ellipsoidal particle. His equation was later modified to account for the motion of cylindrical particles or rods [20, 21] and is written as

$$\dot{\phi} = \frac{r_e^2}{r_e^2+1}\left(-\sin\phi\cos\phi\frac{\partial u_x}{\partial x} - \sin^2\phi\frac{\partial u_x}{\partial y} + \cos^2\phi\frac{\partial u_y}{\partial x} + \sin\phi\cos\phi\frac{\partial u_y}{\partial y}\right) - \frac{1}{r_e^2+1}\left(-\sin\phi\cos\phi\frac{\partial u_x}{\partial x} - \cos^2\phi\frac{\partial u_x}{\partial y} + \sin^2\phi\frac{\partial u_y}{\partial x} + \sin\phi\cos\phi\frac{\partial u_y}{\partial y}\right) \tag{7.8}$$

Here, r_e is the ratio of the major dimensions of the particle, L/D. Note that for the infinite L/D case, Eq. 7.8 reduces to Eq. 7.6.

7.2.4 Folgar-Tucker Model

A simplification of the Jeffery model is to assume a dilute suspension (i.e., very few fibers or fillers are present and they do not interact with each other during flow). In polymer processing, this is usually not a valid assumption. In compression molding, for example, in a charge with 20–50% fiber content by volume the fibers are so closely packed that one cannot see through a resin-less bed of fibers, even for very thin parts. This means that as a fiber rotates during flow, it bumps into its neighbors, making the fiber-fiber interaction a major inhibitor of fiber rotation.

Folgar and Tucker [21, 22] derived a model for the orientation behavior of fibers in concentrated suspensions. For the case of planar flow, Folgar and Tucker's model states:

$$\dot{\phi} = \frac{-C_1\dot{\gamma}}{\psi}\frac{\partial\psi}{\partial\phi} - \cos\phi\sin\phi\frac{\partial u_x}{\partial x} - \sin^2\phi\frac{\partial u_x}{\partial y} + \cos^2\phi\frac{\partial u_y}{\partial x} + \sin\phi\cos\phi\frac{\partial u_y}{\partial y} \tag{7.9}$$

Here, $\dot{\gamma}$ is the *magnitude of the strain rate tensor* and C_I is a phenomenological coefficient that models the interactions between the fibers. Folgar and Tucker's *interaction coefficient*, C_I, varies between 0 for a fiber without interaction with its neighbors, and 1 for a closely packed bed of fibers. For a fiber reinforced polyester resin mat with 20–50% volume fiber content, C_I usually ranges between 0.03 and 0.06. When Eq. 7.9 is substituted into Eq. 7.5, the transient governing equation for fiber orientation distribution with fiber interaction built-in, becomes

$$\frac{\partial\psi}{\partial t} = -C_1\dot{\gamma}\frac{\partial^2\psi}{\partial\phi^2} - \frac{\partial\psi}{\partial\phi}\left(-sc\frac{\partial u_x}{\partial x} - s^2\frac{\partial u_x}{\partial y} + c^2\frac{\partial u_y}{\partial x} + sc\frac{\partial u_y}{\partial y}\right) - \psi\frac{\partial}{\partial\phi}\left(-sc\frac{\partial u_x}{\partial x} - s^2\frac{\partial u_x}{\partial y} + c^2\frac{\partial u_y}{\partial y} + sc\frac{\partial u_y}{\partial y}\right) \tag{7.10}$$

where s and c represent $\sin\phi$ and $\cos\phi$, respectively. The Folgar-Tucker model can easily be solved numerically. Using fiber reinforced thermoset composites as an example, the numerical solution of fiber orientation is discussed in the next section.

7.2.5 Tensor Representation of Fiber Orientation

Advani and Tucker [17, 23] developed a more efficient method to represent fiber orientation using orientation tensors. Their technique dramatically reduced the computational requirements when solving orientation problems using the Folgar-Tucker model.

Instead of representing the orientation of a fiber in a planar geometry by its angle, ϕ, Advani and Tucker used the components of a unit vector p directed along the axis of the fiber. The components of p are related to ϕ,

$$p_1 = \cos\phi \quad \text{and} \tag{7.11a}$$

$$p_2 = \sin\phi \tag{7.11b}$$

where, $p_i\left(i=1,2\right)$ are the two-dimensional Cartesian components of p. A suitably compact and general description of fiber orientation state is provided by the tensor of the form

$$a_{ij} = \langle p_i p_j \rangle \quad \text{and} \tag{7.12}$$

$$a_{ijkl} = \langle p_i p_j p_k p_l \rangle \tag{7.13}$$

Here the angle brackets < > represent an average overall possible direction of p, weighted by the probability distribution function, and a_{ij} is called the second-order orientation tensor and a_{ijkl} the fourth-order tensor. The properties of these tensors are discussed extensively by Advani and Tucker [24]. For the present, note that a_{ij} is symmetric and its trace equals unity. The advantage of using the tensor representation is that only a few numbers are required to describe the orientation state at any point in space. For planar orientations there are four components of a_{ij}, but only two are independent. Advani and Tucker were concerned with planar orientation in SMC only and used a_{11} and a_{22} to describe the direction and distribution of orientation at a point. Once the orientation tensor a_{ij} is known, the mechanical properties of the composite can be predicted.

The Folgar-Tucker model for single fiber motion in a concentrated suspension can be combined with the equation of continuity to produce an *equation of change* for the probability function and/or the orientation tensor [17, 25]. The result of the second-order orientation tensors is

$$\frac{Da_{ij}}{Dt} = -\frac{1}{2}\left(\omega_{ik}a_{kj} - a_{ik}\omega_{kj}\right) + \frac{1}{2}\lambda\left(\dot{\gamma}_{ik}a_{kj} + a_{ik}\dot{\gamma}_k - 2\dot{\gamma}_{kl}a_{ijkl}\right) + 2C_1\dot{\gamma}\left(\delta_{ij} - \alpha a_{ij}\right) \tag{7.14}$$

where δ_{ij} is the unit tensor and α equals 3 for three-dimensional orientation and 2 for planar orientation. Here, ω_{ij} and γ_{ij} are the velocity and the rate of deformation tensors, defined in terms of velocity gradients as

$$\omega_{ij} = \frac{\partial u_j}{\partial x_i} - \frac{\partial u_i}{\partial x_j} \quad \text{and} \tag{7.15}$$

$$\dot{\gamma}_{ij} = \frac{\partial u_j}{\partial x_i} + \frac{\partial u_i}{\partial x_j} \tag{7.16}$$

The material derivative in Eq. 7.14 appears on the left-hand side because the fibers are conveyed with the fluid. This casts the model of Folgar and Tucker into a useful form for computer simulation.

To calculate components of a_{ij} from Eq. 7.14, a_{ijkl} must be replaced by a suitable closure approximation. Combinations of the unit tensor and the components of a_{ij} can be used to form the approximation. Various closure approximations in planar and three-dimensional flow fields have been extensively tested by Advani and Tucker [17] and Cintra and Tucker [27]. It has been shown that Cintra and Tucker's *orthotropic closure approximation* performs best.

To obtain the orientation state of the fibers during the simulation of mold filling, Eq. 7.14 can be solved in the context of a filling simulation using a finite element/control volume approach. Only two equations for a_{11} and a_{12} need to be solved. The other components depend on these, and can be replaced on the right-hand side of Eq. 7.14 using $a_{21} = a_{12}$ and $a_{22} = 1 - a_{11}$.

Nodes that lie within the charge at any given time are treated with a conventional Galerkin finite element method. The spatial orientation field is discretized using nodal values of the independent tensor components a_{11} and a_{12} together with element shape function.

The same mesh and linear shape functions that were used in the filling simulation are used for fiber orientation. The resulting finite element equations for fiber orientation may be compactly expressed in a matrix form as

$$\begin{bmatrix} C_{ij} & 0 \\ 0 & C_{ij} \end{bmatrix} \begin{Bmatrix} \dot{a}_{11j} \\ \dot{a}_{12j} \end{Bmatrix} + \begin{bmatrix} K_{Iij} & K_{IIIij} \\ K_{IIij} & K_{IVij} \end{bmatrix} \begin{Bmatrix} a_{11j} \\ a_{12j} \end{Bmatrix} = \begin{Bmatrix} R_i \\ Q_i \end{Bmatrix} \tag{7.17}$$

Here, the dot denotes ordinary differentiation with respect to time. This nonlinear system of ordinary differential equation was solved using fully implicit time stepping and a Newton-Raphson technique. The initial condition is provided by the orientation state of the fibers in the initial charge.

Advani [17] compared their model to the experiments and found that, overall, there is good agreement between experimental and simulation results. In recent years, further advancements in fiber orientation prediction models were done by Phelps and Tucker [28] who proposed an anisotropic rotational diffusion model.

7.2.5.1 Predicting Orientation in Complex Parts Using Computer Simulation

Today, computer simulation is commonly used to predict mold filling, fiber orientation, thermal history, residual stresses, and warpage in complex parts.

In injection molding, researchers are making progress regarding solving three-dimensional orientation for complex realistic applications [27, 29]. Crochet and co-workers have solved for the non-isothermal, non-Newtonian filling and fiber orientation in non-planar injection molded parts. They used the Hele-Shaw model [30] to simulate mold filling and Advani and Tucker's tensor representation for the fiber orientation distribution in the final part. They divided the injection molded part into layers and included the fountain flow effect in the heat transfer and fiber orientation calculations. Figure 7.27 presents the fixed finite element mesh used to represent a 100 × 40 × 1 mm plate and the filling pattern during molding. Figure 7.28 presents the isotherms, the instant of fill, in three layers of the plate shown in Fig. 7.27, and Fig. 7.29 shows the fiber orientation distribution for the same layers.

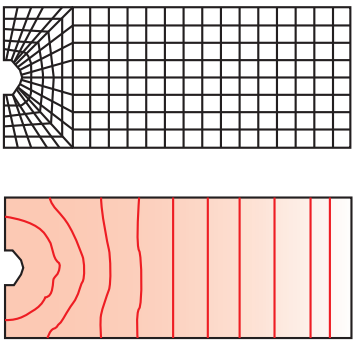

Figure 7.27 Fixed finite element mesh used to represent a 100 × 40 × 1 mm plate and temporary mesh adapted to represent the polymer melt at an arbitrary time during filling

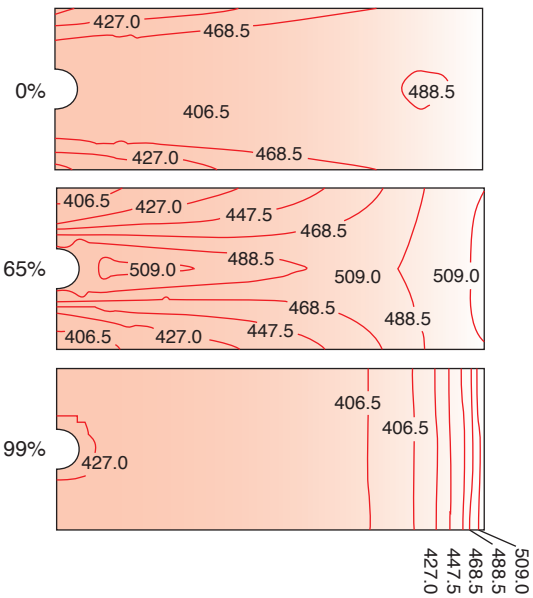

Figure 7.28 Isotherms in three layers at, 0 (center-line), 0.65 and 0.99 mm, the instant of fill

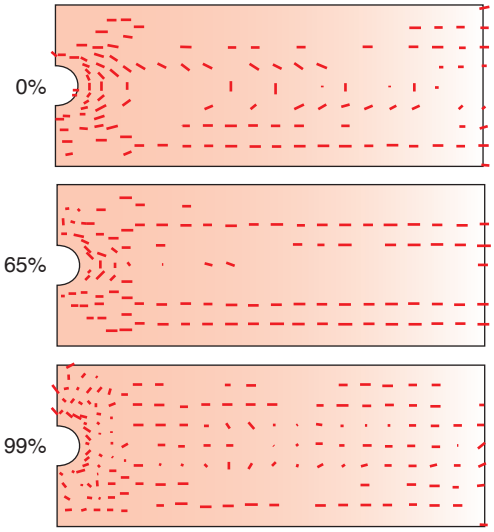

Figure 7.29 Fiber orientation in the same three layers shown in Figure 7.28

Because planar flow governs the compression molding process, the models described earlier work very well to represent the orientation of the fibers during processing and of the final part. The Folgar-Tucker model, Eq. 7.10, is usually solved using the finite difference technique and the velocity gradients in the equation are obtained from mold filling simulation. The initial condition is supplied by fitting $\psi_i(t=0)$ to the measured initial orientation state. For sheet molding compound charges the starting fiber orientation distribution is usually random, or $\psi_i = 1/\pi$.

The model has proven to work well compared to experiments done with extensional flows described in Section 7.1.2. Figure 7.30 compares the measured fiber orientation distributions to the calculated distributions using the Folgar-Tucker model for cases with 67 %, 50 %, and 33 % initial charge mold coverage. To illustrate the effect of fiber orientation on material properties of the final part, Fig. 7.31 [31] shows how the fiber orientation presented in Fig. 7.30 affects the stiffness of the plates.

$C_I = 0.04 C_I = 0.04 C_I = 0.04$

The Folgar-Tucker model has been implemented into various, commercially available compression mold filling simulation programs. To illustrate the prediction of fiber orientation distribution in realistic polymer products, the compression molding process of a truck fender will be used as an example. To compute the fiber orientation, the filling pattern must first be computed. This is usually done by using the control volume approach [32]. The initial charge location and filling pattern during compression molding of the fender is shown in Fig. 7.32, and the finite element discretization used to simulate the process is shown in Fig. 7.33. The fiber orientation distribution field, computed with the Folgar-Tucker model for the com-

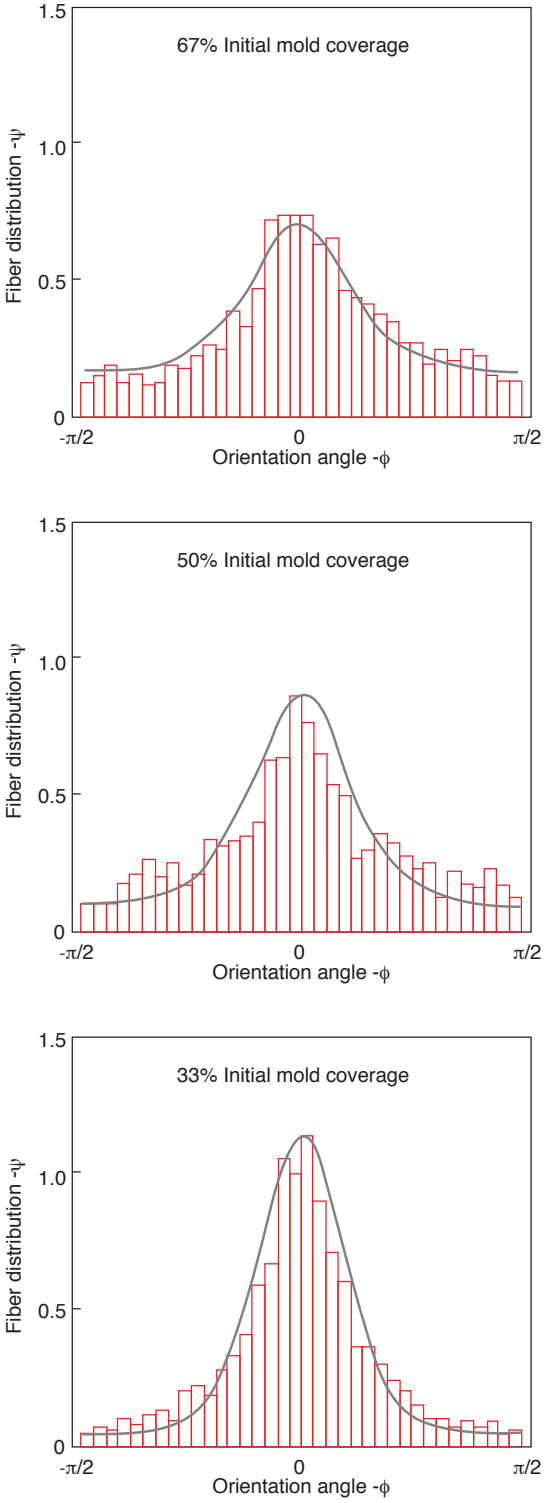

Figure 7.30 Comparison of predicted and experimental fiber orientation distributions for SMC experiments with (a) 67% initial mold coverage and $C_I = 0.04$, (b) 50% initial mold coverage and $C_I = 0.04$ and (c) 33% initial mold coverage and $C_I = 0.04$

pression molded automotive fender under the above conditions, is also shown in Fig. 7.33 [33]. For clarity, the orientation distribution function was plotted in polar coordinates from 0 to 2π and in the center of each finite element that is used for mold filling computation. For more detail about fiber orientation simulation the reader is encouraged to consult the literature [34].

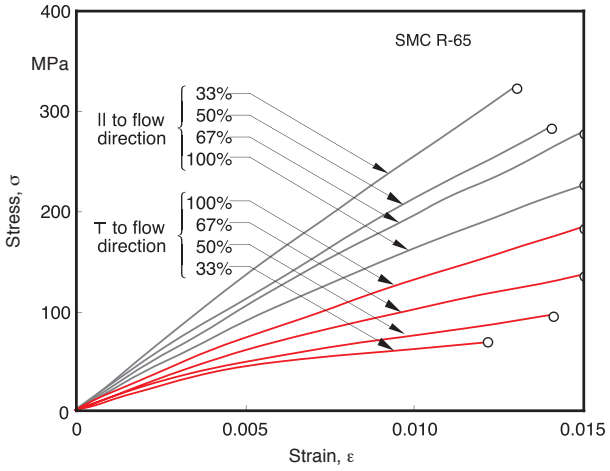

Figure 7.31 Stress-strain curves of 65% glass by volume SMC for various degrees of deformation

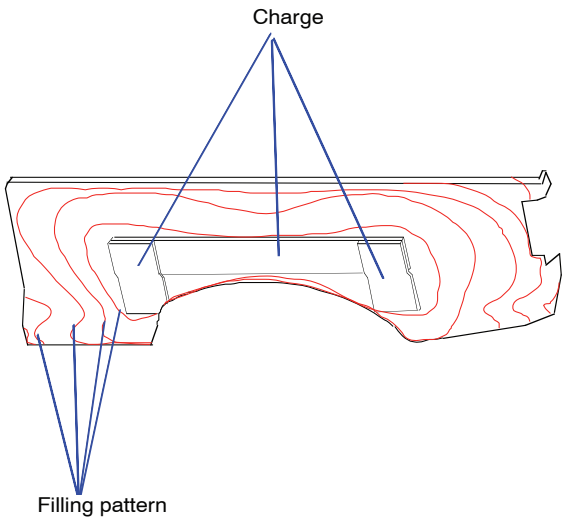

Figure 7.32 Initial charge and filling pattern during compression molding of an automotive fender

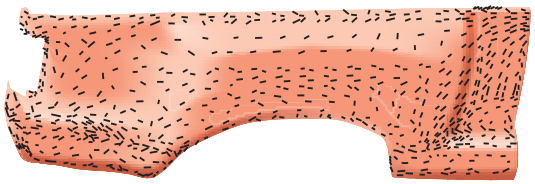

Figure 7.33 Fiber orientation distribution in a compression molded automotive fender

7.3 Fiber Damage

One important aspect when processing fiber reinforced polymers is fiber damage or *fiber attrition*. This is especially true during injection molding where high shear stresses are present. As the polymer is melted and pumped inside the screw section of the injection molding machine and as it is forced through the narrow gate, most fibers shorten in length, reducing the properties of the final part (e.g., stiffness and strength).

Figure 7.34 helps explain the mechanism responsible for fiber breakage. The figure shows two fibers rotating in a simple shear flow: fiber "a", which is moving out of its 0° position, has a compressive loading and fiber "b", which is moving into its 0° position, has a tensile loading. It is clear that the tensile loading is not large enough to cause any fiber damage, but the compressive loading is potentially large enough to buckle and break the fiber. A common equation that relates the critical shear stress, τ_{crit}, to elastic modulus, E_f, and to the L/D ratio of the fibers is

$$\tau_{crit} = \frac{\ln(2L/D) - 1.75}{2(L/D)^4} E_f \tag{7.18}$$

where τ_{crit} is the stress required to buckle the fiber. When the stresses are above τ_{crit}, the fiber L/D ratio is reduced. Figure 7.35 shows a dimensionless plot of critical stress versus L/D ratio of a fiber as computed using Eq. 7.18. It is worthwhile to point out that although Eq. 7.18 predicts L/D ratios for certain stress levels, it does not include the uncertainty that leads to fiber L/D ratio distributions – very common in fiber filled systems.

Figure 7.36 presents findings by Thieltges [35] demonstrating that during injection molding most of the fiber damage occurs in the transition section of the plasticating screw. Lesser effects of fiber damage were measured in the metering section of the screw and in the throttle valve of the plasticating machine. The dam-

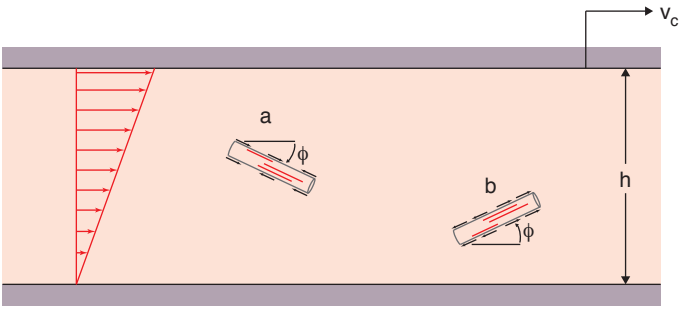

Figure 7.34 Fiber in compression and tension as it rotates during simple shear flow

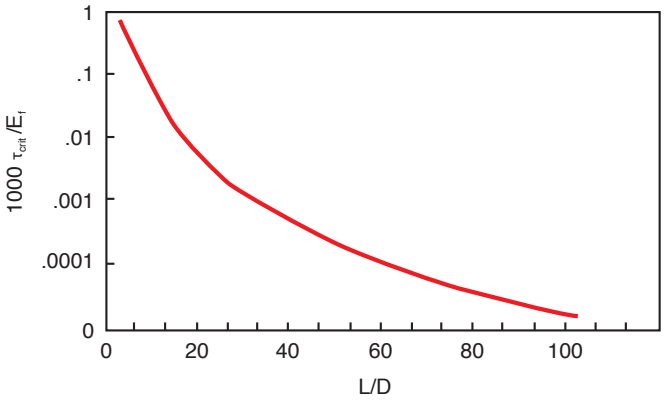

Figure 7.35 Critical stress, τ_{crit}, versus fiber L/D ratio

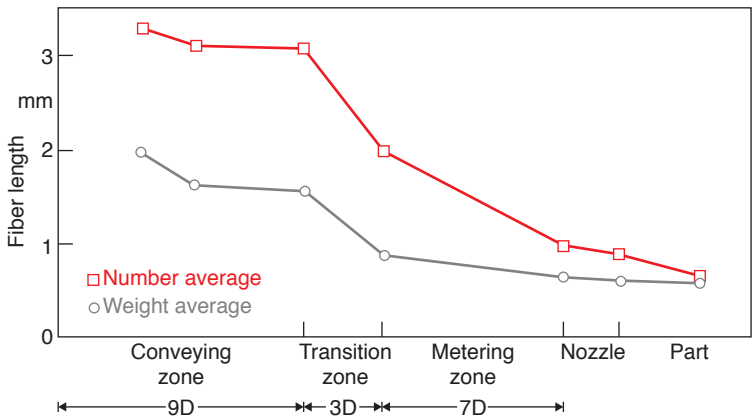

Figure 7.36 Fiber damage measured in the plasticating screw, throttle valve, and mold during injection molding of a polypropylene plate with 40 % fiber content by weight

age observed inside the mold cavity was marginal. However, the small damage observed inside the mold cavity is of great importance because the fibers flowing inside the cavity underwent the highest stresses, further reducing their L/D ratios. Bailey and Kraft [36] also found that fiber length distribution in the injection molded part is not uniform. For example, the skin region of the molding contained much shorter fibers than the core region. Recent work by Loken [37] demonstrated the effect of process conditions on fiber damage. He found that low barrel temperatures and high injection speeds led to higher fiber attrition than high temperatures and low injection speeds. Figure 7.37 presents the cumulative fiber length distribution of three different samples representing a pellet of a PP with 30 % glass fiber content, a sample after gentle processing with high barrel temperatures and low injection speeds, and a third sample with intense processing conditions at low barrel temperature and high injection speeds. The cumulative length distribution $\mathfrak{W}$ is computed using

$$\mathfrak{W}(l) = \frac{1}{\mathfrak{L}} \int_0^l \mathfrak{w}(l)\, dl \; \mathfrak{W}(l) = \frac{1}{\mathfrak{L}} \int_0^l \mathfrak{w}(l)\, dl \tag{7.19}$$

where $\mathfrak{w}(l)$ is the fiber length distribution, $\mathfrak{L}$, is the total fiber length of the sample, and l is the length of individual fibers. It should be noted that the samples with the gentle processing conditions exhibited 12% higher strength than the samples that resulted from more intense processing.

Another mechanism responsible for fiber damage is explained in Fig. 7.38 [38], where the fibers that stick out of partially molten pellets are bent, buckled, and sheared-off during plastication.

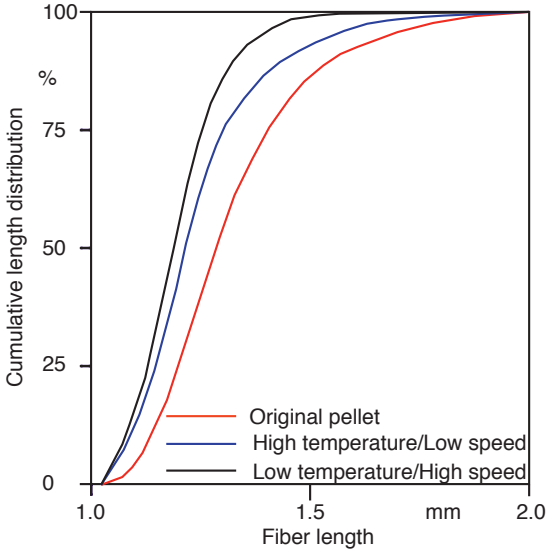

Figure 7.37 Cumulative fiber length distribution of a glass fiber filled polypropylene experiencing different processing conditions

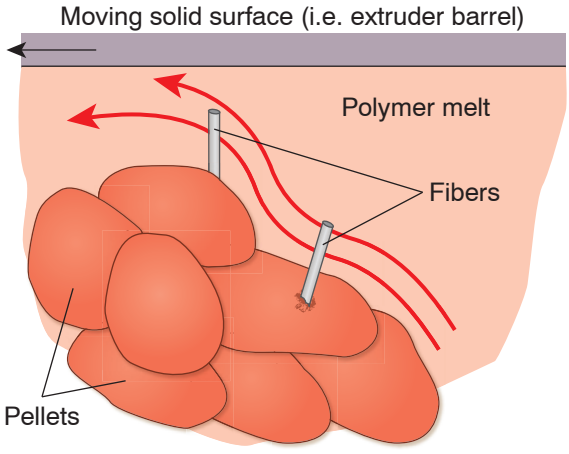

Figure 7.38 Fiber damage mechanism is the interface between solid and melt

Examples

1. Estimate the fiber length after extruding polyamide 66 reinforced with 33% glass fiber. The initial fiber $L/D = 300$, and the fiber diameter is 10 µm. The extruder diameter is 45 mm and the channel depth in the metering section is 5 mm. The extruder rotational speed is 200 rpm. The stiffness of the glass fiber is 90 GPa.
   When solving this problem we can assume a simple shear flow in the metering section of the extruder. The maximum speed is computed using

$$u_0 = R\Omega = 22.5\,\text{mm}\left(200\,\text{rpm}\right)\left(\frac{2\pi}{rev}\right)\left(\frac{1\,\text{min}}{60\,\text{s}}\right) = 471\frac{\text{mm}}{\text{s}} \quad u_0 = R\Omega$$

$$= 22.5\,\text{mm}\left(200\,\text{rpm}\right)\left(\frac{2\pi}{rev}\right)\left(\frac{1\,\text{min}}{60\,\text{s}}\right) = 471\,\text{mm/s}$$

   and the shear with

$$\dot{\gamma} = u_0/h = 471\ \text{mm/s}/5\ \text{mm} = 94\ \text{s}^{-1}$$

   At a rate of deformation of 100 s^{-1} the viscosity of PA 66 is approximately 66 Pa-s leading to a deviatoric stress of 6204 Pa. We can now either use Eq. 7.18 or Fig. 7.35 with a critical stress equal to 6204 Pa, to find a corresponding L/D of approximately 70.

2. Consider a fiber of aspect ratio, L/D = 10 moving in a simple shear flow. Plot the rotational speed of the fiber as a function of angular position, and the angular position as function of time.
   If we apply Eq. 7.8 to simple shear flow, it reduces to

$$\dot{\phi} = \frac{1}{r_e^2+1}\cos^2\phi\frac{\partial u_x}{\partial y} - \frac{r_e^2}{r_e^2+1}\sin^2\phi\frac{\partial u_x}{\partial y} \tag{7.19}$$

   When r_e = 10 (typical for a very short, damaged fiber in fiber reinforced composite parts) the equation for rotational speed is

$$\dot{\phi} = 0.01\cos^2\phi\frac{\partial u_x}{\partial y} - 0.99\sin^2\phi\frac{\partial u_x}{\partial y} \tag{7.20}$$

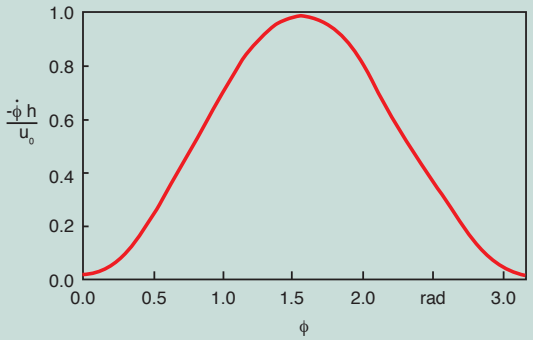

Figure 7.39 Rotational speed of a fiber with L/D = 10 in a simple shear flow, computed using Jeffery's model

Figure 7.39 shows the rotation speed, $\dot{\gamma}$, as a function of angular position. From Eq. 7.20 it is obvious that, at angular position of 0°, there is a very low rotational speed of $0.01\partial uv_x / \partial y$. As the angle moves out of its 0°position, it rapidly increases in speed to a maximum of $0.990\partial u_x / \partial y$ at 90°. Hence, most of the time a fiber is oriented in its 0° position. Figure 7.39 shows this effect by plotting the angular position of the fiber with respect to time. The effect is further increased for higher L/D ratios. Therefore, in shear dominated flows, most of the fibers will be oriented in the direction of the shear plane on which they are traveling. In polymer processes such as extrusion and injection molding, the main mode of deformation is shear. The relationship in Eq. 7.19 and the behavior seen in Fig. 7.40 apply for each plane with its individual gradient $\partial u_x / \partial y$. In processes such as fiber spinning and compression molding, the main modes of deformation are elongational and a similar analysis as done above may be performed.

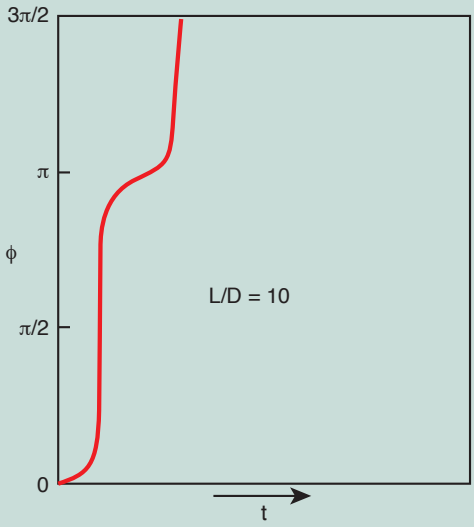

Figure 7.40 Angular position of a fiber with L/D = 10 in a simple shear flow, computed using Jefferey's model

Problems

1. Consider the compression molding process of a circular sheet molding compound (SMC) charge. The charge is composed of 30% by volume glass fibers, 1 in. long, in an unsaturated polyester resin. The flow field during compression molding of a circular charge is described with the following equations: $u_x = x/2$ and $u_y = y/2$. How will the fibers orient, if the initial planar orientation is random? Explain.
2. Does a lower melt temperature during injection molding lead to higher or lower degrees of molecular orientation? Why?
3. Would you use polystyrene to injection mold CD's? Why?
4. When manufacturing a component that includes a small lens, would you place the injection gate near the lens edge, or as far as possible from the lens? Why?
5. Find an injection molded transparent polystyrene component and observe it through cross-polarizers. Determine the location of the gate. Point out the places of highest and lowest orientation within the part.
6. Is there a direct relation between the fringe patterns that you see when observing a transparent component through cross-polarizers and the residual stresses that built up during manufacturing? Why?
7. A 45 mm single screw extruder is used to extrude plates manufactured of polyamide 66 filled with 33% glass fiber by volume. Given that the extruder is rotating at 120 rpm and that the channel depth in the metering section is 5 mm, estimate the average final *L/D* of the fibers.
8. Work out example 7.2 for an aspect ratio, *L/D* = 100. Plot the rotational speed as a function of angular position, and angular position as a function of time.
9. The charge location and filling pattern during compression mold filling of a truck wind deflector is presented in Fig. 7.41 [40]. The part was molded using two sheet molding compound (SMC) charges, one 8-layer charge and another 9-layer charge.
   Is there a knit line in the finished product? If yes, sketch a diagram with its approximate location in the finished part.
   Point out the areas of maximum fiber orientation.
10. Predict the length of the shortest fiber in a fiber filled polyamide 66 part molded at 300 °C with a maximum rate of deformation of 100 s^{-1}.

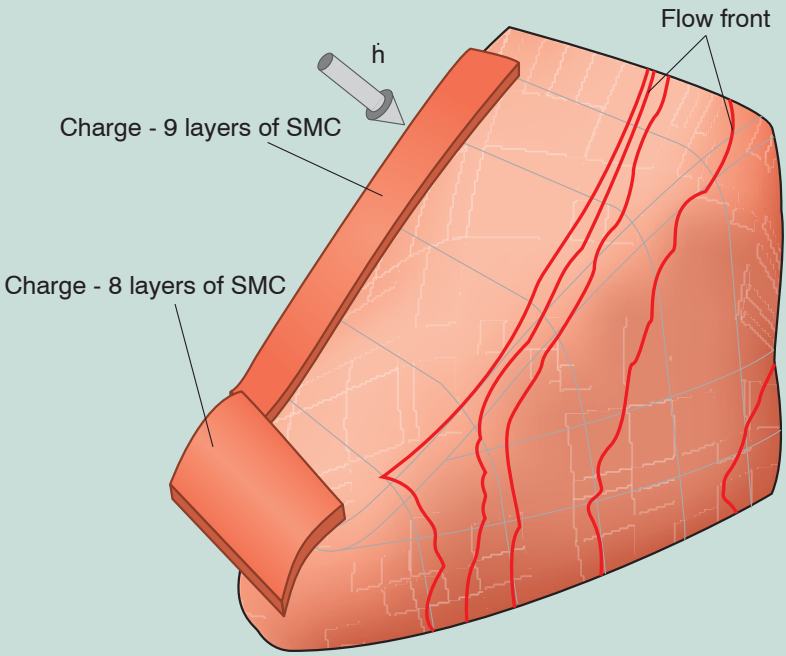

Figure 7.41 Actual mold filling pattern during compression molding of an SMC truck wind deflector

References

[1] Woebken, W., *Kunststoffe, 51*, 547, (1961).

[2] Menges, G., and Wübken, G., *SPE, 31st ANTEC*, (1973).

[3] Wimberger-Friedl, R., *Polym. Eng. Sci.*, 30, 813, (1990).

[4] Wimberger-Friedl, R., Ph.D. Thesis, Eindhoven University of Technology, The Netherlands, (1991).

[5] Menges, G., and Geisbüsch, P., *Colloid & Polymer Science, 260*, 73, (1982).

[6] Bay, R.S., and Tucker III, C.L., *Polym. Comp., 13*, 317, (1992a).

[7] Bay, R.S., and Tucker III, C.L., *Polym. Comp., 13*, 322, (1992b).

[8] Menges, G., Schacht, T., Becker, H., and Ott, S., *Intern. Polym. Proc., 2,* 77, (1987).

[9] Leibfried, D., Ph.D. Thesis, IKV, RWTH-Aachen, Germany, (1970).

[10] Wübken, G., Ph.D. Thesis, IKV, RWTH-Aachen, (1974).

[11] Mavrides, H., Hrymak, A.N., and Vlachopoulos, J., *Polym. Eng. Sci.*, 26, 449, (1986).

[12] Ibid.

[13] Mavrides, H., Hrymak, A.N., and Vlachopoulos, J., *J. Rheol.*, 32, 639, (1988).

[14] Barone, M.R., and Caulk, D.A., *J. Appl. Mech.*, 53, 361, (1986).

[15] Lee, C.-C., Folgar, F., and Tucker III, C.L., *J. Eng. Ind.*, 106, 114, (1984).

[16] Jackson, W.C., Advani, S.G., and Tucker III, C.L., *J. Comp. Mat., 20*, 539, (1986).

[17] Advani, S.G., Ph.D. Thesis, University of Illinois at Urbana-Champaign, (1987).

[18] Barone, M.R., and Osswald, T.A., *Polym. Comp., 9*, 158, (1988).

[19] Jeffery, G.B., *Proc. Roy. Soc., A102*, 161, (1922).

[20] Burgers, J.M., *Verh. K. Akad. Wet., 16*, 8, (1938).

[21] Folgar, F.P., Ph.D. Thesis, University of Illinois at Urbana-Champaign, (1983).

[22] Folgar, F.P., and Tucker III, C.L., *J. Reinf. Plast. Comp.*, 3, 98, (1984).

[23] Advani, S.G. and Tucker III, C.L., *Polym. Comp.*, *11*, 164, (1990).

[24] Advani, S.G. and Tucker III, C.L., *J. Rheol.*, 31, 751 (1987).

[25] Folgar, F. and Tucker III, C.L., *J. Reinf. Plast. Comp., 3*, 98 (1983).

[26] Jackson, W.C., Advani, S.G., and Tucker III, C.L., *J. Comp. Mat., 20,* 539, (1986).

[27] 40. Cintra, J.S., and Tucker III, C.L., *J. Rheol.*, 39:6, 1095 (1995).

[28] Phelps, J.H. and Tucker III, C.L., *Journal of Non-Newtonian Fluid Mechanics*, *156*, 165–176, (2009).

[29] Crochet, M.J., Dupret, F., and Verleye, V., *Flow and Rheology in Polymer Composites Manufacturing*, Ed. S.G. Advani, Elsevier, Amsterdam, (1994).

[30] Hele-Shaw, H.S., *Proc. Roy. Inst., 16,* 49, (1899).

[31] Chen, C.Y., and Tucker III, C.L., *J. Reinf. Compos., 3,* 120, (1984).

[32] Osswald, T.A., and Tucker III, C.L., *Int. Polym. Process.,* 5, 79, (1990).

[33] Gramann, P.J., Sun, E.M., and Osswald, T.A., *SPE 52nd Antec,* (1994).

[34] Tucker III, C.L., and Advani, S.G., *Flow and Rheology in Polymer Composites Manufacturing*, Ed. Advani, Elsevier, Amsterdam, (1994).

[35] Thieltges, H.-P., Ph.D. Thesis, RWTH-Aachen, Germany, (1992).

[36] Bailey, R., and Kraft, H., *Intern. Polym. Proc., 2*, 94, (1987).

[37] Loken, T., M.S. Thesis, University of Wisconsin-Madison, Madison, USA, (2011)

[38] Mittal, R.K., Gupta, V.B., and Sharma, P.K., *Composites Sciences and Tech.,* 31, 295, (1988).

[39] Osswald, T.A., Ph.D. Thesis, University of Illinois at Urbana-Champaign, (1986).

8 Solidification of Polymers

Solidification is the process during which a material undergoes a phase change and hardens. The phase change occurs as a result of either a reduction in material temperature or a chemical curing reaction. As discussed in previous chapters, a thermoplastic polymer hardens as the temperature of the material is lowered below either the melting temperature for a semi-crystalline polymer or the glass transition temperature for an amorphous thermoplastic. A thermoplastic has the ability to soften again as the temperature of the material is raised above the solidification temperature. On the other hand, the solidification of a thermosetting polymer leads to crosslinking of molecules. The effects of crosslinking are irreversible and lead to a network that hinders the free movement of the polymer chains, independent of the material temperature.

8.1 Solidification of Thermoplastics

The term "solidification" is often misused to describe the hardening of amorphous thermoplastics. The solidification of most materials is defined at a discrete temperature, whereas amorphous polymers do not exhibit a sharp transition between the liquid and the solid states. Instead, an amorphous thermoplastic polymer vitrifies as the material temperature drops below the glass transition temperature, T_g. A semi-crystalline polymer does have a distinct transition temperature between the melt and the solid state, the melting temperature, T_m.

8.1.1 Thermodynamics During Cooling

As heat is removed from a polymer melt, the molecules lose their ability to move freely, thus making the melt highly viscous. As amorphous polymers cool, the molecules slowly become closer packed, thus changing the viscous material into a leathery or rubberlike substance. Once the material has cooled below the glass

transition temperature, T_g, the polymer becomes stiff and brittle. It should be pointed out that the glass transition temperature is affected by cooling rate. Higher cooling rates "freeze-in" free volume between the molecules, leading to higher glass transition temperatures. At the glass transition temperature, the specific volume and enthalpy curves experience a significant change in slope. This can be seen for polystyrene in the enthalpy-temperature curve shown in Fig. 8.1. With semi-crystalline thermoplastics, at a crystallization temperature near the melting temperature, the molecules start arranging themselves in small crystalline and amorphous regions, creating a very complicated morphology. During the process of crystalline structure formation, a quantum of energy, often called *heat of crystallization* or *heat of fusion*, is released and must be conducted out of the material before the cooling process can continue. The heat of fusion is reflected in the shape of the enthalpy-temperature curve as shown for polyamide 66, polyethylene, and polypropylene in Fig. 8.1. At the onset of crystalline growth, the material becomes rubbery yet not brittle, because the amorphous regions are still above the glass transition temperature. As explained earlier, the glass transition temperature for some semi-crystalline polymers is far below room temperature, making them tougher than amorphous polymers. For common semi-crystalline polymers, the degree of crystallization can range between 30 and 70 %. This means that 30 – 70 % of the molecules form crystals and the rest remain in an amorphous state. The degree of crystallization is highest for those materials with short molecules because they can crystallize faster and more easily.

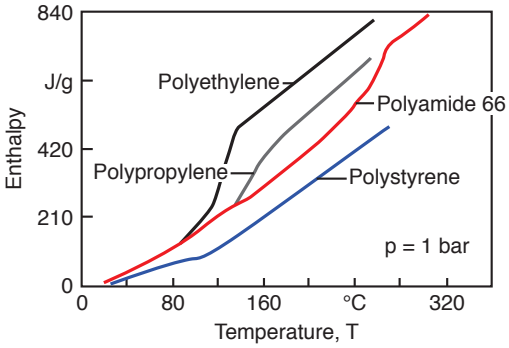

Figure 8.1 Enthalpy as a function of temperature for various thermoplastics

Figure 8.2 [1] depicts the volumetric temperature dependence of a polymer. In the melt state, the chains have "empty spaces" in which molecules can move freely. Hence, undercooled polymer molecules can still move as long as space is available. The point at which this free movement ends for a molecule or segment of chains is called the glass transition temperature or solidification point. As pointed out in Fig. 8.2, the free volume is frozen-in as well. In the case of crystallization, ideally, the volume should jump to a lower specific volume. However, even here small

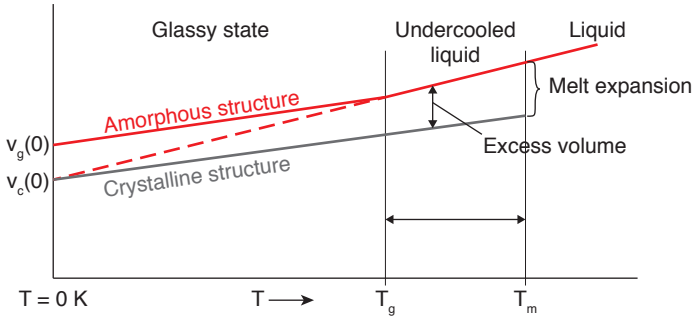

Figure 8.2 Thermal expansion model for thermoplastic polymers

amorphous regions remain permitting a slow flow or material creep. This free volume reduces to nothing at absolute zero temperature at which heat transport can no longer occur.

The specific volume of a polymer changes with pressure even at the glass transition temperature. This is demonstrated for an amorphous thermoplastic in Fig. 8.3 and for a semi-crystalline thermoplastic in Fig. 8.4.

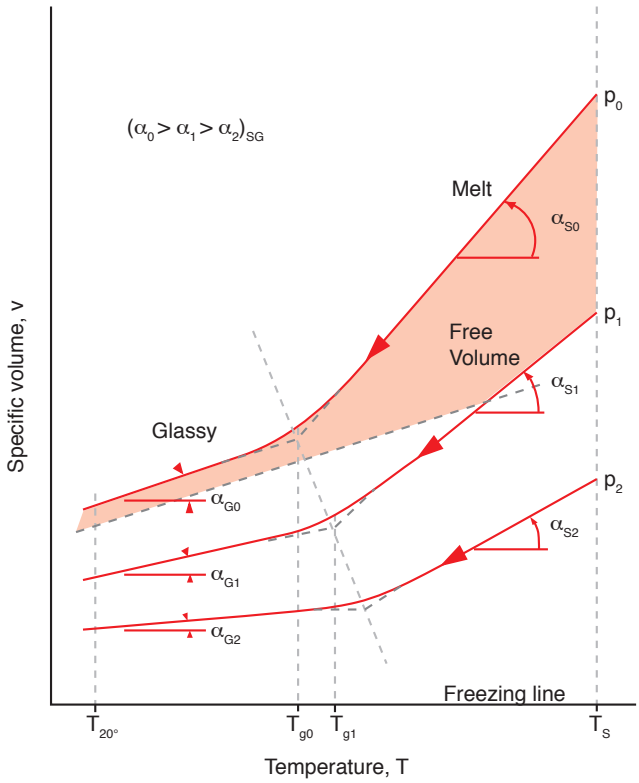

Figure 8.3 Schematic of a p-v-T diagram for amorphous thermoplastics

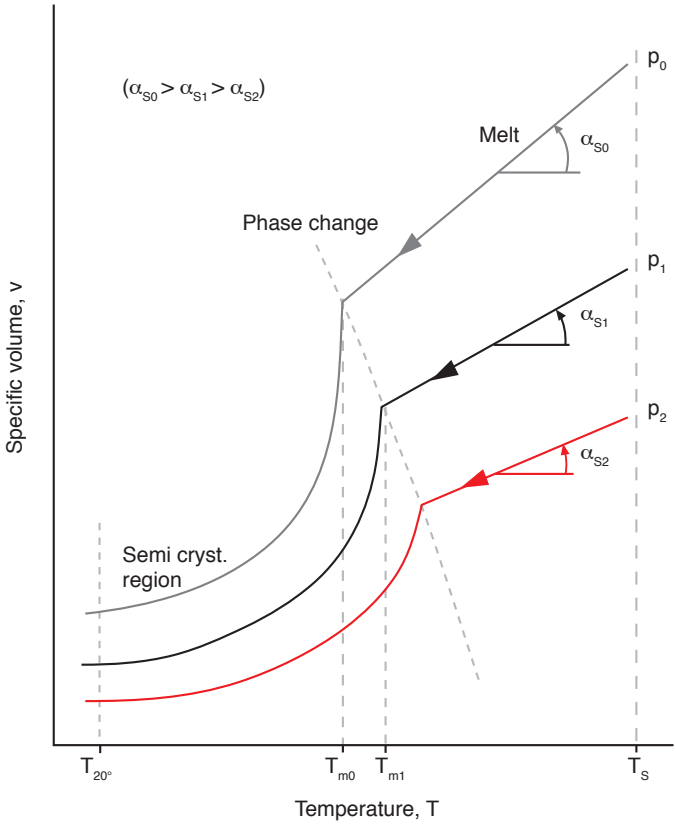

Figure 8.4 Schematic of a p-v-T diagram for semi-crystalline thermoplastics

It should be noted here that the size of the frozen-in free volume depends on the rate at which a material is cooled; high cooling rates result in a large free volume. In practice this is very important. When the frozen-in free volume is large, the part is less brittle. On the other hand, high cooling rates lead to parts that are highly permeable, which may allow the diffusion of gases or liquids through container walls. The cooling rate is also directly related to the dimensional stability of the final part. The effect of high cooling rates can often be mitigated by heating the part to a temperature that enables the molecules to move freely; this will allow further crystallization by additional chain folding. This process has a great effect on the structure and properties of the crystals and is referred to as *annealing*. In general, this only signifies a qualitative improvement of polymer parts. It also affects shrinkage and warpage during service life of a polymer component, especially when thermally loaded.

All these aspects have a great impact on processing. For example, when extruding amorphous thermoplastic profiles, the material can be sufficiently cooled inside the die so that the extrudate has enough rigidity to carry its own weight as it is pulled away from the die. Semi-crystalline polymers with low molecular weights

have a viscosity above the melting temperature that is too low to be able to withstand their own weight as the extrudate exits the die. Temperatures below the melting temperature, T_m, however cannot be used because they would lead to solidification inside the die. Similar problems are encountered with the thermoforming process in which the material must be heated to a point so that it can be formed into its final shape, yet it has to be able to withstand its own weight.

Semi-crystalline polymers are also at a disadvantage regarding the injection molding process. Because of the heat needed for crystallization, more heat must be removed to solidify the part; and because there is more shrinkage, longer packing times and larger pressures must be employed. All this implies longer cycle times and more shrinkage. High cooling rates during injection molding of semi-crystalline polymers will reduce the degree of crystallization. However, the amorphous state of the polymer molecules may lead to some crystallization after manufacturing, which will result in further shrinkage and warpage of the final part. It is quite common to follow the whole injection molding process in the p-v-T diagrams presented in Figs. 8.3 and 8.4, and thus predict how much the molded component has shrunk.

8.1.2 Morphological Structure

Morphology is the order or arrangement of the polymer structure. The possible "order" between a molecule or molecule segment and its neighbors can vary from a very ordered highly crystalline polymeric structure to an amorphous structure (i.e., a structure in greatest disorder or random). The possible range of order and disorder is clearly depicted on the left side of Fig. 8.5. For example, a purely amorphous polymer is formed only by the non-crystalline or amorphous chain structure, whereas the semi-crystalline polymer displays a combination of all the possible structures represented on the left side of Fig. 8.5.

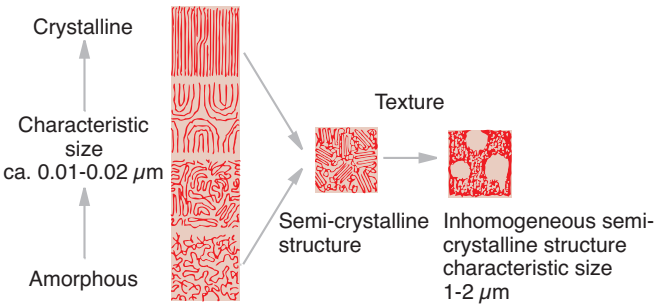

Figure 8.5 Schematic diagram of possible molecular structures that occur in thermoplastic polymers

The image of a semi-crystalline structure as shown in the middle of Fig. 8.5 can be captured with an electron microscope. A macroscopic structure, shown on the right hand side of the figure, can be captured with an optical microscope. An optical microscope can capture coarser macro-morphological structures, such as the spherulites in semi-crystalline polymers.

An amorphous polymer is defined as having a purely random structure. However it is not quite clear if a "purely amorphous" polymer as such exists. Electron microscopic observations have shown amorphous polymers that are composed of relatively stiff chains and that show a certain degree of macromolecular structure and order, for example, globular regions or fibrillic structures. Nevertheless, these types of amorphous polymers are still found to be optically isotropic. Even polymers with soft and flexible macromolecules, such as polyisoprene, whose molecular structure was first considered to be random, sometimes show band-like and globular regions. These bundle-like structures are relatively weak and short-lived when the material experiences stresses. The shear thinning viscosity effect of polymers sometimes is attributed to the breaking of such macromolecular structures.

8.1.3 Crystallization

Early on, before the existence of macromolecules had been recognized, the presence of highly crystalline structures had been suspected. Such structures were discovered when undercooling or when stretching cellulose and natural rubber. Later, it was found that a crystalline order also existed in synthetic macromolecular materials such as polyamide, polyethylene, and polyvinyl. Because of the polymolecularity of macromolecular materials, a 100 % degree of crystallization cannot be achieved. Hence, these polymers are referred to as semi-crystalline. It is common to assume that the semi-crystalline structures are formed by small regions of alignment or crystallites connected by random or amorphous polymer molecules.

With the use of electron microscopes and sophisticated optical microscopes the various existing crystalline structures are now well recognized. They can be listed as follows [2, 3]:

- *Single crystals*. These can form in solutions and help in the study of crystal formation. Here, plate-like crystals and sometimes whiskers are generated.
- *Spherulites*. As a polymer melt solidifies, several folded chain lamellae spherulites will form which are up to 0.1 mm in diameter. A typical example of a spherulitic structure is shown in Fig. 8.6 for a POM. The spherulitic growth in a polypropylene melt is shown in Fig. 8.7.
- *Deformed crystals*. If a semi-crystalline polymer is deformed while undergoing crystallization, oriented lamellae will form instead of spherulites.

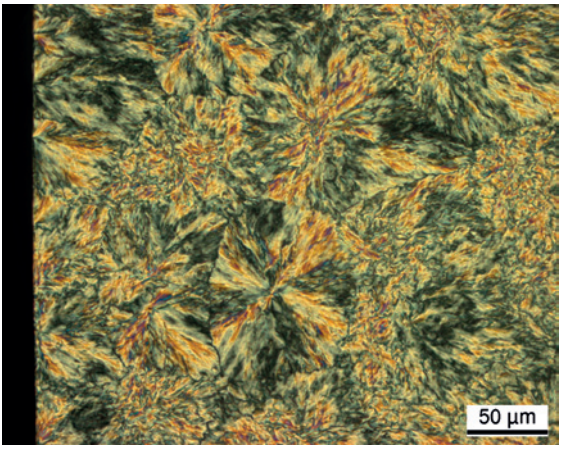

Figure 8.6 Polarized microscopic image of the spherulitic structure in polyacetal (POM) (Courtesy of the Institute of Plastics Technology, LKT, University of Erlangen-Nuremberg)

- *Shish-kebab*. In addition to spherulitic crystals, which are formed by plate- and ribbon-like structures, there are also shish-kebab crystals, which are formed by circular plates and whiskers. Shish-kebab structures are generated when the melt undergoes a shear deformation during solidification. A typical example of a shish-kebab crystal is shown in Fig. 8.8 [4].

The crystallization fraction can be described by the *Avrami equation* [5], written as follows:

$$x(t) = 1 - e^{-Zt^n} \tag{8.1}$$

where Z is a molecular weight and temperature dependent crystallization rate and n the Avrami exponent. However, because a polymer cannot reach 100 % crystallization, the above equation should be multiplied by the maximum possible degree of crystallization, x_∞.

$$x(t) = x_\infty \left(1 - e^{-Zt^n}\right) \tag{8.2}$$

The Avrami exponent, n, ranges between 1 and 4, depending on the type of nucleation and growth. For example, the Avrami exponent for spherulitic growth activated by sporadic nuclei is approx. 4, disc-like growth 3, and rod-like growth 2. If the growth is activated by instantaneous nuclei, the Avrami exponent is lowered by 1.0 for all cases. The crystalline growth rates of various polymers differ significantly from one to another. This is demonstrated in Table 8.1, which shows the maximum growth rate for various thermoplastics. The crystalline mass fraction can be measured experimentally with a differential scanning calorimeter (DSC).

A more in-depth coverage of crystallization and structure development during processing is given by Eder and Janeschitz-Kriegl [7].

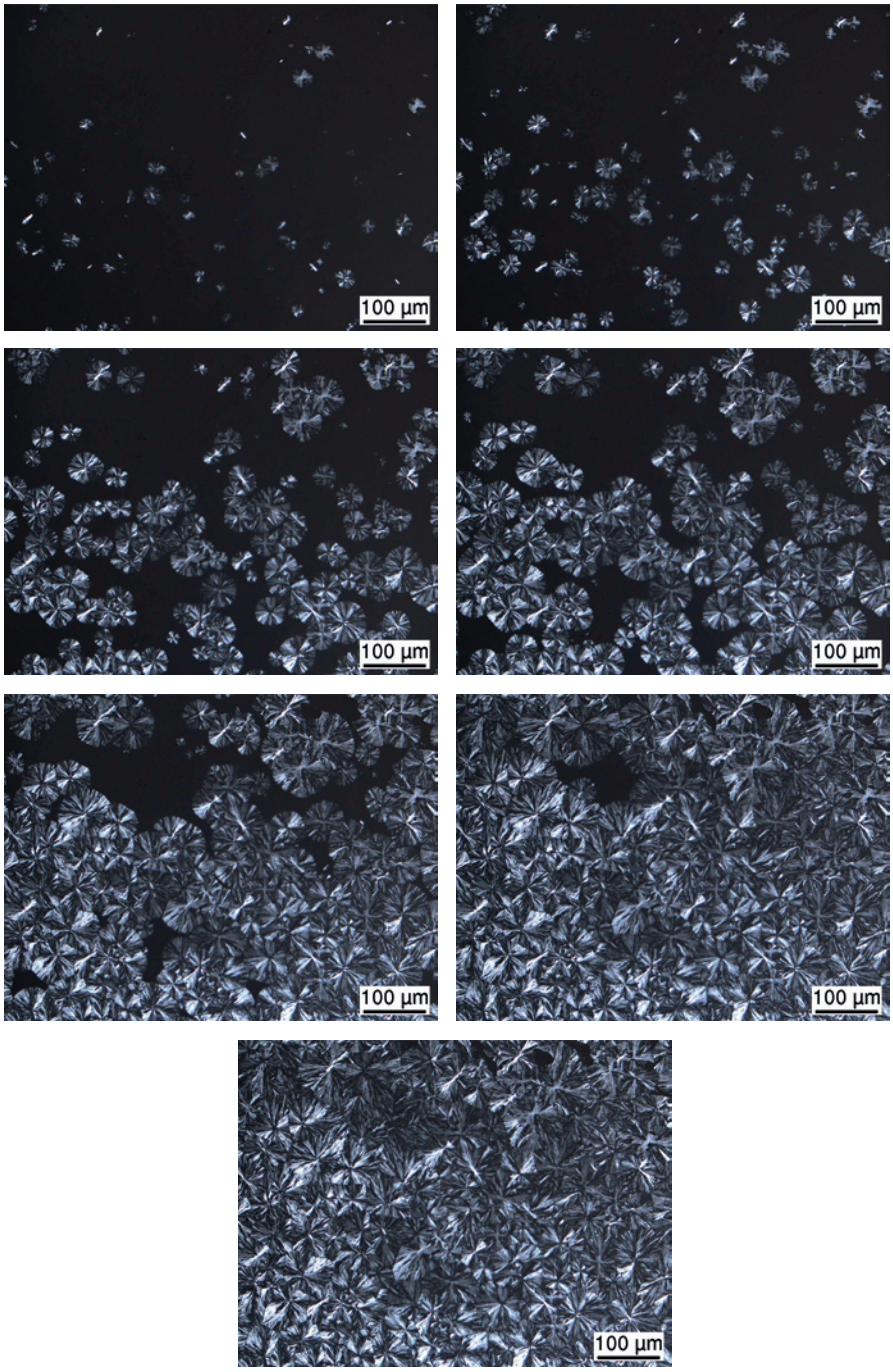

Figure 8.7 Development of the spherulitic structure in polypropylene as it was cooled from 170 to 40 °C at a cooling rate of 20 °C/minute. Images were taken at approximately 20 minute intervals (Courtesy of the Institute of Plastics Technology, LKT, University of Erlangen-Nuremberg)

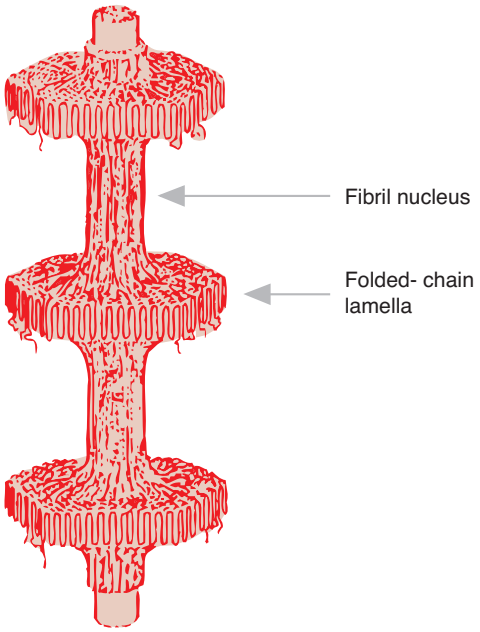

Figure 8.8 Model of the shish-kebab morphology

Table 8.1 Maximum Crystalline Growth Rate and Maximum Degree of Crystallinity for Various Thermoplastics

Polymer	Growth rate (μ/min)	Maximum crystallinity (%)
Polyethylene	>1000	80
Polyamide 66	1000	70
Polyamide 6	200	35
Isotactic polypropylene	20	63
Polyethylene terephthalate	7	50
Isotactic polystyrene	0.30	32
Polycarbonate	0.01	25

8.1.4 Heat Transfer During Solidification

Polymer parts are generally thin; therefore, the energy equation[1] can be simplified to a one-dimensional problem. Thus, using the coordinate description shown in Fig. 8.9 the energy equation can be reduced to

$$\rho C_p \frac{\partial T}{\partial t} = k \frac{\partial^2 T}{\partial z^2} \tag{8.3}$$

1 The energy equation is discussed in Chapter 4 and can be found in its complete form in the Appendix.

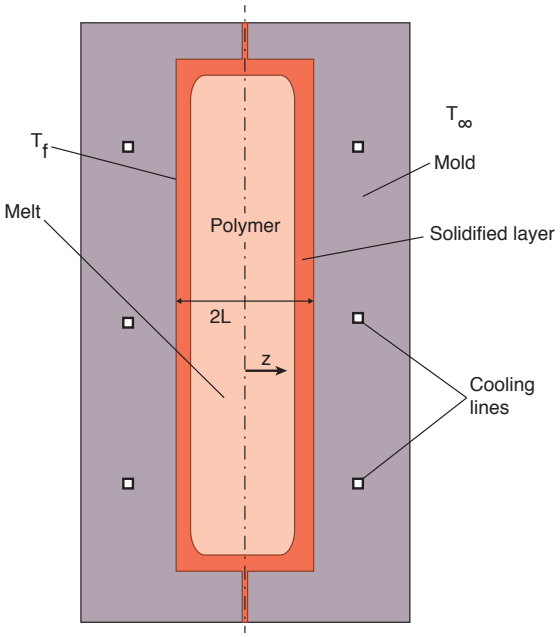

Figure 8.9 Schematic diagram of polymer melt inside an injection mold

Another assumption is a symmetry boundary condition (which also reduces warpage, usually a requirement):

$$\frac{\partial T}{\partial z} = 0 \quad \text{at} \quad z = 0 \tag{8.4}$$

If the sheet is cooled via forced convection or the part is inside a perfectly cooled mold, the final temperature of the part can be assumed to be the second boundary condition:

$$T = T_f \tag{8.5}$$

A typical temperature history for a polystyrene plate (its properties are presented in Table 8.2 [8]) is shown in Fig. 8.10. Once the material's temperature drops below the glass transition temperature, T_g, it can be considered solidified. This is shown schematically in Fig. 8.11. Of importance here is the position of the solidification

Table 8.2 Material Properties for Polystyrene

K	= 0.117 W/mK
C_p	= 1185 J/kgK
ρ	= 1040 kg/m^3
T_g	= 80 °C
E	= 3.2E9 Pa
v	= 0.33

front, $X(t)$. Once the solidification front equals the plate's dimension L, the solidification process is complete. From Fig. 8.10 it can be shown that the rate of solidification decreases as the solidified front moves further away from the cooled surface. For amorphous thermoplastics, the well-known *Neumann solution* can be used to

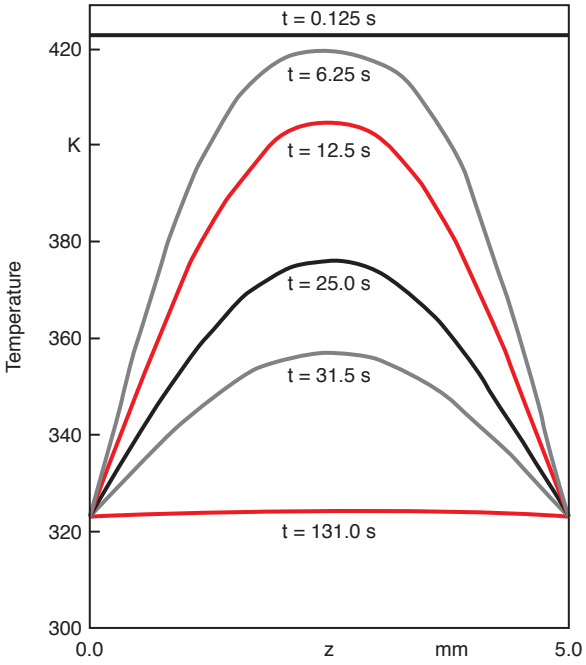

Figure 8.10 Temperature history of polystyrene cooled inside a 5 mm thick mold

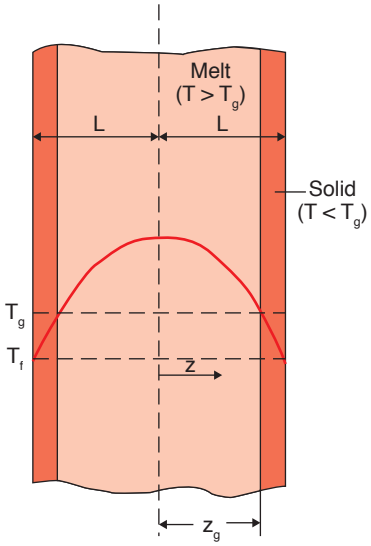

Figure 8.11 Schematic diagram of the cooling process of a polymer plate

estimate the growth of the glassy or solidified layer. The Neumann solution is written as

$$X(t) \propto \sqrt{\alpha t} \tag{8.6}$$

where α is the thermal diffusivity of the polymer. It must be pointed out here that for the Neumann solution, the growth rate of the solidified layer is infinite as time goes to zero.

The solidification process in semi-crystalline materials is more complicated due to the heat of fusion or heat of crystallization, nucleation rate, etc. When measuring the specific heat as the material crystallizes, a peak that represents the heat of fusion is detected (see Fig. 4.12). Figure 8.12 shows the calculated temperature distribution in a semi-crystalline polypropylene plate during cooling. The material properties used for the calculations are shown in Table 8.3 [8]. Here, the material that is below the melting temperature, T_m, is considered solid[2]. Experimental evidence [9] has demonstrated that the growth rate of the crystallized layer in semi-crystalline polymers is finite. This is mainly due to the fact that at the beginning nucleation occurs at a finite rate. Hence, the Neumann solution presented in Eq. 8.6, as well as the widely used *Stefan condition* [10], do not hold for semi-crystalline polymers. This is clearly demonstrated in Fig. 8.13 [10], which presents measured thickness of crystallized layers as a function of time for polypropylene plates quenched at three different temperatures. For further reading on this important topic the reader is encouraged to consult the literature [11, 12].

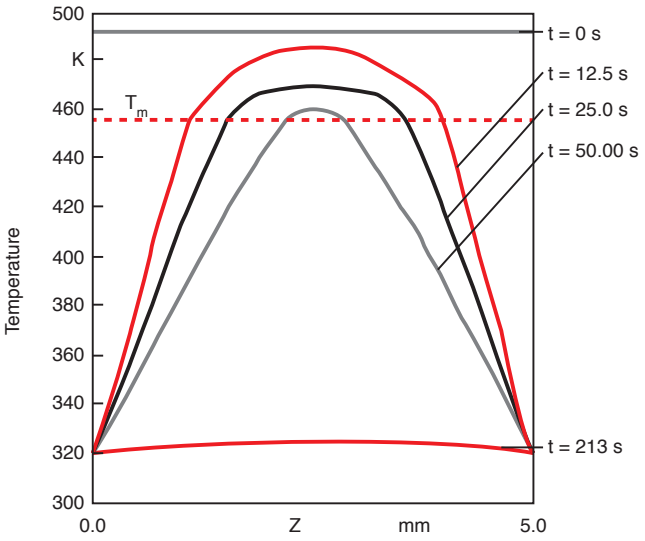

Figure 8.12 Temperature history of polypropylene cooled inside a 5 mm thick mold

2 It is well-known that the growth of the crystalline layer in semi-crystalline polymers is maximal somewhat below the melting temperature, at a temperature T_c. The growth speed of nuclei is zero at the melting temperature and at the glass transition temperature.

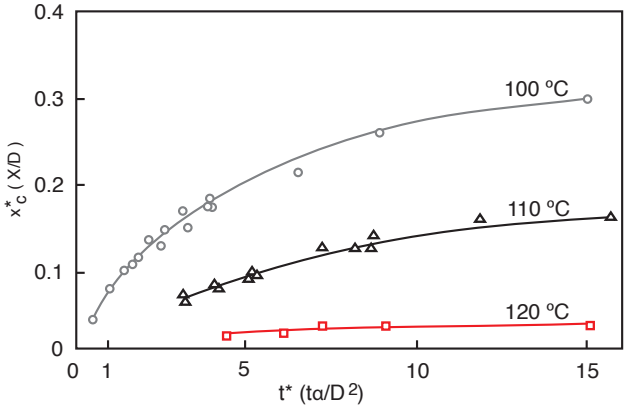

Figure 8.13 Dimensionless thickness of the crystallized layers as a function of dimensionless time for various temperatures of the quenching surface

Table 8.3 Material Properties for Polypropylene

K	=	0.117 W/mK
$C_{p,\,solid}$	=	1800 J/kgK
$C_{p,\,melt}$	=	2300 J/kgK
ρ	=	930 kg/m³
T_g	=	−18 °C
T_m	=	186 °C
λ	=	209 kJ/kg

8.2 Solidification of Thermosets

The solidification process of thermosets, such as phenolics, unsaturated polyesters, epoxy resins, and polyurethanes is dominated by an exothermic chemical reaction called curing reaction. A curing reaction is an irreversible process that results in a structure of molecules that are more or less crosslinked. Some thermosets cure under heat and others cure at room temperature. For thermosets that cure at room temperature the reaction starts immediately after mixing two components, where the mixing is usually part of the process. However, even with these thermosets, the reaction is accelerated by the heat released during the chemical reaction, or the *exotherm*. In addition, it is also possible to activate crosslinking by absorption of moisture or radiation, such as ultraviolet, electron beam, and laser energy sources [13].

In processing, thermosets are often grouped into three distinct categories, namely those that undergo a *heat activated cure*, those that are dominated by a *mixing activated cure*, and those that are activated by the *absorption of humidity or radiation*.

Examples of heat activated thermosets are phenolics; examples of mixing activated cure are epoxy resins and polyurethane.

8.2.1 Curing Reaction

In a cured thermoset, the molecules are rigid, formed by short groups that are connected by randomly distributed links. The fully reacted or solidified thermosetting polymer does not react to heat as observed with thermoplastic polymers. A thermoset may soften somewhat upon heating, but then it will degrade at high temperatures. Due to the high crosslinking density, a thermoset component behaves as an elastic material over a large range of temperatures. However, it is brittle with breaking strains of usually 1 to 3 %. The most common example is phenolic, one of the most rigid thermosets, which consists of carbon atoms with large aromatic rings that impede motion, making it stiff and brittle. Its general structure after crosslinking was shown in Figs. 3.22 and 3.23.

Thermosets can be identified in three categories: thermosets that cure via *condensation polymerization,* those that undergo *addition polymerization,* and those that cure via *free radical polymerization.*

Condensation polymerization is defined as the growth process that results from combining two or more monomers with reactive end-groups together with by-products such as alcohol, water, or acid. A common thermoset that polymerizes or solidifies via condensation polymerization is phenol formaldehyde, discussed in Chapter 3. The by-product of the phenolic curing reaction is water. Examples of addition polymerization are polyurethanes and epoxies.

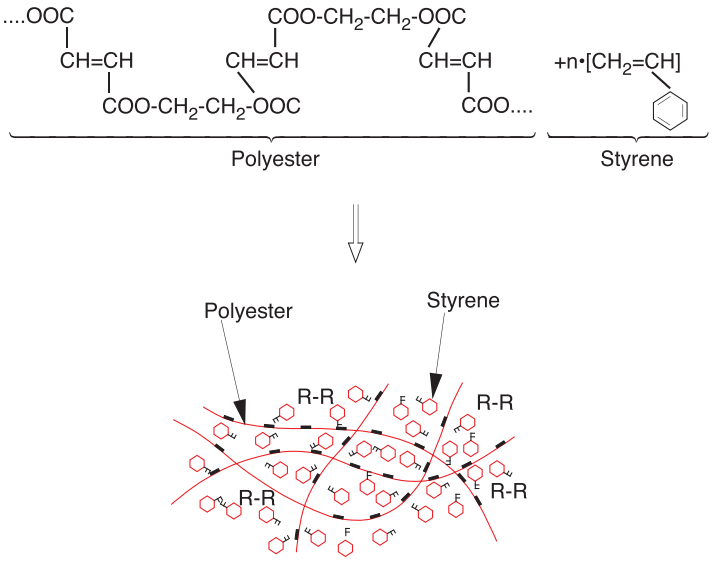

Figure 8.14 Symbolic and schematic representations of uncured unsaturated polyester

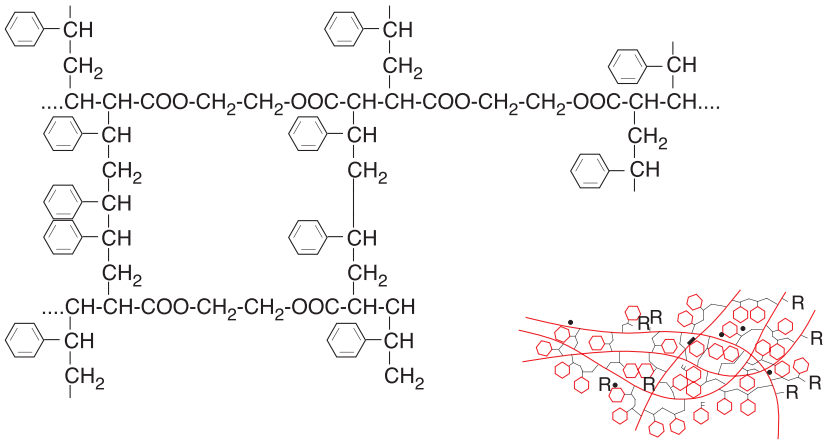

Figure 8.15 Symbolic and schematic representations of cured unsaturated polyester

An example of a crosslinking reaction of a thermoset by *free radical reaction* is the co-polymerization of unsaturated polyester with styrene molecules, shown in Fig. 8.14. The molecules contain several carbon-carbon double bonds, which act as cross-linking sites during curing. An example of the resulting network after the chemical reaction is shown in Fig. 8.15.

8.2.2 Cure Kinetics

As discussed earlier, with regard to processing thermosets can be grouped into two general categories: *heat activated cure* and *mixing activated cure* thermosets. However, no matter which category a thermoset belongs to, its curing reaction can be described by the reaction between two chemical groups denoted by A and B that link two segments of a polymer chain. The reaction can be followed by tracing the concentrations C_A or C_B of unreacted *As* or *Bs*. If the initial concentration of *As* and *Bs* is defined as C_{A_0} and C_{B_0}, the degree of cure can be described by

$$C^* = \frac{C_{A_0} - C_A}{C_{A_0}} \tag{8.7}$$

The degree of cure or conversion, C^*, equals zero when there has been no reaction and equals one when all *As* have reacted and the reaction is complete. However, it is impossible to monitor reacted and unreacted *As* and *Bs* during the curing reaction of a thermoset polymer. It is known though that the exothermic heat released during curing can be used to monitor the conversion, C^*. When several small samples of unreacted thermoset polymer are placed in a differential scanning calorimeter (DSC), each at a different heating rate, every sample will release the same amount of heat, Q_T. This occurs because every crosslinking that occurs during a

reaction releases a small quantum of energy in the form of heat. Figure 8.16 [14] shows the heat rate released during isothermal cure of a vinyl ester at various temperatures.

The degree of cure can be defined by the following relation

$$C^* = \frac{Q}{Q_T} \tag{8.8}$$

where Q is the heat released up to an arbitrary time τ, and is defined by

$$Q = \int_0^{\tau} \dot{Q} dt \tag{8.9}$$

DSC data is commonly fitted to empirical models that accurately describe the curing reaction. Hence, the rate of cure can be described by the exotherm, $\dot{Q}$, and the total heat released during the curing reaction, Q_T, as

$$\frac{dC^*}{dt} = \frac{\dot{Q}}{Q_T} \tag{8.10}$$

With the use of Eq. 8.10, it is now easy to take the DSC data and find the models describing the curing reaction.

During cure, thermoset resins exhibit three distinct phases; viscous liquid, gel, and solid. Each of these three stages is marked by dramatic changes in the thermomechanical properties of the resin. The transformation of a reactive thermosetting liquid to a glassy solid generally involves two distinct macroscopic transitions:

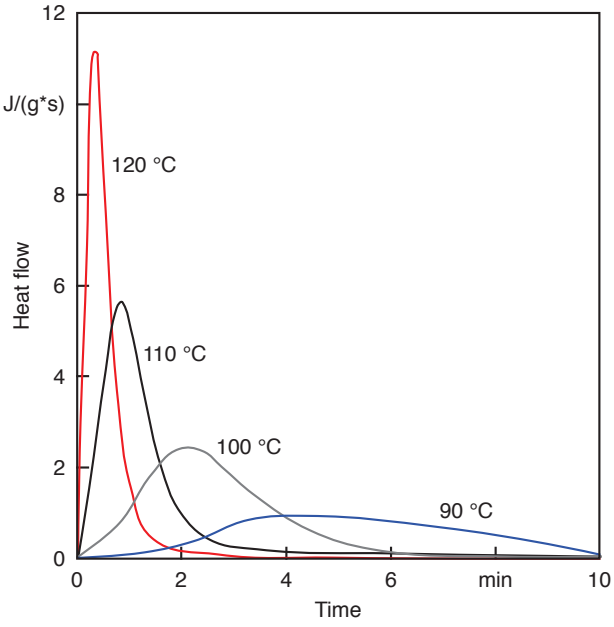

Figure 8.16 DSC scans of the isothermal curing reaction of vinyl ester at various temperatures

molecular gelation and vitrification. Molecular gelation is defined as the time or temperature at which covalent bonds connect across the resin to form a three-dimensional network that gives rise to long range elastic behavior in the macroscopic fluid. This point is also referred to as the gel point, where $C^* = C_g$. As a thermosetting resin cures, the cross-linking begins to hinder molecular movement, leading to a rise in the glass transition temperature. Eventually, when T_g nears the processing temperature, the rate of curing reduces significantly, eventually dominated by diffusion. At this point the resin has reached its vitrification point. Figure 8.17, which presents the degree of cure as a function of time, illustrates how an epoxy resin reaches a maximum degree of cure at various processing temperatures. The resin processed at 200 °C reaches 100% cure because the glass transition temperature of fully cured epoxy is 190 °C, less than the processing temperature. On the other hand, the sample processed at 180 °C reaches 97% cure and the one processed at 160 °C only reaches 87% cure.

Figures 8.16 and 8.17 also illustrate how the curing reaction is accelerated as the processing temperature is increased. The curing reaction of thermally cured thermoset resins is not immediate, thus the blend can be stored in a refrigerator for a short period of time without initiating any significant curing reaction.

The behavior of curing thermosetting resins can be represented with the generalized time-temperature-transformation (TTT) cure diagram developed by Enns and Gillham [16]; it can be used to relate the material properties of thermosets as a function of time and the processing temperature as shown in Fig. 8.18.

The various lines in the diagram represent constant degrees of cure. The curve labeled $C^* = C_g$ represents the gel point and $C^* = 1$ the fully cured resin. Both curves

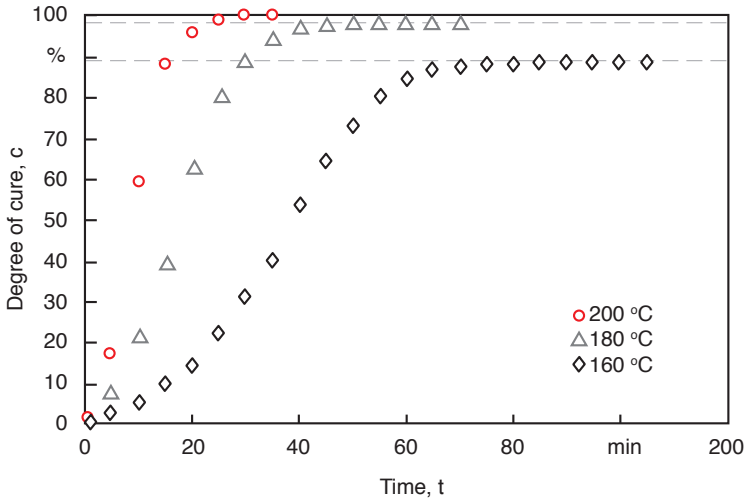

Figure 8.17 Degree of cure as a function time for an epoxy resin measured using isothermal DSC

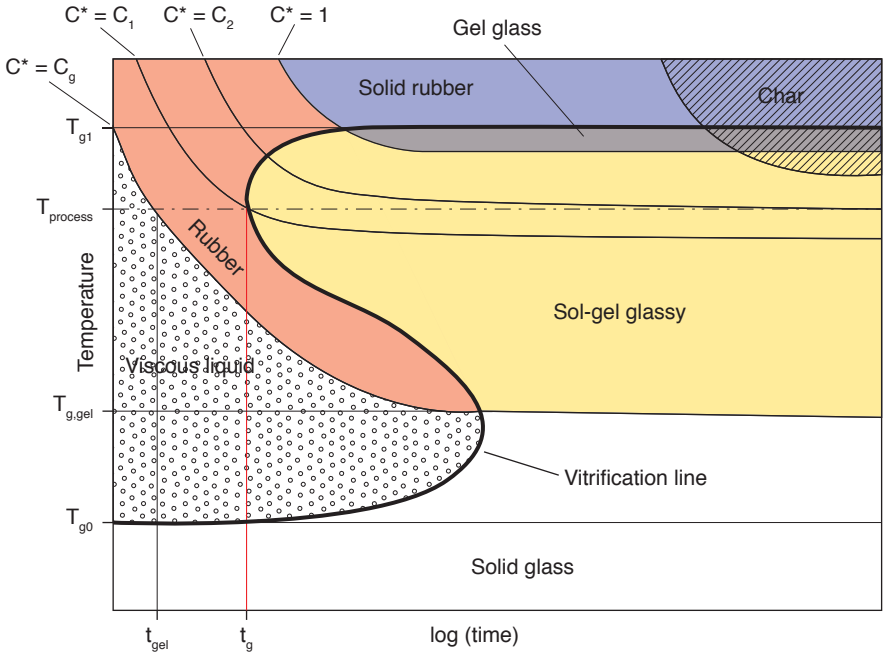

Figure 8.18 Time-temperature-transformation (TTT) diagram for a thermoset

have their corresponding glass transition temperatures, T_{g1} and $T_{g\,gel}$, for the fully cured resin and for the resin at its gel point, respectively. The glass transition temperature of the uncured resin, T_{g0}, and an S-shaped curve labeled "vitrification line", are also depicted. The *vitrification line* represents the boundary at which the glass transition temperature becomes the processing temperature. Hence, to the left of the vitrification curve the curing process is controlled by a very slow diffusion process. The TTT-diagram shows an arbitrary process temperature. The material being processed reaches the gel point at $t = t_{gel}$ and the vitrification line at $t = t_g$. At this point the material has reached a degree of cure of C_1 and glass transition temperature of the resin is equal to the processing temperature. The material continues to cure very slowly (diffusion controlled) until it reaches a degree of cure just below C_2. There are also various regions labeled in the diagram. The one labeled "viscous liquid" represents the resin from the beginning of processing until the gel point has been reached. The flow and deformation that occurs during processing or shaping must occur within this region. The region labeled "char" must be avoided during processing, because at high processing temperatures the polymer will eventually undergo thermal degradation.

The model that best represents the curing kinetics of thermosetting resins as reflected in a TTT-diagram is a diffusion reaction model modified by Kamal-Sourour [17, 18, 19]. To model autocatalytic cure kinetics, the model can be applied as

$$\frac{dC^*}{dt} = \left(k_1 + k_2 C^{*m}\right)\left(1 - C^*\right)^n \tag{8.11}$$

where m and n are reaction orders, and k_1 and k_2 are constants defined by

$$\frac{1}{k_i} = \frac{1}{k_1^c} + \frac{1}{k_D} \tag{8.12}$$

Here, k_i^c are Arrhenius overall rate constants defined by

$$k_1^c = a_1 e^{-E_1/RT} \tag{8.13}$$

and

$$k_2^c = a_2 e^{-E_2/RT} \tag{8.14}$$

where a_1 and a_2 are fitting parameters, E_1 and E_2, activation energies and R the ideal gas constant. The constant k_D in Eq. 8.12 is the diffusion rate constant defined as

$$k_D = a_D e^{-E_D/RT} e^{-b/f} \tag{8.15}$$

where a_D and b are adjustable parameters, E_D is the activation energy of the diffusion process, and f is the equilibrium fractional free volume given by

$$f = 0.00048\left(T - T_g\right) + 0.025 \tag{8.16}$$

where T_g is the instantaneous glass transition temperature during cure. Equation (8.12) shows that the overall rate constant is governed at one extreme by the Arrhenius rate constant (when $k_D \gg k_i^c$), which is the case prior to vitrification, and at the other extreme by the diffusion rate constant (when $k_D \ll k_i^c$, which is the case well after vitrification. For a system exhibiting a unique one-to-one relationship between the glass transition temperature and conversion, DiBenedetto's equation [20] is one of the easiest approaches for stoichiometric ratios to express this relationship using only a single parameter as

$$T_g = T_{g0} + \frac{\left(T_{g1} - T_{g0}\right)\lambda C^*}{1 - \left(1 - \lambda\right)C^*} \tag{8.17}$$

where T_{g0} is the glass transition temperature of the uncured resin, T_{g1} is the glass transition temperature of the fully reacted network, and λ is a structure dependent parameter theoretically equated to

$$\lambda = \frac{\Delta C_{p0}}{\Delta C_{p1}} \tag{8.18}$$

The values of ΔC_{p0} and ΔC_{p1} are the differences in the heat capacity between the glassy and rubbery state for the uncured resin and the fully cured network, respectively. However the parameter λ can also be used as a fitting parameter.

Mixing activated cure materials such as polyurethanes will instantly start releasing exothermic heat after the mixture of its two components has occurred. The proposed *Castro-Macosko curing model* accurately fits this behavior and is written as [15]

$$\frac{dC^*}{dt} = k_0 e^{-E/RT}\left(1 - C^*\right)^2 \tag{8.19}$$

8.2.3 Heat Transfer During Cure

A well-known problem in thick section components is that the thermal and curing gradients become more complicated and difficult to analyze because the temperature and curing behavior of the part are highly dependent on both the mold temperature and part geometry [21, 22]. A thicker part will result in higher temperatures and a more complex cure distribution during processing. This phenomenon becomes a major concern during the manufacture of thick components because high temperatures may lead to thermal degradation. It is important to develop a relatively easy way to determine temperatures developing during molding and curing or demolding times. For example, a one-dimensional form of the energy equation that includes the exothermic energy generated during curing can be solved:

$$\rho C_P \frac{\partial T}{\partial t} = k\frac{\partial^2 T}{\partial z^2} + \rho \dot{Q} \tag{8.20}$$

Assuming the material is confined between two mold halves at equal temperatures, the use of a symmetric boundary condition at the center of the part is valid:

$$\frac{\partial T}{\partial z} = 0 \quad \text{at} \quad z = 0 \tag{8.21}$$

and

$$T = T_m \tag{8.22}$$

at the mold wall.

With the use of the finite difference technique and a six constant model that represents dC^*/dt, Barone and Caulk [23] solved Eqs. 8.20 – 8.22 for the curing of sheet molding compound (SMC). The SMC was composed of an unsaturated polyester resin with 40.7 % calcium carbonate and 30 % glass fiber by weight. Figures 8.19 and 8.20 show typical temperature and degree of cure distributions, respectively, during the solidification of a 10 mm thick part as computed by Barone and Caulk. In Fig. 8.19, the temperature rise resulting from exothermic reaction is obvious. This temperature rise increases in thicker parts and with increasing mold temperatures. Figure 8.21 is a plot of the time to reach 80 % cure versus thickness of the part for various mold temperatures. The shaded area represents the conditions

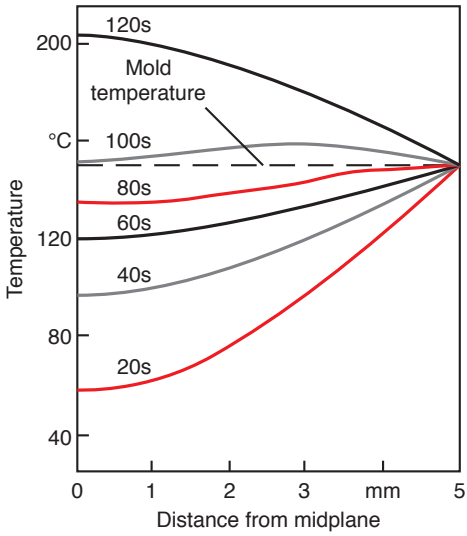

Figure 8.19 Temperature profile history of a 10 mm thick SMC plate

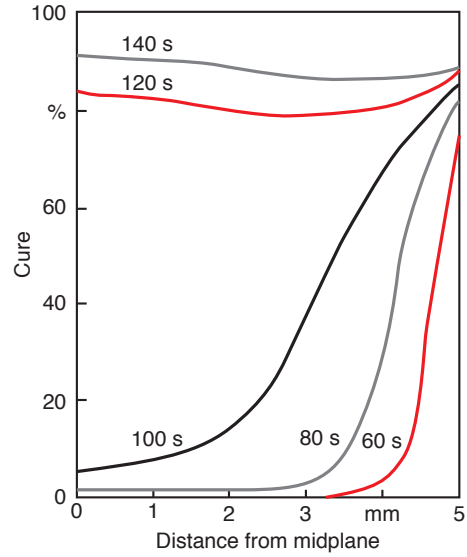

Figure 8.20 Curing profile history of a 10 mm thick SMC plate

at which the internal temperature within the part exceeds 200 °C because of the exothermic reaction. Temperatures above 200 °C may lead to material degradation and high residual stresses in the final part.

Improper processing conditions can result in a non-uniform curing distribution, which may lead to voids, cracks, or imperfections inside the part. It is of great importance to know the appropriate processing conditions, which will both avoid the over-heating problem and speed up the manufacturing process.

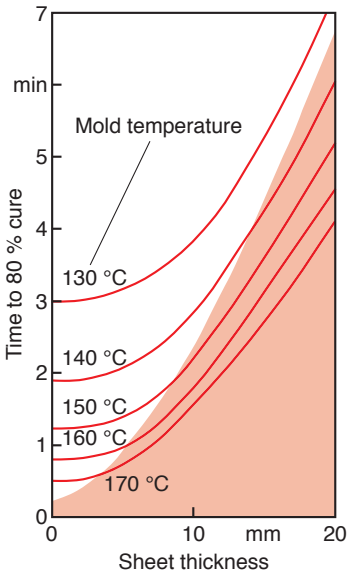

Figure 8.21 Cure times versus plate thickness for various mold temperatures. Shaded region represents the conditions at which thermal degradation may occur

8.3 Residual Stresses and Warpage of Polymeric Parts

Some major problems encountered when molding polymeric parts are the control and prediction of the component's shape at room temperature. For example, the resulting *sink marks* in the final product are caused by the shrinkage of the material during cooling[3] or curing. A common geometry that usually leads to a sink mark is a ribbed structure. The size of the sink mark, which is often only a cosmetic problem, is not only related to the material and processing conditions, but also to the geometry of the part. A rib that is thick in relation to the flange thickness will result in significant sinking on the flat side of the part.

Warpage in the final product is often caused by processing conditions that cause non-symmetric residual stress distributions through the thickness of the part. Thermoplastic parts most affected by residual stresses are those that are manufactured by injection molding. The formation of residual stresses in injection molded parts is attributed to two major coupled factors: cooling and flow stresses. The first and most important factor is the residual stress that is formed because of the rapid cooling or quenching of the part inside the mold cavity. As will be discussed and explained later in this chapter, this dominant factor is the reason why most ther-

3 In injection molding one can mitigate this problem by continuously pumping polymer melt into the mold cavity as the part cools until the gate freezes shut.

moplastic parts have residual stresses that are tensile in the central core of the part and compressive on the surface. Typical residual stress distributions are shown in Fig. 8.22 [24], which presents experimental[4] results for PMMA and PS plates cooled at different conditions.

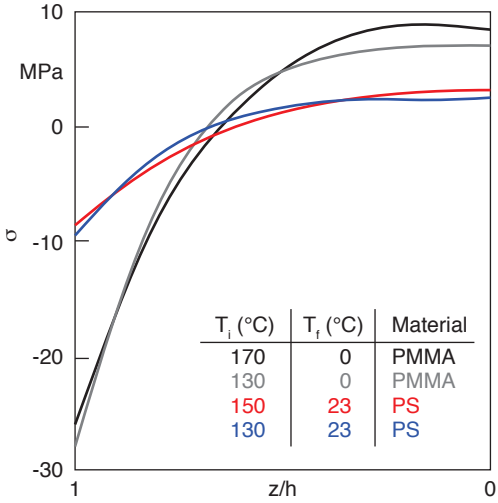

Figure 8.22 Residual stress distribution for 3 mm thick PMMA plates cooled from 170 °C and 130 °C to 0 °C, and for 2.6 mm thick PS plates cooled from 150 °C and 130 °C to 23 °C

Residual stresses in injection molded parts are also formed by the shear and normal stresses that exist during flow of the polymer melt inside the mold cavity during the filling and packing stage. These tensile flow induced stresses are often very small compared to the stresses that build up during cooling. However, at low injection temperatures, these stresses can be significant in size, possibly leading to parts with residual tensile stresses on the surface. Figure 8.23 [25] demonstrates this concept with PS plates molded at different injection temperatures. The figure presents residual stress distributions through the thickness of the plate perpendicular and parallel to the flow direction. Isayev [24, 25] has also demonstrated that flow stresses reach a maximum near the gate. The resulting tensile residual stresses are of particular concern because they may lead to *stress cracking* of the polymer component.

The development of models and simulations to predict shrinkage and warpage during the manufacturing of plastic parts is necessary to understand and control the complex thermomechanical behavior the material undergoes during processing. Shrinkage and warpage result from material inhomogeneities and anisotropy caused by mold filling, molecular or fiber orientation, curing or solidification behavior, poor thermal mold lay-out, and improper processing conditions. Shrink-

4 The experimental residual stress distributions where directly computed from curvature measurements obtained by the layer removal method.

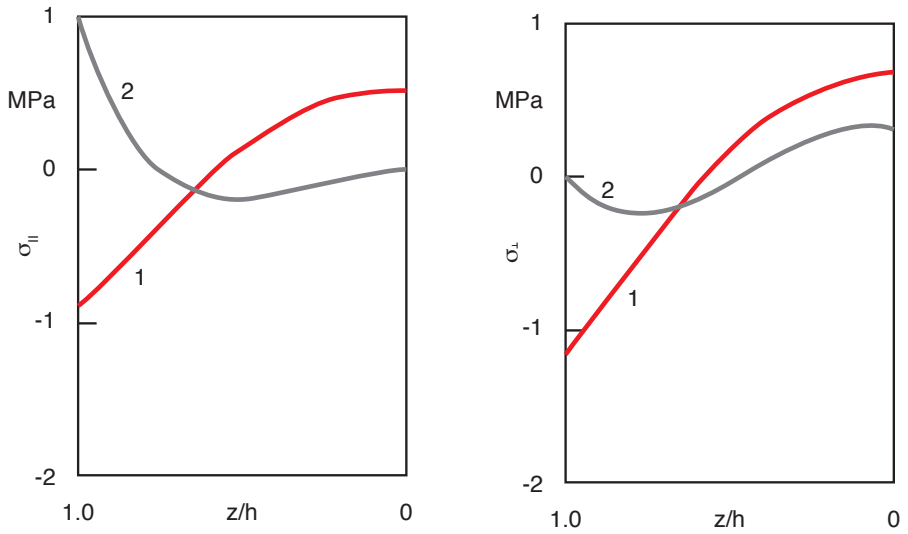

Figure 8.23 Residual stress distribution parallel and perpendicular to the flow direction for a 2.54 mm thick PS plate cooled from 244 °C (1) and 210 °C (2) to 60 °C

age and warpage are directly related to residual stresses. Transient thermal or solidification behavior as well as material anisotropies can lead to the build-up of residual stresses during manufacturing. Such process-induced residual stresses can significantly affect the mechanical performance of a component by inducing warpage or initiating cracks and delamination in composite parts. It is hoped that an accurate prediction of the molding process and of the generation of residual stresses will allow for the design of better molds with appropriate processing conditions.

This section presents basic concepts of the thermomechanical behavior during the manufacturing process of polymeric parts. The formation of residual stresses during the fabrication of plastic parts is introduced first, followed by a review of simple models used to compute residual stresses and associated warpage of plates and beams under different thermal loadings. Several models, which characterize the transient mechanical and thermomechanical behavior of thermoplastic polymers, will be reviewed and discussed next. Using these existing models, residual stresses, shrinkage, and warpage of injection molded thermoplastic parts can be predicted. Furthermore, results from the literature are presented. Because thermoset polymers behave quite differently from thermoplastic polymers during molding, other models need to be introduced to compute the thermomechanical behavior of thermoset polymers. Based on these models, results for predicting residual stresses and the resulting shrinkage and warpage for both thin and thick thermoset parts are also discussed.

8.3.1 Residual Stress Models

The formation of residual stresses is most critical during the solidification of polymer components inside injection molds. To illustrate residual stress build-up during injection molding, the plate shaped injection molding cavity shown in Fig. 8.9 is considered. As a first order approximation, it can be assumed that a hard polymer shell forms around the melt pool as the material is quenched by the cool mold surfaces. Neglecting the packing stage during the injection molding cycle, this rigid frame contains the polymer as it cools and shrinks during solidification. The shrinkage of the polymer is, in part, compensated by the deflection of the rigid surfaces, a deformation that occurs with little effort. In fact, if the packing stage is left out, it is a common experimental observation that between 85 to 90 % of the polymer's volumetric changes are compensated by shrinkage through the thickness of the part [26]. To understand which material properties, boundary conditions, and processing conditions affect the residual stresses in a solidified polymer component, the cooling process of an injection molded amorphous polymer plate inside the mold cavity will be considered. For simplicity, in the following analysis we include only the thermal stresses resulting from the solidification of an injection molded article as it is quenched from an initial temperature, T_i, to a final temperature, T_f (Fig. 8.9). However, it is important to point out again that, in injection molded parts, the solidification process starts during mold filling, and that flow continues during the post-filling or packing stage. This results in frozen-in flow stresses that are of the same order as the thermal stresses. Baaijens [27] calculated the residual stresses in injection molded parts, including the viscoelastic behavior of the polymer and the flow and thermal stresses. With his calculations he demonstrated that the flow induced stresses are significant and that a major portion of these stresses are created during the post-filling stage in the injection molding cycle. This is in agreement with experimental evidence from Isayev [24] and Wimberger-Friedl [28].

In Fig. 8.9 the plate thickness, $2L$, denotes the characteristic dimension across the z-direction and is considered to be much smaller than the plate's other dimensions. This is a common assumption for most polymer parts. It is assumed that the polymer behaves like a viscous liquid above T_g and like an elastic solid below T_g. The resulting residual stresses form because the cooling of the plate (from the outside to the inside) causes the outer layers to solidify first without any resistance from the hot liquid core. As the inner layers solidify and cool, their shrinkage is resisted by the solidified outer surface, thus, leading to a residual stress that is tensile in the center and compressive at the surface. Hence, the residual stress build-up must depend on material and process dependent temperatures, space, thermal properties, elastic properties, and on time. This can be expressed as

$$\sigma = \sigma\left\{T_i - T_f, T_g - T_f, L, z, \beta, k, h, \alpha, E, \nu, t\right\} \tag{8.23}$$

where β is the thermal expansion coefficient, k the thermal conductivity, α the thermal diffusivity, E the elastic modulus, v Poisson's ratio, and t time. Using the dimensional analysis and assuming that stress relaxation effects are negligible, the final residual stress can be written as

$$\frac{\sigma(1-\nu)}{E} = f\left(Bi, \hat{z}\varepsilon_T\right) \tag{8.24}$$

where $\hat{z}$ is a dimensionless coordinate defined by z/L and Bi is the Biot number defined by the ratio of convective heat removal to heat conduction that is calculated with

$$Bi = \frac{hL}{k} \tag{8.25}$$

A large Biot number signifies a process where the heat is removed from the surface of the part at a high rate. This is typical of fast quench processes, which result in both high temperature gradients and residual stresses. Predicted temperature distributions in a process with a large Biot number are shown in Fig. 8.24 a. On the other hand, a low Biot number describes a process where the heat is removed from the part's surface at a very low rate, resulting in parts with fairly constant temperatures. The predicted temperature fields for low Biot number processes, as shown in Fig. 8.24 b, will lead to low residual stresses in the final part.

The third quantity, ε_T, found in Eq. 8.24 is the thermal strain that will lead to residual stress. It is a quantity that measures the influence of processing conditions on residual stress formation and is defined by

$$\varepsilon_T = \beta\left(T_g - T_f\right) \tag{8.26}$$

The limits of the thermal strain are described by

$$\varepsilon_T = 0 \tag{8.27}$$

if $T_f = T_g$ and

$$\varepsilon_T = \text{Maximum} \tag{8.28}$$

if $T_i = T_g$

These limits can be explained. A polymer that is only allowed to cool to T_g, where $T_f = T_m$, does not have a chance to build up any residual stresses, because these can only exist below the glass transition temperature and not in the liquid state. On the other hand, a polymer that is initially at the glass transition temperature and cools to another temperature perceives all its strain in the solid state, hence, conceivably translating them completely into stresses.

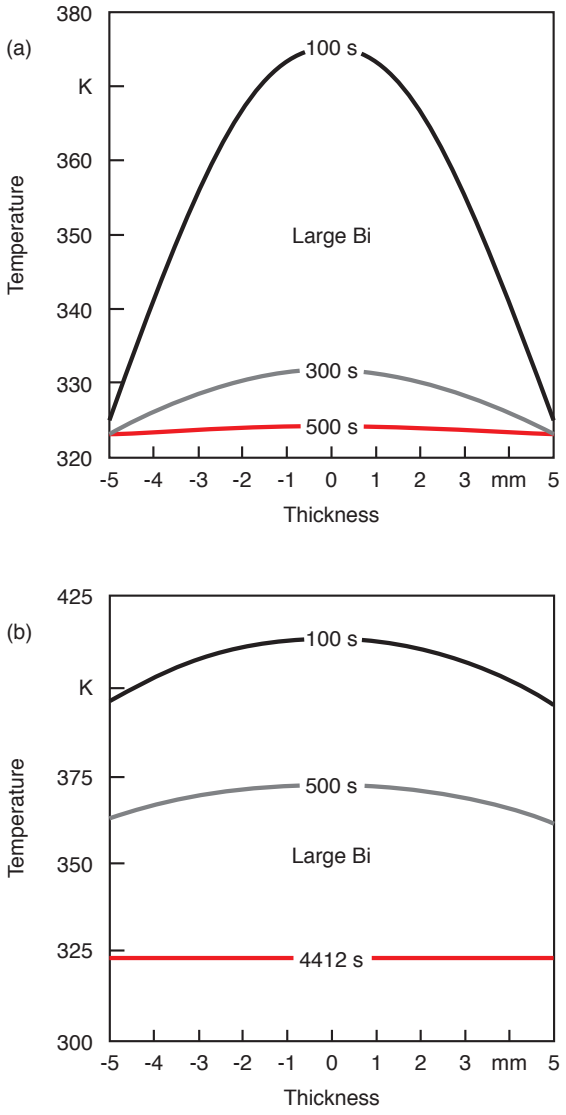

Figure 8.24 Effect of Biot number on the temperature distribution history in a cooling plate: (a) large Bi (b) small Bi

8.3.1.1 Residual Stress Model Without Phase Change Effects

Once the part has solidified, the parabolic temperature distribution will lead to a parabolic residual stress distribution that is compressive in the outer surfaces of the component and tensile in the inner core. Assuming no residual stress build-up during phase change, a simple function based on the parabolic temperature distribution can be used to approximate the residual stress distribution in thin sections [28]:

$$\sigma = -\frac{2}{3}\frac{E\beta}{1-\nu}\left(T_s - T_f\right)\left(\frac{6z^2}{4L^2} - \frac{1}{2}\right) \tag{8.29}$$

Here, T_s denotes the solidification temperature: the glass transition temperature for amorphous thermoplastics, or the melting temperature for semi-crystalline polymers. Equation 8.29 was derived by assuming static equilibrium (e.g., the integral of the stresses through the thickness must be zero). We do not present the full derivation here, because a more general approach is presented in the next section. Figure 8.25 [29] compares the compressive stresses measured on the surface of PMMA samples to Eq. 8.29.

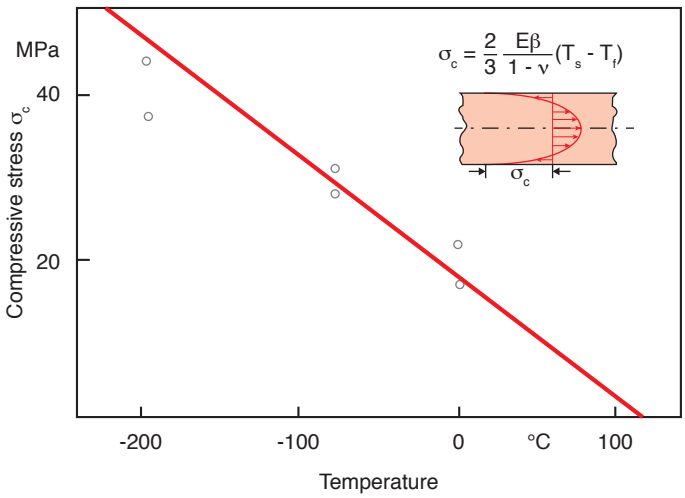

Figure 8.25 Comparison between computed, Eq. (8.29), and measured compressive stresses on the surface ($z = L$) of injection molded PMMA plates

8.3.1.2 Model to Predict Residual Stresses with Phase Change Effects

As the plate shown in Fig. 8.9 cools, it develops a solidified layer that continues to grow until the whole plate hardens. Figure 8.11 shows a cross-section of the plate at an arbitrary point in time. At any instance of time, t, the location that has just reached T_g is defined as $Z_g(t)$. To solve for the residual stress distribution, the energy equation, Eq. 8.3, must be solved while satisfying the force balance equation within the solidified material. At the centerline, the symmetry boundary condition can be used, Eq. 8.4, and a convective boundary condition on the outer surface of the plate is needed.

$$h\left(T_s - T_f\right) = -k\frac{\partial T}{\partial z} \quad \text{at} \quad z = L \tag{8.30}$$

The strain at any time and position is usually defined as the sum of its elastic, thermal, and viscous strain components:

$$\varepsilon(t) = \varepsilon_E + \varepsilon_{th} + \varepsilon_v \tag{8.31}$$

where ε_E is the elastic strain, ε_v the viscous strain, and ε_{th} the thermal strain, which occurs only after the material is below the glass transition temperature. The thermal strain can be written as

$$\varepsilon_{th} = \beta\left(T\left(z,t\right)-T_g\right) \tag{8.32}$$

The viscous strain is the strain the layer undergoes just before solidifying, caused by thermal contraction and viscous flow. The viscous strain occurs under a negligible stress and is not felt by the layer that has just solidified. Each layer has a different viscous strain equal to the overall strain of the plate, $\varepsilon\left(t\right)$, the instant that layer has solidified, which makes the viscous strain a function of space. Solving for the elastic strain results in

$$\sigma\left(z,t\right)=\frac{E}{1-v}\left(\varepsilon\left(t\right)-\beta\left(T\left(z,t\right)-T_g\right)-\varepsilon_v\left(z\right)\right) \tag{8.33}$$

To solve for the total strain of the plate, the stresses must approach equilibrium and add up to zero, as

$$\int_{-L}^{L}\sigma\left(z,t\right)dz=0 \tag{8.34}$$

Because the plate can be considered symmetric and the stresses are zero above the glass transition temperature, we can write

$$\int_{z_g(t)}^{L}\sigma\left(z,t\right)dz=0 \tag{8.35}$$

Substituting Eq. 8.33 into Eq. 8.35 gives

$$\int_{z_g(t)}^{L}\left(\varepsilon\left(t\right)-\beta\left(T\left(z,t\right)-T_g\right)-\varepsilon_v\left(z\right)\right)dz=0 \tag{8.36}$$

However, the plate's total strain is constant through the thickness and can be integrated out and solved for as

$$\varepsilon\left(t\right)=\frac{1}{L-z_g\left(t\right)}\int_{z_g(t)}^{L}\left(\beta\left(T\left(z,t\right)-T_g\right)+\varepsilon_v\left(z\right)\right)dz \tag{8.37}$$

The total strain $\varepsilon\left(t\right)$ and its viscous component ε_v are unknown but equal to each other and can be found by solving both Eq. 8.37 and the energy equation, Eq. 8.3, with a convective boundary condition. The energy equation can be solved numerically by using the finite difference method. The same grid points used for the energy equation can be used for the integration of Eq. 8.37. The solution is achieved in successive time steps from the beginning of cooling until the whole plate has reached the glass transition temperature, at which point the whole viscous strain distribution is known. Now, the part needs to be cooled until its final temperature of $T=T_f$ has been reached. The final residual stress distribution can be computed as

$$\sigma\left(z\right)=\frac{E}{1-v}\left(\varepsilon_{tot}-\beta\left(T_f-T_g\right)-\varepsilon_v\left(z\right)\right) \tag{8.38}$$

The total strain of the plate is unknown and can be found by solving the equilibrium equation, Eq. 8.34, using the final residual stress distribution as

$$\varepsilon_{tot} = \frac{1}{L}\int_0^L \left(\beta\left(T_f - T_g\right) - \varepsilon_v(z)\right)dz \tag{8.39}$$

Figures 8.26 and 8.27 show residual stress distributions for several Biot numbers and values of Θ_g, respectively. The value Θ_g is the dimensionless temperature that leads to a residual stress build-up and is defined by

$$\Theta_g = \frac{T_g - T_f}{T_i - T_f} \tag{8.40}$$

In Figure 8.25 the model described in this section is also compared to the residual stress distribution of Eq. 8.29. In this comparison, the influence of phase change effects becomes evident.

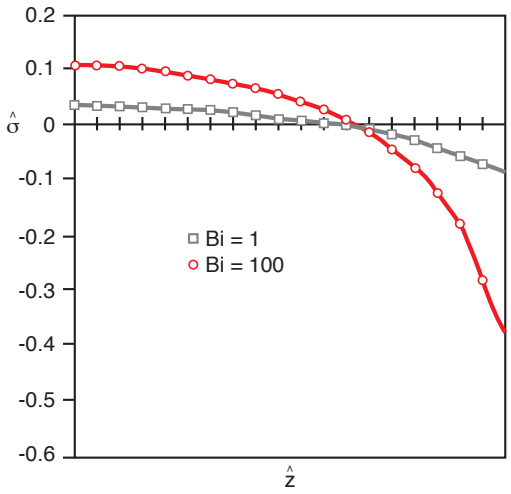

Figure 8.26 Residual stress distributions as a function of Biot number in a polystyrene plate after cooling

Equations 8.37–8.39 can be modified and solved together with the energy equation for thermosets, Eq. 8.20, to compute the residual distributions in thermosetting parts. Here, T_g must be replaced with the temperature of the material at the time it solidified (e.g., when its conversion was 80 %).

8.3.2 Other Simple Models to Predict Residual Stresses and Warpage

In practice, the complexity of part geometry and cooling channel design in the manufacture of plastic parts can result in non-symmetric mold wall temperature variations, which in turn lead to warpage of the part after it is ejected from the mold. We will present a simple model to evaluate residual stress and warpage of a flat plate caused by non-uniform mold temperatures (Fig. 8.26 a), temperature rise

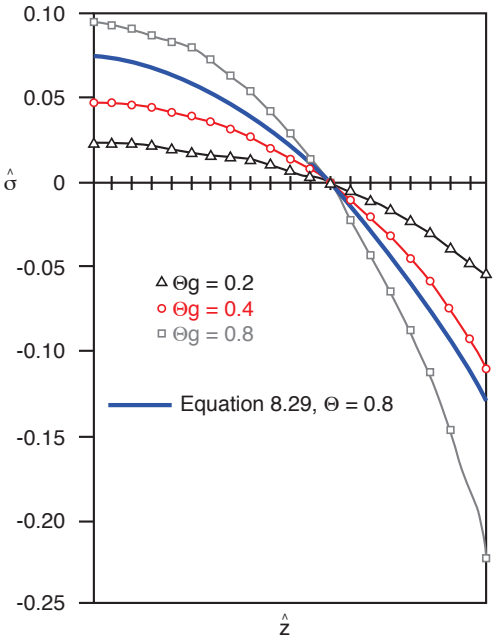

Figure 8.27 Residual stress distributions as a function of thermal boundary conditions in a polystyrene plate after cooling

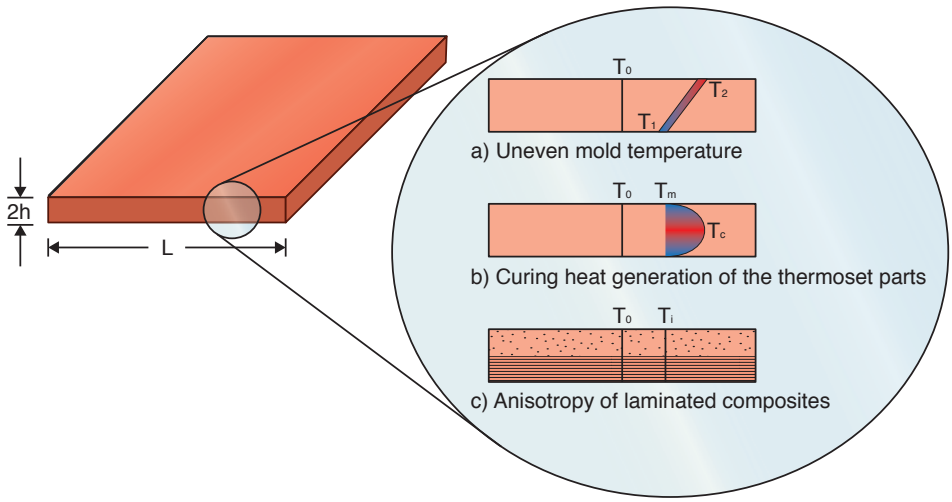

Figure 8.28 Possible causes of residual stress build-up across the thickness of a part

due to exothermic curing reaction in thermoset parts (Fig. 8.26 b), and by non-symmetric stress distributions in laminated composites (Fig. 8.26 c). In general, the stress distribution has to satisfy the equilibrium equation as defined in Eq. 8.33, where the stress-strain relation is defined as

$$\sigma(z) = \frac{E}{(1-\nu)}\left(\varepsilon_{tot} - \beta\Delta T(z) - \varepsilon_v(z)\right) \tag{8.41}$$

Here, ε_{tot} is the total or actual shrinkage of the plate, ΔT the change in temperature, E Young's modulus, v Poisson's ratio, and β the thermal expansion coefficient. For simplicity, the viscous strain is often neglected, assuming the part is thin enough that it solidifies at once. Based on classical shell theory and using the stress distribution, one can additionally compute a thermal moment as follows:

$$M = w\int_{-L}^{L} \sigma(z)\, z dz \tag{8.42}$$

where w is the width of the plate. In the following analyses Eqs. 8.39 – 8.42 will be used to compute residual stress and warpage for various cases. If the part is fixed as it is cooled to its final temperature, the total strain, ε_{tot}, is zero. In such a case, residual stress is dominated by thermal strain.

8.3.2.1 Uneven Mold Temperature

During molding, the mold wall surface temperatures may vary in the order of 10 °C due to improper thermal mold layout (Fig. 8.26 a). Furthermore, the temperatures on the mold surface may vary depending on where the heating or cooling lines are positioned. However, in the current example, we assume that this effect is negligible. The amount of warpage caused by temperature variations between the two mold halves can easily be computed using the equations of the last section. The temperature field across the thickness of a part can be described by

$$T = \left[\frac{1}{2}(T_1 + T_2) + \frac{1}{2}(T_1 - T_2)\frac{z}{L}\right] \tag{8.43}$$

After substituting Eqs. 8.34 and 8.43 into Eq. 8.41, the stress distribution throughout the thickness can be obtained:

$$\sigma = \frac{\beta E}{2(1-v)}\left[(T_2 - T_1)\frac{z}{L}\right] \tag{8.44}$$

Substituting Eq. 8.44 into Eq. 8.42, the thermal moment M becomes

$$M = \frac{w\beta E L^2}{3(1-v)}(T_2 - T_1) \tag{8.45}$$

For a part whose width, w, is much smaller than its length, ℓ, we can assume a cantilevered geometry as shown in Fig. 8.29. For this geometry the deflection, δ, that results from a moment, M, can be written as

$$\delta = \frac{M\ell^2}{2EI} \tag{8.46}$$

where the area moment of inertia, I, is written as

$$I = \frac{1}{12} w(2L)^3 \tag{8.47}$$

Substituting Eqs. 8.45 and 8.47 into Eq. 8.46 we get

$$\delta = \frac{\beta \ell^2}{4L}(T_2 - T_1) \tag{8.48}$$

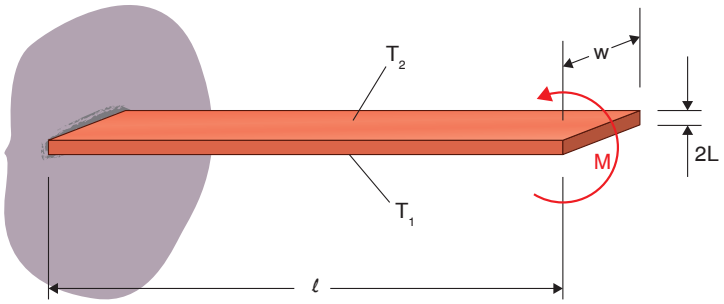

Figure 8.29 Simplified geometry of a thin slender part

8.3.2.2 Residual Stress in a Thin Thermoset Part

In addition to uneven mold temperatures, the exothermic curing reaction is a known problem when manufacturing thermoset parts. Heat release during such reactions can cause the transient temperature inside the part to be higher than the mold wall temperatures. Typical temperature and curing history plots are shown in Figs. 8.17 and 8.18. Note that such a temperature distribution dominates the final residual stress distribution. Here, a simple elastic model is presented to approximate the residual stress distribution. The temperature field in the calculation can be described by a parabolic curve

$$T(z) = T_c + (T_m - T_c)\frac{z^2}{L^2} \tag{8.49}$$

where T_c and T_m are the temperature at the center of the plate and the mold surface, respectively.

We assume the part to be cooled elastically to room temperature, T_0. Using Eq. 8.41, the stress distribution can be expressed by

$$\sigma(z) = \frac{E}{(1-\nu)}\left[\varepsilon_{tot} - \beta\left(T_0 - (z)\right)\right] \tag{8.50}$$

Because the above equation has to satisfy the equilibrium equation, Eq. 8.34, the total strain can be obtained by integrating the stress field across the thickness

$$\varepsilon_{tot} = \frac{\beta}{L}\left[T_0 - \frac{2}{3}T_c - \frac{1}{3}T_m\right] \tag{8.51}$$

Substituting Eq. 8.51 into Eq. 8.39, the residual stress distribution becomes

$$\sigma(z) = \frac{\beta E}{(1-\nu)}\left[\frac{1}{3}(T_c - T_m) - (T_c - T_m)\frac{z^2}{L^2}\right] \tag{8.52}$$

After defining the non-dimensional parameters, $\hat{\sigma}$ and $\hat{z}$, as

$$\hat{\sigma} \equiv \frac{(1-\nu)\sigma}{E\beta(T_c - T_m)} \tag{8.53}$$

and

$$\hat{z} \equiv \frac{z}{L} \tag{8.54}$$

Eq. 8.52 can be normalized as

$$\hat{\sigma}(\hat{z}) = \frac{1}{3} - \hat{z}^2 \tag{8.55}$$

The non-dimensional residual stress distribution across the thickness of the part is depicted in Fig. 8.30. The stresses in the outer layer are compressive while tensile stresses are found in the inner layers. A maximum compressive non-dimensional stress of ⅔ is located on the surface and a maximum tensile stress of ⅓ occurs at the center of the part.

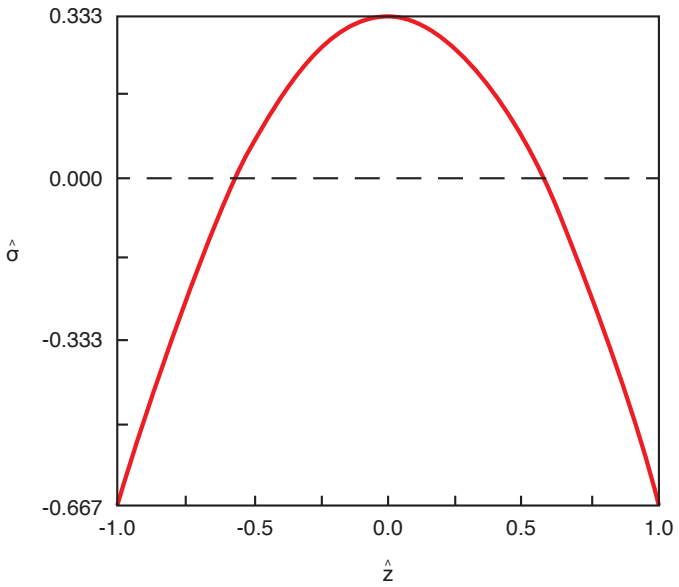

Figure 8.30 Normalized residual stress distribution in a thin thermoset part

8.3.2.3 Anisotropy Induced Curvature Change

In the manufacturing of large and thin laminate structures or fiber reinforced composite parts with a large fiber-length/part-thickness ratio, the final part exhibits a higher thermal expansion coefficient in the thickness direction than in the surface direction. If the part is curved, it will undergo an angular distortion, as shown in Fig. 8.31, which is a consequence of the anisotropy of the composites. This phenomenon is usually called the *spring-forward* effect or *anisotropy induced curvature change* [32]. Through-thickness thermal strains, which are caused by different thermal expansion coefficients, can lead to an angle distortion of a cylindrical shell experiencing a temperature change. As demonstrated in Fig. 8.31, when a curved part undergoes a temperature change of ΔT, the curved angle, θ, will change by

$\Delta\theta$. The resulting $\Delta\theta$, therefore, is dependent on the angle θ the temperature change ΔT, and the difference of the thermal expansion coefficients in the r and θ directions [33]

$$\Delta\theta = (\beta_r - \beta_\theta)\theta\Delta T = \Delta\beta\theta\,\Delta T \tag{8.56}$$

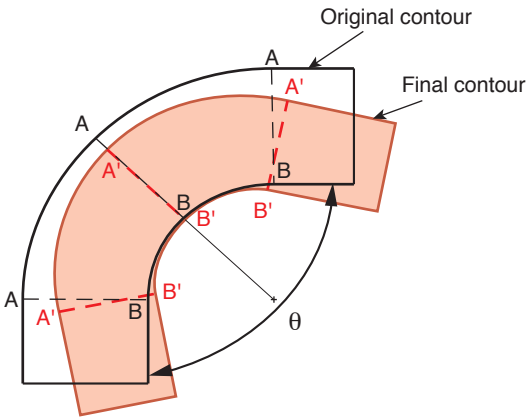

Figure 8.31 Schematic diagram of the spring-forward effect

In plate analysis, the inclusion of anisotropies that lead to curvature changes is very involved. Hence, it is easier to introduce the curvature change by an equivalent thermal moment [34]:

$$M = \frac{E}{(1-\nu)}\frac{\Delta\beta\,\Delta T}{R}\frac{L^3}{12} \tag{8.57}$$

where R represents the local radius of curvature.

8.3.3 Predicting Warpage in Actual Parts

Shrinkage and warpage are directly related to residual stresses that result from locally varying strain fields occurring during the curing or solidification stage of a manufacturing process. Such strain gradients are caused by non-uniform thermomechanical properties and temperature variations inside the mold cavity. Shrinkage due to cure can also play a dominant role in the residual stress development in thermosetting polymers and becomes important for fiber reinforced thermosets when sink marks appearing in thick sections or ribbed parts are a concern.

When processing thermoplastic materials, shrinkage and warpage in a final product depend on the molecular orientation and residual stresses that form during processing. The molecular or fiber orientation and the residual stresses inside the part in turn depend on the flow and heat transfer during the mold filling, packing, and cooling stage of the injection molding process. Kabanemi et al. [35] used a

three-dimensional finite element approach to solve the thermal history and residual stress build-up in injection molded parts. To predict the residual stress in the finished part, they characterized the thermomechanical response of the polymer from melt to room temperature, or used the p-v-T behavior to stress-strain behavior. Bushko and Stokes [36, 37] used a thermorheologically simple thermoviscoelastic material model to predict residual stresses and warpage in flat plates. With their model, they found that packing pressure had a significant effect on the shrinkage of the final part but little effect on the residual stress build-up. Wang and co-workers have developed unified simulation programs to model the filling and post-filling stages in injection molding [38–41]. In their models they perform a simultaneous analysis of heat transfer, compressible fluid flow, fiber orientation, and residual stress build-up in the material during flow and cooling using a finite element/control volume approach for flow, finite difference techniques for heat transfer, and finite element methods for fiber orientation and thermomechanical analysis.

The shrinkage and warpage in thin compression molded fiber reinforced thermoset plates were predicted by various researchers [42] using fully three-dimensional finite element models and simplified finite element plate models. More recently [4, 44], the through-thickness properties, temperature, and curing variations that lead to warpage have been represented with equivalent moments. By eliminating the thickness dimensions from their analysis, they significantly reduced computation costs and maintained agreement with experimental results. At the same time, they were able to use the same finite element meshes used in common commercial codes to predict mold filling and fiber orientation in the final part.

The governing equations used for the stress analysis of polymer components are derived using the principle of virtual work. Here, the stresses are represented as a function of local strain and residual stress $\{\sigma_0\}$.

$$\{\sigma\} = [E]\{\varepsilon\} - [E]\{\varepsilon_{tot}\} + \{\sigma_0\} \tag{8.58}$$

In Eq. 8.58 the modulus matrix [E] is anisotropic and temperature or degree of cure dependent and $\{\varepsilon_{tot}\}$ is the total internal strain that occurs due to curing, cooling, or heating during a time step. Two kinds of internal strains should be included when simulating the thermomechanical behavior of polymer parts. One is a thermal strain caused by temperature change and the other is a curing strain resulting from crosslinking polymerization of thermoset resins. Thus, the total internal strain can be expressed by

$$\{\varepsilon_{tot}\} = \{\varepsilon_0^{th}\} + \{\varepsilon_0^{c}\} \tag{8.59}$$

Here, the superscript *th* denotes the thermal strain and *c* the curing strain. The thermal strains can be represented in terms of temperature change and thermal expansion coefficients

$$\left\{\varepsilon_0^{th}\right\}T = \Delta T\left\{\alpha_{xx}\alpha_{yy}\alpha_{zz}000\right\} \tag{8.60}$$

The anisotropic thermal expansion coefficient, caused by fiber orientation, is perhaps the largest cause of warpage in fiber reinforced parts. Figure 8.32 demonstrates how, for typical thermoset composite parts, the thermal shrinkage parallel to the main orientation direction is about half of the shrinkage normal to the main orientation direction[5].

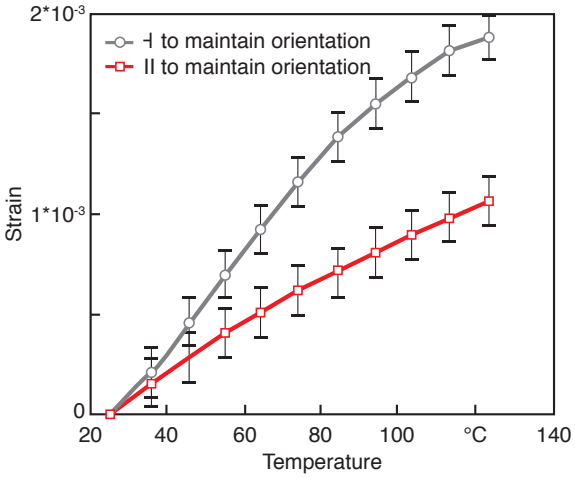

Figure 8.32 Experimentally measured thermal strains in an SMC plate with a fiber orientation distribution that resulted from a 25% initial mold coverage charge

To calculate the residual stress development during the manufacturing process, the heat transfer equation is coupled to the stress-strain analysis through constitutive equations. Figure 8.33 compares the mold geometry with part geometry for

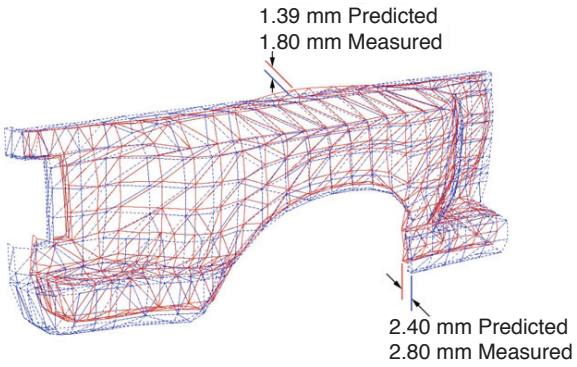

Figure 8.33 Simulated displacements of an automotive body panel. Displacements were magnified by a factor of 20

5 The thermal shrinkage was measured from a rectangular plate molded with a charge that covered 25% of the mold surface and that was allowed to flow only in one direction.

the truck fender shown in Fig. 7.32, after mold removal and cooling, computed using the above model. The fiber content by volume in the part was 21 % ($\phi = 0.21$) and the material properties for the glass fiber and the unsaturated polyester resin are listed in Table 8.4.

Table 8.4 Mechanical and Thermomechanical Properties for Various Materials

	Fiberglass	Polyester	Epoxy
E (MPa)	7.3×10^4	2.75×10^3	4.1×10^3
v	0.25	0.34	0.37
β (mm/mm/K)	5.0×10^{-6}	3.7×10^{-5}	5.76×10^{-5}

Minimizing warpage is one of the biggest concerns for the design engineer. One way to reduce warpage is by introducing a temperature gradient between the upper and lower mold halves. Again, this through-thickness temperature gradient will introduce a thermal moment, which increases or decreases the warpage. Also, by changing the formulation of the polyester resin, the coefficient of thermal expansion of the matrix can be reduced, making it similar to the coefficient of the glass fiber. Theoretically, reduction of the coefficients for the matrix would decrease the in-plane differential shrinkage, which in turn could help reduce the final warpage. Furthermore, the fiber content also has a great effect on the deformation of a body panel. Here, although the warpage is actually caused by the existence of fibers inside the resin, the increase of fiber content adds to the stiffness of the part, which in turn reduces warpage. Further reduction in warpage can also be achieved by changing the size and location of the initial charge, a trial-and-error solution, which is still the most feasible with today's technology.

Examples

1. Three small samples of an epoxy resin were subjected to a temperature rise from 50 °C to 300 °C in a differential scanning calorimeter using three different heating rates: 2.78 K/min, 5.66 K/min and 11.11 K/min. Table 8.5 presents the exothermal heat released during the tests. Determine the total heat of reaction using the data measured with the 2.78 K/min heating rate. Plot the degree of cure as a function of time.
   In order to compute the degree of cure as a function of time we use Eq. 8.8

$$C_i^* = \frac{Q_i}{Q_T}$$

   where

$$Q_i = \int_0^{\tau_i} \dot{Q}\, dt = \sum_{j=1}^{i} \dot{Q}_j \Delta t$$

and

$$Q_T = \int_0^{\infty} \dot{Q} dt = \sum_{j=1}^{n} \dot{Q}_j \Delta t$$

where n is the total number of data points and Δt is the time step. Because the data are given in terms of temperature, we must transform the temperature step to time using the heating rate 2.78 K/min using

$$\Delta t = \frac{10\,\text{K}}{2.78\ \text{K/min}}$$

The above leads to a total heat of reaction, Q_T, of 785.4 J/g or 785.4 kJ/kg. The degree of cure as a function of temperature is plotted in Fig. 8.34.

Table 8.5 DSC Data for an Epoxy Resin

T (°C)	Q $\left(\frac{\text{J}}{\text{g} \cdot \text{min}}\right)$		
	2.78 K/min	5.66 K/min	11.11 K/min
50	0.	0.	0.
60	0.	0.	0.
70	0.01	0.	0.01
80	0.02	0.01	0.02
90	0.03	0.01	0.03
100	0.06	0.04	0.06
110	0.12	0.09	0.12
120	0.22	0.16	0.21
130	0.38	0.28	0.37
140	0.65	0.49	0.62
150	1.11	0.82	1.03
160	1.91	1.35	1.66
170	3.38	2.23	2.668
180	6.23	3.69	4.24
190	12.21	6.23	6.76
200	24.97	10.86	10.94
210	47.10	19.76	18.08
220	60.09	37.23	30.79
230	39.40	68.36	53.89
240	15.0	103.36	94.37
250	4.29	100.09	152.83
260	0.98	55.65	196.48
270	0.17	19.99	168.68
280	0.018	5.17	90.54
290	0.	0.92	31.62
300	0.	0.09	7.06

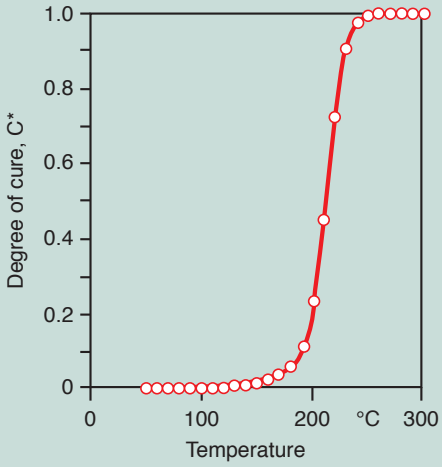

Figure 8.34 Degree of cure as function of temperature for a heating rate of 2.78 K/min

Problems

1. Determine the constants for the curing model presented in Eq. 8.11 for the vinyl ester presented in Fig. 8.16.
2. Write a finite difference program to solve for the transient temperature distribution in a cooling amorphous polymer plate. Test the program with the data given for polystyrene in Table 8.2 for a 2 mm thick plate.
3. Using the momentum balance presented in Eq. 8.34, derive the residual stress distribution, Eq. 8.29, in a cooling polymer plate neglecting the effects of phase change.
4. A 1 mm thick polystyrene ruler is injection molded. For a resin with a glass transition temperature around 100 °C and a final ambient temperature of 20 °C, estimate the residual stress at the surface of the part shortly after demolding. Assume a Young's modulus of 3200 MPa and a thermal expansion coefficient of 7×10^{-5} mm/mm/°C. Neglect phase change effects.
5. For a standard 30 cm long, 3 cm wide, and 1 mm thick ruler, how much warpage would occur with a 5 °C temperature difference between the mold halves? Assume a Young's modulus of 3200 MPa and a thermal expansion coefficient of 7×10^{-5} mm/mm/°C.
6. Write a finite difference program to solve for the transient temperature distribution in a cooling amorphous polymer plate. Solve Eqs. 8.31 – 8.39 along with the predicted temperatures to estimate the residual stress in the final plate. Compare the residual stress distribution for a 2 and a 5 mm thick polystyrene plate.
7. A long and thin composite plate made from unsaturated polyester and unidirectional glass fiber (1000 × 20 × 2 mm) is molded in a thermally

unbalanced mold. One mold side is at 140 °C and the other at 150 °C. Assuming the temperature distribution is at steady state the instant the part solidifies, what is the residual stress distribution in the plate before it is allowed to warp. $E_{composite} = 20$ GPa. Towards which direction would the plate warp, the hot side or cooler side?

8. Figure 8.35 presents a schematic of the cross-section of an SMC pick-up truck box. In the finished product, the average through the thickness thermal expansion coefficient, β_3, is 2×10^{-5} mm/mm/K, and the average planar thermal expansion coefficient, β_1 or β_2 is 8×10^{-6} mm/mm/K. Estimate the amount and direction that the side walls will warp, if any.

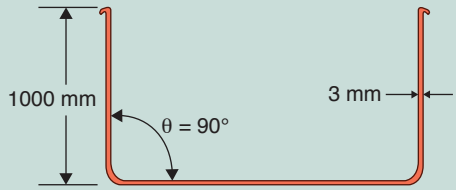

Figure 8.35 Schematic of an SMC pick-up truck cross-section

9. Using the data given in Example 8.1, plot the degree of cure for heating rates of 5.66 K/min and 11.11 K/min. What are the characteristic curing times for all three heating rates?
10. A number of metals used for mold construction are listed below. Determine which material provides the lowest residual stresses possible. Explain.

Material	Thermal conductivity (W/mK)
Stainless steel	70
Low carbon steel	54
Iron	80
Copper	401
Silver	420

11. A thin part is to be manufactured by injection molding using a thermoset polymer and the following properties and conditions:

    $E = 4.1 \times 10^3$ Pa

    $\beta = 5.76 \times 10^{-5}$ mm/mm/K

    $T_m = 23$ °C

    $T_C = 200$ °C

    $Z = 2$ mm

    Graph residual stress distribution, using Equations 8.52 – 55 to prove that it is in agreement with Figure 8.30.
12. Explain the influence of the cooling rate on the solidification process. Does it influence the glass transition temperature?

References

[1] Van Krevelen, D. W., *Properties of Polymers*, 4th ed., Elsevier, Amsterdam, (2009).

[2] Ehrenstein, G. W., *Polymeric Materials: Structure, Properties and Applications*, Hanser Publishers, Munich, (2001).

[3] Menges, G., and Winkel, E., *Kunststoffe, 72*, 2, 91, (1982).

[4] Tadmor, Z., and Gogos, C. G., *Principles of Polymer Processing*, 2nd ed., John Wiley & Sons, New York, (2006).

[5] Avrami, M., *J. Chem. Phys., 7*, 1103, (1939).

[6] Sharples, A., Polymer Science, *A Materials Science Handbook*, Chapter 4, A. D. Jenkins, Ed., North Holland Publishing Company, Amsterdam, (1972).

[7] Eder, G., and Janeschitz-Kriegl, H., *Material Science and Technology, Vol. 18.*, Ed. H. E. H. Meijer, Verlag Chemie, Weinheim, (1995).

[8] Brandrup, J., and Immergut, E. H., *Polymer Handbook*, John Wiley & Sons, New York, (1975).

[9] Krobath, G., Liedauer, S., and Janeschitz-Kriegl, H., *Polymer Bulletin, 14*, 1, (1985).

[10] Stefan, J., *Ann. Phys. and Chem., N.F., 42*, 269, (1891).

[11] Eder, G., and Janeschitz-Kriegl, H., *Polymer Bulletin, 11*, 93, (1984).

[12] Janeschitz-Kriegl, H., and Krobath, G., *Intern. Polym. Process., 3*, 175, (1988).

[13] Randell, D. R., *Radiation Curing Polymers*, Burlington House, London, (1987).

[14] Palmese, G. R., Andersen, O., and Karbhari, V. M., *Advanced Composites X: Proceedings of the 10th Annual ASM/ESD Advance Composites Conference*, Dearborn, MI, ASM International, Material Park, (1994).

[15] Macosco, C. W., *RIM Fundamentals of Reaction Injection Molding*, Hanser Publishers, Munich, (1989).

[16] Enns, J. B. and Gillham, J. K., "Time-Temperature-Transformation (TTT) Cure Diagram: Modeling the Cure Behavior of Thermosets", *J. Appl. Polym. Sci., 28*, 2567 (1983).

[17] Kamal, M. R., "Thermoset Characterization for Moldability Analysis", *Polym. Eng. Sci., 14* (3), 231 (1974).

[18] Rabinowitch, E., *Trans. Faraday Soc., 33*, 1225 (1937).

[19] Havlicek, I. and Dusek, K., in *Crosslinked Epoxies*, 417, B. Sedlacek and J. Kahovec, Eds., Walter de Gruyter, New York (1987).

[20] DiBenedetto, A. T., *J. Polym. Sci. Polym. Phys., ed., 25*, 1949 (1987).

[21] Bogetti, T. A. and Gillespie, J. W., *45th SPI Conf. Proc.,* (1990).

[22] Bogetti, T. A. and Gillespie, J. W., *21st Int. SAMPE Tech. Conf.,* (1989).

[23] Barone, M. R. and Caulk, D. A., *Int. J. Heat Mass Transfer, 22* , 1021, (1979).

[24] Isayev, A. I., and Crouthamel, D. L., *Polym. Plast. Technol., 22*, 177, (1984).

[25] Isayev, A.I., *Polym. Eng. Sci., 23*, 271, (1983).

[26] Wübken, G., Ph.D. Thesis, IKV, RWTH-Aachen, Germany, (1974).

[27] Baaijens, F.P.T., *Rheol. Acta, 30*, 284, (1991).

[28] Wimberger-Friedl, R., *Polym. Eng. Sci., 30* , 813, (1990).

[29] Ehrenstein, G.W., *Mit Kunststoffen konstruieren*, Hanser Publishers, Munich, (2007).

[30] Timoshenko, S. P. and Krieger, S. W., *Mechanics of Composite Materials*, McGraw-Hill, New York, (1959).

[31] Faupel, J.H. and Fisher, F.E., *Engineering Design*, McGraw-Hill, New York, (1981).

[32] Lee, C.-C., GenCorp Research, Akron OH, Personal communication (1994).

[33] O'Neill, J.M., Rogers, T.G., and Spencer, A.J.M., *Math. Eng. Ind., 2,* 65, (1988).

[34] Tseng, S.C., and Osswald, T.A., *Polymer Composites*, *15*, 270, (1994).

[35] Kabanemi, K.K., and Crochet, M.J., *Intern. Polym. Proc, 7*, 60, (1992).

[36] Bushko, W.C., and Stokes, V.K., *Polym. Eng. Sci., 35,* 351, (1995).

[37] Bushko, W.C., and Stokes, V.K., *Polym. Eng. Sci., 35,* 365, (1995).

[38] Chiang, H.H., Hieber, C.A., and Wang, K.K., *Polym. Eng. Sci., 31*, 116, (1991).

[39] Chiang, H.H., Hieber, C.A., and Wang, K.K., *Polym. Eng. Sci., 31*, 125, (1991).

[40] Chiang, H.H., Himasekhar, K., Santhanam, N., and Wang, K.K., *J. Eng. Mater.Tech., 115*, 37, (1993).

[41] Chiang, H.H., Santhanam, N., Himasekhar, K., and Wang, K.K., *Advances in Computer Aided Engineering (CAE) of Polymer Processing, MD-Vol. 49,* ASME, New York, (1994).

[42] Osswald, T.A., *J. Thermoplast. Comp. Mater., 4*, 173, (1991).

[43] Tseng, S.C., Ph.D. Thesis, Dept. of Mech. Eng., University of Wisconsin-Madison, (1993).

[44] Tseng, S.C., and Osswald, T.A., *Polymer Composites, 15*, 270, (1994).

PART 3

Engineering Design Properties

9 Mechanical Behavior of Polymers

Polymeric materials are implemented into various designs because of their low cost, processability, and desirable material properties. Of interest to the design engineer are the short and long-term responses of a loaded component. Properties for short-term responses are usually acquired through short-term tensile tests and impact tests, whereas long-term responses depend on properties measured using techniques such as the creep and the dynamic test.

9.1 Basic Concepts of Stress and Strain

Strictly speaking, polymers cannot be modeled using linear theory of elasticity. However, the stress-strain response of a linear elastic model for the polymer component can suffice in the evaluation of a design and the prediction of the behavior of the component during loading.

For a full three-dimensional model, as shown for a small material element in Fig. 9.1, there are six components of stress and strain. The stress-strain relation for a linear elastic material is defined by the following equations:

$$\sigma_{xx} = EI_{\varepsilon} + 2G\varepsilon_{xx} \tag{9.1}$$

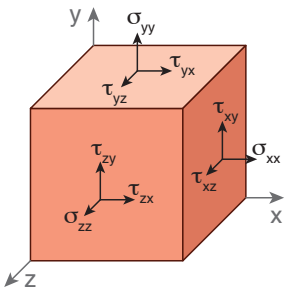

Figure 9.1 Differential material element with coordinate and stress definition

$$\sigma_{yy} = EI_{\varepsilon} + 2G\varepsilon_{yy} \tag{9.2}$$

$$\sigma_{zz} = EI_{\varepsilon} + 2G\varepsilon_{zz} \tag{9.3}$$

$$\tau_{xy} = G\gamma_{xy} \tag{9.4}$$

$$\tau_{yz} = G\gamma_{yz} \tag{9.5}$$

$$\tau_{zx} = G\gamma_{zx} \tag{9.6}$$

where

$$E = \frac{vE}{(1+v)(1-2v)} \tag{9.7}$$

and I_{ε} is the first invariant of the strain tensor and represents the volumetric expansion of the material which is defined by

$$I_{\varepsilon} = \varepsilon_{xx} + \varepsilon_{yy} + \varepsilon_{zz} \tag{9.8}$$

The elastic constants E, v and G represent the modulus of elasticity, Poisson's ratio and shear modulus, respectively. The shear modulus, or modulus of rigidity, can be written in terms of E and v as

$$G = \frac{E}{2(1+v)} \tag{9.9}$$

The above equations can be simplified for different geometries and load cases. Two of the most important simplified models, the plane stress and plane strain models, are discussed in the following.

9.1.1 Plane Stress

A common model describing the geometry and loading of many components is the plane stress model. The model reduces the problem to two dimensions by assuming that the geometry of the part can be described on the x-y plane with a relatively small thickness in the z-direction. In such a case, $\sigma_{zz} = \tau_{zx} = \tau_{yz} = 0$ and Eqs. 9.1 – 9.6 reduce to

$$\sigma_{xx} = \frac{E}{1-v^2}\left(\varepsilon_{xx} + v\varepsilon_{yy}\right) \tag{9.10}$$

$$\sigma_{yy} = \frac{E}{1-v^2}\left(v\varepsilon_{xx} + \varepsilon_{yy}\right) \text{ and} \tag{9.11}$$

$$\tau_{xy} = G\gamma_{xy} \tag{9.12}$$

9.1.2 Plane Strain

Another common model used to describe components is the plane strain model. Similar to the plane stress model, the geometry can be described on an x-y plane with an infinite thickness in the z-direction. This problem is also two-dimensional, with negligible strain in the z-direction but with a resultant σ_{zz}. For this case, Eqs. 9.1–9.8 reduce to

$$\sigma_{xx} = \frac{E(1-v)}{(1+v)(1-2v)}\left(\varepsilon_{xx} + \frac{v}{1-v}\,\varepsilon_{yy}\right) \tag{9.13}$$

$$\sigma_{yy} = \frac{E(1-v)}{(1+v)(1-2v)}\left(\frac{v}{1-v}\,\varepsilon_{xx} + \varepsilon_{yy}\right) \tag{9.14}$$

$$\tau_{xy} = G\gamma_{xy} \tag{9.15}$$

■ 9.2 Viscoelastic Behavior of Polymers

It has already been said that a polymer, at a specific temperature and molecular weight, may behave like a liquid or like a solid, depending on the speed (time scale) at which its molecules are deformed. This behavior, which ranges between liquid and solid, is generally referred to as the viscoelastic behavior or material response. In this chapter we will limit the discussion to *linear viscoelasticity*, which is valid for polymer systems that are undergoing *small deformations*. *Non-linear viscoelasticity*, required when modeling *large deformations* such as those encountered in flowing polymer melts, is covered in detail in Chapter 5.

In linear viscoelasticity, the *stress relaxation test* is often used, along with the *time-temperature superposition principle* and the *Boltzmann superposition principle*, to explain the behavior of polymeric materials during deformation. Figure 9.2 presents

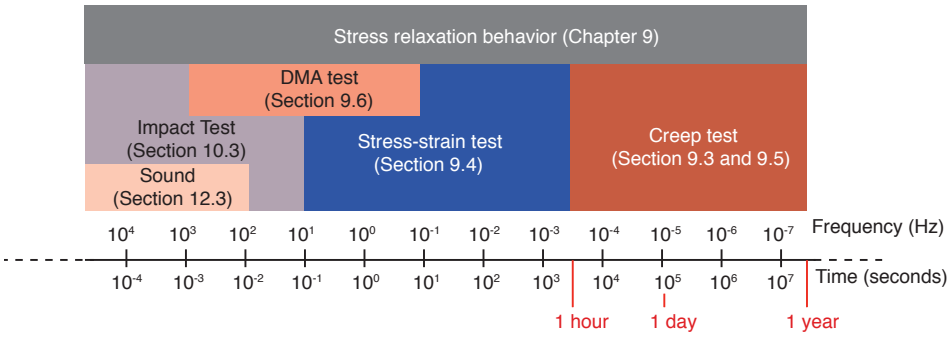

Figure 9.2 Mechanical behavior of polymers with time scale as a reference

a general overview of mechanical behavior and mechanical testing of polymers with time scale, or frequency for cyclic loading, as a reference. The figure also presents the various sections in this book where the different behaviors or responses are covered.

9.2.1 Stress Relaxation Test

In a stress relaxation test, a polymer test specimen is deformed by fixed amount, ε_0, and the stress required to hold that amount of deformation is recorded over time. This test is very cumbersome to perform, so the design engineer and the material scientist have tended to ignore it. In fact, the standard relaxation test ASTM D2991 was dropped from the standards in 1990. Rheologists and scientists, however, have been consistently using the stress relaxation test to interpret the viscoelastic behavior of polymers.

Figure 9.3 [1] presents the stress relaxation modulus measured for polyisobutylene[1] at various temperatures. Here, the stress relaxation modulus is defined by

$$E_r(t) = \frac{\sigma(t)}{\varepsilon_0} \tag{9.16}$$

where ε_0 is the applied strain and $\sigma(t)$ is the stress being measured. From the test results it is clear that stress relaxation is time and temperature dependent, especially near the glass transition temperature where the slope of the curve is maximal. In the case of the polyisobutylene shown in Fig. 9.3, the glass transition temperature is about −70 °C. The measurements were completed in an experimental time window between a few seconds and one day. The tests performed at lower temperatures were used to record the initial relaxation while the tests performed at higher temperatures only captured the end of relaxation of the rapidly decaying stresses.

It is well known that high temperatures lead to small molecular relaxation times[2] and low temperatures lead to materials with large relaxation times. This is due to the fact that at low temperatures the free volume between the molecules is reduced, restricting or slowing down their movement. At high temperatures, the free volume is larger and the molecules can move with more ease. Hence, when changing temperature, the shape of creep[3] or relaxation test results remain the same except that they are horizontally shifted to the left or right, which represent lower or higher response times, respectively.

1 Better known as chewing gum.

2 By relaxation time we usually refer to the time it takes for applied stresses to relax within a material.

3 In a creep test the polymer specimen is loaded to a constant stress, and the strain response is recorded over time.

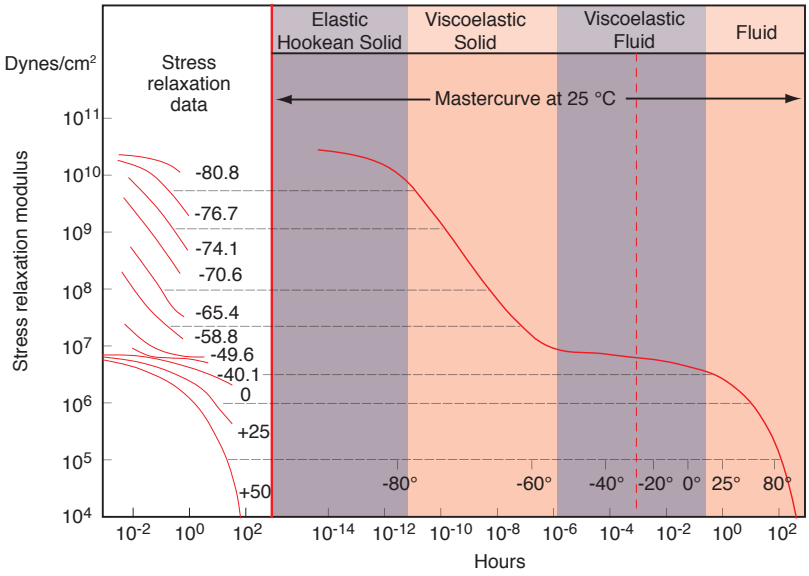

Figure 9.3 Relaxation modulus curves for polyisobutylene at various temperatures and corresponding master curve at 25 °C

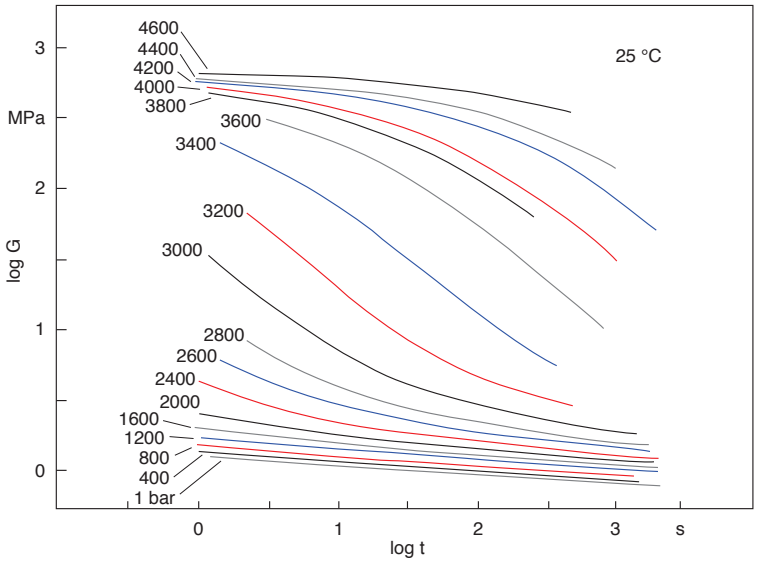

Figure 9.4 Shear relaxation modulus for a chlorosulfonated polyethylene at various pressures

The same behavior is observed if the pressure is varied. As the pressure is increased, the free volume between the molecules is reduced, slowing down molecular movement. Here, an increase in pressure is equivalent to a decrease in temperature. In the melt state, the viscosity of a polymer increases with pressure. Figure 9.4 [2] is presented to illustrate the effect of pressure on stress relaxation.

9.2.2 Time-Temperature Superposition (WLF-Equation)

The time-temperature equivalence seen in stress relaxation test results can be used to reduce data at various temperatures to one general *master curve* for a reference temperature, T_{ref}. To generate a master curve at the reference temperature, the curves shown in the left of Fig. 9.3 must be shifted horizontally, maintaining the reference curve stationary. Density changes are usually small and can be neglected, eliminating the need to perform tedious corrections. The master curve for the data in Fig. 9.3 is shown on the right side of the figure. Each curve was shifted horizontally until the ends of all the curves became superimposed. The amount that each curve was shifted can be plotted with respect to the temperature difference taken from the reference temperature. For the data in Fig. 9.3 the shift factor is shown in the plot in Fig. 9.5. The amounts the curves where shifted are represented by

$$\log t - \log t_{ref} = \log\left(\frac{t}{t_{ref}}\right) = \log a_T \tag{9.17}$$

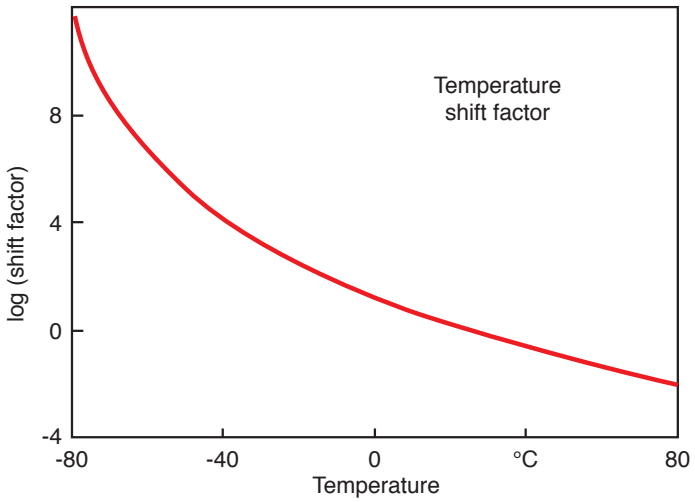

Figure 9.5 Plot of the shift factor as a function of temperature used to generate the master curve plotted in Figure 9.3

Although the results in Figure 9.5 where shifted to a reference temperature of 298 K (25 °C), Williams, Landel and Ferry [3] chose $T_{ref} = 243$ K for

$$\log a_T = \frac{-8.86\left(T - T_{ref}\right)}{101.6 + T - T_{ref}} \tag{9.18}$$

which holds for nearly all polymers, if the chosen reference temperature is 45 K above the glass transition temperature. In general, the horizontal shift, $\log a_T$,

between the relaxation responses at various temperatures to a reference temperature can be computed using the well-known Williams-Landel-Ferry [3] (WLF) equation. The WLF equation is given by

$$\log a_T = -\frac{C_1\left(T - T_{ref}\right)}{C_2 + \left(T - T_{ref}\right)} \tag{9.19}$$

where C_1 and C_2 are material dependent constants. It has been shown that with the assumption C_1 = 17.44 and C_2 = 51.6, Eq. 9.19 fits a wide variety of polymers well as long as the glass transition temperature is chosen as the reference temperature. These values for C_1 and C_2 are often referred to as universal constants. Often, the WLF equation must be adjusted until it fits the experimental data. Master curves of stress relaxation tests are important because the polymer's behavior can be traced over much longer periods of time than when determined experimentally.

9.2.3 The Boltzmann Superposition Principle

In addition to the *time-temperature superposition principle (WLF),* the *Boltzmann superposition principle* is of extreme importance in the theory of linear viscoelasticity. The Boltzmann superposition principle states that the deformation of a polymer component is the sum or superposition of all strains that result from various loads acting on the part at different times. This means that the response of a material to a specific load is independent of already existing loads. Hence, we can compute the deformation of a polymer specimen upon which several loads act at different points in time by simply adding all strain responses. The Boltzmann superposition principle is schematically illustrated in Fig. 9.6. Mathematically, the Boltzmann superposition principle can be stated as follows

$$\varepsilon = \sigma_0 J\left(t - t_0\right) + \left(\sigma_1 - \sigma_0\right) J\left(t - t_1\right) + \ldots + \left(\sigma_i - \sigma_{i-1}\right) J\left(t - t_i\right) + \ldots \tag{9.20}$$

where J represents the material's compliance[4]. However, not all loadings and deformations consist of finite step changes, and Eq. 9.20 can be written in integral form as

$$\varepsilon\left(t\right) = \int_{\sigma(-\infty)}^{\sigma(t)} J\left(t - t'\right) d\sigma\left(t'\right) \tag{9.21}$$

which can also be written as

$$\varepsilon\left(t\right) = \int_{-\infty}^{t} J\left(t - t'\right) \dot{\sigma}\left(t'\right) dt' \tag{9.22}$$

Furthermore, one can invert Eq. 9.22 and write

$$\sigma\left(t\right) = \int_{-\infty}^{t} G\left(t - t'\right) \dot{\varepsilon} dt' \tag{9.23}$$

4 The compliance is the inverse of the stiffness, $J = 1/E$.

The Boltzmann superposition principle holds as long as the polymer follows a linear viscoelastic behavior.

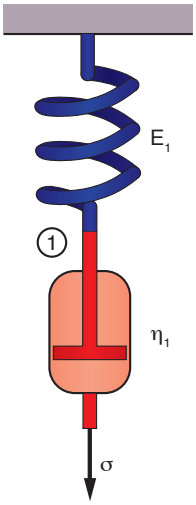

Figure 9.6 Schematic demonstration of Boltzmann's superposition principle; A, B, and C are sudden load changes

9.3 Applying Linear Viscoelasticity to Describe the Behavior of Polymers

As should be clear from the stress relaxation behavior, most polymers exhibit a viscous as well as an elastic response to stress and strain. This puts them in the category of viscoelastic materials. Various combinations of elastic and viscous elements have been used to approximate the material behavior of polymeric melts. The main assumptions made in linear viscoelasticity is that the deformations must be small and that various loadings at different times are simply superimposed on one another as stated by *Boltzmann's superposition principle*. Several models exist to simulate the linear viscoelastic behavior of polymers. These physical models are generally composed of one or several elements, such as dashpots, springs, or friction elements that represent viscous, elastic, or yielding properties, respectively. All models must satisfy the momentum balance and continuity or deformation equation, along with the appropriate constitutive laws. The most commonly used constitutive equations are the viscous – the dashpot – or *Newtonian model,* which is written as

$$\sigma = \eta\dot{\varepsilon} \tag{9.24}$$

and the linear elastic – the spring – or *Hookean model*, which is represented by

$$\sigma = E\varepsilon \tag{9.25}$$

where η and E are the viscosity and Young's modulus, respectively.

9.3.1 The Maxwell Model

For clarity, let us first derive the stress-strain behavior for a Maxwell model shown in Fig. 9.7. The total strain, ε, in the model has an elastic, ε_e, and a viscous, ε_v, strain contribution and can be represented as follows:

$$\varepsilon = \varepsilon_e + \varepsilon_v \tag{9.26}$$

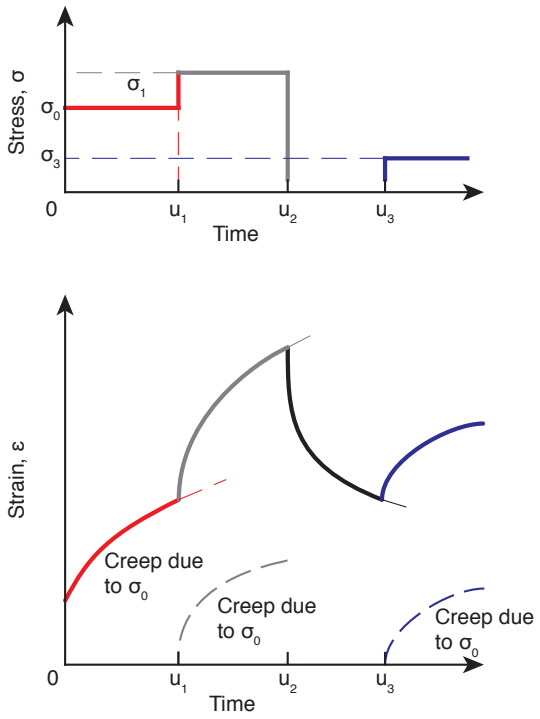

Figure 9.7 Schematic diagram of the Maxwell model

Similarly, the strain rates are written as

$$\dot{\varepsilon} = \dot{\varepsilon}_e + \dot{\varepsilon}_v \tag{9.27}$$

Assuming the spring follows Hooke's law, the following relation holds

$$\dot{\varepsilon}_e = \frac{\dot{\sigma}}{E} \tag{9.28}$$

The viscous portion, represented by the dash pot, is written as follows

$$\dot{\varepsilon}_v = \frac{\sigma}{\eta} \tag{9.29}$$

Combining Eqs. 9.27–9.29 results in

$$\dot{\varepsilon} = \frac{\dot{\sigma}}{E} + \frac{\sigma}{\eta} \tag{9.30}$$

which can be rewritten as

$$\sigma + \frac{\eta}{E}\frac{d\sigma}{dt} = \eta\frac{d\varepsilon}{dt} \tag{9.31}$$

which is often referred to as the governing equation for Maxwell's model in *differential form.*

Maintaining the material at a constant deformation, such as in the relaxation test, the differential equation, Eq. 9.31, reduces to

$$\sigma + \frac{\eta}{E}\dot{\sigma} = 0 \tag{9.32}$$

Integrating Eq. 9.32 results in

$$\sigma = \sigma_0 e^{-t/\lambda} \tag{9.33}$$

where λ is known as the *relaxation time*. The relaxation response of the constant strain Maxwell model is compared to the four-parameter Maxwell model in Fig. 9.16. Using Eq. 9.33 one can show how, after $t = \lambda$, the stresses relax to 37 % of their initial value, $e^{-1} = 0.37$. When estimating relaxation of stresses, four relaxation times (4λ) are often used. Hence, by using $t = 4\lambda$ in Eq. 9.33 the stresses have relaxed to 1.8 % of their original value. Using the Boltzmann superposition principle and Eq. 9.33 we can write the governing equation for the Maxwell model in *integral form* as

$$\sigma(t) = \int_{-\infty}^{t} Ee^{-(t-t')/\lambda}\dot{\varepsilon}dt \tag{9.34}$$

9.3.2 Kelvin Model

Depending on the time scale, the Maxwell model emulates solids – short time scales – as well as liquids – long time scales – while the Kelvin model is exclusively used to model viscoelastic solids. The Kelvin model, sometimes also called the Kelvin-Voigt model, is shown in Fig. 9.8. It is the simplest model that can be used to represent the behavior of a solid polymer component at the beginning of loading.

The momentum balance for the Kelvin model is stated as

$$\sigma = \sigma_1 + \sigma_2 \tag{9.35}$$

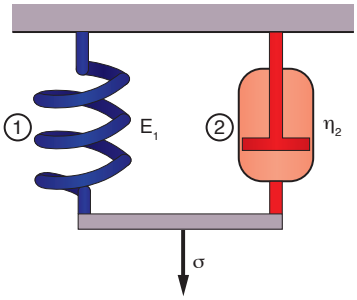

Figure 9.8 Schematic diagram of the Kelvin model

and the continuity equation is represented by

$$\varepsilon = \varepsilon_1 = \varepsilon_2 \tag{9.36}$$

Using Eq. 9.36 with the constitutive relations in Eqs. 9.24 and 9.25, the governing equation, Eq. 9.35, can be rewritten as

$$\sigma = E\varepsilon + \eta\dot{\varepsilon} \tag{9.37}$$

Using Eq. 9.37, the strain in a creep test in the Kelvin model can be solved for as

$$\varepsilon(t) = \frac{\sigma_0}{E}\left(-e^{-t/\lambda}\right) \tag{9.38}$$

where λ, (η/E), is the relaxation time. The creep modulus is defined as

$$E_c(t) = \frac{E}{\left(1-e^{-t/\lambda}\right)} \tag{9.39}$$

The creep response of the Kelvin model is shown in Fig. 9.9.

In the Kelvin model the stress does not relax and remains constant at

$$\sigma = E\varepsilon_0 \tag{9.40}$$

which is shown in Fig. 9.9.

Because the stresses do not relax in a Kelvin model, the full shape of the original component or specimen can be recovered. The strain recovery response can be written as

$$\varepsilon(t) = \varepsilon_0 e^{-t/\lambda} \tag{9.41}$$

and is shown in Fig. 9.9.

We can also consider the response of a Kelvin model subjected to a sinusoidal strain given by

$$\varepsilon(t) = \varepsilon_0 \sin(\omega t) \tag{9.42}$$

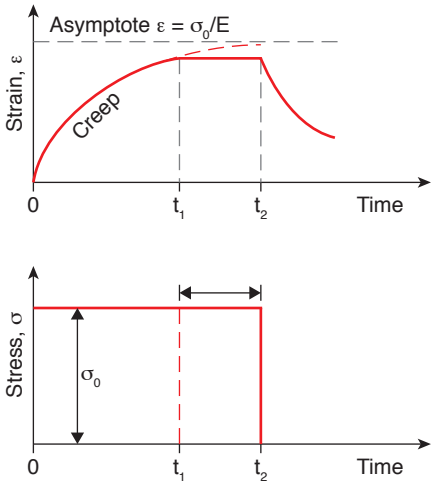

Figure 9.9 Creep, relaxation, and recovery response of the Kelvin model

where ε_0 is the strain amplitude and ω is the frequency. Differentiating Eq. 9.42 and substituting into Eq. 9.37 results in

$$\sigma(t) = E\varepsilon_0 \sin(\omega t) + \eta\omega\varepsilon_0 \cos(\omega t) \tag{9.43}$$

Dividing Eq. 9.43 by the strain amplitude results in the *complex modulus*. In Eq. 9.43 we recognize the *storage modulus*

$$E' = E \tag{9.44}$$

and the loss modulus

$$E'' = \eta\omega \tag{9.45}$$

9.3.3 Jeffrey Model

As shown in Fig. 9.10, the Jeffrey model is a Kelvin model with a dashpot. This extra feature adds the missing long-term creep behavior to the Kelvin model.

The momentum balance of the Jeffrey model is represented by two equations as

$$\sigma = \sigma_3 \quad \text{and} \tag{9.46}$$

$$\sigma = \sigma_1 + \sigma_2 \tag{9.47}$$

as is the continuity equation by

$$\varepsilon_1 = \varepsilon_2 \quad \text{and} \tag{9.48}$$

$$\varepsilon = \varepsilon_2 + \varepsilon_3 \tag{9.49}$$

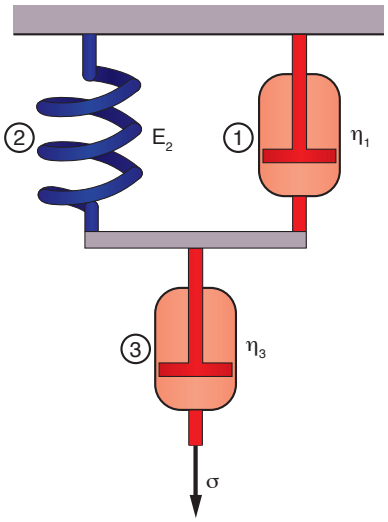

Figure 9.10 Schematic diagram of the Jeffrey model

Combining Eq. 9.46 – 9.49 and applying the constitutive equations gives

$$\sigma + \left(\frac{\eta_1 + \eta_3}{E_2}\right)\dot{\sigma} = \eta_3\dot{\varepsilon} + \left(\frac{\eta_3\eta_1}{E_2}\right)\ddot{\varepsilon} \tag{9.50}$$

which is sometimes written as

$$\sigma + \lambda_1\dot{\sigma} = \eta_0\left(\dot{\varepsilon} + \lambda_2\ddot{\varepsilon}\right) \tag{9.51}$$

Using Eq. 9.51, the strain in a creep test in the Jeffrey model can be solved for as

$$\varepsilon(t) = \frac{\sigma_0}{E}\left(1 - e^{-t/\lambda_2}\right) + \frac{\sigma_0}{\eta_0}t \tag{9.52}$$

and is depicted in Fig. 9.11. The creep modulus of the Jeffrey model is written as

$$E_c(t) = \left(\frac{\left(1 - e^{-t/\lambda_2}\right)}{E} + \frac{t}{\eta_3}\right)^{-1} \tag{9.53}$$

The stress relaxation of the Jeffrey model is derived from the governing equation, Eq. 9.51 as

$$\sigma = \sigma_0 e^{-t/\lambda_1} \tag{9.54}$$

and is also represented in Fig. 9.11.

The unrelaxed stress is recovered in the same way as in the Kelvin model

$$\varepsilon(t) = \varepsilon_0 e^{-t/\lambda} \tag{9.55}$$

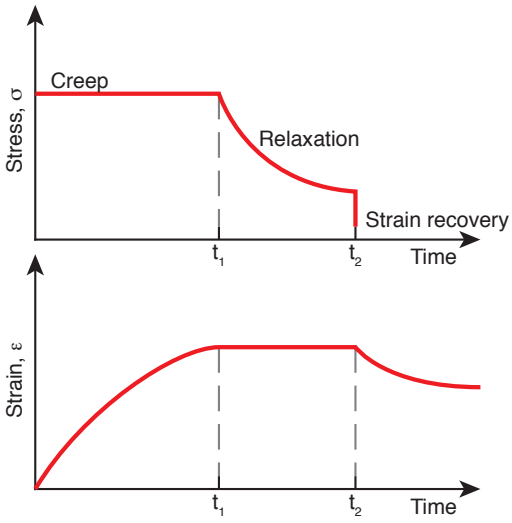

Figure 9.11 Creep, relaxation, and recovery response of the Jeffrey model

9.3.4 Standard Linear Solid Model

The standard linear solid model, shown in Fig. 9.12, is a commonly used model to simulate the short-term behavior of solid polymer components. The momentum balance of the standard linear solid model is expressed with two equations as

$$\sigma = \sigma_1 + \sigma_2 \tag{9.56}$$

and

$$\sigma_1 = \sigma_3 \tag{9.57}$$

Continuity or deformation is represented with

$$\varepsilon = \varepsilon_1 + \varepsilon_3 \tag{9.58}$$

and

$$\varepsilon = \varepsilon_2 \tag{9.59}$$

When we combine Eqs. 9.56–9.59 and use the constitutive equations for the spring and dashpot elements, we get the governing equation for the standard linear solid model:

$$\eta\dot{\sigma} + E_1\sigma = \eta\left(E_1 + E_2\right)\dot{\varepsilon} + E_1E_2\varepsilon \tag{9.60}$$

Using Eq. 9.60, the strain in a creep test in the standard linear solid model can be solved for as

$$\varepsilon = \frac{\sigma_0}{E_2} + \left(\frac{\sigma_0}{E_1 + E_2} - \frac{\sigma_0}{E_2}\right)e^{-\left(E_1E_2/\eta\left(E_1+E_2\right)\right)t} \tag{9.61}$$

and is plotted in Fig. 9.13.

The stress relaxation of the standard linear solid model can be derived by integrating Eq. 9.60 and is represented by

$$\sigma = \varepsilon_0 \left(E_2 + E_1 \right) e^{-(E_1/\eta)t} \tag{9.62}$$

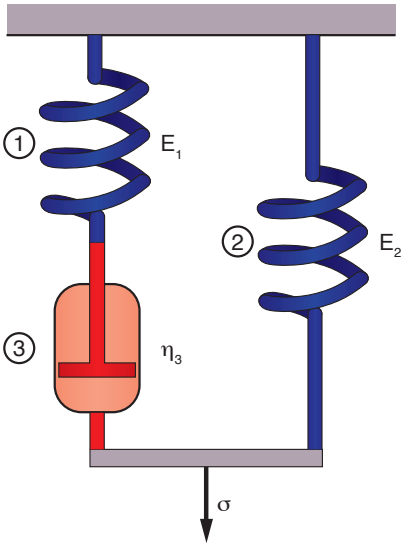

Figure 9.12 Schematic diagram of the standard linear solid model

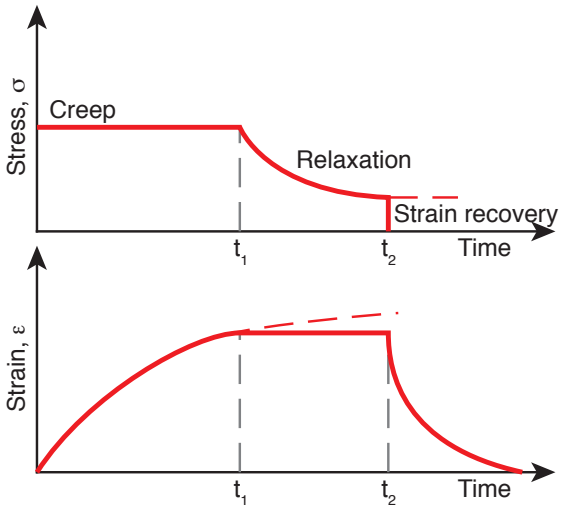

Figure 9.13 Creep, relaxation, and recovery response of the standard linear solid model

9.3.5 The Generalized Maxwell Model

The generalized Maxwell model, also known as the Maxwell-Wiechert model, shown in Fig. 9.14, is a generalized model that consists of an arbitrary number of Maxwell models connected in parallel, allowing a more accurate simulation to fit experimentally generated mechanical behavior.

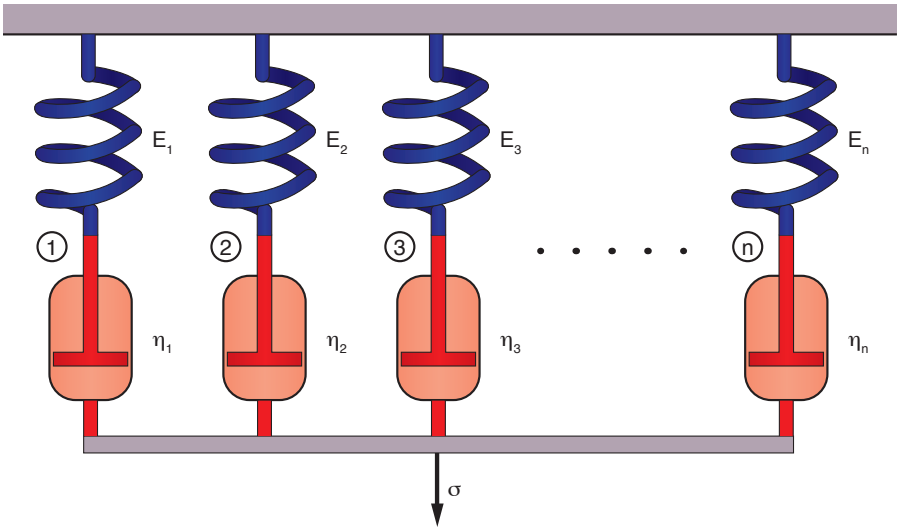

Figure 9.14 Schematic diagram of the Maxwell-Wiechert model

The momentum balance in the *i*th Maxwell element of the Maxwell-Wiechert model is expressed as

$$\sigma_1 = \sigma_{i1} = \sigma_{i2} \tag{9.63}$$

and the full momentum balance for a model with *n* elements is written as

$$\sigma = \sum_{i=1}^{n} \sigma_i \tag{9.64}$$

Continuity or deformation for the *i*th Maxwell element is expressed as

$$\varepsilon_i = \varepsilon_{i1} + \varepsilon_{i2} \tag{9.65}$$

and for the full model

$$\varepsilon = \varepsilon_1 = \varepsilon_2 = \varepsilon_i \ldots \tag{9.66}$$

The governing equation for the Maxwell-Wiechert model is written as

$$\dot{\varepsilon} = \frac{\dot{\sigma}_i}{E_i} + \frac{\sigma_i}{\eta_i} \tag{9.67}$$

The stress relaxation of the Maxwell-Wiechert model can be derived by integrating Eq. 9.67 and substituting the resulting stress into Eq. 9.64. Dividing by the applied strain ε_0 results in an expression for the relaxation model which is written as

$$E(t) = \sum_{i=1}^{n} E_i e^{-(1/\lambda_i)t} \tag{9.68}$$

which represents a model with n relaxation times and where $\lambda_i = \eta_i / E_i$. As an example, we can approximate the relaxation behavior of polyisobutylene by using a Maxwell-Wiechert model having two Maxwell elements with $\lambda_1 = 10^{-8}$ h and $\lambda_2 = 100$ h, and $E_1 = 3 \times 10^9$ Pa and $E_2 = 10^6$ Pa. Figure 9.15 compares the experimental relaxation modulus with the model. One can see that although there are big differences between the two curves, the model, with its two relaxation times, does at least qualitatively represent the experimental values.

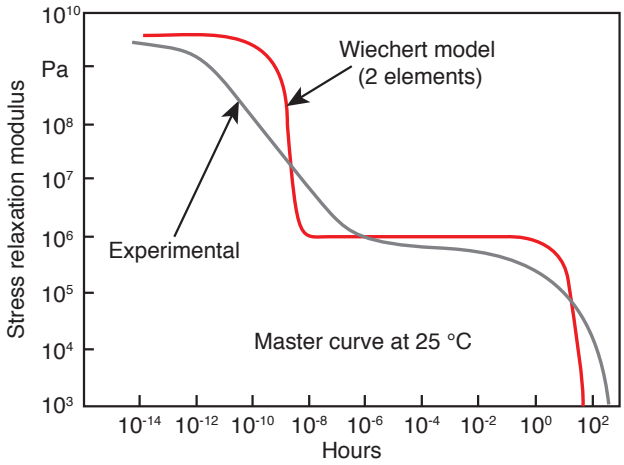

Figure 9.15 Comparison of the experimental stress relaxation for polyisobutylene with a two-component Maxwell-Wiechert model response

For a better fit with experimental data it is common to use several spring-dash pot models in parallel, such as shown in Fig. 9.16 [4]. The curve shown in the figure fits a four-parameter model with experimental relaxation and retardation data for a common polystyrene with a molecular weight of 260,000 g/mole. For this specific material, the relaxation behavior of the injected melt into a hot cavity, at a reference temperature of 113 °C, is described by

$$\frac{\varepsilon}{\varepsilon_a} = 0.25\left(e^{-8.75t/\lambda} + e^{-1.0t/\lambda} + e^{-0.28t/\lambda} + e^{-0.0583t/\lambda}\right) \tag{9.69}$$

where ε_a is the strain after relaxation and is defined by

$$\varepsilon_a = \frac{l_a - l_0}{l_0} = \frac{S_0}{1 - S_0} \tag{9.70}$$

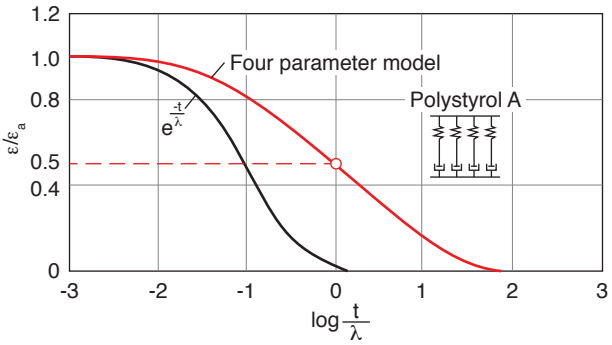

Figure 9.16 Relaxation response of a Maxwell model and a four-parameter Maxwell model

Here, l_a and l_0 represent the length of the stretched and relaxed sample, respectively, and S_0 represents the total shrinkage.

The terms $\frac{\lambda}{8.75}, \lambda, \frac{\lambda}{0.28}, \frac{\lambda}{0.0583}$, in Eq. 9.69 represent four individual relaxation times for this specific polystyrene, modeled using the four-parameter model. The relaxation time, λ, correlates with the time it takes for the initial strain to relax to one-half its initial value. This relaxation time is also temperature dependent, as shown for various polymers in Fig. 9.17. Figure 9.17 shows how the shapes of the curves are all similar, only shifted by a certain temperature. It is important to note that the relaxation and retardation behavior of all amorphous thermoplastics is similar.

Wübken [5] performed similar tests with different amorphous thermoplastics, and he found that, indeed, in all cases the measurements showed a correlation between

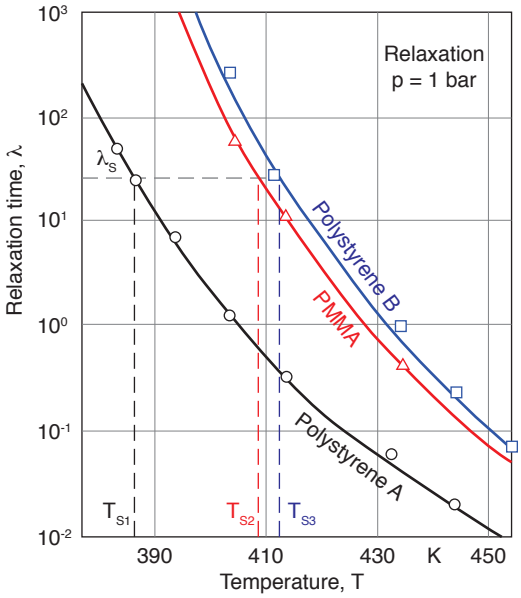

Figure 9.17 Relaxation time as a function of temperature for various thermoplastics

time and temperature such as described by the WLF [3] equation. The data fit by the four-parameter model was generated via two different experiments: a relaxation test inside an injection mold between 100 and 180 °C, and a retardation test outside of the mold between 72 and 100 °C. The measured data are shown in Figs. 9.18 and 9.19 for the relaxation and retardation tests, respectively. The curves shown in both graphs were shifted horizontally to generate one master curve as shown in Fig. 9.20. The solid line in the figure is the four-parameter fit represented by Eq. 9.69.

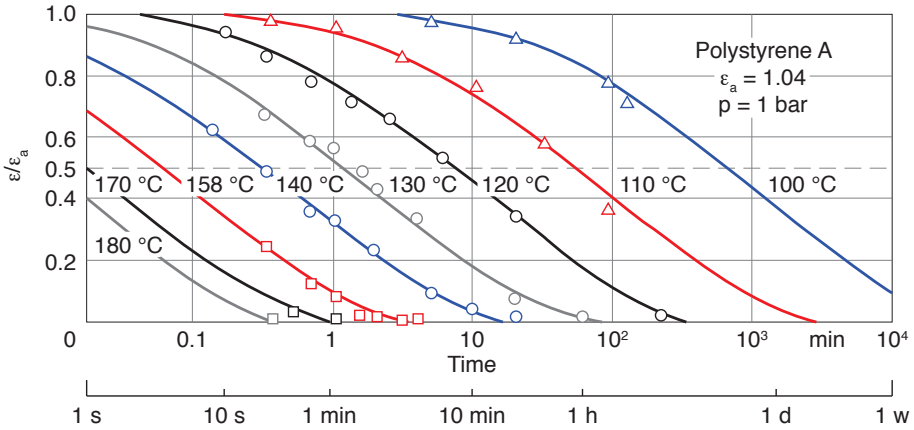

Figure 9.18 Relaxation response, inside an injection mold, of a polystyrene specimen at various temperatures

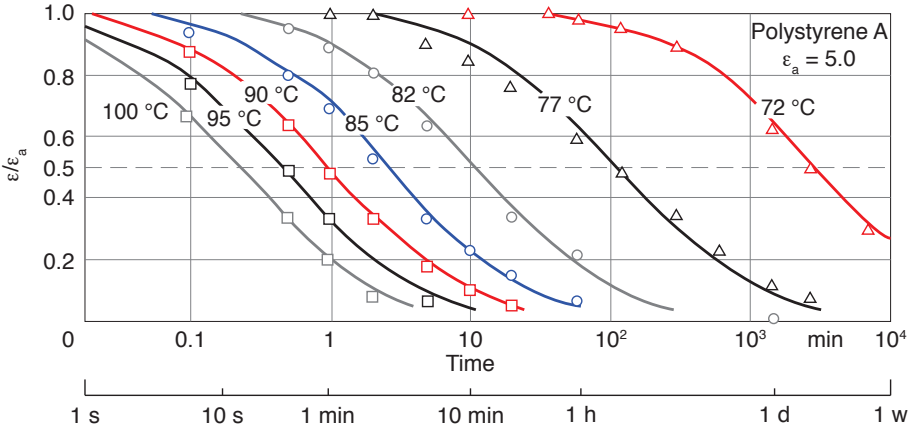

Figure 9.19 Recovery or retardation response after injection molding of a polystyrene specimen at various temperatures

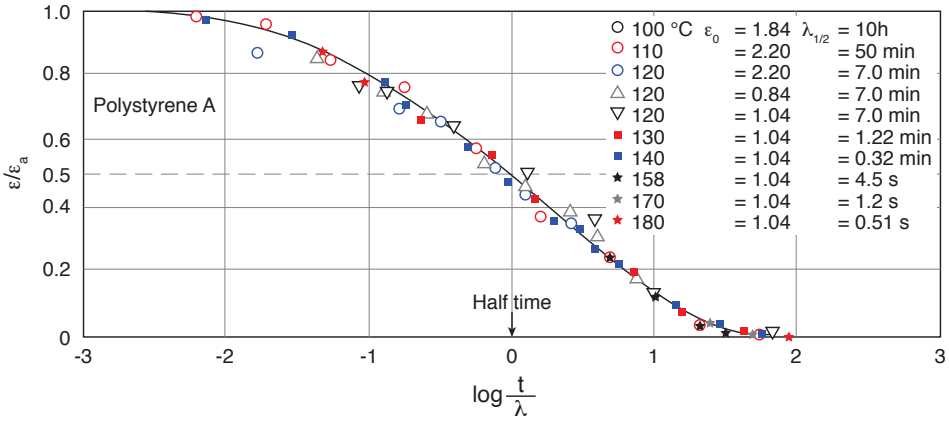

Figure 9.20 Master curve for the relaxation response, inside an injection mold, of a polystyrene specimen at various temperatures

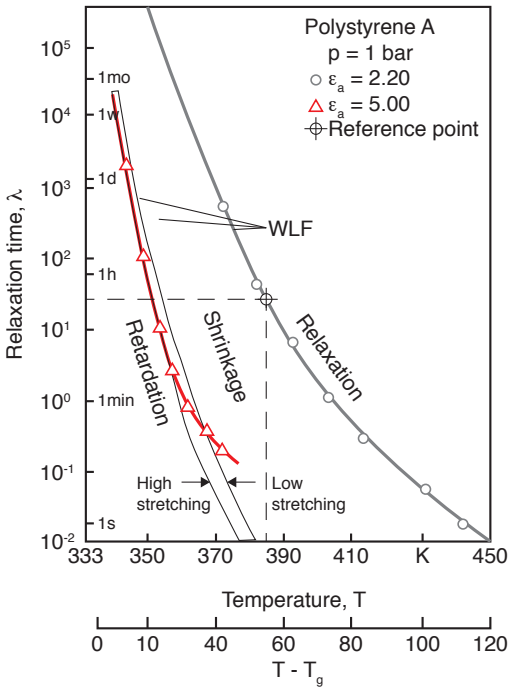

Figure 9.21 Relaxation and retardation times as a function of temperature for polystyrene

Hence, appropriate T_{ref} and I values must be found. However, the reference temperature is not quite independent of the relaxation behavior of the polymer but is related to the material properties. For the polystyrene A in Fig. 9.21, $T_{ref} = 113$ °C, or about 48 °C above T_g. For example, for the polystyrene A of Fig. 9.21, the relaxation time, λ, can be computed by

$$\text{Relaxation:} \quad \log(\lambda) = \log(27) - \frac{8.86(T - T_s)}{101.6 + (T - T_s)} \tag{9.71}$$

$$\text{Creep:} \quad \log(\lambda) = \log(0.0018) - \frac{8.86(T - T_s)}{101.6 + (T - T_s)} \tag{9.72}$$

where the constants 27 and 0.0018 are the relaxation times, λ, in minutes, at the reference temperature of 113 °C.

As discussed earlier, similar to the temperature induced shift, there is also a shift due to pressure. If we refer to Fig. 9.22, which shows the influence of pressure on T_g, we can see that this effect can easily be included into the WLF equation i. e., there is approximately a 2 °C shift in the glass transition temperature of polystyrene for every 100 bar of pressure rise [5].

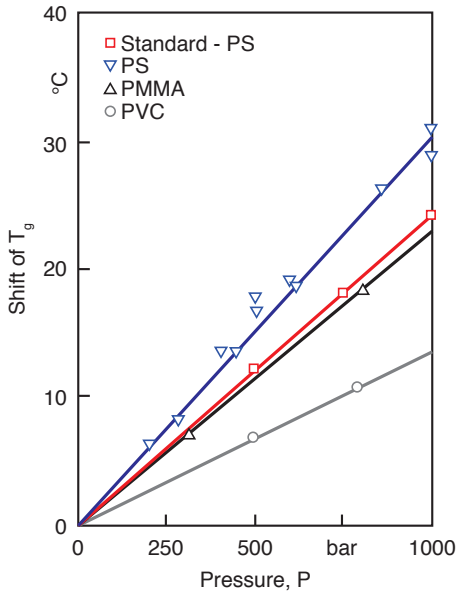

Figure 9.22 Influence of hydrostatic pressure on the glass transition temperature for various amorphous thermoplastics

9.4 The Short-Term Tensile Test

The most commonly used mechanical test is the short-term stress-strain tensile test. Stress-strain curves for selected polymers are displayed in Fig. 9.23 [6]. For comparison, the figure also presents stress-strain curves for copper and steel. It becomes evident from Fig. 9.23 that although they have much lower tensile strengths, many engineering polymers exhibit much higher strains at break.

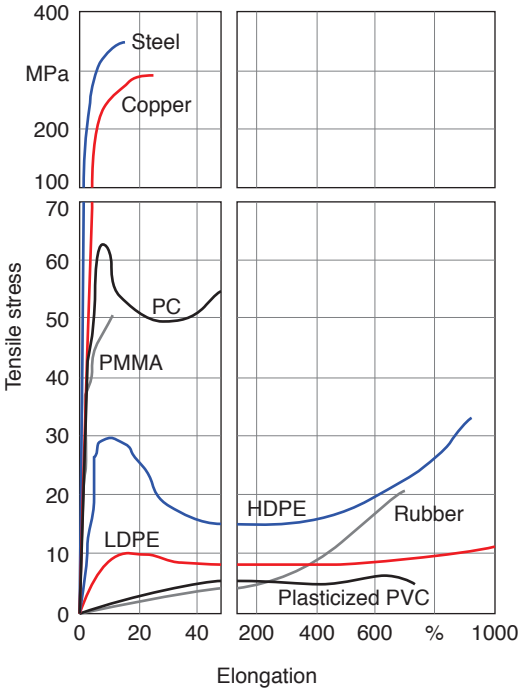

Figure 9.23 Tensile stress-strain curves for several materials

The next two sections discuss the short-term tensile test for elastomers and thermoplastic polymers separately. The main reason for identifying two separate topics is that the deformation of a cross-linked elastomer and an uncross-linked thermoplastic vary greatly. The deformation in a cross-linked polymer is in general reversible, whereas the deformation in typical uncross-linked polymers is associated with molecular chain relaxation, which makes the process time-dependent, and sometimes irreversible.

9.4.1 Rubber Elasticity

The main feature of elastomeric materials is that they can undergo very large and reversible deformations because the curled-up polymer chains stretch during deformation but are hindered in sliding past each other by the crosslinks between the molecules. Once a load is released, most of the molecules return to their coiled shape. As an elastomeric polymer component is deformed, the slope of the stress-strain curve drops significantly as the uncurled molecules provide less resistance and entanglement, allowing them to move more freely. Eventually, at deformations of about 400%, the slope starts to increase because the polymer chains are fully stretched. This is followed by polymer chain breakage or crystallization, which ends with fracture of the component. Stress-deformation curves for natural rubber

(NR) [7] and a rubber compound [8] composed of 70 parts of styrene-butadiene-rubber (SBR) and 30 parts of natural rubber are presented in Fig. 9.24. Because of the large deformations (typically several hundred percent), the stress-strain data are usually expressed in terms of extension ratio, λ, defined by

$$\lambda = \frac{L}{L_0} \tag{9.73}$$

where L represents the instantaneous length and L_0 the initial length of the specimen.

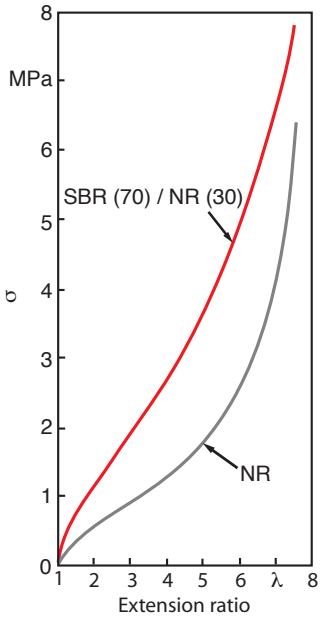

Figure 9.24 Experimental stress-extension curves for NR and a SBR/NR compound

Based on kinetic theory of rubber elasticity [7, 9] simple expressions can be derived to predict the stress as a function of extension. For a component in uniaxial extension, or compression, the stress can be computed as[5]

$$\sigma = G_0\left(\lambda - \frac{1}{\lambda^2}\right) \tag{9.74}$$

where G_0 is the shear modulus at zero extension, which for rubbers can be approximated by

$$G_0 = \frac{E_0}{3} \tag{9.75}$$

with E_0 as the elastic tensile modulus at zero extension.

5 A similar equation exists for equibiaxial extension (inflation) of thin sheets. This equation is written as follows $\sigma = G_0\left(\lambda^2 - 1/\lambda^4\right)$.

Figure 9.25 [7] compares the kinetic theory model with the experimental data for natural rubber presented in Fig. 9.24. The agreement is good up to about 50% extension $(\lambda = 1.5)$. However, Eq. 9.74 can be used to approximate the stress-strain behavior up to 600% extension $(\lambda = 7.0)$. For compression, the model agrees much better with experiments, as shown for natural rubber in Fig. 9.26 [7]. Fortunately, rubber products are rarely deformed more than 25% in compression or tension, a fact that often justifies the use of Eq. 9.74.

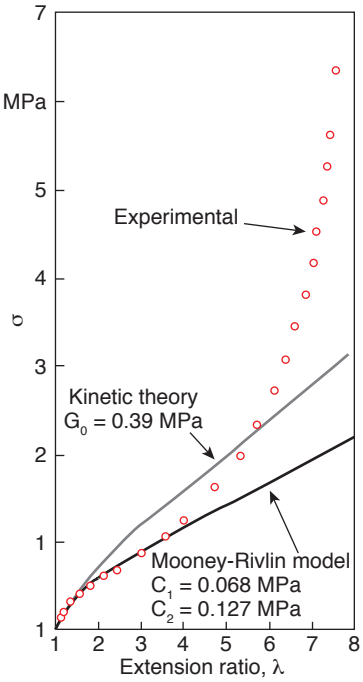

Figure 9.25 Comparison of theoretical and experimental stress-extension curves for natural rubber

A more complex model representing the deformation behavior of elastomers in the region in which the stress-strain curve is reversible is the *Mooney-Rivlin* equation [10, 11] written as

$$\sigma = 2\left(\lambda - \frac{1}{\lambda^2}\right)\left(C_1 + \frac{C_2}{\lambda}\right) \tag{9.76}$$

which can be rearranged to give

$$\frac{\sigma}{2\left(\lambda - \frac{1}{\lambda^2}\right)} = C_1 + \frac{C_2}{\lambda} \tag{9.77}$$

A plot of the *reduced stress*, $\sigma/2\left(\lambda - 1/\lambda^2\right)$, versus $1/\lambda$ is usually referred to as a *Mooney plot* and should be linear with a slope of C_2 and an ordinate of $(C_1 + C_2)$ at $1/\lambda = 1$. A typical Mooney plot is presented in Fig. 9.27 [12] for a natural rubber with different formulations and times of vulcanization.

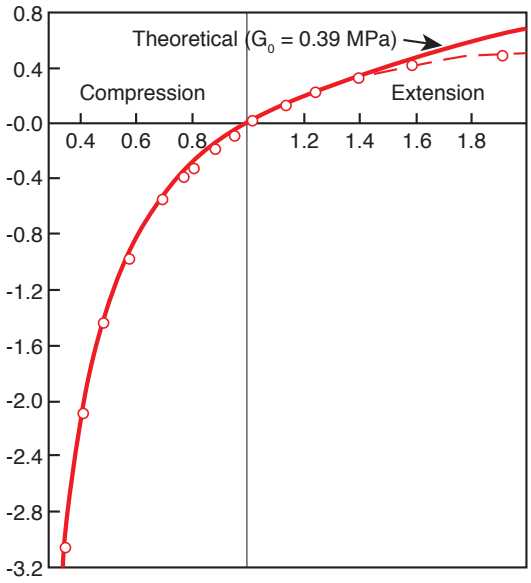

Figure 9.26 Experimental and theoretical stress-extension and compression curves for natural rubber

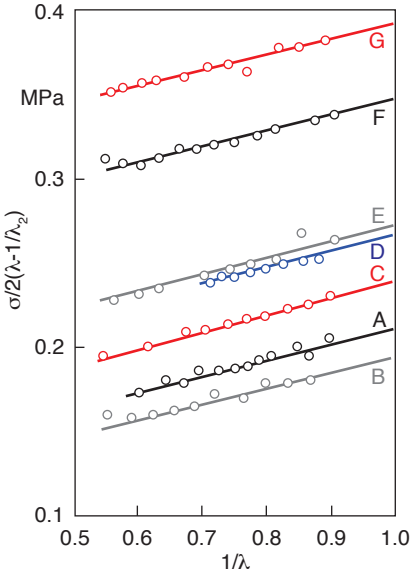

Figure 9.27 Mooney plots for rubber with various degrees of vulcanization

Descriptions of the various rubber formulations tested are presented in Table 9.1 [12]. It can be seen that C_2 shows little change, even with different rubber composition, and is approximately 0.1 Mpa. On the other hand, C_1 changes with degree of vulcanization and composition. A comparison between the Mooney-Rivlin model, the kinetic theory model, and experimental data for natural rubber is found in Fig. 9.25. For this material, the Mooney-Rivlin model represents the experimental data quite well up to extension ratios of 3.5.

Table 9.1 Compounding Details of the Vulcanizates Used by Gumbrell et al. [12]

Mix	A	B	C	D	E	F	G
Rubber	100	100	100	100	100	100	100
Sulfur	3.0	3.0	3.0	3.0	3.25	4.0	4.0
Zinc oxide	5.0	5.0	5.0	5.0	5.0	5.0	5.0
Stearic acid	1.0	1.0	1.0	1.0	1.0	1.0	1.0
Benzothiazyl disulphide	0.5	0.5	0.5	0.75		1.0	0.5
Mercaptobenzothiazyl disulphide		0.5	0.5	0.25		0.3	
Zinc dimethyl dithiocarbamate				0.1		0.15	
Diphinyl guanidine					1.25		1.0
Antioxidant	1.0	1.0	1.0	1.0	1.0	1.0	1.0
Time of vulcanization at 141.5 °C (min)	45	10	30	20	60	10	12

Finally, it should be noted that the stiffness and strength of rubber is increased by filling with carbon black. The most common expression for describing the effect of carbon black content on the modulus of rubber was originally derived by Guth and Simha [13] for the viscosity of particle suspensions, and later used by Guth [14] to predict the modulus of filled polymers. The Guth equation can be written as

$$\frac{G_f}{G_0} = 1 + 2.5\phi + 14.1\phi^2 \tag{9.78}$$

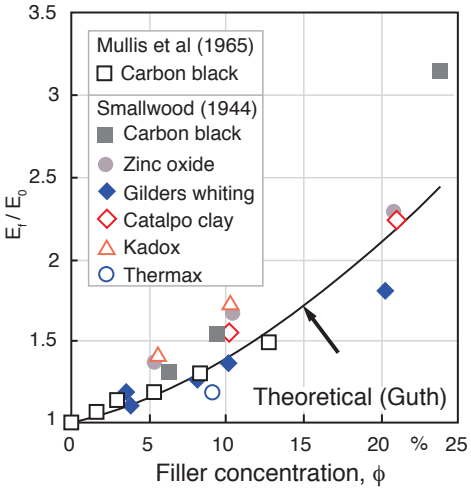

Figure 9.28 Effect of filler on modulus of natural rubber

where G_f is the shear modulus of the filled material and ϕ the volume fraction of particulate filler. The above expression is compared to experiments [15, 16] in Fig. 9.28.

9.4.2 The Tensile Test and Thermoplastic Polymers

Of all the mechanical tests done on thermoplastic polymers, the tensile test is the least understood, and the results are often misinterpreted and misused. Because the test was inherited from other materials that have linear elastic stress-strain responses, it is often inappropriate for testing polymers. However, standardized tests such as DIN 53457 and ASTM D638 are available to evaluate the stress-strain behavior of polymeric materials.

The DIN 53457, for example, is performed at a constant elongational strain rate of 1 % per minute, and the resulting data are used to determine the *short-term modulus.* The ASTM D638 test also uses one rate of deformation per material to measure the modulus; a slow speed for brittle materials and a fast speed for ductile ones. However, these tests do not reflect the actual rate of deformation experienced by the narrow portion of the test specimen, making it difficult to maintain a constant speed within the region of interest.

Extensive work was done by Knausenberger and Menges [17] where the rate of deformation of the test specimen is maintained constant. This is achieved by optically measuring the deformation on the specimen itself, as schematically demonstrated in Fig. 9.29 [17], and using that information as a feedback to control the elongational speed of the testing machine. The Knausenberger-Menges technique

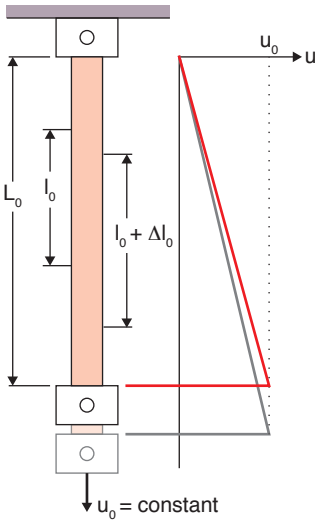

Figure 9.29 Flat tensile bar with velocity distribution

allows the testing engineer to measure the stress-strain response at various strain rates, ensuring in each test that the rate of deformation in the narrow section of the test specimen is accurately controlled. The resulting data can be used to determine the viscoelastic properties of polymers ranging from impact to long-term responses. A typical test performed on PMMA at various strain rates at room temperature is shown in Fig. 9.30. The increased curvature in the results with slow elongational speeds suggests that stress relaxation plays a significant role during the test.

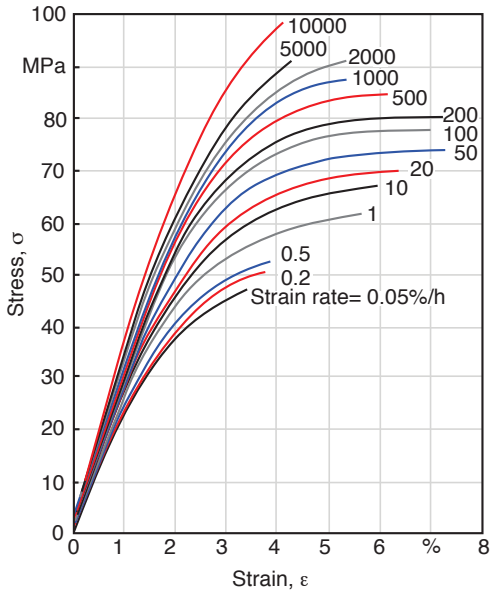

Figure 9.30 Stress-strain behavior of PMMA at various strain rates

It can be shown that for small strains, or in linear viscoelasticity, the *secant modulus*, described by

$$E_s = \frac{\sigma}{\varepsilon} \tag{9.79}$$

and the tangent modulus, defined by

$$E_t = \frac{d\sigma}{d\varepsilon} \tag{9.80}$$

are independent of strain rate and are functions only of time and temperature. This is demonstrated in Fig. 9.31 [18]. The figure shows two stress-strain responses: one at a slow elongational strain rate, $\dot{\varepsilon}_1$, and one at twice the speed, defined by $\dot{\varepsilon}_2$. The tangent modulus at ε_1 in the curve with $\dot{\varepsilon}_1$ is identical to the tangent modulus at ε_2 in the curve with ε_2, where ε_1 and ε_2 occurred at the same time. For small strains the tangent modulus, E_t, is identical to the relaxation modulus, E_r, measured with a stress relaxation test. This is important because the complex stress

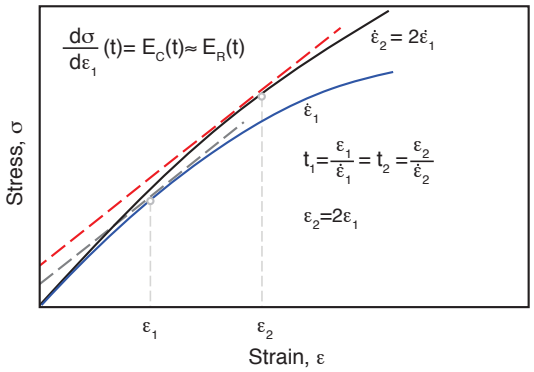

Figure 9.31 Schematic of the stress-strain behavior of a viscoelastic material at two rates of deformation

relaxation test can be replaced by the relatively simple short-term tensile test by plotting the tangent modulus versus time.

Generic stress-strain curves and stiffness and compliance plots for amorphous and semi-crystalline thermoplastics are shown in Fig. 9.32 [19]. For amorphous thermoplastics the stress-strain behavior in the curves of Fig. 9.32 can typically be approximated by

$$\sigma(T,t) = E_0(T,t)\left(1 - D_1(T,t)\varepsilon\right)\varepsilon \tag{9.81}$$

and in a short-term test a semi-crystalline polymer would behave more like

$$\sigma(T,t) = E_0(T,t)\frac{\varepsilon}{1 + D_2(T,t)\varepsilon} \tag{9.82}$$

where E_0, D_1 and D_2 are time- and temperature-dependent material properties. However, below the glass transition temperature, the stress-strain curve of an amorphous polymer has a long and much steeper rise, with less relaxation effects, as shown in Fig. 9.32 and Eq. 9.81. In the stress-strain response of semi-crystalline polymers, on the other hand, the amorphous regions make themselves visible in long-term tensile tests. Hence, Eqs. 9.81 and 9.82 can be written in a more general form as

$$\sigma = E_0\varepsilon\frac{1 - D_1\varepsilon}{1 + D_2\varepsilon} \tag{9.83}$$

The coefficients in Eq. 9.83 can be determined for various rates of deformation. For example, the curves in Fig. 9.33 [20] show the coefficient E_0 for an amorphous unplasticized PVC measured at various strain rates, $\dot{\varepsilon}$, and temperatures. The curves in the figure suggest that there is a direct relationship between temperature and strain rate or time. It can be seen that the curves, separated by equal temperature differences, are shifted from each other at equal distances, $\log(a_T)$, where

$$a_T = \frac{\dot{\varepsilon}_{ref}}{\dot{\varepsilon}} \tag{9.84}$$

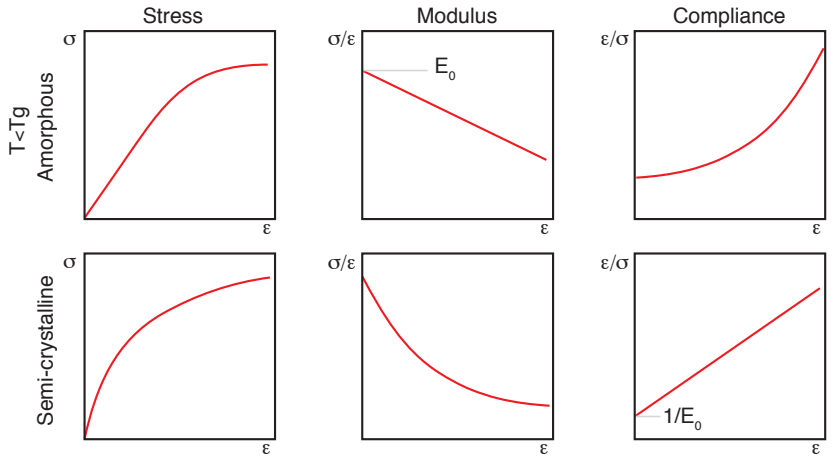

Figure 9.32 Schematic of the stress-strain response, modulus, and compliance of amorphous and semi-crystalline thermoplastics at constant rates of deformation

Since strain rate is directly related to time, one can make use of Arrhenius' relation between relaxation time, λ, and a reference relaxation time, λ_{ref}, stated by

$$\frac{\lambda}{\lambda_{ref}} = e^{-A/KT} \tag{9.85}$$

where A is the activation energy, T temperature, and K a material property. The modified form of the Arrhenius equation for shifting the data can be written as

$$\log\left(a_T\right) = K\left(\frac{1}{T} - \frac{1}{T_{ref}}\right) \tag{9.86}$$

where T_{ref} is the reference temperature. The material constant K can be calculated by using data from Fig. 9.33, as shown in the sample graphical shift displayed in the figure. The coefficient K, which can be solved for by using

$$K = \frac{\log\left(\dot{\varepsilon}_{ref} / \dot{\varepsilon}\right)}{1/T - 1/T_{ref}} \tag{9.87}$$

turns out to be 10,000 for the conditions shown in Fig. 9.33. This is true unless the test temperature is above the glass transition temperature, at which point the shift factor, a_T, and the coefficient K become functions of strain rate, as well as of time and temperature. This is demonstrated for unplasticized PVC in Fig. 9.34 [20]. For the temperature range below T_g, displayed in Fig. 9.33, the data can easily be shifted, allowing the generation of a *master curve* at the reference temperature, T_{ref}. Figure 9.35 [20] shows such master curves for the three coefficients E_0, D_1 and D_2 in Eq. 9.83 for the amorphous PVC shown in Figs. 9.33 and 9.34. For comparison, Fig. 9.36 [20] shows E_0 and D_2 for a high density polyethylene at 23 °C as a function of strain rate.

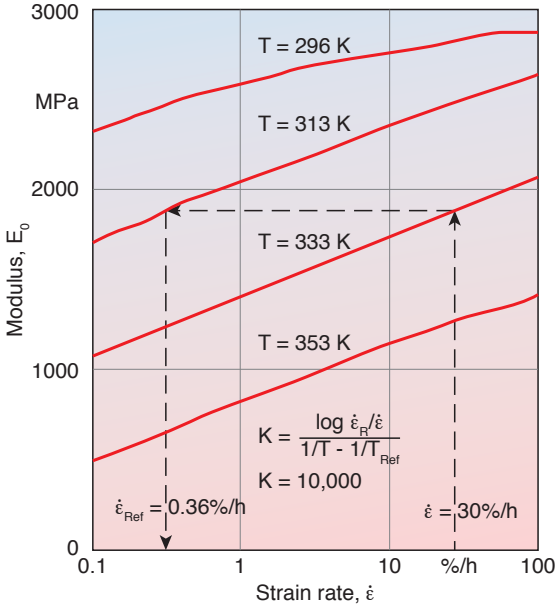

Figure 9.33 Plot of the elastic property E_0 and determining strain rate shift for an unplasticized PVC

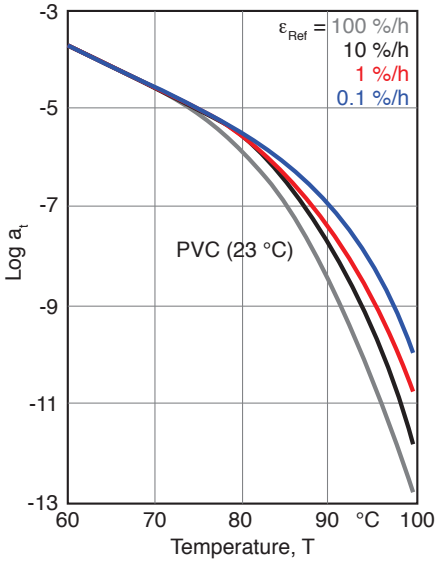

Figure 9.34 Time-temperature shift factor for an unplasticized PVC at several rates of deformation

The values of E_0, D_1 and D_2 can be easily calculated for each strain rate from the stress-strain diagram [21]. The modulus E_0 simply corresponds to the tangent modulus at small deformations where

$$\sigma \approx E_0 \varepsilon \tag{9.88}$$

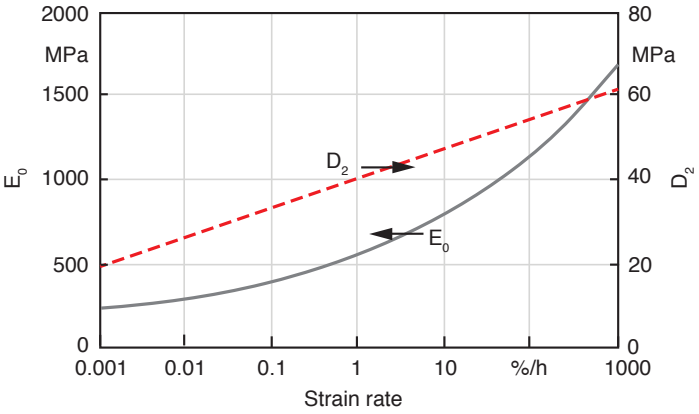

Figure 9.35 Master curves for E_0, D_1, and D_2 for an amorphous unplasticized PVC

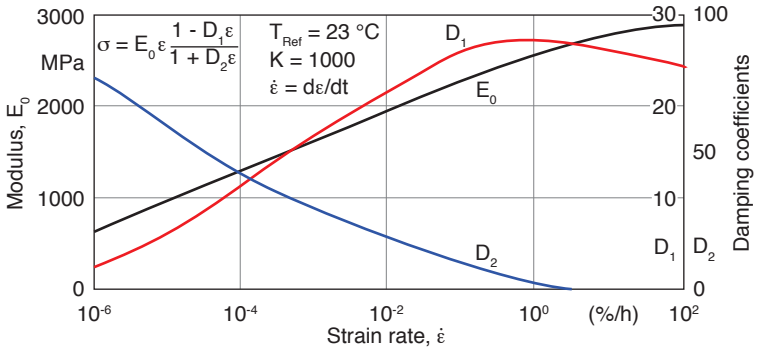

Figure 9.36 Coefficients E_0 and D_2 for a high density polyethylene at 23 °C

Assuming that for amorphous thermoplastics $D_2 \approx 0$ when $T \ll T_g$ and for semi-crystalline thermoplastics $D_1 \approx 0$ when $T \gg T_g$ we can compute D_1 and D_2 from

$$D_1 = \frac{\sigma_2 \varepsilon_1 - \sigma_1 \varepsilon_2}{\sigma_2 \varepsilon_1^2 - \sigma_1 \varepsilon_2^2} \tag{9.89}$$

$$D_2 = \frac{\sigma_1 \varepsilon_2 - \sigma_2 \varepsilon_1}{\varepsilon_1 \varepsilon_2 (\sigma_2 - \sigma_1)} \tag{9.90}$$

By introducing the values of E_0, D_1, and D_2, plotted in Fig. 9.35, into Eq. 9.83 one can generate long-term behavior curves as shown in the isochronous plots in Fig. 9.37 [20]. Here, the stress-strain behavior of unplasticized PVC is presented at constant times from 0.1 to 1000 hours of loading time. This is done by simply determining which strain rate results in a certain value of strain for a specific isochronous curve (time), then reading the values of E_0, D_1, and D_2 from the graphs and computing the corresponding stress using Eq. 9.83. With this technique and the application of the time-temperature superposition on short-term tests, the long-term behavior of polymers, which is usually measured using time consuming creep or relaxation tests, can be approximated.

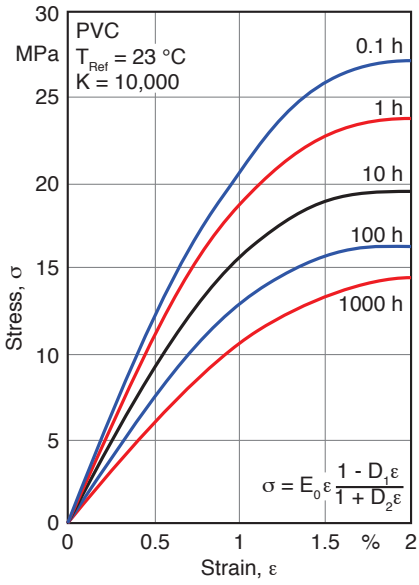

Figure 9.37 Isochronous stress-strain curves for an unplasticized PVC

As a final note, similar to the effect of a rise in temperature, a solvent can increase the overall toughness of the material at the sacrifice of its strength and stiffness. This is shown in Fig. 9.38 [20] for a PVC plasticized with 10 and 20 % dioctylphthalate (DOP), respectively. Figure 9.39 [20] shows the coefficients E_0 and D_2 for a PVC plasticized with 10 and 20 % DOP. Figure 9.40 [20] demonstrates the similar effects of temperature and plasticizer.

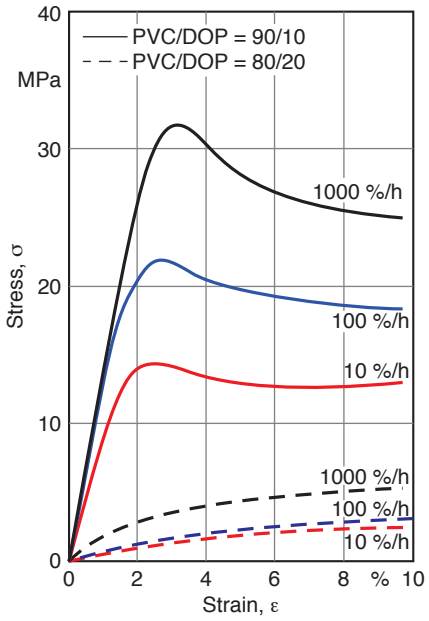

Figure 9.38 Stress-strain responses at various rates of deformation for a plasticized PVC with two plasticizer (DOP) concentrations

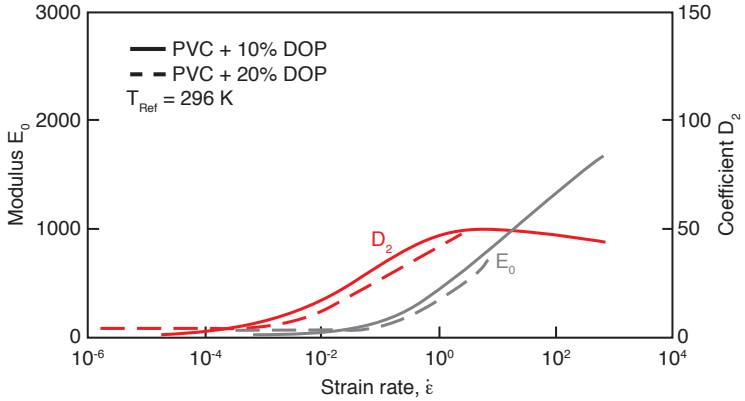

Figure 9.39 Coefficients E_0 and D_2 for polyvinyl chloride plasticized with 10% and 20% DOP, respectively

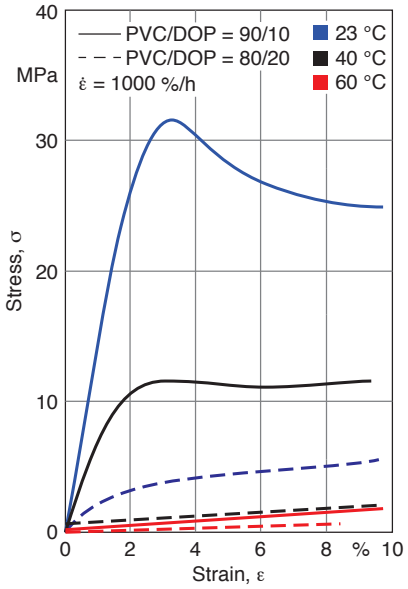

Figure 9.40 Stress-strain responses at various temperatures for a plasticized PVC with two plasticizer (DOP) concentrations

9.5 Creep Test

The stress relaxation and the creep test are well-known long-term tests that reflect time dependent behavior caused by the ability of the molecules to slide past each other when subjected to a stress. The stress relaxation test, discussed earlier, is difficult to perform and is therefore often approximated by data acquired through the more commonly used *creep test.* The stress relaxation of a polymer is often thought of as the inverse of creep.

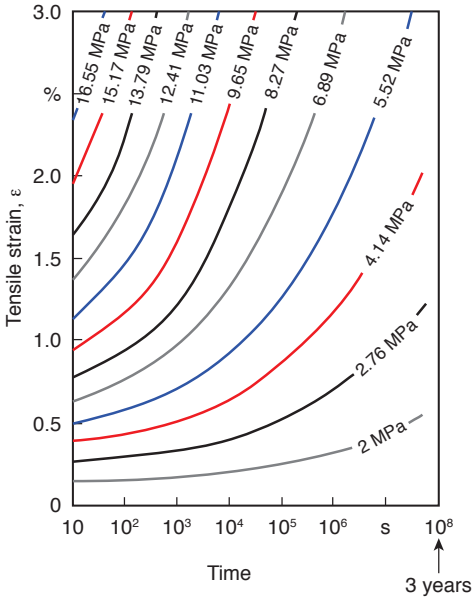

Figure 9.41 Creep response of a propylene-ethylene copolymer at 20 °C

The creep test, which can be performed either in shear, compression, or tension, measures the flow of a polymer component under a constant load. It is a common test that measures the strain, ε, as a function of stress, time, and temperature. Standard creep tests such as DIN 53 444 and ASTM D2990 can be used. Creep tests are performed at a constant temperature using a range of applied stress, as shown in Fig. 9.41 [22], where the creep responses of a polypropylene copolymer are presented for a range of stresses in a graph with a log scale for time. When plotting creep data in a log-log graph, in the majority of the cases, the creep curves reduce to straight lines as shown for polypropylene in Fig. 9.42 [6]. Hence, the

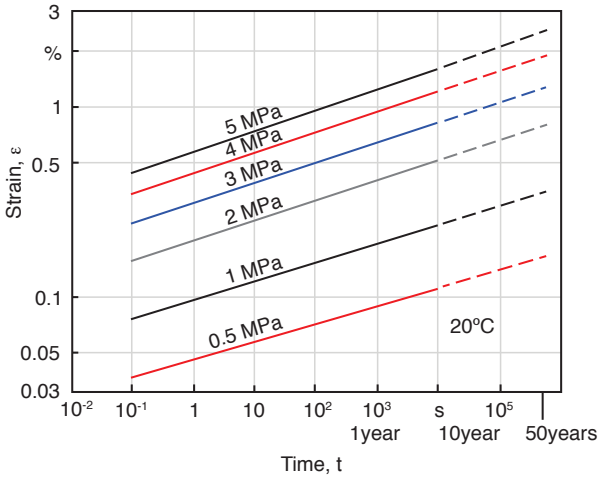

Figure 9.42 Creep response of a polypropylene plotted on a log-log scale

creep behavior of most polymers can be approximated with a power-law model represented by

$$\varepsilon(t) = M(\sigma, T)t^n \tag{9.91}$$

where M and n are material-dependent properties.

Similar to the stress relaxation test, the creep behavior of a polymer depends heavily on the material temperature during testing, exhibiting the highest rates of deformation around the glass transition temperature. This is demonstrated in Fig. 9.43 [23], which presents the creep compliance of plasticized PVC.

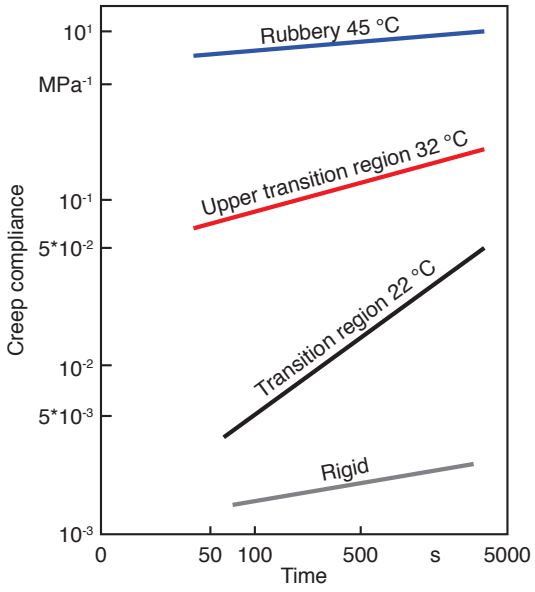

Figure 9.43 Creep compliance of a plasticized PVC at different temperatures

Creep data is very often presented in terms of creep modulus, E_c, defined by

$$E_c = \frac{\sigma_0}{\varepsilon(t)} \tag{9.92}$$

Figure 9.44 [24] presents the creep modulus for various materials as a function of time.

Depending on the time scale of the experiment, a property that also varies considerably during testing is Poisson's ratio, ν. Figure 9.45 [19] shows Poisson's ratio for PMMA deformed at rates (%/h) between 10^{-2} (creep) and 10^3 (impact). The limits are $\nu = 0.5$ (fluid) for high temperatures or very slow deformation speeds and $\nu = 0.33$ (solid) at low temperatures or high deformation speeds.

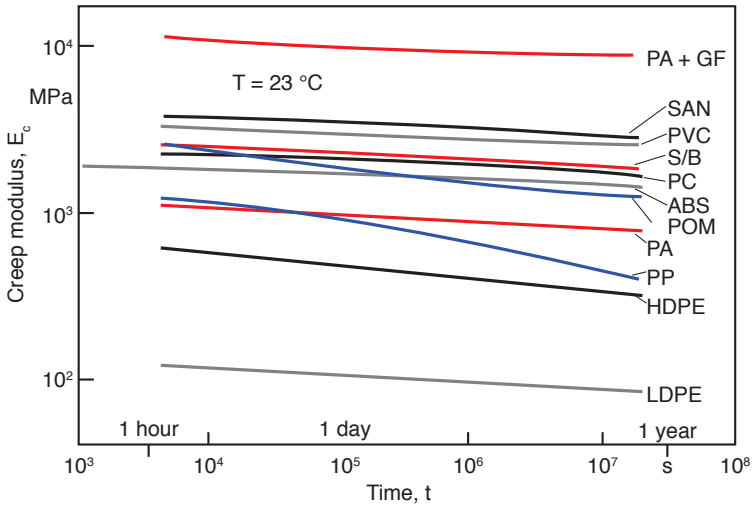

Figure 9.44 Time dependence of creep moduli for several polymers

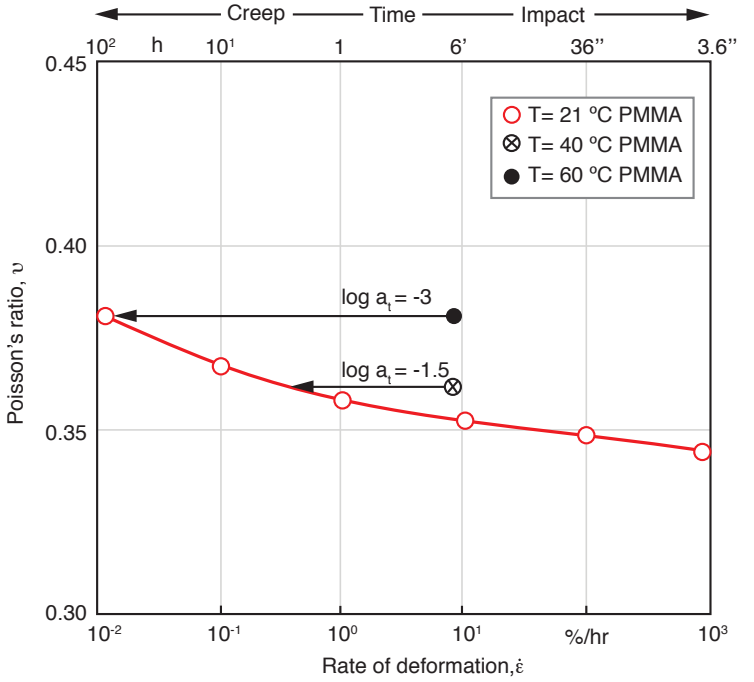

Figure 9.45 Poisson's ratio as a function of rate of deformation for PMMA at various temperatures

9.5.1 Isochronous and Isometric Creep Plots

Typical creep test data, as shown in Fig. 9.41, can be manipulated to be displayed as short-term stress-strain tests or as stress relaxation tests. These manipulated creep-test-data curves are called *isochronous* and *isometric* graphs.

An isochronous plot of the creep data is generated by cutting sections through the creep curves at constant times and plotting the stress as a function of strain. The isochronous curves of the creep data displayed in Fig. 9.41 are presented in Fig. 9.46 [22]. Similar curves can also be generated by performing a series of *short creep tests*, where a specimen is loaded at a specific stress for a short period of time, typically around 100 s [25]. The load is then removed, and the specimen is allowed to relax for a period of 4 times longer than the time of the creep test. The specimen is then reloaded at a different stress, and the test is repeated until a sufficient number of points have been created to plot an isochronous graph. This procedure is less time-consuming than the regular creep test and is often used to predict the short-term behavior of polymers. However, it should be pointed out that the short-term tests described earlier are more accurate and cheaper to perform.

The isometric or "equal size" plots of the creep data are generated by taking constant strain sections of the creep curves and by plotting the stress as a function of time. Isometric curves of the polypropylene creep data presented in Fig. 9.41 are shown in Fig. 9.47 [22]. This plot resembles the stress relaxation test results and is often used in the same manner. When we divide the stress axis by the strain, we can also plot the modulus versus time.

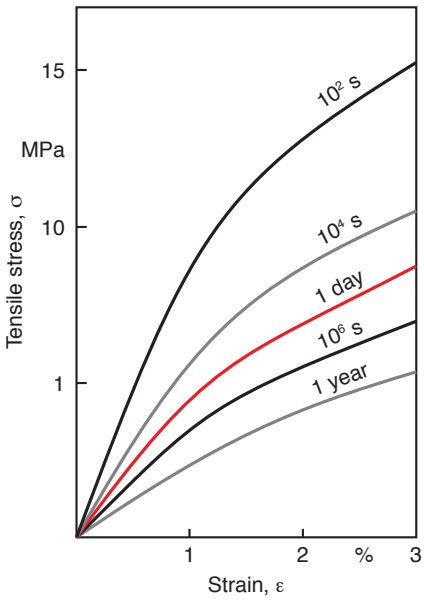

Figure 9.46 Isochronous stress-strain curves for the propylene-ethylene copolymer creep responses shown in Figure 9.41

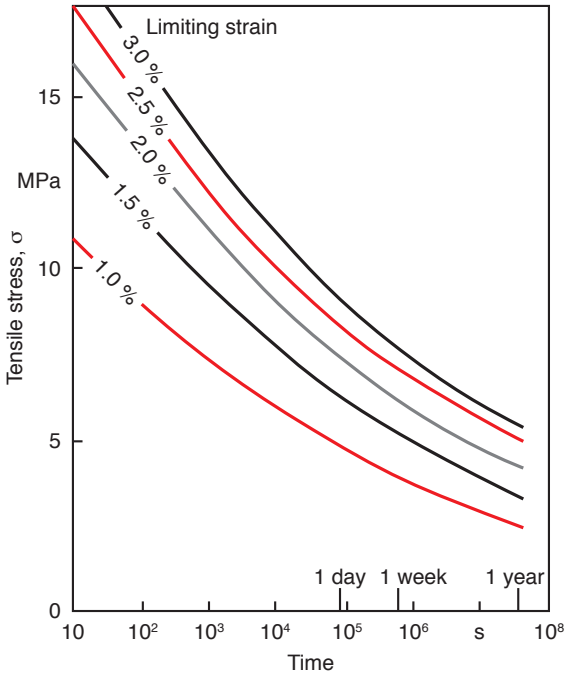

Figure 9.47 Isometric stress-time curves for the propylene-ethylene copolymer creep responses shown in Figure 9.41

■ 9.6 Dynamic Mechanical Tests

As is done to measure rheological behavior of polymer melts, short time scale mechanical behavior of polymers can also be evaluated using oscillatory tests.

9.6.1 Torsion Pendulum

The simplest dynamic mechanical test is the torsion pendulum. The standard procedure for the torsional pendulum, schematically shown in Fig. 9.48 [26], is described in DIN 53445 and ASTM D2236. The technique is applicable to virtually all plastics over a wide range of temperatures; from the temperature of liquid nitrogen, −180 °C to 50 – 80 °C above the glass transition temperature in amorphous thermoplastics and up to the melting temperature in semi-crystalline thermoplastics. Torsional tests for thermoset polymers can reach the degradation temperatures of the material.

The torsion pendulum apparatus is made of an inertia wheel, grips, and the specimen contained in a temperature-controlled chamber. The rectangular test specimen can be cut from a polymer sheet or part, or it can be made by injection molding.

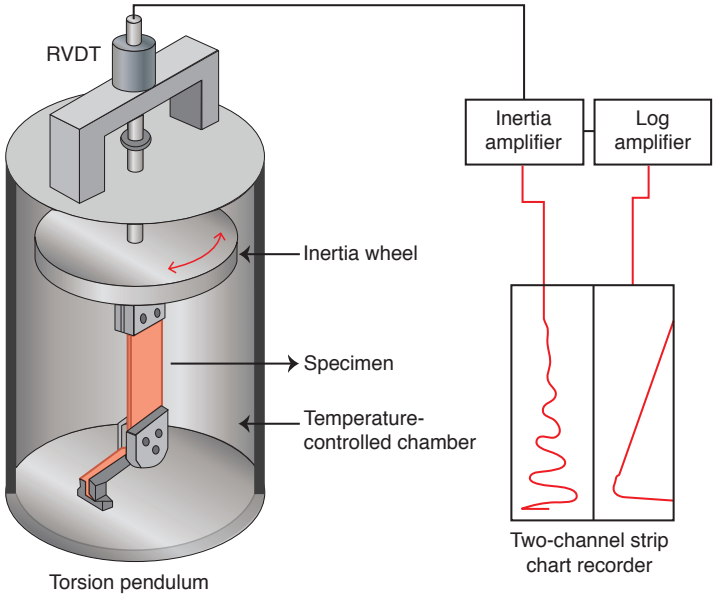

Figure 9.48 Schematic diagram of the torsion pendulum test equipment

To execute the test, the inertia wheel is deflected, then released and allowed to oscillate freely. The angular displacement or twist of the specimen is recorded over time. The frequency of the oscillations is directly related to the elastic shear modulus of the specimen, G', and the decay of the amplitude is related to the damping or *logarithmic decrement*, Δ, of the material. The elastic shear modulus (Pascals) can be computed using the relation[6]

$$G' = \frac{6.4\pi^2 ILf^2}{\mu bt^3} \tag{9.93}$$

where I is the polar moment of inertia (g/cm^2), L the specimen length (cm), f the frequency (Hz), b the width of the specimen, t the thickness of the specimen, and μ a shape factor, which depends on the width-to-thickness ratio. Typical values of μ are listed in Table 9.2 [23]. The logarithmic decrement can be computed using

$$\Delta = \ln\left(\frac{A_n}{A_{n+1}}\right) \tag{9.94}$$

where A_n represents the amplitude of the nth oscillation.[7] Although the elastic shear modulus, G', and the logarithmic decrement, Δ, are sufficient to characterize a material, one can also compute the loss modulus G'' by using

$$G'' = \left(\frac{G'\Delta}{\pi}\right) \tag{9.95}$$

6 For more detail, please consult ASTM D2236.

7 When $\Delta > 1$, a correction factor must be used to compute G'. See ASTM D2236.

Table 9.2 Shape Factor μ for Various Rectangular Cross-Sections

Ratio of specimen width to thickness	μ
1.0	2.249
1.2	2.658
1.4	2.990
1.6	3.250
1.8	3.479
2.0	3.659
2.5	3.990
3.0	4.213
4.0	4.493
5.0	4.662
10.0	4.997
50.0	5.266
∞	5.333

The logarithmic decrement can also be written in terms of *loss tangent*, $\tan\delta$, where δ is the out-of-phase angle between the strain and stress responses. The loss tangent is defined as

$$\tan\delta = \frac{G''}{G'} = \frac{\Delta}{\pi} \tag{9.96}$$

Figures 9.49 [6] and 9.50 [6] show the elastic shear modulus and the loss tangent for high impact polystyrene, and various polypropylene grades, respectively. In the graph for high impact polystyrene, the glass transition temperatures for polystyrene at 120 °C and for butadiene at −50 °C, are visible. For the polypropylene grades, the glass transition temperatures and the melting temperatures can be seen. The vertical scale in plots such as Figs. 9.49 and 9.50 is usually a logarithmic

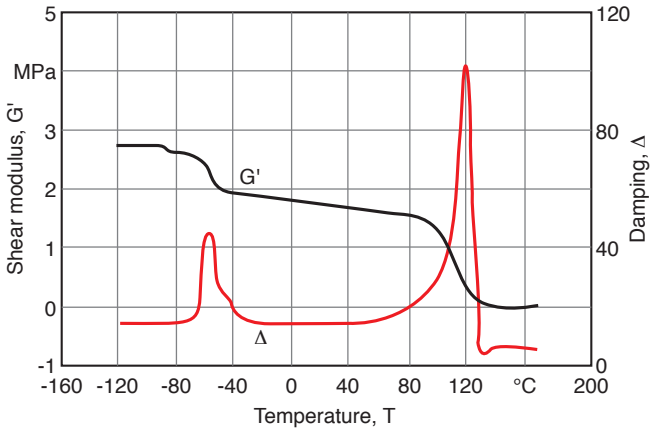

Figure 9.49 Elastic shear modulus and loss tangent for HIPS

scale. However, a linear scale better describes the mechanical behavior of polymers in design aspects. Figure 9.51 [6] presents the elastic shear modulus on a linear scale for several thermoplastic polymers as a function of temperature.

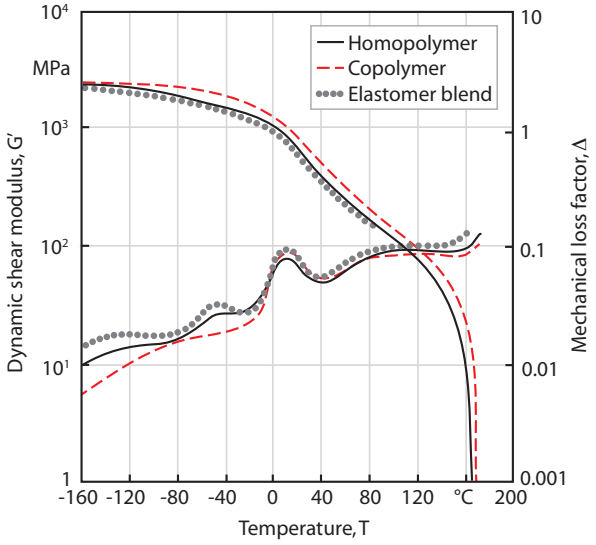

Figure 9.50 Elastic shear modulus and loss tangent for various polypropylene grades

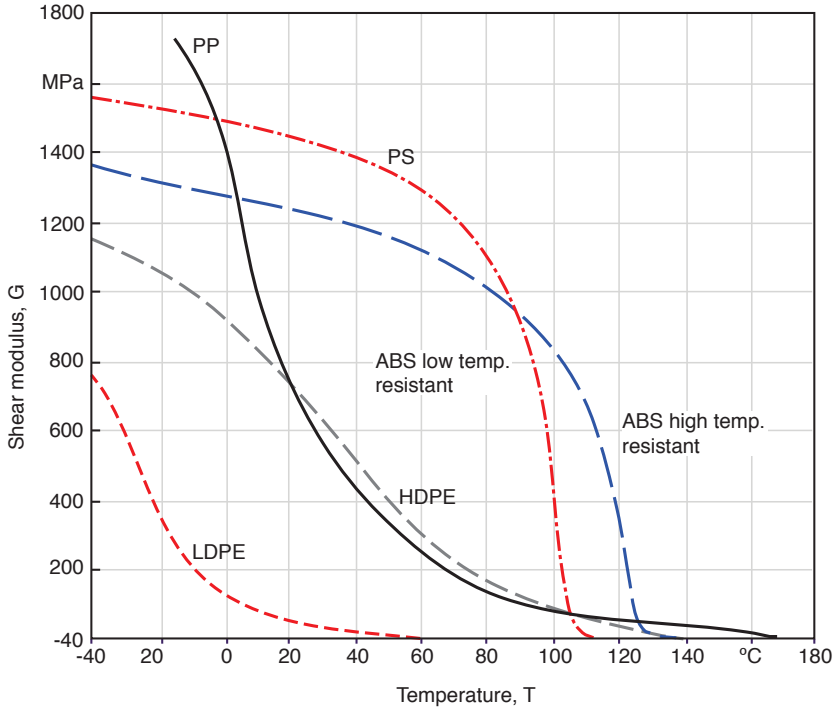

Figure 9.51 Elastic shear modulus for several thermoplastics

9.6.2 Sinusoidal Oscillatory Test

In the sinusoidal oscillatory test, a specimen is excited with a low frequency stress input that is recorded along with the strain response. The shapes of the test specimen and the testing procedure vary significantly from test to test. The various tests and their corresponding specimens are described by ASTM D4065 and the terminology, such as the one already used in Eqs. 9.93–9.96, is described by ASTM D4092.

If the test specimen in a sinusoidal oscillatory test is perfectly elastic, the stress input and strain response would be as follows:

$$\tau(t) = \tau_0 \cos \omega t \tag{9.97}$$

$$\gamma(t) = \gamma_0 \cos \omega t \tag{9.98}$$

For an ideally viscous test specimen, the strain response would lag $\pi/2$ radians behind the stress input:

$$\tau(t) = \tau_0 \cos \omega t \tag{9.99}$$

$$\gamma(t) = \gamma_0 \cos\left(\omega t - \frac{\pi}{2}\right) \tag{9.100}$$

Polymers behave somewhere in between the perfectly elastic and the perfectly viscous materials and their response is described by

$$\tau(t) = \tau_0 \cos \omega t \quad \text{and} \tag{9.101}$$

$$\gamma(t) = \gamma_0 \cos(\omega t - \delta) \tag{9.102}$$

The shear modulus takes a complex form of

$$G^* = \frac{\tau(t)}{\gamma(t)} = \frac{\tau_0 e^{i\delta}}{\gamma_0} = \frac{\tau_0}{\gamma_0}(\cos\delta + i \sin\delta) = G' + G'' \tag{9.103}$$

which is graphically represented in Fig. 9.52. G' is usually referred to as *storage modulus* and G'' as *loss modulus*. The ratio of loss modulus to storage modulus is referred to as *loss tangent:*

$$\tan\delta = \frac{G''}{G'} \tag{9.104}$$

Models such as the Maxwell model described by Eq. 9.31 can also be used to simulate the dynamic response of polymers. In a dynamic test[8] the strain input is given by

$$\varepsilon = \varepsilon_0 \sin(\omega t) \tag{9.105}$$

8 The dynamic test is discussed in more detail in Chapter 8.

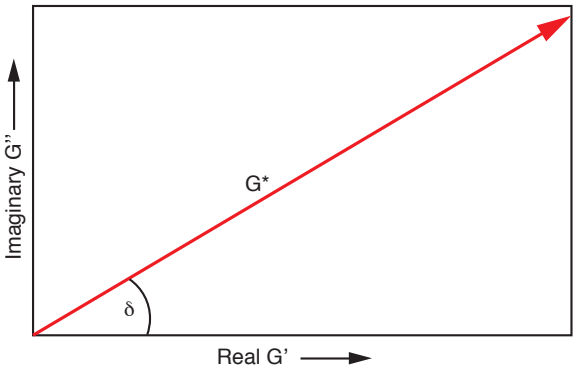

Figure 9.52 Vector representation of the complex shear modulus

where ε_0 is the strain amplitude and ω the frequency in radians per second. Differentiating Eq. 9.105, combining with Eq. 9.31, and integrating results in

$$\sigma = \left(\frac{E\varepsilon_0\omega\lambda}{1+(\omega\lambda)^2}\right)\left(\omega\lambda\sin(\omega t)+\cos(\omega t)\right) \tag{9.106}$$

for a steady state response. Dividing Eq. 9.70 by the amplitude of the strain input results in a complex modulus, which is formed by an elastic component, that is in-phase with the strain input, and a viscous component. The elastic term is generally called the *storage modulus* and is defined by

$$E' = \left(\frac{E(\omega\lambda)^2}{1+(\omega\lambda)^2}\right) \tag{9.107}$$

and the viscous term, usually referred to as the *loss modulus*, is given by

$$E'' = \left(\frac{E\omega\lambda}{1+(\omega\lambda)^2}\right) \tag{9.108}$$

We can also consider the response of a Maxwell-Wiechert model subjected to a sinusoidal strain given by Eq. 9.42. In a similar analysis to that presented for the Kelvin model and for the Maxwell model, the *storage modulus* is given by

$$E' = \sum_{i=1}^{n}\left(\frac{E_i(\omega_i\lambda_i)^2}{1+(\omega_i\lambda_i)^2}\right) \tag{9.109}$$

and the viscous term or the *loss modulus*, is given by

$$E'' = \sum_{i=1}^{n}\left(\frac{E_i\omega_i\lambda_i}{1+(\omega_i\lambda_i)^2}\right) \tag{9.110}$$

9.7 Effects of Structure and Composition on Mechanical Properties

The shear modulus versus temperature diagram is a very useful description of the mechanical behavior of certain materials. It is possible to generate a general shear modulus versus temperature diagram for all polymers by using a reduced temperature described by

$$T_{red} = \frac{293K}{T_g} \tag{9.111}$$

Figure 9.53 [27] shows this diagram with the shear modulus of several polymers. The upper left side of the curve represents the stiff and brittle crosslinked materials, and the upper right side represents the semi-crystalline thermoplastics whose glass transition temperature is below room temperature. The lower right side of the curve represents elastomers, positioned accordingly on the curve depending on their degree of crosslinking.

9.7.1 Amorphous Thermoplastics

Amorphous thermoplastics exhibit "useful" behavior below their glass transition temperature. Figure 9.54 shows the shear modulus of an unplasticized PVC with respect to temperature. In this figure we observe that the material solidifies at the glass transition temperature, between 80 and 90 °C. We note that one cannot exactly pinpoint T_g but rather a range within which it will occur. In fact, at 60 °C the stiffness already dramatically drops as the U-PVC starts to soften. Below −10 °C, the U-PVC becomes very stiff and brittle, making it useful only between −10 °C and 60 °C for most applications. As mentioned before, the properties of thermoplastics can be modified by adding plasticizing agents. This is shown for PVC in Fig. 9.55, where the shear modulus drops at much lower temperatures when a plasticizing agent is added.

Often the tensile stress and strain at failure are plotted as a function of temperature. Figure 9.56 shows this for a typical amorphous thermoplastic. The figure shows how the material is brittle below the glass transition temperature and, therefore, fails at low strains. As the temperature increases, the strength of the amorphous thermoplastic decreases, as it becomes leathery in texture and is able to withstand larger deformations. Above T_g, the strength decreases significantly, as the maximum strain continues to increase, until the flow properties have been reached at which point the mechanical strength is negligible. This occurs around the "flow temperature" marked as T_f in the diagram. If the temperature is further

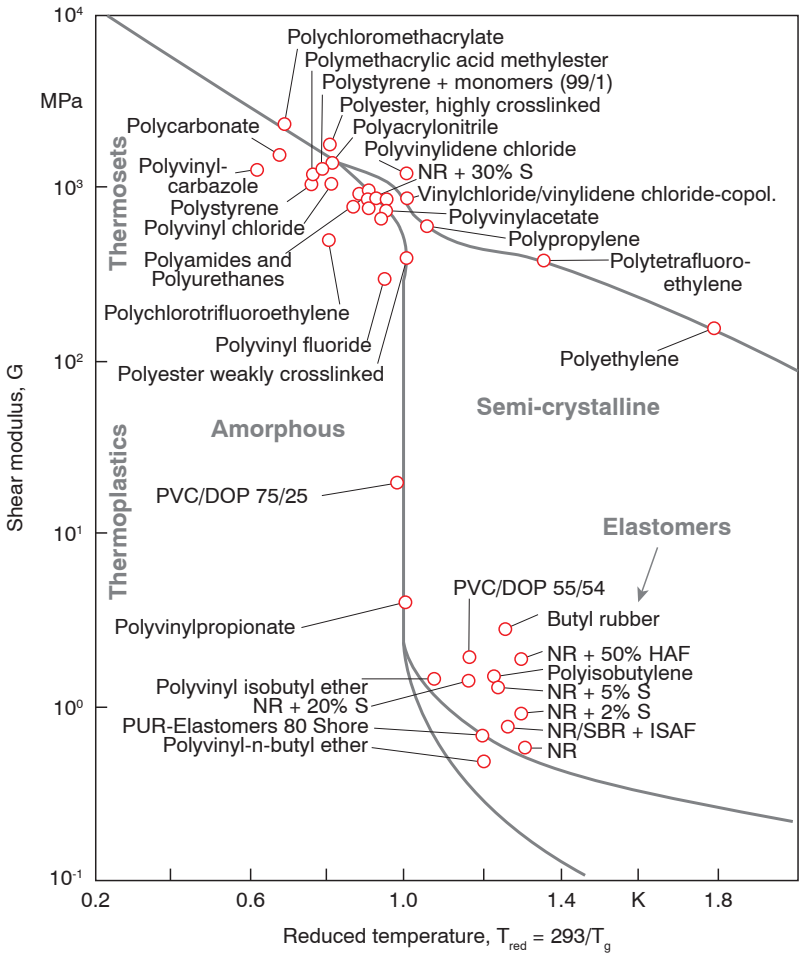

Figure 9.53 Shear modulus of several polymers as a function of reduced glass transition temperature

increased, the material will eventually thermally degrade at the degradation temperature, T_d.

Some amorphous thermoplastics can be made high impact resistant (less brittle) through copolymerization. The most common example is acrylonitrile-butadiene-styrene, also known as ABS. Since butadiene chains vitrify at temperatures below −50 °C, ABS is very tough at room temperature in contrast to polystyrene and acrylics by themselves. Due to the different glass transition temperatures present in the materials forming the blend, ABS shows two general transition regions, one around −50 °C and the other at 110 °C, visible in both the logarithmic decrement and the shear modulus.

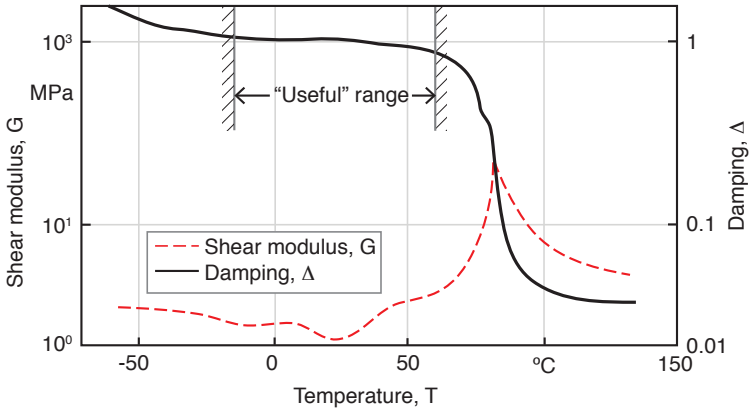

Figure 9.54 Shear modulus and mechanical damping for an unplasticized PVC

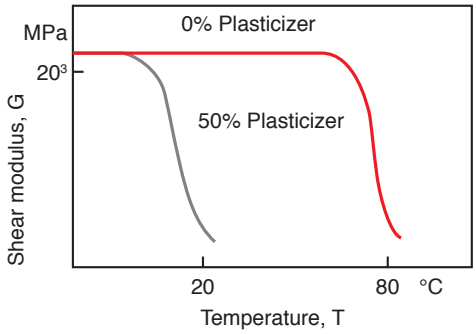

Figure 9.55 Shear modulus as a function of temperature for a PVC with and without a plasticizing agent

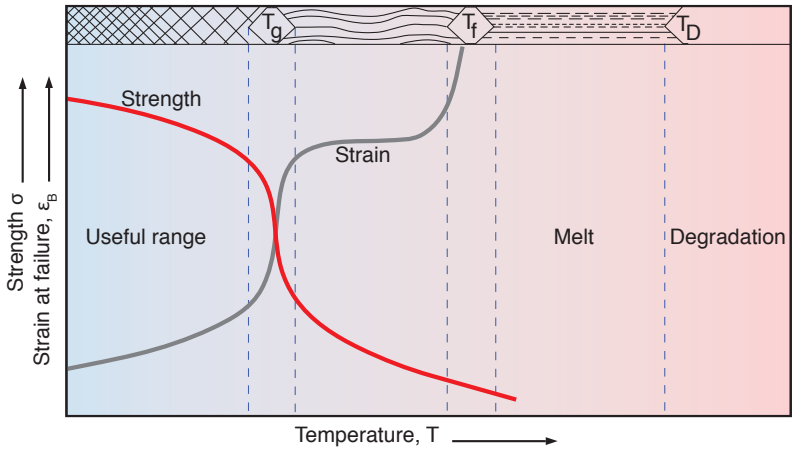

Figure 9.56 Tensile strength and strain at failure as a function of temperature for an amorphous thermoplastic

9.7.2 Semi-Crystalline Thermoplastics

The properties of semi-crystalline thermoplastics can also be analyzed by plotting mechanical properties with respect to temperature. An interesting example is shown in Fig. 9.57, which presents plots of shear modulus versus temperature for polystyrenes with different molecular structures after having gone through different stereo-specific polymerization techniques: low molecular weight PS (A), a high molecular weight PS (B), a semi-crystalline PS (C), and a crosslinked PS (D). In Fig. 9.57 we can see that the low molecular weight material flows before the high molecular weight one, simply due to the fact that the shorter chains can slide past each other more easily – reflected in the lower viscosity of the low molecular weight polymer. The semi-crystalline PS shows a certain amount of stiffness between its glass transition temperature at around 100 °C and its melting temperature at 230 °C. Because a semi-crystalline polystyrene is still brittle at room temperature, it is not very useful to the polymer industry. Figure 9.57 also demonstrates that a crosslinked polystyrene will not melt.

Semi-crystalline thermoplastics are leathery and tough at room temperature because their atactic and amorphous regions vitrify at much lower temperatures.

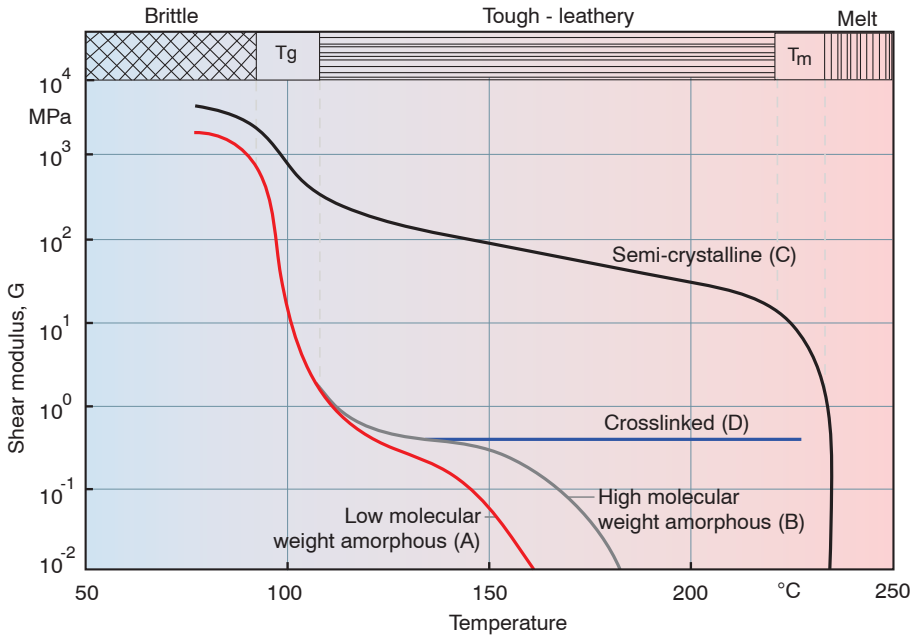

Figure 9.57 Shear modulus curves for amorphous, semi-crystalline, and crosslinked polystyrene; (A) low molecular weight amorphous, (B) high molecular weight amorphous, (C) semi-crystalline, (D) cross-linked

Figure 9.58 shows the shear modulus plotted versus temperature for polypropylene at various degrees of crystallinity. In each case the amorphous regions "solidify" at around 0 °C, whereas the melting temperature goes up significantly with increasing degree of crystallinity. The brittle behavior of polypropylene at 0 °C can sometimes pose a problem in design. This problem can be mitigated through copolymerization – in this case PP copolymerized with ethylene or with elastomers such as ethylene-propylene-diene terpolymer (EPDM).

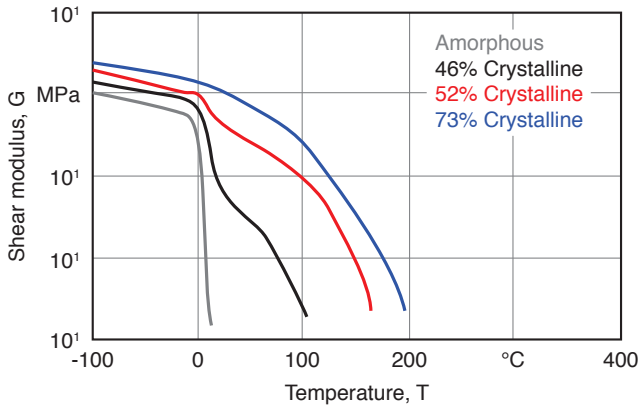

Figure 9.58 Shear modulus for polypropylene with various degrees of crystallinity

The tensile stress and the strain at failure for a common semi-crystalline thermoplastic are shown in Fig. 9.59. The figure shows an increase in toughness between the glass transition temperature and the melting temperature. The range between T_g and T_m applies to most semi-crystalline thermoplastics.

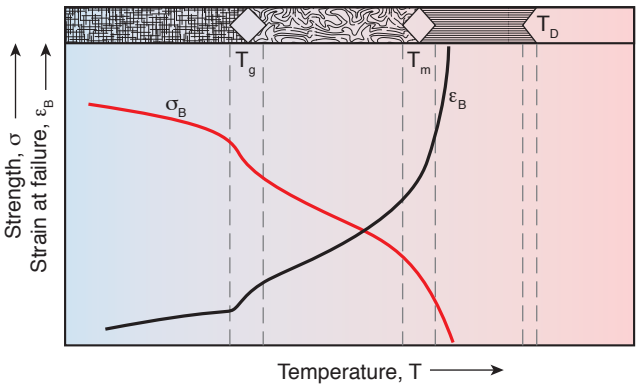

Figure 9.59 Tensile strength and strain at failure as a function of temperature for a semi-crystalline thermoplastic

9.7.3 Oriented Thermoplastics

If a thermoplastic is deformed at a temperature high enough so that the polymer chains can slide past each other but low enough such that the relaxation time is much longer than the time it takes to stretch the material, the orientation generated during stretching is retained within the polymer component. We note that the amount of stretching, L/L_0, is not always proportional to the degree of orientation within the component; for example, if the temperature is too high during stretching, the molecules may have a chance to fully relax, resulting in a component with little or no orientation. Any degree of orientation results in property variations within thermoplastic polymers. Figure 9.60 [28] shows the influence stretching has on various properties of common amorphous thermoplastics. The stretching will lead to decreased strength and stiffness properties perpendicular to the orientation and increased properties parallel to the direction of deformation. In addition, highly oriented materials tend to split along the orientation direction under small loads.

In amorphous thermoplastics the stretching that leads to permanent property changes occurs approx. 20 to 40 °C above the glass transition temperature, T_g, whereas with semi-crystalline thermoplastics they occur approx. 10 to 20 °C below the melting temperature, T_m. After stretching a semi-crystalline polymer, it must be annealed at temperatures high enough that the amorphous regions relax. During stretching the spherulites break up as whole blocks of lamellae slide out, shown schematically in Fig. 9.61 [29]. Whole lamellae can also rotate such that by sufficiently high stretching, all molecules are oriented in the same direction. The lamellae blocks are now interconnected by what is generally called *tie molecules*. If this material is annealed in a fixed position, a very regular, oriented structure can be generated. This highly oriented material becomes dimensionally stable at elevated temperatures, including temperatures slightly below the annealing or fixing temperature. However, if the component is not fixed during the annealing process, the structure before stretching would be recovered. Figure 9.62 shows stress-strain plots for polyethylene with various morphological structures. If the material is stretched such that a needle-like or fibrilic morphological structure results, the resulting stiffness of the material is very high. Obviously, a more realistic structure that would result from stretching would lead to a stacked, plate-like structure with lower stiffness and ultimate strength. An unstretched morphological structure would be composed of spherulites and exhibit much lower stiffness and ultimate strength. The strength of fibrilic structures is taken advantage of when making synthetic fibers. Figure 9.63 shows theoretical and achievable elastic moduli of various synthetic fiber materials.

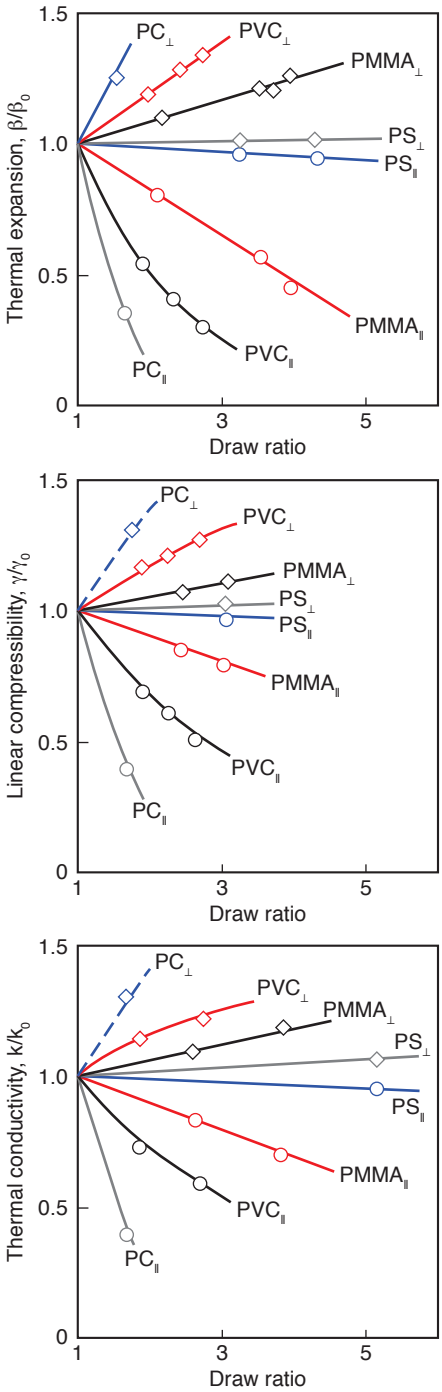

Figure 9.60 Influence of stretch on different properties of amorphous thermoplastics: (top) thermal expansion, (center) linear compressibility, (bottom) thermal conductivity

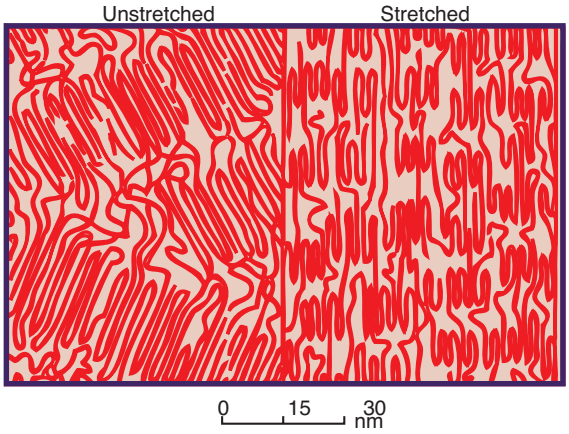

Figure 9.61 Schematic of the sliding and re-orientation of crystalline blocks in semi-crystalline thermoplastics

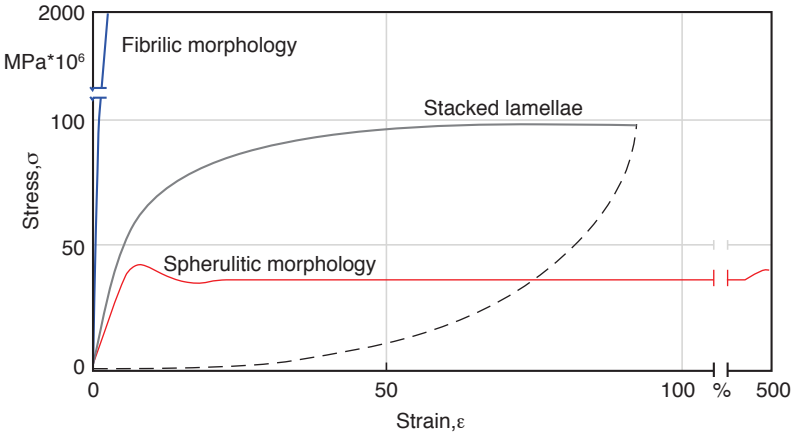

Figure 9.62 Stress-strain behavior of polyethylene with various morphologies

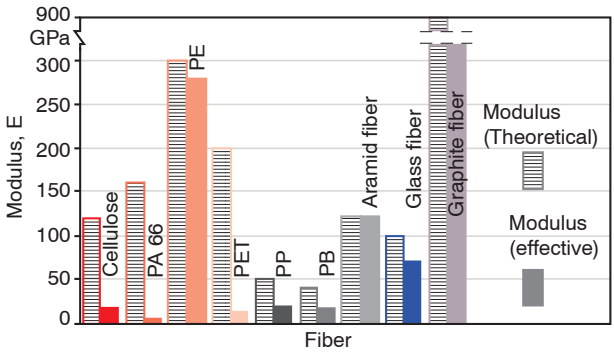

Figure 9.63 Tensile modulus for various fibers

High-stiffness and high-strength synthetic fibers are becoming increasingly important for lightweight, high-strength applications. Extended-chain ultra-high molecular weight polyethylene fibers have only been available commercially since the mid-1980s. The fibers are manufactured by drawing or extending fibers of small diameters at temperatures below the melting point. The modulus and strength of the fiber increase with the drawing ratio or stretch. Due to intermolecular entanglement, the natural draw ratio of high molecular weight high-density polyethylene[9] is only 5. To increase the draw ratio by a factor of 10 or 100, polyethylene must be processed in a solvent such as paraffin oil or paraffin wax.

Figure 9.64 [30] presents the tensile modulus of super-drawn, ultra-high molecular weight high-density polyethylene fibers as a function of draw ratio. It can be seen that at draw ratios of 250, a maximum modulus of 200 GPa is reached. In addition to amorphous and semi-crystalline thermoplastics, there is a whole family of thermoplastic materials whose molecules do not relax and, thus, retain their orientation even in the melt state. This class of thermoplastics is the *liquid crystalline polymers*. One such material is the aramid fiber, most commonly known by its trade name, Kevlar, which has been available in the market for many years. To demon-

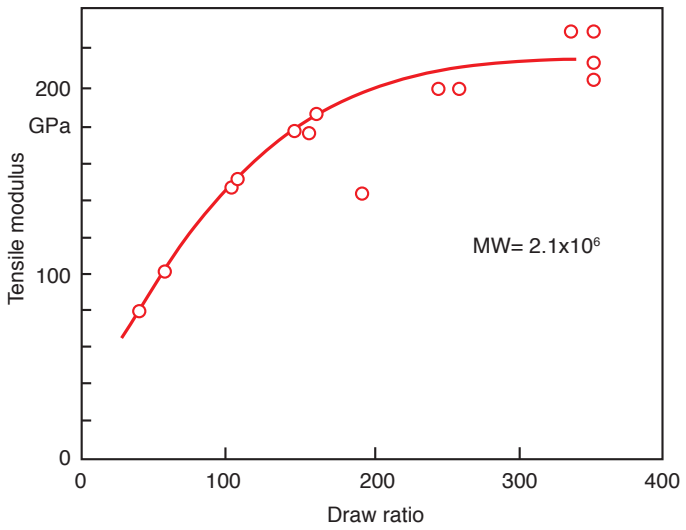

Figure 9.64 Tensile modulus as a function of draw ratio for a UHMWPE ($M_w \sim 2 \times 10^6$)

9 It is interesting that a semi-crystalline thermoplastic stretches more at low molecular weights than at high molecular weights. This contradicts what we expect from theory that longer molecules allow the component to stretch following the relation $\lambda_{max} \approx M^{0.5}$. An explanation for this may be the *trapped entanglements* found in high molecular weight, semi-crystalline polymers that act as semi-permanent crosslinks that rip at smaller deformations.

strate the structure of liquid crystalline polymers, successive enlargement of an aramid pellet is shown in Fig. 9.65 [31]. For comparison, Table 9.3 presents mechanical properties of aramid and polyethylene fibers and other materials.

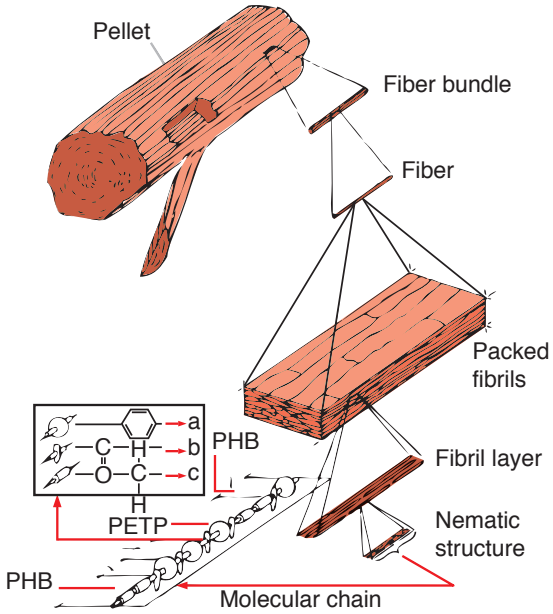

Figure 9.65 Schematic of the structure of a LC-PET

Table 9.3 Mechanical Properties of Selected Fibers

Fiber	Tensile strength (MPA)	Tensile modulus (GPa)	Elongation at break (%)	Specific gravity
Polyethylene	3000	172	2.7	0.97
Aramid	2760	124	2.5	1.44
Graphite	2410	379	0.6	1.81
S-glass	4585	90	2.75	2.50

The anisotropy of the oriented material can be approximated by assuming that there are covalent bonds joining the molecular chains along the orientation direction, whereas only van der Waals forces act in the two directions perpendicular to the main orientation. With this so-called 1:2 rule, we can write

$$a_{\parallel} + 2a_{\perp} = 3a_0 \quad \text{and} \tag{9.112}$$

$$a_1 + 2a_2 = 3a_0 \tag{9.113}$$

where a_0 is the property for the isotropic material, a_1 and a_2 are the values for the fully oriented material, and $a_{\parallel}$ and $a_{\perp}$ are the values that correspond to the parallel and perpendicular directions with respect to the main orientation. The actual degree of orientation in the above analysis is unknown. The 1 : 2 rule can be applied to strength properties such as elastic modulus and Poisson's ratio as well as to thermal expansion coefficient and thermal diffusivity. For the elastic modulus, we can write

$$\frac{1}{E_{\parallel}} + \frac{2}{E_{\perp}} = \frac{3}{E_0} \tag{9.114}$$

This rule can be used to approximate mechanical properties of synthetic fibers. For example, a polypropylene fiber will have a tensile elastic modulus of 700 MPa compared to an elastic modulus of 30 MPa for the isotropic material.

9.7.4 Crosslinked Polymers

Crosslinked polymers, such as thermosets and elastomers, behave completely differently than their counterparts, thermoplastic polymers. In crosslinked systems, the mechanical behavior is also best reflected by the plot of the shear modulus versus temperature. Figure 9.66 compares the shear modulus between highly crosslinked, crosslinked, and non-crosslinked polymers. The coarse crosslinked system, typical of elastomers, has a low modulus above the glass transition temperature. The glass transition temperature of these materials is usually below −50 °C, so they are soft and flexible at room temperature. On the other hand, highly crosslinked systems, typical in thermosets, show a smaller decrease in stiffness as the material is raised above the glass transition temperature; the decrease in properties becomes smaller as the degree of crosslinking increases. Figure 9.67 shows ultimate tensile strength and strain curves plotted versus temperature. It is clear that the strength remains fairly constant up to the thermal degradation temperature of the material.

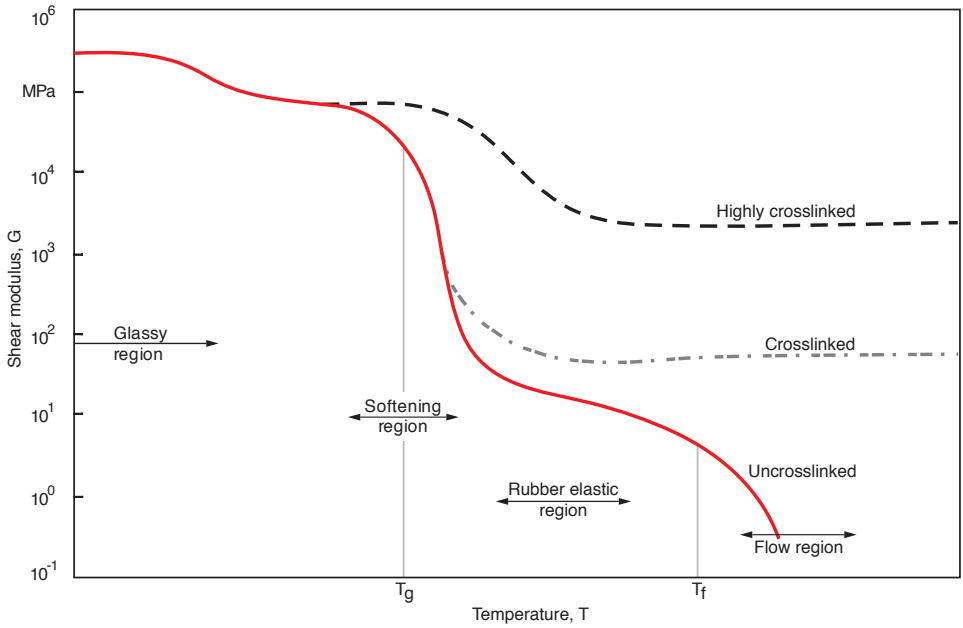

Figure 9.66 Shear modulus and behavior of cross-linked and non-crosslinked polymers

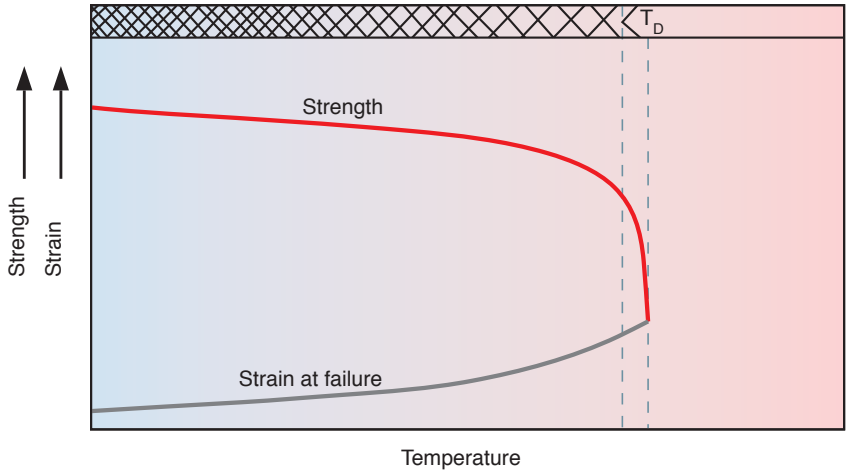

Figure 9.67 Tensile strength and strain at failure as a function of temperature for typical thermosets

9.8 Mechanical Behavior of Filled and Reinforced Polymers

When we talk about fillers, we refer to materials that are intentionally placed in polymers to make them stronger, lighter, electrically conductive, or cheaper. Any filler will affect the mechanical behavior of a polymeric material. For example, long fibers will make it stiffer but usually denser, whereas foaming will make it more compliant but much lighter. On the other hand, a filler such as calcium carbonate will decrease the polymer's toughness while making it considerably cheaper. Figure 9.68 [32] shows a schematic plot of the change in stiffness as a function of volume fraction for several types of filler materials.

Figure 9.69 shows the increase in dynamic shear modulus for polybutylene terephthalate with 10 and 30% glass fiber content. However, fillers often decrease the strength properties of polymers – this is discussed in more detail in the next chapter.

However, when we refer to reinforced plastics, we talk about polymers (matrix) whose properties have been enhanced by introducing a reinforcement (fibers) of higher stiffness and strength. Such a material is usually called a *fiber reinforced polymer* (FRP) or a *fiber reinforced composite* (FRC). The purpose of introducing a fiber into a matrix is to transfer the load from the weaker material to the stronger one. This load transfer occurs over the length of the fiber as schematically represented in Fig. 9.70. The length it takes to complete the load transfer from the

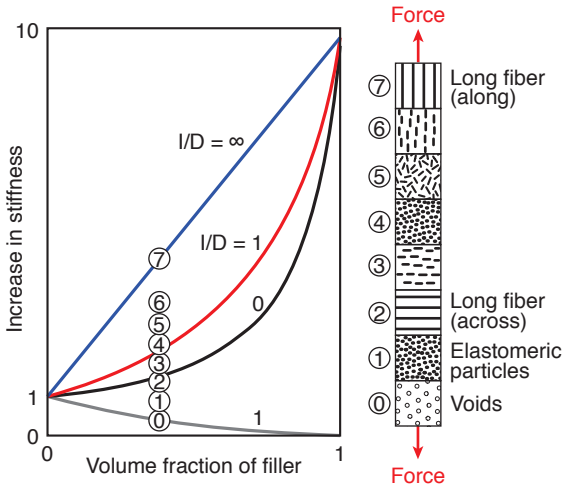

Figure 9.68 Relation between stiffness and filler type and orientation in polymeric materials

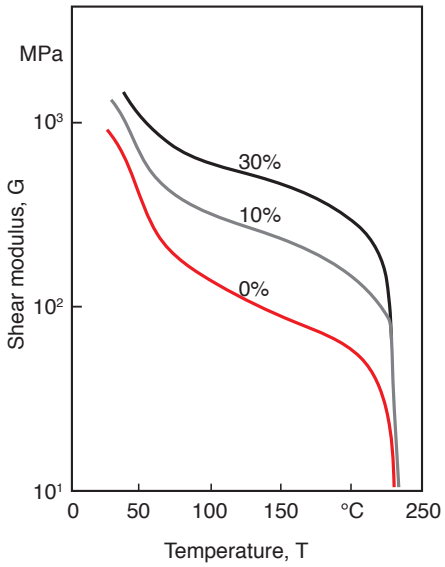

Figure 9.69 Shear modulus for a polybutylene terephthalate with various levels of glass fiber content by weight

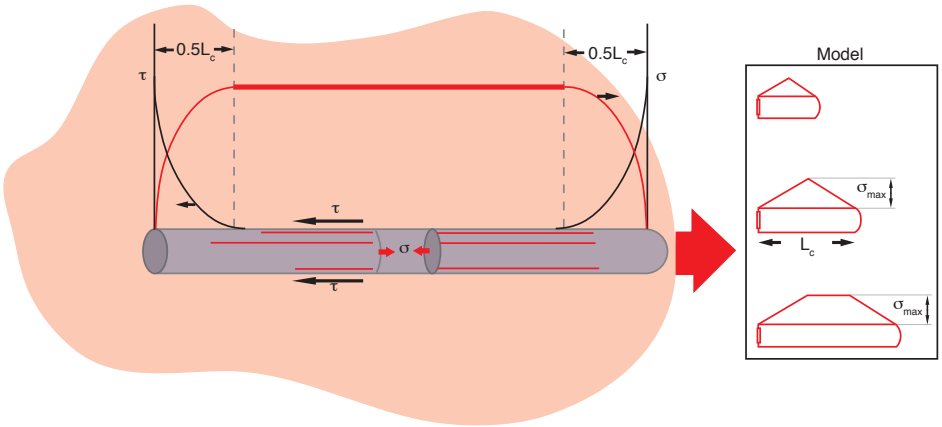

Figure 9.70 Schematic diagram of load transfer from matrix to fiber in a composite

matrix to the fiber, without fiber or matrix fracture, is usually referred to as critical length, L_c. For the specific case with perfect adhesion between fiber and matrix, the critical length can be computed as

$$L_c = D\frac{\sigma_{uf}}{2\tau_{um}} \tag{9.115}$$

where D is the fiber diameter, σ_{uf} is the tensile strength of the fiber and τ_{um} is the shear strength of the matrix. Although Eq. 9.115 predicts L/D as low as 10, experimental evidence suggests that aspect ratios of 100 or higher are required to

achieve maximum strength [33]. If composites have fibers that are shorter than their critical length, they are referred to as *short fiber composites*, and if the fibers are longer, they are referred to as *long fiber composites* [34].

9.8.1 Anisotropic Strain-Stress Relation

As discussed in Chapter 6, filled polymers are often anisotropic, and the relations presented in Eqs. 9.1 – 9.15 are not valid. The three-dimensional anisotropic strain-stress relation where, for simplicity, x, y, and z have been replaced by 1, 2, and 3, respectively, is often written as

$$\varepsilon_{11} = \frac{1}{E_{11}}\sigma_{11} - \frac{\nu_{21}}{E_{22}}\sigma_{22} - \frac{\nu_{31}}{E_{33}}\sigma_{33} \tag{9.116}$$

$$\varepsilon_{22} = -\frac{\nu_{12}}{E_{11}}\sigma_{11} + \frac{1}{E_{22}}\sigma_{22} - \frac{\nu_{32}}{E_{33}}\sigma_{33} \tag{9.117}$$

$$\varepsilon_{33} = -\frac{\nu_{13}}{E_{11}}\sigma_{11} - \frac{\nu_{23}}{E_{22}}\sigma_{22} + \frac{1}{E_{33}}\sigma_{33} \tag{9.118}$$

$$\gamma_{12} = \frac{1}{G_{12}}\tau_{12} \tag{9.119}$$

$$\gamma_{23} = \frac{1}{G_{23}}\tau_{23} \tag{9.120}$$

$$\gamma_{31} = \frac{1}{G_{31}}\tau_{31} \tag{9.121}$$

and in matrix form for the more general case:

$$\begin{Bmatrix} \varepsilon_{11} \\ \varepsilon_{22} \\ \varepsilon_{33} \\ \gamma_{12} \\ \gamma_{23} \\ \gamma_{31} \end{Bmatrix} = \begin{bmatrix} S_{11} & S_{12} & S_{13} & S_{14} & S_{15} & S_{16} \\ S_{21} & S_{22} & S_{23} & S_{24} & S_{25} & S_{26} \\ S_{31} & S_{32} & S_{33} & S_{34} & S_{35} & S_{36} \\ S_{41} & S_{42} & S_{43} & S_{44} & S_{45} & S_{46} \\ S_{51} & S_{52} & S_{53} & S_{54} & S_{55} & S_{56} \\ S_{61} & S_{62} & S_{63} & S_{64} & S_{65} & S_{66} \end{bmatrix} \begin{Bmatrix} \sigma_{11} \\ \sigma_{22} \\ \sigma_{33} \\ \tau_{12} \\ \tau_{23} \\ \tau_{31} \end{Bmatrix} \tag{9.122}$$

where coupling between the shear terms and the elongational terms can be introduced.

9.8.2 Aligned Fiber Reinforced Composite Laminates

The most often applied form of the above equations is the two-dimensional model used to analyze the behavior of aligned fiber reinforced laminates, such as that shown schematically in Fig. 9.71. For this simplified case, Eqs. 9.116–9.121 reduce to

$$\varepsilon_L = \frac{1}{E_L}\sigma_L - \frac{\nu_{TL}}{E_T}\sigma_T \tag{9.123}$$

$$\varepsilon_T = -\frac{\nu_{LT}}{E_L}\sigma_L + \frac{1}{E_T}\sigma_T \tag{9.124}$$

$$\gamma_{LT} = \frac{1}{G_{LT}}\tau_{LT} \tag{9.125}$$

which can also be written as

$$\{\varepsilon_{LT}\} = [S_{LT}]\{\sigma_{LT}\} \tag{9.126}$$

where the subscripts L and T define the longitudinal and transverse directions, respectively, as described in Fig. 9.71, and $[S_{LT}]$ is referred to as the compliance matrix.

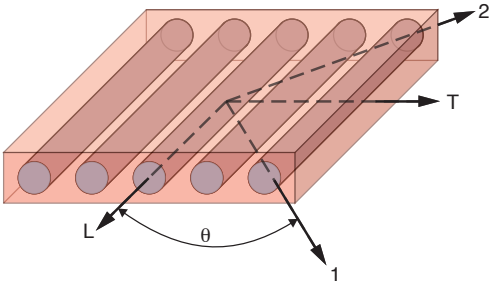

Figure 9.71 Schematic diagram of unidirectional continuous fiber reinforced laminated structure

The longitudinal and transverse properties can be calculated using the widely used Halpin-Tsai model [35] as

$$E_L = E_m\left(\frac{1-\xi\eta\phi}{1-\eta\phi}\right) \tag{9.127}$$

$$E_T = E_m\left(\frac{1-\eta\phi}{1-\eta\phi}\right) \tag{9.128}$$

$$G_{LT} = G_m\left(\frac{1-\lambda\phi}{1-\lambda\phi}\right) = G_m\frac{\nu_{LT}}{\nu_m} \tag{9.129}$$

where

$$\eta = \frac{\left(\frac{E_f}{E_m} - 1\right)}{\left(\frac{E_f}{E_m} + \xi\right)} \tag{9.130}$$

$$\lambda = \frac{\left(\frac{G_f}{G_m} - 1\right)}{\left(\frac{G_f}{G_m} + 1\right)} \tag{9.131}$$

$$\xi = 2\left(\frac{L}{D}\right) \tag{9.132}$$

Here, the subscripts t and m represent the fiber and matrix, respectively; L the fiber length; D the fiber diameter; ϕ the volume fiber fraction, which can be expressed in terms of weight fraction, ψ, as

$$\phi = \frac{\psi}{\psi + (1+\psi)(\rho_f/\rho_m)} \tag{9.133}$$

It should be pointed out that, in addition to the Halpin-Tsai model, there are several other models in use today to predict the elastic properties of aligned fiber reinforced laminates [36, 38]. Most models predict the longitudinal modulus quite accurately, as shown in Fig. 9.72 [36], which compares measured values to computed values using the *mixing rule*. This comes as no surprise, because experimental evidence clearly shows that longitudinal modulus is directly proportional to the fiber content for composites with unidirectional reinforcement. However, differences do exist between the models when predicting the transverse modulus, as shown in Fig. 9.73 [36].

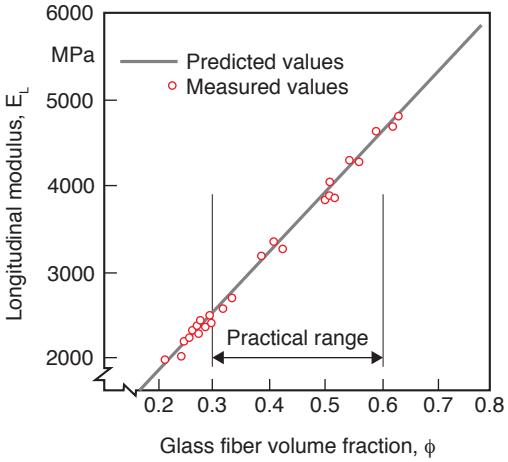

Figure 9.72 Measured and predicted longitudinal modulus for an unsaturated polyester/aligned glass fiber composite laminate as a function of volume fraction of glass content

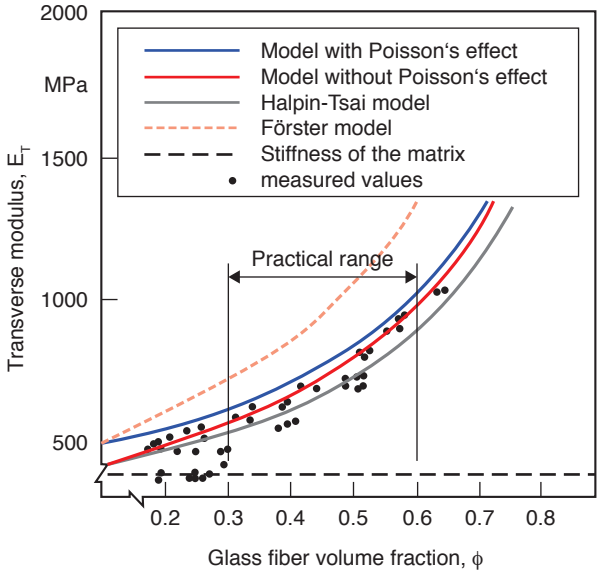

Figure 9.73 Measured and predicted transverse modulus for an unsaturated polyester/aligned glass fiber composite laminate as a function of volume fraction of glass content

9.8.3 Transformation of Fiber Reinforced Composite Laminate Properties

The loading in a laminated structure is not always aligned with the transverse and longitudinal directions of the reinforcement. Hence, it is often necessary to rotate the laminate and its properties by an angle θ. Figure 9.71 depicts the laminate's material coordinate system $L-T$ and a rotated arbitrary coordinate system 1–2. If we rotate the axes from the 1–2 system to the $L-T$ system, we can transform the stress components using

$$\begin{Bmatrix} \sigma_L \\ \sigma_T \\ \tau_{LT} \end{Bmatrix} = \begin{bmatrix} c^2 & s^2 & 2sc \\ s^2 & c^2 & -2sc \\ -sc & sc & (c^2 - s^2) \end{bmatrix} \begin{Bmatrix} \sigma_{11} \\ \sigma_{22} \\ \tau_{12} \end{Bmatrix} \quad \text{or} \tag{9.134}$$

$$\{\sigma_{LT}\} = [T_\sigma]\{\sigma_{12}\} \tag{9.135}$$

The transformation of the strain components carry an extra ½ term for the shear strains and is written as

$$\begin{Bmatrix} \varepsilon_L \\ \varepsilon_T \\ \gamma_{LT} \end{Bmatrix} = \begin{bmatrix} c^2 & s^2 & sc \\ s^2 & c^2 & -sc \\ -2sc & 2sc & (c^2 - s^2) \end{bmatrix} \begin{Bmatrix} \varepsilon_{11} \\ \varepsilon_{22} \\ \gamma_{12} \end{Bmatrix} \text{or} \tag{9.136}$$

$$\{\varepsilon_{LT}\} = [T_\varepsilon]\{\varepsilon_{12}\} \tag{9.137}$$

Combining Eq. 9.126 with the above transformations, we can write

$$\left[T_{\varepsilon}\right]\left\{\varepsilon_{12}\right\}=\left[S_{LT}\right]\left[T\sigma\right]\left\{\sigma_{12}\right\} \tag{9.138}$$

or

$$\left\{\varepsilon_{12}\right\}=\left[T_{\varepsilon}\right]^{-1}\left[S_{LT}\right]\left[T\sigma\right]\left\{\sigma_{12}\right\} \tag{9.139}$$

The compliance matrix in the $L-T$ coordinate system has four independent components and the 1–2 system has six. The inverse of $\left[T_{e}\right]$ is equivalent to rotating the coordinates back by $-\theta$. This leads to

$$\begin{Bmatrix} S_{11} \\ S_{22} \\ S_{12} \\ S_{44} \\ S_{14} \\ S_{24} \end{Bmatrix} = \begin{bmatrix} c^4 & s^4 & 2c^2s^2 & c^2s^2 \\ s^4 & c^4 & 2s^2c^2 & c^2s^2 \\ c^2s^2 & c^2s^2 & (c^4+s^4) & -c^2s^2 \\ 4c^2s^2 & 4c^2s^2 & -8c^2s^2 & (c^2-s^2)^2 \\ 2c^3s & -2cs^3 & 2(cs^3-c^3s) & (cs^3-c^3s) \\ 2cs^3 & -2c^3s & 2(c^3s-s^3) & (c^3s-s^3) \end{bmatrix} \begin{Bmatrix} S_{LL} \\ S_{TT} \\ S_{LT} \\ S_{SS} \end{Bmatrix} \tag{9.140}$$

or

$$\left\{S_{12}\right\}=\left[R\left(\theta\right)\right]\left\{S_{LT}\right\} \tag{9.141}$$

The engineering elastic constants in the 1–2 system can easily be computed:

$$E_{11}=\frac{1}{S_{11}} \tag{9.142}$$

$$E_{22}=\frac{1}{S_{22}} \tag{9.143}$$

$$G_{12}=\frac{1}{S_{44}} \tag{9.144}$$

$$v_{12}=-\frac{S_{12}}{S_{11}} \tag{9.145}$$

$$v_{21}=-\frac{S_{12}}{S_{22}} \tag{9.146}$$

$$\eta_{14}=\frac{S_{14}}{S_{11}} \tag{9.147}$$

$$\eta_{24}=\frac{S_{24}}{S_{22}} \tag{9.148}$$

$$\eta_{41} = \frac{S_{41}}{S_{44}} \tag{9.149}$$

$$\eta_{42} = \frac{S_{42}}{S_{44}} \tag{9.150}$$

Figure 9.74 [38] shows how the stiffness decreases as one rotates away from the longitudinal axis for an aligned fiber reinforced composite with different volume fraction fiber contents. From the figure it is evident that for high volume fraction fiber contents only a slight misalignment of the fibers from the loading direction results in a drastic reduction of the properties. Along with the predicted stiffness properties, the figure also presents the stiffness for a composite with 0.56 volume fraction of fibers measured at various angles from the longitudinal axis of the composite. The measured and the predicted values agree quite well.

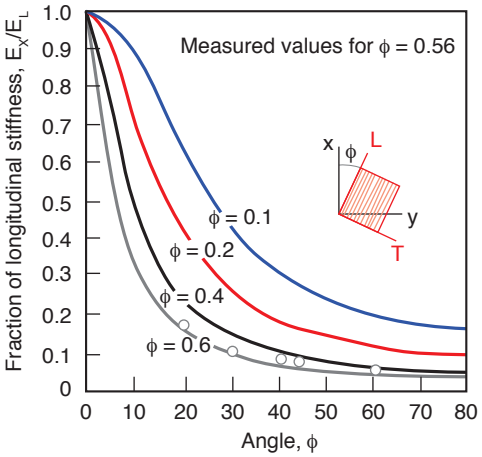

Figure 9.74 Measured and predicted elastic modulus in a unidirectional fiber reinforced laminate as a function of angle between loading and fiber direction

9.8.4 Reinforced Composite Laminates with a Fiber Orientation Distribution Function

The above transformation can be used to compute the properties of planar systems with a fiber orientation distribution function. This is done by superposing aligned fiber laminates rotated away from the principal 1–2 coordinate system by an angle θ and with a volume fiber fraction given by $\psi(\theta)$. The transformation is written as

$$\{S_{12}\} = \int_{-\pi/2}^{\pi/2} \left(\left[R(\theta) \right] \{S_{LT}\} \psi(\theta) \right) d\theta \tag{9.151}$$

which can be written in discrete terms to be used with a fiber orientation distribution function attained from computer simulation:

$$\{S_{12}\} = \sum_{i=1}^{N} \left(\left[R\left(\theta_i\right) \right] \{S_{LT}\} \psi\left(\theta_i\right) \right) \Delta\theta \tag{9.152}$$

Using Eq. 9.151, one can easily predict the stiffness properties of a part with randomly oriented fibers, where $\psi(\theta) = 1/\pi$, using[10]

$$\frac{1}{E_{11}} = \frac{1}{E_{22}} = \frac{1}{E_{\text{Random}}} = \frac{3}{8}\frac{1}{E_L} + \frac{3}{8}\frac{1}{E_T} - \frac{2}{8}\frac{\nu_{LT}}{E_L} + \frac{1}{8}\frac{1}{G_{LT}} \tag{9.153}$$

9.9 Strength Stability Under Heat

As mentioned earlier, polymers soften and eventually flow as they are heated. It is, therefore, important to know what the limiting temperatures are at which a polymer component can still be loaded with moderate deformations. Three tests are commonly performed on polymer specimens to determine this limiting temperature for a specific material. They are the *Vicat temperature test* (DIN 53460), shown in Fig. 9.75[11], the *Martens temperature test* (DIN 53458 or 53462), and the *heat-distortion temperature* (HDT) test (ASTM D 648-72) shown in Fig. 9.76[12].

In the Vicat temperature test, a needle loaded with weights is pushed against a plastic specimen inside a glycol bath. This is shown schematically in Fig. 9.75. The uniformly heated glycol bath rises in temperature during the test. The *Vicat number* or Vicat temperature is measured when the needle has penetrated the specimen by 1 mm. The advantage of this test method is that the test results are not influenced by the part geometry or manufacturing technique. The practical temperature limit for thermoplastics, for example to make sure that the finished part does not deform under its own weight, lies around 15 K below the Vicat temperature.

10 The incorrect expression $E_{Random} = 3/8E_L + 5/8E_T$ is often successfully used for low fiber content to approximate the stiffness of the composite with randomly oriented fibers. However, using this equation for composites with large differences between E_L and E_T may lead to an overestimate of stiffness by 50 %.

11 Courtesy of BASF

12 Courtesy of BASF

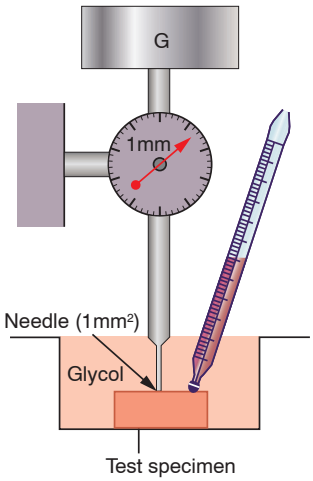

Figure 9.75 Apparatus to determine a material's shape stability under heat using the Vicat temperature test

To determine the heat distortion temperature, the standard specimen lies in a fluid bath on two knife edges separated by a 10 cm distance. A bending force is applied on the center of the specimen. Similar to the Vicat temperature test, the bath's temperature is increased during the test. The HDT is the temperature at which the specimen has bent 0.2 mm to 0.3 mm (see Fig. 9.76). The Vicat temperature is relatively independent of the shape and type of part, whereas the heat-distortion-data are influenced by the shaping and pretreatment of the test sample. Table 9.4 shows the heat distortion temperature for selected thermoplastics measured using ASTM D648.

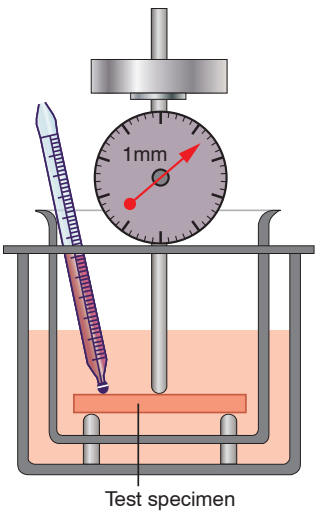

Figure 9.76 Apparatus to determine a material's shape stability under heat using the heat-distortion-temperature test (HDT)

In the Martens temperature test, the temperature at which a cantilevered beam has bent 6 mm is recorded. The test sample is placed in a convection oven with a

constantly rising temperature. In Europe, the HDT test has replaced the *Martens temperature test.*

It is important to point out that these test methods do not provide enough information to determine the allowable operating temperature of molded plastic components subjected to a stress. Heat distortion data is excellent when comparing the performance of different materials and should only be used as a reference, not as a direct design criterion.

Table 9.4 Heat Distortion Temperature for Selected Thermoplastics

Material	HDT (°C) 1.86 MPa	0.45 MPa
HDPE	50	50
PP	45	120
uPVC	60	82
PMMA	60	100
PA 66	105	200
PC	130	145

Examples

1. For the poly-α-methylstyrene stress relaxation data in Fig. 9.77 [39], create a master creep curve at T_g (204 °C).
   - Identify the glassy, rubbery, viscous, and viscoelastic regions of the master curve. Identify each region with a spring-dashpot diagram. Develop a plot of the shift factor, $\log(a_T)$ versus T, used to create your master curve. $\log(a_T)$ is the horizontal distance that the curve at temperature T was slid to coincide with the master curve.
   - What is the relaxation time of the polymer at the glass transition temperature?

   The master creep curve for the above data is generated by sliding the individual relaxation curves horizontally until they match with their neighbors, using a fixed scale for a hypothetical curve at 204 °C. Because the curve does not exist for the desired temperature we can interpolate between 208.6 °C and 199.4 °C. The resulting master curve is presented in Fig. 9.78.

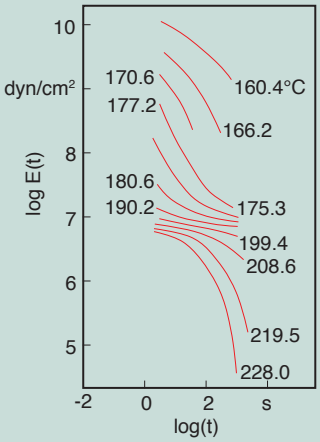

Figure 9.77 Stress relaxation data for poly-α-methylstyrene

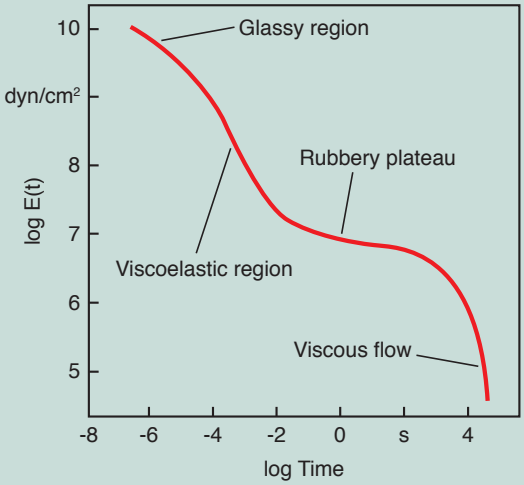

Figure 9.78 Master curve for poly-α-methylstyrene at 204 °C

The amount each curve must be shifted from the master curve to their initial position is the shift factor, $\log(a_T)$. Figure 9.79 represents the shift factor versus temperature. The solid line indicates the shift factor predicted by the WLF equation.

The relaxation time for the poly-α-methylstyrene presented here is $10^{4.5}$ s, or 31,623 s (8.8 h). The relaxation time for the remaining temperatures can be computed using the shift factor curve.

2. A loaded high-density polyethylene component is not to exceed 4% strain after 60 days of loading at room temperature. Using the short term data presented in Fig. 9.80 estimate the maximum allowable stress within the component.

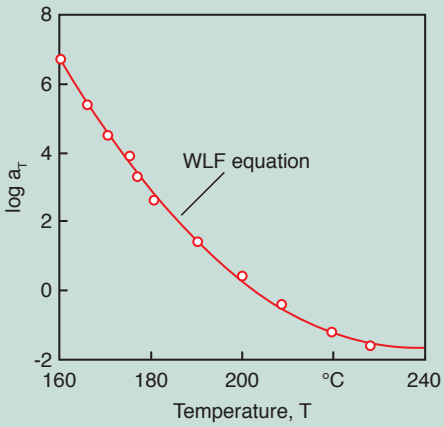

Figure 9.79 Shift factor and WLF curves for T_{ref} = 204 °C

Figure 9.80 presents constants E_0 and D_2 as a function of rate of the deformation, $\dot{\varepsilon}$. The time given in this design is 60 days (1440 h) and the strain is 4%. Therefore, the average rate of deformation is $4\%/1440\ \text{h} = 0.0028\ \%/\text{h}$. At that rate, we read $E_0 = 250$ MPa and $D_2 = 28$. We can now use Eq. 9.82 to compute the allowable stress

$$\sigma = \frac{E_0\varepsilon}{1 + D_2\varepsilon} = \frac{250\ \text{MPa}(0.04)}{1 + 28(0.04)} = 4.72\ \text{MPa}$$

It should be noted that the prescribed strain of 4% is quite high. As a rule of thumb, a component that is subjected to a long-term load should not have strains larger than 2% to avoid creep rupture. Hence, if we reduce our allowable strain to 2%, the rate of deformation during the 60 days should be $\dot{\varepsilon} = 2\%/1440\text{h} = 0.0014\ \%/\text{h}$. At the new rate we read $E_0 = 245$ MPa and $D_2 = 26$ from Fig. 9.80. Using the new constants, the maximum allowable stress for a 2% strain in 60 days is 3.22 MPa.

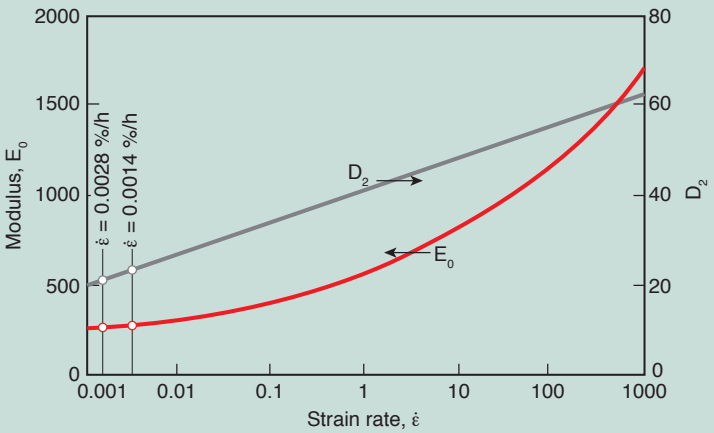

Figure 9.80 Coefficients for PE-HD short term data

3. In a special laboratory experiment, a PMMA pipe is used to cap a tank that is pressurized at 2 MPa, as shown in Fig. 9.81. The 3 mm thick pipe has a 50 mm internal diameter and is 300 mm long. Estimate the diameter change of the pipe after one year of testing? Use the creep data given below [40].

   To solve this problem we can use the thin pressure vessel approximation, working with an average diameter, $\bar{D} = 53$ mm. This is a case of biaxial stress, composed of a hoop stress, σ_H, and an axial stress, σ_A, defined by

$$\sigma_H = \frac{p\bar{D}}{2h} = 17.67 \text{ MPa and } \sigma_A = \frac{p\bar{D}}{4h} = 8.83 \text{ MPa}$$

   where, p is the pressure and h is the thickness. These stresses are constant and will cause the pipe to creep. Using the PMMA creep data we can generate a 1 year isochronous curve, which is presented in Fig.9.83. The strains that correspond to stresses of 17.67 MPa and 8.83 MPa are $\varepsilon_H = 1.32$ % and $\varepsilon_A = 0.6$ %, respectively. Because this is a biaxial case, we must correct the hoop strain using Poisson's effect before computing the diameter change. For this we use

$$\varepsilon_H' = \varepsilon_H - \nu\varepsilon_A$$

   However, because we were not given Poisson's ratio, ν, we assume a value of ⅓. Thus,

$$\varepsilon_H' = 1.32 - (1/3)0.6 = 1.12 \%$$

   To compute the diameter change we use

$$\varepsilon_H' = \Delta D/D$$

   Hence,

$$\Delta D = (53 \text{ mm})\ (0.0112) = 0.594 \text{ mm}$$

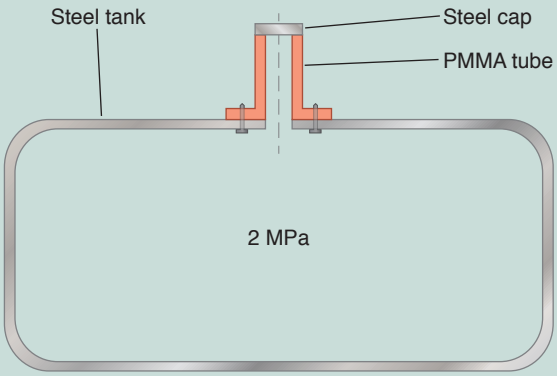

Figure 9.81 Schematic of the apparatus described in Example 9.2

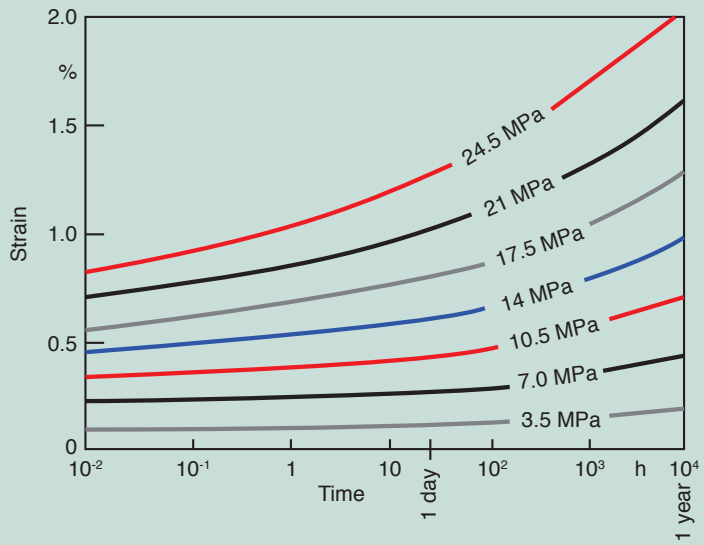

Figure 9.82 PMMA creep data

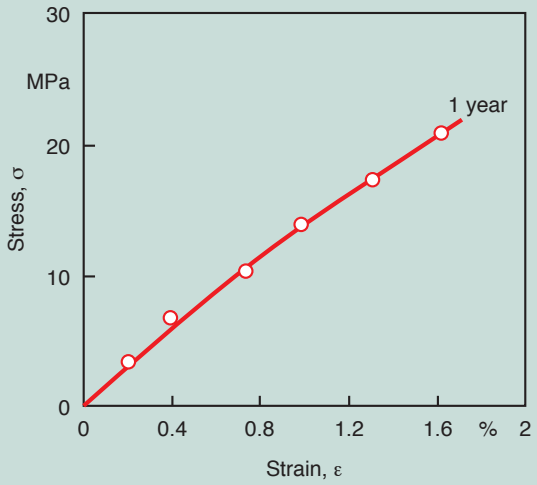

Figure 9.83 A 1 year isochronous curve for PMMA

4. In the assembly shown in Fig. 9.84, a tubular polypropylene feature is pressed on a 15 mm long metal stud. The inner diameter of the 1 mm thick PP tubular element is 10 mm. The metal stud is slightly oversized with a diameter of 10.15 mm. With a coefficient of friction $\mu = 0.3$ estimate the force required to disassemble the parts shortly after assembly and after one year. Use the creep data given in Fig. 9.85.

This is a classic constant strain, ε_0, stress relaxation problem. The initial hoop stress that holds the assembly together can be quite high. However, as time passes the hoop stress relaxes and it becomes easier to disassemble the two components. The strain in the system after assembly is computed using

$$\varepsilon_0 = {}^{\Delta D}/_{\overline{D}} = {}^{0.16\text{ mm}}/_{11\text{ mm}} = 0.0145 \rightarrow 1.45\,\%$$

In order to follow the hoop stress history after assembly we generate a 1.45% isometric curve, which is shown in Fig. 9.86.

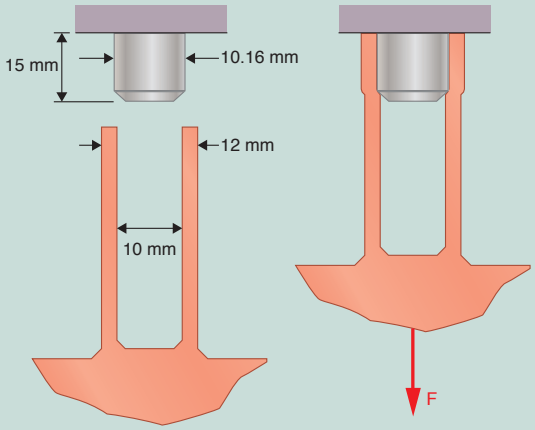

Figure 9.84 Assembly for Example 9.3

From the isochronous curve we can deduce that the hoop stress, σ_H, is 13.7 MPa shortly after assembly and about 5 MPa one year after assembly. The pressure acting on the metal stud, due to the hoop stress, can be computed using

$$p = {}^{2h\sigma_H}/_{\overline{D}}$$

which gives $p = 2.49$ MPa right after assembly and $p = 0.91$ MPa after one year. From the pressure and the friction we can calculate the disassembly force with

$$F = \mu p\left(\pi D_i L\right)$$

where $L = 15$ mm is the length of the stud. Using the above equation, the computed force necessary to pull the two components apart is 358 N (80 lb) after assembly and 130 N (29 lb) after one year.

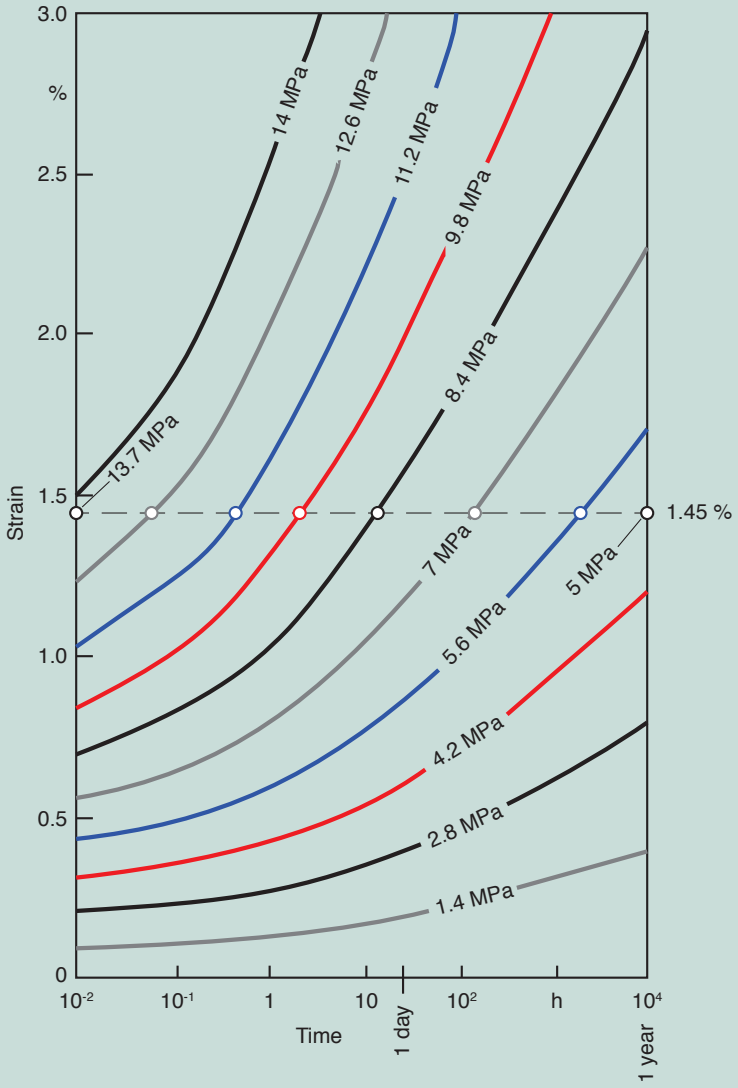

Figure 9.85 PP creep data

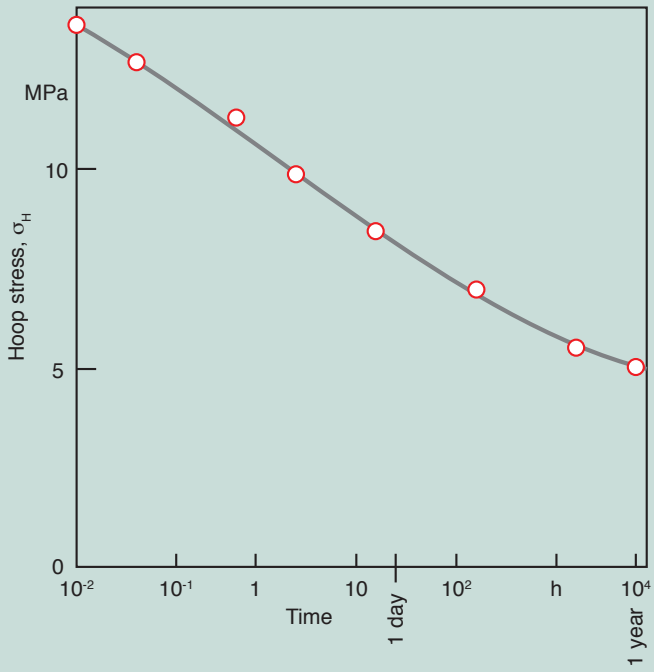

Figure 9.86 Isochronous curve for PP at 1.45% strain

5. You are asked to design a polypropylene bracket of circular cross-section, as depicted in Fig. 9.87, to hold a 10 N load for a one year period. The maximum strain you would like the bracket to feel is 2%. Calculate the diameter of the bracket using the PP creep data given in Example 9.3.

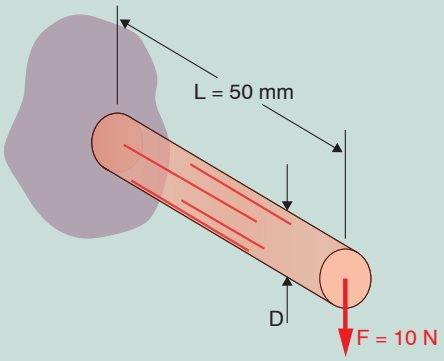

Figure 9.87 Cantilevered bracket of circular cross-section

In this design, the instant the bracket is loaded it will begin to creep. Because the life of the system is designed to be one year, with a maximum strain of 2%, we will work with a 1 year isochronous curve (Fig. 9.88), generated using Fig. 9.85.

From the isochronous curve we find that 6.5 MPa is the stress that corresponds to a 2% strain. In a cantilevered beam, the maximum stresses occur in the upper (tensile) and lower (compressive) points where the bracket joins the wall. For a cantilevered system we use

$$\sigma = \frac{Mc}{I} \quad \text{where} \quad \begin{cases} c = D/2 \\ M = FL \\ I = \dfrac{\pi D^4}{64} \end{cases}$$

Hence, we can solve for D using

$$D = \sqrt[3]{\frac{32FL}{\pi\sigma}} = \sqrt[3]{\frac{32\,(10\text{ N})(0.05\text{ m})}{\pi\ \ 6.5\times10^6\text{ Pa}}} = 9.2\text{ mm}$$

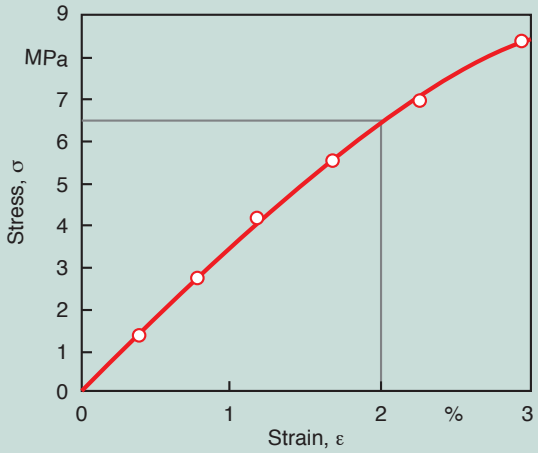

Figure 9.88 A 1 year isochronous curve for PP

At this point it is important to mention that this design has many flaws. First, a solid cross-section such as this will result in a long cycle time during manufacturing due to the slow cooling. In addition, thick cross-sections result in large amounts of shrinkage, especially with a semi-crystalline material such as polypropylene. Finally, the bending strength of a solid circular cross-section is only a fraction (lower than 20%) of the bending strength that an I-beam could deliver. This means that by changing the cross-sectional geometry of the beam, we would only need 20% or less of the material required for the present design.

Problems

1. Is it true that by decreasing the temperature of a polymer you can increase its relaxation time?
2. If you know the relaxation time of a polymer at one temperature, can you use the WLF equation to estimate the relaxation time of the same material at a different temperature? Explain.
3. You are to extrude a polystyrene tube at an average speed of is 0.1 m/s. The relaxation time, λ, of the polystyrene at the processing temperature is 1 second. The die land length is 0.02 m. Will elasticity play a significant role in your process?
4. Figure 9.89 presents some creep compliance data for polystyrene at various temperatures [41]. Create a master curve at 109.8 °C by graphically sliding the curves at some temperatures horizontally until they line up.

   Identify the glassy, rubbery, and viscoelastic regions of the master curve.

   Develop a plot of the shift factor, $\log(a_T)$ versus T, used to create your master curve. $\log(a_T)$ is the horizontal distance that the curve at temperature T was slid to coincide with the master curve. Compare your graphical result with the WLF equation.

   Note: The WLF equation is for a master curve at T_g (85 °C for this PS), but your master curve is for 109.8 °C, so be sure you make a fair comparison.

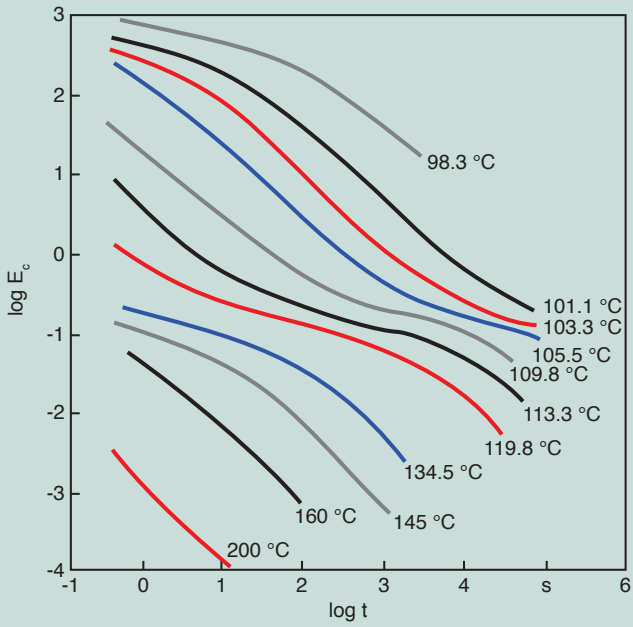

Figure 9.89 Creep modulus as a function of time for polystyrene

5. Figure 9.90 presents relaxation data for polycarbonate at various temperatures [42]. Create a master curve at 25 °C by graphically sliding the curves at the various temperatures horizontally until they line up.

   Identify the glassy, rubbery, and viscoelastic regions of the master curve.

   Develop a plot of the shift factor, $\log(a_T)$ versus T, used to create your master curve. $\log(a_T)$ is the horizontal distance that the curve at temperature T was slid to coincide with the master curve.

   Compare your graphical result with the WLF equation. Note that the resulting master curve is far from the glass transition temperature of polycarbonate.

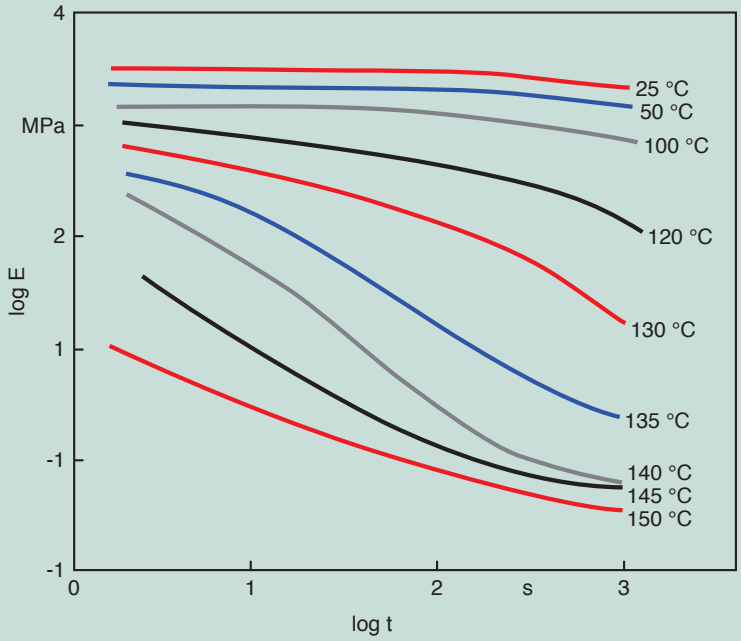

Figure 9.90 Relaxation modulus as a function of time for polycarbonate

6. Figure 9.4 presents shear relaxation data for a chlorosulfonated polyethylene at various pressures. Create a master curve at 1 bar by graphically sliding the curves at the various pressures horizontally until they line up. On the same graph draw the master curve at a pressure of 1200 bar, a high pressure encountered during injection molding.
7. Using the coefficients E_0 and D_2 for the high-density polyethylene presented in Fig. 9.91, compute the stress for 0%, 2%, 4%, and 6% strain and reconstruct the stress-strain curve for a specimen tested at 23 °C with a 100%/h deformation rate.

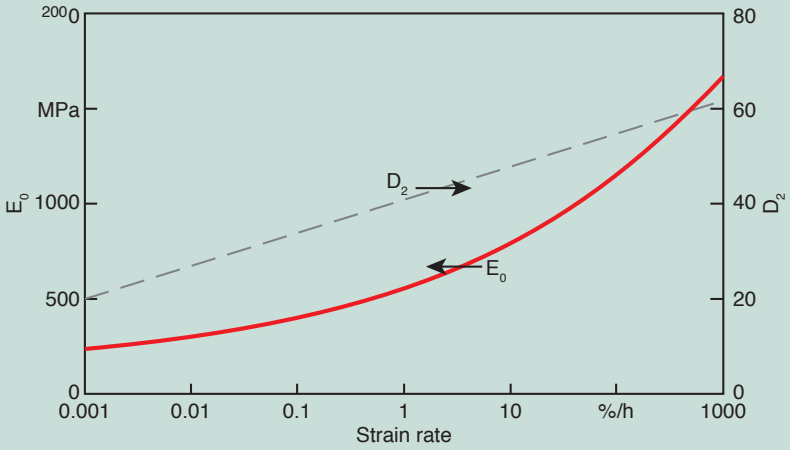

Figure 9.91 Coefficients E_0 and D_2 for a high density polyethylene at 23 °C

8. For the above material calculate the 1% strain secant modulus for 6 min, 1 h, 10 h, and 100 h. Plot the data and comment on your results.
9. Using the time-temperature superposition principle described below, plot the stress-strain curve of Problem 9.1 for $T = 40$.

$$\log\left(\dot{\varepsilon}_{ref}/\dot{\varepsilon}\right) = k\left(1/T - 1/T_{ref}\right), \text{ with } k = 10400 \text{ K}$$

10. Generate a 2 year isochronous curve for the polypropylene curve presented in Fig. 9.42. Using this curve, estimate the thickness of a 50 mm diameter polypropylene pipe whose maximum allowable strain in a 2 year period should be 2% while subjected to a 200 kPa internal pressure. **Note:** neglect effect of biaxial state of stress.
11. After a continuous 1 year operation, what is the diameter change of a cast acrylic tube that is part of a fluids experimental set-up that transports air at a pressure of 10 bar. Use the following
    - Tube inside diameter = 50 mm,
    - Tube thickness = 3 mm,
    - Tube length = 300 mm.

    Use the 20 °C creep curves given in Fig. 9.82.
12. You are to re-design the 50 mm long solid polypropylene circular bracket described in Example 9.4 using a hollow circular cross-section with a 2 mm thickness. How much material are you saving?
13. A cast iron pump housing has a polypropylene cover. The cover is tightened with steel bolts causing a compressive strain of 1.5% on the edge of the plate. When will the pump start leaking if it generates internal pressures of up to 4 MPa? Use the creep data given in Fig. 9.41.

14. Rework Example 9.3 using polyacetal data given in Fig. 9.92.

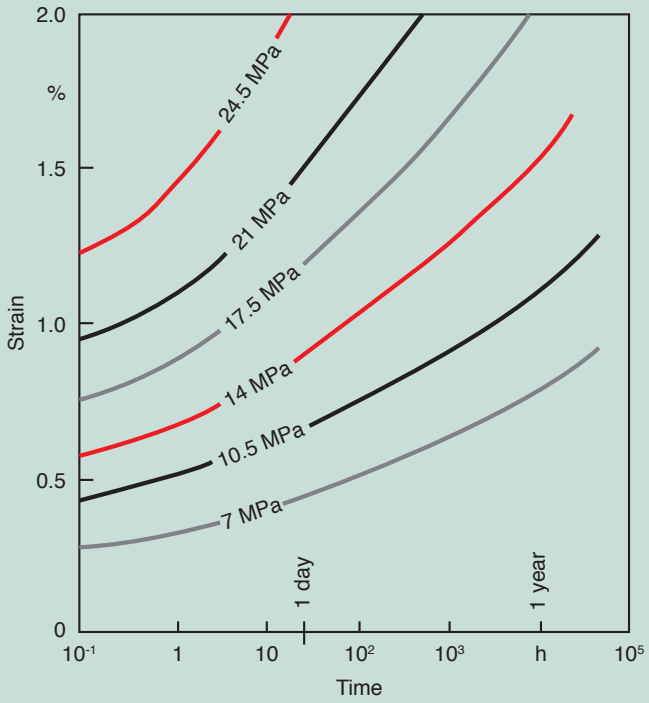

Figure 9.92 Creep data for polyacetal [25]

15. Two metal pipes are to be connected using a polypropylene fitting as shown in Fig. 9.93. The tubes are inserted onto the fitting causing a 1% hoop strain.

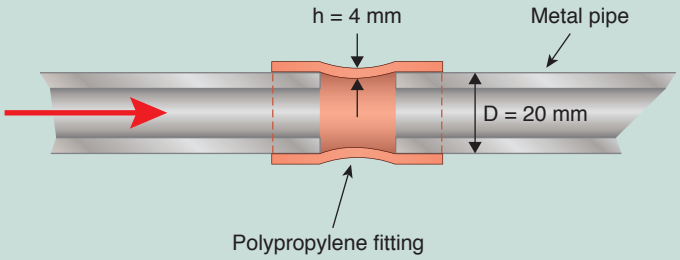

Figure 9.93 Polypropylene snap-fit assembly

Using the creep curves given in Fig. 9.85, estimate the initial hoop stress in the polypropylene fitting.

The pressure of the water inside the tubes is 5 MPa. Estimate how long this design will be water-proof.

What initial hoop strain do you recommend to make the design water proof for 1 year?

Draw a 1 day isochronous stress-strain curve.

16. Derive the equation given for Young's modulus, E_{random}, for a plate with randomly oriented fibers. Assume that the fiber length is much larger than the thickness of the plate.
17. Similar to the Halpin-Tsai model, the mixing rule is another common technique to compute the properties of a unidirectional fiber reinforced composite part. The mixing rule for the longitudinal modulus is written as

$$E_L = \phi E_f + \left(1-\right) E_m$$

Plot E_L as a function of ϕ for $E_f / E_m = 2, 10,$ and 20.

18. You are to design two long fiber reinforced cylindrical structural components. Component A is to be loaded axially. Component B is to be loaded in torsion.

What is the ideal orientation of the fibers for each component?

If you were to choose between pultrusion, filament winding, and injection molding, which process would you choose to manufacture your components? Why?

19. You are asked to design a polyacetal snap-fit as depicted in Fig. 9.94. Find the maximum force between the two components shortly after assembly and after one year. Use the creep data presented in Fig. 9.92 [25].

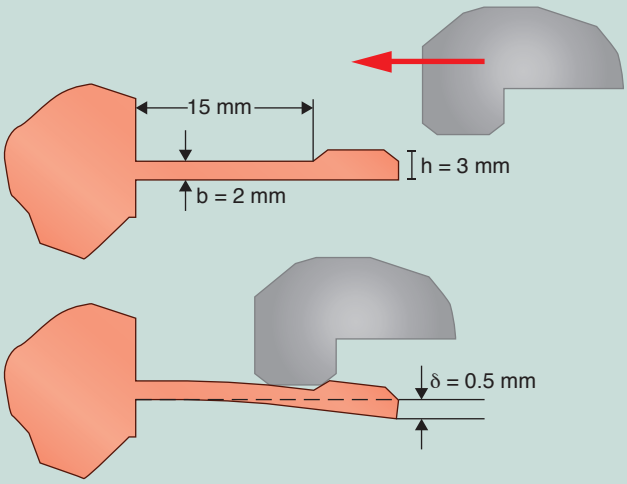

Figure 9.94 Polyacetal snap-fit assembly

20. In a certain design, in which creep plays a significant role, you need to decide between a polyacetal and a polypropylene component. Your maximum allowable strain is 2% after one year. Which one would you choose if cost plays a major role in your design decision? To help you solve this problem, use the creep data presented in Figs. 9.85 and 9.92 for POM and PP, respectively, and the cost data presented in Chapter 1.
21. In Problem 9.14, what would your decision be if weight played a higher role than cost?
22. A polypropylene pipe with a mean diameter of 30 cm is designed for a pressure of 10 bar. Calculate the appropriate value for its wall thickness.
23. A natural rubber tensile bar is extended to 1.5 times its length with a stress of 1 MPa. If the same natural rubber is filled with carbon black to a volume fraction of 30%, estimate the shear modulus.

References

[1] Castiff, E. and Tobolsky, A.V.J., *Colloid Sci., 10*, 375, (1955).

[2] Fillers, R.W., and Tschoegl, N.W., *Trans. Soc. Rheol, 21*, 51 (1977).

[3] Williams, M.L., Landel, R.F., and Ferry, J.D., *J. Amer. Chem. Soc., 77*, 3701, (1955).

[4] Wübken, G., Ph.D. Thesis, IKV, RWTH-Aachen, (1974).

[5] Münstedt, H., *Rheol. Acta, 14*, 1077, (1975).

[6] Domininghaus, H., Elsner, P., Eyerer, P., and Hirth, T., *Kunststoffe – Eigenschaften und Anwendungen*, Springer, Munich, (2012).

[7] Treloar, L.R.G., *The Physics of Rubber Elasticity*, 3rd. ed., Clarendon Press, Oxford, (1975).

[8] ICIPC, Medellín, Colombia.

[9] Ward, I.M., and Hadley, D.W., *An Introduction to Mechanical Properties of Solid Polymers*, John Wiley & Sons, Chichester, (1993).

[10] Mooney, M., *J. Appl. Phys., 11*, 582, (1940).

[11] Rivlin, R.S., and Saunders, D.W., *Phil. Trans. Roy. Soc., A243*, 251, (1951).

[12] Gumbrell, S.M., Mullins, L., and Rivlin, R.S., *Trans. Faraday Soc., 49*, 1495, (1953).

[13] Guth, E., and Simha, R., *Kolloid-Zeitschrift, 74*, 266, (1936).

[14] Guth, E., *Proceedings of the American Physical Society*, (1937): *Physical Review, 53*, 321, (1938).

[15] Smallwood, H.M., *J. Appl. Phys., 15*, 758, (1944).

[16] Mullins, L., and Tobin, N.R. N.R., *J. Appl. Polym. Sci., 9*, 2993, (1965).

[17] Knausenberger, R., and Menges, G., *SPE Technical Papers*, 39th ANTEC, 240, (1981).

[18] Retting, W., *Rhelogica Acta, 8*, 258, (1969).

[19] Schmachtenberg, E., Ph. D. Thesis, IKV, RWTH-Aachen, Germany, (1985).

[20] Krämer, S., Ph. D. Thesis, IKV, RWTH-Aachen, Germany, (1987).

[21] Weng, M., Ph. D. Thesis, IKV, RWTH-Aachen, Germany, (1988).

[22] ASTM, Plastics (II), 08.02, ASTM D2990, (2009).

[23] Nielsen, L. E., *Mechanical Properties of Polymers*, Van Nostrand Reinhold, New York, (1962).

[24] Menges, G., Haberstroh, E., Michaeli, W., and Schmachtenberg, E., *Menges Werkstoffkunde Kunststoffe*, Hanser Publishers, Munich, (2011)

[25] Crawford, R. J., *Plastics Engineering*, 2nd ed., 47, Pergamon Press, Oxford, (1987).

[26] O'Toole, J. L., *Modern Plastics Encyclopedia*, McGraw Hill, New York, (1983).

[27] Thimm, Th., *Plastomere, Elastomere, Duromere, Kautschuk und Gummi, 14*, 8, 233, (1961).

[28] Henning, F., *Kunststoffe, 65*, 401, (1975).

[29] Hosemann, R., *Kristall und Technik, 11*, 1139, (1976).

[30] Zachariades, A. E., and Kanamoto, T., *High Modulus Polymers*, A. E. Zachariades, and R. S. Porter, Eds., Marcel Dekker, Inc., New York, (1988).

[31] Becker, H., Diploma Thesis, IKV, RWTH-Aachen, Germany, (1986).

[32] Wende, A., *Glasfaserverstärkte Plaste*, VEB Deutscher Verlag für die Grundstoff-Industrie, Leipzig, (1969).

[33] Nielsen, L. E., and Landel, R. F., *Mechanical Properties of Polymers and Composites*, 2nd ed., Marcel Dekker, Inc., New York, (1994).

[34] Krishnamachari, S. I., *Applied Stress Analysis of Plastics*, Van Nostrand Reinhold, New York, (1993).

[35] Tsai, S. W., Halpin, J. C., and Pagano, N. J., *Composite Materials Workshop*, Technomic Publishing Co., Stamford, (1968).

[36] Brintrup, H., Ph. D. Thesis, IKV, RWTH-Aachen, Germany (1974).

[37] Ehrenstein, G. W., *Faserverbundkunststoffe*, Hanser Publishers, Munich, (1992).

[38] Menges, G., and Bintrup, H., Chapter 4 in *Polymere Werkstoffe*, Georg Thieme Verlag Stuttgart, (1984).

[39] Fujimoto, T., Ozaki, M., and Nagasawa, M., *J. Polymer Sci., 2*, 6, (1968).

[40] Powell, P. C., *Engineering with Polymers*, Chapman and Hall, London, (1983).

[41] Pazek, D. J., *J. Polym. Sci., A-2*, (6), 621, (1968).

[42] Carreau, P. J., De Kee, D. C. R., and Chhabra, R. P., *Rheology of Polymeric Systems*, Hanser Publishers, Munich, (1997).

10 Failure and Damage of Polymers

Failure of a component is a designer's and an engineer's biggest headache. The field of study that analyzes failed products or predicts failure is very large and complex. With polymers, failure is caused by mechanical, thermal, chemical, or other environmental influences. This chapter begins with a small overview of fracture mechanics. Here, simple models are presented that can be used to quantify the strength of polymers. The subsequent sections cover short-term behavior, impact strength, creep rupture, fatigue, wear, and environmental effects.

10.1 Fracture Mechanics

A common and relatively simple approach to analyzing failure of polymer components is derived from linear elastic fracture mechanics (LEFM). The main assumption when using LEFM is that the material under consideration behaves like a linear elastic solid. The technique has been found to work well even for those materials for which the region near the crack tip behaves non-elastically as long as the material exhibits elastic behavior everywhere else. When a polymer component is loaded at relatively high speeds, its behavior can be considered elastic, justifying the usage of linear elastic fracture mechanics to analyze its failure. In fact, polymer components made of a ductile material will often undergo a brittle failure when subjected to impact.

However, LEFM is not appropriate to model the fracture behavior in viscoelastic media or where extensive plasticity is present during deformation. For these cases, *J-integrals* can be used to determine energy change during fracture. LEFM does not apply to long-term tests, such as creep rupture, because the mechanical properties of the component or test specimen are viscoelastic. If the time scale of the loaded component is carried to the extreme, say on the order of a few months or years, the material behavior is viscous.

The next sections will discuss linear elastic as well as linear viscoelastic fracture mechanics, applying them to quantitatively analyze strength properties of cracked polymer components or parts with sharp notches or stress concentrators.

10.1.1 Fracture Predictions Based on the Stress Intensity Factor

From the basic three crack growth modes of failure, shown in Fig. 10.1, mode I most resembles an internal crack growing under a tensile load. For the analysis, consider the cracked body displayed in Fig. 10.2 with a crack length of *2a* and an applied stress σ. Near, but not at the crack tip, the stress in the direction of loading can be approximated by

$$\sigma_y = \frac{K_{I\,c}}{\sqrt{2\pi r}} \tag{10.1}$$

where *r* is the distance from the crack tip and K_{Ic} is the *critical stress intensity factor* needed for mode *I* crack growth and failure, defined by

$$K_{Ic} = \sigma\sqrt{\pi a} \tag{10.2}$$

This stress intensity factor depends on crack size relative to component size, crack shape, boundary conditions, and other conditions. Hence, a more general form of Eq. 10.2 is given by

$$K_{Ic} = Y\sigma\sqrt{\pi a} \tag{10.3}$$

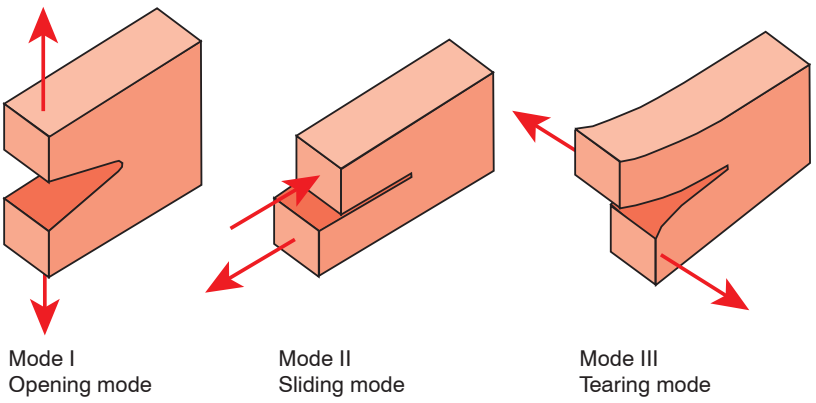

Figure 10.1 Three modes of crack loadings

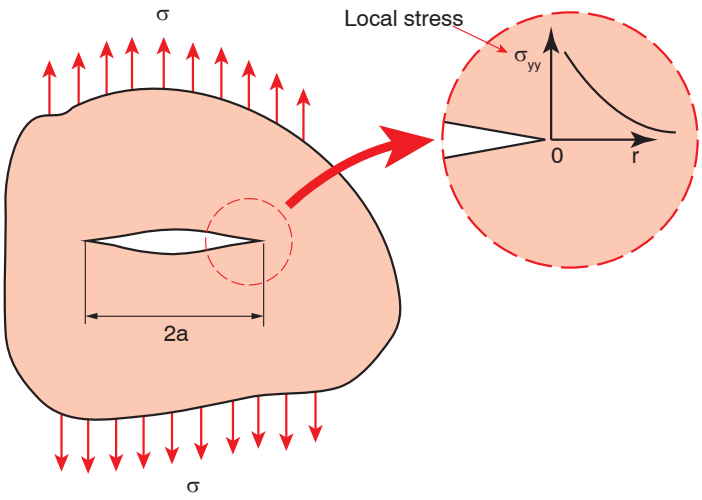

Figure 10.2 Stress near a crack tip in an infinite plate

where Y is a dimensionless correction factor tabulated for various geometries in Table 10.1. In a linear elastic solid, fracture occurs instantaneously at a combination of stress and crack size that results in a critical stress intensity factor, K_{Ic}. The critical stress intensity factor is a material property that depends on the temperature, grade of polymer, orientation, etc., where a large value implies a tough material. Table 10.2 [1, 2] shows stress intensity factors, also called *fracture toughness*, for common polymers.

Table 10.1 Values for Geometry Factor Y for Various Crack Configurations

Central crack	$Y = \sqrt{\frac{W}{\pi a}\tan\left(\frac{\pi a}{W}\right)}$
Double edge crack	$Y = \sqrt{\frac{W}{\pi a}\tan\left(\frac{\pi a}{W}\right) + \frac{0.2W}{\pi a}\sin\left(\frac{\pi a}{W}\right)}$
Single edge crack	$Y = 1.12 - 0.23\left(\frac{a}{w}\right) + 10.6\left(\frac{a}{w}\right)^2 - 21.7\left(\frac{a}{w}\right)^3 + 30.4\left(\frac{a}{w}\right)^4$

Table 10.2 Values of Plane Stress Intensity Factor and Strain Toughness for Various Materials

Material	K_{Ic} (MN/m$^{3/2}$)	G_{Ic} (kJ/m^2)
ABS	2–4	5
Acetal	4	1.2–2
Epoxy	0.3–0.5	0.1–0.3
LDPE	1	6.5
MDPE-HDPE	0.5–5	3.5–6.5
Polyamide 66	3	0.25–4
Polycarbonate	1–2.6	5
Polyester-glass reinforced	5–7	5–7
Polypropylene copolymer	3–4.5	8
Polystyrene	0.7–1.1	0.3–0.8
PMMA	1.1	1.3
uPVC	1–4	1.3–1.4
Aluminum alloy	37	20
Glass	0.75	0.01–0.02
Steel-mild	50	12
Steel alloy	150	107
Wood	0.5	0.12

10.1.2 Fracture Predictions Based on an Energy Balance

To analyze a mode I crack growth case using an energy balance and LEFM, consider the cracked body used in the previous analysis, where the actual forces are used instead of stresses, as displayed in Fig. 10.3. The crack width is also $2a$, and

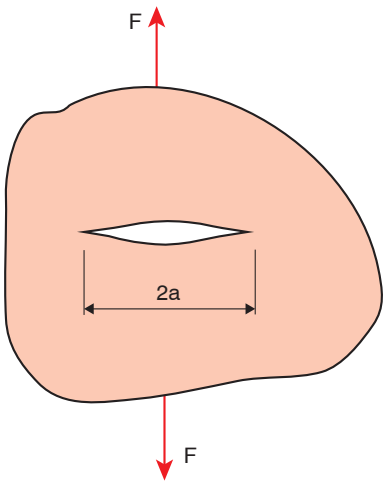

Figure 10.3 Load applied on a cracked specimen

the body is subjected to a load F. The load-displacement behavior of the cracked body is described by the solid line in Fig. 10.4. The elastic energy stored in the loaded component is given by the area under the curve:

$$U_e = \frac{1}{2} FX \tag{10.4}$$

As the crack grows by an amount Δa, the stiffness of the component decreases as shown by the dashed line in Fig. 10.4, and the elastic energy changes to

$$U_e' = \frac{1}{2}\left(F + \Delta F\right)\left(X + \Delta X\right) \tag{10.5}$$

The change in stored elastic energy for the body with the growing crack is described by

$$\Delta U = U_e - U_e' \tag{10.6}$$

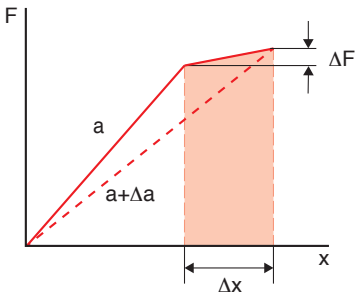

Figure 10.4 Linear elastic behavior of a cracked specimen

The external work done as the crack grows the distance Δa is defined by the shaded area in Fig. 10.4 and can be written as

$$\Delta U_c = \left(F + \frac{\Delta F}{2}\right) \Delta X \tag{10.7}$$

By subtracting Eq. 10.6 from Eq. 10.7 we can compute the energy required to generate new surfaces during fracture:

$$\Delta U_c - \Delta U = \frac{1}{2}\left(F\Delta X - X\Delta F\right) \tag{10.8}$$

Griffith's hypothesis [3], commonly used as a fracture criterion, states that for a crack to increase in size, the rate of stored elastic energy decrease must be larger or equal to the rate at which surface energy is created during crack growth. Griffith's hypothesis can be related to the expression in Eqs. 10.6 and 10.7 as

$$\frac{1}{t}\frac{\partial\left(U_c - U\right)}{\partial a} \geq G_{Ic} \tag{10.9}$$

where t is the thickness of the specimen and G_{Ic} defines the energy required to increase a crack by a unit length in a component of unit width and is usually referred to as the *elastic energy release rate*, the *toughness,* or the *critical energy release rate.* Equations 10.6, 10.7, and 10.9 can be combined to give

$$G_{Ic} = \frac{1}{2}\left(F\frac{\partial x}{\partial a} - X\frac{\partial F}{\partial a} \right) \tag{10.10}$$

Making use of the compliance defined by

$$J = \frac{X}{F} \tag{10.11}$$

and defining the force at the onset of crack propagation by F_c, we can rewrite Eq. 10.10 as

$$G_{Ic} = \frac{F_c^2}{2t}\frac{\partial J}{\partial a} \tag{10.12}$$

This equation describes the fundamental material property, G_{Ic}, as a function of applied force at fracture and the rate at which compliance changes with respect to crack size. Equation 10.12 is more useful when written in terms of stress as

$$G_{Ic} = \frac{\pi\sigma_c^2 a}{E} \tag{10.13}$$

This equation only applies for plane stress and must be redefined for the plane strain case as

$$G_{Ic} = \frac{\pi\sigma_c^2 a}{E}\left(1-\nu^2\right) \tag{10.14}$$

Table 10.2 also displays typical values of toughness for common materials.

By substituting Eq. 10.3 into Eqs. 10.13 and 10.14, we can relate the stress intensity factor K_{Ic} and the toughness G_{Ic} with

$$G_{Ic} = \frac{K_{Ic}^2}{Y^2 E} \tag{10.15}$$

for the plane stress case and

$$G_{Ic} = \frac{K_{Ic}^2}{Y^2 E}\left(1-\nu^2\right) \tag{10.16}$$

for the plane strain case.

10.1.3 Linear Viscoelastic Fracture Predictions Based on *J*-Integrals

Because of the presence of viscous components and the relatively large crack-tip plastic zone during deformation, the elastic energy release rate, G_{Ic}, is not an appropriate measure of the energy release or toughness during fracture of many thermoplastic polymers. The *J*-integral concept was developed by Rice [4] to describe the strain energy transfer into the crack tip region and, using the notation in Fig. 10.5, is defined by

$$J_{Ic} = \int_{\Gamma} W dy - \int_{\Gamma} \underline{T} \frac{\partial \underline{u}}{\partial x} ds \tag{10.17}$$

where W represents the strain energy density, $\underline{T}$ the traction vector, and $\underline{u}$ the displacement vector. As with G_{Ic}, J_{Ic} is a measure of the energy release rate, thus, analogous to Fig. 10.4. We can consider Fig. 10.6 to determine the energy release in a viscoelastic material with a growing crack. Again, the shaded area in the curve represents the energy release rate, which, apart from second order effects, is the same for constant load and constant deformation and for a specimen of thickness t can be computed by

$$\Delta U = J_{Ic} t \Delta a \tag{10.18}$$

which gives

$$J_{Ic} = -\frac{1}{t}\left(\frac{\partial U}{\partial a}\right) \tag{10.19}$$

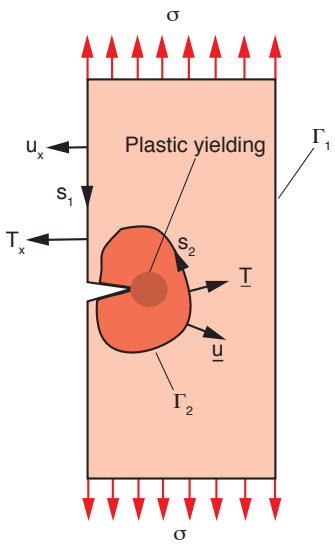

Figure 10.5 Strain energy transfer into the crack tip region of a component

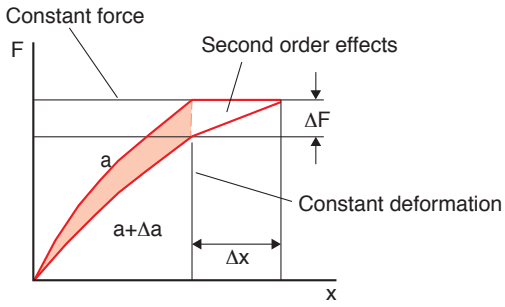

Figure 10.6 Non-linear behavior of a cracked specimen

At fracture, J_{Ic} can be related to the crack opening displacement, δ, and the yield stress, σ_y, by

$$J_{Ic} = \sigma_y \delta \tag{10.20}$$

One important feature of the *J*-integral as defined in Eq. 10.17 is that it is path-independent, so any convenient path can be chosen where stresses and displacements are known. A good choice for a path is one that completely encloses the crack tip with the plastic region but which lies within the elastic region of the body. Another property of the *J*-integral is that for linear elastic cases, $J_{Ic} = G_{Ic}$.

10.2 Short-Term Tensile Strength

As discussed in the previous chapter, short-term tensile tests DIN 53457 and ASTM D638 are available to test the stress-strain behavior of polymeric materials at room temperature (23 °C)[1]. The resulting data is plotted in a stress-strain curve that reflects the type of material and the mode of failure associated with the test polymer. When regarding polymeric materials from the failure mode point of view, there are two general types of fracture: *brittle* and *ductile*. However, depending on the temperature, environment, and whether a component is notched or not, a material can fail either way. Figure 10.7 shows a diagram developed by Vincent [5] that helps the engineer to distinguish between the different modes of failure of various thermoplastics. The figure represents a plot of brittle stress at about –180 °C (σ_B) versus yield stress at –20 °C (Δ) and 20 °C( ).

20 °C (???)

10.2.1 Brittle Failure

Brittle failure usually occurs with thermoplastics below their glass transition temperature, T_g, and with highly cross-linked polymers. However, as discussed later in this chapter, brittle failure also occurs in creep rupture and fatigue tests performed at temperatures above the glass transition temperature of the polymer. Typically, it occurs at very small strains – perhaps 1 % or less – and it is generally associated with amorphous thermoplastics below their glass transition temperature. Figure 10.8 shows the stress-strain curve for an injection molded polystyrene ASTM D638M type I test specimen shown in Fig. 10.9. The stress strain curve has a con-

1 We believe that it is imperative that the rate of deformation within the tensile specimen be maintained constant. In Chapter 9 we presented the Knausenberger-Menges technique that maintains this condition using optical techniques.

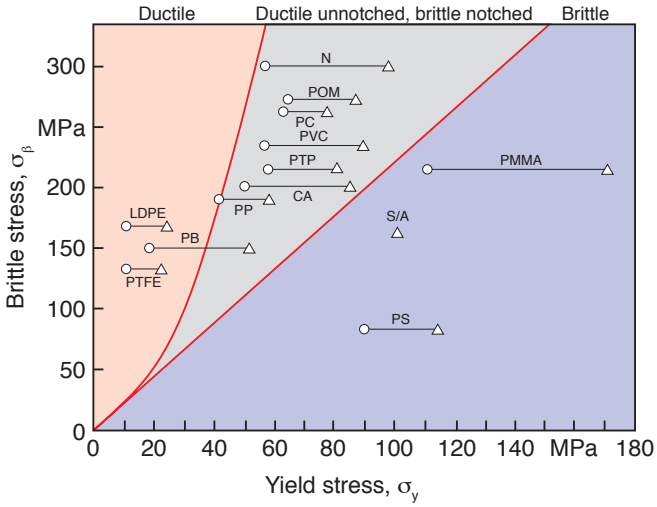

Figure 10.7 Brittle stress at -180 °C versus yield stress at -20 °C (Δ) and 20 °C ( ) for various polymers

20 °C (???)

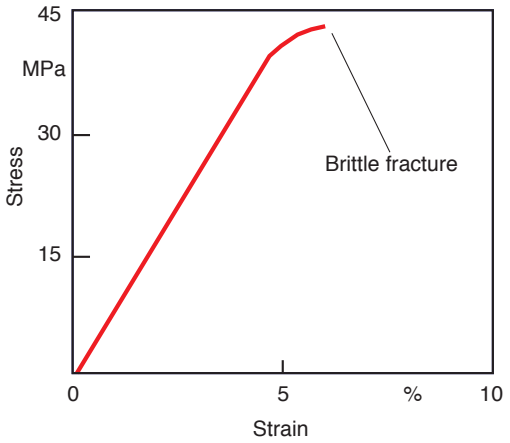

Figure 10.8 Stress-strain curve for a polystyrene at room temperature

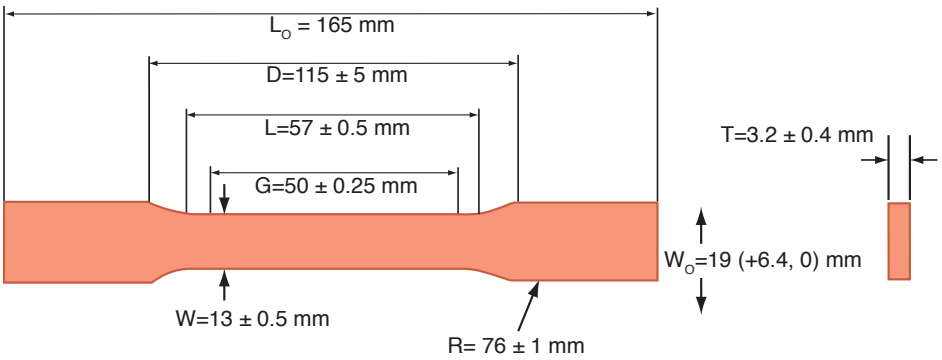

Figure 10.9 ASTM D638 test specimen

stant slope until the point where small microcracks form just before failure. These small microcracks form in the plane perpendicular to the maximum principal stress and are nucleated at points of high stress concentrations, such as scratches, dust particles in the material or material inhomogeneities. These cracks, which are more commonly known as*crazes*, impair clarity and reflect light, which makes them particularly obvious in transparent materials.

Figure 10.10 [6] shows electron micrographs of the center and edge of a craze in a polystyrene specimen. As can be seen in the micrograph, the craze boundaries are connected by load bearing fibrils, which make them less dangerous than actual cracks. Crazing is directly related to the speed at which the component or test specimen is being deformed. At high deformation speeds, the crazes are small and form shortly before failure, which makes them difficult to detect. At slow rates of deformation, crazes tend to be large and occur early on during loading. A typical craze is about 0.5 μm wide at the center and 200 μm long.[2] However, the length and width of a craze are material-dependent.

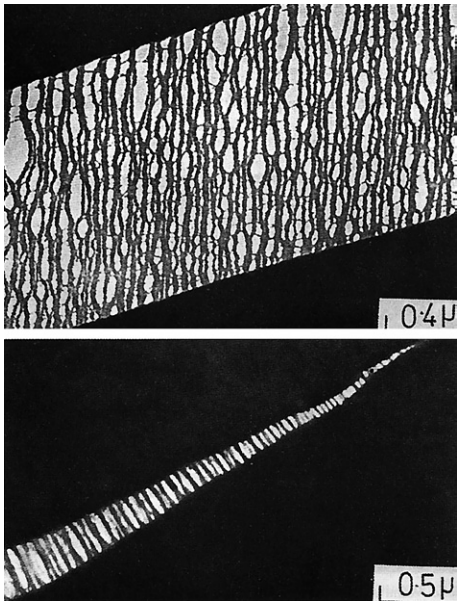

Figure 10.10 Electron micrographs of the center and edge of a craze in a polystyrene specimen

Figure 10.11 [7] shows the relation between stress, strain, craze size formation, and failure. By extrapolating the craze formation line, one can see that at high stress, crazes form at the same time as failure. When crazes form under static loading, they do not pose immediate danger to the polymer component. However, crazes

2 The length of a craze will vary between 10 μm and 1000 μm.

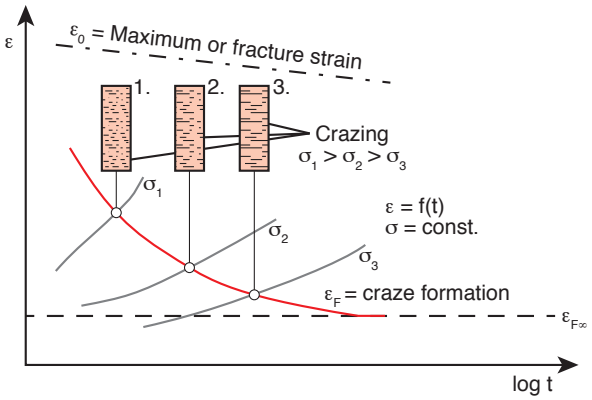

Figure 10.11 Relation between stress, strain, time, and craze formation

are irreversible, and they imply permanent damage within the material. It should also be noted that once crazes and microcracks have formed, the material no longer obeys the laws of linear viscoelasticity. The limit strain at which microcracks will form is sometimes depicted by $\varepsilon_F \chi$. Complex models exist, beyond the scope of this book, which relate the critical strain to the surface energy within a craze [8].

Figure 10.12 [7] shows the relationship between strain, time, and damage for PMMA. The bottom of the figure shows the time-temperature superposition. For example, the damage that occurs at 10 hours at 23 °C will occur at 10^5 hours for a component at 60 °C. It is interesting to see how the critical strain, $\varepsilon_F \chi$, is delayed as the temperature of the polymer component rises.

Figure 10.13 [7] shows a plot of critical strain versus temperature for an impact resistant polystyrene and compares the damage behavior curve to the shear modulus. The two curves are almost mirror images of each other and demonstrate that

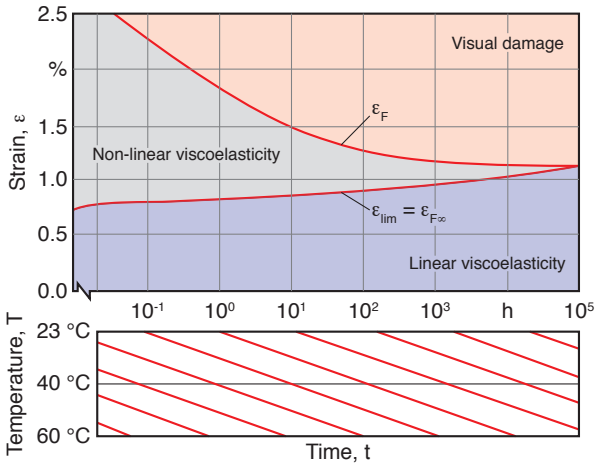

Figure 10.12 Strain limits for linear viscoelasticity

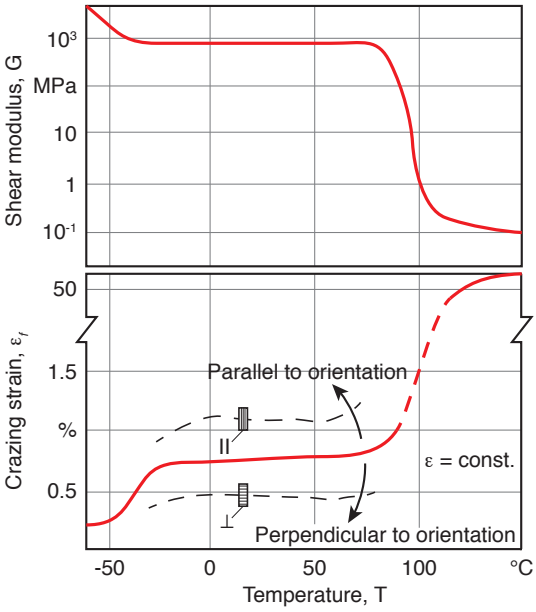

Figure 10.13 Shear modulus and crazing strain as a function of temperature for a high impact polystyrene

the formation of microcracks is inversely proportional to the stiffness of the material. The figure also demonstrates the influence of orientation on the onset of microcracks. As expected, in a component loaded perpendicular to the orientation, or across the polymer chains, the microcracks form earlier than in one loaded parallel to the orientation direction.

10.2.2 Ductile Failure

In semi-crystalline thermoplastics ductile failure occurs at temperatures between the glass transition temperature, T_g, and the melting temperature, T_m. A ductile failure is a succession of several events, as is clearly shown in the stress-strain diagram for polypropylene in Fig. 10.14 and explained in the following paragraphs.

At first, the semi-crystalline polymer behaves like an elastic solid whose deformation is reversible. For the polypropylene sample test results shown in Fig. 10.14, this linear elastic behavior holds for deformations of up to 0.5%. This behavior takes place when the component's load is applied and released fairly quickly, without causing a permanent damage to the material and allowing the component to return to its original shape. This is graphically depicted in Fig. 10.15 [7].

If the load is increased or the process is slowed, the stress-strain curve becomes non-linear, reflected by the reduction of rate of stress increase. At this point, microcracks form in the interface between neighboring spherulites, as shown in the photograph of Fig. 10.16 [9] and schematically in Fig. 10.17 [7].

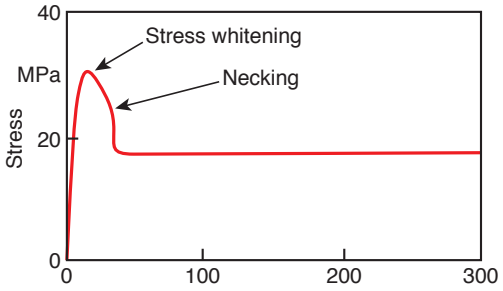

Figure 10.14 Stress-strain curve for a polypropylene at room temperature

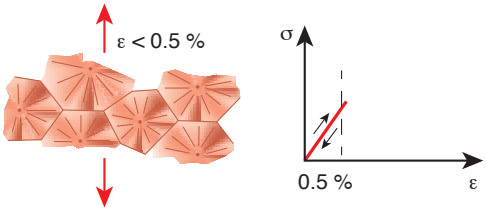

Figure 10.15 Elastic deformation within a spherulitic structure

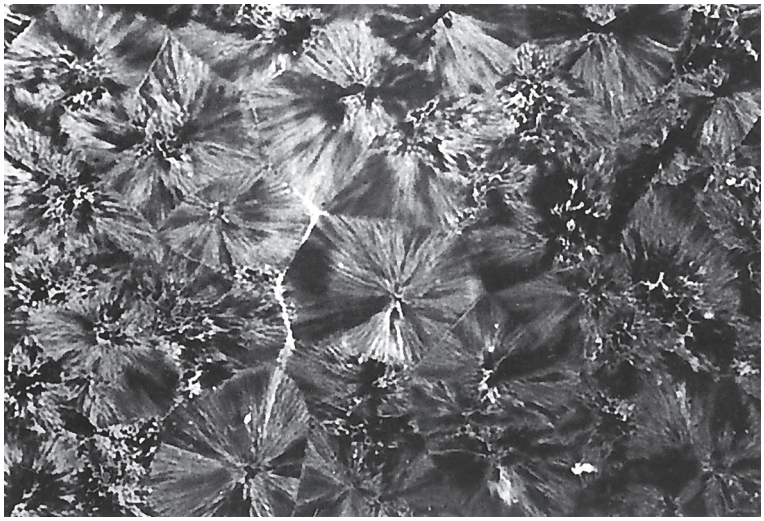

Figure 10.16 Micrograph of crack formation at inter-spherulitic boundaries (polypropylene)

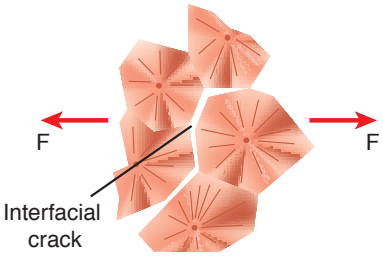

Figure 10.17 Schematic of crack formation at inter-spherulitic boundaries

The formation of such microcracks, also called *stress whitening*, is an irreversible process, causing a permanent deformation in the polymer component. Other than the white coloration that makes itself noticeable in the stressed component, the cracks are not visible to the naked eye. These microcracks are fairly constant in length, typically about the size of the spherulites. Their formation and growth, and their relation to the stress-strain behavior of a semi-crystalline polymer, are depicted in Fig. 10.18 [7].

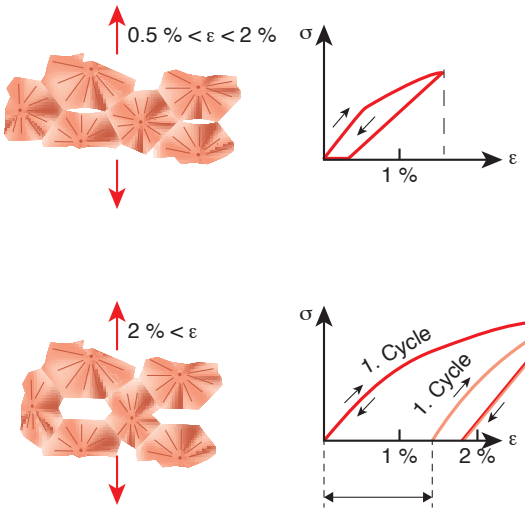

Figure 10.18 Relation between microcrack formation and the stress-strain behavior of a semi-crystalline polymer

Figure 10.14 shows that by further deforming the specimen, the stress-strain curve reaches a maximum called the *yield point* or *yield strength*. Beyond the yield point the stress drops, an event that is followed by *necking*, a localized reduction in cross-sectional area. Once necking has occurred, the specimen or component continues a long cold drawing process during which the spherulitic structure is first deformed and then broken up, creating highly oriented regions within the polymer component. Figure 10.19 shows the progression of the necked region during tensile tests of polypropylene samples. This mode of failure is common in semi-crys-

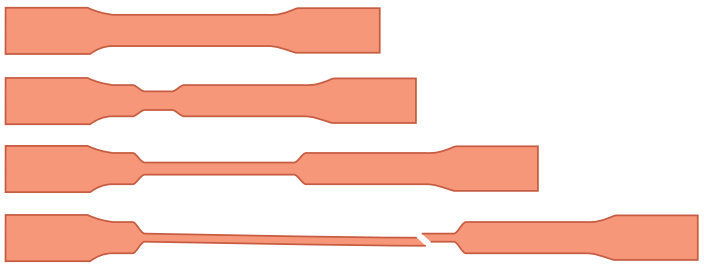

Figure 10.19 Necking progression of a polypropylene specimen during a tensile test

Figure 10.20 Necking of a polyethylene automotive fan blade [11]

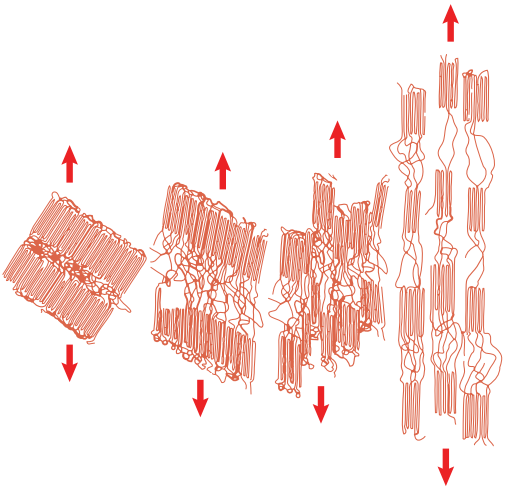

Figure 10.21 Molecular model used to represent necking and drawing during a tensile test

talline components, such as the one shown in Fig. 10.20 for a polyethylene automotive fan blade.

Necking and cold drawing can be explained with the molecular model [10] shown in Fig. 10.21. Once the amorphous ties between lamellae have been completely extended, a slip-tilting of the lamellae is induced. As deformation continues, lamellae fragments get aligned in the direction of draw, forming fibrils of alternating crystal blocks and stretched amorphous regions.

10.2.3 Failure of Highly Filled Systems or Composites

A polymer that usually fails under a brittle fracture can be toughened by adding filler particles. The most common examples for this effect are high impact polystyrene (HIPS) and ABS. In both these systems, brittle polymers (acrylic, and polystyrene) were toughened by the inclusion of rubbery particles into the material as

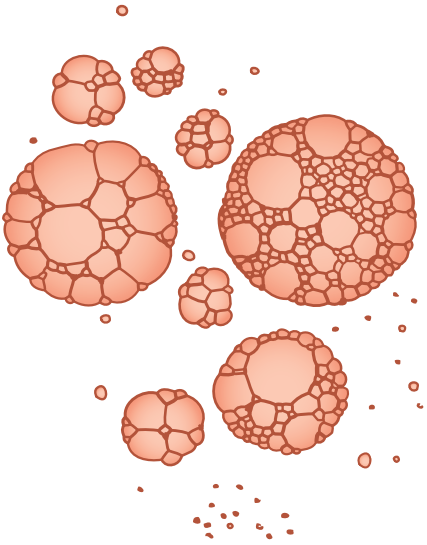

Figure 10.22 Schematic of the structure of a high impact polystyrene

shown in the schematic of the structure of HIPS in Fig. 10.22 [12]. This increase in toughness is reflected in the stress-strain behavior of HIPS shown in Fig. 10.23, where the rubbery elastic behavior of the rubber particles lowered the stiffness and ultimate strength of the material but increased its toughness. The rubber particles halt the propagation of a growing craze. Typically, the crazes that form in such systems are only as large as the characteristic gap between filler particles. This creates a system that has a large number of small crazes instead of the small number of large crazes present in the unfilled polymer. Table 10.3 [2] presents the effect of volume fraction of rubber particles on the mechanical and fracture properties of rubber-modified polystyrene. The impact strength and the fracture strain are maximized at a rubber particle volume fraction of about 20 %.

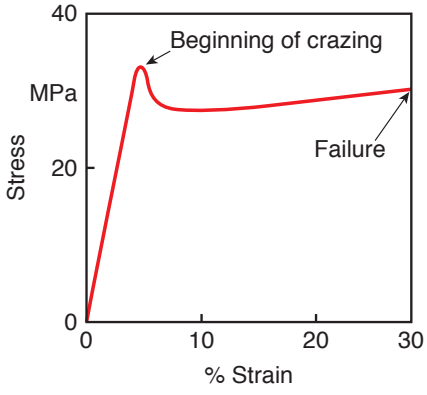

Figure 10.23 Stress-strain curve of a high impact polystyrene

Table 10.3 Effect of Rubber Particle Volume Fraction, ϕ, on the Properties of Rubber Modified Polystyrene

Volume fraction ϕ	Tensile modulus (GPa)	Impact strength (MJ/m^3)	Fracture strain (%)
0.06	2.8	0.42	3
0.12	2.4	1.90	20
0.22	1.9	11.6	45
0.30	1.0	5.6	34
0.78	0.55	1.2	8

This increase in toughness can be observed even if the filler material is also brittle. Electron micrographs of such systems have shown that cracks propagate until they encounter a filler particle, which often stops the propagation [2]. In thermosetting polymers, this effect is commonly referred to as *crack pinning*. Figure 10.24 compares plots of impact-absorbed energy as a function of specimen size for unfilled epoxy and epoxies filled with irregular-shaped silica with 55 and 64 wt.%, respectively. The factor $tw\tilde{a}$ in Fig. 10.24 is a product of the specimen's cross-sectional area, tw, where t is the specimen's thickness and w the specimen's width, and $\tilde{a}$ is a crack factor described in section 10.3.2 and tabulated in Tables 10.6 and 10.7 for Charpy and Izod impact tests, respectively.

The failure of a fiber-filled material begins at the interface between filler or reinforcement and the matrix, as shown in the electron micrograph presented in Fig. 10.25 [13] . The micrograph was taken when a glass fiber filled polyester specimen was placed under load and shows the breakage of the adhesion between imbedded glass fibers and their matrix. This breakage is generally referred to as *debonding*.

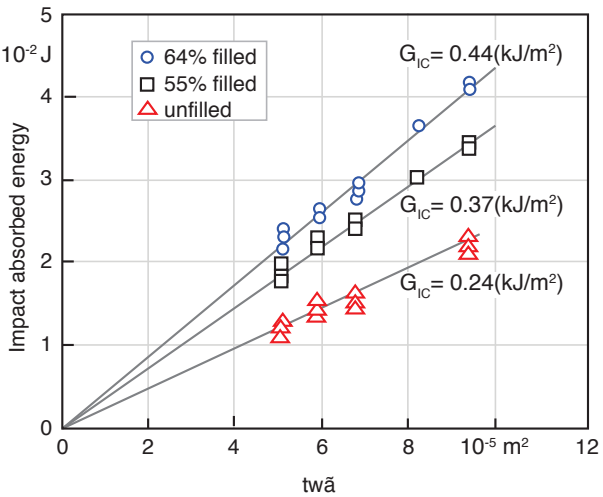

Figure 10.24 Impact absorbed energy as a function of specimen size for unfilled epoxy and epoxies filled with irregular-shaped silica with 55 and 64 wt.%

Figure 10.25 Electron micrograph of crack formation between polyester matrix and a glass fiber

This initial microcrack formation is reflected in a stress-strain curve by the deviation from the linear range of the elastic constants. In fact, the failure is analogous to the microcracks that form between spherulites when a semi-crystalline polymer is deformed.

■ 10.3 Impact Strength[3]

In practice, nearly all polymer components are subjected to impact loads. Because many polymers are tough and ductile, they are often well suited for this type of loading. However, under specific conditions even the most ductile materials, such as polypropylene, can fail in a brittle manner at very low strains. These types of failure are prone to occur at low temperatures and at very high deformation rates.

According to several researchers [14, 15] a significantly high rate of deformation leads to complete embrittlement of polymers, which results in a lower threshold of elongation at break. Menges and Boden designed a special high-speed elongational testing device that was used to measure the minimum work required to break the specimens. The minimum strain, ε_{min}, which can be measured with such a device, is a safe value to use in calculations for design purposes. It is safe to assume that if this minimum strain value is exceeded at any point in the component, initial fracture has already occurred. Table 10.4 [16, 17] presents minimum elongation at break values for selected thermoplastics on impact loading.

3 The term "impact strength" is widely misused, because what is actually referred to is energy absorbed before failure.

Table 10.4 Minimum Elongation at Break on Impact Loading

Polymer	ε_{min} (%)
HMW-PMMA	2.2
PA 6 + 25% SFR	1.8
PP	1.8
uPVC	2.0
POM	4.0
PC + 20% SFR	4.0
PC	6.0

Table 10.5 Minimum Stress at Break on Impact Loading

Polymer	σ_{min} (MPa)
HMW-PMMA	135
PA 6 + 25% SFR	175
uPVC	125
POM	> 130
PC + 20% SFR	> 110
PC	> 70

On the other hand, the stiffness and the stress at break of the material under consideration increase with the rate of deformation. Table 10.5 [16] presents data for the stress at break, σ_{min}, for selected thermoplastics on impact loading. This stress corresponds to the point at which the minimum elongation at break has just been reached.

Figure 10.26 summarizes the stress-strain and fracture behavior of a HMW-PMMA tested at various rates of deformation. The area under the stress-strain curves represents the *volume-specific energy to fracture (w)*. For impact, the elongation at break of 2.2% and the stress at break of 135 MPa represent a minimum of volume-specific energy, because the stress increases with higher rates of deformation, but the elongation at break remains constant. Hence, if we assume a linear behavior, the *minimum volume-specific energy absorption* up to fracture can be calculated using

$$w_{min} = 0.5\sigma_{max}\varepsilon_{min} \tag{10.21}$$

If the stress-strain distribution in the polymer component is known, the minimum energy absorption capacity can be estimated using w_{min}. It can be assumed that failure occurs when w_{min} is exceeded in any part of the loaded component. This

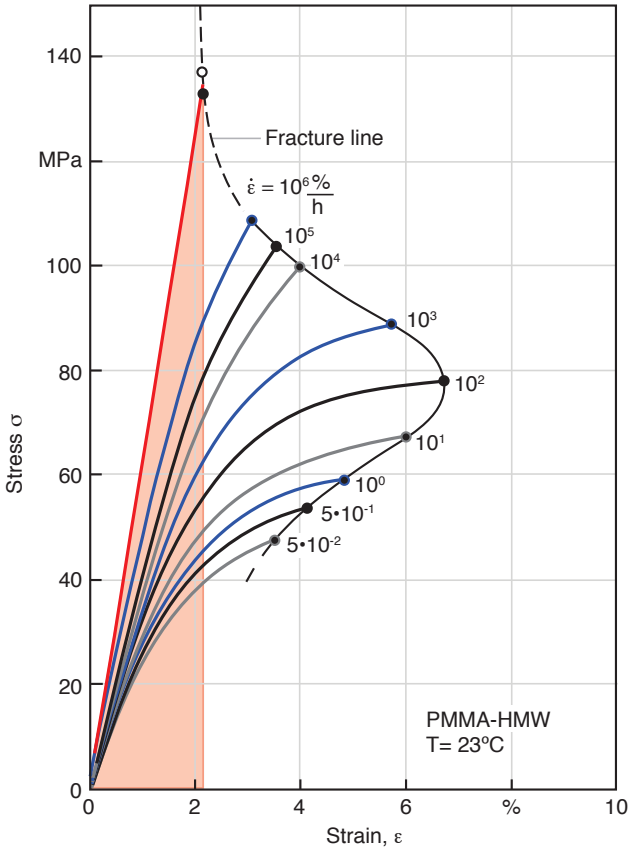

Fig. 10.26 Stress-strain behavior of HMW-PMMA at various rates of deformation

minimum volume-specific energy absorption, w_{min}, can be used as a design parameter. It was also used by Rest [18] for fiber-reinforced polymeric materials.

Glass fiber reinforced thermoplastics generally undergo brittle failure. Figure 10.27 [16] shows how the impact resistance of a polyamide 6 material was dramatically reduced by the addition of glass reinforcement. Interesting to note is that the impact resistance of polyamide 6 with 6% and 30% glass reinforcement is essentially the same when compared to the unfilled material. However, a specimen with a sharp notch that resembles a crack will have a higher impact resistance if it is glass reinforced. Figure 10.28 [16] illustrates this by showing a plot of Izod test data for polyamide 6 specimens and for polyamide 6 specimens filled with 30% glass reinforcement as a function of notch radius. Here, the data for a small notch radius reflect the energy it takes to propagate the crack through the specimen. The data for a large notch radius approach the energy it takes to both initiate and propagate a crack. In a filled polymer, a filler can sometimes increase the impact resistance of the component. For example, the volume fraction of crazes in a rubber particle filled polystyrene increases with increasing particle content. Figure 10.29

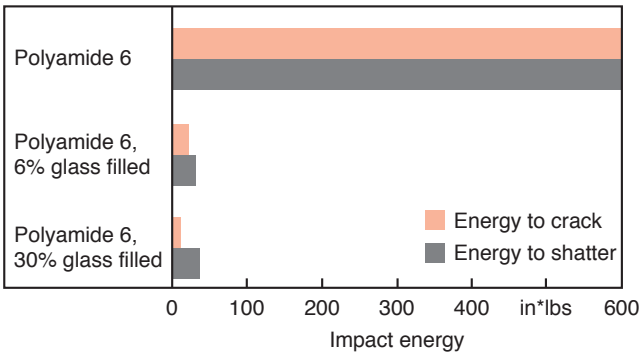

Figure 10.27 Effect of glass fiber content on energy required to generate a crack and break fiber filled polyamide 6 specimens

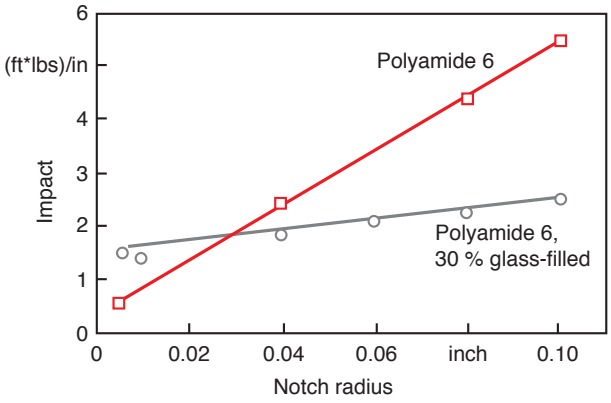

Figure 10.28 Impact strength as a function of notch tip radius for a filled and an unfilled polyamide 6

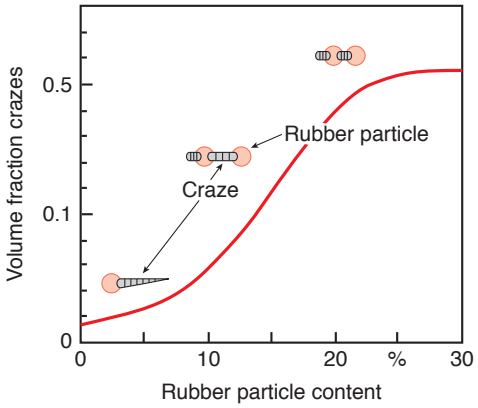

Figure 10.29 Volume fraction of craze voids as a function of rubber particle content in a high impact polystyrene

shows the volume fraction of craze voids as a function of rubber particle content in a high impact polystyrene. The figure also schematically depicts the relation between rubber particle content and craze geometry.

The impact strength of a copolymer and polymer blend of the same materials can be quite different, as shown in Fig. 10.30. From the figure it is clear that the pro-

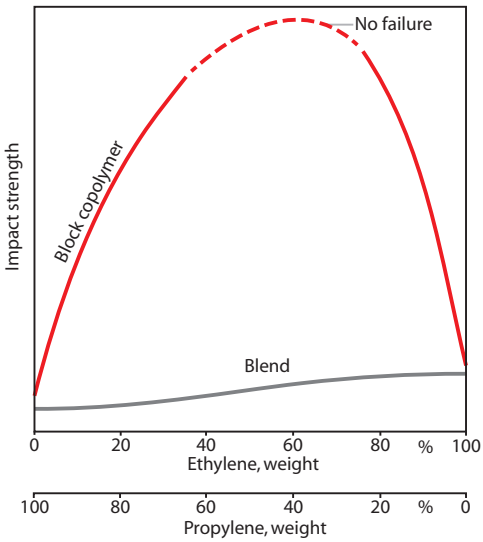

Figure 10.30 Impact strength of a propylene-ethylene copolymer and a polypropylene-polyethylene polymer blend

pylene-ethylene copolymer, which is an elastomer, has a much higher impact resistance than the basic polypropylene-polyethylene blend. It should be pointed out here that elastomers usually fail by ripping. The ripping or tear strength of elastomers can be tested using the ASTM D1004, ASTM D1938, or DIN 53507 test methods. The latter two methods make use of rectangular test specimens with clean slits cut along the center. A typical tear propagation test for an elastomer composed of 75 parts of natural rubber (NR) and 25 parts of styrene butadiene rubber (SBR) is presented in Fig. 10.31[4]. The tear strength of elastomers can be increased by introducing certain types of particulate fillers. For example, a well

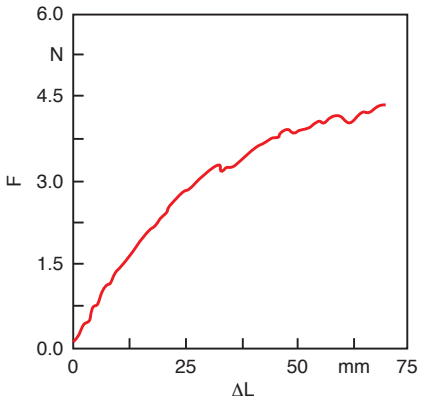

Figure 10.31 Tear propagation test for an elastomer composed of 75 parts of natural rubber (NR) and 25 parts of styrene butadiene rubber (SBR)

4 Courtesy of ICIPC, Medellín, Colombia.

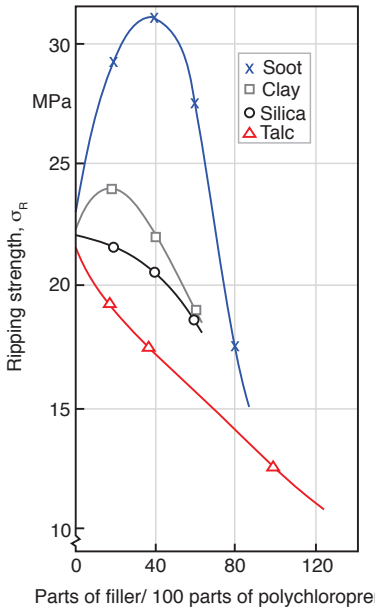

Figure 10.32 Ripping strength of a polychloroprene elastomer as a function of filler content for different types of fillers

dispersed carbon black filler can double the ripping strength of a typical elastomer. Figure 10.32 [7] shows the effect that different types of fillers have on the ripping strength of a polychloroprene elastomer.

In general, one can say that if the filler particles are well dispersed and have diameters between 20 nm and 80 nm, they will reinforce the matrix. Larger particles will act as microscopic stress concentrators and will lower the strength of the polymer component. A case where the filler adversely affects the polymer matrix is presented in Fig. 10.33 [7], where the strength of PVC is lowered with the addition of a calcium carbonate powder.

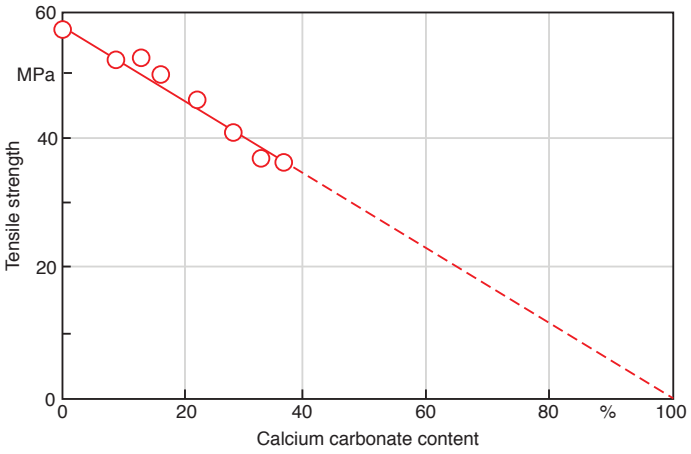

Figure 10.33 Tensile strength of PVC as a function of calcium carbonate content

10.3.1 Impact Test Methods

Impact tests are widely used to evaluate a material's capability to withstand high velocity impact loadings. The most common impact tests are the *Izod* and the *Charpy* tests. The Izod test evaluates the impact resistance of a cantilevered notched bending specimen as it is struck by a swinging hammer. Figure 10.34 [19] shows a typical Izod-type impact machine, and Fig. 10.35 [19] shows a detailed view of the

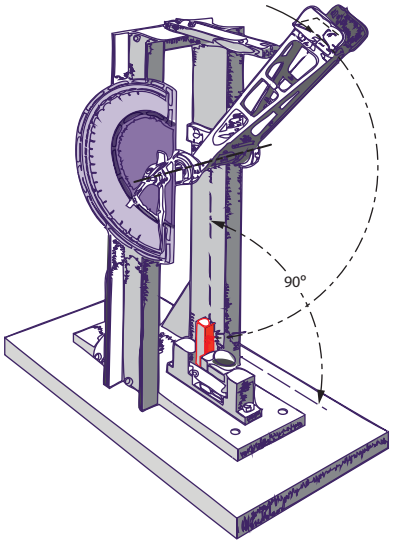

Figure 10.34 Cantilever beam Izod impact machine

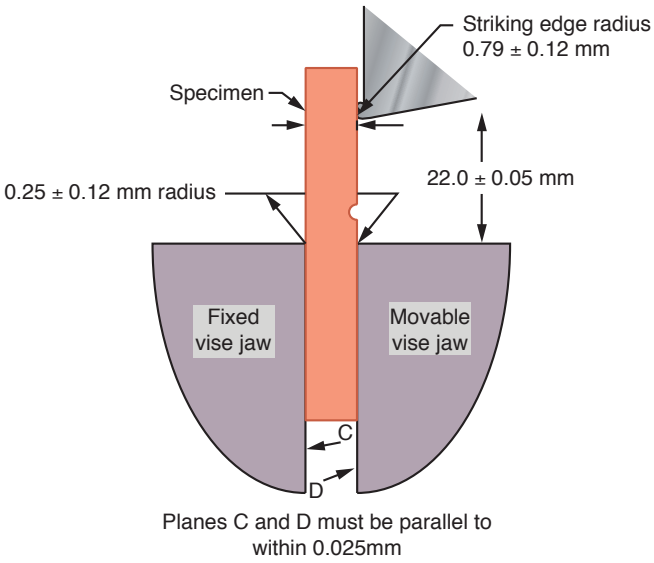

Figure 10.35 Schematic of the clamp, specimen, and striking hammer in an Izod impact test

specimen, the clamp, and the striking hammer. The pendulum or hammer is released from a predetermined height and after striking the specimen, it travels to a recorded height. The energy absorbed by the breaking specimen is computed from the difference between the two heights. The standard test method that describes the Izod impact test is the ASTM-D 256 test. There are several variations of the Izod test. These variations include positioning the test specimen such that the stresses in the notch are tensile or compressive by having the notch face away or toward the swinging pendulum, respectively. In addition, the clamping force exerted on the test specimen can have a great effect on the test results. The Charpy test evaluates the bending impact strength of a small notched or unnotched, simply supported specimen that is struck by a hammer similar to the Izod impact tester [19]. The notched Charpy test is done such that the notch faces away from the swinging hammer, creating tensile stresses within the notch, see Fig. 10.36. Both, the standard ASTM D256 and DIN 53453 test, describe the Charpy impact test.

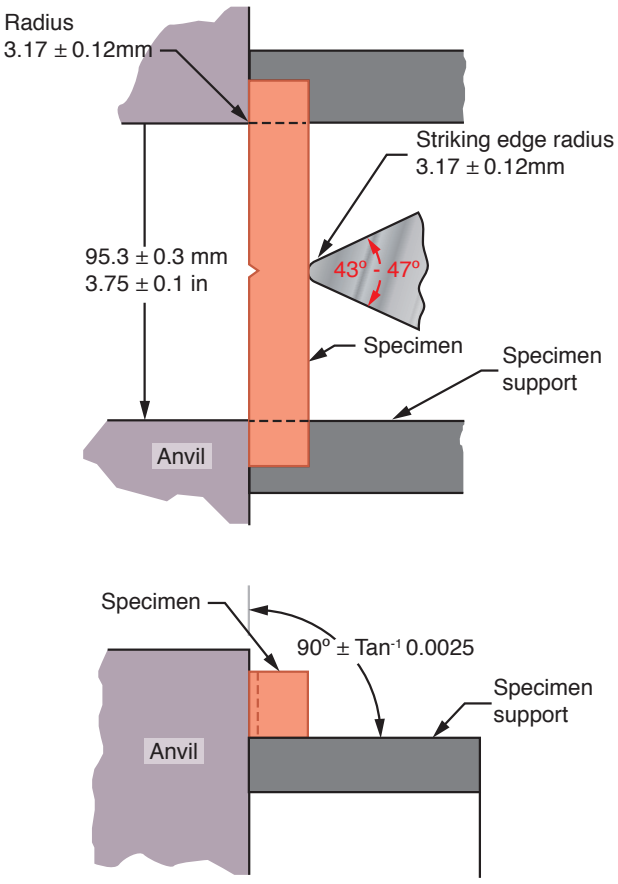

Figure 10.36 Schematic of the clamp, specimen, and striking hammer in a Charpy impact test

A variable of both tests is the notch tip radius. Depending on the type of material, the notch tip radius may significantly influence the impact resistance of the specimen. Figure 10.37 [2] presents impact strength for various thermoplastics as a function of notch tip radius. As expected, impact strength is significantly reduced with decreasing notch radius. Another factor that influences the impact resistance of polymeric materials is the temperature. This is clearly demonstrated in Fig. 10.38 [2], in which PVC specimens with several notch radii are tested at various temperatures. In addition, the impact test sometimes brings out brittle failure in materials that undergo a ductile breakage in a short-term tensile test. The brittle behavior is sometimes developed by lowering the temperature of the specimen or by decreasing the notch tip radius. Figure 10.39 [1] shows the brittle to ductile behavior regimes as a function of temperature for several thermoplastic polymers.

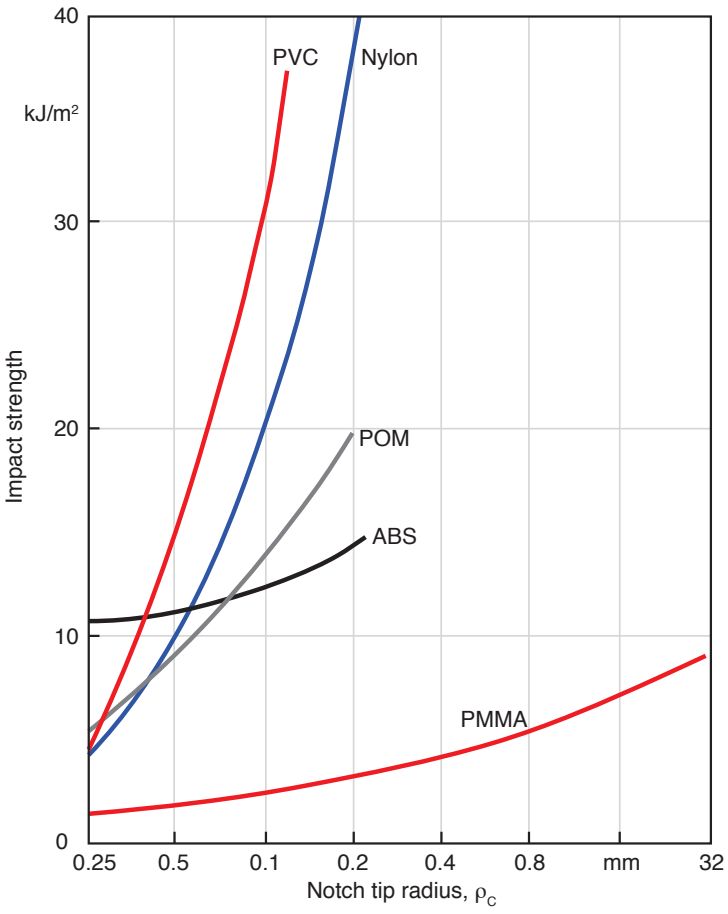

Figure 10.37 Impact strength as a function of notch tip radius for various polymers

Another impact test worth mentioning is the *falling dart* test. This test is well suited for specimens that are too thin or flexible to be tested using the Charpy or Izod tests. This test, described by the ASTM 3029 and DIN 53 453 standard methods, also works well to determine the fracture toughness of a finished product with large. Figure 10.40 shows a schematic of a typical falling dart test set-up [19]. The test consists of dropping a *tup*, with a spherical tip and otherwise variable shape and weight on a usually circular test specimen that is clamped around the periphery. The weight of the tup and the height from which it is dropped are the test variables. The energy needed to fracture the test specimen is directly computed from the potential energy of the tup before it is released, written as

$$U_p = mgh \tag{10.22}$$

where m is the mass of the tup, h the height from which it is dropped, and g gravity. It is assumed that the potential energy is fully transformed into kinetic energy

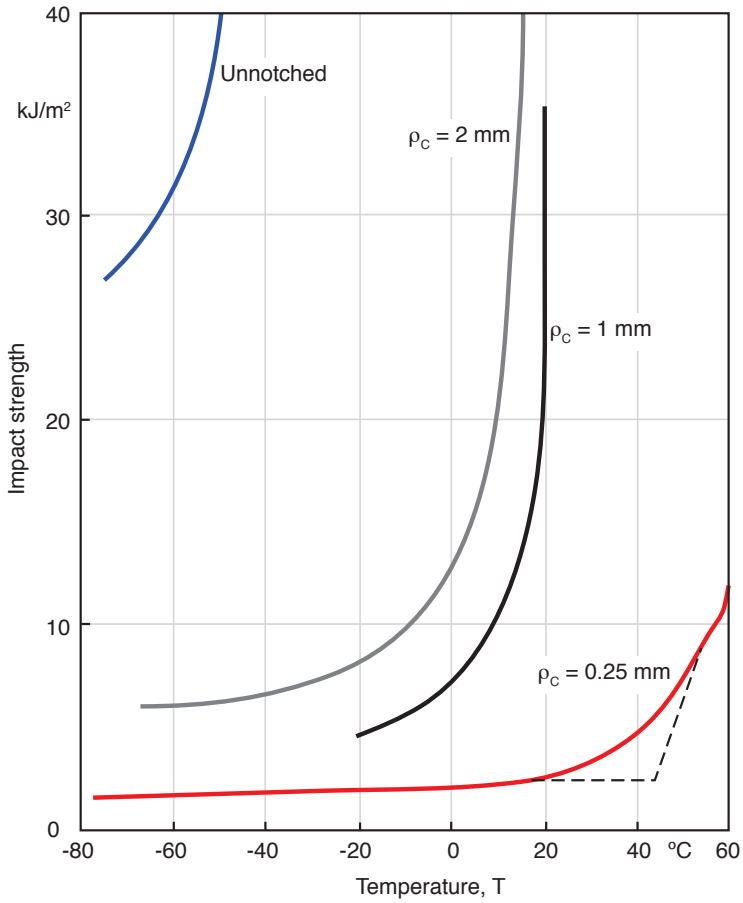

Figure 10.38 Impact strength of PVC as a function of temperature for various notch tip radii

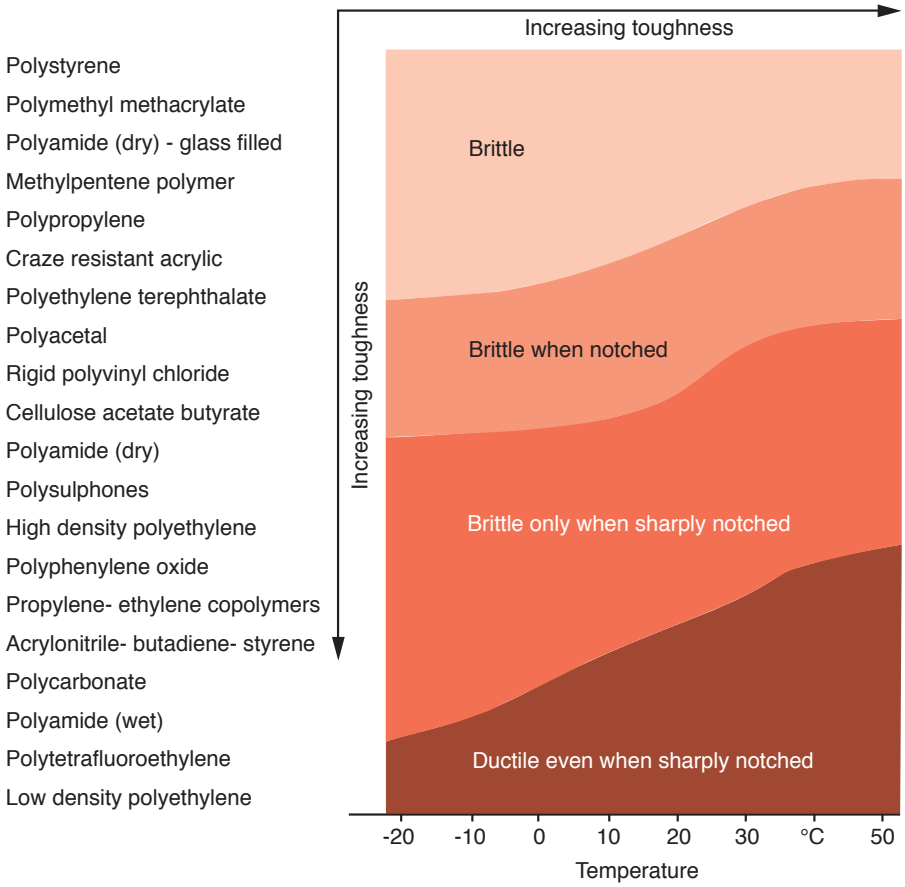

Figure 10.39 Brittle to ductile behavior regimes as a function of temperature for several thermoplastic polymers

and, in turn, into fracture energy. The test itself is much simpler than the Charpy and Izod tests, because Eq. 10.22 can be used to interpret the results directly. However, a large number of tests are required to determine the energy required for fracture.

10.3.2 Fracture Mechanics Analysis of Impact Failure

Although the most common interpretation of impact tests is qualitative, it is possible to use linear elastic fracture mechanics to quantitatively evaluate impact test results. Using LEFM, it is common to compute the material's fracture toughness G_{Ic} from impact test results. Obviously, LEFM is only valid if the Izod or Charpy test specimen is assumed to follow linear elastic behavior and contains a sharp notch. At the onset of crack propagation, Eq. 10.4, which gives the elastic energy stored in the loaded test specimen, can be rewritten in terms of compliance, J, as

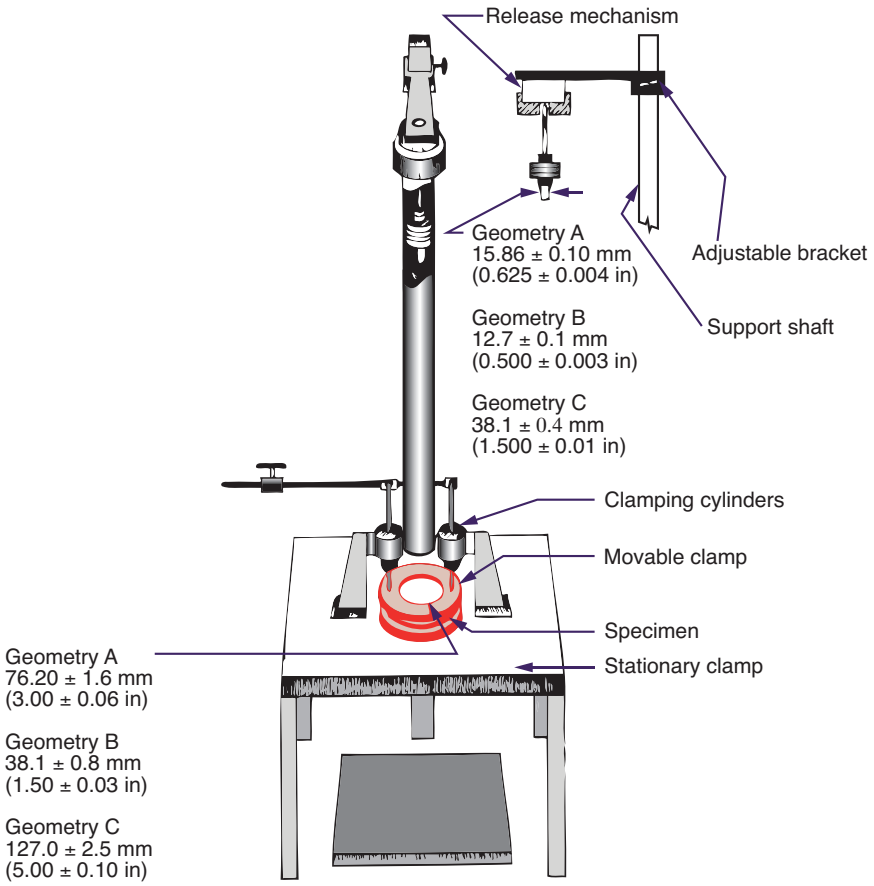

Figure 10.40 Schematic of a drop weight impact tester

$$U_e = \frac{1}{2} F_c^2 J \tag{10.23}$$

Solving for F_c in Eq. 10.12 and substituting into Eq. 10.23 results in

$$U_e = G_{Ic} t \left(\frac{J}{\partial J / \partial a} \right) \tag{10.24}$$

Introducing the test specimen's width, w, and a geometrical crack factor, $\tilde{a}$, given by

$$\tilde{a} = \left(\frac{1}{J} \frac{\partial J}{\partial a} \right)^{-1} \tag{10.25}$$

we can write Eq. 10.24 as

$$U_e = G_{Ic} w t \tilde{a} \tag{10.26}$$

The parameter $\tilde{a}$ is found in Table 10.6 [20] for various Charpy impact test specimens and in Table 10.7 [20] for various Izod impact test specimens. The elastic

energy absorbed by the test specimen during fracture, U_e, can also be represented by energy lost by the pendulum, U_L. This allows the test engineer to relate impact test results to the fracture toughness G_{Ic} of a material. When plotting U_e versus $tw\tilde{a}$, the kinetic effects lead to a positive intercept on the U_e axis. This can be corrected by subtracting the kinetic effects, U_k, from U_e. The kinetic effects can be computed using [20]

$$U_k = (1+e)\left(1+\frac{1}{2}\frac{m}{M}(1-e)\right)m\left(\frac{M}{m+M}\right)V^2 \tag{10.27}$$

where m is the mass of the specimen, M the mass of the tup, V the velocity, and e the coefficient of restitution.

Figure 10.41 contains both Charpy and Izod test result data for a medium density polyethylene [20] as plots of U_e versus $tw\tilde{a}$ with kinetic energy corrections. We can now calculate G_{Ic} from the slope of the curve (Eq. 10.26).

However, as mentioned earlier for polymers that undergo significant plastic deformation before failure, Eq. 10.26 does not apply and the *J*-integral must be used. Here, by taking the Charpy or Izod specimen and assuming full yield, having a plastic hinge between the tip of the crack and the specimen wall opposite to the cracked side, we can calculate the energy by using

$$U_e = \frac{\delta}{2}\sigma_y t(w-a) \tag{10.28}$$

Table 10.6 Charpy Impact Test Geometric Crack Factors $\tilde{a}$

a/w	$2L/w = 4$	$2L/w = 6$	$2L/w = 8$	$2L/w = 10$	$2L/w = 12$
0.04	1.681	2.456	3.197	3.904	4.580
0.06	1.183	1.715	2..220	2.700	3.155
0.08	0.933	1.340	1.725	2.089	2.432
0.10	0.781	1.112	1.423	1.716	1.990
0.12	0.680	0.957	1.217	1.461	1.688
0.14	0.605	0.844	1.067	1.274	1.467
0.16	0.550	0.757	0.950	1.130	1.297
0.18	0.505	0.688	0.858	1.015	1.161
0.20	0.468	0.631	0.781	0.921	1.050
0.22	0.438	0.584	0.718	0.842	0.956
0.24	0.413	0.543	0.664	0.775	0.877
0.26	0.391	0.508	0.616	0.716	0.808
0.28	0.371	0.477	0.575	0.665	0.748
0.30	0.354	0.450	0.538	0.619	0.694
0.32	0.339	0.425	0.505	0.578	0.647
0.34	0.324	0.403	0.475	0.542	0.603

Table 10.6 Charpy Impact Test Geometric Crack Factors $\tilde{a}$ *(continued)*

a/w	$2L/w = 4$	$2L/w = 6$	$2L/w = 8$	$2L/w = 10$	$2L/w = 12$
0.36	0.311	0.382	0.447	0.508	0.564
0.38	0.299	0.363	0.422	0.477	0.527
0.42	0.276	0.328	0.376	0.421	0.462
0.44	0.265	0.311	0.355	0.395	0.433
0.46	0.254	0.296	0.335	0.371	0.405
0.48	0.244	0.281	0.316	0.349	0.379
0.50	0.233	0.267	0.298	0.327	0.355
0.52	0.224	0.253	0.281	0.307	0.332
0.54	0.214	0.240	0.265	0.88	0.310
0.56	0.205	0.228	0.249	0.270	0.290
0.58	0.196	0.216	0.235	0.253	0.271
0.60	0.187	0.205	0.222	0.238	0.253

Table 10.7 Izod Impact Test Geometric Crack Factors $\tilde{a}$

a/w	$2L/w = 4$	$2L/w = 6$	$2L/w = 8$	$2L/w = 10$	$2L/w = 12$
0.06	1.540	1.744	1.850	2.040	–
0.08	1.273	1.400	1.485	1.675	1.906
0.10	1.060	1.165	1.230	1.360	1.570
0.12	0.911	1.008	1.056	1.153	1.294
0.14	0.795	0.890	0.932	1.010	1.114
0.16	0.708	0.788	0.830	0.900	0.990
0.18	0.650	0.706	0.741	0.809	0.890
0.20	0.600	0.642	0.670	0.730	0.810
0.22	0.560	0.595	0.614	0.669	0.750
0.24	0.529	0.555	0.572	0.617	0.697
0.26	0.500	0.525	0.538	0.577	0.656
0.28	0.473	0.500	0.510	0.545	0.618
0.30	0.452	0.480	0.489	0.519	0.587
0.32	0.434	0.463	0.470	0.500	0.561
0.34	0.420	0.446	0.454	0.481	0.538
0.36	0.410	0.432	0.440	0.468	0.514
0.38	0.397	0.420	0.430	0.454	0.494
0.40	0.387	0.410	0.420	0.441	0.478
0.42	0.380	0.400	0.411	0.431	0.460
0.44	0.375	0.396	0.402	0.423	0.454
0.46	0.369	0.390	0.395	0.415	0.434
0.48	0.364	0.385	0.390	0.408	0.422
0.50	0.360	0.379	0.385	0.399	0.411

Using the relation in Eq. 10.20 with Eq. 10.28 we can write

$$J_{Ic} = \frac{2U_e}{A} \tag{10.29}$$

where $t(w-a)$ was replaced by A or the cross-sectional area of the specimen where fracture occurs. Figure 10.42 gives results for U_e as a function of A for high-impact polystyrene. The results show close agreement between the Charpy and Izod test methods and indicate that a linear correlation exists, as predicted with Eq. 10.29.

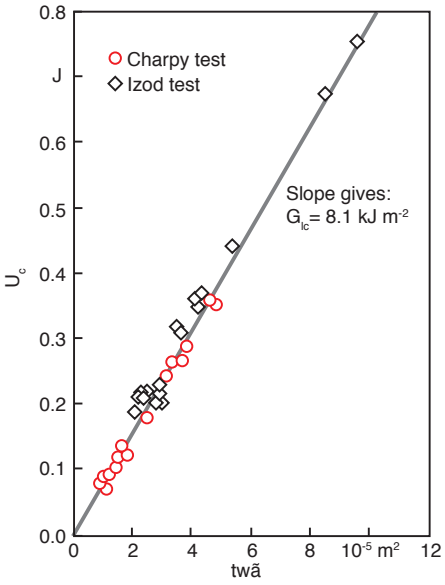

Figure 10.41 Elastic energy absorbed at impact fracture as a function of test specimen cross-sectional geometry for a medium-density polyethylene

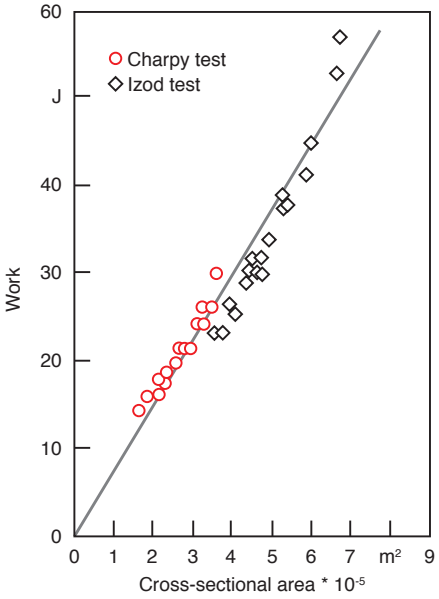

Figure 10.42 Elastic energy absorbed as a function of cross-sectional fracture area for a high impact polystyrene test specimen

10.4 Creep Rupture

During creep, a loaded polymer component will gradually increase in length until fracture or failure occurs. This phenomenon is usually referred to as *creep rupture* or, sometimes, as *static fatigue*. During creep, a component is loaded under a constant stress, constantly straining until the material cannot withstand further deformation, causing it to rupture. At high stresses, the rupture occurs sooner than at lower stresses. However, at low enough stresses, failure may never occur. The time it takes for a component or test specimen to fail depends on temperature, load, manufacturing process, environment, and other factors. It is important to point out that damage is often present and visible before creep rupture occurs. This is clearly demonstrated in Fig. 10.43 [7], which presents isochronous creep curves for polymethyl methacrylate at three different temperatures. The regions of linear and non-linear viscoelasticity and of visual damage are highlighted in the figure.

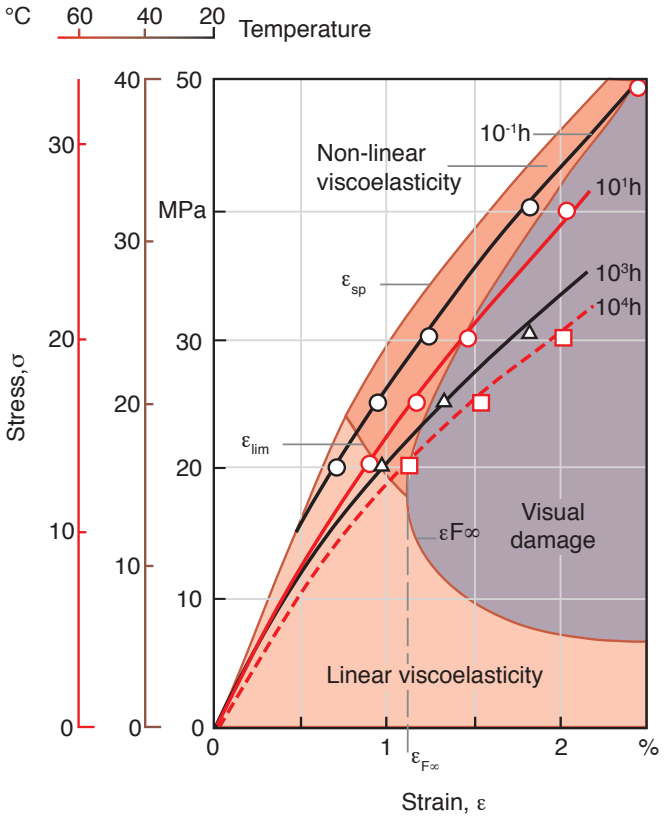

Figure 10.43 Isochronous creep curves for PMMA at three different temperatures

10.4.1 Creep Rupture Tests

The standard test to measure creep rupture is the same as the creep test discussed in the previous chapter. Results from creep rupture tests are usually presented in graphs of applied stress versus the logarithm of time to rupture. A sample of creep rupture behavior for several thermoplastics is presented in Fig. 10.44 [21]. As the scale in the figure suggests, the tests were carried out with loadings that cause the material to fail within a few weeks. An example of a creep rupture test that ran for 10 years is shown in Fig. 10.45 [22, 23]. Here, the creep rupture of high density polyethylene pipes under internal pressures was tested at different temperatures. Two general regions with different slopes become obvious in the plots. The points to the left of the knee represent pipes that underwent a ductile failure, whereas

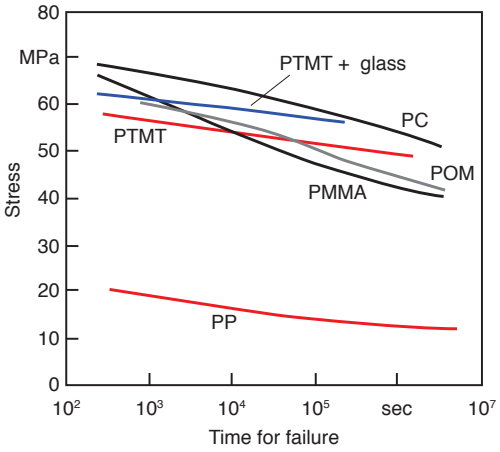

Figure 10.44 Creep rupture behavior for various thermoplastics

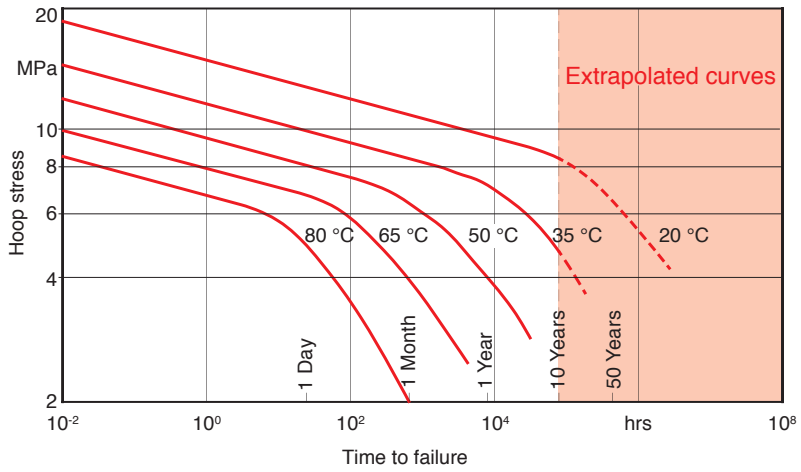

Figure 10.45 Creep rupture behavior as a function of temperature for a high density polyethylene

those points to the right represent the pipes that suffered brittle failure. As pointed out, generating a graph such as the one presented in Fig. 10.45, is an extremely involved and lengthy task that takes several years of testing.[5] Usually, these types of tests are carried out to 1,000 h (6 weeks) or 10,000 h (60 weeks) as shown in Fig. 10.46[6] for a polyamide 6 with 30% glass fibers tested at different temperatures. Once the steeper slope, which is typical of the brittle fracture, has been reached, the line can be extrapolated with some degree of confidence to estimate values of creep rupture at future times.

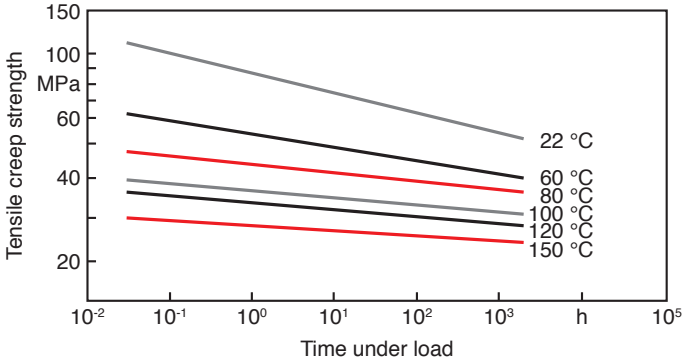

Figure 10.46 Creep rupture behavior as a function of temperature for a polyamide 6 with 30% glass fibers (Durethan BKV 30)

Although the creep test is considered a long-term test, in principle it is difficult to actually distinguish it from monotonic stress-strain tests or even impact tests. In fact, one can plot the full behavior of the material, from impact to creep, on the same graph as shown for PMMA under tensile loads at room temperature in Fig. 10.47 [7].

Figure 10.47 represents strain as a function of the logarithm of time. The strain line that represents rupture is denoted by ε_B. This line represents the maximum attainable strain before failure as a function of time. Obviously, a material tested under an impact tensile loading will strain much less than the same material tested in a creep test. Of interest in Fig. 10.47 are the two constant stress lines denoted by σ_1 and σ_2. The following example will help the reader interpret Fig. 10.47. It can be seen that a PMMA specimen loaded to a hypothetical stress of σ_1 will behave as a linear viscoelastic material up to a strain of 1%, at which point the first microcracks start forming or craze nucleation begins. The crazing appears a little later after the specimen's deformation is slightly over 2%. The test specimen continues

5 These tests where done between 1958 and 1968 at Hoechst AG, Germany.

6 Courtesy Bayer AG.

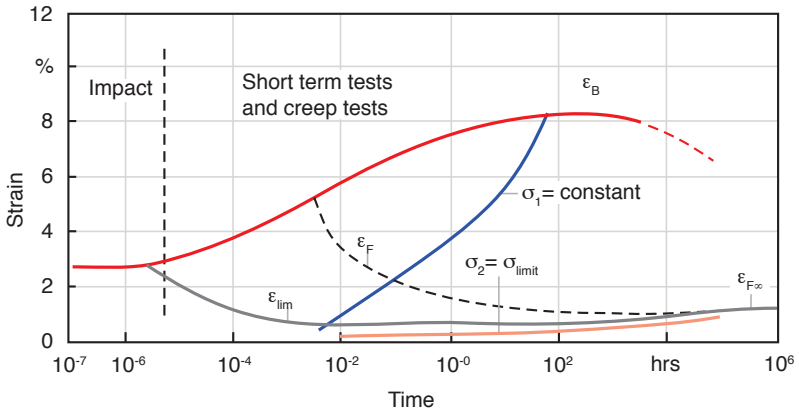

Figure 10.47 Plot of material behavior at room temperature, from impact to creep, for a PMMA under tensile load

to strain for the next 100 h until it ruptures at a strain of about 8 %. From the figure it can be deduced that the first signs of crazing can occur days and perhaps months or years before the material actually fractures. The stress line denoted by σ_2, where $\sigma_1 > \sigma_2$, is a limiting stress under which the component will not craze. Figure 10.47 also demonstrates that a component loaded at high speeds (i. e., impact) will craze and fail at the same strain. A limiting strain of 2.2 % is shown.

Because these tests take a long time to perform, it is often useful to test the material at higher temperatures, where a similar behavior occurs in a shorter period of

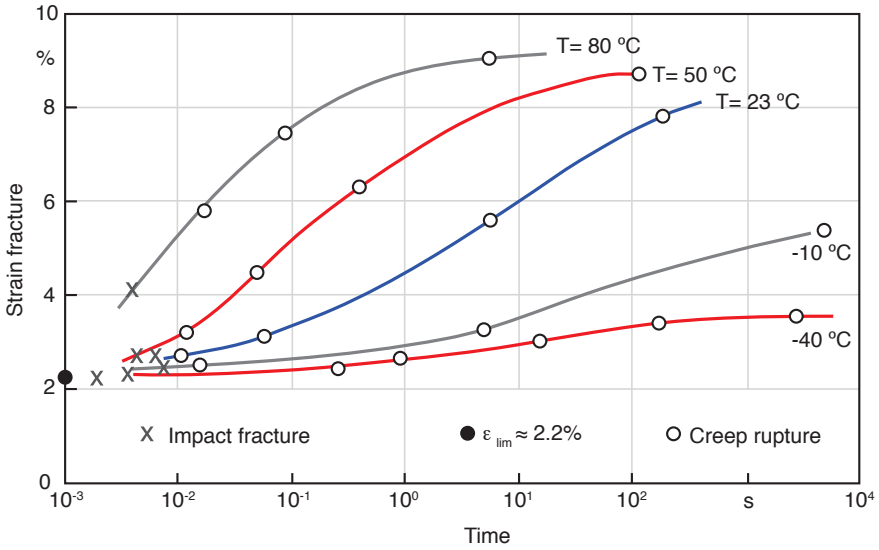

Figure 10.48 Strain at fracture for a PMMA in creep tests at various temperatures

time. Figure 10.48 [7] shows tests performed on PMMA samples at five different temperatures. When comparing the results in Fig. 10.48 to the curve presented in Fig. 10.47, a clear time-temperature superposition becomes visible. In the applied stress versus logarithm of time to rupture curves, such as the one shown in Fig. 10.45, the time-temperature superposition is also evident.

10.4.2 Fracture Mechanics Analysis of Creep Rupture

Crack growth rates during static tests have been found to have a power law relation with the stress intensity factor K_{Ic}, as

$$\frac{da}{dt} = AK_{Ic}^{m} \tag{10.30}$$

where A and m are material properties and K_{Ic} can be computed using Eq. 10.3 which results in

$$\frac{da}{dt} = A\left(Y\sigma\right)^{m}\left(\pi a\right)^{m/2} \tag{10.31}$$

By ignoring the time it takes for crack initiation, this equation may be used to predict a conservative time for creep rupture of a polymer component. If we integrate Eq. 10.31, we can predict the time it takes for a crack to grow from a length a_1 to a length a_2 by using

$$t = \frac{2\left(a_1^{1-m/2} - a_2^{1-m/2}\right)}{\left[\left(m-2\right)C_1\left(Y\sigma\sqrt{\pi}\right)^{m}\right]} \tag{10.32}$$

Experimental evidence shows that for slow crack growth, the value of m is large, and ranges between 7 and 25. Hence, the time it takes for a crack to grow between a_1 and a_2 is dominated by the initial crack length, because a small crack will grow much slower than a large one.

10.5 Fatigue

Dynamic loading of any material that leads to failure after a certain number of cycles is called *fatigue* or *dynamic fatigue*. Dynamic fatigue is of extreme importance because a cyclic or fluctuating load will cause a component to fail at much lower stresses than it does under monotonic loads.

10.5.1 Fatigue Test Methods

The standard fatigue tests for polymeric materials are the ASTM-D 671 test and the DIN 50100 test. In the ASTM test, a cantilever beam, shown in Fig. 10.49 [19], is held in a vise and bent at the other end by a yoke that is attached to a rotating, variably eccentric shaft. A constant stress throughout the test region in the specimen is achieved by its triangular shape.

Fatigue testing results are plotted as stress amplitude versus number of cycles to failure. These graphs are usually called *S-N curves*, a term inherited from metal fatigue testing [24]. Figure 10.50 [25] presents S-N curves for several thermoplastic and thermoset polymers tested at a 30-Hz frequency and about a zero mean stress, σ_m.

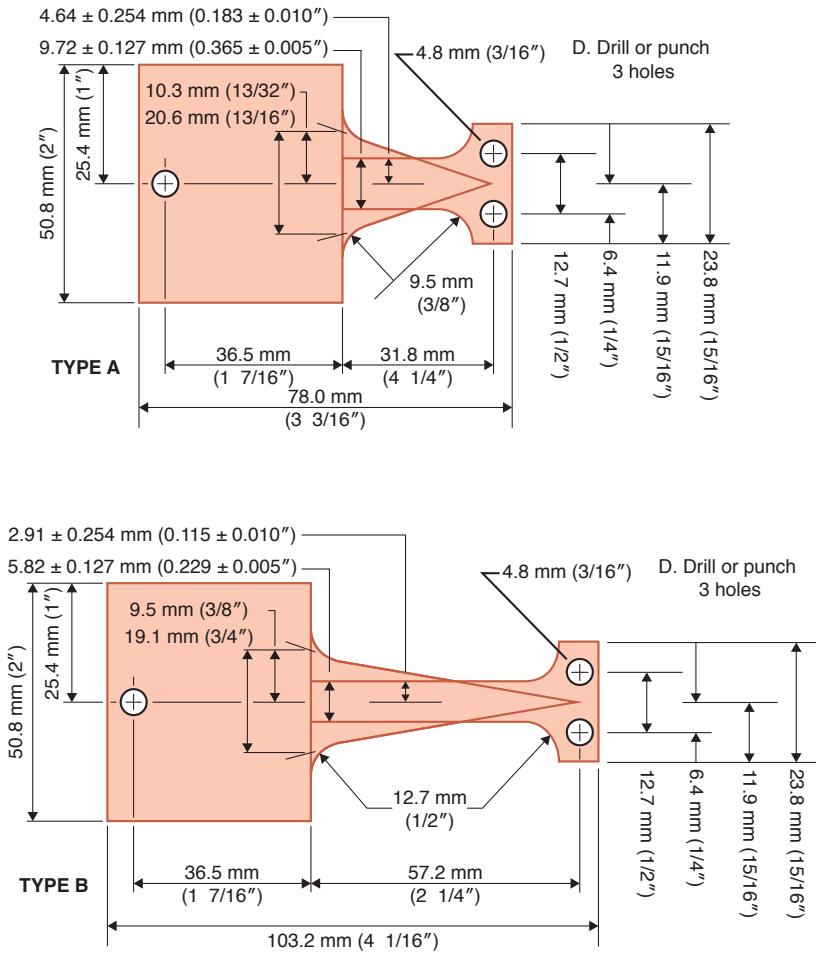

Figure 10.49 ASTM constant force fatigue test specimens

We must point out here that most fatigue data presented in the literature and in resin supplier data sheets do not present the frequency, specimen geometry, or environmental conditions at which the tests were performed. Hence, such data is not suitable for use in design. The data we present in this section is only intended to illustrate the various problems that arise when measuring fatigue life of a polymer. The information should also serve to reflect trends and as a comparison between various materials and conditions.

Fatigue in plastics is strongly dependent on the environment, the temperature, the frequency of loading, the surface, and other conditions. For example, due to surface irregularities and scratches, crack initiation at the surface is more likely in a polymer component that has been machined than in one that was injection molded. As mentioned in Chapter 5, an injection molded article is formed by several layers with different orientation. In such parts the outer layers act as a protective skin that inhibits crack initiation. In an injection molded article, cracks are more likely to initiate inside the component by defects such as weld lines and filler particles. The gate region is also a prime initiator of fatigue cracks. Corrosive environments also accelerate crack initiation and failure via fatigue. Corrosive environments and weathering will be discussed in more detail later in this chapter.

It is interesting to point out in Fig. 10.50 that thermoset polymers show higher fatigue strength than thermoplastics. An obvious cause for this is their greater

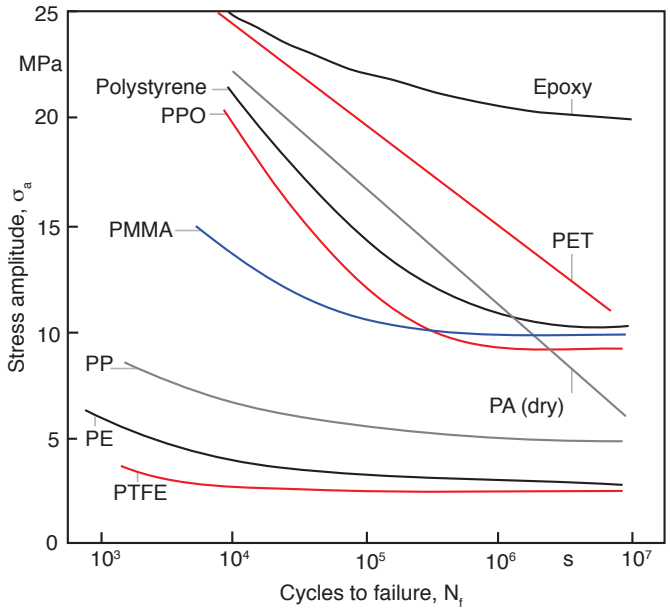

Figure 10.50 Stress-life (S-N) curves for several thermoplastic and thermoset polymers tested at a 30-Hz frequency about a zero mean stress

rigidity. However, more important is the lower internal damping or friction, which reduces temperature rise during testing. Temperature rise during testing is one of the main factors that lead to failure when experimentally testing thermoplastic polymers under cyclic loads. The heat generation during testing is caused by the combination of internal frictional or hysteretic heating and low thermal conductivity. At a low frequency and low stress level, the temperature inside the polymer specimen will rise and eventually reach thermal equilibrium when the heat generated by hysteretic heating equals the heat removed from the specimen by conduction. As the frequency is increased, viscous heat is generated faster, causing the temperature to rise even further. This phenomenon is shown in Fig. 10.51 [21] in which the temperature rise during uniaxial cyclic testing of polyacetal is plotted. After thermal equilibrium has been reached, a specimen eventually fails by conventional brittle fatigue, assuming the stress is above the endurance limit.

However, if the frequency or stress level is increased even further, the temperature will rise to the point at which the test specimen softens and ruptures before reaching thermal equilibrium. This mode of failure is usually referred to as *thermal fatigue*. This effect is clearly demonstrated in Fig. 10.52 [21]. The points marked T denote those specimens that failed due to thermal fatigue. The other points represent the specimens that failed by conventional mechanical fatigue. A better picture of how frequency plays a significant role in fatigue testing of polymeric materials is generated by plotting results such as those shown in Fig. 10.52 [21] for several

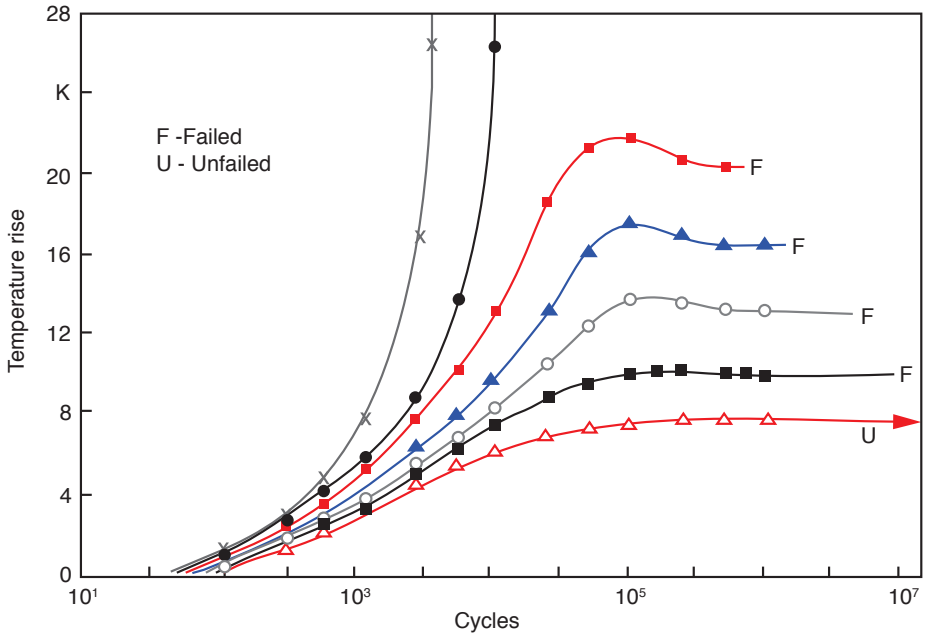

Figure 10.51 Temperature rise during uniaxial cycling under various stresses at 5-Hz

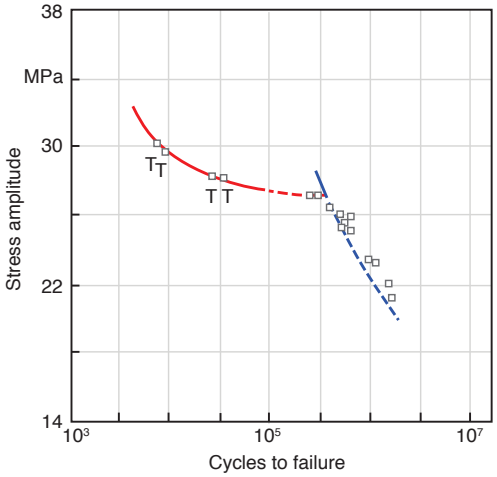

Figure 10.52 Fatigue and thermal failures in acetal tested at 1.67 Hz

frequencies (Fig. 10.53 [21]). The temperature rise in the component depends on the geometry and size of the test specimen. For example, thicker specimens will cool slower and are less likely to reach thermal equilibrium. Similarly, material around a stress concentrator will be subjected to higher stresses, which will result in temperatures that are higher than the rest of the specimen, leading to crack initiation caused by localized thermal fatigue. To neglect the effect of thermal

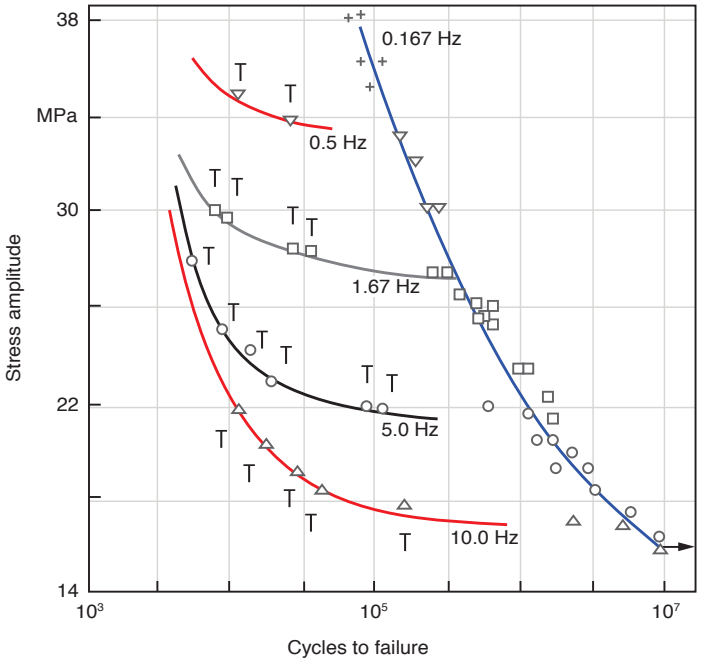

Figure 10.53 Fatigue and thermal failures in acetal tested at various frequencies

fatigue, cyclic tests with polymers must be performed at very low frequencies that make them much lengthier than those performed with metals and other materials that exhibit high thermal conductivity.

As mentioned earlier, stress concentrations have a great impact on the fatigue life of a component. Figures 10.54[7] and 10.55 compare S-N curves for uPVC and polyamide 66, respectively, for specimens with and without a 3 mm

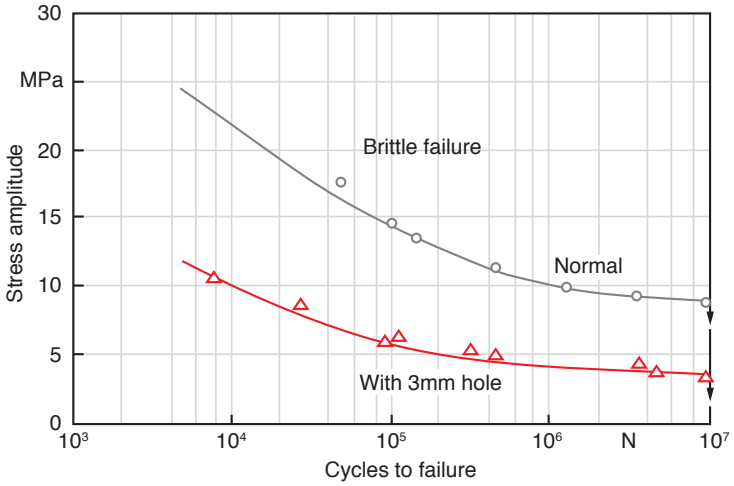

Figure 10.54 Fatigue curves for an uPVC using specimens with and without 3 mm hole stress concentrators, tested at 23 °C and 7-Hz with a zero mean stress

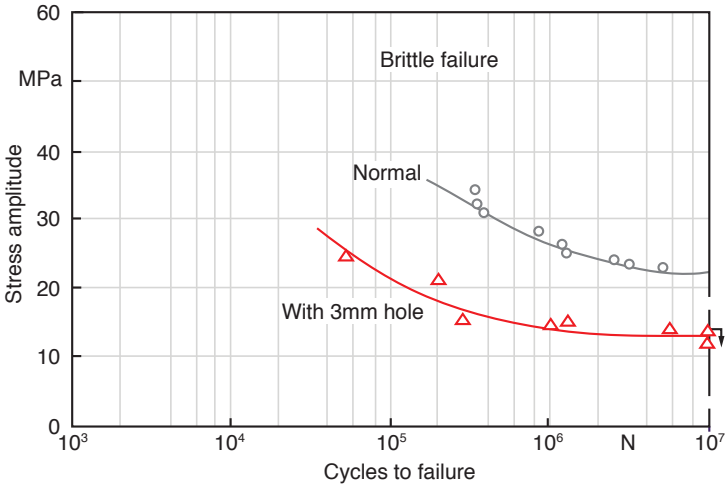

Figure 10.55 Fatigue curves for polyamide 66 (Durethan A30S) using specimens with and without 3 mm hole stress concentrators, tested at 23 °C and 7-Hz with a zero mean stress

7 All courtesy of Bayer AG, Germany.

circular hole acting as a stress concentrator. Material irregularities caused by filler particles or by weld lines also affect the fatigue of a component. Figures 10.56 and 10.57 compare S-N curves for regular PC and ABS test specimens to fatigue behavior of specimens with a weld line and specimens with a 3-mm circular hole.

Up to this point, we assumed a zero mean stress, σ_m. However, many polymer components that are subjected to cyclic loading have other loads and stresses applied

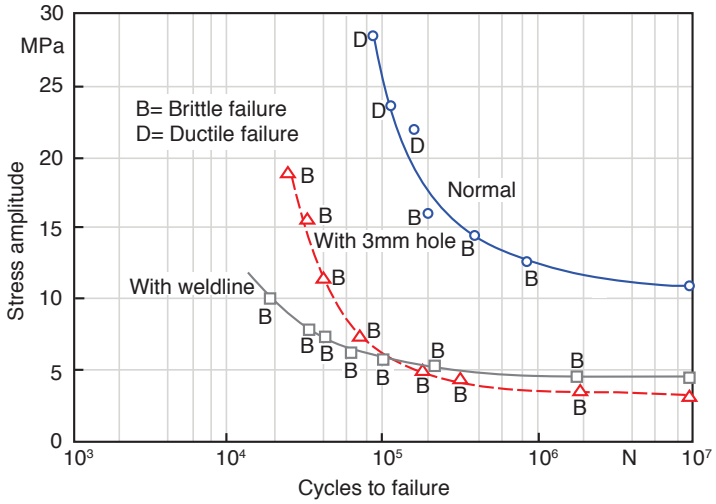

Figure 10.56 Fatigue curves for polycarbonate (Makrolon 2800) using regular specimens and specimens with 3 mm hole stress concentrators and weld lines, tested at 23 °C and 7-Hz with a zero mean stress

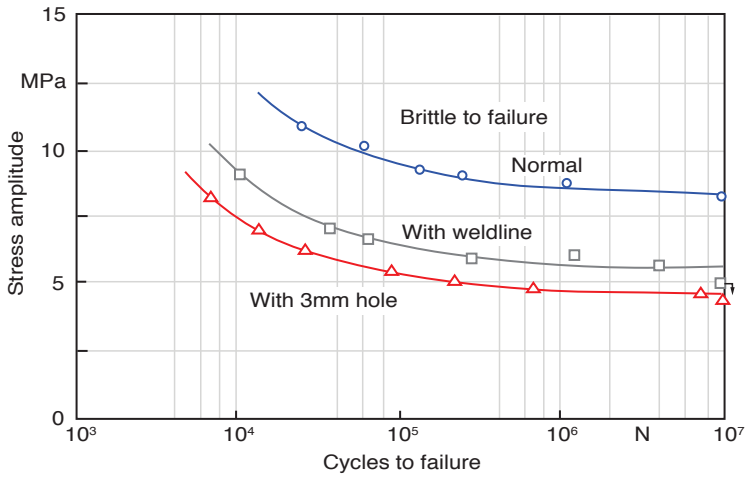

Figure 10.57 Fatigue curves for ABS (Novodur PH/AT) using regular specimens and specimens with 3 mm hole stress concentrators and weld lines tested at 23 °C and 7-Hz with a zero mean stress

to them, leading to non-zero mean stress values. This superposition of two types of loading will lead to a combination of creep, caused by the mean stress, and fatigue, caused by the cyclic stress, σ_a. Test results from experiments with cyclic loading and non-zero mean stresses are complicated by the fact that some specimens fail due to creep and others due to conventional brittle fatigue. Figure 10.58 illustrates this phenomenon for both cases with and without thermal fatigue, comparing them to experiments in which a simple static loading is applied. For cases with two or more dynamic loadings with different stress or strain amplitudes, a similar strain deformation progression is observed. Figure 10.59 [26] presents the strain progression in polyacetal specimens in which two stress amplitudes, one above and one below the linear viscoelastic range of the material, are applied. The strain progression, $\Delta\varepsilon$, is the added creep per cycle caused by different loadings, similar to *ratcheting* effects in metal components where different loadings are combined.

Fiber-reinforced composite polymers are stiffer and less susceptible to fatigue failure. Reinforced plastics have also been found to have lower hysteretic heating effects, making them less likely to fail by thermal fatigue. Figure 10.60 [27] presents the flexural fatigue behavior for glass fiber filled and unfilled polyamide 66 tested at 20 °C and a 0.5 Hz frequency with a zero mean stress. Parallel to the fiber orientation, the fatigue life was longer than the life of the specimens tested perpendicular to the orientation direction and the unfilled material specimens. The fatigue life of the unfilled specimen and the behavior perpendicular to the orienta-

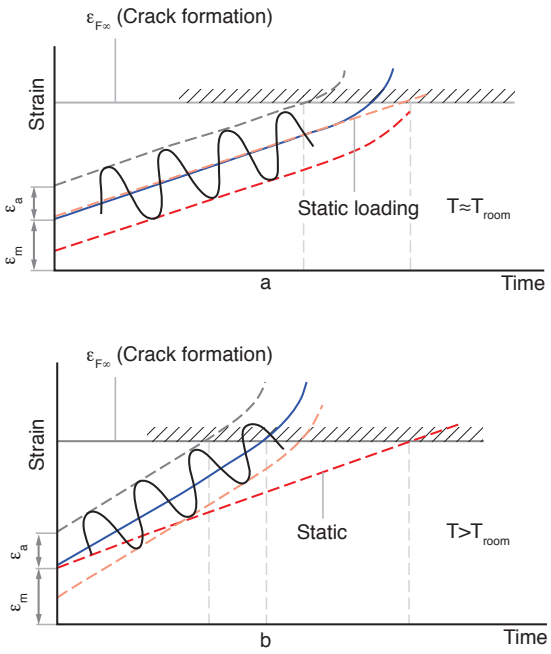

Figure 10.58 Creep and thermal fatigue effects during cyclic loading

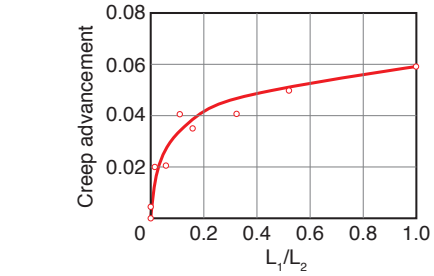

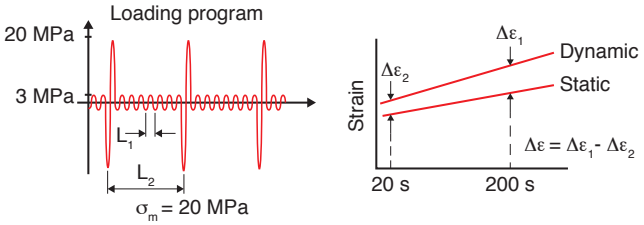

Figure 10.59 Strain progression in polyacetal specimens during fatigue tests with two stress amplitudes

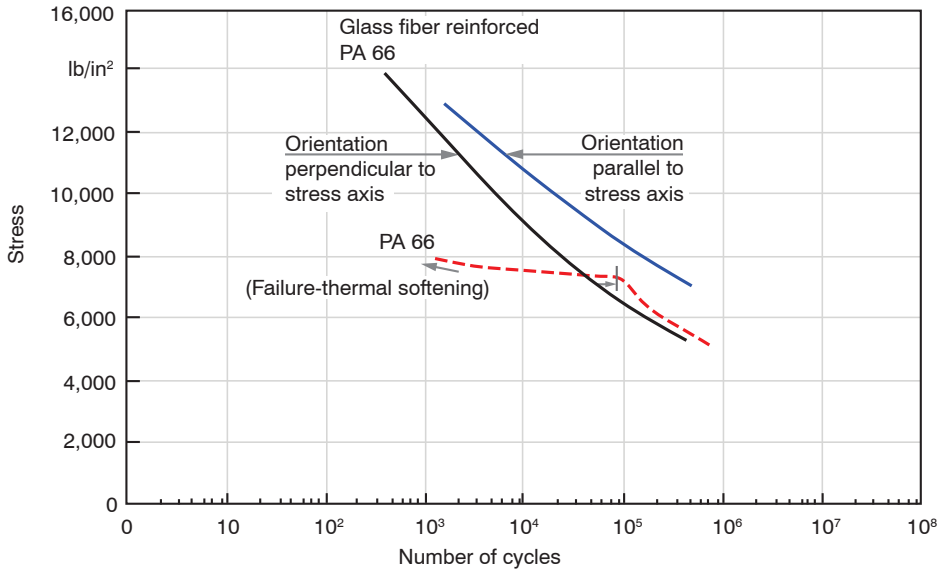

Figure 10.60 Flexural fatigue curves for a polyamide 66 and a glass fiber filled polyamide 66 tested at 20 °C and 0.5 Hz with a zero mean stress

tion direction were similar. However, the unfilled material failed by thermal fatigue at high stresses, whereas both the specimens tested perpendicular and parallel to the orientation direction failed by conventional fatigue at high stress levels. Fiber reinforced systems generally follow a sequence of events during failure consisting of debonding, cracking, and separation [28]. Figure 10.61 [29] clearly demonstrates this sequence of events with a glass-filled polyester mat tested at 20 °C and a fre-

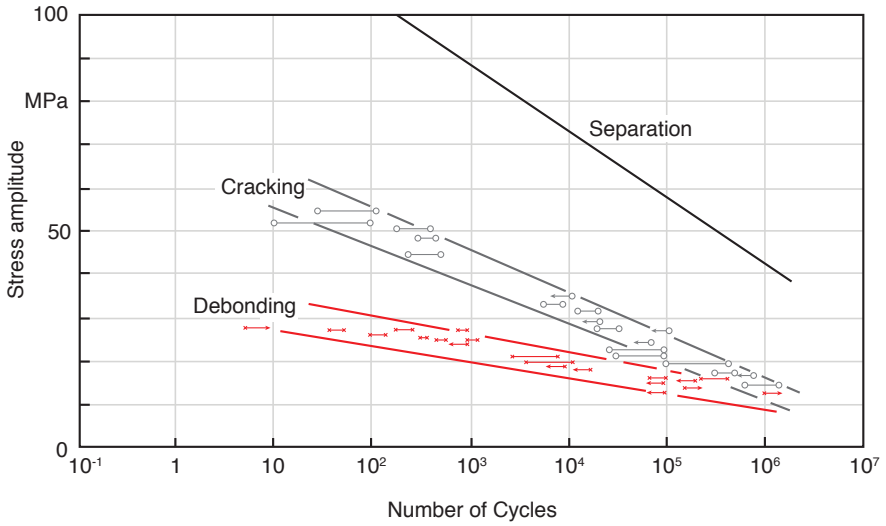

Figure 10.61 Fatigue curves for a glass filled polyester mat tested at 20 °C and a frequency of 1.67 Hz

quency of 1.67 Hz. In most composites, debonding occurs after just a few cycles. It should be pointed out that reinforced polymer composites often do not exhibit an endurance limit, making it necessary to use factors of safety between 3 and 4. The fracture by fatigue is generally preceded by cracking of the matrix material, which gives a visual warning of imminent failure. It is important to mention that the fatigue life of thermoset composites is also affected by temperature. Figure 10.62 [30] shows the tensile strength versus number of cycles to failure for a 50% glass fiber filled unsaturated polyester tested at 23 °C and at 93 °C. At ambient temperature, the material exhibits an endurance limit of about 65 MPa, which is reduced to 52 MPa at 93 °C.

10.5.2 Fracture Mechanics Analysis of Fatigue Failure

Crack growth rates during cyclic fatigue tests are related to the stress intensity factor difference, ΔK_{Ic},

$$\frac{da}{dt} = B\left(\Delta K_{Ic}\right)^n \tag{10.33}$$

where B and n are material properties and $\Delta K_{Ic} = K_{Ic\,\max} - K_{Ic\,\min}$ can be computed using Eq. 10.3 with the maximum and minimum alternating stresses. Crack growth behavior for several polymers is shown in Fig. 10.63 [29, 31]. Hertzberg and Manson [29] also show that for some materials, the crack growth rate is reduced somewhat with increasing test frequency.

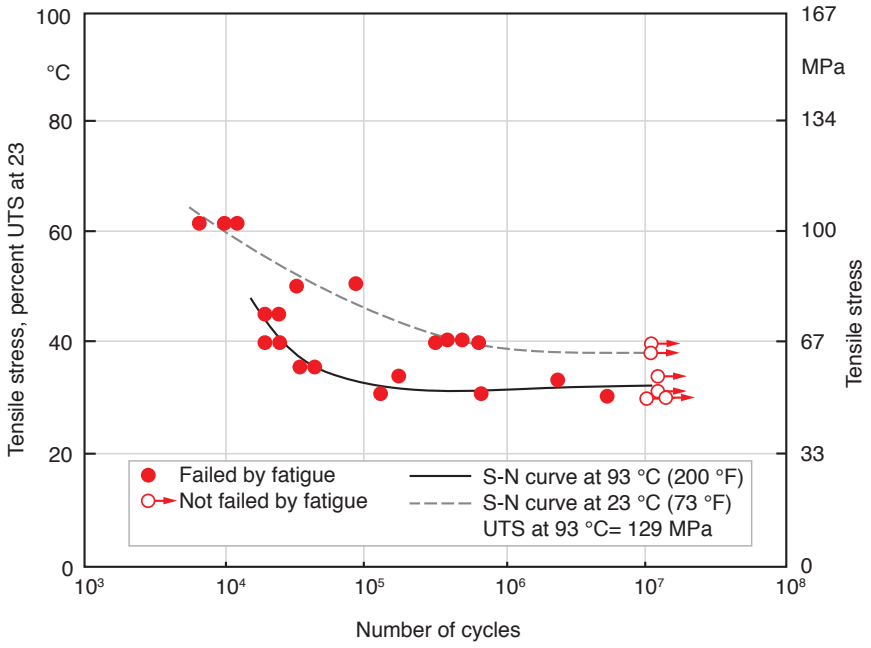

Figure 10.62 Fatigue curves for a 50 wt.% glass fiber reinforced polyester resin sheet molding compound tested at 23 °C and 93 °C and 10 Hz

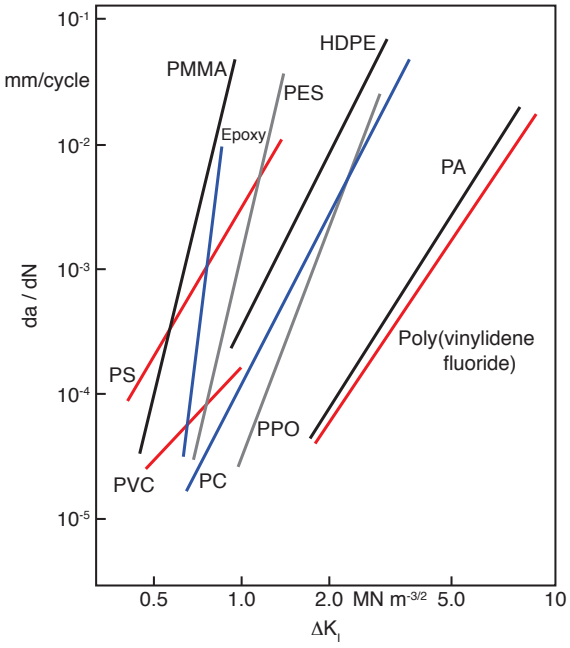

Figure 10.63 Crack growth rate during fatigue for various polymers

10.6 Friction and Wear

Friction is the resistance that two surfaces experience as they slide or try to slide past each other. Friction can be dry (i.e., direct surface-surface interaction) or lubricated, where the surfaces are separated by a thin film of a lubricating fluid.

The force that arises in a dry friction environment can be computed using *Coulomb's law of friction* as

$$F = \mu N \tag{10.34}$$

where F is the force in surface or sliding direction, N the normal force, and μ the coefficient of friction. Coefficients of friction between several polymers and different surfaces are listed in Table 10.8 [7]. However, when dealing with polymers, the process of two surfaces sliding past each other is complicated by the fact that enormous amounts of frictional heat can be generated and stored near the surface due to the low thermal conductivity of the material. The analysis of friction between polymer surfaces is complicated further by environmental effects, such as relative humidity, and by the likeliness of a polymer surface to deform when stressed, such as shown in Fig. 10.64 [7]. The top two figures illustrate metal-metal friction, whereas the bottom figures illustrate metal-polymer friction.

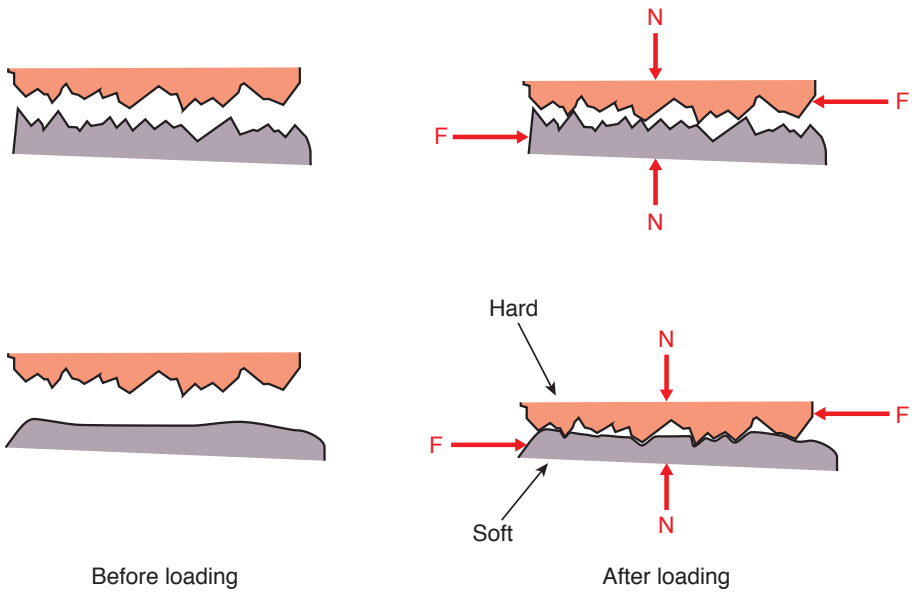

Figure 10.64 Effect of surface finish and hardness on frictional force build-up

Table 10.8 Coefficient of Friction for Various Polymers

Specimen	Partner	Velocity (mm/s)					
		0.03	0.1	0.4	0.8	3.0	10.6
Dry friction							
PP^{i}	PP^{s}	0.54	0.65	0.71	0.77	0.77	0.71
PA^{i}	PA^{i}	0.63	–	0.69	0.70	0.70	0.65
PP^{s}	PP^{s}	0.26	0.29	0.22	0.21	0.31	0.27
PA^{m}	PA^{m}	0.42	–	0.44	0.46	0.46	0.47
Steel	PP^{s}	0.24	0.26	0.27	0.29	0.30	0.31
Steel	PA^{m}	0.33	–	0.33	0.33	0.30	0.30
PP^{s}	Steel	0.33	0.34	0.37	0.37	0.38	0.38
PA^{m}	Steel	0.39	–	0.41	0.41	0.40	0.40
Water lubricated							
PP^{s}	PP^{s}	0.25	0.26	0.29	0.30	0.28	0.31
PA^{m}	PA^{m}	0.27	–	0.24	0.22	0.21	0.19
Steel	PP^{s}	0.23	0.25	0.26	0.26	0.26	0.22
PP^{s}	Steel	0.25	0.25	0.26	0.26	0.25	0.25
PA^{m}	Steel	0.20	–	0.23	0.23	0.22	0.18
Oil lubricated							
PP^{s}	PP^{s}	0.29	0.26	0.24	0.25	0.22	0.21
PA^{m}	PA^{m}	0.22	–	0.15	0.13	0.11	0.08
Steel	PP^{s}	0.17	0.17	0.16	0.16	0.14	0.14
Steel	PA^{m}	0.16	–	0.11	0.09	0.08	0.08
PP^{s}	Steel	0.31	0.30	0.30	0.29	0.27	0.25
PA^{m}	Steel	0.26	–	0.15	0.12	0.07	0.04

Note ^{i} = injection molded, ^{s} = sandblasted, ^{m} = machined

Temperature plays a significant role with regard to the coefficient of friction μ as clearly demonstrated in Fig. 10.65 for polyamide 66 and polyethylene. In the case of polyethylene, the friction first decreases with temperature. At 100 °C the friction increases because the polymer surface becomes tacky. The friction coefficient starts to drop as the melt temperature is approached. A similar behavior is seen for the polyamide.

As mentioned earlier, temperature increases can be caused by the energy released by the frictional forces. A temperature increase in time, due to friction between surfaces of the same material, can be estimated using

$$\Delta T = \frac{2\dot{Q}\sqrt{t}}{\sqrt{\pi}\sqrt{k\rho C_p}} \tag{10.35}$$

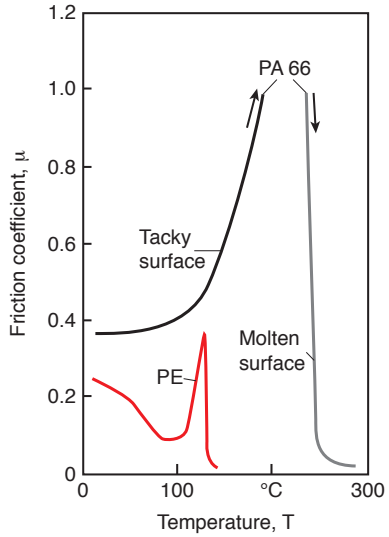

Figure 10.65 Temperature effect on coefficient of friction for a polyamide 66 and a high density polyethylene

where k is the thermal conductivity of the polymer, ρ the density, C_p the specific heat and $\dot{Q}$ the rate of energy created by the frictional forces, which can be computed using

$$\dot{Q} = Fv \tag{10.36}$$

where v is speed between the sliding surfaces.

Wear is also affected by the temperature of the environment. Figure 10.66[8] shows how wear rates increase dramatically as the surface temperature of the polymer increases, causing it to become tacky.

Table 10.9 [32] presents relative volumetric wear values for selected polymers and beechwood, using the volumetric wear of steel St 37 as a reference.

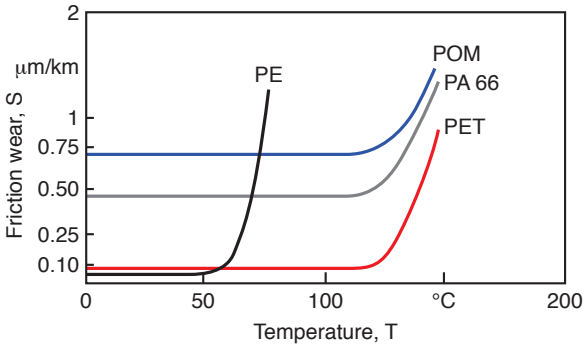

Figure 10.66 Wear as a function of temperature for various thermoplastics

8 Courtesy of BASF.

Table 10.9 Relative Volumetric Wear

Polymer	Density (g/cm^3)	Wear/Wear$_{steel}$
Steel	7.45	1.0
Beechwood	0.83	17.9
PMMA	1.31	11.2
PVC-U	1.33	5.8
HDPE	0.92	3.8
PP	0.90	2.8
HDPE	0.95	2.1
PA 66	1.13	1.0
UHMW-HDPE	0.94	0.6

10.7 Stability of Polymer Structures

The failure of certain structures is often determined by the stiffness of the structural element and not by the strength of the material. Such a failure is commonly referred to as *buckling*. The common example of buckling is the failure of a slender column under compressive load. Slender columns with hinged ends have a critical load, F_{crit}, defined by

$$F_{crit} = \frac{\pi^2 EI}{L^2} \tag{10.37}$$

where E is the modulus, I the area moment of inertia, and L the length of the column. If we use the relation $I = Ar^2$, where A is the cross-sectional area of the column and r is the radius of gyration, we can rewrite Eq. 10.37 as

$$\frac{F_{crit}}{A} = \frac{\pi^2 EI}{\left(L/r\right)^2} = \frac{\pi^2 EI}{\lambda^2} \tag{10.38}$$

where F_{crit}/A is often referred to as critical unit load and λ the slenderness ratio. For a square cross-section of dimensions $a \times a$ the slenderness ratio is defined by

$$\lambda = \frac{L}{a}\sqrt{12} \tag{10.39}$$

Menges and Dolfen performed a series of compression tests on glass fiber reinforced unsaturated polyester specimens with square cross-sections. Figure 10.67 [33] presents the unit loads and compressive strains at failure of the composite columns as functions of slenderness ratio. Their experiments demonstrated that for slenderness ratios smaller than 20, the columns failed in a shear delamination mode, while columns with slenderness ratios larger than 20 failed by buckling. Similarly, Gaube and Menges [7] performed experiments with various shell struc-

tures. Figure 10.68 presents the critical strain as a function of slenderness ratio and shows that in all cases buckling of polymer structures occurred below the value predicted by classical stability theory.

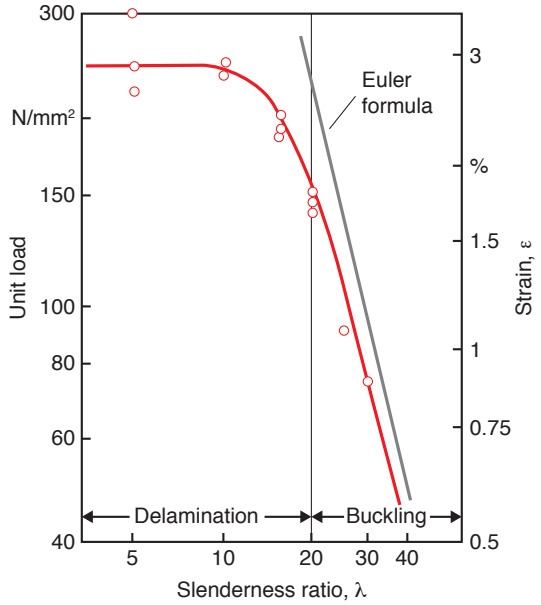

Figure 10.67 Delamination and buckling of glass reinforced UPE columns

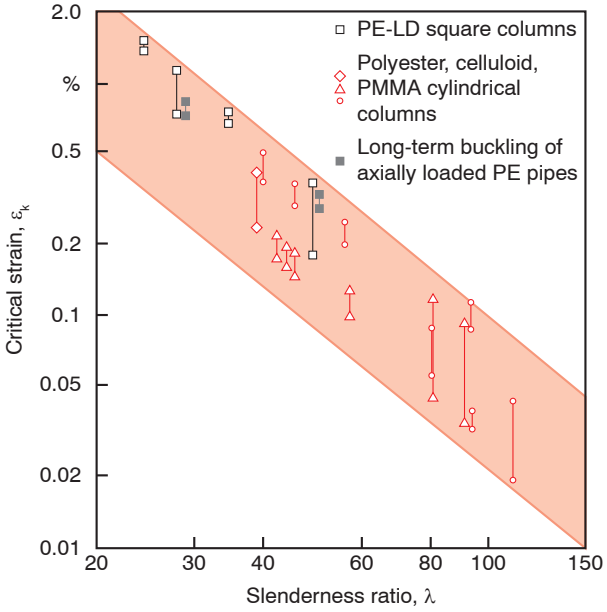

Figure 10.68 Buckling of columns and tubes

10.8 Environmental Effects on Polymer Failure

The environment or the media in contact with a loaded or unloaded component plays a significant role regarding its properties, life span, and mode of failure. The environment can be a natural one, such as rain, hail, solar ultra-violet radiation, extreme temperatures, etc., or an artificially created one, such as solvents, oils, detergents, high temperature environments, among others. Damage in a polymer component due to natural environmental influences is usually referred to as *weathering*.

10.8.1 Weathering

When exposed to the elements, polymeric materials begin to exhibit environmental cracks, which lead to early failure at stress levels significantly lower than those in the absence of these environments. Figure 10.69 [35] shows an electron micrograph of the surface of a high-density polyethylene beer crate after nine years of use and exposure to weather. The surface of the HDPE exhibits brittle cracks, which resulted from ultra violet rays, moisture, and extremes in temperature.

Figure 10.69 Electron micrograph of the surface of a high density polyethylene beer crate after nine years of use and exposure to weather

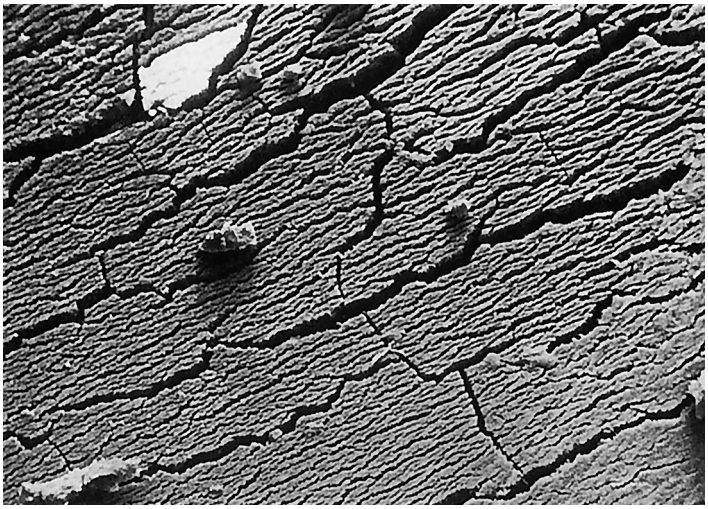

Figure 10.70 Surface of a polyoxymethylene specimen irradiated with ultra-violet light for 100 h in a laboratory environment

Standard tests such as the DIN 53486 test are available to evaluate the effects of weathering on properties of polymeric materials. It is often unclear which weathering aspects or which combination of these aspects influences material decays the most. Hence, laboratory tests are often done to isolate individual weathering factors such as ultra-violet radiation. For example, Fig. 10.70 shows the surface of a polyoxymethylene specimen irradiated with ultra violet light for 100 h in a laboratory environment. The DIN 53487 Xenotest is a standard test to expose polymer test specimens to UV radiation in a controlled environment. Figure 10.71 is a plot of impact strength of notched PMMA specimens as a function of hours of UV radiation exposure in a controlled DIN 53487 test and years of weathering under stand-

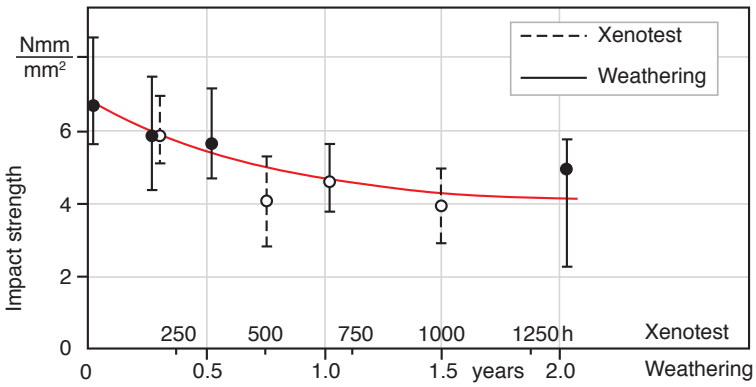

Figure 10.71 Impact strength of notched PMMA specimens as a function of hours of UV radiation exposure in a controlled test and weathering exposure time

ard DIN 53486 conditions. The correlation between the two tests is clear. The ASTM-D 4674 test evaluates the color stability of polymer specimens exposed to ultra-violet radiation. Standard tests also exist to test materials for specific applications such as the ASTM-D 2561 test, which evaluates the environmental stress cracking resistance of blow molded polyethylene containers.

As can be seen, the effect of ultra-violet radiation, moisture, and extreme temperature is detrimental to the mechanical properties of plastic parts. One example in which weathering completely destroys the strength properties of a material is shown for PVC in Fig. 10.72. The figure presents the decay of the impact strength of PVC pipes exposed to weathering in the United Kingdom [34]. As can be seen, the impact strength rapidly decreases in the first six months and is only 11 % of its original value after only two years. The location and climate of a region can have a significant impact on the weathering of polymer components. Figure 10.73 [34]

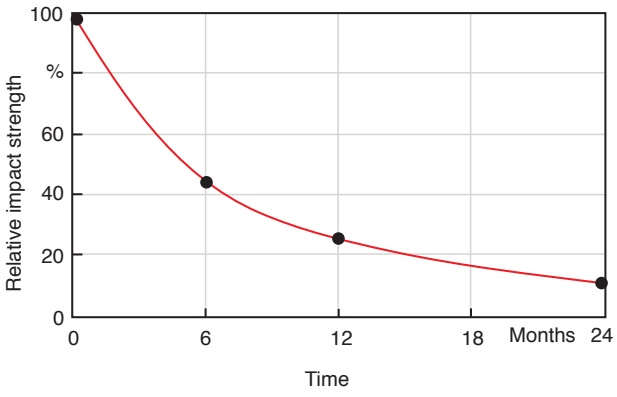

Figure 10.72 Impact strength of PVC pipe as a function weathering exposure time in the United Kingdom

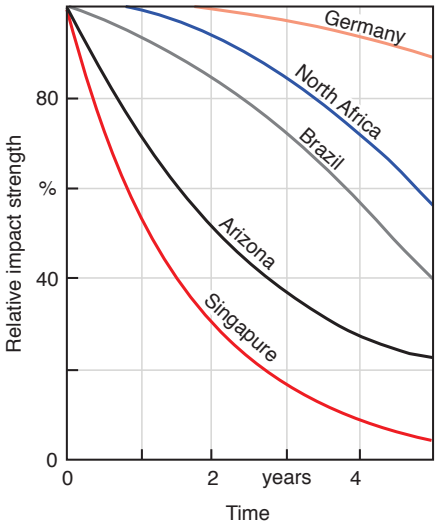

Figure 10.73 Impact strength as a function of weathering time of uPVC exposed at different geographic locations

shows the decrease in impact strength of rigid PVC as a function of time at five different locations. After five years of weathering, the PVC exposed in Germany still has 95 % of its original impact strength, whereas the samples exposed in Singapore have less than 5 % of their initial strength. The degradation in PVC samples is also accompanied by discoloration, as presented in Fig. 10.74 [34]. The figure shows discoloration of white PVC as a function of time at various locations. The samples exposed in Arizona showed significantly higher discoloration than those exposed in Pennsylvania and Florida.

The strength losses and discoloration in a weathering process are mainly attributed to the ultra-violet rays received from sunshine. This can be demonstrated by plotting properties as a function of actual sunshine received instead of time exposed. Figure 10.75 [35] is a plot of percent of initial impact strength for an ABS as a function of total hours of exposure to sun light in three different locations: Florida, Arizona, and West Virginia. The curve reveals the fact that by "normalizing" the curves with respect to exposure to actual sunshine, the three different sites with three completely different weather conditions[9] lead to the same relation between impact strength and total sunshine.

The effect of weathering can often be mitigated by the use of pigments, such as TiO_2 or carbon black, which absorb ultra-violet radiation, making it more difficult to penetrate the surface of a polymer component. The most important pigment is

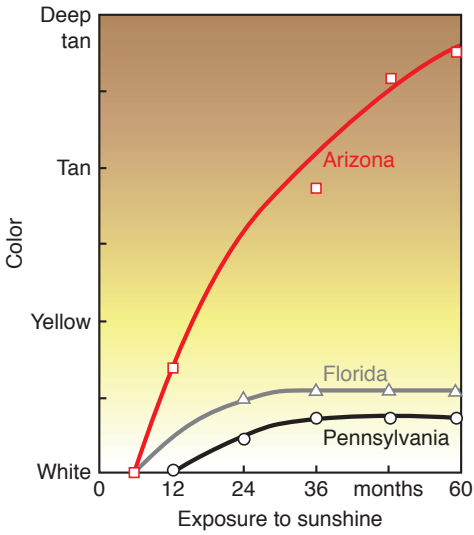

Figure 10.74 Discoloration as a function of weathering time of white PVC exposed at different geographic locations

9 Florida has a subtropical coastal climate with an annual rainfall of 952 mm and sunshine of 2750 hours. Arizona has a hot dry climate with 116 mm of rainfall and 3850 hours of sunshine. West Virginia has a milder climate with 992 mm of rainfall and 2150 hours of sunshine [28].

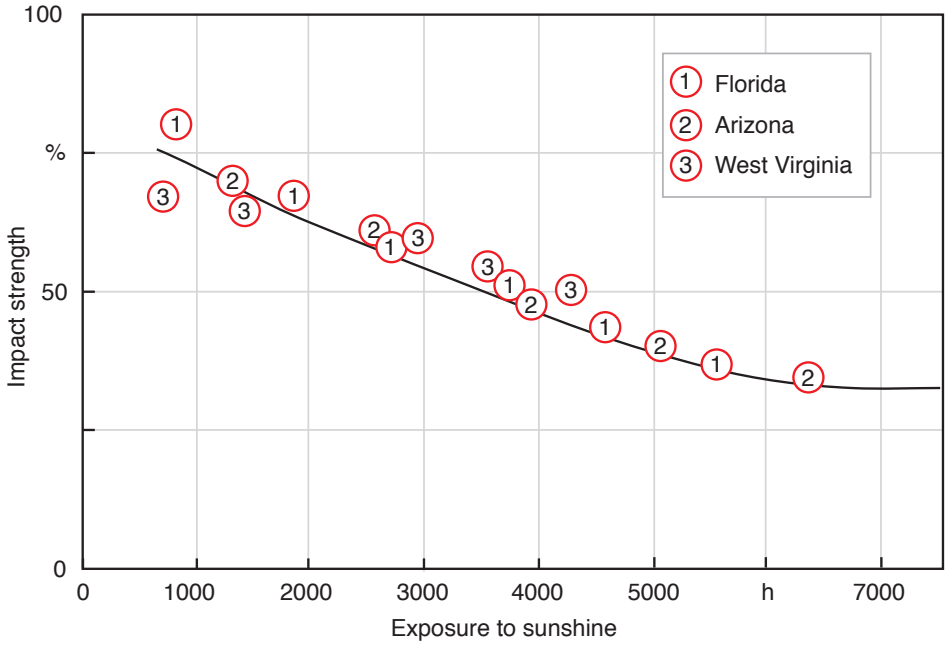

Figure 10.75 Impact strength of an ABS as a function of hours of exposure to actual sunshine

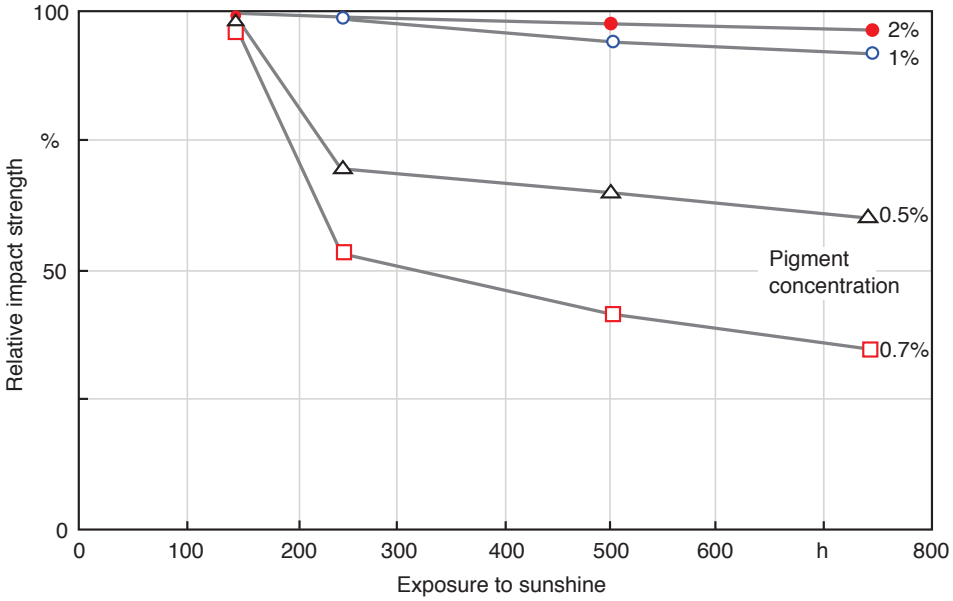

Figure 10.76 Influence of pigment concentration on the impact strength reduction of ABS specimens exposed to weather

carbon black. For example, ABS with white and black pigments exhibits a noticeable improvement in properties after exposure to ultra-violet radiation. Figure 10.76 [35] shows the reduction of impact strength in ABS samples as a function of exposure time to sunshine for four pigment concentrations: 0.5 %, 0.7 %, 1 %, and 2 %. It is clear that the optimal pigment concentration is around 1 %. Beyond 1 % of pigmentation there is little improvement in properties.

10.8.2 Chemical Degradation

Liquid environments can have positive and negative effects on the properties of polymeric materials. Some chemicals or solvents can have detrimental effects on a polymer component. Figure 10.77 [25] shows results of creep rupture tests done on PVC tubes as a function of hoop stress. It can be seen that the life span of the tubes in contact with iso-octane and isopropanol was significantly reduced as compared to the tubes in contact with water. The measured data for the pipes that contained iso-octane clearly show a slope reduction with a visible endurance limit, making it possible to do long-life predictions. On the other hand, the isopropanol samples do not exhibit such a slope reduction, suggesting that isopropanol is a harmful environment which acts as a solving agent and leads to gradual degradation of the PVC surface.

The question, whether a chemical is harmful to a specific polymeric material must be addressed if the polymer component is to be placed in such an environment. Similar to polymer solutions, a chemical reaction between a polymer and another substance is governed by the Gibbs free energy equation, as discussed in Chap-

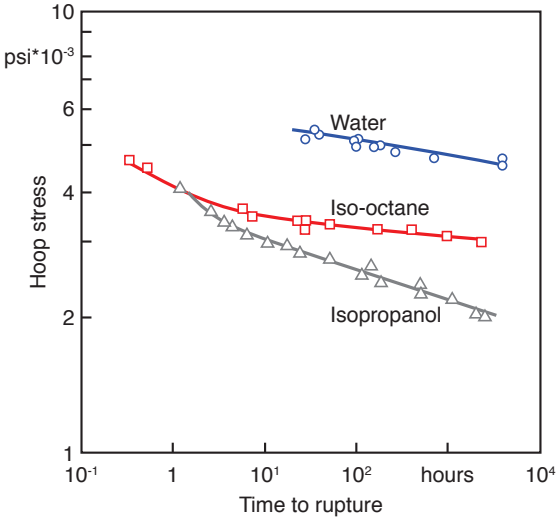

Figure 10.77 Effect of different environments on the stress rupture life of PVC pipe at 23 °C

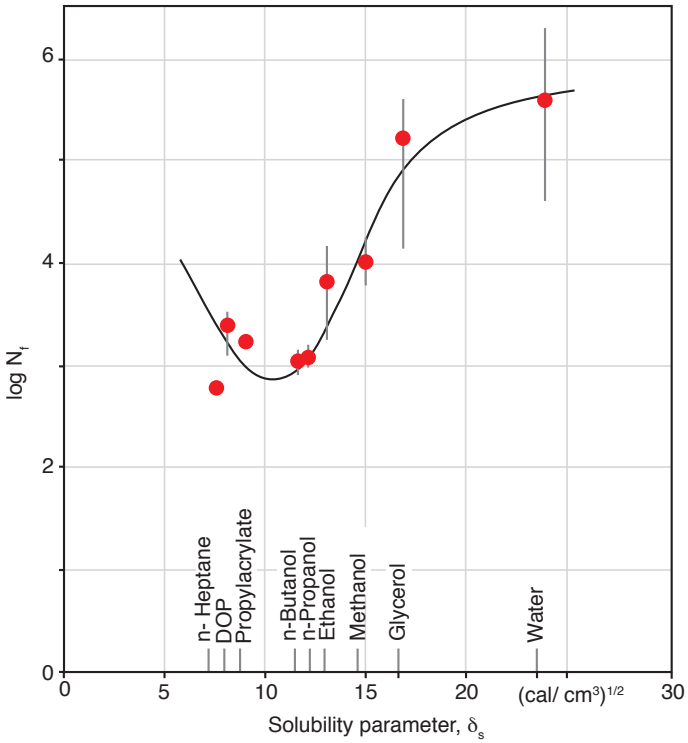

Figure 10.78 Effect of solubility parameter of the surrounding media on the fatigue life of polystyrene specimens

ter 6. If the change in enthalpy, ΔH, is negative, a chemical reaction will occur between the polymer and the solvent.

The effect of the solubility parameter of several solvents on the fatigue response of polystyrene samples is presented in Fig. 10.78 [31]. Here, the relation in Eq. 6.24 becomes evident; as the absolute difference between the solubility parameter of polystyrene, which is 9.1 $(cal/cm^3)^{1/2}$, and the solubility parameter of the solvent decreases, the fatigue life drops significantly.

It should be pointed out again that some substances are more likely to be absorbed by the polymer than others[10]. A polymer whose solubility parameter is close to the solubility parameter of the polymer is more likely to generate stress cracks and fail. This is illustrated in Fig. 10.79 [36], which shows the strain for crack formation in polyphenylene oxide samples as a function of solubility parameter[11] of various solutions. The specimens in those solutions that were ± 1 $(cal/cm^3)^{1/2}$ away from the solubility parameter of the polymer generated cracks at fairly low strains,

10 Please refer to Chapter 13.

11 Please refer to Chapter 6.

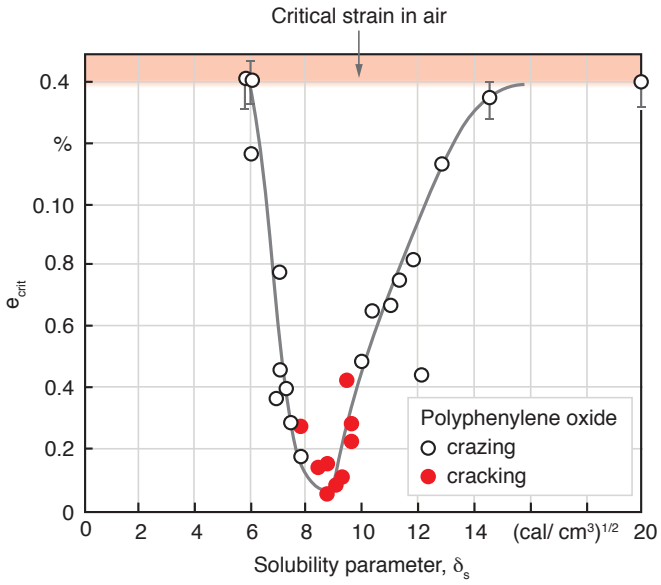

Figure 10.79 Strains at failure as a function of solubility parameter for polyphenylene oxide specimens: (•) cracking, (O) crazing

whereas those specimens in solutions with a solubility parameter further away from the solubility of the polymer formed crazes at much higher strains.

Environmental stress cracking or stress corrosion in a polymer component only occurs when crazes or microcracks are present. Hence, stress corrosion in a hostile environment can be avoided if the strain within the component is below the critical strain, ε_{fx}.

10.8.3 Thermal Degradation of Polymers

Because plastics are organic materials, they are threatened by chain breaking, splitting off of substituents, and oxidation. This degradation generally follows a reaction that can be described by the Arrhenius principle. The period of dwell or residence time permitted before thermal degradation occurs is given by

$$t_{\text{permitted}} \sim \exp\left(\frac{\Delta}{RT}\right) \tag{10.40}$$

where Δ is the activation energy of the polymer, R the gas constant and T the absolute temperature.

A material that is especially sensitive to thermal degradation is PVC; furthermore, the hydrogen chloride that results during degradation attacks metal parts. Ferrous metals act as catalyzers and accelerate degradation.

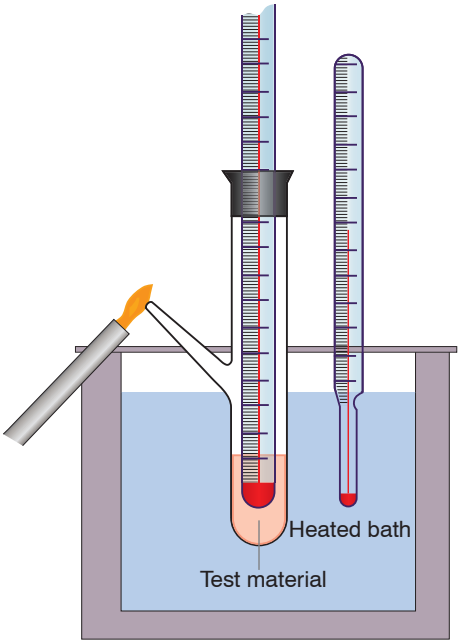

Figure 10.80 Test procedure to determine flash point of polymers

An easy method for determining the flash point of molding batches is by burning the hydrocarbons that are released at certain temperatures. This is shown schematically in Fig. 10.80[12] . For PVC one should use a vial with soda lye, instead of a flame, to determine the conversion of chlorine.

Thermogravimetry (TGA) is another widely used method to determine the resistance to decomposition or degradation of polymers at high temperatures. For this purpose, the test sample is warmed up in air or in a protective gas while placed on a highly sensitive scale. The change in weight of the test sample is then observed and recorded (see Chapter 3). It is also very useful to observe color changes in a sample while they are heated inside an oven. For example, to analyze the effect of processing additives, polymers are kneaded for different amounts of time, pressed onto a plate, and placed inside a heated oven. The time when a color change occurs is recorded to identify the occurrence of degradation.

12 Courtesy of BASF.

Examples

1. Charpy impact tests were performed on PVC samples with crack lengths of 1, 2, 3, 4, and 5 mm. The energy absorbed by the specimen during impact was 0.1, 0.062, 0.046, 0.037, and 0.031 J. The specimen's cross-section was 10 mm x 10 mm, and its length 40 mm. For a PVC modulus of 2 GPa, what is the material's fracture toughness?
   We must first compute a/w and read $\tilde{a}$ from Table 10.6, where w = 10 mm and L = 40 mm. Next we can calculate $tw\tilde{a}$ using Table 10.6), where w = 10 mm. Table 10.10 tabulates all the data.
   We can now plot U versus $tw\tilde{a}$ and estimate the fracture toughness from the slope, as shown in Fig. 10.82.

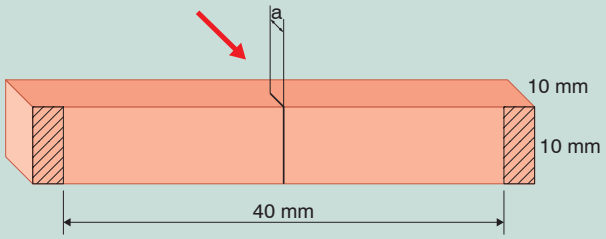

Figure 10.81 Sample geometry for Example 10.1

Table 10.10 Tabulated Data for Example 10.1

a (mm)	a/w	$\tilde{a}$	$Dw\tilde{a}$ (m^2)	U (J)
1	0.1	0.781	78.1×10^{-6}	0.1
2	0.2	0.468	46.8×10^{-6}	0.062
3	0.3	0.354	35.4×10^{-6}	0.0465
4	0.4	0.287	28.7×10^{-6}	0.037
5	0.5	0.233	23.3×10^{-6}	0.031

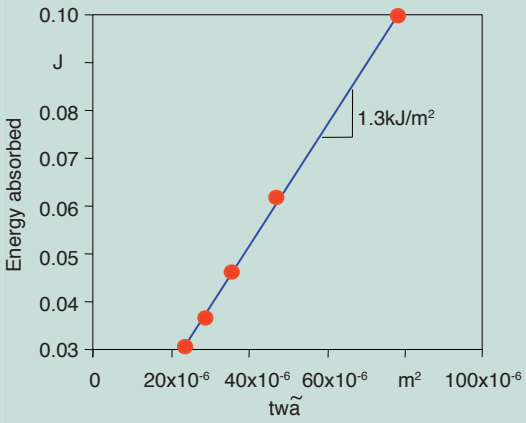

Figure 10.82 Fracture toughness plot for Example 10.1

We can also compute the critical stress intensity factor K_{Ic} using

$$K_{Ic} = \sqrt{EG_{Ic}} = 1.61 \text{MN m}^{-3/2}$$

2. You are asked to design a cylindrical, 200 mm diameter, 5 mm thick polycarbonate pressure vessel, as depicted in Fig. 10.83. To attach a fixture, the pressure vessel has a series of 0.5 mm deep grooves along its length. During its life, the pressure vessel will experience occasional pressure surges. Using the data given below, estimate the critical pressure inside the vessel that will result in fracture.

$$G_{Ic} = 5 \text{ kJ/m}^2, \quad E = 2.1 \text{ GPa}, \quad \nu = 0.33$$

This problem can be solved using Eq. 10.14

$$G_{Ic} = \frac{\pi \sigma_c^2 a}{E}\left(1 - \nu^2\right)$$

where, σ_c is the hoop stress given by

$$\sigma_c = \frac{p\bar{D}}{2h}$$

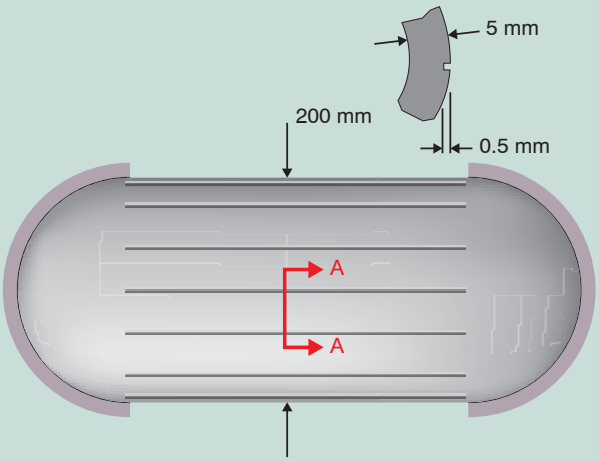

Figure 10.83 Pressure vessel geometry for Example 10.2

Note that since the vessel is axially restricted, the axial stress can be neglected. We can now solve for the pressure that will lead to failure using

$$p = \left[\frac{G_{Ic}}{\pi a}\frac{4Eh^2}{\left(1-\nu^2\right)\bar{D}^2}\right]^{1/2} = \left[\frac{5 \text{ kJ/m}^2}{\pi\left(0.5\text{mm}\right)}\frac{4\left(2.1 \text{ GPa}\right)\ 5\text{mm}^2}{\left(1-.33^2\right)\left(197.5\text{mm}\right)^2}\right]^{1/2} = 4.39 \text{ MPa}\left(645 \text{ psi}\right)$$

Problems

1. Is polystyrene an appropriate material to use for safety goggles? Why?
2. A high impact strength polycarbonate has a stress intensity factor, K_{Ic}, of 2.6 MN/m$^{3/2}$, and a strain toughness, G_{Ic} of 5.0 kJ/m^2. The polycarbonate will be used to assemble a hockey face guard. The face guard will fit onto the helmet using several snap-fits located on the helmet. This requires 1.5 mm deep grooves on the polycarbonate face guard. To what maximum stresses will you be able to subject the face guard in the region of the grooves?
3. Someone in your company designed high-density polyethylene water pipes to transport cold and hot water at pressures of 1.5 bar. The hot water will be at 50 °C, and you can assume the cold water to be at room temperature. The pipe's inner diameter is 50 mm with a wall thickness of 1 mm. Would you approve this product with a 5 year warranty for the above specifications? Why?
4. A PS-HI test specimen with a 20 mm x 1 mm cross-section and 2 mm long central crack is carrying a 100 N load. Plot the stress distribution near, but not at the crack tip.
5. A PS component with 0.5 mm long crazes is being stressed between – 5 MPa and + 5 MPa. At what rate is the length of the crazes growing? Estimate the number of cycles to failure.
6. A creeping PS component loaded to a stress of 2 MPa is showing the formation of small crazes that measure approximately 200 µm. Estimate the time it takes for the crazes to grow to a length of 500 µm. Use m = 7 and m = 25.

References

[1] Crawford, R.J., *Plastics Engineering*, 2nd ed., Pergamon Press, (1987).

[2] Kinloch, A.J., Young, R.J., *Fracture Behavior of Polymers*, Applied Science Publishers, London, (1983).

[3] Griffith, A.A., *Phil. Trans. Roy. Soc., A221*, 163, (1920).

[4] Rice, J.R., *J. Appl. Mech., 35*, 379, (1965).

[5] Vincent, P.I., *Plastics, 29*, 79 (1964).

[6] Beahan, P., Bevis, M., and Hull, D., *Phil. Mag., 24*, 1267, (1971).

[7] Menges, G., Haberstroh, E., Michaeli, W., and Schmachtenberg, E., *Menges Werkstoffkunde Kunststoffe*, Hanser Publishers, Munich (2011).

[8] Nicolay, Ph.D. Thesis, IKV, RWTH-Aachen, (1976).

[9] Menges, G., and Alf, E., *Kunststoffe, 62*, 259, (1972).

[10] Schultz, J. M., *Polymer Materials Science*, Prentice-Hall, Englewood Cliffs, N.J., (1974).

[11] Ehrenstein, G. W., *Polymeric Materials*, Hanser Publishers, Munich, (2001).

[12] Engel, L., Klingele, H., Ehrenstein, G. W., and Schaper, H., *Scanning Electron Microscopy of Plastics Failure*, Hanser Publishers, Munich, (2010)

[13] Roskothen, H. J., Ph. D. Thesis, IKV, RWTH-Aachen, (1974).

[14] Boyer, R. F., *Polymer Eng. Sci., 8,* 161, (1968).

[15] Boden, H. E., Ph.D. Thesis, IKV, RWTH-Aachen, Germany, (1983).

[16] Menges, G., and Boden, H.-E., *Failure of Plastics*, Chapter 9, in Eds. W. Brostow, and R.D. Corneliussen, Hanser Publishers, Munich, (1986).

[17] Andrews, E. H., *Fracture in Polymers*, Oliver and Body, London, (1968).

[18] Rest, H., Ph. D. Thesis, IKV-Aachen, (1984).

[19] ASTM, Vol .08.01, Plastics (I): C 177-D 1600, ASTM-D 256, (2010).

[20] Plati, E. and Williams, J. G., *Polym. Eng. Sci., 15,* 470, (1975).

[21] Crawford, R. J., and Benham, P. P., *Polymer, 16*, 908, (1975).

[22] Richard, K., Gaube, E., and Diedrich, G., *Kunststoffe, 49*, 516, (1959).

[23] Gaube, E. and Kausch, H. H., *Kunststoffe, 63,* 391, (1973).

[24] Bannantine, J. A., Comer, J. J., and Handrock, J. L., *Fundamentals of Metal Fatigue Analysis*, Prentice Hall, Englewood Cliffs, (1990).

[25] Riddell, M. N., *Plast. Eng., 40*, 4, 71, (1974).

[26] Kleinemeier, B., Ph. D. Thesis, IKW-Aachen, Germany, (1979).

[27] Bucknall, C. B., Gotham, K. V., and Vincent, P. I., in *Polymer Science. A Materials Handbook*, Chapter 10 Ed. A. D. Jenkins, Vol. 1, American Elsevier, New York, (1972).

[28] Owen, M. J., Smith, T. R., and Dukes, R., *Plast.Polym., 37*, 227, (1969).

[29] Hertzberg, R. W., and Manson, J. A., *Fatigue of Engineering Plastics*, Academic Press, New York, (1980).

[30] Denton, D. L., *The Mechanical Properties of an SMC-R50 Composite*, Owens-Corning Fiberglas Corp., (1979).

[31] Hertzberg, R. W., Manson, J. A., and Skibo, M. D., *Polym. Eng. Sci., 15*, 252, (1975).

[32] Domininghaus, H., Elsner, P., Eyerer, P., and Hirth, T., *Kunststoffe – Eigenschaften und Anwendungen*, Springer, Munich, (2012).

[33] Dolfen, E., Ph. D. Thesis, IKV, RWTH-Aachen, (1978).

[34] Davis, A. and Sims, D., *Weathering of Polymers*, Applied Science Publishers, London, (1983).

[35] Ruhnke, G. M. and Biritz, L. F., *Kunststoffe, 62*, 250, (1972).

[36] Bernier, G. A., and Kambour, R. P., *Macromolecules, 1*, 393, (1968).

11 Electrical Properties of Polymers

In contrast to metals, common polymers are poor electron conductors. Similar to mechanical properties, their electric properties depend to a great extent on the flexibility of the polymer's molecular blocks. The intent of this chapter is to familiarize the reader with electrical properties of polymers by discussing their dielectric, conductive, and magnetic properties.

11.1 Dielectric Behavior[1]

11.1.1 Dielectric Coefficient

The most commonly used electrical property is the dielectric coefficient, ε_r. Let us begin the discussion on dielectricity by looking at a disk condenser charged by the circuit shown in Fig 11.1. The accumulated charge, Q, is proportional to the consumed voltage, U:

$$Q = CU \tag{11.1}$$

where the proportionality constant, C, is called *capacitance*. The capacitance for the disk condenser in a vacuum, also valid for air, is defined by

$$C_0 = \varepsilon_0 \frac{A}{d} \tag{11.2}$$

where ε_0 is the vacuum's dielectric coefficient, A the disk's area, and d the separation between the plates. Hence, the condenser's charge is given by

$$Q_0 = C_0 U \tag{11.3}$$

1 Parts of this chapter are based on the lecture notes of Prof. H. Hersping at the RWTH-Aachen, Germany, (1972).

If we replace the vacuum or air between the disks of the condenser by a real dielectric, the charge increases, for the same voltage U, by the factor ε_r represented by

$$Q = \varepsilon_r Q_0 \tag{11.4}$$

and the capacity changes to

$$C = \varepsilon_r C_0 = \varepsilon_r \varepsilon_0 \frac{A}{d} \tag{11.5}$$

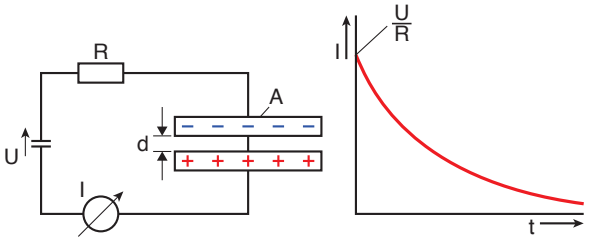

Figure 11.1 Condenser circuit used to measure capacitance properties

The constant ε_r is often called the *relative dielectric coefficient*. It is dimensionless, and it is dependent on the material, temperature, and frequency. However, the charge changes when a dielectric material is inserted between the plates. This change in charge is caused by the influence of the electric field developing polarization charges in the dielectric. This is more clearly represented in Fig. 11.2. The new charges that develop between the condenser's metal disks are called Q_p. Hence, the total charge becomes

$$Q = Q_0 + Q_p \tag{11.6}$$

In general terms, the charge is expressed per unit area as

$$\frac{Q}{A} = \frac{Q_0}{A} + \frac{Q_p}{A} = D \tag{11.7}$$

where D is the total charge per unit area. Introducing the *electric field intensity*, E, Eq. 11.2 can be rewritten as

$$E = \frac{U}{d} = \frac{1}{\varepsilon_0}\frac{Q_0}{A} = \frac{1}{\varepsilon_0 \varepsilon_r}\frac{Q}{A} \tag{11.8}$$

which results in

$$\frac{Q_0}{A} = \varepsilon_0 E \tag{11.9}$$

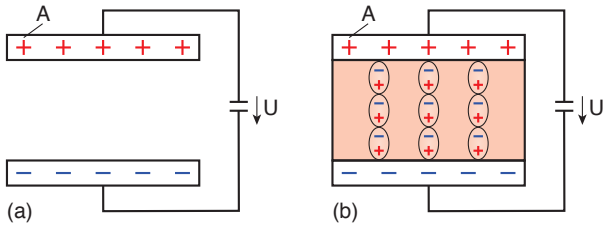

Figure 11.2 Polarization charges a) without a dielectric, b) with a dielectric

If the charged condenser is separated from the voltage source beforehand, the voltage of the condenser will decrease with insertion of a dielectric. Thus, the inserted dielectric also increases the capacity of the condenser. Let us define the charge density of the polarization surface as

$$P = \frac{Q_p}{A} \tag{11.10}$$

This causes the total charge per unit area to become

$$D = \varepsilon_0 E + P \tag{11.11}$$

which can be rewritten as

$$P = D - \varepsilon_0 E \tag{11.12}$$

No field can develop within metallic condenser plates because of the high electric conductivity. Therefore, using the dielectric charge density per unit area, Eqs. 11.7 and 11.8 can be combined to give

$$D = \varepsilon_0 \varepsilon_r E \tag{11.13}$$

Substituting this result into Eq. 11.12, we get

$$P = \varepsilon_0 \varepsilon_r E - \varepsilon_0 E \tag{11.14}$$

or

$$P = \varepsilon_0 \left[\varepsilon_r - 1\right] E = \varepsilon_0 \chi E \tag{11.15}$$

The factor χ is generally referred to as *dielectric susceptibility*. It is a measurement of the ability of a material to be a polarizer.

Table 11.1 lists the relative dielectric coefficients of important polymers. The measurements were conducted using the standard test DIN 53 483 in condensers of different geometries, which in turn depended on the sample type. The ASTM standard test is described by ASTM D150. Figures 11.3 [1] and 11.4 [1] present the dielectric coefficient for selected polymers as a function of temperature and frequency, respectively.

Table 11.1 Relative Dielectric Coefficient, ε_r, of Various Polymers [2]

Polymer	Relative dielectric coefficient, ε_r	
	800 Hz	10^6 Hz
Expanded polystyrene	1.05	1.05
Polytetrafluoroethylene	2.05	2.05
Polyethylene (density dependent)	2.3 – 2.4	2.3 – 2.4
Polystyrene	2.5	2.5
Polypropylene	2.3	2.3
Polyphenylene ether	2.7	2.7
Polycarbonate	3.0	3.0
Polyethylene terephthalate	3.0 – 4.0	3.0 – 4.0
ABS	4.6	3.4
Cellulose acetate, type 433	5.3	4.6
Polyamide 6 (moisture content dependent)	3.7 – 7.0	
Polyamide 66 (moisture content dependent)	3.6 – 5.0	
Epoxy resin (unfilled)		2.5 – 5.4
Phenolic type 31.5	6.0 – 9.0	6.0
Phenol type 74	6.0 – 10.0	4.0 – 7.0
Urea type 131.5	6.0 – 7.0	6.0 – 8.0
Melamine type 154	5.0	10.0

11.1.2 Mechanisms of Dielectrical Polarization

The two most important molecular mechanisms causing polarization of a dielectric in an electric field are *displacement polarization* and *orientation polarization*.

Under the influence of an electric field, the charges deform in field direction by aligning with the atomic nucleus (electron polarization) or with the ions (ionic polarization). This is usually called *displacement polarization* and is shown in Fig. 11.5.

Because of their structure, some molecules possess a dipole moment in the spaces that are free of an electric field. Hence, when these molecules enter an electric field, they will orient according to the strength of the field. This is generally referred to as *orientation polarization* and is schematically shown in Fig. 11.5.

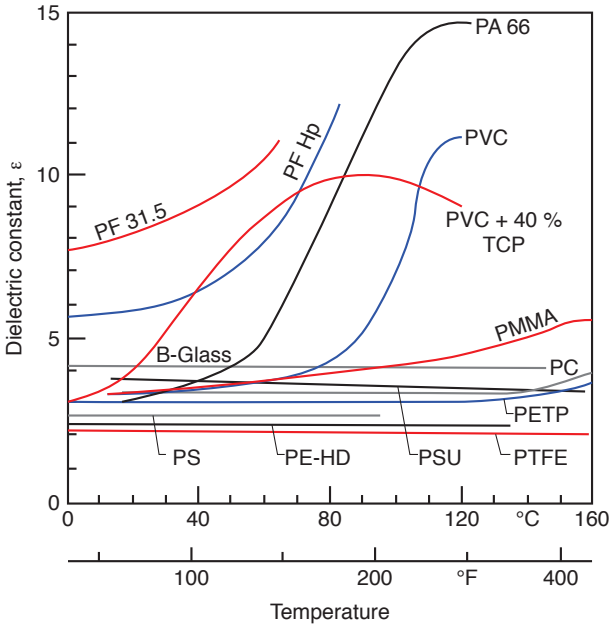

Figure 11.3 Dielectric constant as a function of temperature for various polymers

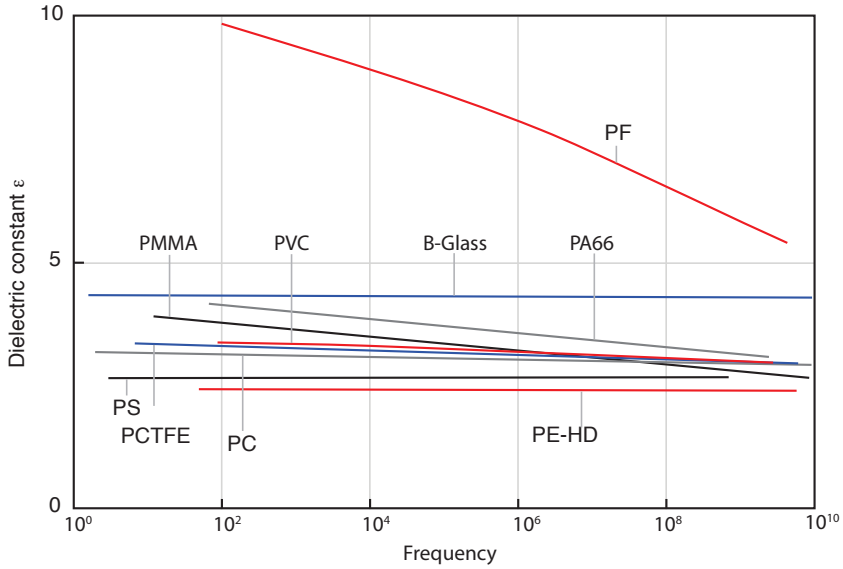

Figure 11.4 Dielectric constant as a function of frequency for various polymers

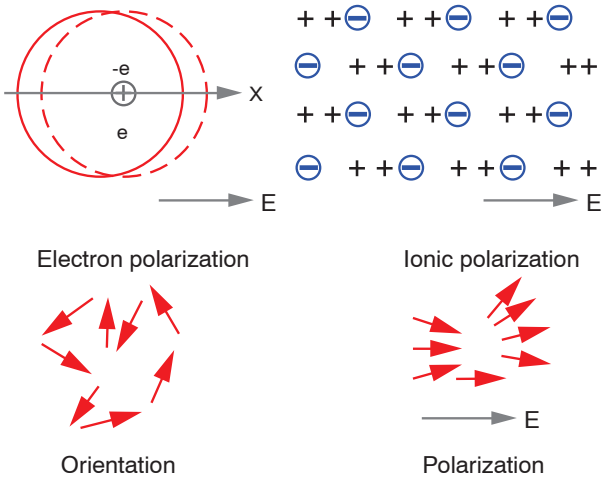

Figure 11.5 Polarization processes

It takes some time to displace or deform the molecular dipoles in the field direction and even longer time for the orientation polarization and the more viscous the surrounding medium is, the longer this process takes. In alternating fields of high frequency, the dipole movement can lag behind at certain frequencies. This is called dielectric relaxation, which leads to dielectric losses that appear as dielectric heating of the polar molecules.

In contrast to this, the changes during displacement polarization happen so quickly that it can even follow a light wave. Hence, the refractive index, n, of light is determined by the displacement contribution, ε_v, of the dielectric constant[2]. The relation between n and ε_v is given by

$$n = \sqrt{\varepsilon_v} \tag{11.16}$$

This provides a means to measure polarization properties because the polarization of electrons determines the refractive index of polymers. It should be noted that ion or molecular segments of polymers are mainly stimulated in the middle of the infrared spectrum.

A number of polymers have permanent dipoles. The best known polar polymer is polyvinyl chloride, and C = O groups also represent a permanent dipole. Therefore, polymers with that kind of building block suffer dielectric losses in alternating fields of certain frequencies. For example, Fig. 11.6 shows the frequency dependence of susceptibility.

2 For a more in-depth coverage of optical properties the reader is referred to Chapter 12 of this book.

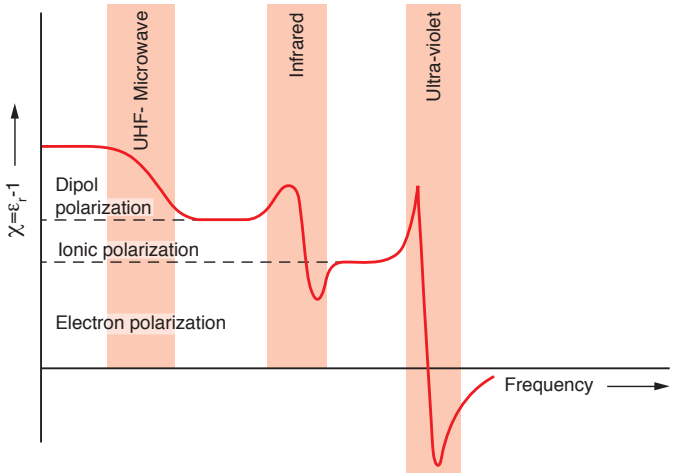

Figure 11.6 Frequency dependence of different polarization cases

In addition, the influence of fillers on the relative dielectric coefficient is of considerable practical interest. The rule of mixtures can be used to calculate the effective dielectric coefficient of a matrix with fillers that are assumed to be of spherical shape as

$$\varepsilon_{\text{eff}} = \varepsilon_{\text{matrix}}\left(1-3\phi\frac{\varepsilon_{\text{matrix}}-\varepsilon_{\text{filler}}}{2\varepsilon_{\text{matrix}}+\varepsilon_{\text{filler}}}\right) \tag{11.17}$$

Materials with air entrapments, such as foams, have a filler dielectric coefficient of $\varepsilon_{air}=1$; thus, the effective dielectric coefficient of the material reduces to

$$\varepsilon_{\text{foam}} = \varepsilon_{\text{matri}_{\text{X}}}\left(1-3\phi\frac{\varepsilon_{\text{matrix}}-1}{2\varepsilon_{\text{matrix}}+1}\right) \tag{11.18}$$

and, for metal fillers, where $\varepsilon_{metal}=\infty$, it can be written as

$$\varepsilon_{\text{eff}} = \varepsilon_{\text{matrix}}\left(1+3\phi\right) \tag{11.19}$$

Whether a molecule is stimulated to its resonant frequency in alternating fields or not depends on its relaxation time. The relaxation time, in turn, depends on viscosity, η, temperature, T, and radius, r, of the molecule. The following relationship can be used:

$$\lambda_m \sim \frac{\eta r^3}{T} \tag{11.20}$$

The parameter λ_m is the time a molecule needs to move back to its original shape after a small deformation. Hence, the resonance frequency, f_m, can be computed using

$$f_m = \frac{\omega_m}{2\pi} = \frac{1}{2\pi\lambda_m} \tag{11.21}$$

where ω_m is the frequency in rad/s.

11.1.3 Dielectric Dissipation Factor

The movement of molecules, for example, during dipole polarization or ion polarization in an alternating electric field, leads to internal friction and, therefore, to the heating of the dielectric. The equivalent circuit shown in Fig. 11.7 is used here to explain this phenomenon. Assume an alternating current is passing through this circuit, with the effective value of U volts and an angular frequency ω defined by

$$\omega = 2\pi f \tag{11.22}$$

where f is the frequency in Hz. Through such a system, a complex current I^* will flow, composed of a resistive or loss component, I_r, and a capacitive component, I_c. The vector diagram in Fig. 11.8 shows that with

$$I_r = U/R \tag{11.23}$$

and

$$I_c = \omega CU \tag{11.24}$$

we can write

$$I^* = U/R + i\omega CU \tag{11.25}$$

Here, i represents an imaginary component oriented in the imaginary axis of the vector diagram in Fig. 11.8. An alternating current applied to a condenser free of any current loss components would result in

$$\frac{I_r}{I_c} = \tan\delta \to 0 \tag{11.26}$$

In such a case, the condenser current is purely capacitive, which leads to no losses at all. This results in a voltage that is lagging the current by 90°, as demonstrated in Fig. 11.9. Accordingly, capacitance also consists of a real component and an imaginary component.

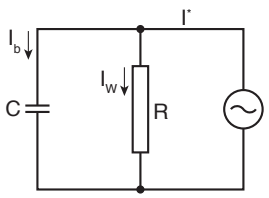

Figure 11.7 Equivalent circuit diagram for the losses in a dielectric